NUREG/CR-6809
SAND2003-0839P
ANA-01-0330

Posttest Analysis of the NUPEC/NRC 1:4 Scale Prestressed Concrete Containment Vessel Model

ANATECH Corporation

Sandia National Laboratories

U.S. Nuclear Regulatory Commission
Office of Nuclear Regulatory Research
Washington, DC 20555-0001

NUREG/CR-6809
SAND2003-0839P
ANATECH Report. ANA-01-0330

Posttest Analysis of the NUPEC/NRC 1:4 Scale Prestressed Concrete Containment Vessel Model

Manuscript Completed: March 2003
Date Published: March 2003

Prepared by
R. A. Dameron
B. E. Hansen
D. R. Parker
Y. R. Rashid

ANATECH Corp.
5435 Oberlin Drive
San Diego, CA 92121

Sandia Project Monitor: M. Hessheimer

Work performed under Sandia Contract No. AO-5464

Sandia National Laboratories
Albuquerque, NM 87185
Operated by
Sandia Corporation
for the U.S. Department of Energy

Prepared for
NRC Project Manager: J. F. Costello
U.S. Nuclear Regulatory Commission
Office of Nuclear Regulatory Research
Division of Engineering
Washington, DC 20555-0001
NRC Job Code Y6131

ABSTRACT

The Nuclear Power Engineering Corporation of Japan and the U.S. Nuclear Regulatory Commission, Office of Nuclear Regulatory Research, are cosponsoring and jointly funding a Cooperative Containment Research Program at Sandia National Laboratories (SNL) in Albuquerque, New Mexico. As a part of the program, a prestressed concrete containment vessel (PCCV) model was subjected to a series of overpressurization tests at SNL beginning in July 2000 and culminating in a functional failure mode or Limit State Test (LST) in September 2000 and a Structural Failure Mode Test (SFMT) in November 2001. The PCCV model, uniformly scaled at 1:4, represents the containment structure of an actual Pressurized Water Reactor (PWR) plant (OHI-3) in Japan. The objectives of the internal pressurization tests were to obtain measurement data on the structural response of the model to pressure loading beyond design basis accident in order to validate analytical modeling, find pressure capacity of the model, and observe its failure mechanisms.

This report compares results of pretest analytical studies of the PCCV model to the PCCV high pressure test measurements and describes results of posttest analytical studies. These analyses were performed by ANATECH Corp. under contract with SNL. The posttest analysis represents the third phase of a comprehensive PCCV analysis effort. The first phase consisted of preliminary analyses to determine what finite element models would be necessary for the pretest prediction analyses, and the second phase consisted of the pretest prediction analyses.

The principal objectives of the posttest analyses were: (1) to provide insights to improve the analytical methods for predicting the structural response and failure modes of a prestressed concrete containment, and (2) to evaluate by analysis any phenomena or failure mode observed during the test that had not been explicitly predicted by analysis. The posttest activities documented herein also include reviewing the effects of and "correcting" the test data for external factors that were not explicitly considered in the analyses, such as ambient temperature variations and artificial response data created by the instrumentation.

In addition to documenting the comparisons between measured behavior and predicted behavior of the liner, concrete, rebar, and tendons, a variety of failure modes and locations were investigated. Global analysis helped identify possible modes; other analyses investigated localized failure modes or modes specifically associated with 3D behavior. Liner tearing failure at the midheight of the cylinder near penetrations and a shear/bending failure at the base of the cylinder wall were both found to be competing failure modes. More detailed modeling of these locations placed a higher likelihood of failure on the liner tearing mode at the cylinder midheight near a major penetration. The most likely location for the liner tearing failure was near the Equipment Hatch at the ending point of a vertical T-anchor, near where the liner is attached to the thickened liner insert plate. The pressure at which the local analysis computed liner strains that reached the failure limits (indicating tearing and leakage) was 3.2 times the design pressure (Pd) of 0.39 MPa or 1.27 MPa. During the LST, liner tearing and leakage failure was first detected at a pressure of 2.4-2.5 Pd, and subsequent increase in pressure to 3.3 Pd resulted in further tearing at many strain concentration locations and increasing leakage. This report compares measured strains near as many of these strain concentrations as possible to the predictions from the global and local penetration analyses. The report also describes reanalysis of existing models and new analysis of new models, including representation of typical liner seam details aimed at simulating some local as-built conditions that existed in the test.

The LST resulted in liner tearing and leakage, but not in a structural failure. Structural damage was limited to concrete cracking and the overall structural response (displacements, rebar and tendon strains, etc.) was only slightly beyond yield. (Global hoop strains at the midheight of the cylinder only reached 0.4%, approximately twice the yield strain in steel.) In order to provide additional structural response data for comparison with in-elastic response conditions, the PCCV model was resealed, filled nearly full with water, and repressurized during the SFMT to a maximum pressure of 3.6 Pd when a catastrophic rupture occurred. A comparison of pretest and post-LST analysis results to the SFMT data and additional analyses, to provide some insight into the mechanisms leading to the structural failure, are also included in this report.

The report closes with summary and conclusions on the accuracy and adequacy of the pretest prediction analysis. The summary attempts to also draw lessons learned from previous containment research and highlight the new and unique lessons learned from the 1:4 scale PCCV project, such as the modeling and behavior of prestressing and some unique

liner seam details. These conclusions are then used to establish guidelines for containment analysis. The relevance of this research to U.S. plants is also discussed.

CONTENTS

FIGURES

Figure Page

TABLES

EXECUTIVE SUMMARY

The Nuclear Power Engineering Corporation (NUPEC) of Japan and the U.S. Nuclear Regulatory Commission (NRC), Office of Nuclear Regulatory Research, are cosponsoring and jointly funding a Cooperative Containment Research Program at Sandia National Laboratories[1] (SNL) in Albuquerque, New Mexico. As a part of the program, a prestressed concrete containment vessel (PCCV) model was subjected to a series of overpressurization tests at SNL beginning in July 2000 and culminating in a functional failure mode or Limit State Test (LST) in September 2000 and a Structural Failure Mode Test (SFMT) in November 2001. The PCCV model, uniformly scaled at 1:4, represents of the containment structure of an actual Pressurized Water Reactor (PWR) plant (OHI-3) in Japan. The objectives of the internal pressurization tests were to obtain measurement data of the model's structural response to pressure loading beyond design basis accident in order to validate analytical modeling, find pressure capacity of the model, and observe its failure mechanisms. This report documents a comparison of the pre-test analyses with the test results and describes the posttest analyses performed to improve the simulation of model behavior.

The pretest and posttest analyses described herein were performed by ANATECH Corp. under contract with SNL. The current work represents the third phase of a comprehensive PCCV analysis effort. The first phase consisted of preliminary analyses to determine what finite element models would be necessary for the pretest prediction analyses, and the second phase consisted of the pretest prediction analyses. The principal objectives of the posttest analyses are: (1) to provide insights to improve the analytical methods for predicting the structural response and failure modes of a prestressed concrete containment, and (2) to evaluate by analysis any phenomena or failure mode observed during the test that was not explicitly predicted by analysis.

The first two chapters summarize the events of the high pressure LST, including the observed failure modes and corresponding pressures and a final set of analyses conducted immediately prior to the test, but after publication of the formal pretest analyses in [1] and [2]. The ABAQUS general purpose finite element program with the ANACAP-U concrete and steel constitutive modeling modules were used for the analysis. Tendons and their prestressing were modeled to replicate expected tendon stress-strain behavior and friction effects. Concrete cracking was simulated with the "smeared crack" approach, where cracking is introduced at the finite element integration points. The failure predictions consisted of liner tearing locations, all occurring near the midheight of the cylinder near penetrations and weld seams with "rat-hole" details. The most likely location for the liner tearing failure was predicted to be near the Equipment Hatch (E/H) at the ending point of a vertical T-anchor, near where the liner is attached to the thickened liner insert plate. The failure pressure was predicted to be 3.2 times the design pressure (Pd) of 0.39 MPa or 1.27 MPa. During the LST, liner tearing and leakage failure was first detected at a pressure of 2.4-2.5 Pd, and a subsequent increase in pressure to 3.3 Pd resulted in further tearing at many strain concentration locations and increased leakage. Subsequent chapters compare measured strains near as many of these strain concentrations as possible to the predictions from local analyses, and also describe reanalysis of existing models and new analyses, such as liner seam models aimed at simulating some of the model's as-built conditions.

The models that constituted the final pretest predictions were the global axisymmetric, the semi-global three-dimensional cylinder midheight (3DCM) model, and local penetration models of the E/H, Personnel Airlock (A/L), and Mainsteam (M/S) penetrations. The local failure predictions were all driven by response versus pressure histories calculated by the 3DCM model. The only changes made between the 1999 pretest predictions reported in [1] and the final (2000) pretest predictions were to material properties and prestressing levels. Because visual inspection of the model revealed the existence of micro-cracking (probably due to curing and shrinkage) throughout the cylinder, the concrete tensile strength was reduced to a cracking strain of $\varepsilon_{cr} = 40 \times 10^{-6}$, based on prior experience with similar test structures. A new suite of concrete compressive tests became available in February, 2000, so these were also incorporated into the final pretest analyses.

ANATECH was also tasked with reviewing and correcting measurements taken during the LST. This effort focused on identifying artifacts in the response data resulting from uncontrollable, external influences on the model and those that

---

1 This work is jointly sponsored by the Nuclear Power Engineering Corporation and the U.S. Nuclear Regulatory Commission. The work of the Nuclear Power Engineering Corporation is performed under the auspices of the Ministry of Economy, Trade and Industry, Japan. Sandia is a multiprogram laboratory operated by Sandia Corporation, a Lockheed Martin Company, for the U.S. Department of Energy under Contract Number DE-AC04-94AL85000

were a byproduct of the instrumentation. The effects and phenomena addressed in the "data correction" effort were ambient temperature variations, rigid body motion of the model, and strain localization. The details of these corrections are described in the test report; however, the phenomena and corresponding corrections are summarized in Chapter 3.

In reviewing the PCCV test data, the 55 Standard Output Locations (SOLs) used for the Round Robin prediction exercise held in 1999 were very useful comparison points. In Chapter 4, the published and final pretest analyses are compared to the test data at each SOL. All analysis data curves were "rezeroed" to the first point of the test data, i.e. the data reading occurring at the start of the test. This slightly shifted the analysis data, but it simplified the comparison of the response to internal pressure and eliminated differences in the response to dead load and prestressing and that could occur from creep or other time-dependent effects. This is justified because most of the PCCV instrumentation was initialized in March, 2000; after dead loads were applied, the model was prestressed, and subjected to six months of daily temperature cycling and low- pressure testing prior to the start of the LST (September, 2000).

The overall conclusions from the comparisons of the pretest analysis with the LST are as follows:

- Radial displacements in the cylinder wall were well predicted by global axisymmetric analysis, but dome and overall vertical displacements were significantly overpredicted.
- Wall-base juncture behavior, including many rebar and liner strain measurements, were well predicted by the detailed wall-base juncture (axisymmetric) modeling.
- Functional failure (i.e. leakage in excess of 1% mass/day) at a pressure of 2.5 Pd occurred at a liner tear in an area of high strain that was not predicted by analysis, but was probably amplified due to defects associated with weld seam repair.
- Maximum pressure, 187.9 psig (3.30 Pd), which was primarily the onset of global yielding, was closely predicted by analysis, but the predicted failure mode itself did not manifest. Note that the maximum pressure achieved during the LST was also limited by the capacity of the pressurization system to balance the increasing leak rate after functional failure occurred.
- The average radial displacement at the midheight of the cylinder of 20mm at maximum pressure, equivalent to an average hoop strain of 0.37%, is within 10% of that predicted by global analysis (21.9 mm or 0.41%).
- Maximum radial displacement at E/H = 29mm, equivalent hoop strain of 0.0054, was reasonably predicted by 3DCM model, but prediction of displacements at other azimuths–like the buttresses–were poorly predicted by 3DCM model.
- For both the hoop and vertical tendons, there was about 8% to 10% loss of stress between the initial prestressing and the start of the LST caused by long-term effects and by the SFT and SIT.
- Hoop tendon stress distribution simulated by analysis at start of LST shows fair agreement with measurements, implying that the angular friction and anchor set modeling assumptions at the start of the test were reasonable. Vertical tendon stress distribution at the start of the LST were less consistent with the initial modeling assumptions. One tendon, V85, showed significant friction losses below the springline, and the other two instrumented vertical tendons showed only about half of the friction loss in the dome than what was assumed by designers and incorporated in analysis.
- Hoop tendon stress distributions during pressurization showed poor agreement with the pretest analysis. In particular, the gages interior from the ends are underpredicted *and* the anchor forces are overpredicted.
- The cylinder hoop tendon data, in total, shows evidence of the tendons slipping during pressurization. The measurements indicate that the shape of the tendon stress profile completely changes during pressurization. Comparing the increase in the tendon strain to the cylinder hoop strain implies that portions of the tendons are slipping (i.e. tendon strain is greater than the cylinder wall strain) in order for the higher deformation at other azimuths to be accommodated.

Chapter 5 describes the global posttest analyses performed after the LST. To summarize the conclusions:

- Basemat uplift and dome displacements comparisons were significantly improved by redistributing soil basemat springs according to tributary area, improving the dome meridional tendon representation to account for the added stiffness of the overlapping tendons due to the rectilinear "hairpin" layout.
- Comparisons were also improved by using no vertical tendon friction in the cylinder.
- Analysis should not use the "Prestress Hold" option in ABAQUS.

Chapter 6 describes the posttest 3DCM analysis. In the pretest analyses, the 3DCM model was developed to investigate the non-axisymmetric behavior of the cylinder wall and provide more realistic boundary conditions for the penetration's submodels. Buttresses above and below the 3DCM model boundaries have vertical beam stiffnesses that were not accounted for in the pretest analysis. Equivalent spring properties were derived and then applied as radial spring elements. The derivation was performed by adding a 2D plane stress representation of a buttress to the axisymmetric model. The model was then cut at the appropriate 3DCM model horizontal boundary. Zero rotation boundary conditions were applied at the cut boundary and horizontal and vertical tendon prestress was maintained as in the full axisymmetric models. A horizontal displacement was then applied to the cut boundary. Separate models were analyzed with and without the buttress present and the force versus displacement results were differenced; these became the force versus deflection properties assigned to the buttress springs. The only other modeling assumption found to be at significant variance with observed test behavior was the tendon modeling, especially the representation of friction. A lengthy study and series of analyses focused on this variance. Two important observations were made about the hoop tendon measurements as pressure increases:

1. When pressure overcomes prestress, P = 0.59 MPa, tendon stress distributions change from the classical angular friction design assumption to an approximately uniform distribution; then they stay fairly uniform at most higher pressures. Toward the end of the test, some tendon interior forces slightly exceed the force at the anchor.
2. The apparent strain increases in the tendons corresponding to the force/strain gage readings are significantly larger (e.g. 0.48% versus 0.35%, for H53) than the strain that corresponds purely to radial expansion. This can only be explained by force redistribution associated with sliding. Thus the position of the tendon relative to the concrete must be allowed to change after initial prestress in order to adequately simulate tendon behavior during overpressurization.

These observations led to changes and studies of the tendon friction modeling in the 3DCM model. Because the tendon friction behavior observed in the test turned out to be quite complex, the analysis strategies investigated were chosen to at least bracket the observed LST behavior. The last three analyses presented are:

Model 6. Apply prestress. Then, by using the ABAQUS *MODEL CHANGE capability, fix the tendon nodes at their initially deformed position relative to the concrete. In other words, start from classical design prestress with friction and then grout (bond) the tendons.

Model 7. Perform run 5 (the run with only the buttress springs added) up to P = 1.5 Pd (0.59 MPa), then "MODEL CHANGE" all friction elements to non-friction elements (truss ties aligned perpendicular to the tendons. In other words, at P = 1.5 Pd, perfectly grease (unbond) the tendons).

Model 9. After prestress, keep the initial friction elements, but add a new set of friction elements in the reverse orientation so that if points on the tendon move relative to concrete in the reverse direction from that of initial prestress, they will experience reverse direction friction.

In general, the tendon friction simulation runs 6, 7, and 9 show progressively better agreement with test measurements, with run 9 showing quite good agreement at the anchors and at most points interior to the tendon ends. Based on these and the other observations, the results of run 9 were used to drive the submodels for E/H and M/S (and estimated feedwater (F/W)) penetrations posttest analysis. On tendon friction behavior, the test measurements and analytical evidence support the conclusion that tendon friction is important to the tendon behavior, but traditional friction design formulas that predict tendon stress distribution begin to break down once pressurization exceeds the pressure that overcomes prestress (in this case, roughly 1.5 Pd). The coefficient of angular friction appears to lessen, allowing sliding and force redistribution as the vessel expands, but more importantly, some parts of the tendon are forced to reverse direction of travel relative to the duct, reverse it from the direction of travel experienced during prestressing. Under this action, angular friction properties probably still hold, but the direction of friction must change sign from that assumed in a design calculation.

Chapter 7 describes the posttest analyses of the penetration submodels. Liner strains measured in the vicinity of the E/H penetration collar were much lower than predicted by pretest analysis. Since the predicted high strain locations were fundamental to the failure predictions, significant effort was spent reanalyzing the E/H model after the test. With a set of changes that included conversion of the model to the other side of the hatch (away from the buttress) and a correction to the vertical stress boundary condition, posttest E/H model's hoop expansion behavior correlated much better with measured global displacement behavior. The hoop deformation correlation-to-pressure function introduced in the pretest work was no longer needed. Two hypotheses were developed.

Hypothesis 1: The liner in the E/H area had a high degree of bond-friction with concrete, preventing slippage of the liner relative to the concrete; relative slippage is required for elevated strains to develop near local discontinuities like T-anchors and stiffeners.

Hypothesis 2: Formation of a major crack near the edge of the E/H embossment further concentrated the liner strains at the edge of the embossment.

Posttest analysis showed that by preventing relative slip between liner and concrete, the overall behavior of the system (concrete strains, tendon strains, liner strains away from the hatch) remained the same, but the elevated strains close to the collar were eliminated. In the final case, directed cracks were introduced to one row of elements, and a discrete crack was formed by adding double rows of nodes along an assumed crack line. This was found to create an elevated liner strain phenomenon. The mild strain concentration coincides, in location, with rat-hole weld seam details, and in the LST, numerous tears occurred at these details. Based on results of detailed liner rat-hole analysis (Chapter 8), the additional strain concentration associated with these details is enough to generate liner strains at the edge of the embossment in excess of the liner tearing strain criteria. This shows that with discrete crack modeling and local rat-hole modeling, a liner tear could have been predicted to occur as early as 2.8 Pd. Based on the evidence provided by liner strain gages and by acoustic monitoring, one of the tears along this embossment edge may have even occurred as early as 2.5 Pd. (Note that this posttest analysis did not attempt to include as-built liner defects, such as local thinning or residual stresses resulting from initial fabrication or subsequent repairs.) The posttest E/H study thus presents a modeling strategy with results that correlate well with the LST measurements and observations. A somewhat higher strain prediction might be possible if a discrete crack (separate rows of nodes) were propagated all the way through the concrete wall, but this would require a change in rebar modeling strategy–one that is probably not practical even for detailed analysis of containments.

The M/S and F/W penetration hot spots (both analysis and LST observations) occurred near the vertical T-anchor terminations and near the 'equator' of the thickened insert plate surrounding the penetration group, i.e. at the 3:00 and 9:00 positions. For the posttest analysis effort, no changes to the M/S model were necessary, other than updating the applied displacement versus pressure histories that were obtained from 3DCM posttest Model 9. After studying the F/W geometry in the posttest phase of the project, it was determined that the F/W penetration model was so similar to the M/S penetration model that it was not necessary to pursue separate analysis of the F/W model; the posttest M/S model analysis was assumed to be reasonably representative of the F/W penetrations. Several observations could be made from the well-instrumented M/S and F/W locations that are relevant to response predictions around containment penetrations.

- Many of the highest strains recorded during the LST are near the M/S and the F/W.
- There is wide variation in peak strain measurements, even at locations that are theoretically identical in geometry; factors contributing to these differences are: slight variations in liner thickness (due to manufacturing and weld repair grinding), gage position relative to the collar/weld, material properties (including welding heat effects), etc.
- The highest strain measurements can, but do not always, correspond to tear locations. Examples supporting this are: 1) a gage near the F/W tear shows evidence of rising strain prior to tear occurrence, then starting at 2.9 Pd, declining strain due to the stress relief caused by the tear; a gage located near the crack tip, on the other hand, showed quite low strain up to 3.1 Pd and then a sudden jump. This supports a hypothesis that this tear initiated at a pressure of 2.9 Pd at about the 7:30 position (midpoint of the tear) and then between 2.9 Pd and 3.1 Pd, the tear ran around the perimeter of the thickened collar and up to the 9:00 position.

Comparisons of analysis to the M/S and F/W liner strain gages show that the posttest analysis of the M/S penetrations captures the strains measured in the LST quite well for both the M/S and F/W penetrations.

Chapter 8 describes the investigation of the liner tears that occurred away from the penetrations but where welding details may have caused local liner strain concentrations. The PCCV model exhibited 16 distinct locations at which liner tears occurred. All 16 locations were near vertical weld seams, but with some variation in the presence or configuration of a horizontal stiffener or rat-hole. By comparing "before and after" photos taken by SNL and with reference to a posttest metallurgical study [7], it was observed that liner welding irregularities were present at almost all of the tear locations. These irregularities included points of extensive repair, such as grinding, points of discontinuous or missing back-up bars, or points with weld and liner seam fit-up irregular geometry. Some locations, where a seam and rat-hole existed and high strains were measured, but a tear did not occur (e.g., at Location D-7, just below where tear 16 occurred), provide additional evidence of the importance of the welding details to liner tearing. Visual observation showed extensive grinding and weld repair in the liner welds where most of the tears occurred. Ultrasonic measurements showed substantial reductions in thickness near these tears. Measurements showed ~23% thickness reduction in many locations, and more (up to 40% in a few locations). A posttest liner seam analysis study was aimed at answering questions about quantifying the effects of welding irregularities and distinguishing these from strain concentration effects solely related to geometry. A mesh-size sensitivity study was conducted. Analyses were then conducted to assess the effects of material and geometry variations. The first variation was to implement varying material properties near the weld areas. This included assignment of different material properties to the base metal, heat affected zone (HAZ), and weld fusion zone (WFZ) regions of the model. The second variation only modified the material in the WFZ. The final phase incorporated geometry modifications to the model near the weld lines. This included thinning of elements and varying the extent of thinning in the vicinity of the welds due to grinding. The geometry modifications were coupled with modified material properties ranging from uniform to including variations of base metal, HAZ, and WFZ regions. All of the material and geometry variations were based on the data contained in the SNL metallurgical analysis report [7]. The conclusions of the liner seam/rat-hole modeling study are summarized below:

- By comparison with strain gage measurements and posttest liner tear observations, some of the finite element weld seam analyses are able to generate strain fields in and around the rat-holes and liner welds which exceed the liner tearing strain criteria at locations where tears were observed.
- Because of competing mechanisms (between the weld zone and the ends of stiffeners), making yield and ultimate strength adjustments to the HAZ material properties appears to be justified and necessary to correctly predict strain concentration location and intensity.
- The models with back-up bars, nominal geometric properties, and best-estimate material properties yielded the best simulations of defect-free construction of rat-hole/weld-seam details, represented in the PCCV model at locations D7 and J5. However, even models without back-up bars also provided reasonable correlation with gages at these locations.
- A case with severe (~40%) amounts of thinning appears to provide the best simulation of the behavior of tear occurrences in which severe liner thinning (due to weld repair grinding) was reported in [7] to be present and back-up bars were absent; these conditions existed at tears 7, 8, 10, 12, 13, 14, 15, and 16.
- A case specifically representing the "tear 16" detail was performed. This case appears to provide reasonable simulation of the tears that occurred *with* back-up bars present, namely, tears 1, 2, 6, 9, 11, and 16. The severity of the strain at this case also shows that a tear ($\varepsilon_{eff} > 20\%$) at the geometry simulated would have been predicted to occur as early as 3.0 Pd.
- If a section of liner with a rat-hole/liner-seam detail, such as that at tear Locations 7, 12, 13, and 15 is subjected to additionally elevated strain (i.e. strain across the liner model that is larger than free-field global strain) a tear even earlier than 3.0 Pd can be justified. In practice, such a prediction could approximately be made using a strain concentration factor approach. The strain concentration factors (K = peak ε_{eff} divided by global ε_{hoop}) implied by this liner seam study are as follows: K = 48 (tear at stiffener end, no back-up bar); K = 45 (tear at stiffener end, with back-up bar); K = 59 (tear at HAZ, no back-up bar, and 40% thickness reduction due to grinding); K = 91 (tear at tear 16, if a short segment of horizontal weld seam back-up bar is missing)
- Using a model of the rat-hole/seam locations without defects, such as location D-7, showed that liner tears still would have developed by pressure of 3.4 Pd, so liner tearing and leakage would still have been the failure mode (for quasi-static pressurization) even in the absence of liner welding irregularities.

The LST resulted in liner tearing and leakage, but not a structural failure. Structural damage was limited to concrete cracking, and the overall structural response (displacements, rebar and tendon strains, etc.) was only slightly beyond yield. (Global hoop strains at the midheight of the cylinder only reached 0.4%, approximately twice the yield strain in steel.) In order to provide additional structural response data to compare with in-elastic response conditions, the PCCV model was resealed, filled nearly full with water, and repressurized during the SFMT to a maximum pressure of 3.6 Pd when a catastrophic rupture occurred. Chapter 9 includes a brief discussion and comparison of the pretest and post-LST analysis results to the SFMT data and presents the results of a post-SFMT analysis intended to provide some insight into the mechanisms leading to the structural failure.

The SFMT posttest analysis showed that good simulation of the PCCV global behavior through and including tendon rupture is possible with a 3D shell model. The main limitations of the shell model were a lack of local liner strain concentration prediction and a lack of accuracy in the predictions of local wall-base-juncture behavior. However, significant accuracy in global behavior prediction did not seem to be lost when a bonded tendon assumption was used.

The SFMT model provided additional insight as to how the structural failure likely developed. Near the 0 degrees - 6 degrees azimuth of the cylinder, there is a discontinuity of a step-down in inner and outer hoop rebar area of 38% (step-down from alternating D19, D16 bars to a pattern of 1D16/3D13 bars). Then at 3.49 Pd, the wall and tendon strain at the 0 degrees - 6 location is a little higher than all other azimuths, and a tendon rupture occurs. Once this occurs, the analysis shows neighboring tendons rupturing and deformations spreading quickly along this azimuth. It is interesting to note that the analysis predicts that the secondary tendon ruptures spread upward. Shortly after the first rupture at 5.4 m, analysis predicts the tendon ruptures to spread up through 6.5 m. From review of the test video, this appears to agree with observations. By 3.65 Pd, the analysis shows rupture to have spread over a vertical line spanning about 6 m. This also agrees with observations. After wall rupture, a secondary event occurred in the SFMT: through-wall failure around the circumference of the wall at about 1.5 m elevation. While it is difficult to say at what azimuth this failure initiated, it seems clear that this was a shear or combined shear/flexural failure of the wall. The plotting of analysis shear results showed that such failure may have initiated at the buttresses (evidenced by the high shear stresses predicted there) and then "unzipped." Note from the plans that at elev. 1.60 m, there is a step-down in vertical rebar from D19 to D16, which may have focused this shear failure plane. Moreover, at the buttresses, the outer vertical rebar step down occurs slightly lower: at 1.22 m there is a change from a total of nineteen D19 bars down to a total of ten D19 bars placed within the buttress. This may explain why the circumferential failure ran through the buttresses at a slightly lower elevation than the rest of the wall. As a point of comparison, the shear failure threshold calculation performed in the pretest work [1] is compared to the demand (both pretest axisymmetric and posttest SFMT) in Chapter 9. This shows that without the trigger of rupture of the vessel, the capacity (a modified compression field theory calculation) exceeds the demand throughout the pressurization. But with the triggering event of a massive wall rupture, one of two mechanisms may have caused shear demand to exceed capacity: 1) a large deformation of the wall opening, creating large rotations near the base of the wall, would crush the outer concrete of the flexural section and thereby reduce the capacity, or 2) the water jet-induced momentum imbalance would cause added shear demand; this would create tangential shear at some azimuths and would be the maximum at the buttresses; such shear acting in combination with the already high radial shear stresses could have increased shear stress demand enough to induce the shear failure.

The 1:4 scale PCCV test showed the driving response quantity that leads to the limit state of the vessel is the radial expansion of the cylinder. This aspect of response must be predicted correctly in order to reasonably predict vessel capacity and predict, at least approximately, the many other local aspects of response (local liner strains, etc.) that are driven by the cylinder expansion. With this test, as with the 1:6 scale PCCV model, many competing strain concentrations occur around the mid-height of the cylinder. Although it is difficult to predict which local liner detail will tear first, and although some particular response quantities, like basemat uplift, were not predicted exactly by the ANATECH/SNL pretest analysis of the PCCV model, the radial expansion of the cylinder was predicted very accurately. A response mechanism that also appears to have been well predicted was cylinder wall-base flexure and shear, another mechanism that, if predicted grossly incorrectly, could lead to erroneous pressure capacity/failure mode conclusions.

The minimum requirement for a containment overpressure evaluation should certainly be a robust axisymmetric analysis. Other steps, guidelines, and lessons learned are provided in the final chapter of this report. The lessons learned in the current work, which are perhaps the most novel, are those related to tendon friction behavior. As a result of this project, the best calculation methods recommended for tendon friction modeling are, in descending order of preference, 1) an advanced contact friction surface between the tendons and the concrete (not manageable for the current problem size and complexity), 2) pre-set friction ties applied in one direction during prestressing and then added in the other direction during pressurization (3DCM run 9) and 3) if neither of these methods are practical within the scope of the calculation, it is best to start with an "average" stress level (using a friction loss design formula), but assume uniform stress distribution in the tendons throughout pressurization, i.e., an unbonded tendon assumption, and finally 4) same as 3, but using a bonded tendon assumption. It should be recognized for method 4, however, that this can lead to a premature prediction of tendon rupture, because the tendon strain increments during pressurization will match the hoop strain increments of the vessel wall one-to-one, and this was not observed during the PCCV LST.

The relevance of this work to full size U.S. Containments is fundamental. All of the analysis methods tried, calibrated, and validated would be highly applicable to full-scale structures. The posttest work also provides a reasonably simple liner-only mesh approach to predicting local strains near weld seams, and the test itself underscores the need for continuous back-up bars on all liner seam welds. Such is the requirement in the current U.S. design rules.

ACKNOWLEDGMENTS

This pretest analysis effort was sponsored by the U.S. Nuclear Regulatory Commission. The authors would first like to thank Dr. James F. Costello of the NRC for his technical interaction and support throughout the program.

The work described herein was performed by ANATECH for Sandia National Laboratories in Albuquerque under Contract No. AO-5464. Reviews of the posttest analysis plan and the analysis results have been conducted by Mike Hessheimer and other Sandia personnel. The valuable discussions and guidance received during those reviews were critical to the development and presentation of the results. It should also be noted that the analytical models and software developed by ANATECH for the Electric Power Research Institute (EPRI) in their Containment Integrity Program were made freely available by EPRI and proved to be indispensable in the performance of this work.

ABBREVIATIONS

3DCM	entire cylinder midheight region
A/L	airlock
BPS	before prestressing
CIRC	circular cross section
CTL	Construction Technology Laboratories
DOR	data of record
DYN	"dynamic" data
E/H	Equipment Hatch
F/W	Feedwater
HAZ	heat affected zone
LST	Limit State Test
M/S	Mainsteam
NRC	U.S. Nuclear Regulatory Commission
NUPEC	Nuclear Power Engineering Corporation
PCCV	prestressed concrete containment vessel
PSFT	Post System Functionality Test
SFT	System Functionality Test
SFMT	Structural Failure Mode Test
SIT	Structural Integrity Test
SNL	Sandia National Laboratories
SOL	Standard Output Locations
UTS	Ultimate Tensile Strength
WFZ	weld fusion zone

1.0 INTRODUCTION

1.1 Background Leading up to the Limit State Test

Sandia National Laboratories (SNL) is conducting a research program to investigate the integrity of nuclear containment structures. This program is cosponsored by the Nuclear Power Engineering Corporation (NUPEC) of Japan and the U.S. Nuclear Regulatory Commission (NRC). As part of the program, NUPEC constructed a 1:4 scale model of the prestressed concrete containment vessel (PCCV) of a Japanese pressurized water reactor (PWR) plant at SNL's Containment Technology Test Facility in Albuquerque, NM. The model is shown in Figures 1-1 and 1-2. SNL designed and installed an extensive suite of instrumentation during and after the construction of the model and conducted a series of overpressurization model tests leading to both functional and structural failure. One of the key program objectives was to validate methods for predicting structural performance of containment vessels when subjected to beyond-design-basis loadings, such as very high internal pressurization. The NRC-sponsored analysis effort to achieve this objective included 2D and 3D nonlinear finite element modeling of the PCCV model. Such analyses were performed using the nonlinear concrete constitutive model, ANACAP-U, in conjunction with the ABAQUS general purpose finite element code [5]. The analysis effort was conducted in three phases:

1. Preliminary Analysis,
2. Pretest Prediction, and
3. Posttest Data Interpretation and Analysis.

The purpose of the preliminary analysis was to provide a basic understanding of the model response for program planning purposes and to define the scope of the pretest analysis. The preliminary analysis results were not formally documented; however, a summary paper was published [2], and the results are reflected in the pretest analysis that followed. A list of possible failure modes and locations was developed in the preliminary analysis phase prior to conducting the formal pretest analyses. Some of the potential failure modes were specifically addressed by the global analysis, while others were addressed by local models. The results of the preliminary analyses indicated that a liner tearing failure at the midheight of the cylinder near a penetration and a shear/bending failure at the base of the cylinder wall were both found to have a significant probability of occurrence. Recommendations were then made for the pretest analyses, including model refinements and the development of local models to better predict the sequence of competing failure modes were identified.

The principal objectives of the pretest analyses were to (1) exercise advanced analytical methods for predicting structural response of a prestressed concrete containment, (2) gain insight into potential structural failure modes of a prestressed concrete containment, and (3) support planning of test procedures and instrumentation. One requirement of the program was that the pretest analysis predictions be completed and published [1] prior to the high-pressure Limit State Test (LST) of the PCCV model, which was conducted in September, 2000. This meant that the pretest prediction analyses must be completed many months prior to the test. For this reason, the published pretest analysis predictions did not include certain as-built features, actual measured prestressing and associated losses, or creep and temperature effects. Prestress values, losses due to friction, anchor set, and concrete creep were approximated from the assumptions used in the PCCV model design.

In addition to a detailed axisymmetric global model, local models developed for the pretest analysis included: the Equipment Hatch (E/H) region, the Personnel Airlock (A/L) region, and the Mainsteam Penetration (M/S) region. A detailed 3D model of the entire cylinder midheight region (3DCM) was also developed to investigate tendon behavior in the cylinder and 3D effects that drive the local strain concentrations near the penetrations. A highly detailed representation of the wall-basemat juncture region was also added to the 2D axisymmetric model, making total of five pretest analysis models. The pretest analyses described herein were also the basis of the SNL/ANATECH submittal to an international Round Robin Pretest Analysis exercise [3].

The pretest analysis phase of the PCCV model test program refined and demonstrated finite element and material modeling methods and a systematic process for developing pressure response predictions from global 2D, semi-global 3D, and local 3D analysis models. Tendon modeling tasks demonstrated the utility of a new tendon modeling approach in which friction losses are explicitly represented by friction truss tie elements. Tendon stress distributions at various pressures were provided as benchmarks of expected tendon behavior. Capturing the tendon stress distributions in more detail refined the prediction of displacement response and liner strains, especially near the E/H, where this distribution is very complex. **The 3DCM model, with its detailed tendon representation, predicted the rupture of hoop tendons closest to the E/H at a model pressure of about 3.5 Pd. However, this mode was predicted to be precluded by the liner tearing and leakage failure mode.**

Using a strain-based failure criteria that considered the triaxiality of stress and a reduction of ductility in the vicinity of a weld, a liner failure strain criteria of 16% was established. The failure pressure at which a local analysis computed effective plastic strain that reached the failure strain criteria was 3.2 Pd, or 1.3MPa. The location for this liner-tearing failure was near the E/H, adjacent to a vertical liner anchor that terminated near the liner insert plate transition. Other local models showed other candidate liner tear locations, several of which were predicted to occur during the pressure range 3.2 Pd to 3.5 Pd if they were not precluded first by the growth of the first tear and subsequent depressurization of the vessel. A significant candidate tear location was also found near the 90 degree buttress where hoop strains are elevated due to circumferential bending, and weld seams with hoop stiffener "rat-holes" are coincidentally located. Failure at such locations was predicted to occur shortly after failure at the E/H location.

After publishing the pretest analysis results, a final pretest analysis was performed to refine the pretest predictions using the most current as-built model properties. This final pretest analysis was performed primarily to support test operations by providing the ‘best’ predictions of the model’s response for real-time comparison with the actual response. This information was essential to the safe and successful conduct of the test. Since the results of this final pretest analysis were not published in the pretest analysis report [1], a summary of the results are included in Chapter 2 of this report.

1.2 Limit State Test and Structural Failure Mode Test Overview

The following "quick look" observations written a few days after the test by Mike Hessheimer at SNL provide a concise overview of the LST conduct and PCCV model behavior:

> The PCCV Limit State Test (LST) began at 10:00a.m., Tuesday, September 26, 2000 as scheduled. We began pressurizing in increments of 0.2 Pd, repeating the Structural Integrity Test (SIT) pressure sequence we followed on September 12. We continued pressurizing the model to 1.5 Pd, when we conducted a leak check and calculated a leak rate of approximately 0.5% mass/day after 3.5 hours. Based on our experience during the SIT/ILRT we interpreted this as indicating that there was no leakage.
>
> We proceeded to pressurize in increments of 0.1 Pd until we reached 2 Pd at 22:00 Tuesday evening to conduct another leak check. Since there was no evidence of distress, we continued the leak test throughout Tuesday night and Wednesday morning and calculated at leak rate of >0.1% mass/day after holding pressure for approximately 8 hours.
>
> At 07:00, Wednesday, September 28, we continued pressurizing the model in increments of 0.1 Pd until we reached 2.5 Pd around 10:00. At this point, we observed some liner strains approaching 2% and also had some evidence from the acoustic system that there might have been a liner tear. We continued with the planned leak check at this pressure and after 1-1/2 hours, calculated a fairly stable leak rate of 1.5% mass/day (+/- 0.5% mass/day). We decided that this was clear indication of a liner tear/leak and modified our test plan slightly, continuing to pressurize the model in incremental steps of 0.05 Pd, but reducing the hold time at each pressure step to less than 10 minutes.
>
> We were able to continue pressurizing the model to approximately 3 Pd, with increasing evidence of leakage and increasing liner strains. At 3 Pd, it became difficult to increase pressure so we increased the nitrogen flow rate to 3500 scfm. We were able to increase pressure to 3.1 Pd however the pressure dropped steadily after reaching this pressure. We estimated the leak rate at this point to be approximately 100% mass/day. We then increased our nitrogen flow rate to the maximum capacity of the pressurization system (5000 scfm) and were able to increase the pressure to slightly over 3.3 Pd before the leak rate exceeded our capacity to pressurize the model. Since we could no longer increase pressure and we had almost exhausted our supply of nitrogen, the decision was made to begin terminating the test. The isolation valve was closed and we allowed the model to depressurize on it's own. We estimated that the initial terminal leak rate was on the order of 900% mass/day. (The maximum flow rate of nitrogen, 5000 scfm is equivalent to 1000% mass/day.) As the model

> depressurized, we observed a steadily decreasing leak rate (initially decaying at 250% mass/day per hour). We then opened the vent valve to depressurize the model more quickly to 1.0 Pd.
>
> At 1.0 Pd, we were able to inspect the model and observe (hear and feel) nitrogen gas escaping through many small cracks in the concrete and at the tendon anchors. We suspect that the liner acted as a leak chase, allowing nitrogen gas escaping through a tear or tears in the liner to travel between the liner and the concrete until it found an exit path through a crack in the concrete or a conduit in the tendon duct.
>
> At maximum pressure local liner strains approached 6.5% and global hoop strains (computed from the radial displacement) at the mid-height of the cylinder averaged 0.4%. While we observed large liner strains and suspect that the liner may have torn in several locations, the remainder of the structure appears to have suffered very little damage with the exception of more extensive concrete cracking at some locations. There was no indication of tendon or rebar failure.

Plots of the model pressurization versus time, nitrogen flow in versus time, and the flow rates versus time are shown in Figures 1-3 and 1-4. Once the model was depressurized and inspected, a total of 26 liner tears were found at 17 different locations. This observed liner tear map is shown in Figure 1-5. Every tear occurred at or near a vertical weld seam, and some of the tears grew quite large; certainly large enough to account for the depressurization of the model.

Following the LST and post-LST inspection of the model and the data, it became clear that the objectives of the test program were not fully satisfied. Other than concrete cracking, liner tearing, and leakage, the LST did not cause any significant structural damage in the model, and overall structural response (displacements, rebar and tendon strains, etc.) was only slightly beyond the elastic range. In order to provide additional structural response data to compare with inelastic response conditions, the PCCV model was resealed, filled nearly full with water, and repressurized during the Structural Failure Mode Test (SFMT). A maximum pressure of 3.6 Pd was reached when a catastrophic rupture occurred. This was preceded only briefly by tensile failure of several hoop tendons. The condition of the model immediately after the SFMT is shown in Figure 1-6.

1.3 Objectives of Posttest Analysis Work

The scope and objectives of the posttest analysis work are outlined below.

1.3.1 Final Pretest Analysis

A final pretest analysis was performed to support test operations and to account for information (such as tendon prestress levels) learned in the final months prior to the test.

1.3.2 Evaluation of Test Data and Comparison with Pretest Analysis Results

The published and final pretest analysis results are compared to the test data to characterize how well the pretest analyses predicted the behavior and identify areas for improvement or modification in the posttest analyses. In addition to comparing responses for specific transducers, a qualitative assessment on the overall response is also included. Also, the effect of uncontrollable external factors (e.g. variations in ambient thermal response), as well as response artifacts introduced by the instrumentation, were identified and the methods used to 'correct' the data for these effects were developed.

1.3.3 Global Posttest Analysis

The global PCCV axisymmetric model was updated to reflect actual conditions during the LST (e.g., material properties, in-situ stress conditions of concrete and tendons, etc.) and the global model was reanalyzed. The effect of soil stiffness on the basemat and the modeling of the dome tendons were also addressed.

1.3.4 Local Posttest Analyses

The 3DCM model, the local penetration models (E/H, A/L, and M/S), and, to address the liner failure occurrence in some unexpected location, one new model, were developed and analyzed.

1.3.5 Post SFMT Analysis

Selected data from the SFMT was compared to both the pretest and posttest analyses. A simplified 3D shell model was developed to simulate and provide some insight into the sequence of events leading to the catastrophic structural failure.

1.3.6 Posttest Analysis Report

The results of these tasks are documented herein, including a summary of lessons learned and possible analysis methodology enhancements as a result of the PCCV analysis research program.

Figure 1-1. NUPEC/NRC 1:4 Scale PCCV Model Built at Sandia National Laboratories

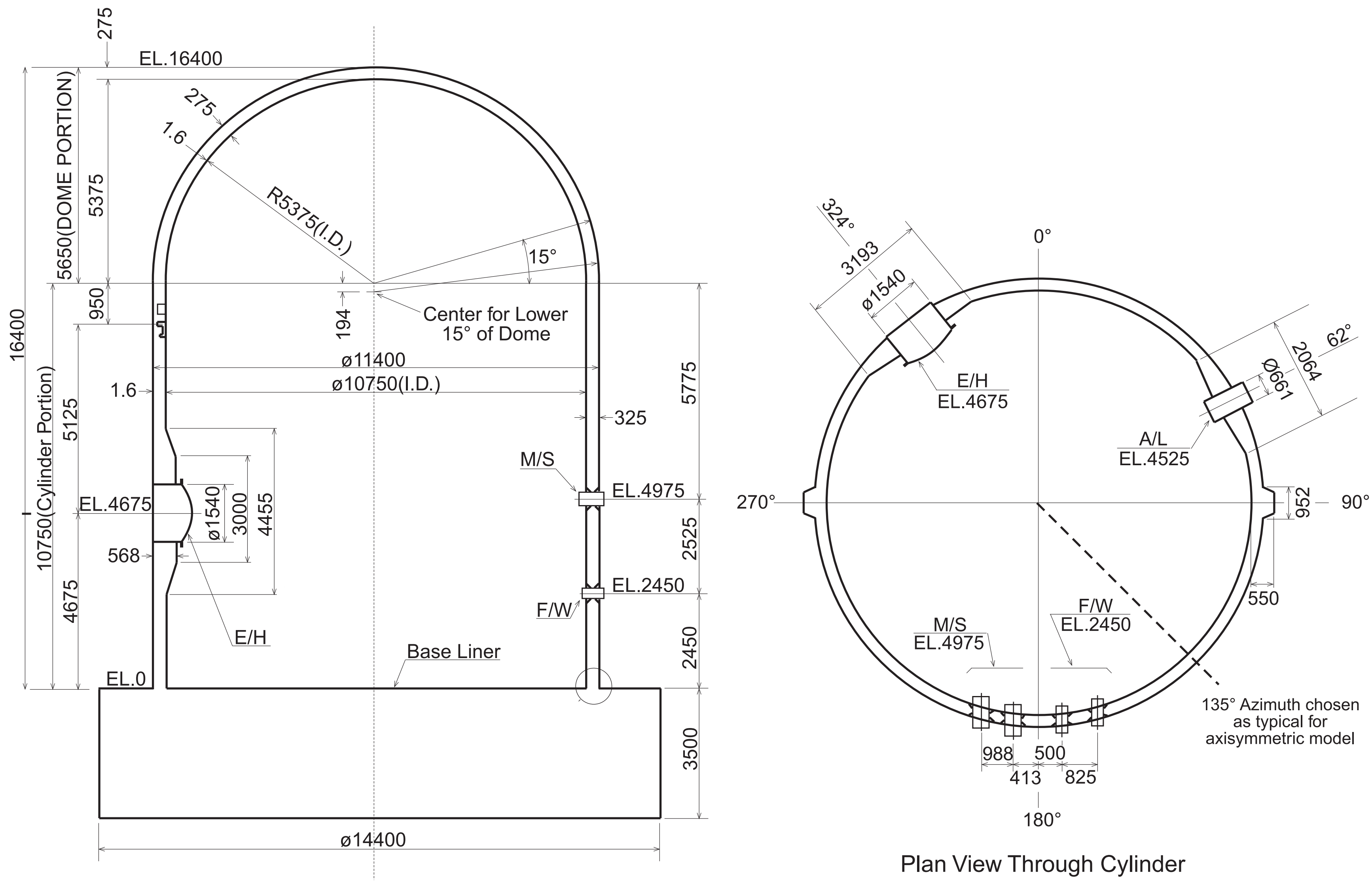

Figure 1-2. 1:4 Scale PCCV Model Geometry (dimensions in mm)

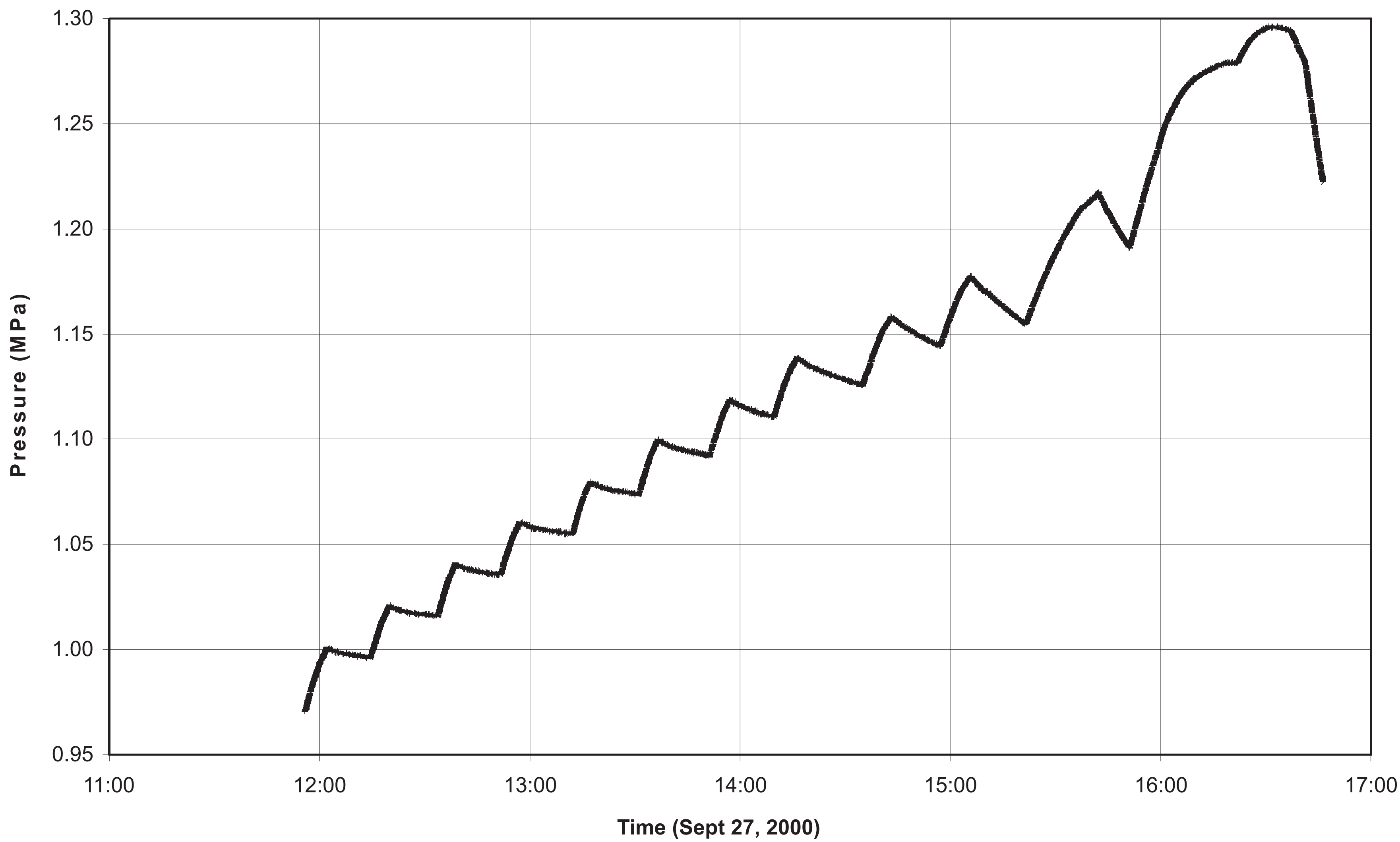

Figure 1-3. LST Pressure Time History (2.5Pd - 3.3Pd)

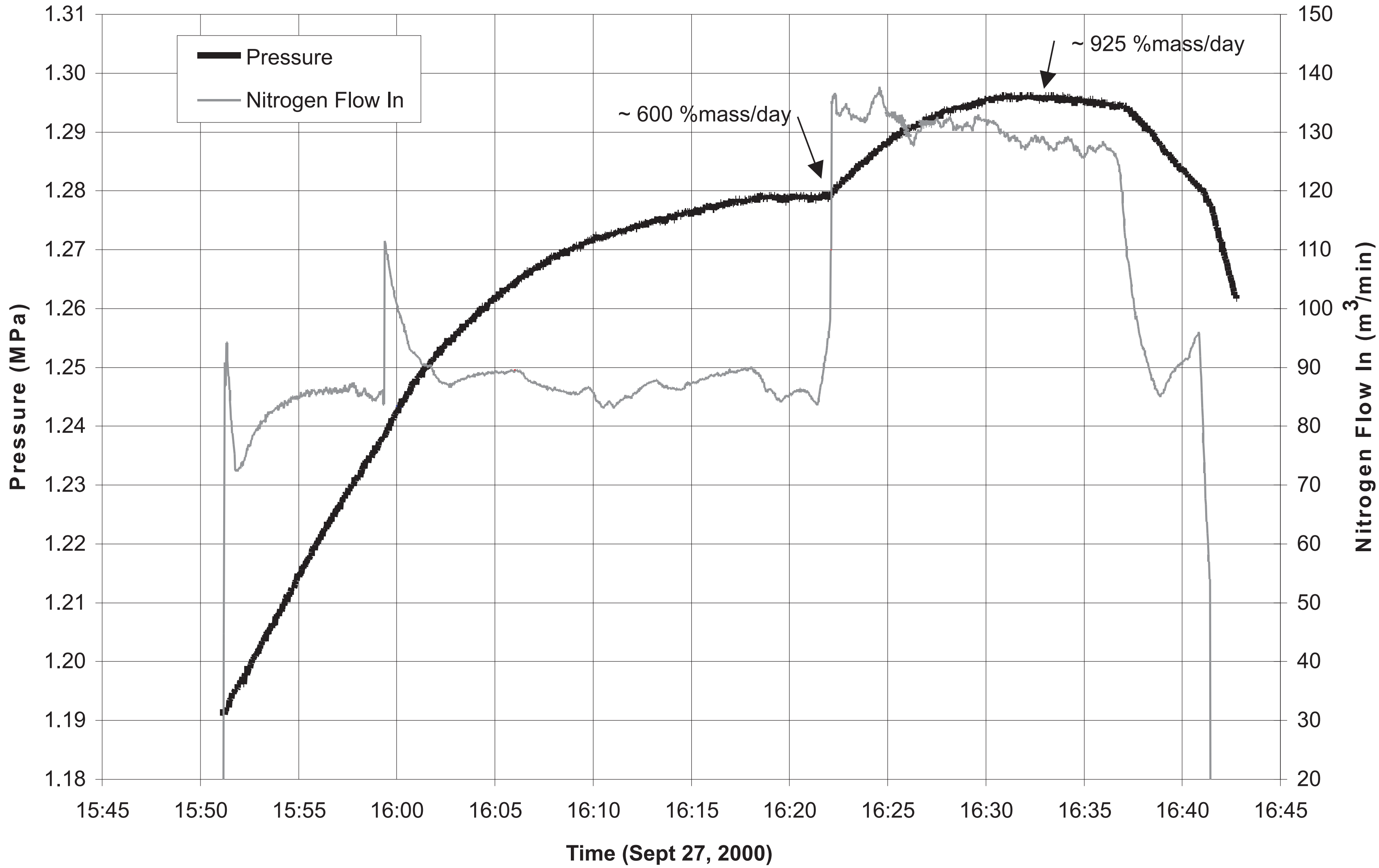

Figure 1-4. LST Pressure and Flow (Final Minutes)

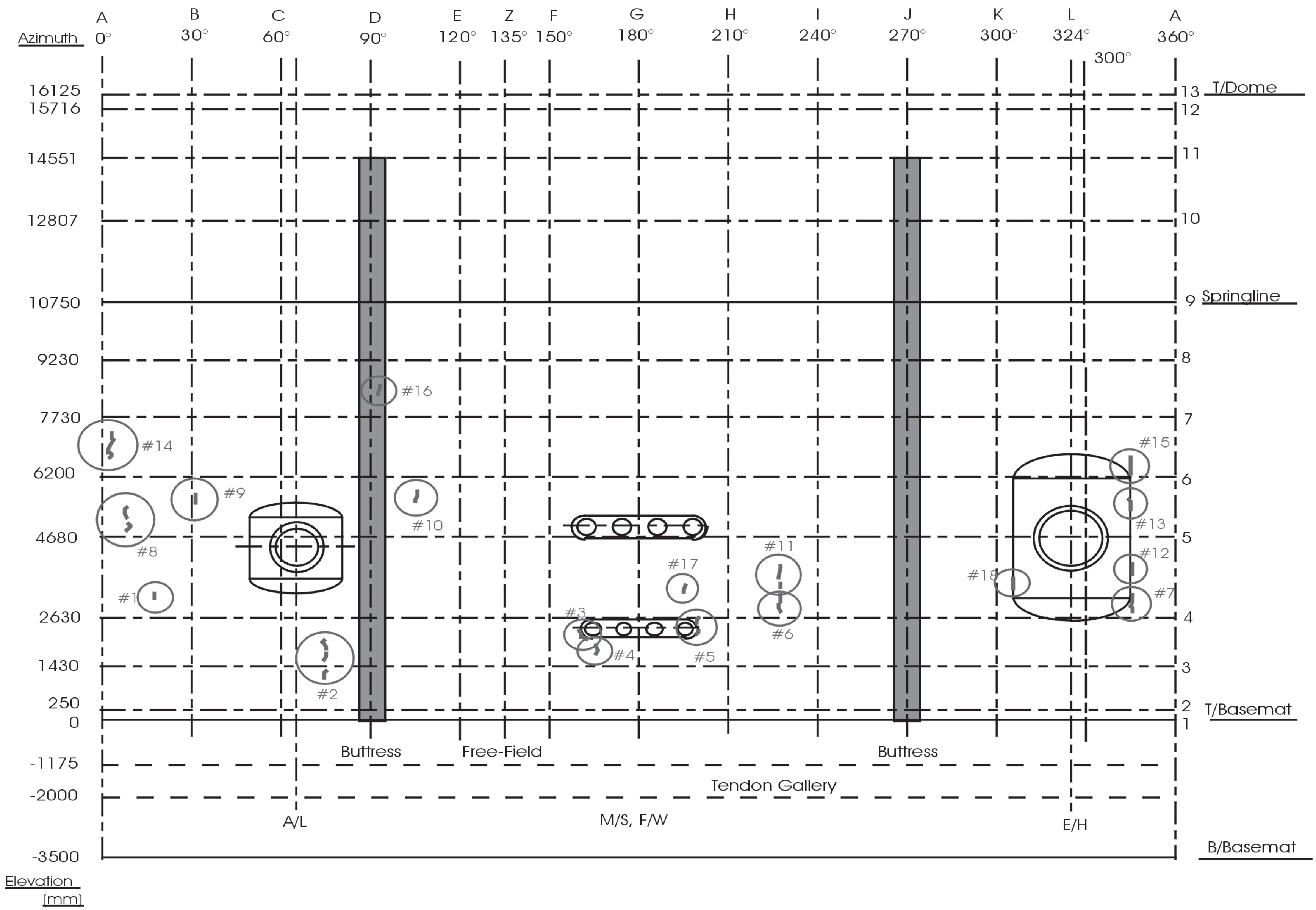

Figure 1-5. Liner Tears Observed After LST

Figure 1-6. PCCV Model after Structural Failure Mode Test

2.0 FINAL PRETEST ANALYSIS

2.1 Scope of Final Pretest Analysis

Pretest prediction analysis of the NUPEC/SNL 1:4 scale PCCV model LST is formally documented in the NUREG CR-6685 Report [1]. Due to the logistics of report preparation and reviewing requirements, the analyses reported therein were performed in the fall of 1999, one year prior to the LST scheduled for September, 2000. A final set of pretest prediction analyses were performed just prior to the test, which incorporated updated properties and in-situ conditions of the model. These final pretest analyses were performed primarily to support test operations by providing the 'best' predictions of the model's response for real-time comparison with the actual response. This information was essential to the safe and successful conduct of the test. The properties and modeling inputs considered for modification were:

1. Concrete material properties,
2. Prestress (stress levels, stress distribution due to friction, and anchor set), and
3. Creep, temperature, and other time dependent effects.

The global axisymmetric, the semi-global 3DCM models, and the local penetration models were reanalyzed. The local failure predictions are all driven by response versus pressure histories calculated by the 3DCM model, but the local models had to be reanalyzed to save the data recently selected for monitoring during the test. How the updated modeling inputs were considered in the final analyses is summarized herein.

2.2 Final Model Inputs

2.2.1 Concrete Material Properties

Because visual inspection of the model reveals the existence of microcracking (probably due to curing and shrinkage) throughout the cylinder, the concrete tensile strength was reduced to correspond to a cracking strain of $\varepsilon_{cr} = 40. \times 10^{-6}$. This is half of the value used in the prior analysis.

A new suite of concrete compressive tests conducted at Construction Technology Laboratories (CTL) became available in February, 2000. The concrete pour designations are shown in Figure 2-1 and the latest test results are tabulated in the CTL test excerpt, Table 2-1. How this data was used in the reanalysis is summarized below.

2.2.1.1 Axisymmetric Analysis

Based on prior analysis, the areas where concrete behavior most influences model behavior are in regions C1 and F3B. A third zone, the rest of the basemat, was also identified separately because of the differences in material specifications for this zone. The zones used for the analysis assumptions are shown in Figure 2-1. The average strengths and moduli assigned for these regions are as follows:

		Region C1	Region F3B	Rest of Basemat
f_c'	=	60.9 MPa (8831 psi)	59.4 MPa (8613 psi)	49.2 MPa (7,134 psi)
E	=	27.1 GPa ($3.93 \cdot 10^6$ psi)	28.0 GPa (4.06×10^6 psi)	26.0 MPa (3.77×10^6 psi)

These figures were computed by averaging the data in Table 2-1, but only using "C1," "F3B," and the average of region "F1," "F2," and "F3A," respectively. The Region C1 and F3B strengths are roughly 22% higher than what was used in the prior prediction analysis, and may, therefore, have a noticeable effect on the cylinder wall flexural behavior. The Young's Moduli are roughly 15% lower than what was used in the prior analysis. Note that the strain at peak stress (provided in e-mail correspondence from M. F. Hessheimer, 7/21/00) is mostly in the range of 0.0025 to 0.0026, so the shape of the stress-strain curve used in the prior analysis is judged to be reasonable with the exception of softening the modulus.

Table 2-1. Strength and Modulus of Elasticity Results

Sample	Test Number	Load, kN	Stress MPa	Average	Modulus GPa	Average
C1T2	4	1,077	59.0	60.9	26.0	27.1
C1T5	1	1,146	62.8		28.2	
C1T6	3	1,109	60.8		27.2	
C2T1	7	1,142	62.6	57.0	25.5	26.6
C2T3	5	959	52.6		26.0	
C2T4	6	1,019	55.9		28.3	
C3T1	8	961	52.7	50.7	18.4	24.4
C3T3	9	1,101	60.4		29.5	
C3T5	2	711	39.0		25.3	
C4T1	11	1,151	63.1	61.8	28.6	28.6
C4T2	10	1,302	71.4		32.4	
C4T3	12	930	51.0		24.9	
D1T2	13	1,316	72.1	71.3	30.8	30.9
D1T3	14	1,293	70.9		30.9	
D1T4	15	1,291	70.8		31.1	
D2T2	16	977	53.6	50.7	28.0	23.6
D2T3	17	799	43.8		15.9	
D2T4	18	996	54.6		26.9	
D3T1	19	1,322	72.5	57.0	31.6	22.5
D3T2	20	873	47.8		17.3	
D3T2	21	922	50.6		18.6	
F1T5	32	1,045	57.3	52.2	22.0	25.8
F1T6	31	1,010	55.3		28.3	
F1T8	33	803	44.0		27.2	
F2T2	30	978	53.6	54.2	27.2	29.5
F2T4	29	911	49.9		28.2	
F2T8	28	1,078	59.1		33.2	
F3AT3	35	790	43.3	41.2	26.4	22.8
F3AT4	36	628	34.4		16.0	
F3AT5	34	839	46.0		26.0	
F3BT2	25	1,316	72.1	59.4	30.6	28.0
F3BT3	26	920	50.4		26.8	
F3BT7	27	1,017	55.8		26.7	
F4T1	22	1,239	67.9	65.9	29.1	30.0
F4T2	23	1,161	63.6		30.2	
F4T2	24	1,205	66.0		30.5	

If all the cylinder and dome pours were averaged, then

$$f'_{c_{avg}} = 58.5\text{MPa}$$

which is within 4% of the C1 value. For this reason, it was decided to use the C1 value throughout the cylinder and dome of the axisymmetric analysis. Similarly, the average value for the basemat is 54.6 MPa or within 8% of the F3B value; therefore, it was decided to use the F3B value, as shown.

2.2.1.2 3DCM Analysis

The 3DCM model encompasses all of region C3 (whose strength is substantially lower than C1) and about half of region C4. For this model, the compressive properties were modified as follows:

$$f_c' = \left(f_{c_{c3}}' + 0.5 f_{c_{c4}}'\right)/1.5 = 54.4MPa\left(7,838\ psi\right)$$

$$E = \left(E_{c3} + 0.5E_{c4}\right)/1.5 = 25.8GPa\left(3.74x10^6\ psi\right)$$

2.2.2 Prestressing

Table 2-2 shows a prestressing data summary, prepared by SNL, which tabulates the averages for measurements of forces, friction, and seating losses.

Table 2-2. Prestressing Data Summary

Avg. Values	Hoop	Vertical
Design Tension Forces	44.4 Tonnes (97.9 K)	49.6 Tonnes (109.3 K)
Jack Force	43.6 Tonnes (96.1 K)	49.0 Tonnes (108.1 K)
Design Lift-off Force	34.1 Tonnes (75.2 K)	46.3 Tonnes (102.1 K)
Jack Lift-off Force	34.0 Tonnes (75.0 K)	44.2 Tonnes (97.5 K)
Load Cell Force (5/4/00)	33.3 Tonnes (73.52 K)	43.6 Tonnes (96.04 K)
Load Cell Force (7/6/00)	33.1 Tonnes (73.04 K)	43.5 Tonnes (95.85 K)
Friction Coeff.	0.18	0.22
Seating Loss (mm)	3.95 mm	4.95 mm
Seating Lost Force	9.56 Tonnes (21.09 K)	4.79 Tonnes (10.56 K)

2.2.2.1 Axisymmetric Analysis

After extensive review of the data, it was decided to use the average load cell force recorded approximately two months after completion of prestressing, on July 6, in the axisymmetric analysis. This includes stress redistributions due to tendon relaxation, seating, and initial effects of creep. Judging by the very limited change from May to July, the July value appears to be a very stable value and it is apparent that creep effects may have been much smaller than anticipated, or partially offset by change in ambient thermal conditions between May and August.

The measured friction coefficients for the hoop and vertical tendons (0.18 and 0.22) were close to the design value assumed prior to the test (0.21). However, there is a great deal of conflicting information in reaching these final friction coefficient conclusions. For example, the measurements for the instrumented vertical tendons show that angular friction may be greatly overstated, but setting losses and "wobble" friction may be understated. The reverse may be true for the hoop tendons. The hoop tendon friction is discussed in more detail for the 3DCM. Since there is no hard-and-fast conclusion on the friction coefficient, it was decided to stay with angular friction that is based on NUPEC's original measurements, namely $\mu = 0.21$ for the hoop tendons. For the vertical tendons, some changes were adopted.

The hoop prestress values relevant to the axisymmetric analysis were recomputed as follows:

Hoop Tendons

The azimuth at which 3.95 mm loss is absorbed/balanced by tendon friction = 39.5˚ from buttress centerline (by separate calculation; see 3DCM discussion)

$T_2 = T_1\, e^{-\mu\alpha}$ $(\mu = 0.21)$

Stress at load cell = 73.04 K/.525 in^2 = 0.96 MPa (139.1 ksi)

Stress at anchor set balance/absorption point = 1.074 MPa (155.7 ksi)

The stresses at the 135˚ azimuth were recalculated as:

$$s_{\text{Group1}} = 155.7e^{-\left(.21x955x\frac{\Pi}{180}\right)} = 109.7\ ksi \quad (757\ MPa)$$

$$s_{\text{Group2}} = 155.7e^{-\left(.21x5.5x\frac{\Pi}{180}\right)} = 152.6\ ksi \quad (1052\ MPa)$$

These hoop prestress values are 5% lower than those used in the earlier analysis.

Vertical Tendons

The strain gage measurements on V46 and V37 (plots attached as Figure 2-2 and 2-3) show much different stress distributions than originally assumed. The axisymmetric model was not originally set up to model vertical tendon anchor set or wobble friction. However, judging by the measurements of Tendon V46, some simulation of stress variation along the straight vertical tendon segments was needed. From Table 2-2, the average force measured in the vertical tendons on July 6, 2000 was 43.47T (95.85k). For Tendon 46, it was 42.18T (93 kips), and there were significant losses along the cylinder barrel section of the model (see Figure 2-2). Without having much additional data, Tendon V46 was used as a prototype for the final axisymmetric analysis vertical tendon stress distribution. As such, the anchor force was set equal to 42.18T (93 kips). The stress at the anchor is therefore

$$\sigma_{\text{vertical}} = 42.18\text{T}/3.393\text{cm}^2 = 1222 \text{ MPa } (177 \text{ ksi}).$$

A friction tie strategy similar to the dome strategy of the earlier axisymmetric models was adopted and implemented as shown in Figures 2-4, 2-5, and 2-6. The resulting stress distribution after prestressing and equilibration is shown in Figure 2-7. The stress results are also shown on the measurement plots in Figures 2-2 and 2-3. The anchor force used is about 8% less than that for the prior pretest analysis. For friction, an angle for the 5 friction ties of 11.70 degrees was selected to achieve the stress losses shown in the figures. This friction tie modeling strategy was explained in detail in the pretest analysis report [1].

2.2.2.2 3DCM Model

The 3DCM model behavior was found to be sensitive to the extent of anchor set; thus more discussion is warranted for making the final tendon stress assumptions for this model.

The 3DCM model spans vertically from hoop tendon H35 to H72. The prestressing tendon tensioning data [1] shows that the average hoop tendon seating loss is 3.95 mm when averaged over all hoop tendons *and* when averaged over H35 to H72. Therefore, it was decided to use 3.95 mm for the seating loss on all hoop tendons. This put the seating loss zone of influence at 39.5 degrees from the buttress centerline, which creates a case that is partway between Case 1 and Case 2 from the early 3DCM anchor set loss sensitivity study [1]. This assumption appears to agree fairly well with the strain gage data points on the hoop tendons that were instrumented (H35, H53, and H68) (see Figures 2-8 to 2-13). The measured strains/forces at the midpoints of H53 and H68 imply that the angular friction may be a little smaller than the design value (0.18 versus 0.21), but the H35 measurements show that near penetrations where the tendon path curves around the penetrations, the effective angular friction may be higher than the design value. For the tendons represented in the 3DCM, it was assumed that the design value 0.21 (as measured by NUPEC in separate mock-up tests) would provide a reasonable average of the varying conditions that occur in the cylinder-midheight region. Note that the initial stress profile of H35 simulated in the 3DCM mimics the plotted measurements, with the minimum stress position at a point closer to the equipment hatch, rather than at the tendon midpoint (90 degrees). This is because of the extra local angle changes that the tendon passes through when sweeping around the E/H.

Although it would be possible to input different hoop tendon stresses in each tendon, it was decided to use the average load cell value of 32.89T (72.5 kips) that existed at the July 6 measurement. The load cell measurements for H40 (End A) and H58 (End A) appear unreasonably low compared to the jacking forces, and an average force seems more appropriate. The target hoop prestress at the anchors, therefore, was

$$s_{anchor} = {32.89T}\Big/{3.393cm^2} = 952MPa\left(138.1ksi\right).$$

The final hoop tendon stress profiles produced are shown in Figures 2-8 through 2-16.

2.2.3 Creep, Temperature, and Other Time Dependent Effects

Judging by the minimal change in the tendon forces between May and July, the effects of creep and shrinkage appear to be much smaller than anticipated. It is difficult, however, to isolate the creep response from other time-dependent effects, such as temperature. Since creep effects will tend to be largest within the first 30 to 60 days after prestressing, using the July 6 measured prestress values accounts for time-dependent effects reasonably well. In general, as is shown in Figures 2-8 to 2-13, the initial levels of prestress arrived at are lower than those measured on individual tendons by between 3% and 10%. This should accommodate creep effects that may occur between July 6 and September 26, but no further creep and temperature effect simulations have been performed other than the one discussed in the pretest analysis report [1].

2.3 Data Presentation

The goals of the final pretest prediction analysis were to update the prediction results with analyses that included the latest material properties and tendon stress conditions. As noted, this was done primarily to support test operations by providing the 'best' predictions of the model's response for real-time comparison to the actual response. The following suites of data were provided for making real-time comparisons during the test:

1. All Standard Output Locations (SOL);

2. Four sets of displacement profile data versus pressure (vertical sections at 90 degrees, 135 degrees, and 324 degrees and a horizontal profile at Elev. 4.7m);

3. Four sets of strain data to be displayed on panels (E/H, A/L, M/S and Wall-Base Juncture).

Some of the more important plots with the published and final pretest predictions are presented in Chapter 4. The radial displacements at the bottom and top of the final 3DCM model are compared to the final axisymmetric model results in Figures 2-17 and 2-18. Comparing to the previous pretest analysis shows a trend of slight reduction in 3DCM radial displacement and an increase in axisymmetric radial displacements. This brings the 3DCM radial displacement results, at 135 degrees, a little closer to the axisymmetric results, but there is still a substantial difference between the two. Developing a final suite of analysis data to compare to test data during the test meant choosing between cylinder radial displacement data predicted by the two different models. To this end, it was decided to use a spatial interpolation scheme to develop a consistent set of displacement data for the entire cylinder. The difference between the 3DCM model and axisymmetric model radial displacements is one of several posttest evaluation topics in this report.

2.4 Conclusions of Final Pretest Analysis

Final changes to the pretest prediction analyses were documented prior to the test and summary results. Based on the final analyses, the general failure mode prediction, liner tearing near the equipment hatch, did not change; nor did the failure (leakage) pressure, 3.2 Pd. The final ranking and predicted sequence of failure locations was previously published in the pretest predictions report [1]. Those predictions are repeated below for reference.

Table 2-3. Possible Liner Tearing Locations in Descending Order of Probability of Occurrence

Most Likely Occurrence	Location
1.	E/H near vertical T-anchor termination (4 locations, Type 3);
2.	E/H near horizontal stiffener termination(4 locations, Type 2);
3.	Near a weld seam with hoop stiffener rat-hole, 5 degrees from the centerline of 90 degree buttress (i.e. 95 degrees; occurs in roughly 6 locations);
4 and 5	Similar to 1 and 2, but near the A/L (7 locations, Types 3 and 2);
6.	Similar to 1, but near the M/S penetration (2 locations, Type 3);
7.	Similar to 1 and 2, but near the feedwater (F/W) penetration (3 locations, Types 3 and 2);
8.	Strain concentration Location Type 4 near F/W penetrations, M/S penetrations.
9.	Liner tear at wall-basemat juncture.

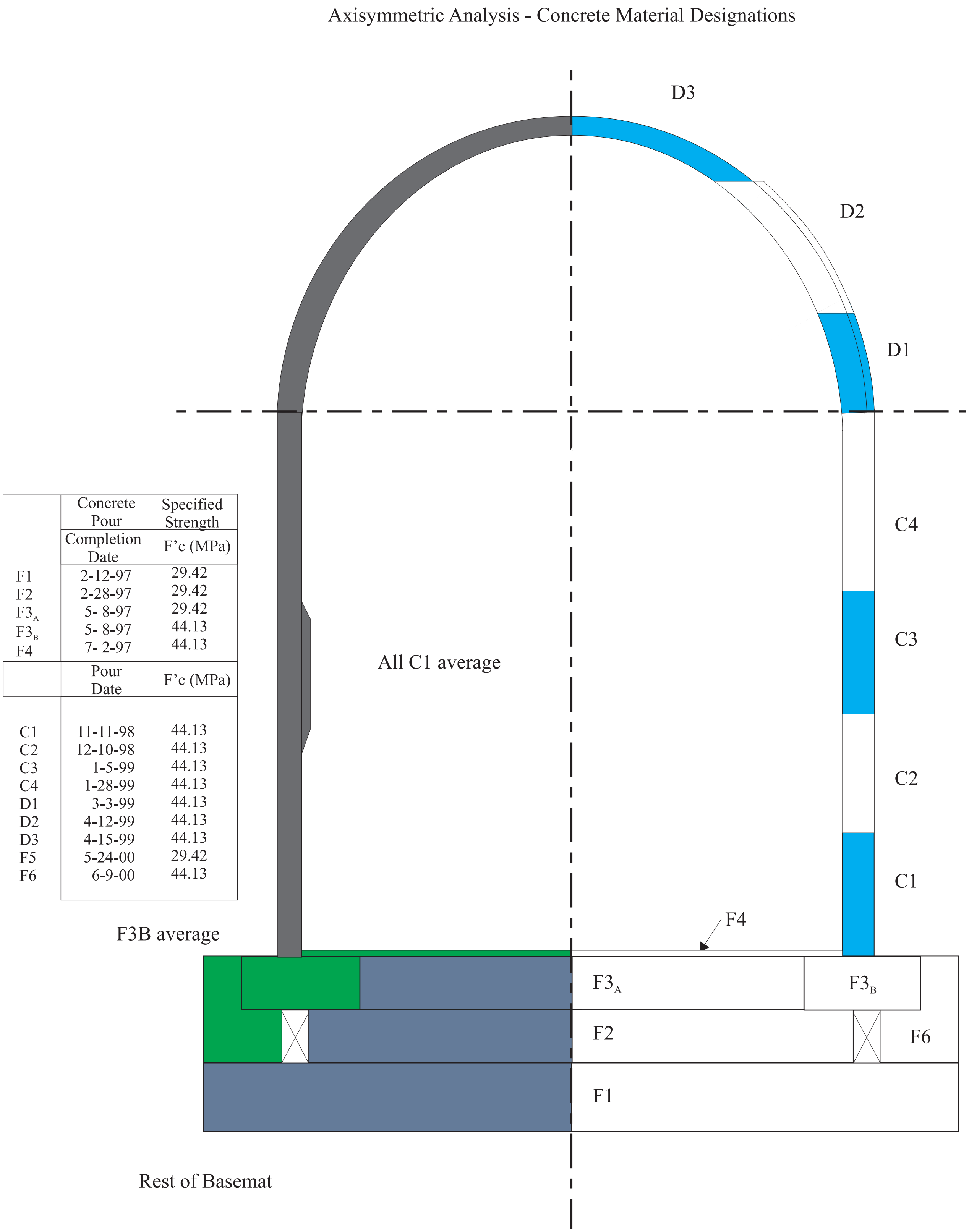

	Concrete Pour Completion Date	Specified Strength F'c (MPa)
F1	2-12-97	29.42
F2	2-28-97	29.42
$F3_A$	5- 8-97	29.42
$F3_B$	5- 8-97	44.13
F4	7- 2-97	44.13
	Pour Date	F'c (MPa)
C1	11-11-98	44.13
C2	12-10-98	44.13
C3	1-5-99	44.13
C4	1-28-99	44.13
D1	3-3-99	44.13
D2	4-12-99	44.13
D3	4-15-99	44.13
F5	5-24-00	29.42
F6	6-9-00	44.13

Figure 2-1. PCCV Model with Revised Concrete Pour Schedule

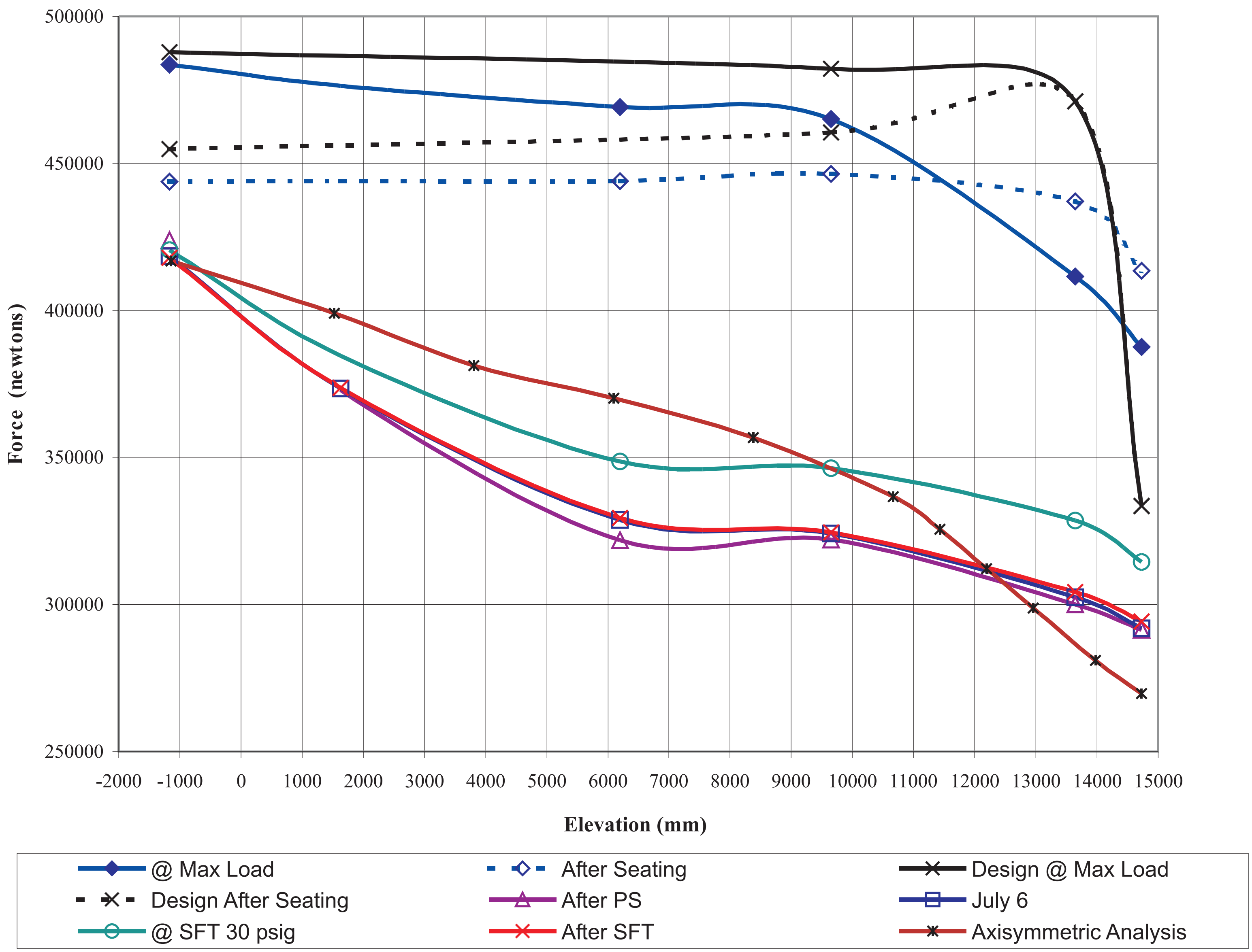

Figure 2-2. Tendon Force Measurements for Vertical Tendon #V46

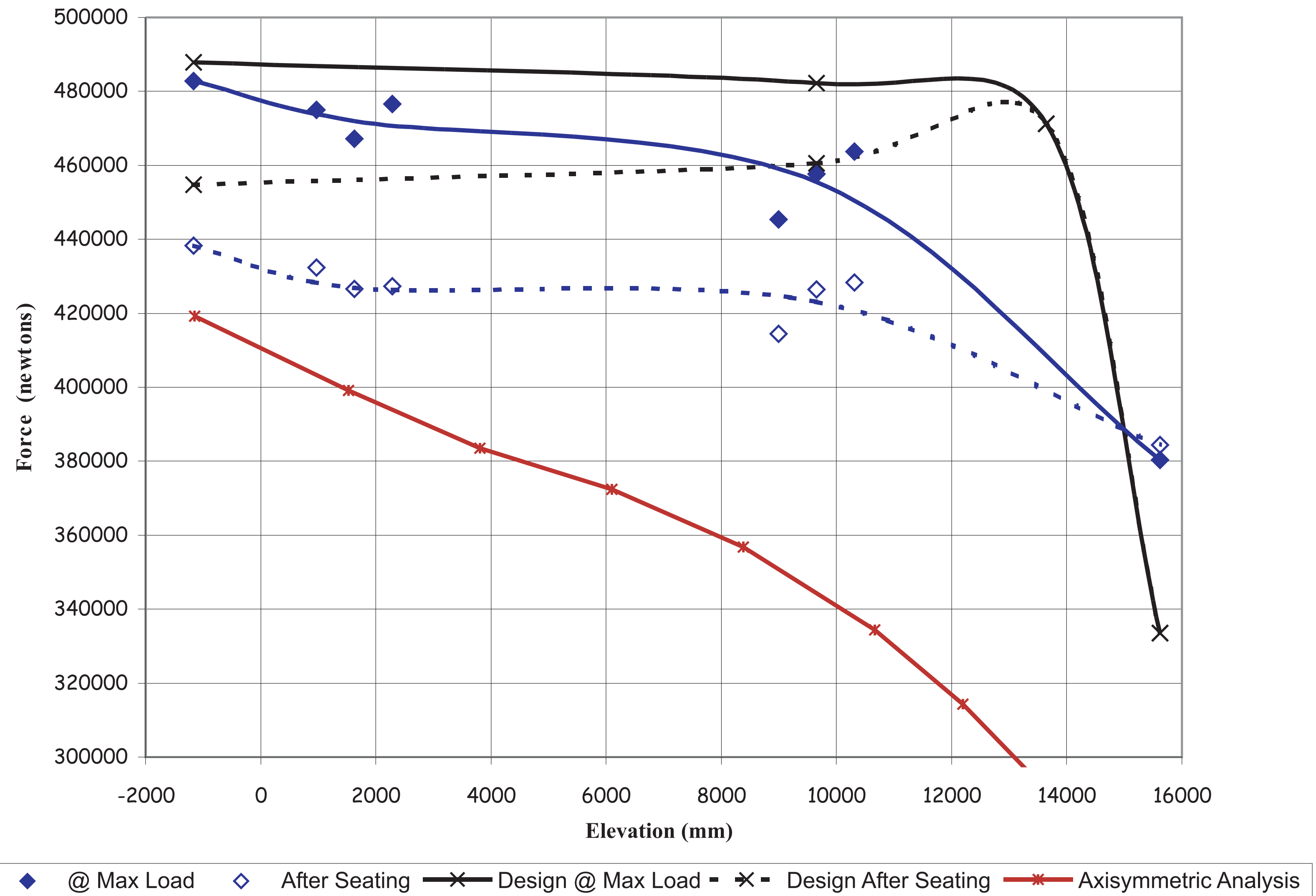

Figure 2-3. Tendon Force Measurements for Vertical Tendon #V37

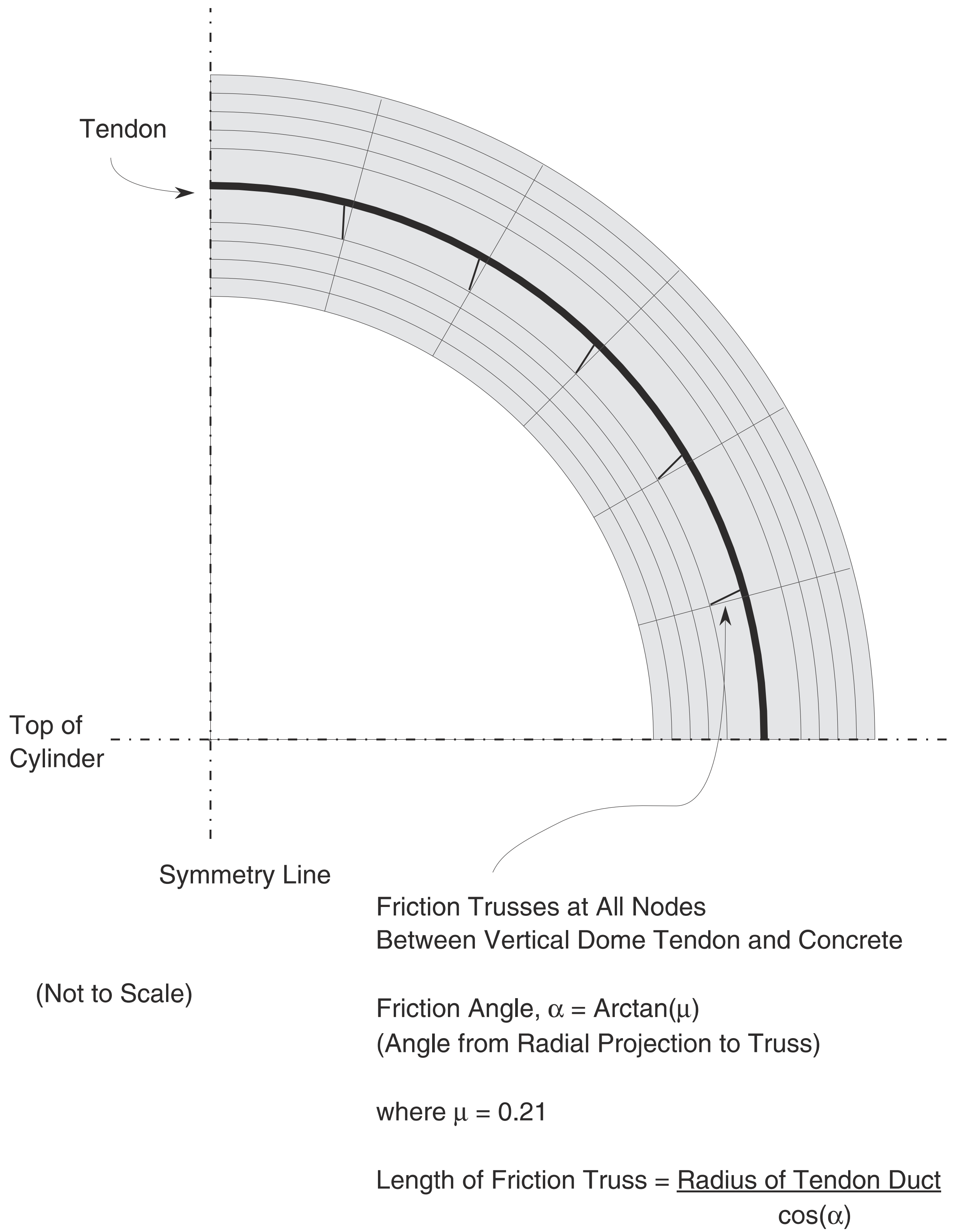

Figure 2-4. Modeling of Tendon Friction Behavior

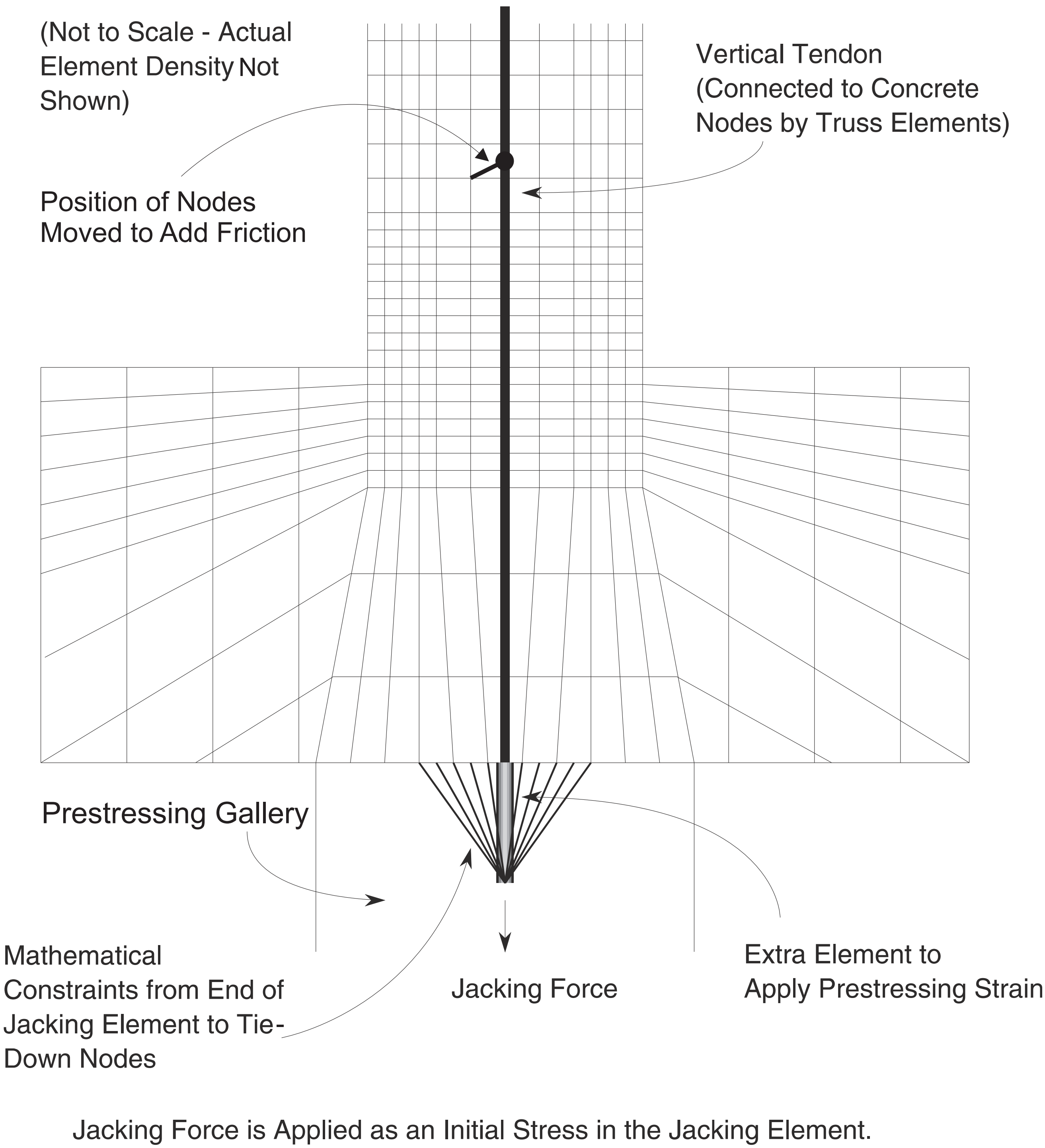

Figure 2-5. Modeling of Prestress Application with Jacking Element

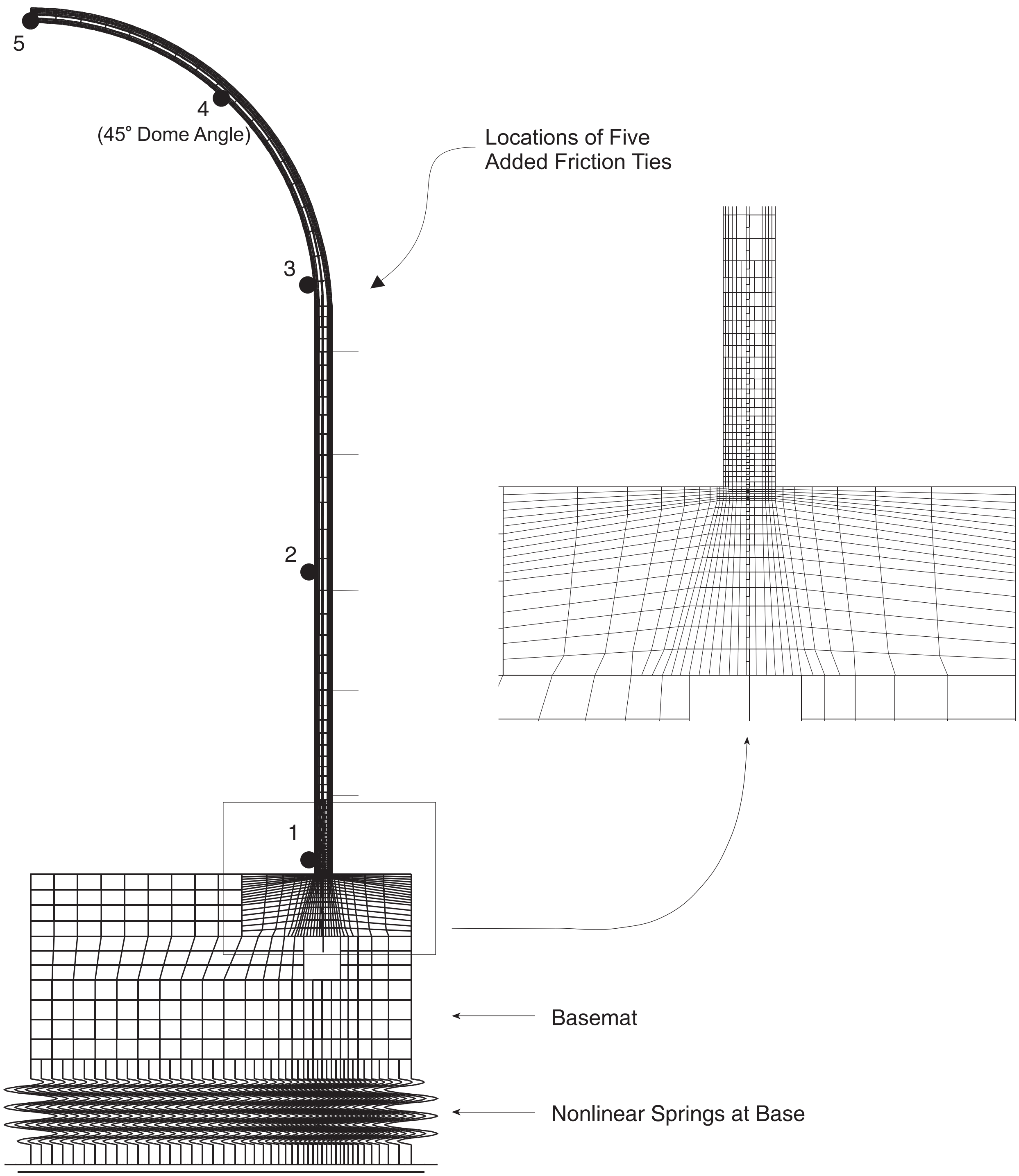

Figure 2-6. Axisymmetric Model of PCCV and Locations for Plotted Output

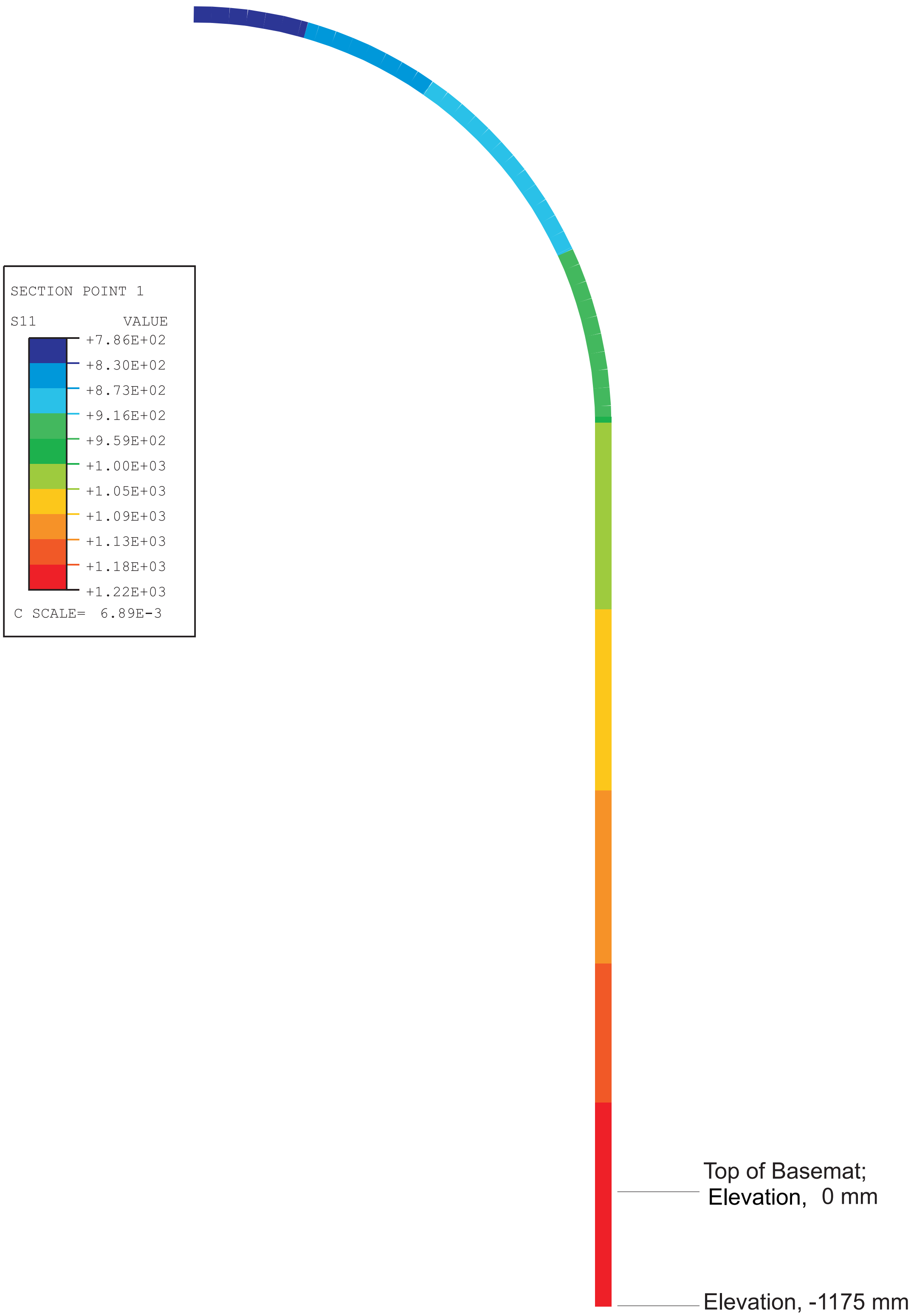

Figure 2-7. Vertical Stress (MPa) in Vertical Tendons after Prestress

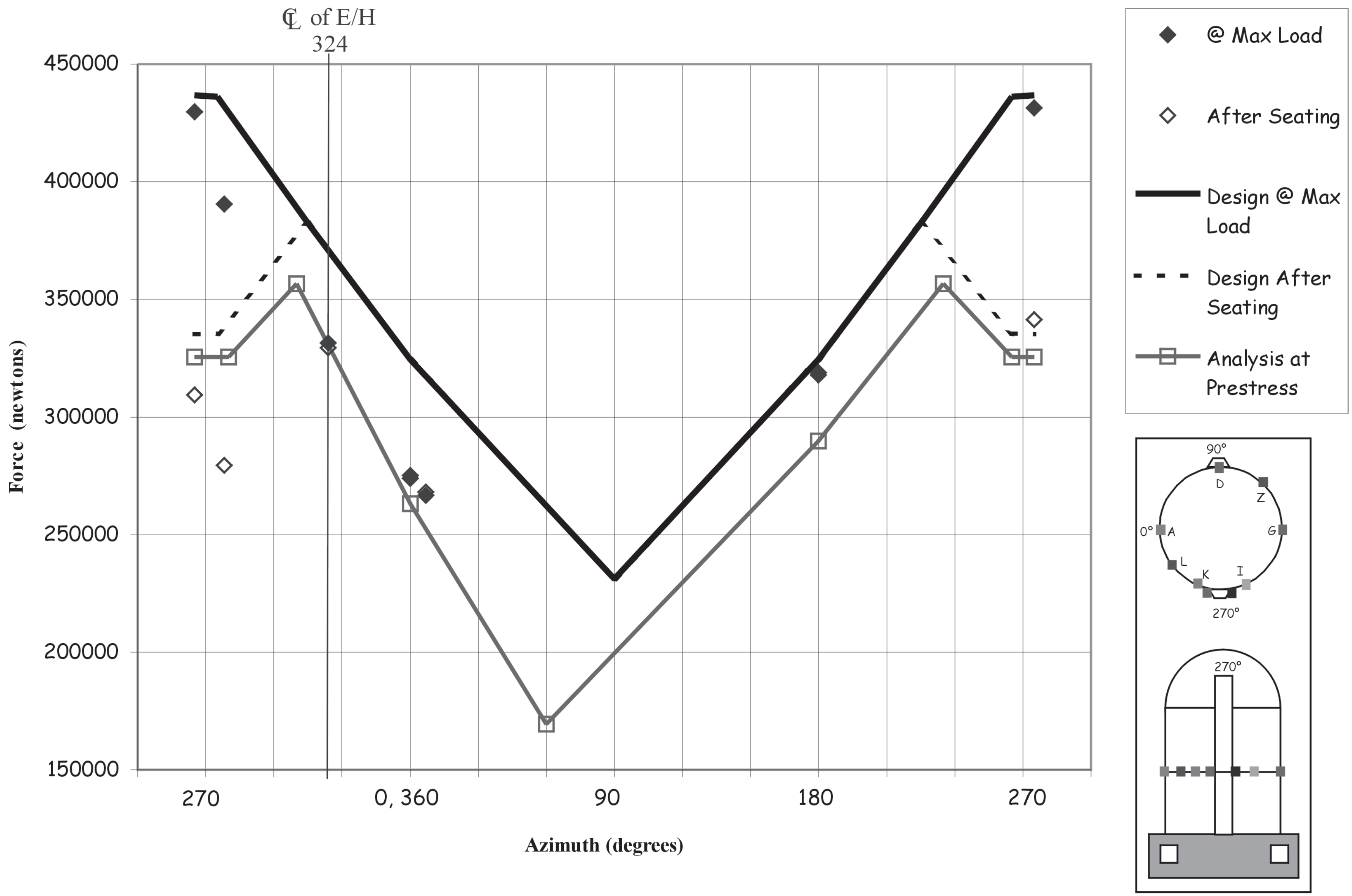

Figure 2-8. Tendon H35 Force Distribution (Strain Gage Data)

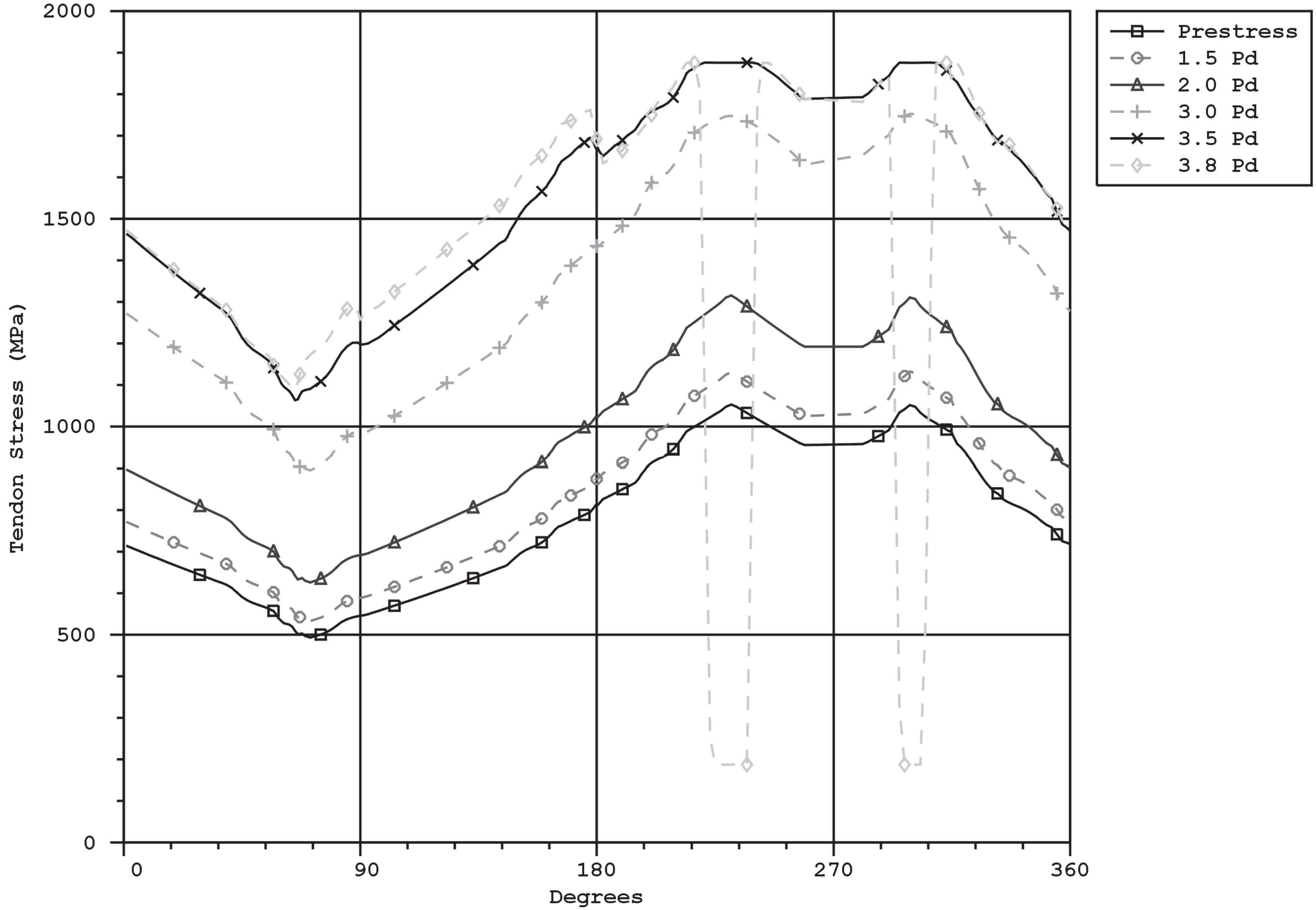

Figure 2-9. Tendon Stress Profile for Instrumented Hoop Tendon #H35

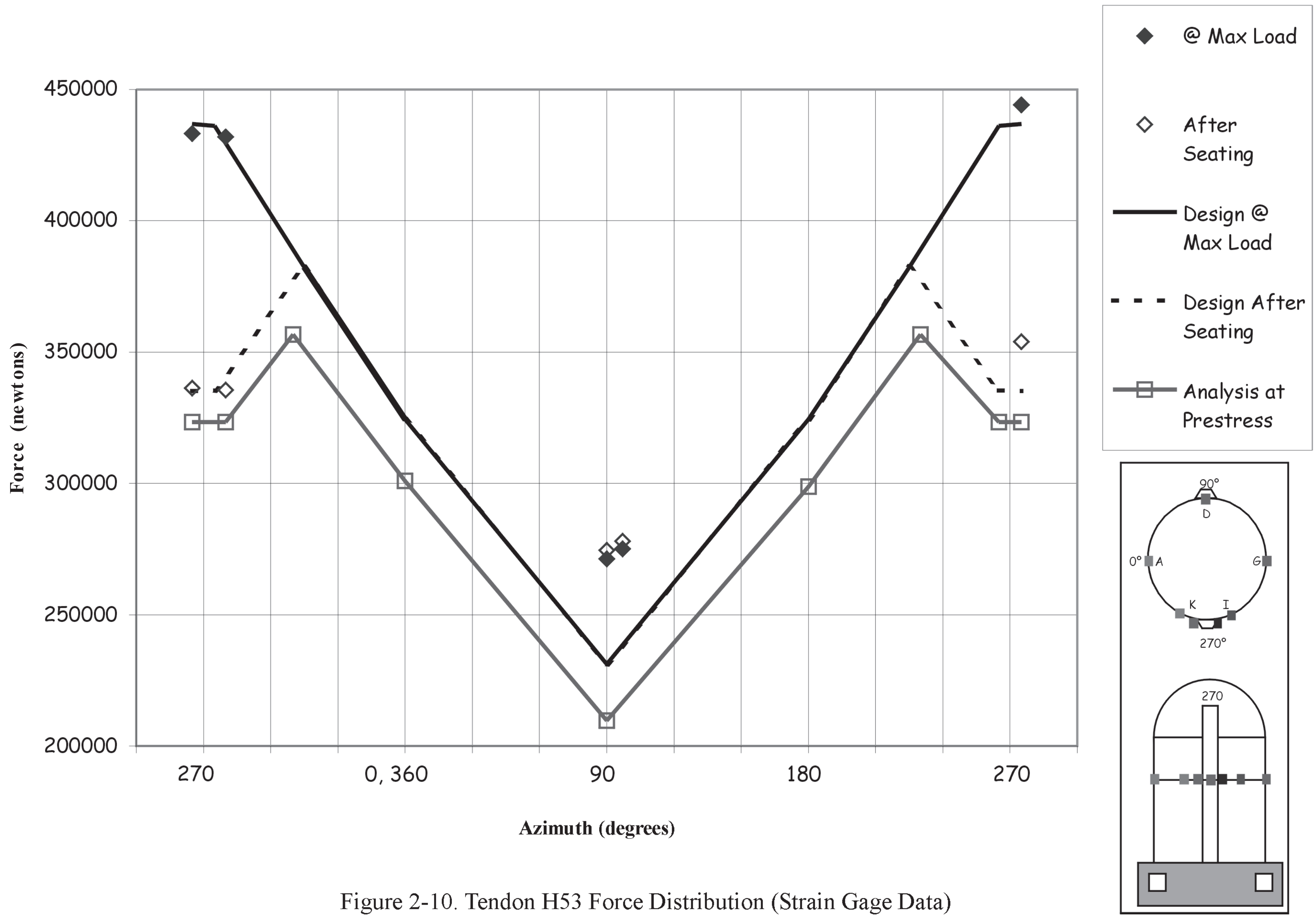

Figure 2-10. Tendon H53 Force Distribution (Strain Gage Data)

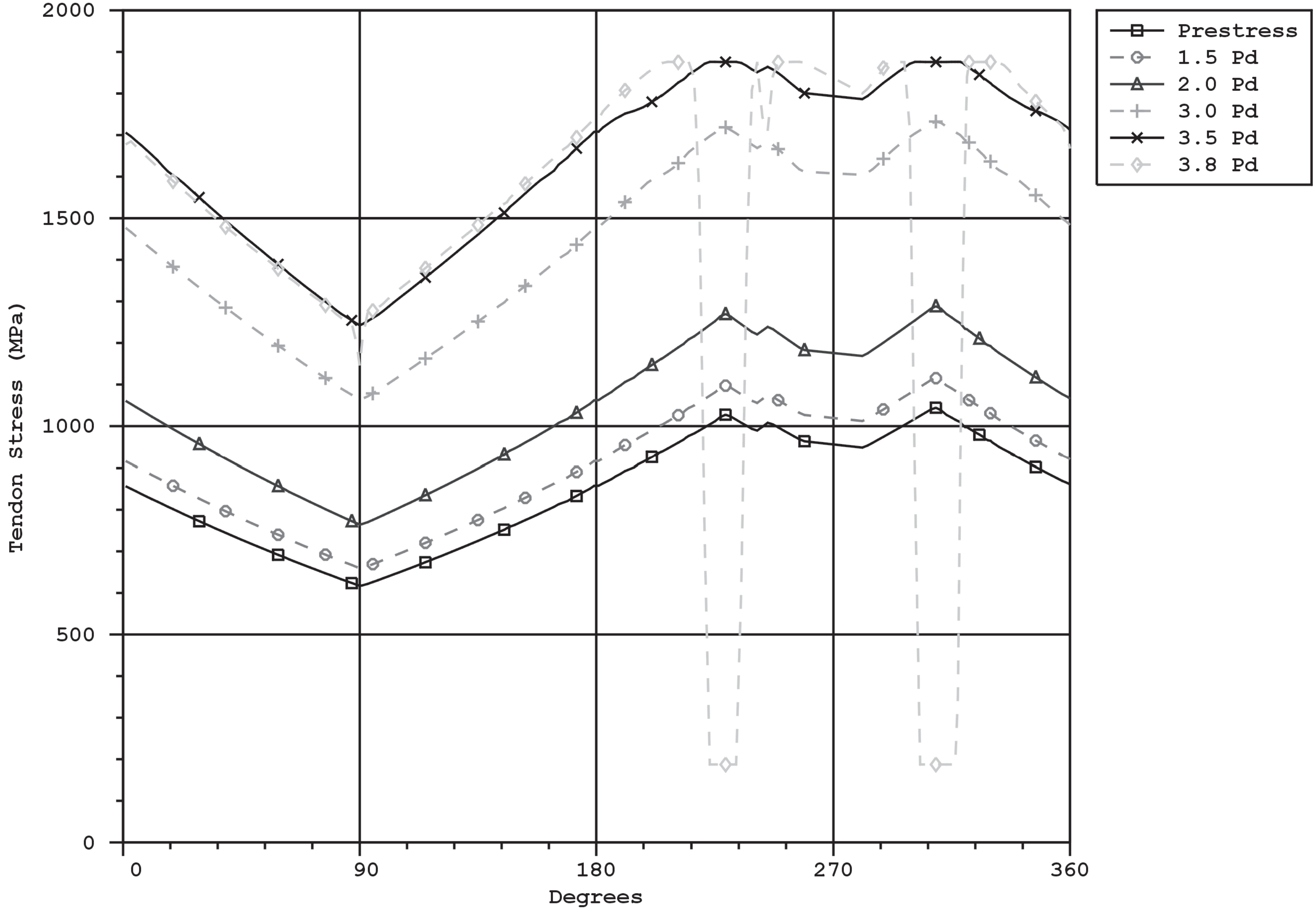

Figure 2-11. Tendon Stress Profile for Instrumented Hoop Tendon #H53

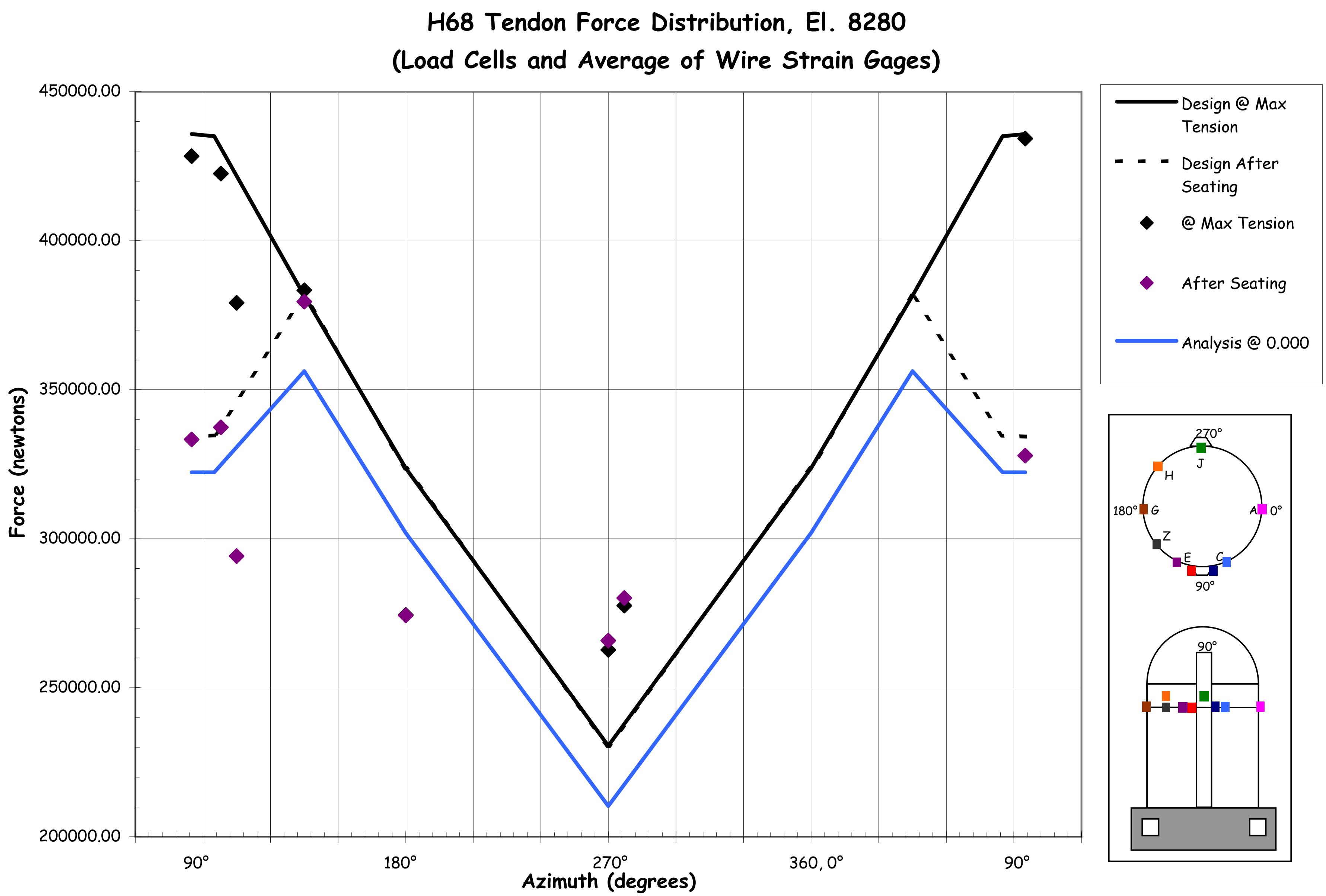

Figure 2-12. Tendon H68 Force Distribution (Strain Gage Data)

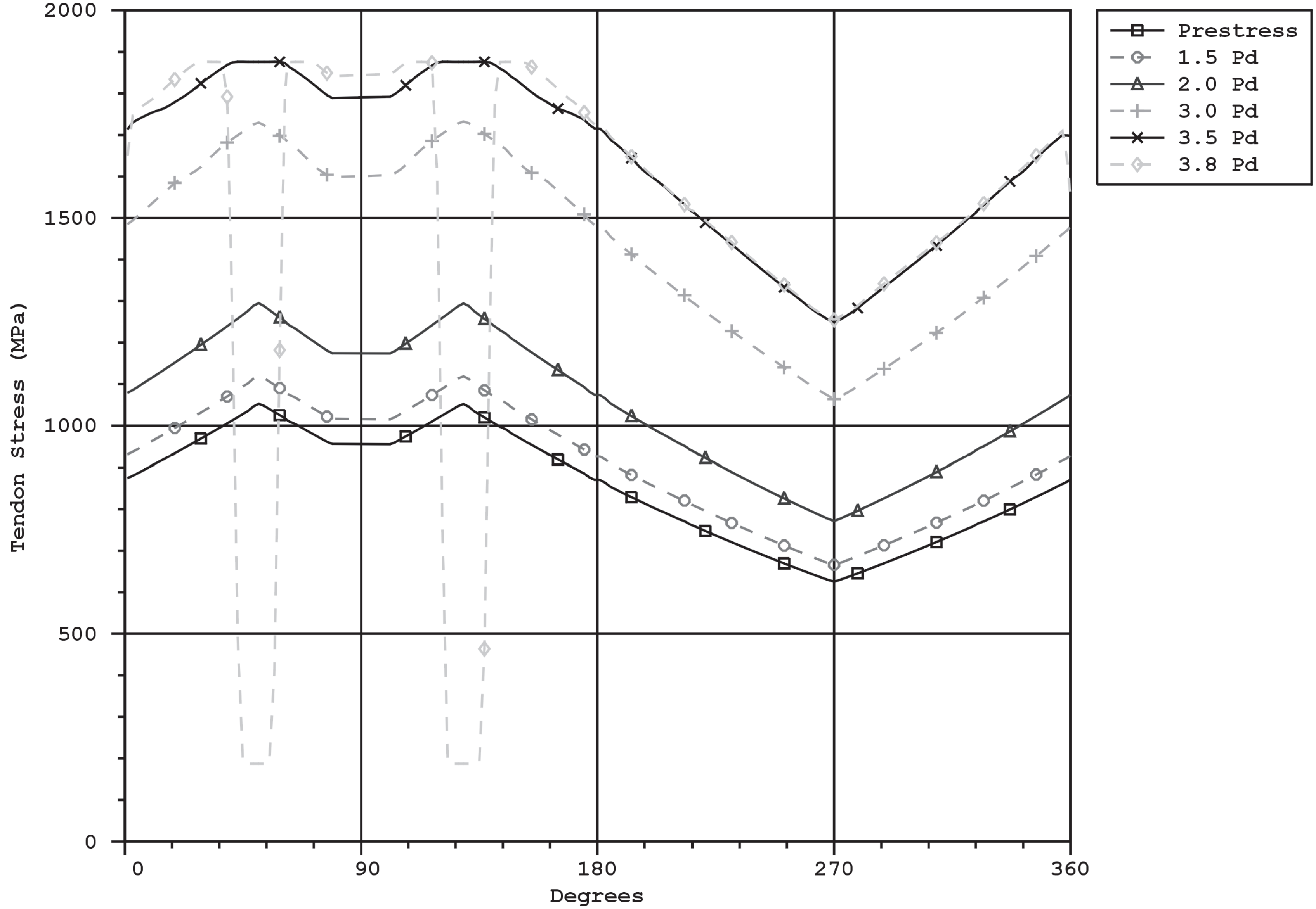

Figure 2-13. Tendon Stress Profile for Instrumented Hoop Tendon #H68

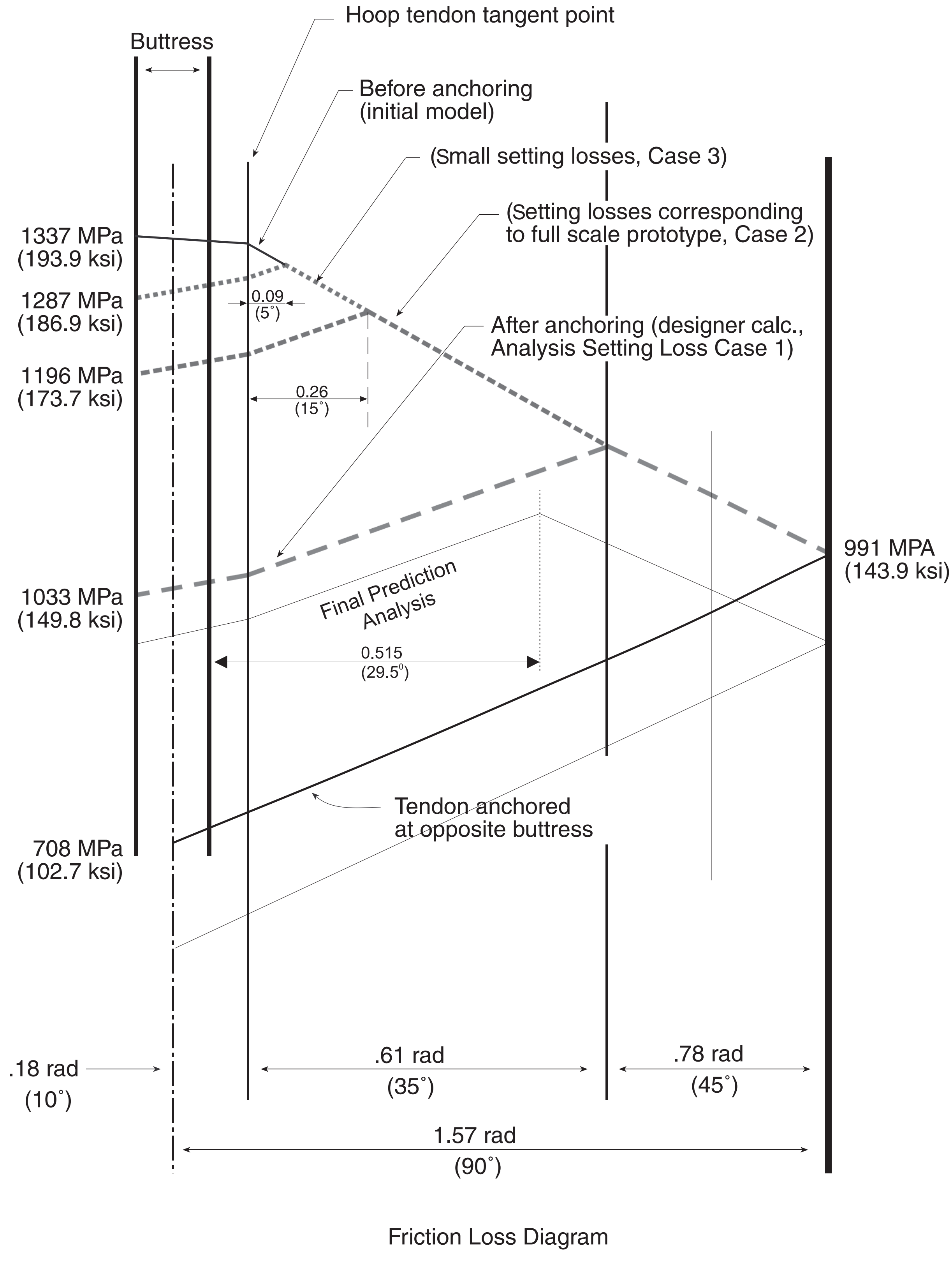

Figure 2-14. Other Setting Loss Cases for Parameter Study

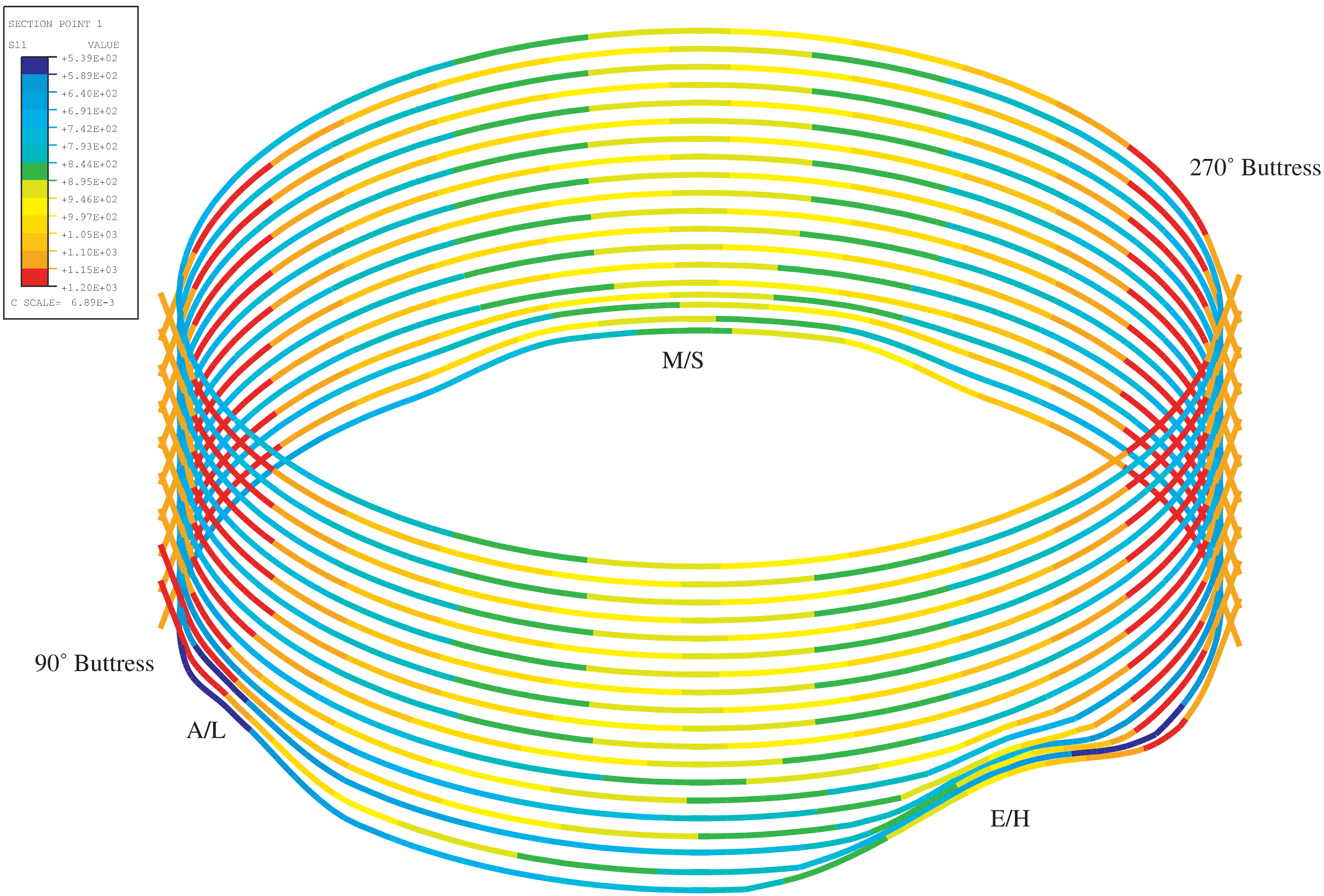

Figure 2-15. Stress Contours (MPa) in Hoop Tendons After Prestress

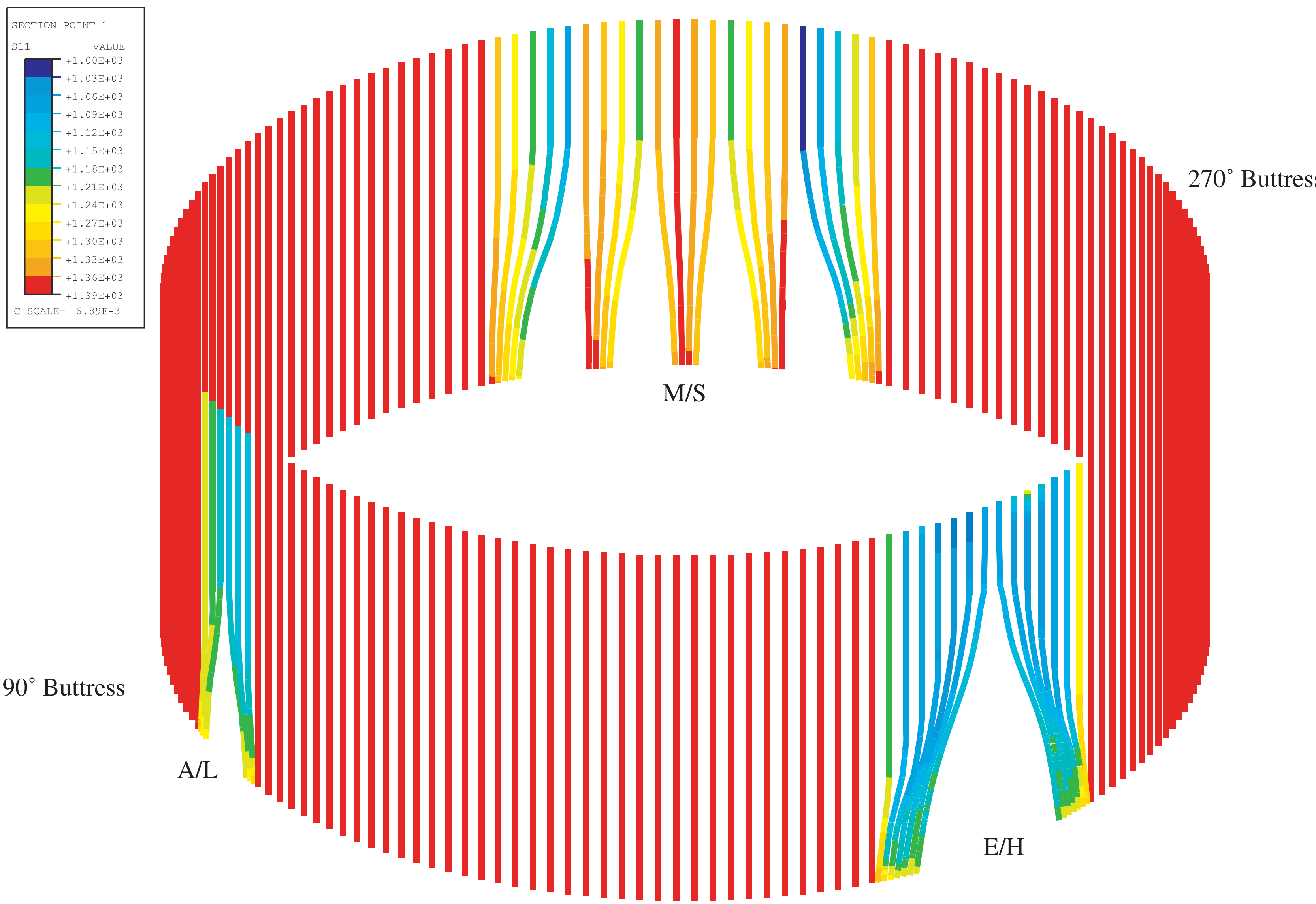

Figure 2-16. Stress Contours (MPa) in Meridional Tendons after Prestress

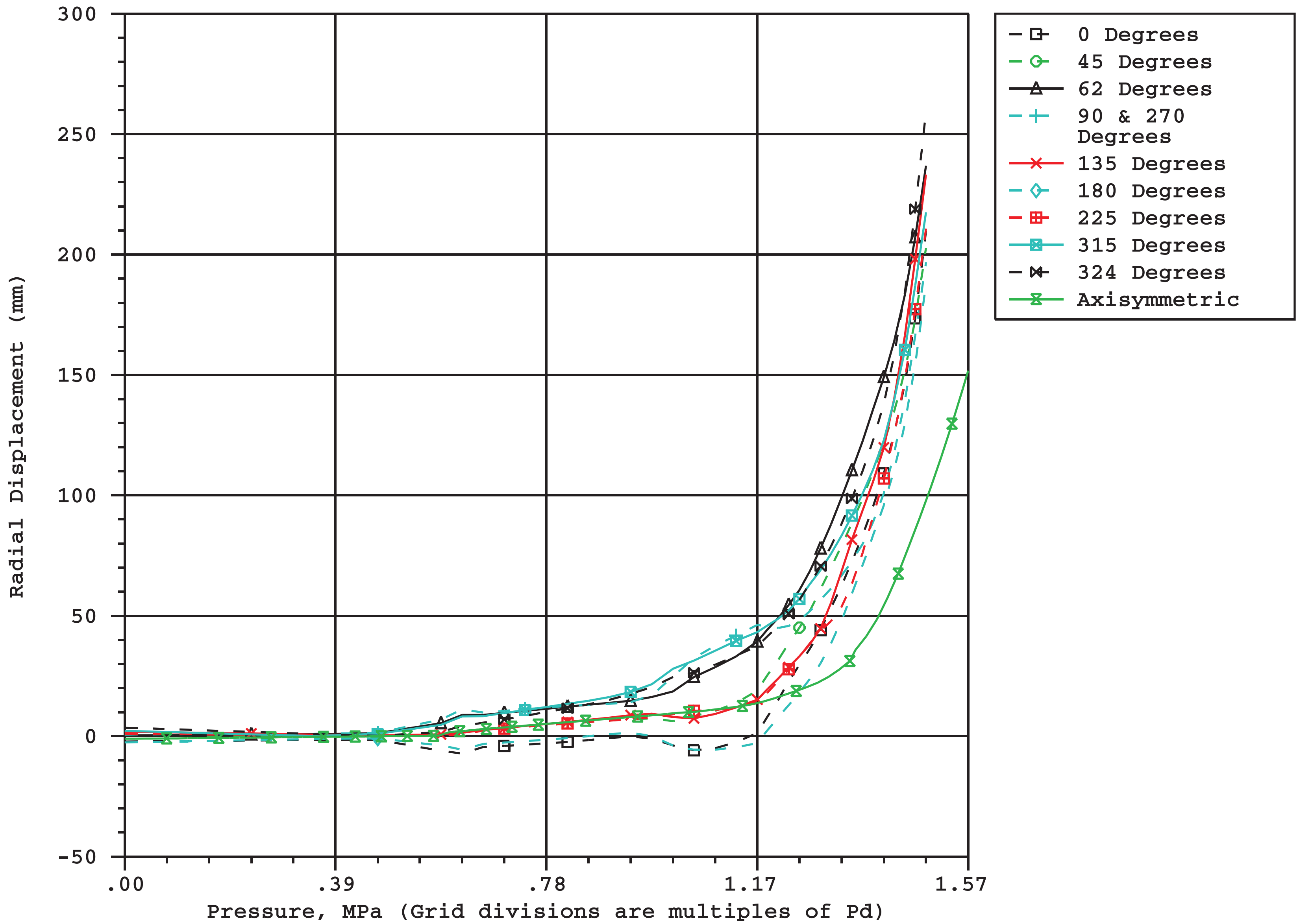

Figure 2-17. Radial Displacement at EL = 4.7 m, 3DCM Compared to Axisymmetric

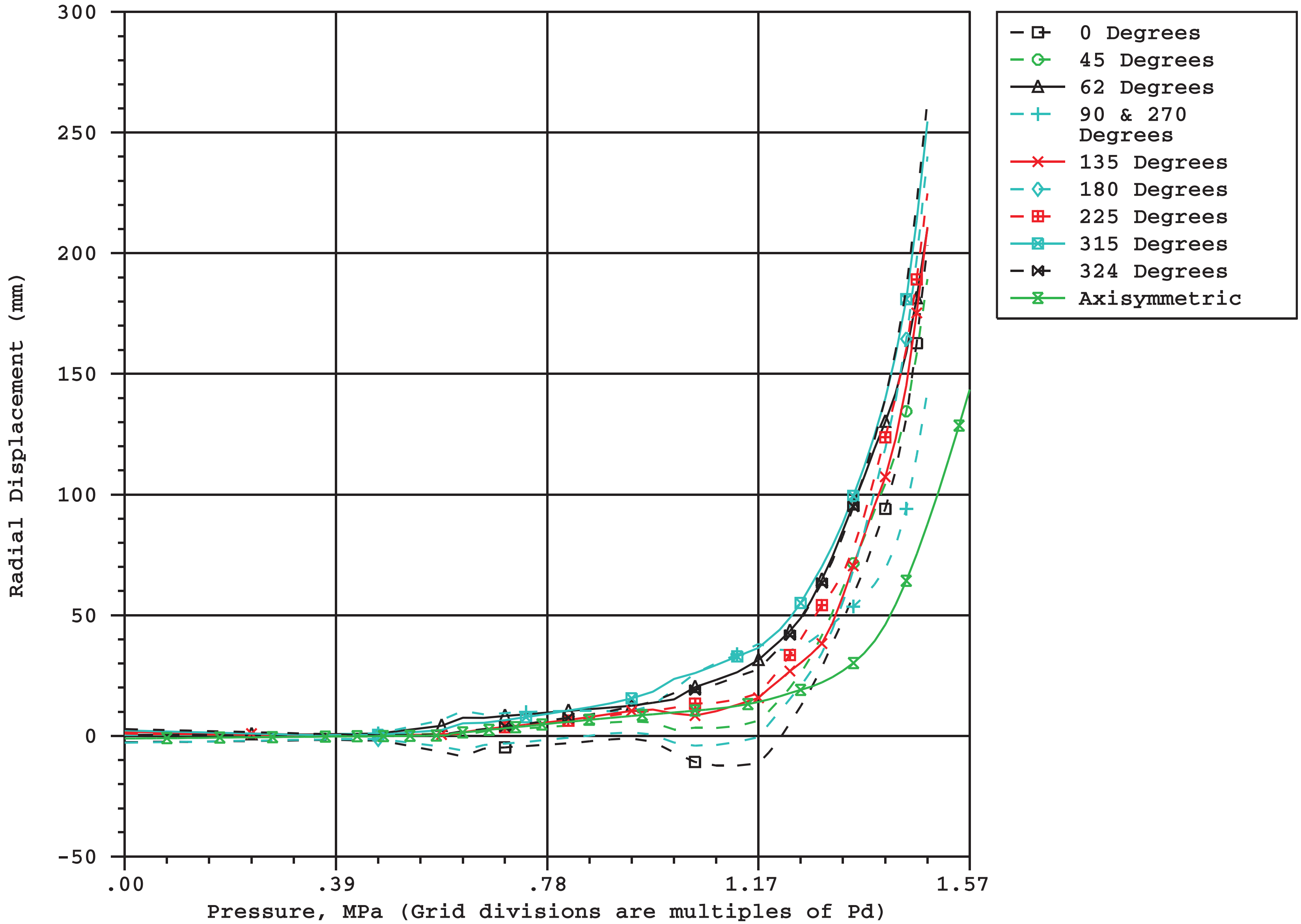

Figure 2-18. Radial Displacement at EL = 8.9 m, 3DCM Compared to Axisymmetric

3.0 TEST MEASUREMENTS

3.1 Overview of Instrumentation

In any experimental program, there are a number of external factors or artifacts of the instrumentation that can influence the data. The goal of this effort was to identify these factors and, to the extent that their influence was significant, adjust the raw data to produce a uniform data set. As part of the posttest analysis effort, ANATECH was also tasked with reviewing the data, identifying significant external influences or artifacts and, if possible, correcting the measurements taken during the LST for these unwanted influences.

A detailed presentation and discussion of the PCCV instrumentation is beyond the scope of this report; a thorough coverage is provided in Ref. 8. This chapter identifies the external influences on the test data and then summarizes the methods to characterize and correct for these influences, if feasible. The details of the corrections are also included in the PCCV test report [8].

The instrumentation measurements in the "data correction" effort, and the effects and phenomena that were addressed, are listed below.

Table 3-1. Instrumentation Measurements

Measurement	Effects Considered for Correction
Displacement	Temperature, Rigid Body Motion
Strains in Special Gaged Rebars	Temperature, Strain Localization
Strains in Liner	Temperature
Pressure	--
Strains in Rebar	Temperature, Strain Localization
Tendon Strains	Temperature
Temperatures	--

3.2 Temperature Effects on Measurements

The data acquisition system was installed and activated more than seven months prior to the LST. Gage measurements taken at various time intervals throughout these seven months provided a vast database of the model's response to changes in ambient temperature. Since the goal of the "data correction" effort is to create a corrected set of data that is free of temperature effects, data were extracted from the database to calibrate correction formulas for each gage. Changes in temperature have a direct influence on the strains and displacements of a free-standing structure. Furthermore, temperature changes have secondary effects on the voltage readouts of strain gages. Both of these effects were considered and quantified in the data correction effort; the former by direct observation of the model response during the calibration periods and the latter by the gage manufacturer. To correct for either phenomena first requires that the temperature be known at every gage, or, in effect, at all possible locations within the PCCV. This information was obtained by developing a temperature mapping algorithm based on interpolation between the matrix of temperature gages. Development of the temperature mapping and data correction algorithms is described in the test report [8].

3.3 Instrumentation Artifacts

In addition to temperature effects, some data artifacts were introduced by the inherent limitations of the instruments themselves or by the methods used to mount them to the structures.

3.3.1 Displacements

While analyses report absolute displacements, that is, in terms of a fixed, global coordinate system, displacement data obtained from experiments are always relative to some other physical structure. In the case of the PCCV model, nearly all the displacements were obtained by measuring the vertical and radial motion of the PCCV relative to the internal instrumentation frame and basemat. The basemat vertical uplift was measured relative to the mudmat. All of these ‘reference’ structures are, themselves, subject to the same influences and loads as the main body of the PCCV model, and therefore also move. A separate set of instruments were applied to these structures to monitor their motion in response the these loads. This data was used to evaluate whether these reference structure motions had a significant influence on the test data. This data is also provided in the test report [8].

With the exception of basemat uplift, the motion of the instrumentation frame to variations in ambient or internal temperature and pressure were negligible relative to the overall motion of the PCCV model, and no corrections were applied to the data.

Regarding the basemat uplift, after the pressure test were completed, it was recognized that the mudmat tended to conform itself to the basemat, and as a result, no relative motion between the basemat and mudmat occurred or was measured. This data was initially interpreted to show that there was no basemat uplift. It was subsequently recognized, therefore, that the vertical displacement transducers on the basemat were not capable of measuring the absolute uplift of the basemat. Unfortunately, no other transducers were available to provide this data and no correction algorithm could be developed. The implications relative to the analysis are described in the next chapter. Fortunately, however, the calculated uplift is relatively small and has very little influence, if any, on the vertical displacement data for the cylinder wall and dome.

3.3.2 Rebar Strains

In addition to the temperature effects described above, there is an additional gage artifact that affects strain gages mounted on deformed rebar. The strain gages used in the PCCV model tests are foil-type resistance gages bonded to the rebar using adhesives. In order to ‘glue’ these gages to the rebar, a relatively flat, smooth surface is required. This surface is obtained by grinding away the local deformations over an area slightly larger than the gage and then polishing this surface. This grinding, while minimized, reduces the cross-sectional area of the rebar at the location where the gage is applied. This locally reduced segment then yields slightly before the rest of the bar, and as a result, strains at the gage location are higher (on the order of 0.5%) than the rest of the bar at stresses just below yield and beyond. This is a significant effect and can be demonstrated analytically for reductions in the cross-sectional area as small as 1%. The phenomena has been illustrated by a series of rebar tensile tests performed at SNL, a few results of which are plotted in Figure 3-1.

This artifact was known from previous experience, and efforts were made to minimize the effect during instrumentation of the rebar. Data was collected on the final bar diameters with the hope that a standardized correction algorithm could be developed.

Recognizing that the rebar gage measurements tend to overpredict the corresponding engineering strain, especially in the range of initial yield (i.e. between $\varepsilon = 0.002$ and $\varepsilon = 0.015$), one possible correction algorithm was developed, as follows. Based on measurements of the instrumented rebar, the typical area reduction as a result of the grinding is 2%. It is assumed that for all strain ε, there is a unique stress, σ, according to the engineering stress-versus engineering strain data. Using the averaged data for the SD390-D13 bars, the yield curve is approximately

ε	σ
.002	58 ksi
.009	60.9 ksi
.013	62.06 ksi
.015	63.075 ksi
.020	66.7 ksi

For a measured local rebar strain, ε_i, the corresponding stress, σ_i, is "looked-up" from the stress-strain data for the bar in question.

The nominal stress in the bar, i.e. outside the locally reduced area, is $\sigma_n = \sigma_i$ / (Area Ratio).

The nominal strain, ε_n, is then returned from the yield function.

This correction is also illustrated in Figure 3-2. Unfortunately, this correction did not account for the complete gage effect. Attempts to apply the correction to all the rebar data did not improve the data, and in some cases made it worse. As a result, it was decided not to apply the correction to the data, but to recognize its presence and consider it, as appropriate, when comparing the data to analyses.

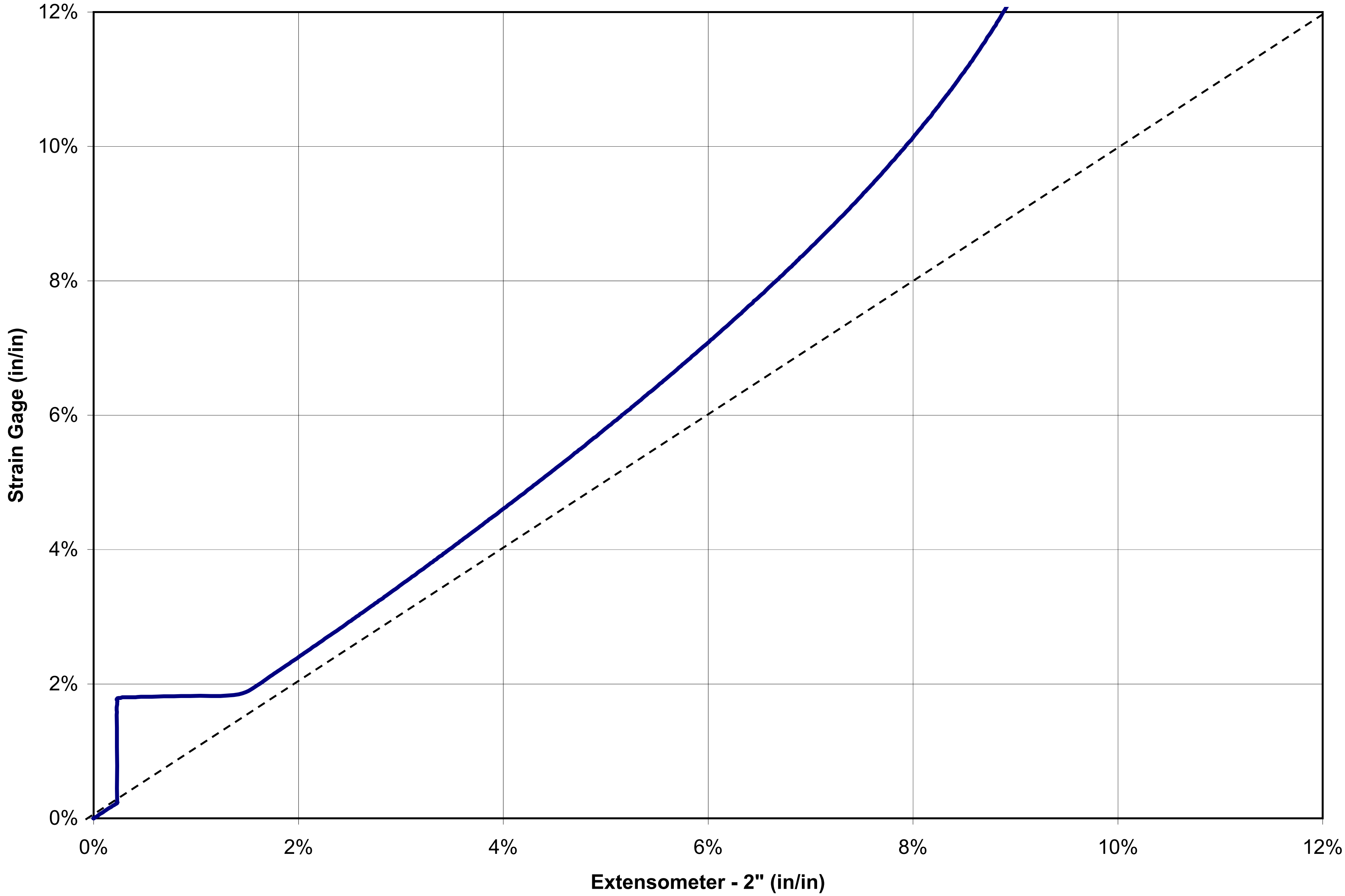

Figure 3-1. Comparison of Strain at Z6 (Azimuth 135 degrees, Elev. 6280)

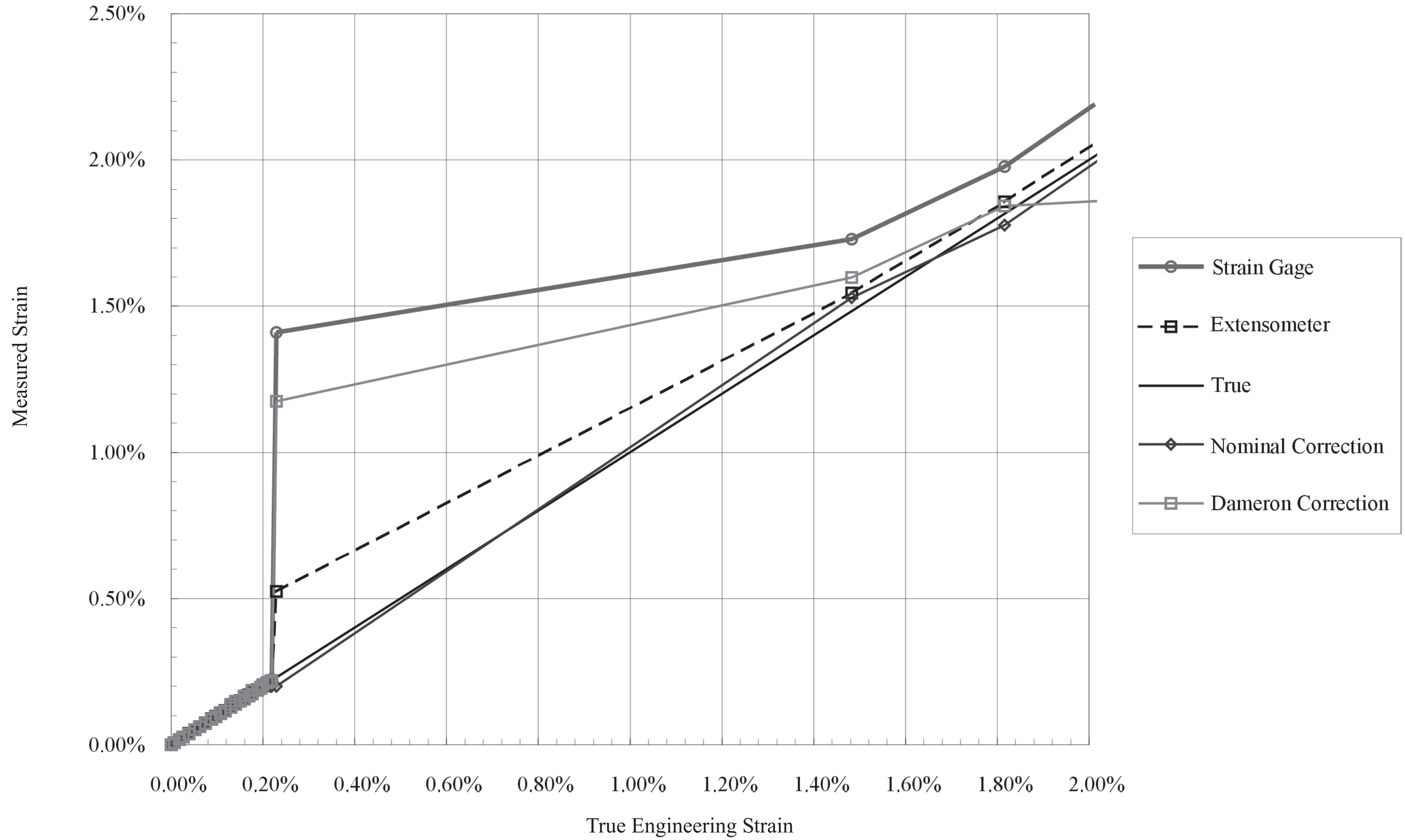

Figure 3-2. Rebar Tensile Test Simulation

4.0 COMPARISONS OF PRETEST ANALYSIS RESULTS WITH THE TEST

The pretest analyses consisted of global axisymmetric analysis and local model analysis. The local models analyzed were: the E/H region, the personnel airlock region, and the M/S penetration region. A detailed 3DCM was also developed to investigate tendon behavior in the cylinder and 3D effects that drive the local strain concentrations near the penetrations. A highly detailed representation of the wall-basemat juncture region was included in the 2D axisymmetric model, making a total of five pretest analysis models. The results of the initial pretest analyses were published in 1999 [1] and were the basis of the SNL/ANATECH contribution to an international Round Robin Pretest Analysis exercise [3]. As described in Chapter 2, a final pretest analysis was completed in 2000, immediately prior to the LST.

This chapter compares the test measurements to both pretest analyses. Test data are compared to the results of the analysis. For example, the results of the 3DCM model, with its explicit tendon representation, are compared to the tendon strain or force data, whereas results of the axisymmetric model are compared to those response data that are relatively independent of the azimuth, such as free-field displacements and the behavior of the wall-base junction and the dome response. The same rationale is used to compare and discuss failure modes.

A set of 55 SOLs, each associated with an actual gage (or set of gages), was identified by the project team to provide a comprehensive suite of data sets for comparison to the round robin analysis results. The SOLs are described in Table 4-1, along with the associated gage(s). After reviewing the PCCV LST data, these locations were indeed useful comparison points. This chapter thus makes extensive use of comparisons at these 55 SOLs. In some cases, to learn more about how the analysis or the test responded at another location, additional plots and comparisons were extracted from the analytical models and the test data.

Table 4-1. Standard Output Locations

Loc. #	Type	Orientation	Az. (deg)	El. (m)	Comments	General Location	Instr. ID (1st)	ID (2nd gage)
1	Displacement	Vertical	135	0	Outside Cylinder	Top of Basemat	DL-M-Z0-01	
2	Displacement	Radial	135	0.25	Inside Liner Surface	Base of Cylinder	DL-R-Z2-01	
3	Displacement	Radial	135	1.43	Inside Liner Surface	Base of Cylinder	DL-R-Z3-01	
4	Displacement	Radial	135	2.63	Inside Liner Surface	Base of Cylinder	DT-R-Z4-01	
5	Displacement	Radial	135	4.68	Inside Liner Surface	E/H elev.	DT-R-Z5-01	
6	Displacement	Radial	135	6.2	Inside Liner Surface	Approximate Midheight	DT-R-Z6-01	
7	Displacement	Radial	135	10.75	Inside Liner Surface	Springline	DT-R-Z9-01	
8	Displacement	Vertical	135	10.75	Inside Liner Surface	Springline	DT-M-Z9-01	
9	Displacement	Horiz. (Rad)	135	14.55	Inside Liner Surface	Dome 45 deg	CP-R-Z11-01	
10	Displacement	Vertical	135	14.55	Inside Liner Surface	Dome 45 deg.	DT-M-Z11-01	
11	Displacement	Vertical	135	16.13	Inside Liner Surface	Dome apex	DT-M-Z13-01	
12	Displacement	Radial	90	6.2	Inside Liner Surface	Midheight @ Buttress	CP-R-D6-01	
13	Displacement	Radial	90	10.75	Inside Liner Surface	Springline @ Buttress	CP-R-D9-01	

Table 4-1. Standard Output Locations

Loc. #	Type	Orientation	Az. (deg)	El. (m)	Comments	General Location	Instr. ID (1st)	ID (2nd gage)
14	Displacement	Radial	324	4.675	Inside Liner Surface	Center of E//H	CP-R-L5-01	
15	Displacement	Radial	62	4.525	Inside Liner Surface	Center of A/L	CP-R-C5-01	
16	Rebar Strain	Meridional	135	0.05	Inner Rebar Layer	Base of Cylinder	RS-M-Z1-01	
17	Rebar Strain	Meridional	135	0.05	Outer Rebar Layer	Base of Cylinder	RS-M-Z1-02	
18	Rebar Strain	Meridional	135	0.25	Inner Rebar Layer	Base of Cylinder	RS-M-Z2-01	
19	Rebar Strain	Meridional	135	0.25	Outer Rebar Layer	Base of Cylinder	RS-M-Z2-02	
20	Rebar Strain	Meridional	135	1.43	Inner Rebar Layer	Base of Cylinder	RS-M-Z3-01	
21	Rebar Strain	Meridional	135	1.43	Outer Rebar Layer	Base of Cylinder	RS-M-Z3-02	
22	Rebar Strain	Hoop	135	6.2	Outer Rebar Layer	Midheight	RS-C-Z6-02	
23	Rebar Strain	Meridional	135	6.2	Outer Rebar Layer	Midheight	RS-M-Z6-02	
24	Rebar Strain	Hoop	135	10.75	Outer Rebar Layer	Springline	RS-C-Z9-02	
25	Rebar Strain	Meridional	135	10.75	Inner Rebar Layer	Springline	RS-M-Z9-01	RS-M-Z9-03
26	Rebar Strain	Meridional	135	10.75	Outer Rebar Layer	Springline	RS-M-Z9-02	RS-M-Z9-04
27	Rebar Strain	Hoop	135	14.55	Outer Rebar Layer	Dome 45 deg.	RS-C-Z11-02	
28	Rebar Strain	Meridional	135	14.55	Inner Rebar Layer	Dome 45 deg.	RS-M-Z11-01	RS-M-Z11-03
29	Rebar Strain	Meridional	135	14.55	Outer Rebar Layer	Dome 45 deg.	RS-M-Z11-02	RS-M-Z11-04
30	Rebar Strain	Meridional	90	0.05	Inner Rebar Layer	Base of Cylinder @ Buttress	RS-M-D1-01	
31	Rebar Strain	Meridional	90	0.05	Outer Rebar Layer	Base of Cylinder @ Buttress	RS-M-D1-02	
32	Rebar Strain	Hoop	90	6.2	Outer Rebar Layer	Midheight @ Buttress	RS-C-D6-02	
33	Rebar Strain	Meridional	90	6.2	Outer Rebar Layer	Midheight @ Buttress	RS-M-D6-02	
34	Liner Strain	Meridional	0	0.01	Inside Liner Surface	Base of Cylinder	LSI-M-A1-01	
35	Liner Strain	Meridional	0	0.01	Outside Liner Surface	Base of Cylinder	LSO-M-A1-03	
36	Liner Strain	Meridional	135	0.25	Inside Liner Surface	Base of Cylinder	LSI-M-Z2-01	

Table 4-1. Standard Output Locations

Loc. #	Type	Orientation	Az. (deg)	El. (m)	Comments	General Location	Instr. ID (1st)	ID (2nd gage)
37	Liner Strain	Hoop	135	0.25	Inside Liner Surface	Base of Cylinder	LSI-C-Z2-01	
38	Liner Strain	Meridional	135	6.2	Inside Liner Surface	Midheight	LSI-M-Z6-01	
39	Liner Strain	Hoop	135	6.2	Inside Liner Surface	Midheight	LSI-C-Z6-01	
40	Liner Strain	Meridional	135	10.75	Inside Liner Surface	Springline	LSI-M-Z9-01	
41	Liner Strain	Hoop	135	10.75	Inside Liner Surface	Springline	LCI-C-Z9-01	
42	Liner Strain	Meridional	135	16.13	Inside Liner Surface	Dome apex	LSI-M-Z13-01	LSI-C-Z13-01
43	Liner Strain	Meridional	90	6.2	Inside Liner Surface	Midheight @ Buttress	LSI-M-D6-01	
44	Liner Strain	Hoop	90	6.2	Inside Liner Surface	Midheight @ Buttress	LSI-C-D6-01	
45	Liner Strain	Hoop	334	4.675	Inside Liner Surface	10 mm from thickened plate	LSI-C-A5-03	
46	Liner Strain	Hoop	58	4.525	Inside Liner Surface	10 mm from thickened plate	LSI-C-C5-03	
47	Base Liner	Radial	135	0	100 mm Inside Cylinder	FF Basemat Liner Strain	LSI-R-Z1-08	
48	Tendon Strain	Hairpin	180	15.6	Tendon - V37	Tendon Apex	TT-M-G12-01	TF-M-G12-01
49	Tendon Strain	Hairpin	135	10.75	Tendon - V46	Tendon Springline	TT-M-Z9-01	TF-M-Z9-01
50	Tendon Strain	Hoop	90	6.58	Tendon - H53	Mid. Tendon	TT-C-D6-01	TT-C-D6-02
51	Tendon Strain	Hoop	180	6.58	Tendon - H53	¼ - Tendon	TT-C-G6-01	TF-C-G6-01
52	Tendon Strain	Hoop	280	6.58	Tendon - H53	Tendon Near Buttress	TT-C-K6-01	TF-C-K6-01
53	Tendon Strain	Hoop	0	4.57	Tendon - H35	Tendon between E/H and A/L	TT-C-A5-01	TT-C-A5-02
54	Tendon Force	Hairpin	241	-1.16	Tendon - V37	Tendon Gallery	TL-—10-03	
55	Tendon Force	Hoop	275	6.58	Tendon - H53	@ Buttress	TL-C-J6-02	

4.1 Displacements

The most fundamental response quantities to compare are displacements, so significant emphasis was placed on measurements and comparisons of these. As discussed later, various local phenomena can significantly influence the measurements of strains in the liner, reinforcement, or tendons, but displacement measurements are regarded as the most reliable source of general response information. Much global strain information can also be inferred from displacement measurement by using, for example, a kinematic relationship such as

$$e_h = \frac{u_r}{R} \, ,$$

where ε_h is the hoop strain, u_r is the radial displacement, and R is the radius.

Meridional strain can also be inferred from the difference in vertical displacement divided by the gage length in between.

Displacements as a function of pressure are compared at SOLs 1 through 14 in Figures 4-1 through 4-4. Each comparison plot includes four curves:

1. LST DOR
2. LST correction (LST DOR corrected for ambient temperature effects, as per Reference [8])
3. 2000 analysis (final pretest analysis performed just prior to the test and discussed in Chapter 2)
4. 1999 analysis (published pretest analysis [1] and [4])

A discussion of each comparison is listed by location, below. One additional adjustment to the analysis results should be noted. To focus on comparing the pressure response of the model, all of the analysis results were shifted so that the calculated zero pressure response matched the data at the start of the test. This eliminated differences that could occur due to creep or other time dependent effects. The only other loading conditions considered in the analyses, besides internal pressurization, were dead load and prestressing loads. Since the PCCV instrumentation was initialized on March 3, 2000, after construction was essentially complete, response to dead load was not measured. The model was then completely prestressed, exposed to six months of ambient temperature fluctuations (during which the model was allowed to creep, shrink, and relax), and finally to preliminary pressure testing prior to the start of the LST. By adjusting the analysis results, differences due to these secondary effects were eliminated from the comparison to the pressure response.

SOL 1. Vertical Displacement at Outside Edge, Top of Basemat. The test data shows virtually no uplift, while the analyses at 3.3 Pd show 2.3mm and 9mm for the 1999 and 2000 analyses, respectively. The apparent discrepancy between the test data and the analysis results may be an artifact from the way basemat uplift was measured during the LST. The displacement gage(s) were mounted to measure the relative displacement between the bottom of the basemat and the top of the underlying mud-mat, since there were no other practical means of referencing a fixed point. In an analysis that uses a very stiff foundation, even very small basemat curvatures create appreciable basemat uplift, but being much more flexible, mud-mat flexure can be assumed to follow basemat flexure. As a result, there could have been appreciable basemat flexure without the mud-mat ever separating from the PCCV basemat and, therefore, no observed relative motion. Unfortunately, there is no way to corroborate the accuracy of the analysis predictions for basemat uplift. The differences between the analyses and the test, and between the analyses themselves, are both noteworthy and are discussed in the revised global posttest analysis in Chapter 5.

SOLs 2, 3, 4, 5, 6, 14, and 15. There is very good agreement (to within +/- 4% over most of the pressurization history) for all of the cylinder radial displacement locations between analysis and test, but a few general observations can be made. The analyses and the test consistently exhibit a sharp jump in displacement at approximately 1.45 Pd (0.57 MPa). This is possibly associated with the onset of hoop cracking in the cylinder, although the data is not entirely conclusive on this point. At first, it was thought this was associated with the 3 hour pressure hold at 1.5 Pd, but the jump in the data occurs just prior to the 1.5 Pd pressure hold. Also, there is no similar jump in data at the 2.0 Pd pressure hold, which was held overnight. The radial displacement at the A/L is somewhat overpredicted beyond 2.8 Pd.

SOLs 7, 8, 9, 10, and 11. There is poor correlation between analysis and test data for these displacements in the dome and springline. Radial displacements at the springline were underpredicted in analysis by roughly a factor of 2. Vertical displacement was also off, but overprediction is understandable, given the significant overprediction of basemat uplift. (The 1999 analysis better predicts this quantity than the 2000 analysis.) The same is true for vertical displacements at the dome 45-degree-angle and the apex, but the radial displacement at the dome 45-degree-angle is well predicted (to within +/- 20%).

SOLs 12 and 13. At the buttress locations, the analysis overpredicted the measured response at the midheight and underpredicted the measured response at the springline. This is consistent with the trends observed in the 3DCM analysis, which is discussed in much more detail in Chapter 6. Note that for SOLs where axisymmetric analysis is inapplicable, only a "2000" results curve is plotted.

4.2 Rebar Comparisons

Rebar comparisons are made in Figures 4-5 through 4-9.

SOLs 16, 17, 18, 19, 20, and 21. This series of locations compares inner and outer meridional rebars in a series near the base of the cylinder wall, which is a zone of significant flexure and shear. In general, the strains in the inner rebar layers agree fairly well with analysis and the outer rebar layers show more noticeable differences. The main reason for this may be simply that the outer rebar strains have quite small amplitudes, since the wall's vertical flexure tends to add tension on the inside and compression on the outside surfaces. It is often difficult to match a test measurement of very small amplitude (i.e., percentage differences may appear large, while in absolute terms, the differences are quite small). The predicted trends do appear to be reasonable, however. It should also be noted that the outer rebars that were gaged are likely to be very close to the neutral axis of bending in the section. Thus, if the analytical prediction of neutral axis location is only off by a few millimeters, the strain predictions immediately adjacent to this could be at large variance with the test model, or even have opposite signs. The inside bars are sufficiently far from the neutral axis of bending to prevent such sensitivity.

SOLs 22 and 23. These locations compare hoop and meridional rebar strain at the cylinder midheight. Agreement with analysis is generally good, although the hoop bar strains late in the test tend to be underpredicted. This difference has been attributed to rebar gage effects, as discussed in Chapter 3. The argument is that the analysis agrees well on radial displacements at this location, so by kinematics, it follows that the prediction of global hoop strain at this location is also good.

SOLs 24, 25, and 26. These locations compare a hoop rebar and an inner and outer meridional rebar at the springline. Again, the hoop rebar strain and inner rebar strain predictions show similar trends to the measurements, while the outer rebar strain is significantly overpredicted. The same observations made at the wall-base juncture apply here. Due to the radial stiffness differential between cylinder and dome, the springline is once again a point of significant meridional bending, with tension on the inside and compression on the outside. (This flexural component is in addition to the underlying tension caused by the pr/2t cylinder stress.) As an indicator, the measurements for the inside meridional bar reaches .0013 by the end of the test (3.3 Pd), while the measurement for the outside bar only reaches .00022.

SOL 27, 28, and 29. These rebar strain measurements in inner and outer hoop and meridional rebar show good agreement to analysis for the hoop rebar, but poor agreement for both meridional rebar. This observation and the dome displacement observation clearly show that the analysis overpredicted vertical deformations in the dome.

SOL 30, 31, 32, and 33. These comparisons are for the meridional (inner and outer) and hoop rebar at the 90 degree buttress. The comparisons of inner meridional rebar strain at the base of the wall are good (to within about 25%), while for the outer meridional rebars they are significantly overpredicted. The previous argument about local bending and proximity to the neutral axis may also apply here. The buttress hoop rebar strain at cylinder midheight is also significantly overpredicted.

4.3 Liner Strain Comparisons

Liner strain comparisons are made in Figures 4-10 through 4-13.

SOL 34, 35, 36, and 37. The first four comparisons are for strains near the wall-base juncture at azimuth 0 degrees and azimuth 135 degrees, inside and outside liner surface. At elevation 0.01 meters, the analysis shows a similar trend to the data, but overpredicts the magnitude. This comparison may be highly influenced by gage placement and by the location for extracting the analytical data. The location is within just a few millimeters of a sharp stiffness discontinuity. There is also some evidence in the test data that the liner base anchor may have begun to pull out of the concrete; if this indeed occurred, it would lessen the severity of the stiffness discontinuity and the meridional strains near the wall-base juncture. Unfortunately, the liner strain gages at azimuth 135 degrees were damaged by welding operations during the PCCV model construction, so the evidence supporting this hypothesis is limited. The meridional and hoop strain comparisons at 0.25 meters elevation show fair agreement. It is interesting to note that the hoop gages at 0.25 meters elevation show positive values during prestress and a negative trend during pressurization. This is counter to the rest of the cylinder and is likely caused by the reverse in vertical curvature that takes place at this elevation, and apparently is a Poisson Effect caused by wall flexure.

SOL 38 and 39. Hoop and meridional strain comparisons at cylinder midheight show similar trends. At approximately 2.8 Pd, the test data indicates significant yielding of the liner in the hoop direction. The analysis results also demonstrate a change in stiffness at this pressure, but not so sharply. Note that the analysis results are purely global response, taken from axisymmetric analysis, while liner strain measurements can be influenced by local details on the liner, such as proximity to stiffeners, weld seams, or even proximity to a concrete crack behind the liner.

SOL 40, 41, and 42. Hoop and meridional strain comparisons at the springline show good agreement (within ~10%) for hoop behavior, but the meridional strain, which is likely influenced significantly by vertical bending behavior, is overpredicted by analysis. This is consistent with the observed trend that vertical deformations in the dome were overpredicted by analysis. The meridional strain comparison at the dome apex shows fairly good agreement (within ~25%).

SOL 43 and 44. These locations compare meridional and hoop strain near the 90 degree buttress at the cylinder midheight. The hoop strain compares very closely, while the meridional strain is overpredicted.

SOL 45 and 46. These locations are intended to capture strain concentration locations near the thickened insert plate of the E/H and A/L, respectively. While at pressures lower than about 2.7 Pd, there is fair agreement with the measurements, clearly the local analyses predicted a strong strain concentration that did not occur in the test. This fundamental difference between the analytical predictions and the test is discussed later in detail.

SOL 47. This location is on the liner at the basemat, 100 mm inside the cylinder. While the strain comparisons at least show a similar trend, there are large differences in magnitude. However, the measured data and the analysis predictions are small, so quantities being compared are also small.

4.4 Tendon Comparisons

Tendon gage versus analysis (pressure histories) comparisons are made in Figure 4-14 and 4-15

SOL 48, 49, and 54. These locations compare strain and load cell force in two vertical (hairpin) tendons. The comparisons of strain are fairly good, while the comparison of load cell force is somewhat overpredicted.

SOL 50, 52, 53, and 55. These locations compare strain for hoop tendon H53 (mid-tendon, near buttress, and between E/H and A/L) and load cell force for hoop tendon H53. The strain comparisons generally show good agreement, except near the buttress, where the analysis overpredicted. The load cell force also shows reasonably good agreement.

An overview of comparisons of analytically predicted to actual tendon behavior is provided in Figures 4-16 through 4-22. These figures combine the test measurement information from load cells and the average of the wire strain gages.

The wire strain gage data was converted to force by SNL using the stress versus strain curves for the total tendon. These were provided in Ref. [8]. The analysis data for the hoop tendon comparisons is from the pretest 3DCM analysis. More hoop tendon comparisons are provided in Chapter 6 in the discussion on the 3DCM. The reader is also directed to those Figures (6-3 to 6-6) for the following discussion.

The hoop tendon data provides the following insights into the PCCV hoop tendon behavior and the predictions of behavior provided by the pretest 3DCM analysis.

1. The initial prestress anchor forces put into the pretest model have the same shape as the basic design friction assumption and roughly 9% lower magnitude. This 9% reduction from design values was incorporated to address the long term losses that occurred between initial seating and the LST. This strategy for initial anchor force, on average, agrees well with the tendon anchor force measurements taken just prior to LST pressurization. These observations are based on comparing the "Analysis @ 0.000" anchor force data to the data points at "9/26/00 10:03 0.00." At H11, H35, H53, H67, and H68, the zero pressure anchor forces are generally in good agreement with the analysis, and are generally 5% to 10% lower than the design assumptions.

2. The shape of the tendon stress distribution at the start of the LST also shows a similar trend compared with measurements, implying that the angular friction and anchor set modeling assumptions at the start of the test (which were made based on standard design assumptions) were reasonable. There is some scatter in the level of agreement, however. Tendon H11 shows about 20% less angular friction loss than assumed, while H35, H53, and H67 show much closer agreement. H68 also shows some scatter in the measured friction loss profile.

3. Some of the hoop tendon stress distributions during pressurization showed poor agreement with the pretest analysis. This is based on comparing the analysis curve at 1.17 MPa (3.0 Pd) to the data at 1.162 MPa. While H11 and H53 show fair agreement at the "interior" gages, the anchor forces are significantly over-predicted. Higher on the cylinder (H53 and H67), the interior gages are underpredicted *and* the anchor forces are overpredicted.

4. The cylinder hoop tendon data, in total, shows evidence of changes in friction orientation (i.e. tendon slipping) during pressurization. H53 and H67 show this particularly well. The data indicate that the shape of the tendon stress profile changes during pressurization. The total force increase on the plot is equivalenced to a hoop strain derived from the radial expansion of the cylinder (i.e., H53 $\Delta\varepsilon$=0.48% and H67 $\Delta\varepsilon$=0.45%, while hoop strain from radial expansion is significantly lower at 0.35% and 0.37%.). This implies that portions of the tendons are slipping to accommodate the higher deformation at other azimuths.

The vertical tendon data (Figures 4-17 through 4-22) provide the following insights.

1. As with the hoop tendons, there was about 8% to 10% loss occurrence between the initial prestressing and the start of the LST caused by long term effects and by the System Functionality Test (SFT) and SIT. This is evidenced in Figures 4-17 and 4-18 for tendon V37, Figures 4-19 and 4-20 for V46, and Figures 4-21 and 4-22 for V85. Only V85 showed significant friction losses above the springline, and the other two gaged vertical tendons showed only about half of the friction loss in the dome than what was assumed by the designers and incorporated in the analysis.

2. Comparisons with the axisymmetric analysis show that assuming no friction along the straight portion of the tendon and much smaller friction in the dome would provide improved simulation of the vertical tendon behavior. (As discussed in Chapter 5, this justifies returning to the 1999 axisymmetric analysis as the better vertical tendon simulation.)

4.5 Wall-Base Juncture Shear Behavior

Another local area of the PCCV model that was studied in detail was the wall-base juncture [1]. Some relatively large concrete strains, driven by shear and flexure were predicted to occur as shown in Figure 4-23, but no failure associated with the shear and flexure mechanism was predicted until P > 4.0 Pd, much larger than the 3.3 Pd reached in the LST. Nevertheless, it is of interest to compare special rebar and liner strain measurements taken in the wall-base juncture area to the pretest analysis. Since it was concluded during the posttest work that the 1999 pretest model provided the more appropriate simulation of the true vertical tendon stresses, and since this modeling detail has significant influence on the wall-base juncture behavior, the comparisons to the test are only made to the 1999 predictions.

Because this area was identified as having a high potential for large strains and liner tearing in the preliminary analysis, a significant effort was made to instrument the liner and wall at several azimuths. Specially fabricated 'gage bars' (not part of the model reinforcing) were installed through the thickness of the wall in an attempt to monitor the local strain distribution. Unfortunately, many of the gages installed on the liner and the gage bars were damaged during construction or subsequent water penetration and were not functional during the LST. The typical arrangement of liner strain gages at the wall-base juncture are shown in Figure 4-24. The 'gage bar' strain gages installed in the area are shown schematically in Figure 4-25. Fortunately, a large number of gages survived at the 135 azimuth, which was chosen to represent the axisymmetric behavior of the model. During the test, many of these gages were monitored in real time using this display screen. The gage numbering shown on the screen is tabulated in Table 4-2. A labeling scheme that facilitates analysis versus test comparisons is shown in Figure 4-26.

Table 4-2. Gage Identification for the Basemat Junction Display Screen

Number on Screen	Gage Name
1	GB-M-Z1-05
2	GB-M-Z1-10
3	RS-R-Z2-02
4	GB-M-Z1-15
5	GB-M-Z1-20
7	GB-M-Z1-09
8	RS-R-Z2-01
9	GB-M-Z1-14
10	GB-M-Z1-19
11	GB-M-Z1-03
13	RS-R-Z-1-02
14	GB-M-Z1-13
15	GB-M-Z1-18
18	RS-R-Z1-01
20	GB-M-Z1-22
24	GB-M-Z1-21
25	RS-M-Z2-01
26	RS-M-Z2-02
27	RS-M-Z1-01
28	RS-M-Z1-02
38	RS-M-Z0-13
39	RS-M-Z0-14

Comparisons between wall-base area liner and rebar strain gages are provided in Figures 4-27 through 4-49. The analysis data was zeroed to the experimental measurements, but a specific gage had to be selected for this zeroing. Which gage was selected is clear from observing which data/gage history curves "match" at P=0. The liner strain comparisons near the base of the wall (Figures 4-27 through 4-32) show similar trends to the analysis. When two liner positions are shown (i.e., B, C, etc.), this is provided to straddle strain gage locations that occur between the two analysis liner locations. Thus, often a particular gage will agree well with one of the pair of analysis points or with an average of the two. In general, the agreement shows that the wall-base liner behavior was well simulated by the analysis.

The level of correlation with the rebar gages (Figures 4-33 through 4-49) was not as good, but such was the case in comparing "free-field" rebar strain data, as well. As described in Chapter 3, in general the rebar strain measurements, upon reaching yield ($\varepsilon \cong 0.002$), tend to significantly overstate the actual strain. It is also quite difficult to pinpoint an analysis location that coincides with a rebar strain gage location. Nevertheless, some of the gages show quite good agreement with analysis. These include Axisymmetric Position D compared to GB-M-A1-04 (Figure 4-34), midway between Positions E and J versus GB-M-Z1-05 (Figure 4-35), Position D vs. GB-M-Z1-10 (Figure 4-38), and Position V (in flexural compression) vs. GB-M-Z1-22 (Figure 4-43) and Position W vs. GB-M-Z1-18 (Figure 4-44). These are all vertical bars, indicating that the analysis captured the wall-base flexure behavior reasonably well.

Figures 4-46, 4-47, 4-48, and 4-49 compare stirrup strains. In general, these would be extremely difficult to match with analysis because stirrup strains are so influenced by the precise location of a major shear crack. Nevertheless, Figure 4-48 for stirrup location AB (shown in yellow on Figure 4-26, at about Elev. 12 inches) shows similar behavior to the gage measurements, indicating that shear behavior was simulated reasonably well. Note that all of the stirrup strains (measured and predicted) are well below yield, indicating that at the end of the LST (3.3 Pd), the model is far from developing shear failure.

4.6 Failures: Predicted and Observed

The 3DCM model predicted rupture of hoop tendons near the E/H with strains exceeding 5% at a model pressure of about 3.5 Pd[1]. However, this mode was predicted to be precluded by the liner tearing and leakage failure mode associated with the local models. The failure pressure at which a local analysis computed effective plastic strain that reached the failure strain of approximately 16% was 3.2 Pd, or 1.3MPa. The location for this liner-tearing failure was near the E/H, adjacent to a vertical liner anchor that terminated near the liner insert plate transition. Other local models showed other candidate liner tear locations, several of which were predicted to occur during the pressure range 3.2 Pd to 3.5 Pd, if they were not precluded first by the growth of the first tear and subsequent depressurization of the vessel. Significant candidate tear locations were also predicted near weld seams with hoop stiffener rat-holes, for example, near the 90-degree buttress where hoop strains are elevated due to circumferential bending. Failure at such locations was predicted to occur shortly after the E/H location.

As discussed in detail in Chapter 8, this last type of tear location was the predominant failure mode observed in the LST. Liner tears occurred in 16 locations, and there is evidence (acoustic and pressure/leak-rate measurements) supporting approximately 2.5 Pd as the pressure of the first tear initiation. Although predicted as a general failure mode, the specific location and pressure were not predicted. The following chapters discuss and present conclusions as to why these specific tear events were not explicitly predicted and why the strain predictions at the highest strain location of the pretest analysis was significantly overpredicted.

While the scope and objectives of the pretest analysis work for the 1:4-scale PCCV did not include a formal probabilistic risk assessment of the failure (leakage) pressure prediction, the final probability of liner tearing/leakage versus pressure was described in probabilistic terms with reference to the final list of candidate tearing locations. Combining probabilities and locations produced the following leakage pressure predictions and confidence intervals, which were published prior to the test. Best estimate (Probability = 0.5), $P_{leakage}$=3.2 Pd=1.3 MPa; upper bound (Probability = 0.9), $P_{leakage}$=3.5 Pd=1.4 MPa; lower bound (Probability = 0.1), $P_{leakage}$=2.75 Pd=1.1 MPa. Referring back to the pretest report where these were derived, the first leakage occurred below the 10% probability. This was an unacceptable prediction, but is easily explained by the presence of extensive flaws near weld seams. Such flaws probably can and should be considered in containment probabilistic calculations. Discussion of these issues as they relate to the test observations is also provided in later chapters.

4.7 Discussion and Conclusions of Analysis vs. Test Comparisons

A good overview of the test versus analysis comparisons in this chapter can be made by combining the response history information into deformed shape comparison plots. This information is provided in Figures 4-50 through 4-53. The plots show displaced shape along a horizontal slice (at Elev. 4.68 m) and three vertical slices (at 135, 324, and 90 degree azimuths) at various pressures compared to analysis. The overall conclusions from these and other comparisons in this chapter are as follows.

- Radial displacements were well predicted by global axisymmetric analysis, but dome and overall vertical displacements were significantly overpredicted.

- Based on the gages available, the wall-base juncture behavior appears to have been well predicted by the detailed wall-base juncture (axisymmetric) modeling.

- Maximum pressure (187.9 psig (3.30 Pd), which was primarily a function of the onset of global yielding, was closely predicted by analysis, but the predicted failure mode did not manifest itself. Note that the maximum pressure achieved during the LST was also limited by the capacity of the pressurization system to balance the increasing leak rate after functional failure occurred.

- An initial small leak occurred at 2.5 Pd that was not predicted by analysis, but this probably occurred due to defects associated with weld seam repair.

- Average radial displacement reached 23mm at 3.3 Pd
  - Average hoop strain = 0.0040 (well predicted by global analysis).

- Maximum radial displacement at E/H = 29mm at 3.3 Pd
  - Equivalent hoop strain = 0.0054 (reasonably well predicted by 3DCM, but prediction of some displacements at other azimuths — like the buttresses — was poor).

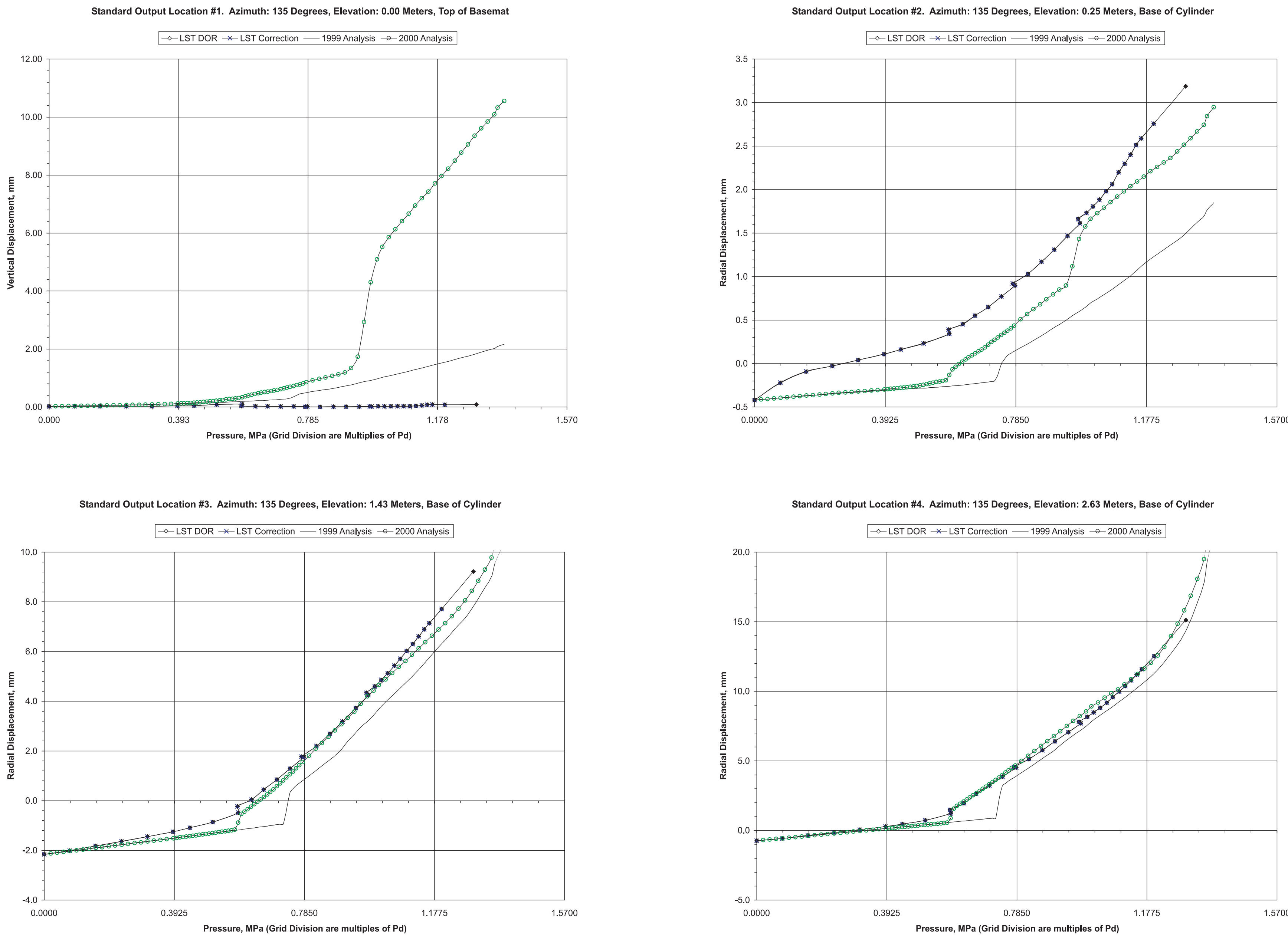

Figure 4-1. Comparisons at Standard Output Location 1, 2, 3, and 4

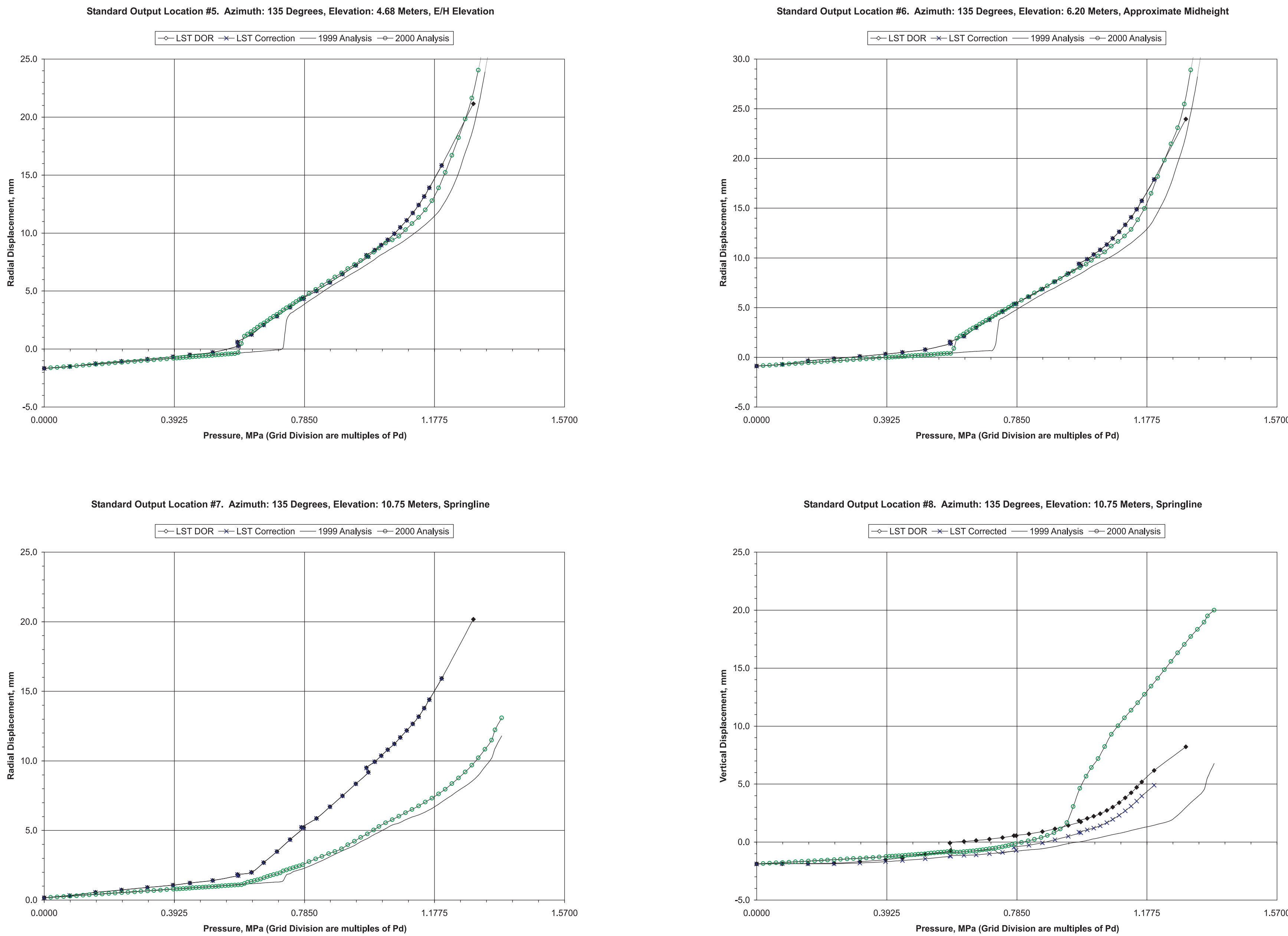

Figure 4-2. Comparisons at Standard Output Location 5, 6, 7, and 8

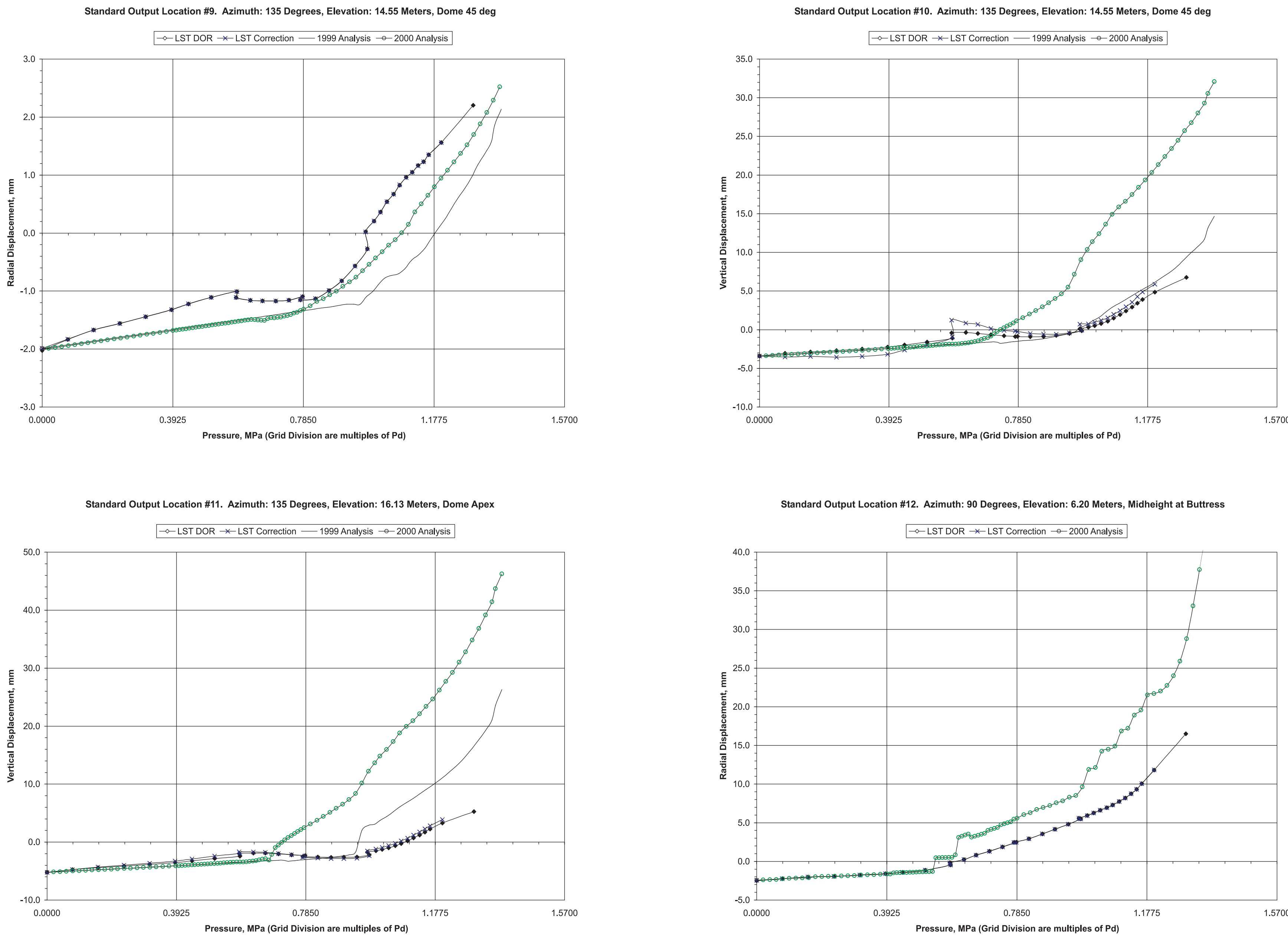

Figure 4-3. Comparisons at Standard Output Location 9, 10, 11, and 12

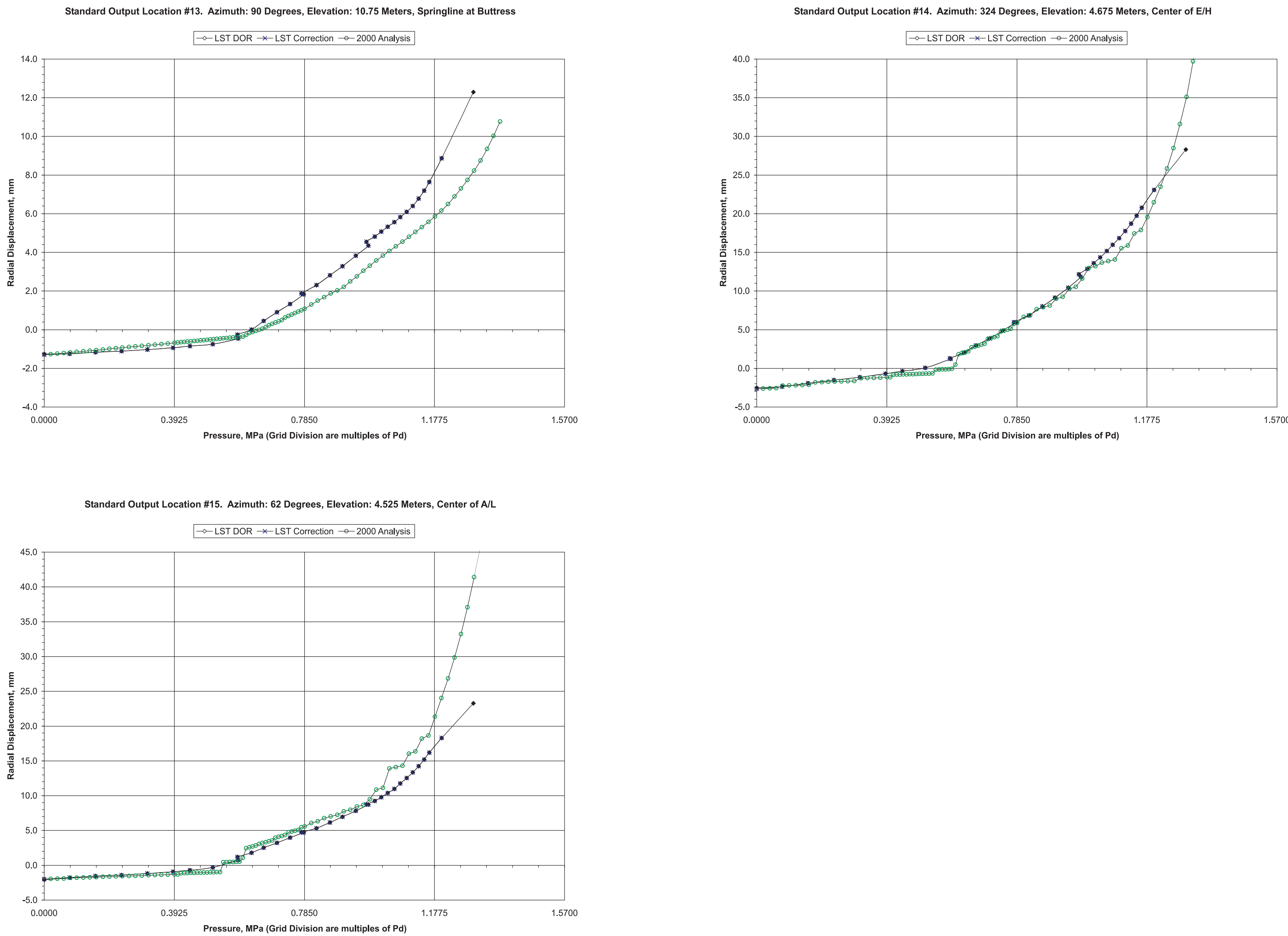

Figure 4-4. Comparisons at Standard Output Location 13, 14, and 15

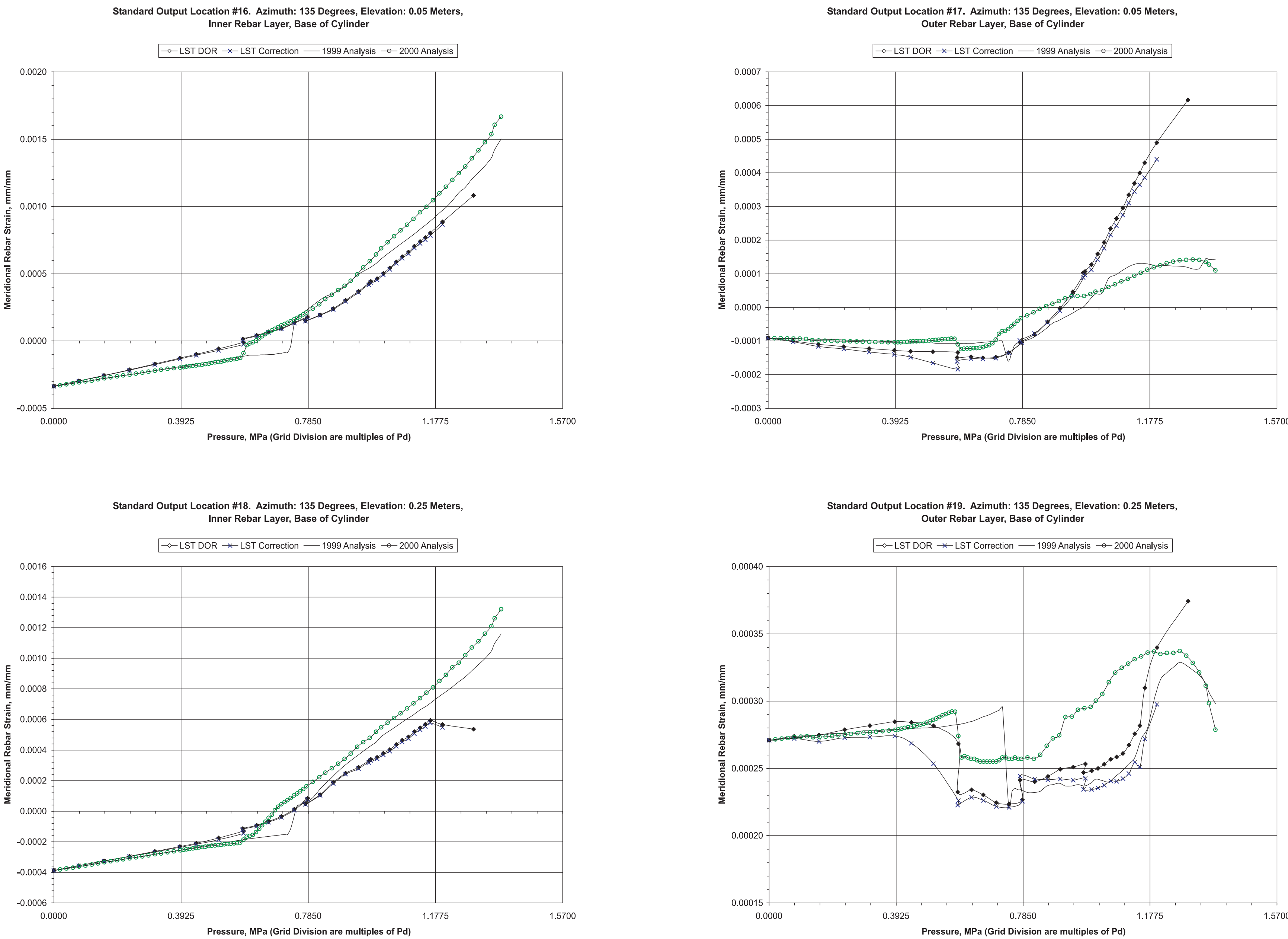

Figure 4-5. Comparisons at Standard Output Location 16, 17, 18, and 19

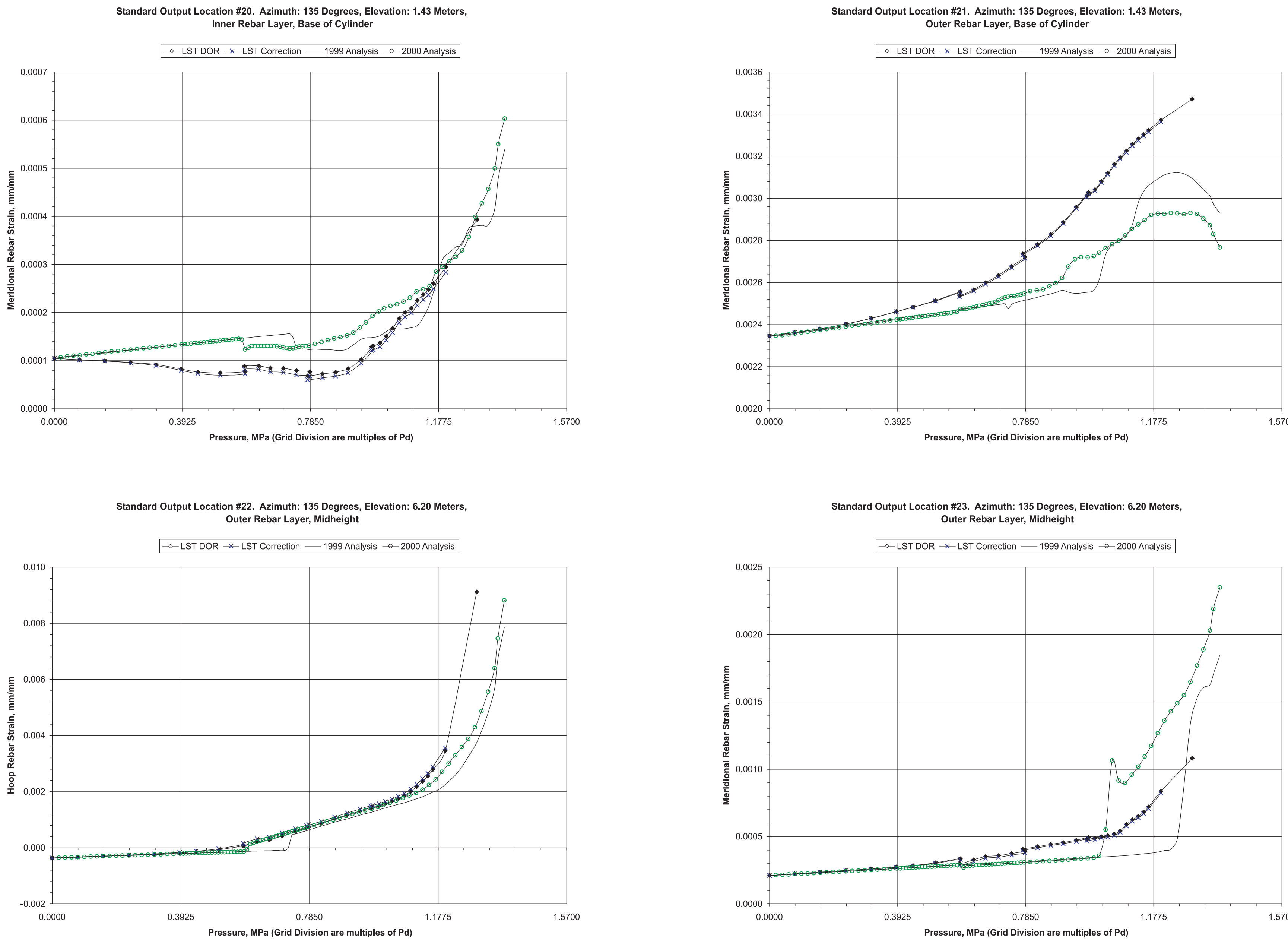

Figure 4-6. Comparisons at Standard Output Location 20, 21, 22, and 23

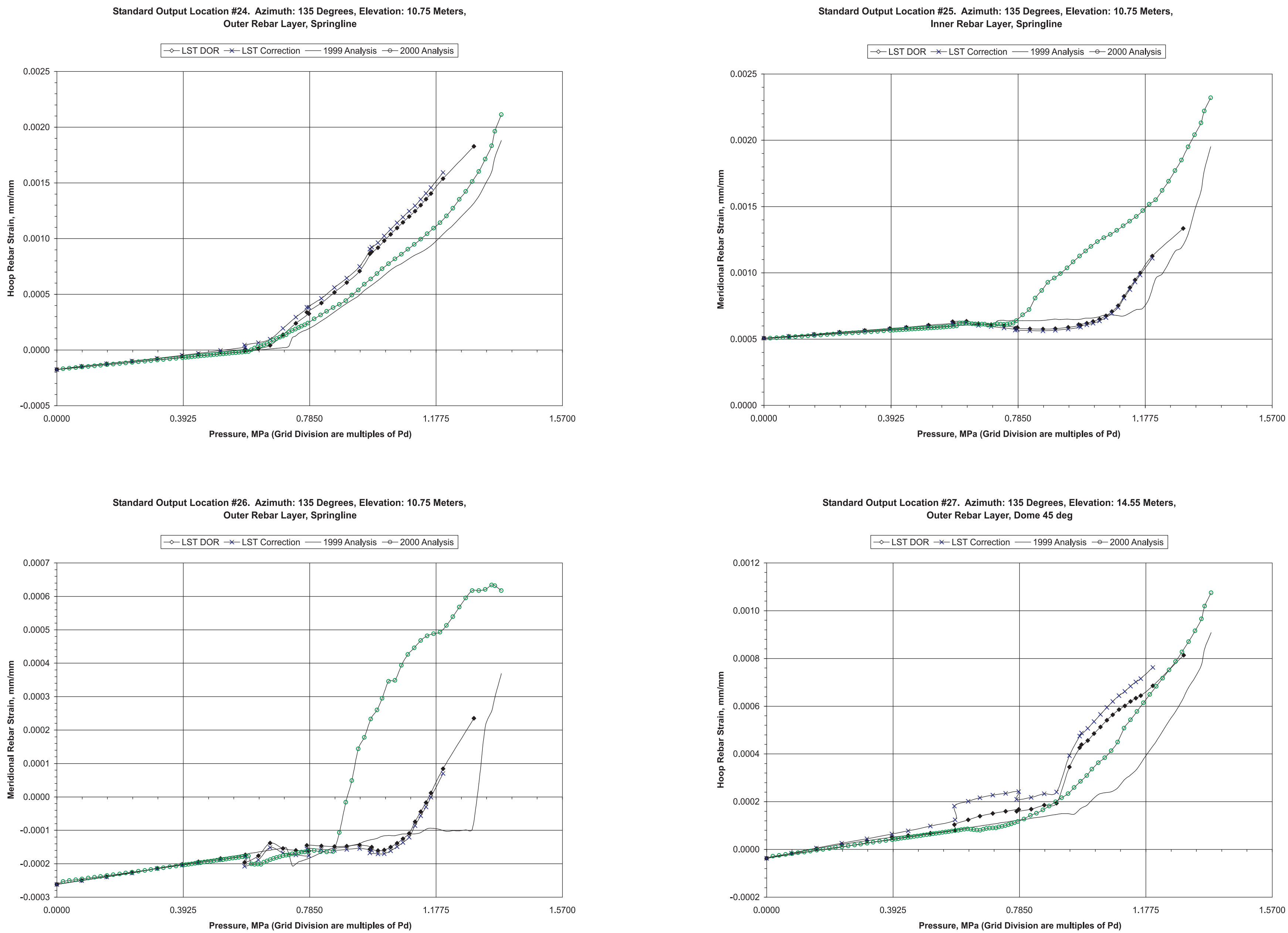

Figure 4-7. Comparisons at Standard Output Location 24, 25, 26, and 27

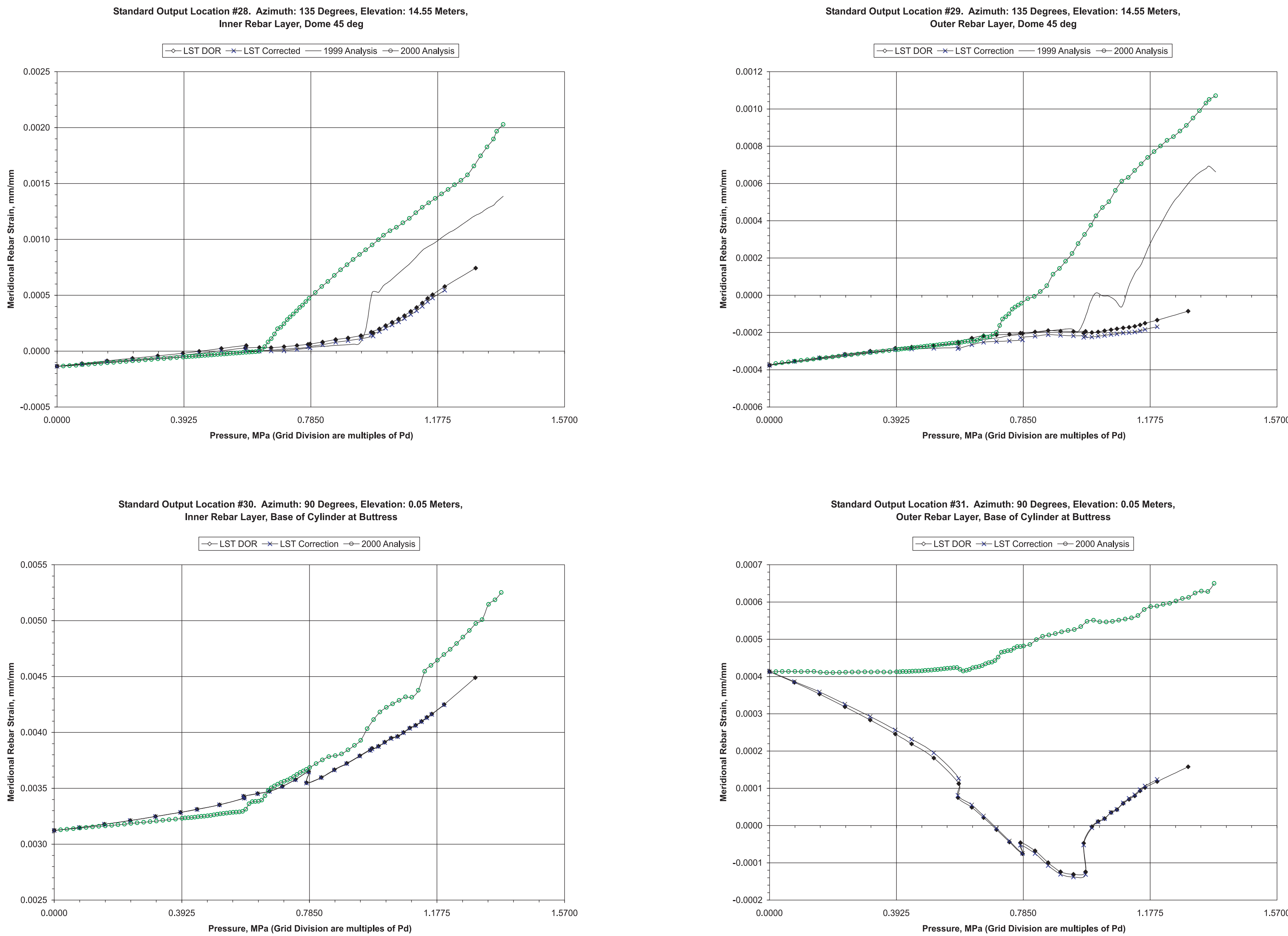

Figure 4-8. Comparisons at Standard Output Location 28, 29, 30, and 31

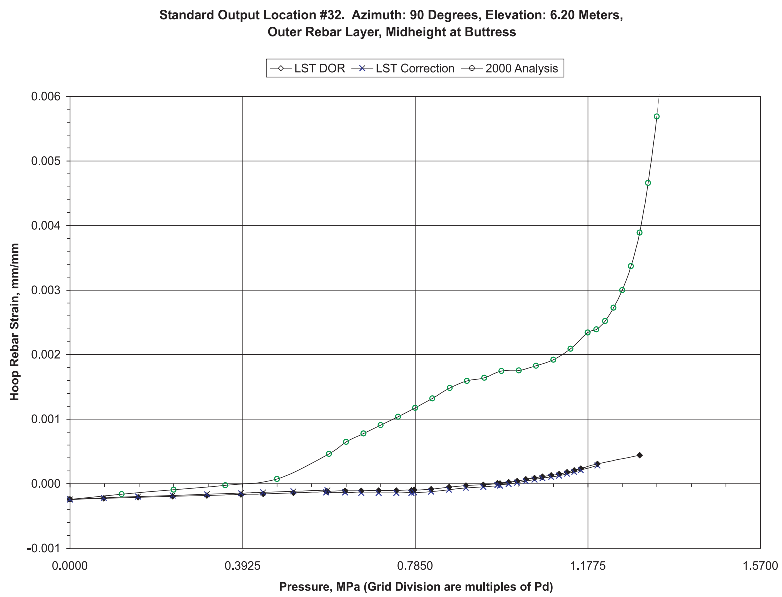

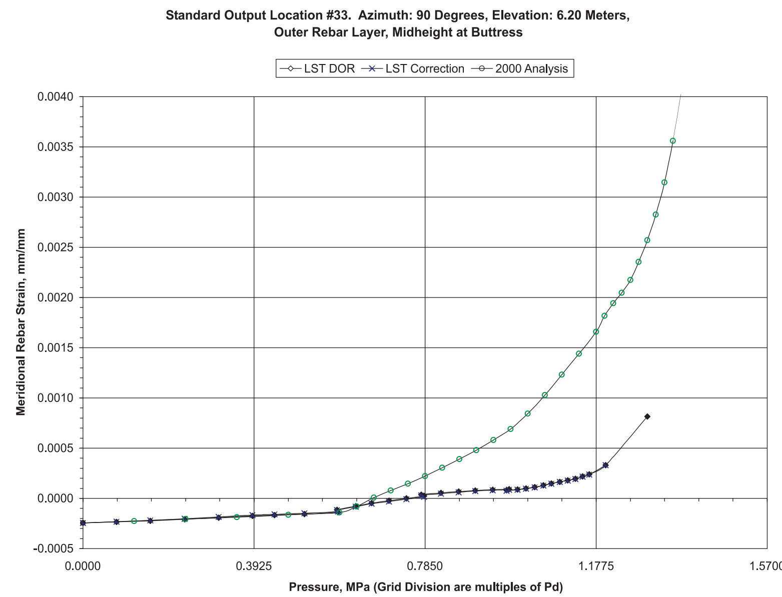

Figure 4-9. Comparisons at Standard Output Location 32 and 33

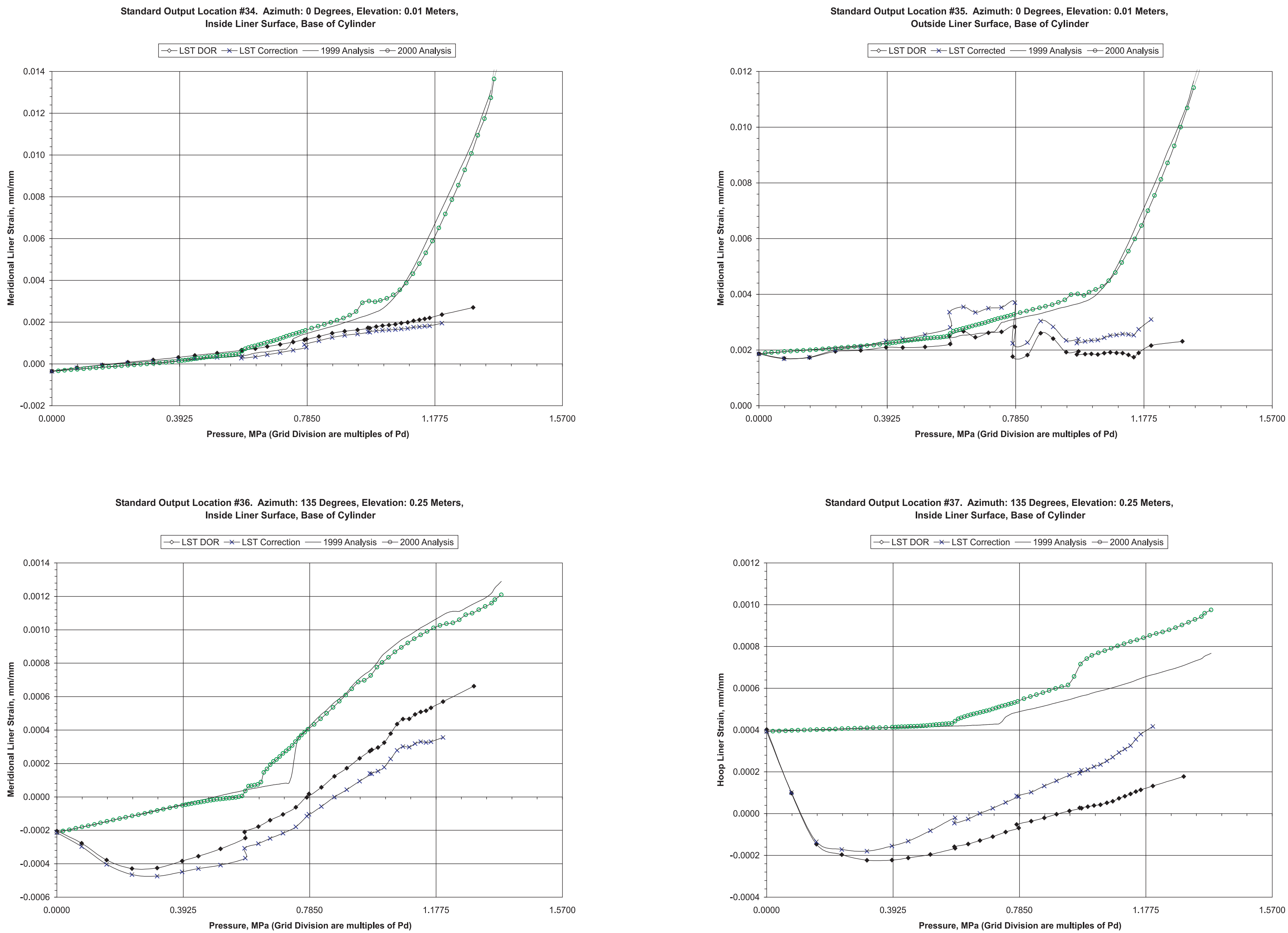

Figure 4-10. Comparisons at Standard Output Location 34, 35, 36, and 37

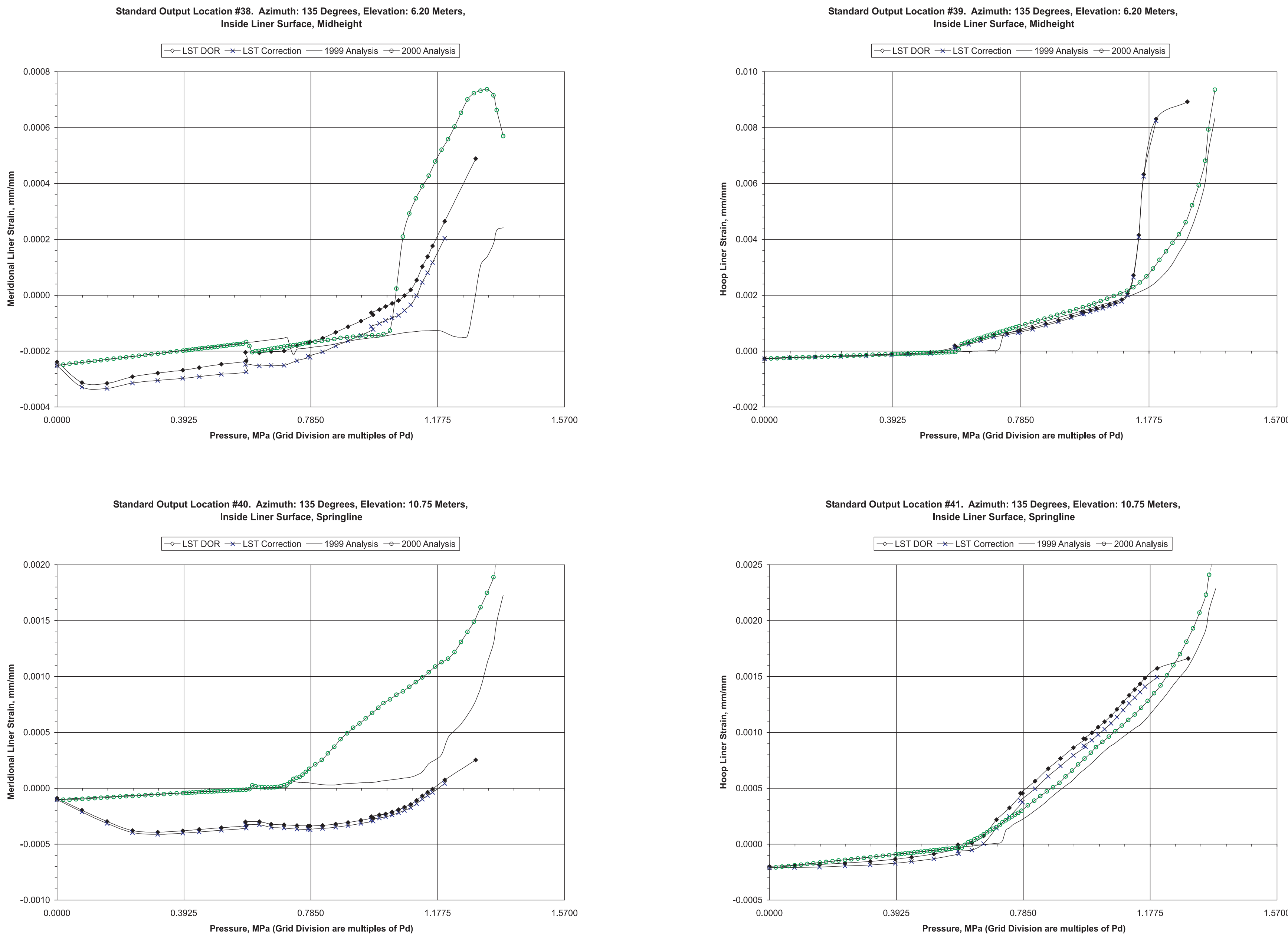

Figure 4-11. Comparisons at Standard Output Location 38, 39, 40, and 41

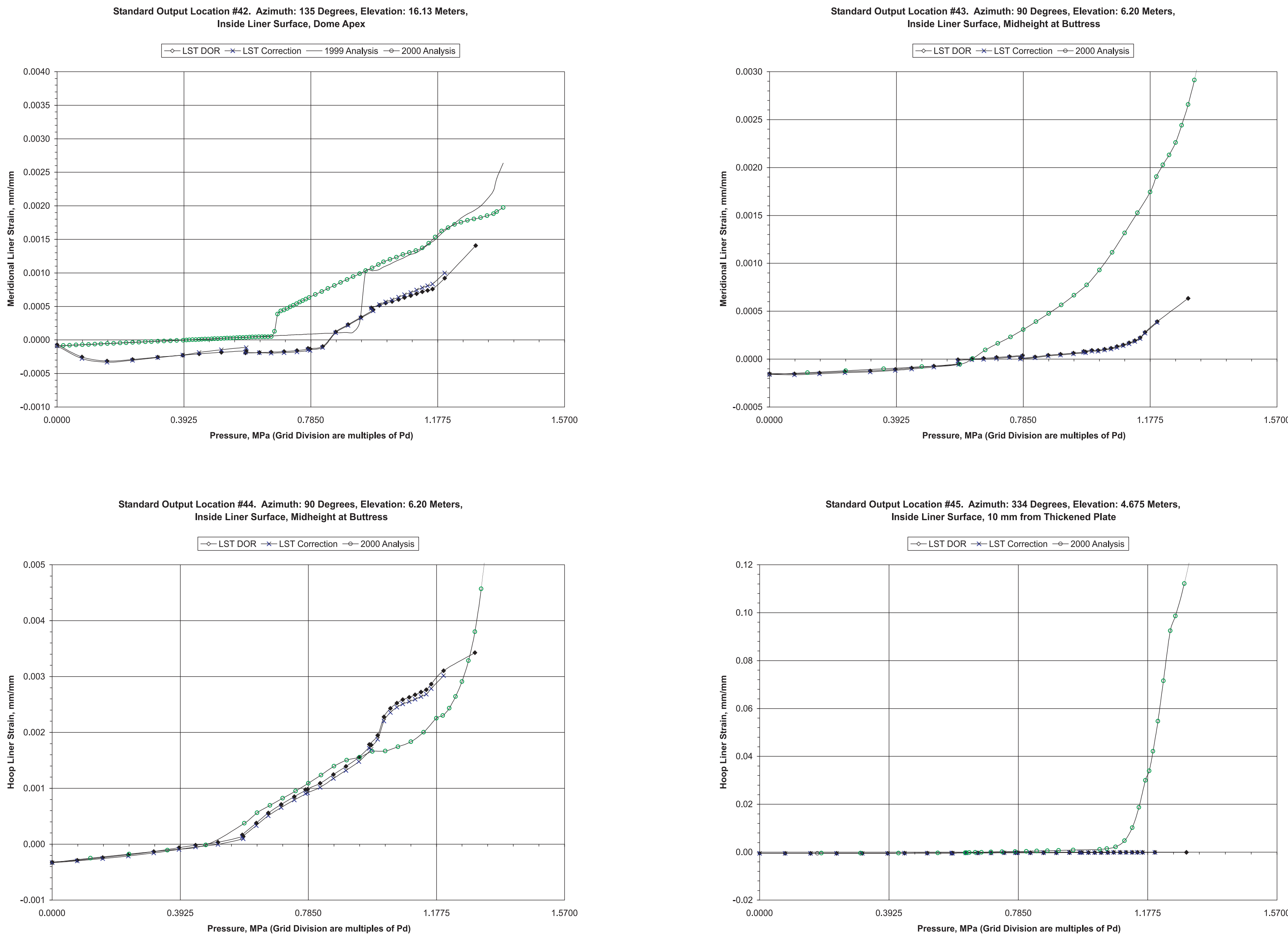

Figure 4-12. Comparisons at Standard Output Location 42, 43, 44, and 45

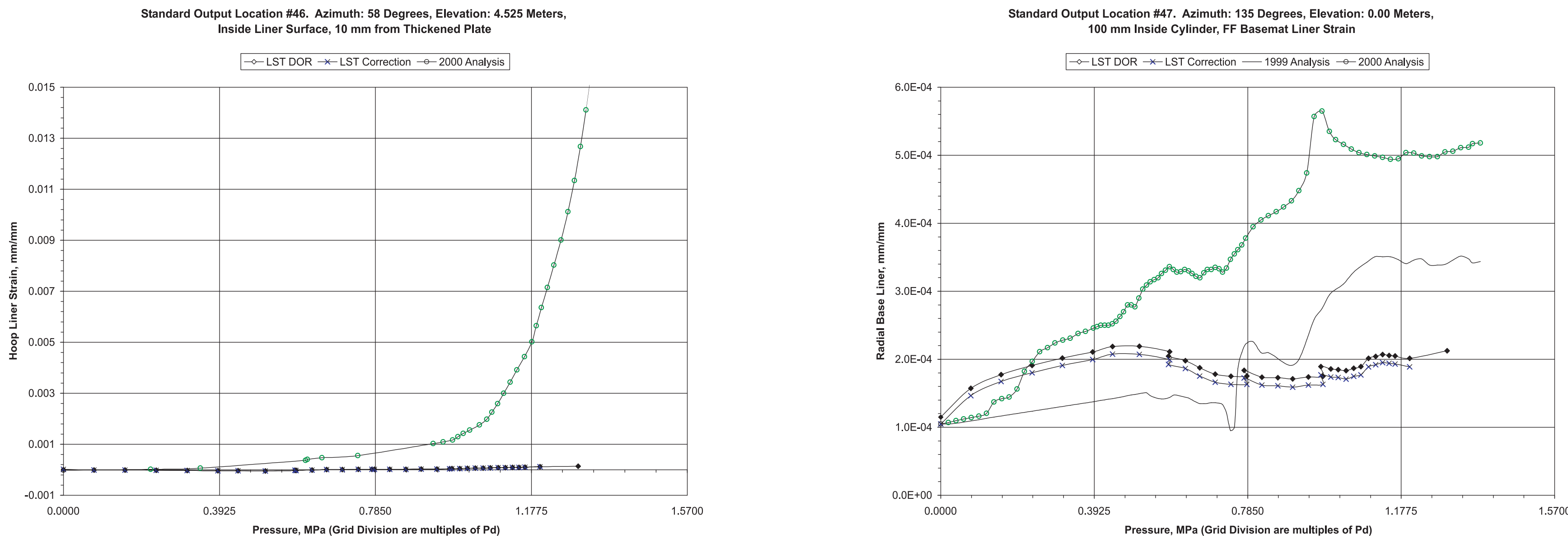

Figure 4-13. Comparisons at Standard Output Location 46 and 47

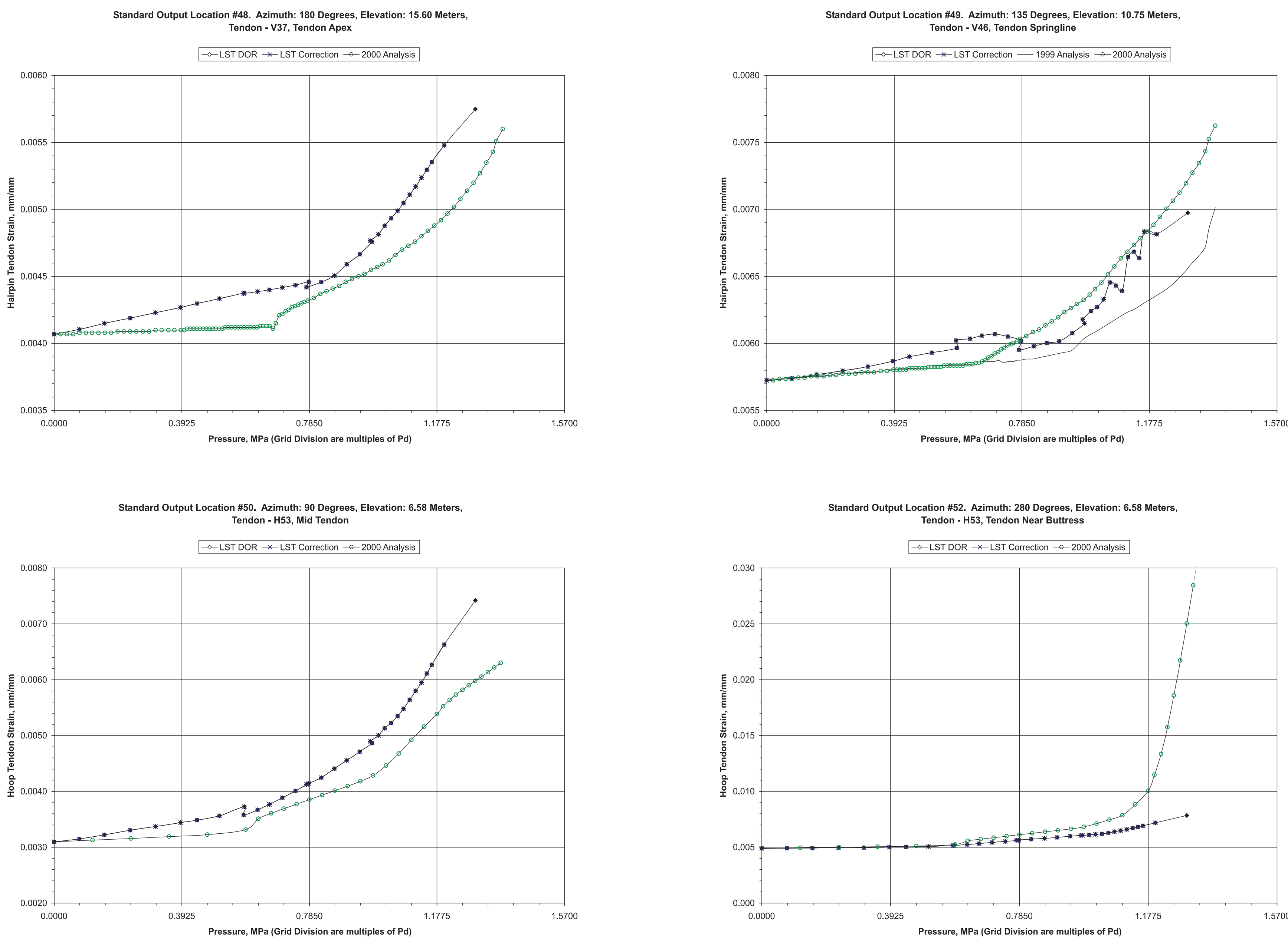

Figure 4-14. Comparisons at Standard Output Location 48, 49, 50, and 52

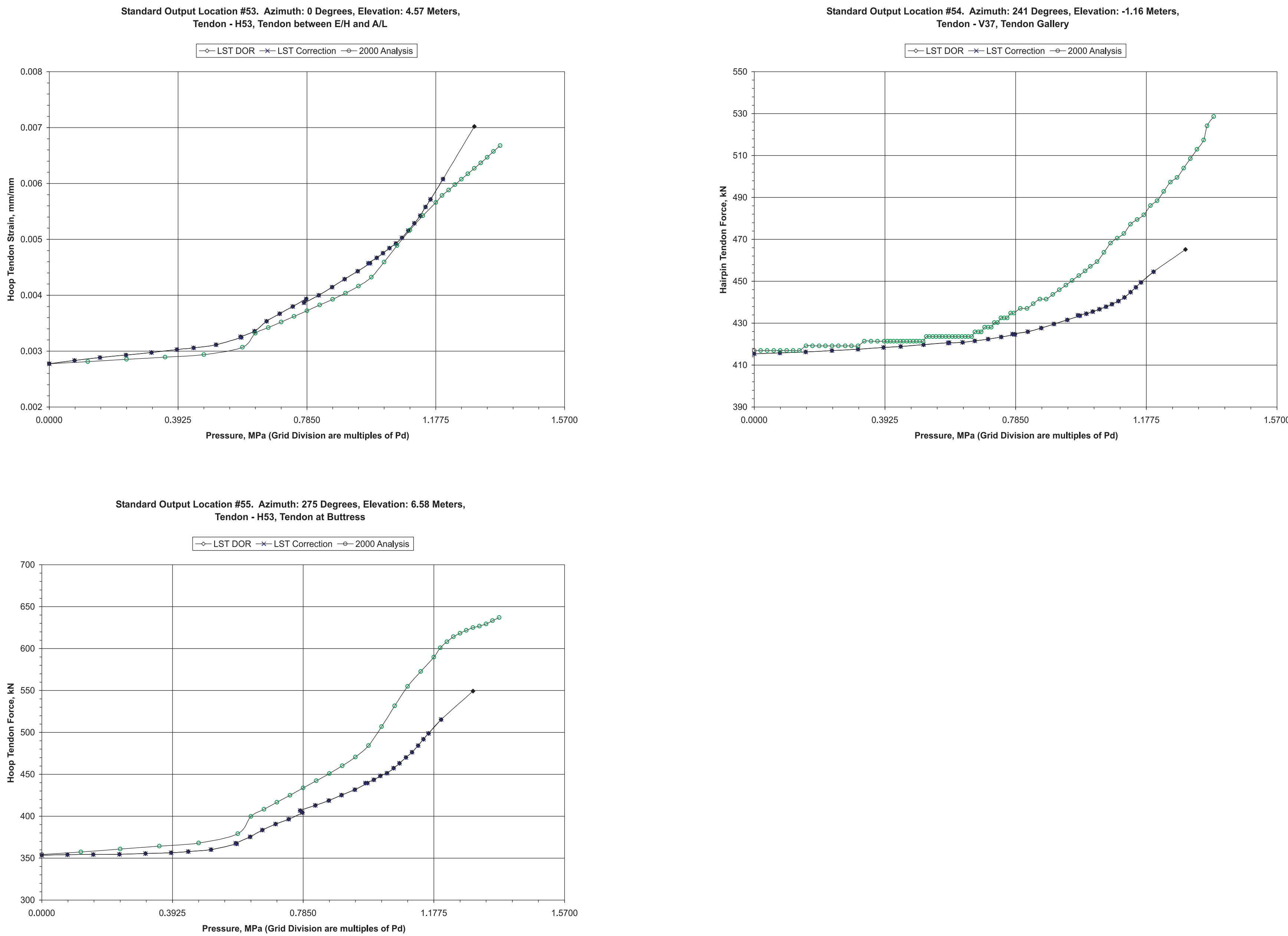

Figure 4-15. Comparisons at Standard Output Location 53, 54, and 55

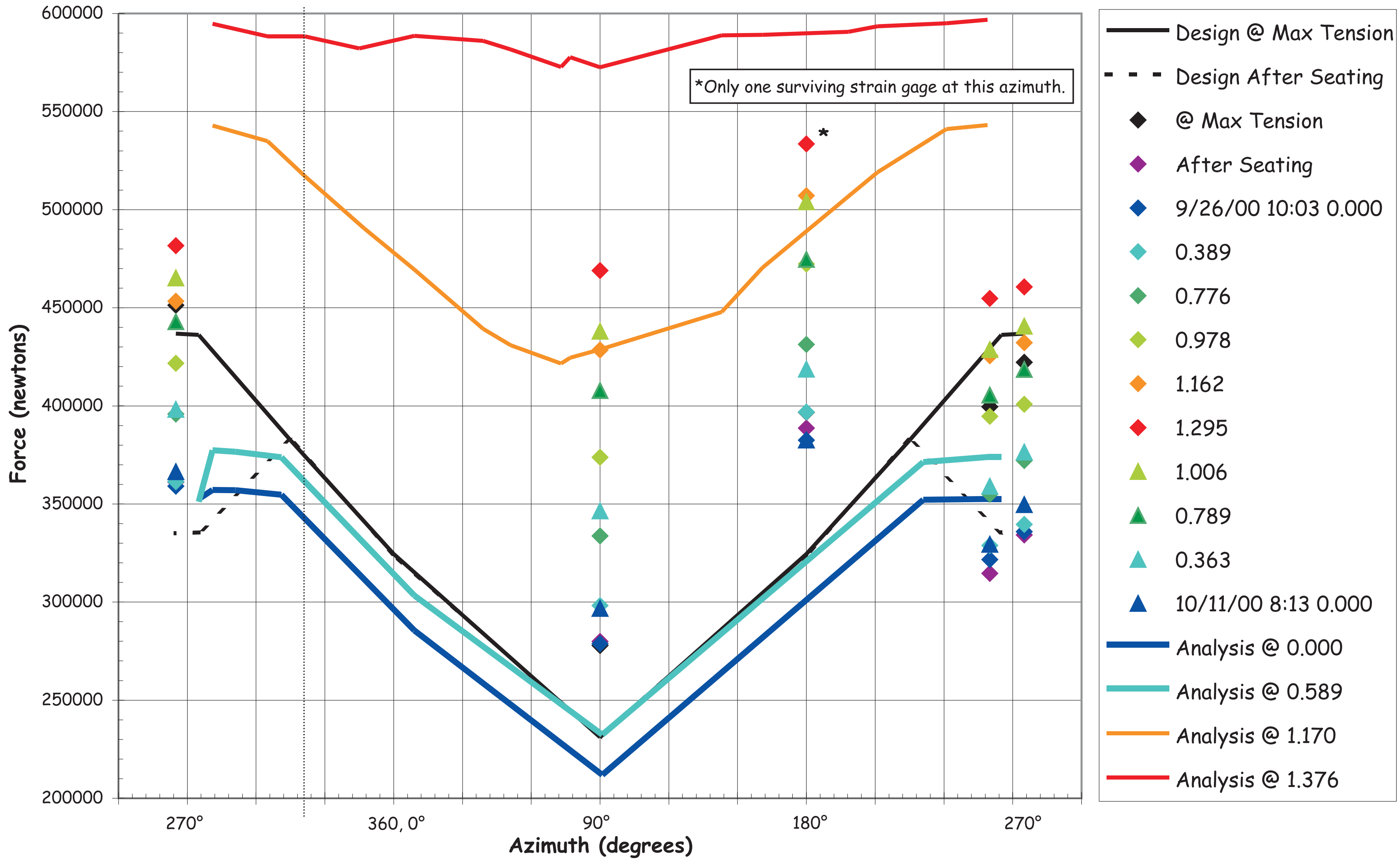

Figure 4-16. H11 Tendon Force Distribution, El. 1854 (Load Cells and Average of Wire Strain Gages)

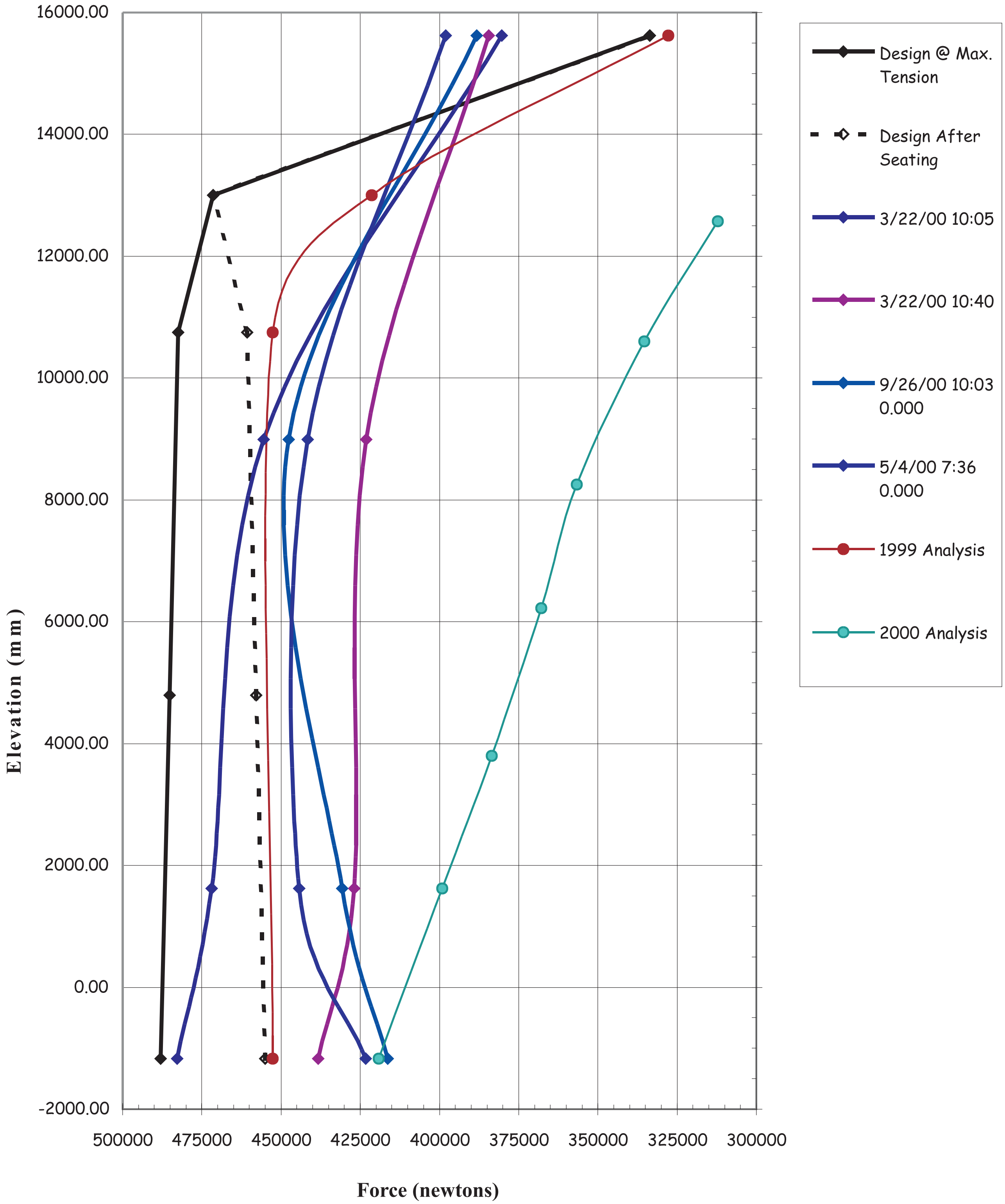

Figure 4-17. V37 Tendon Force Distribution @ Azimuth 240
(Load Cells and Average of Wire Strain Gages)

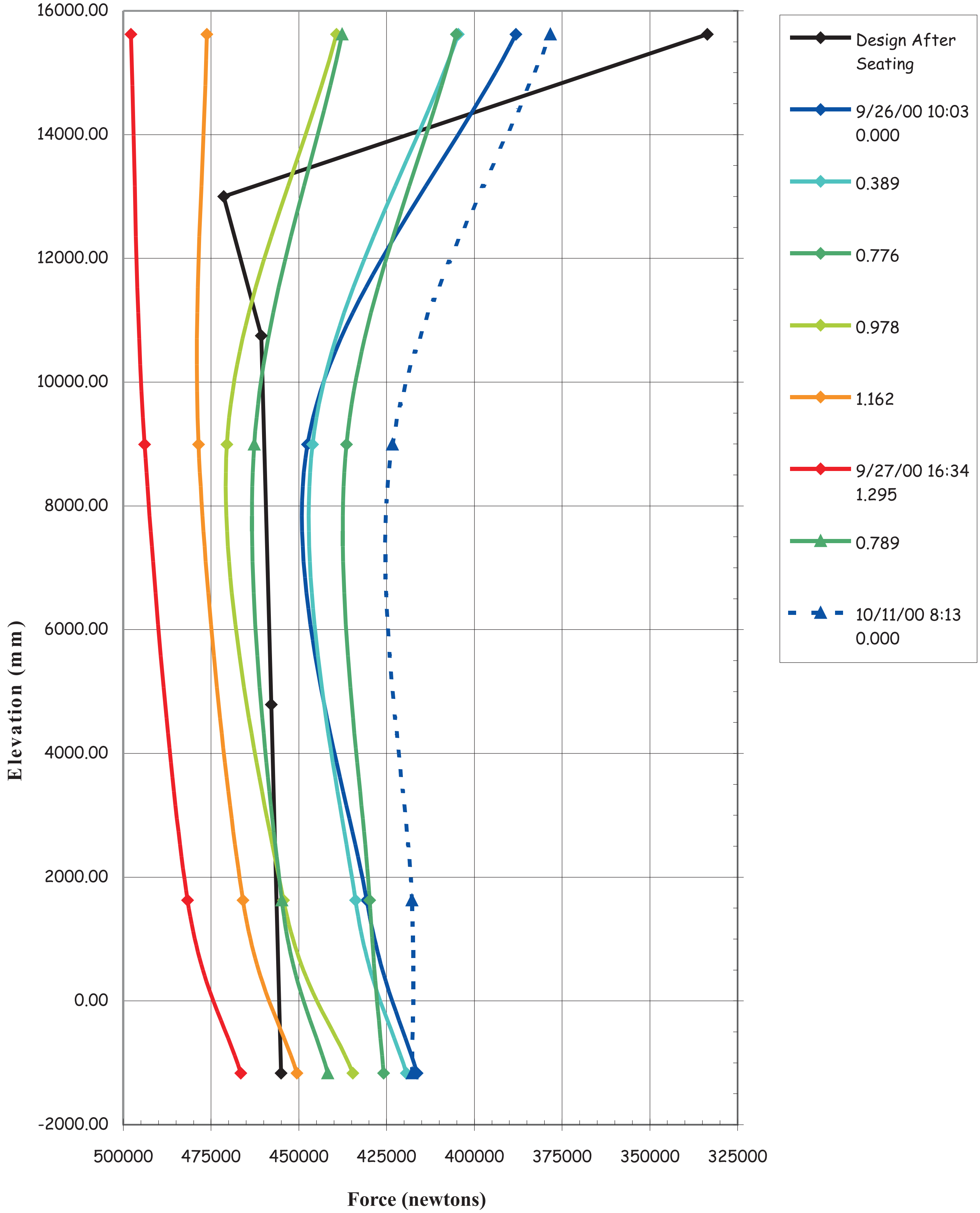

Figure 4-18. V37 Tendon Force Distribution @ Azimuth 240
(Load Cells and Average of Wire Strain Gages)

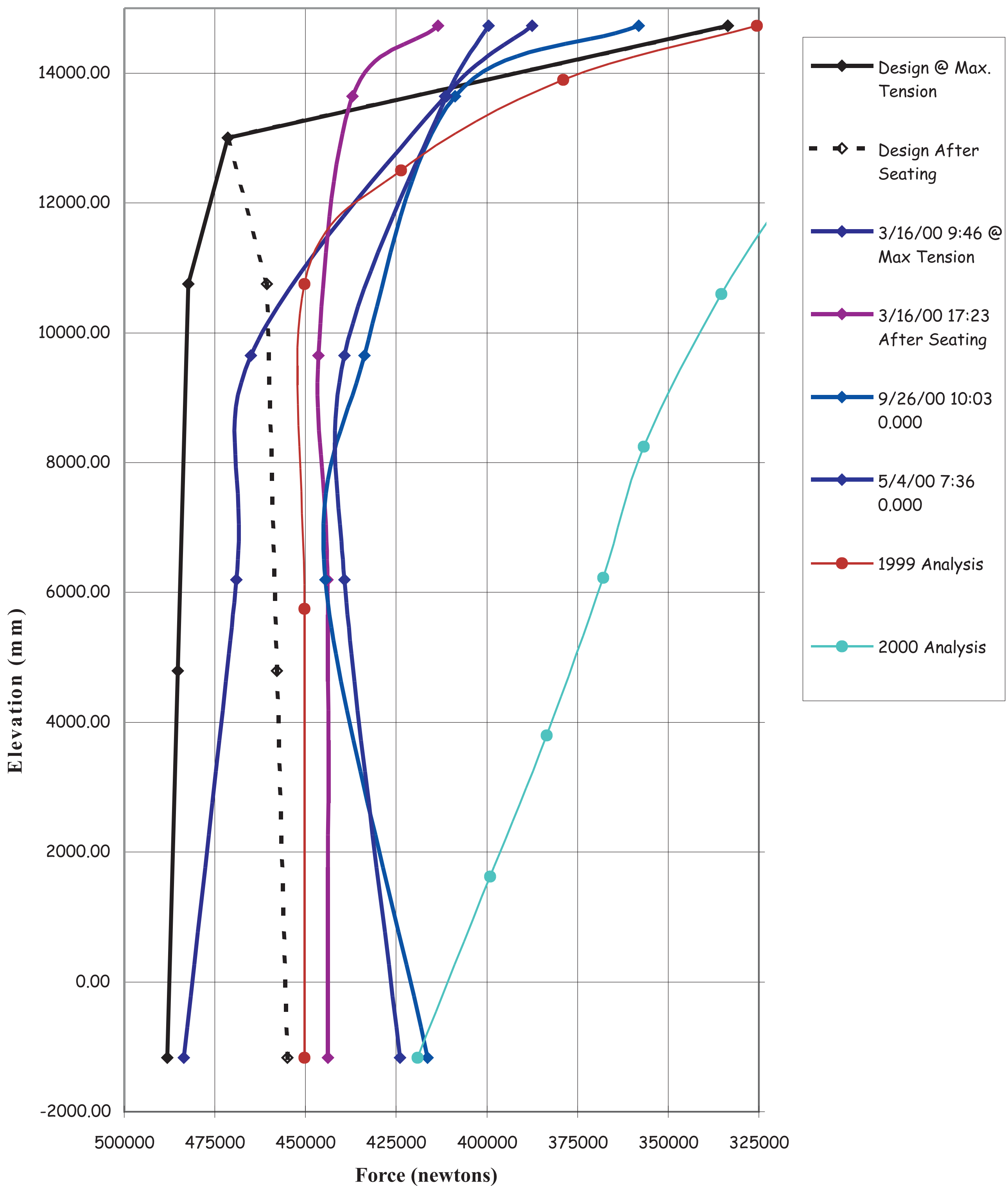

Figure 4-19. V46 Tendon Force Distribution @ Azimuth 135
(Load Cells and Average of Wire Strain Gages)

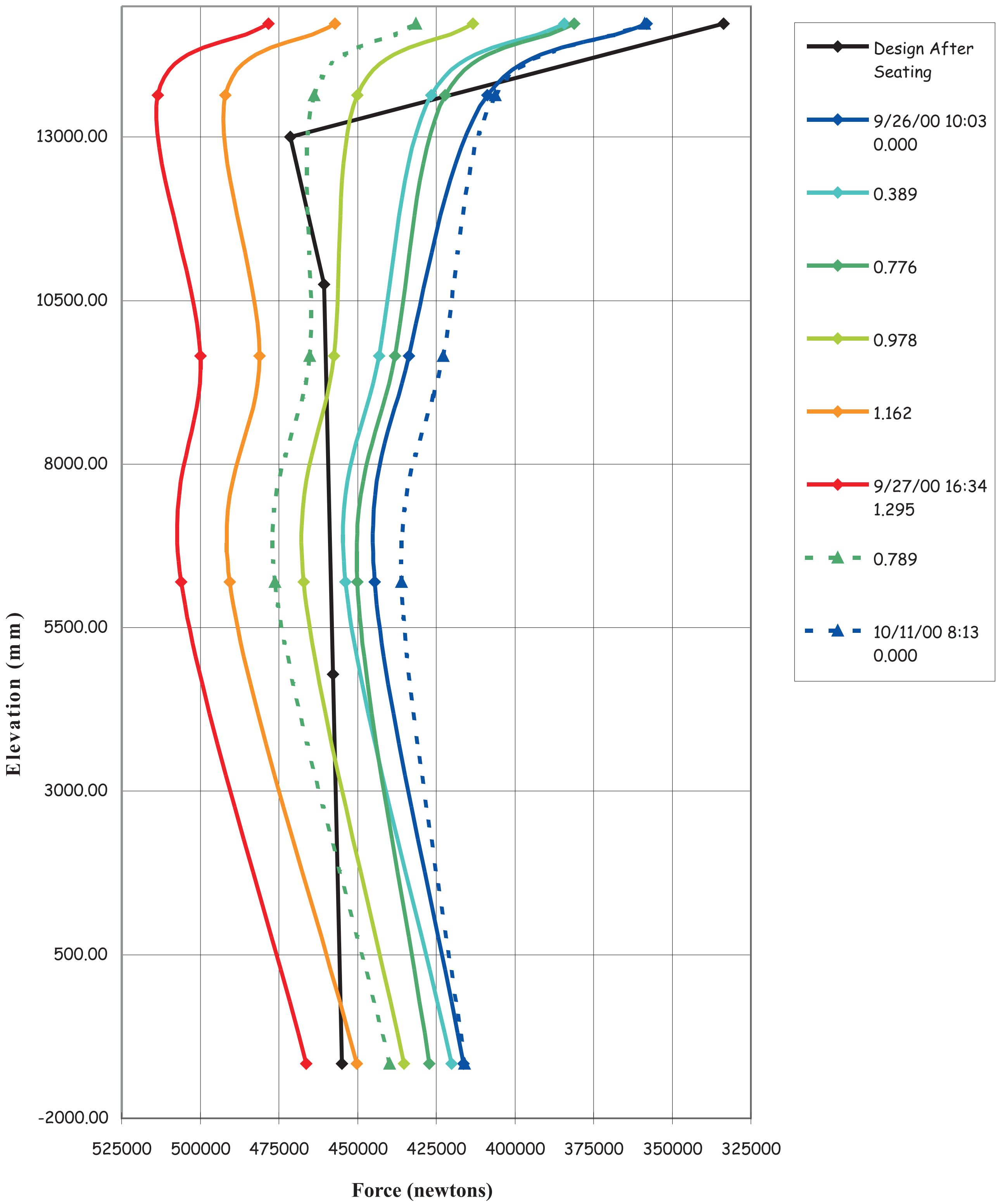

Figure 4-20. V46 Tendon Force Distribution @ Azimuth 135
(Load Cells and Average of Wire Strain Gages)

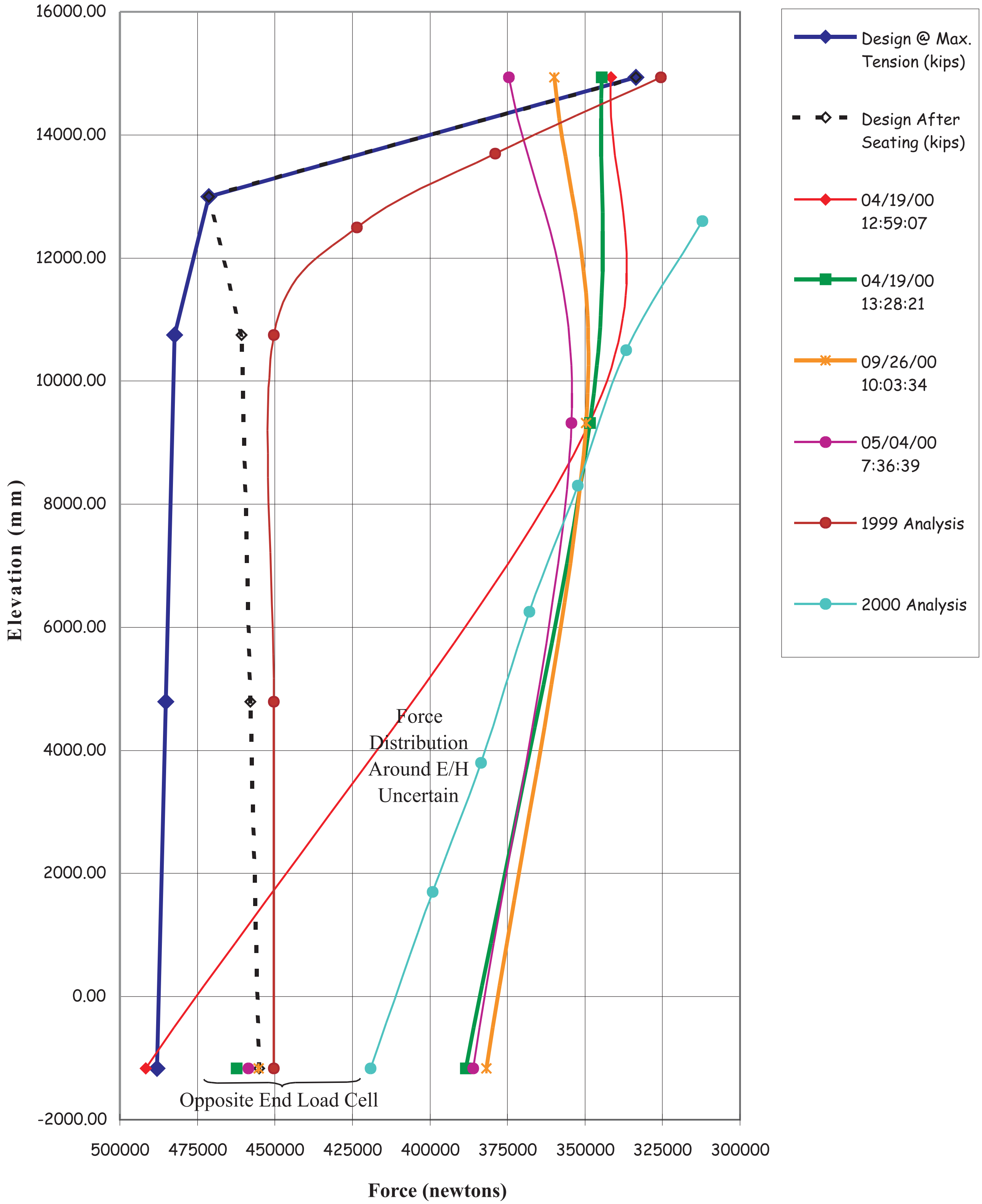

Figure 4-21. V85 Tendon Force Distribution @ Azimuth 325
(Load Cells and Average of Wire Strain Gages)

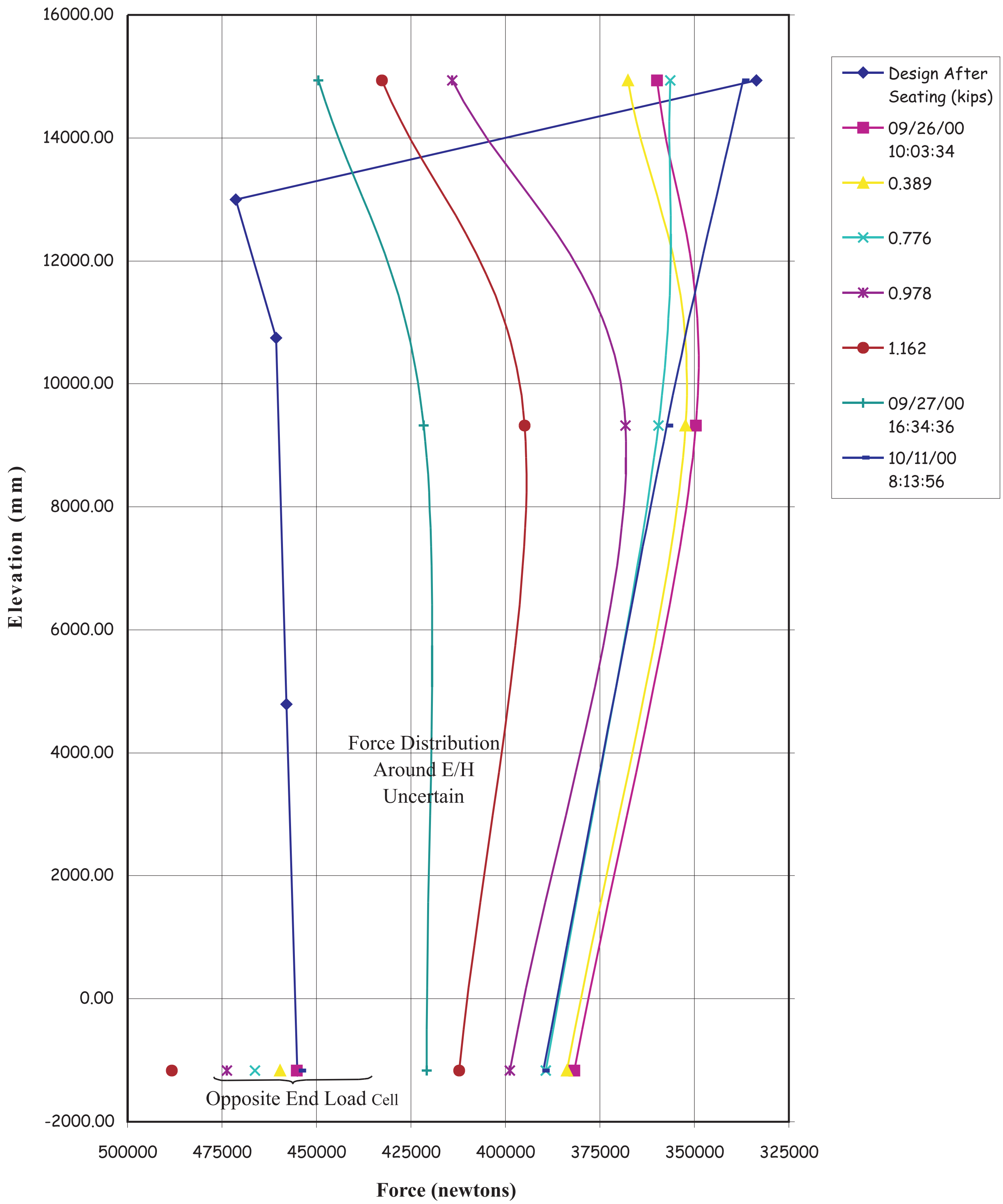

Figure 4-22. V85 Tendon Force Distribution @ Azimuth 325
(Load Cells and Average of Wire Strain Gages)

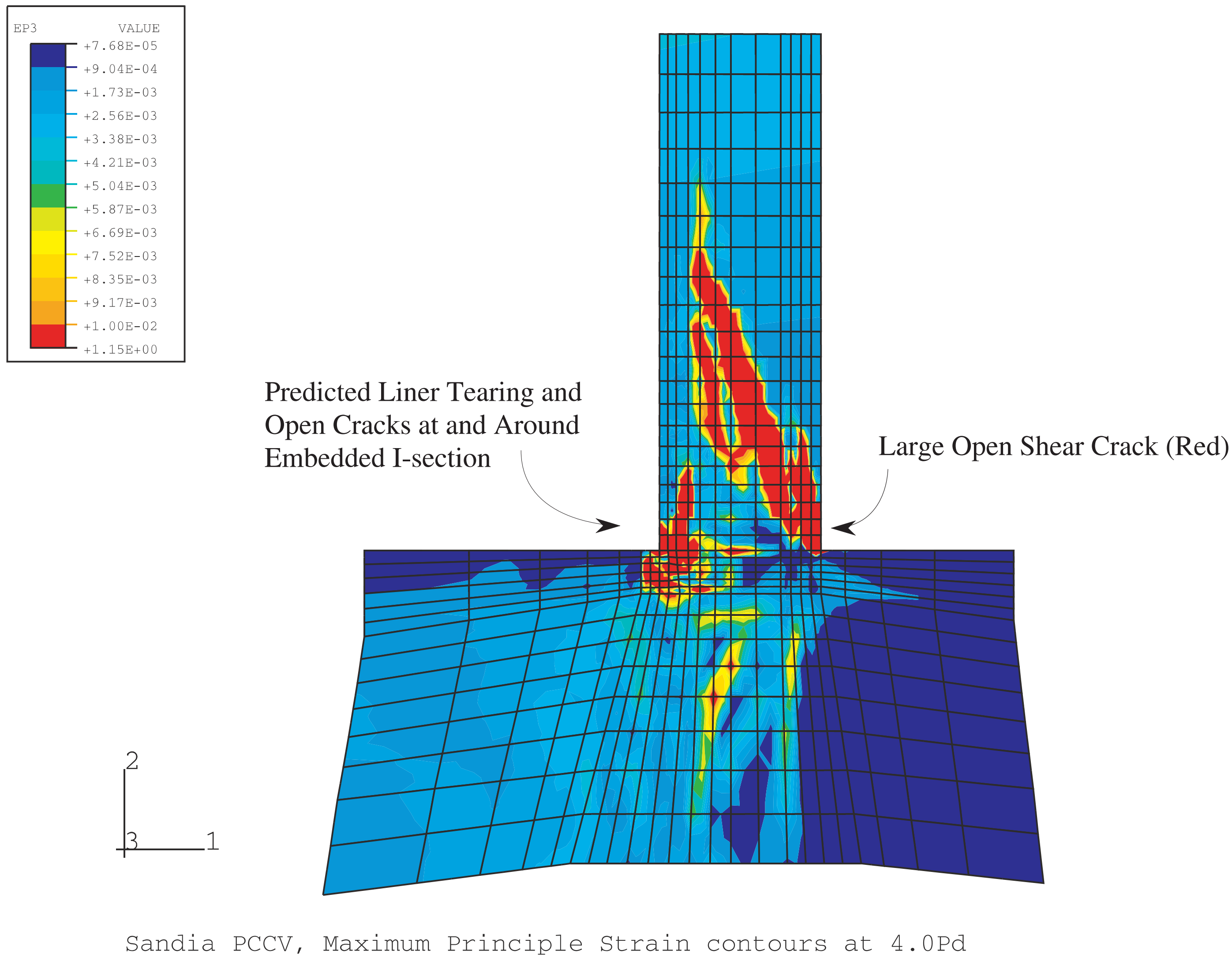

Figure 4-23. Maximum Principle Strain Contours in Wall-Base Region at 4.0 × Pd Showing Open Cracks and Predicted Liner Tearing from 1999 Pretest Analysis

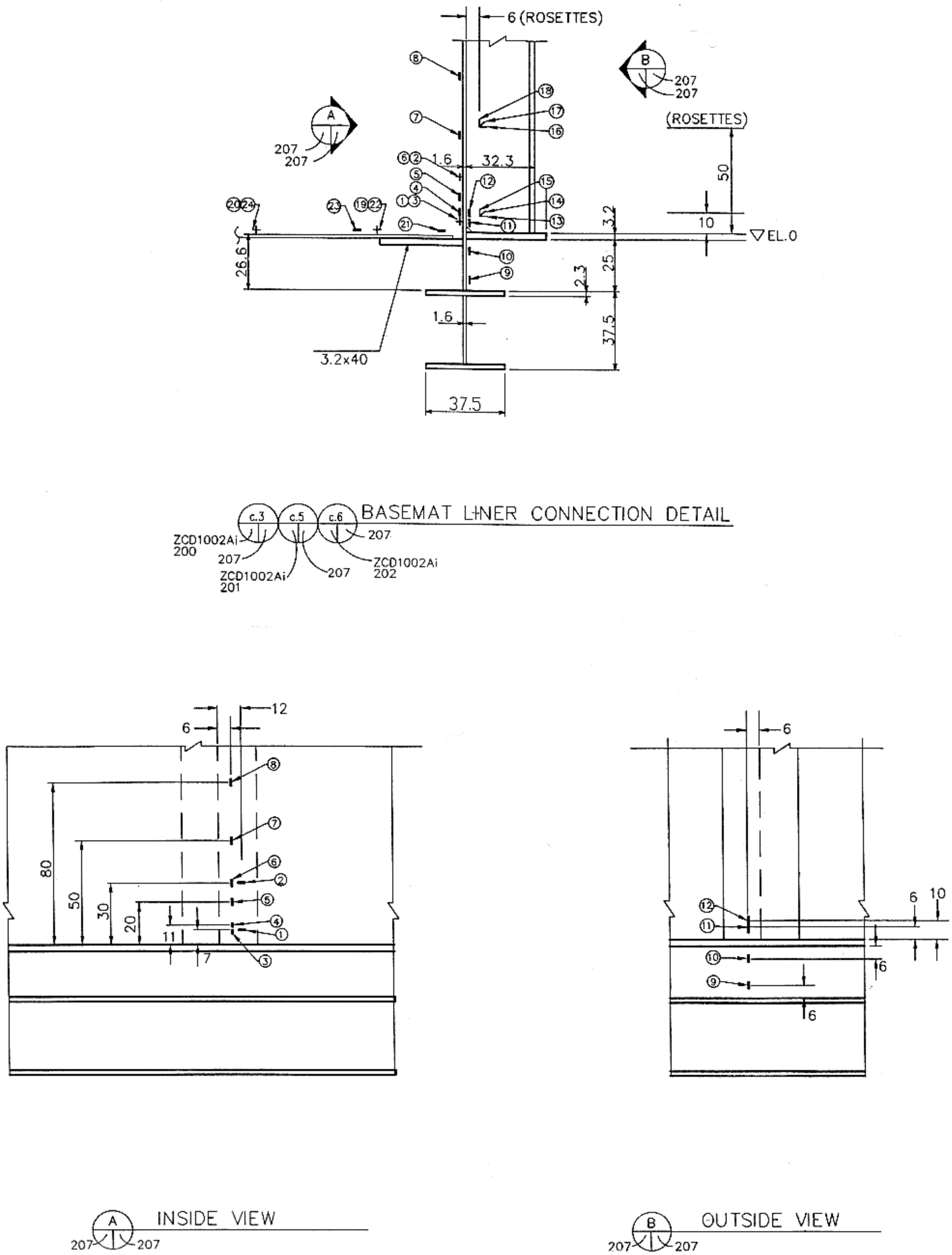

Figure 4-24. Basemat Liner Connection, Liner Instrumentation Details
(From Sheet D-SN-P-207, NUPEC/NRC Structural Behavior Test Model - As Built)

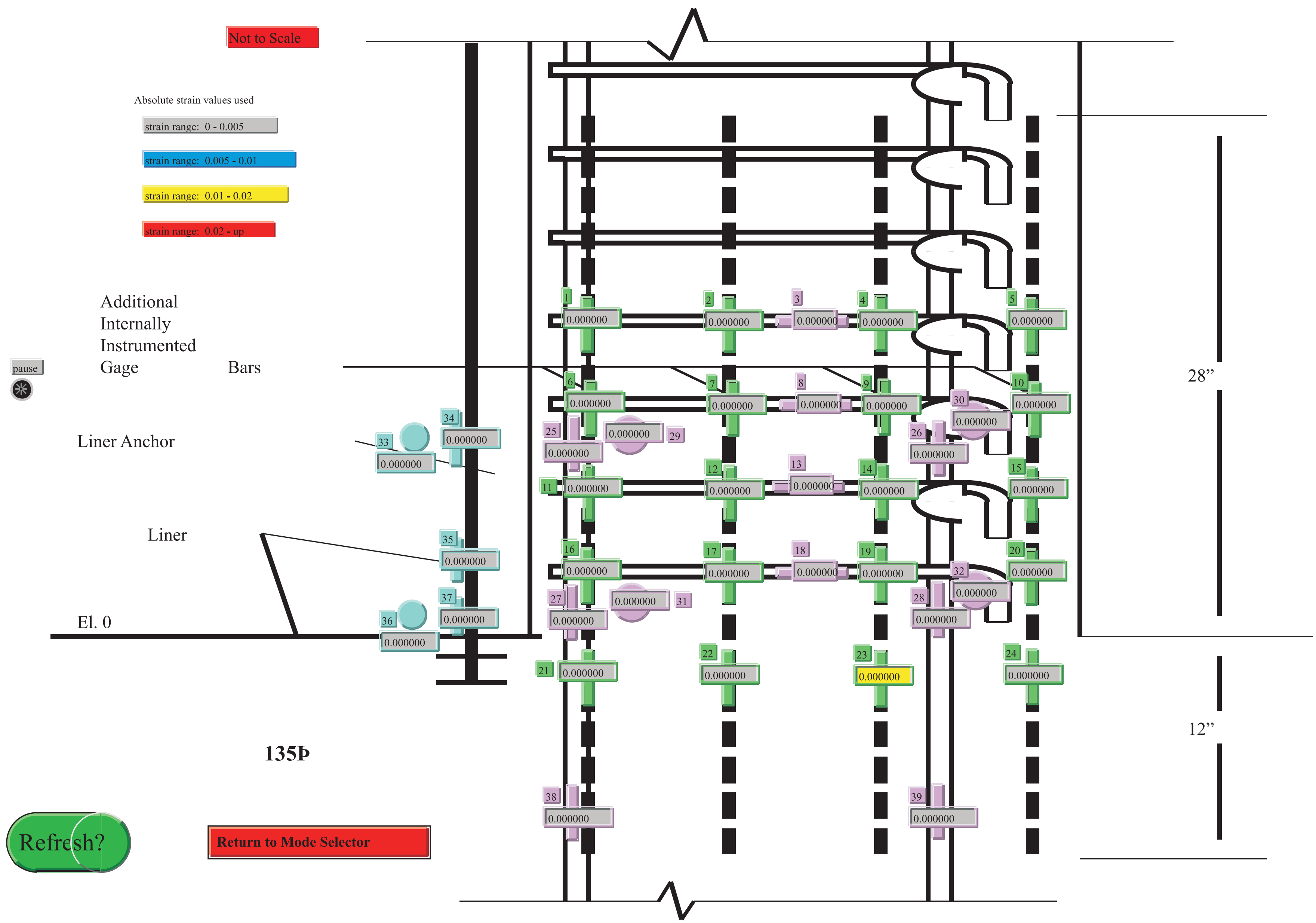

Figure 4-25. Basemat Junction, Gage Bar and Stirrup Strain Gage Locations

Gage Bar Strain Locations (positions A-Z)

Radial Stirrup Strain Locations (positions Z-AC

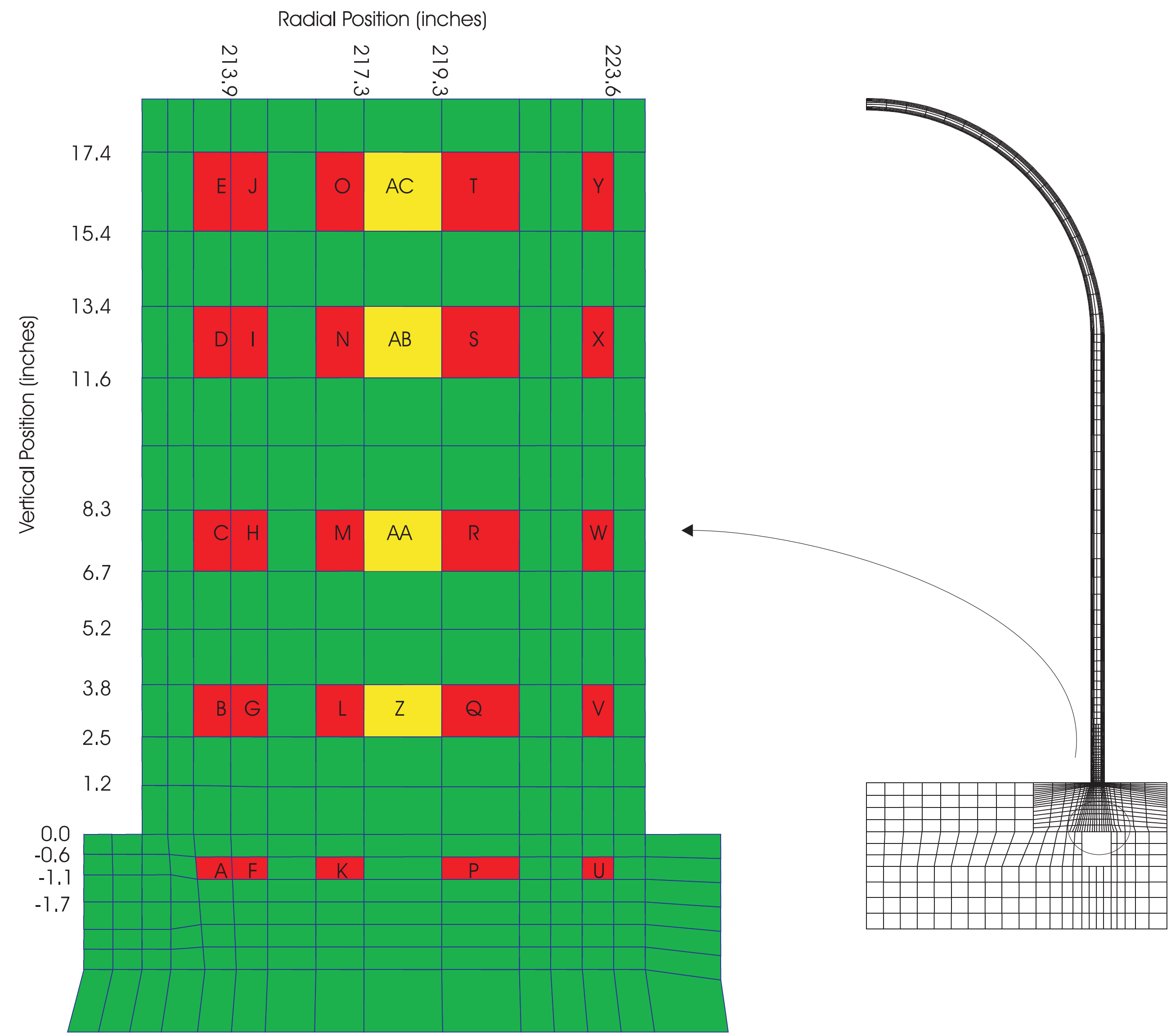

Liner Strain Locations

Position	Elevation
A	-1.27
B	-0.92
C	-0.62
D	-0.36
E	-0.10
F	0.17
G	0.63
H	1.28
I	1.92
J	2.56
K	3.21

Figure 4-26. Axisymmetric Model Gage Bar, Stirrup, and Liner Strain Comparison Locations

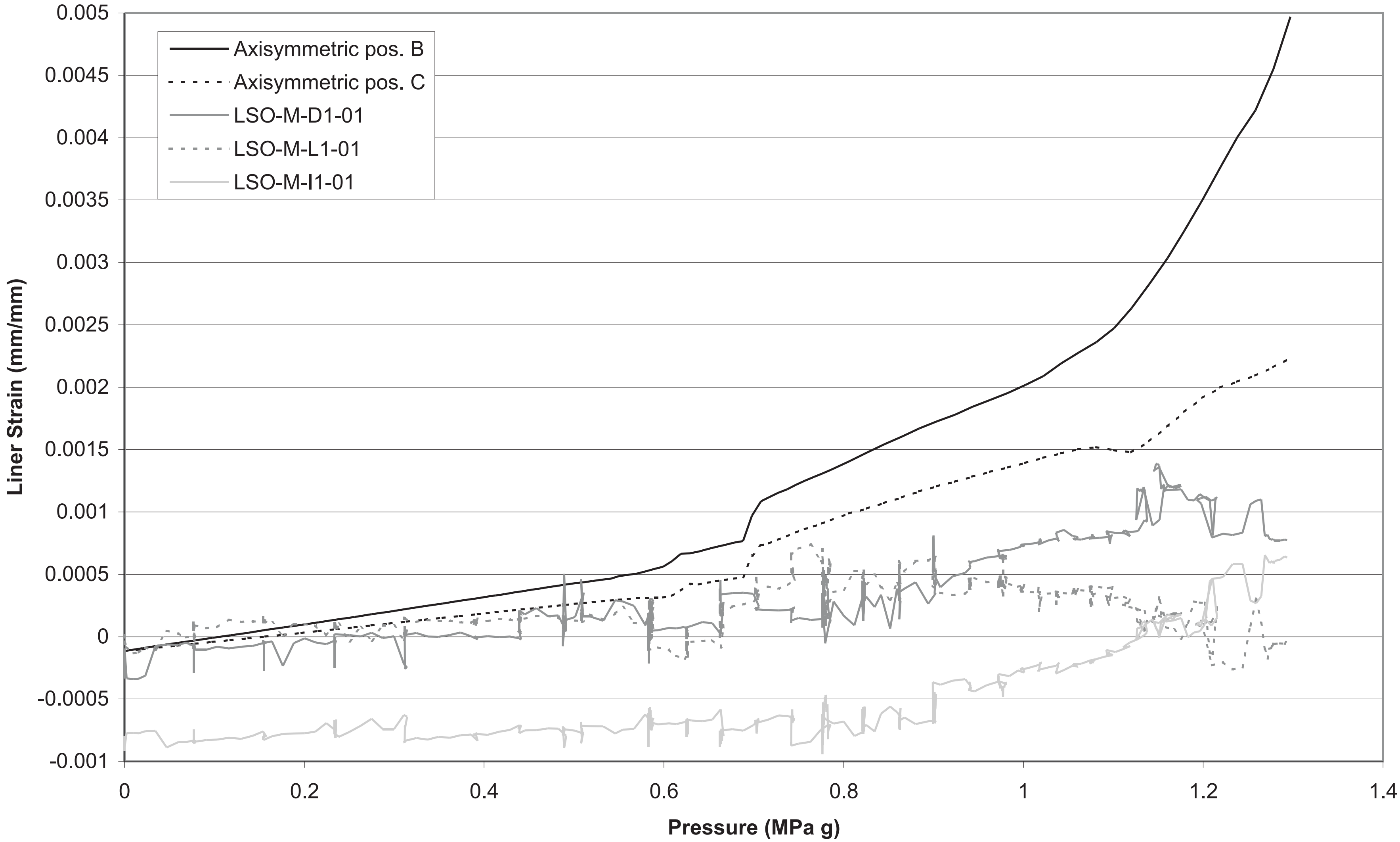

Figure 4-27. 1999 Pretest Analysis vs. LST at Wall Base Liner Position B-C

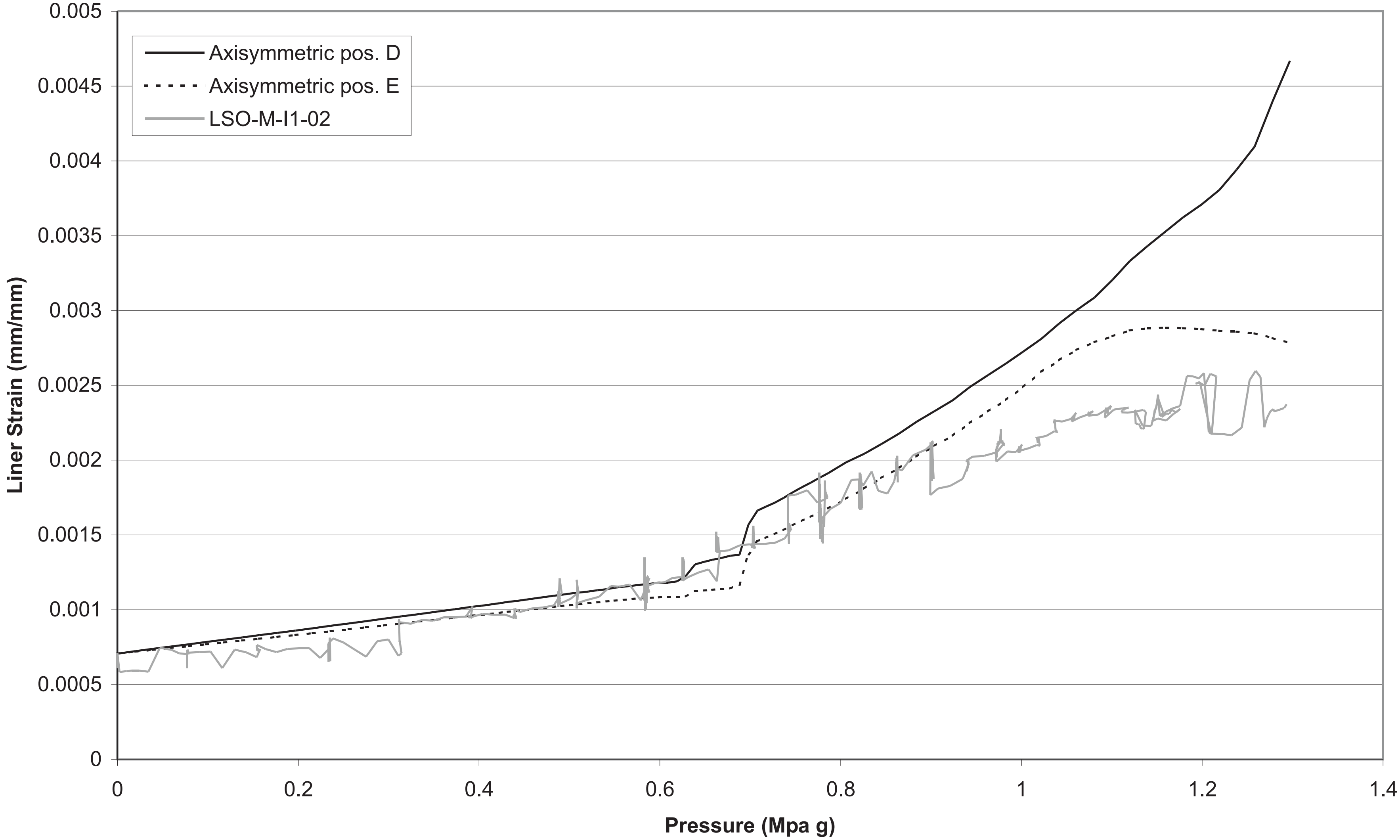

Figure 4-28. 1999 Pretest Analysis vs. LST at Wall Base Liner Position D-E

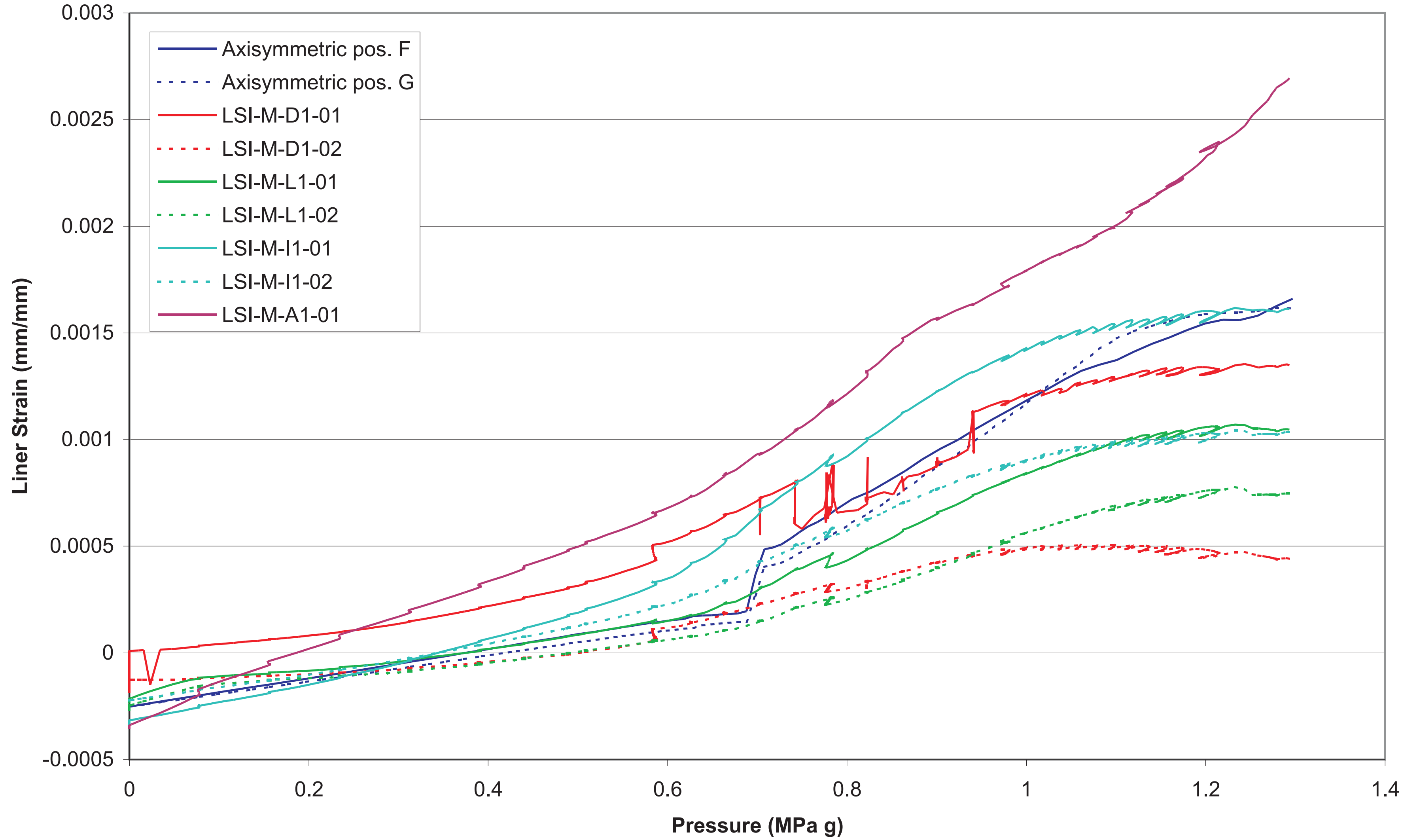

Figure 4-29. 1999 Pretest Analysis vs. LST at Wall Base Liner Position F-G

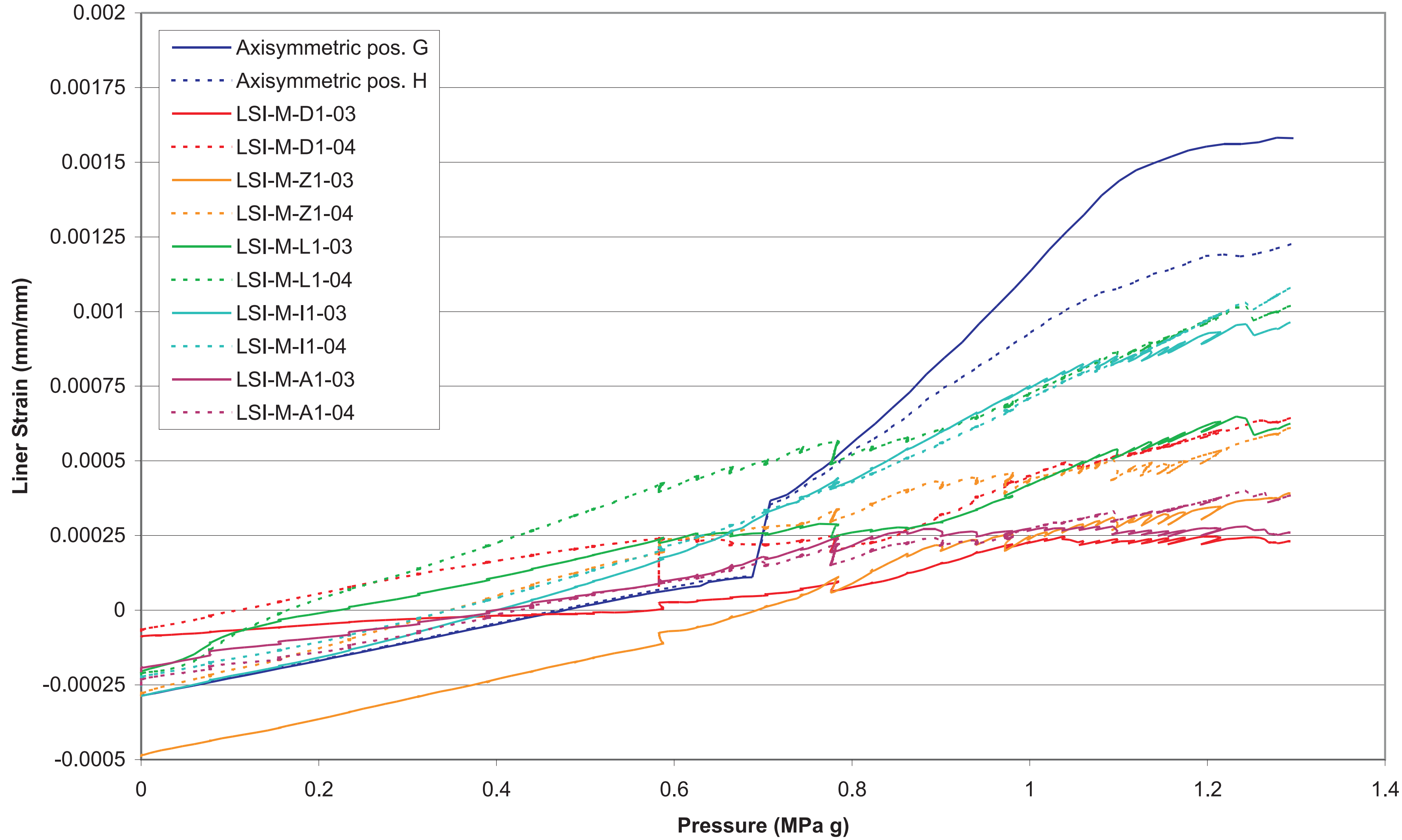

Figure 4-30. 1999 Pretest Analysis vs. LST at Wall Base Liner Position G-H

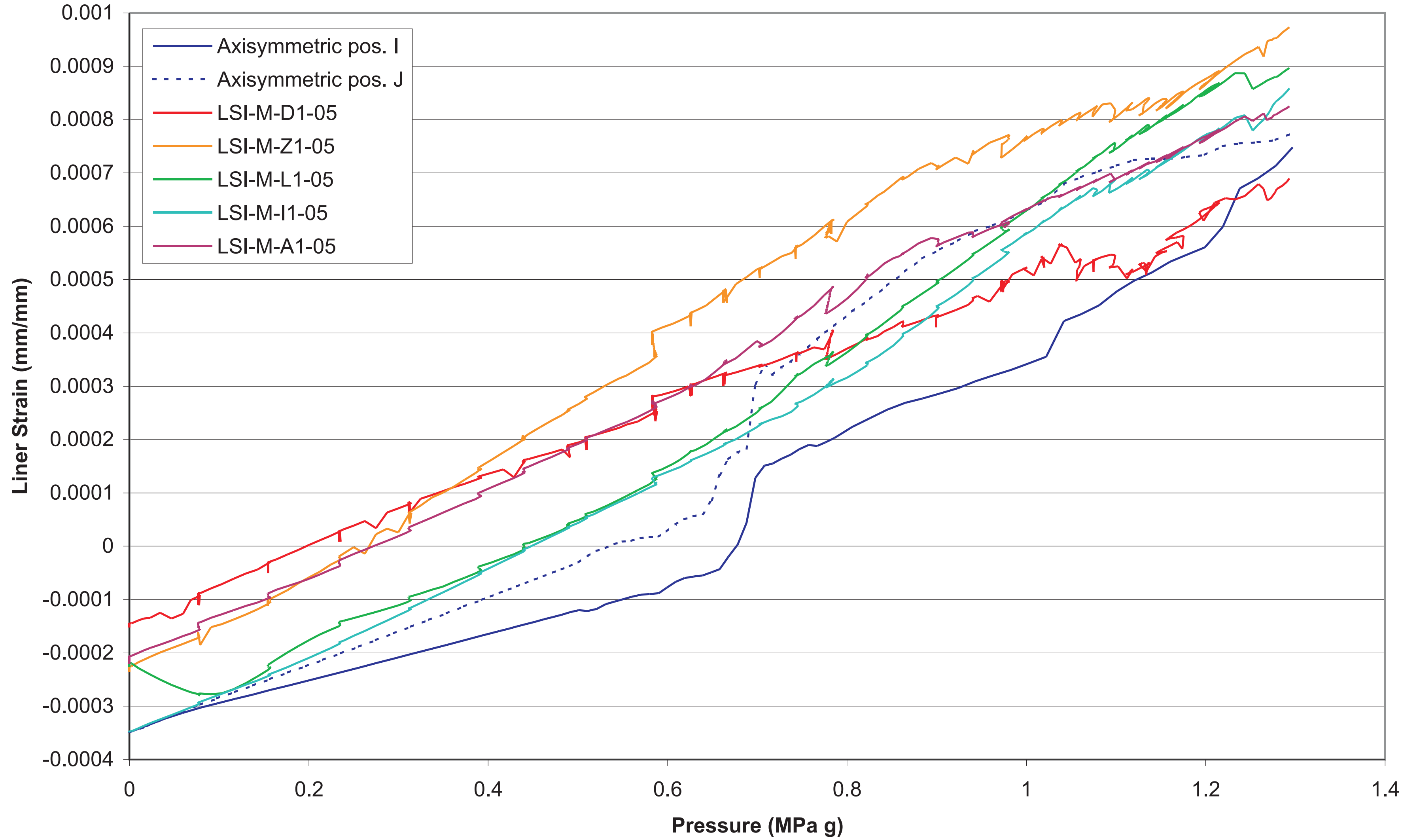

Figure 4-31. 1999 Pretest Analysis vs. LST at Wall Base Liner Position I-J

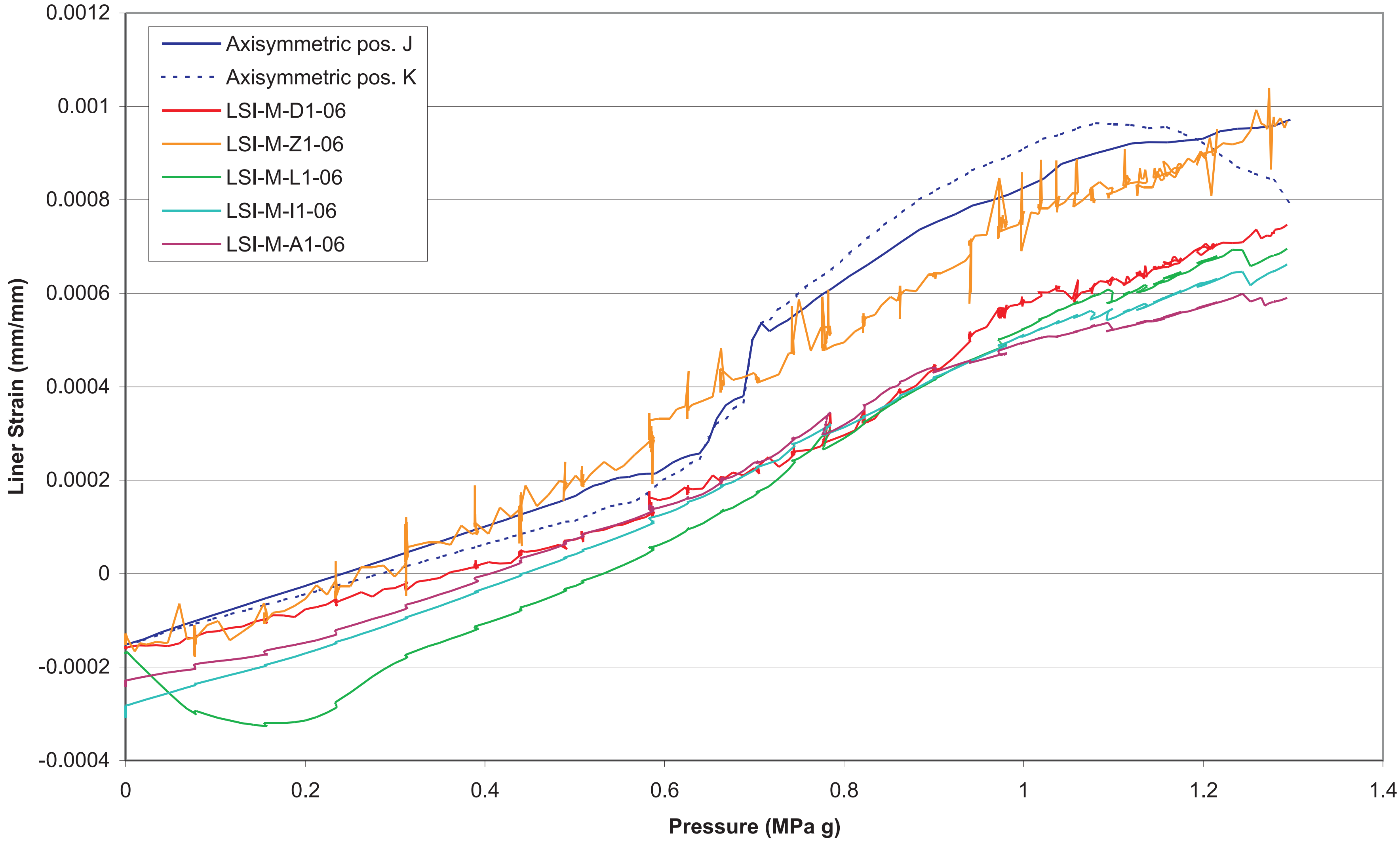

Figure 4-32. 1999 Pretest Analysis vs. LST at Wall Base Liner Position J-K

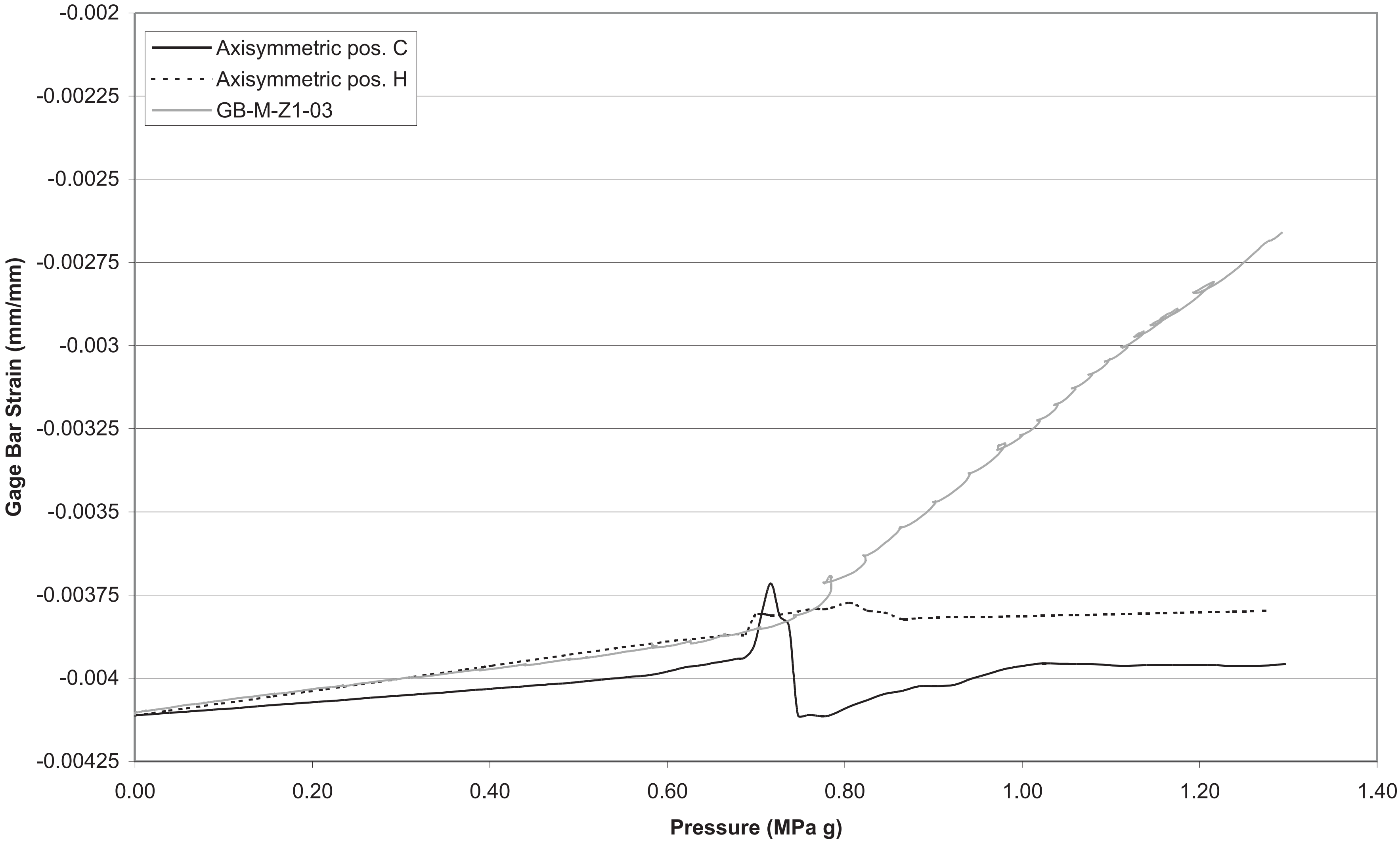

Figure 4-33. 1999 Pretest Analysis vs. LST at Wall Base Gage Bar Position C-H

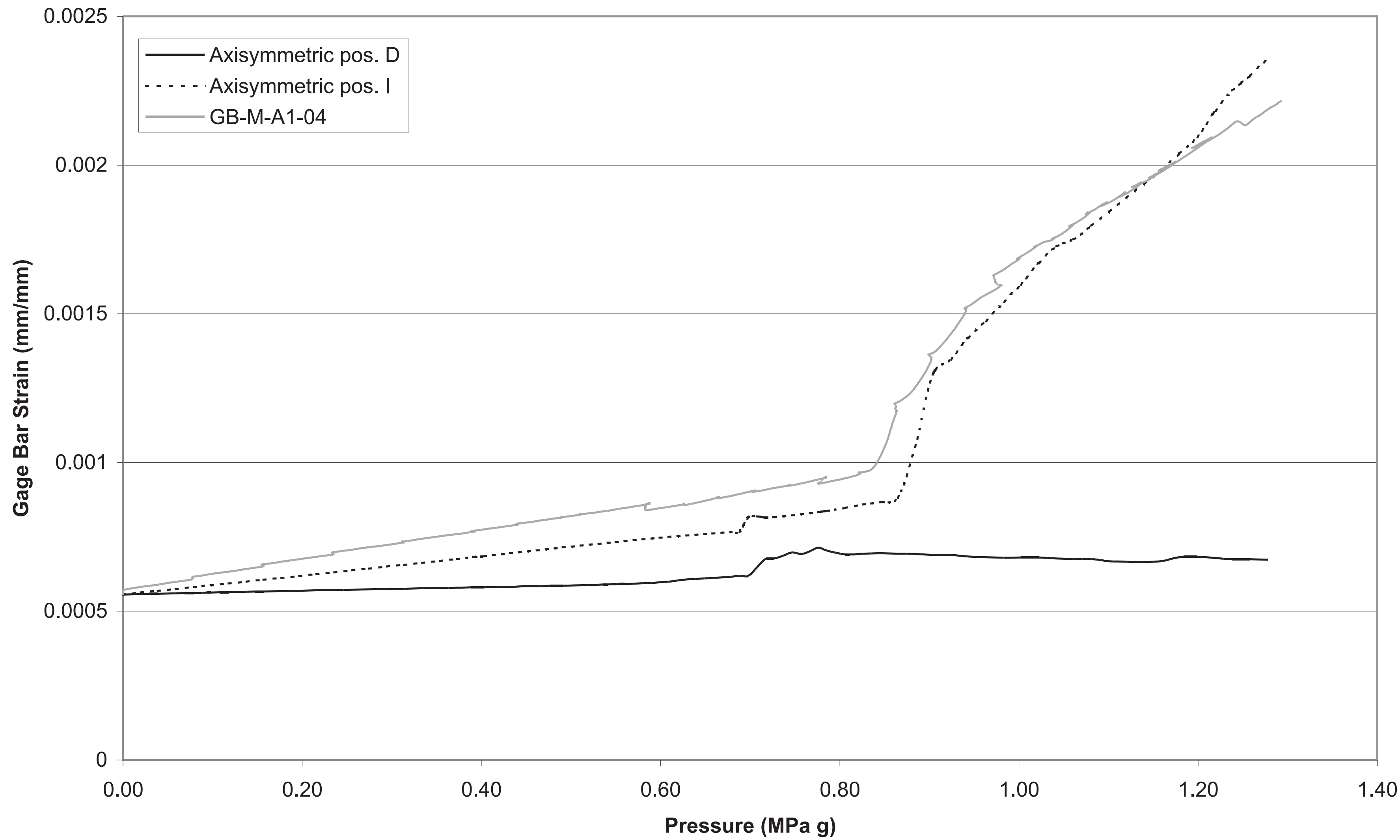

Figure 4-34. 1999 Pretest Analysis vs. LST at Wall Base Gage Bar Position D-I

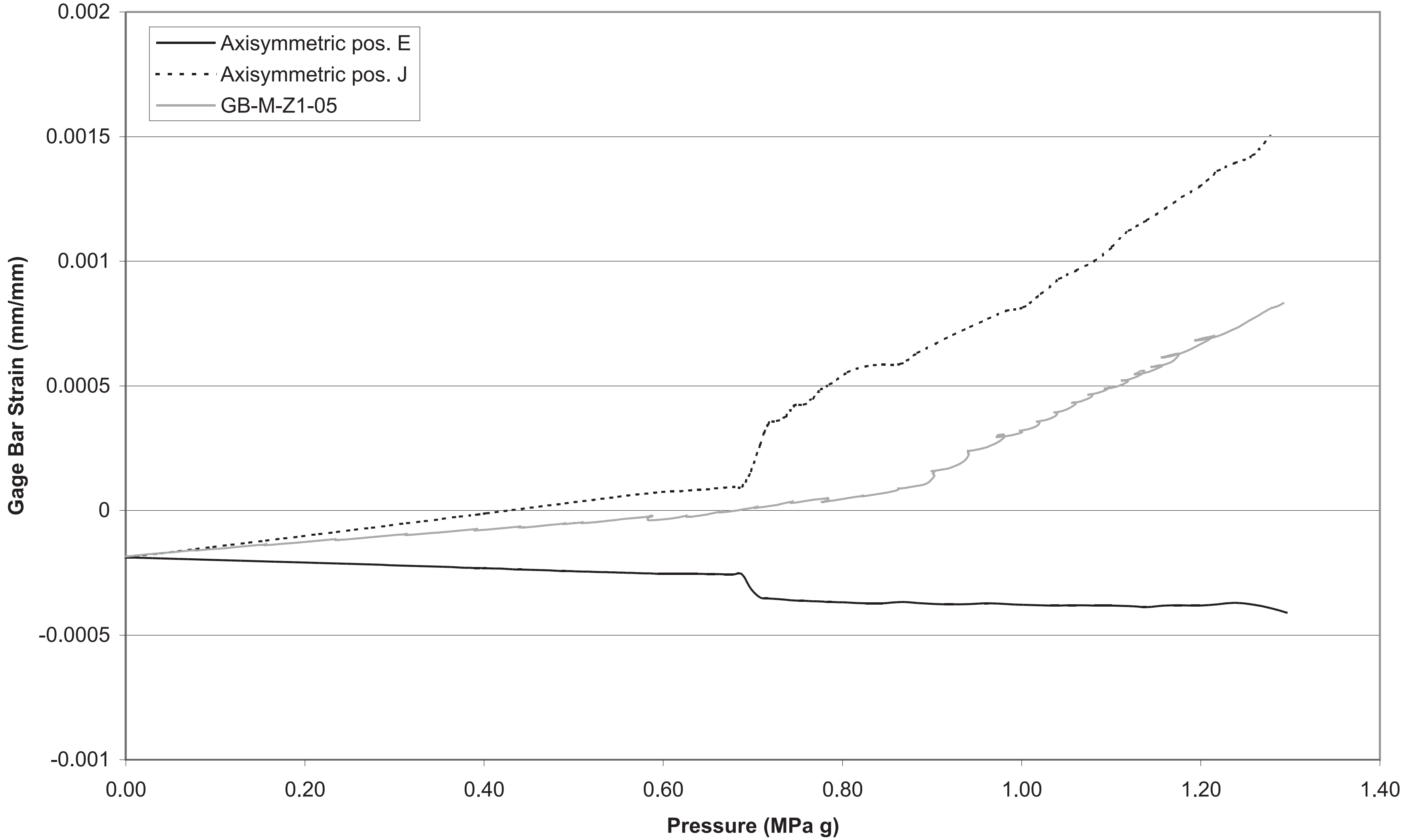

Figure 4-35. 1999 Pretest Analysis vs. LST at Wall Base Gage Bar Position E-J

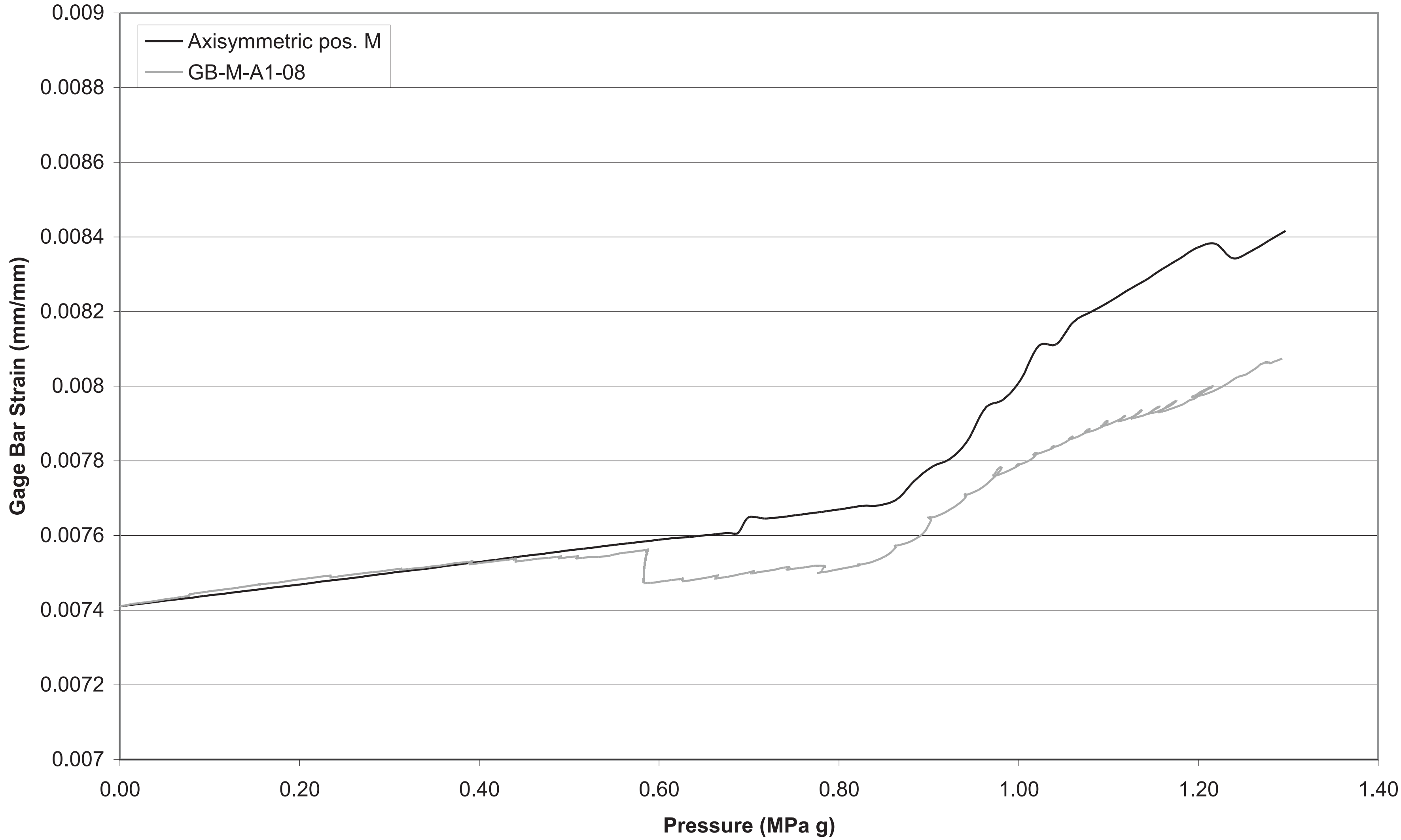

Figure 4-36. 1999 Pretest Analysis vs. LST at Wall Base Gage Bar Position M

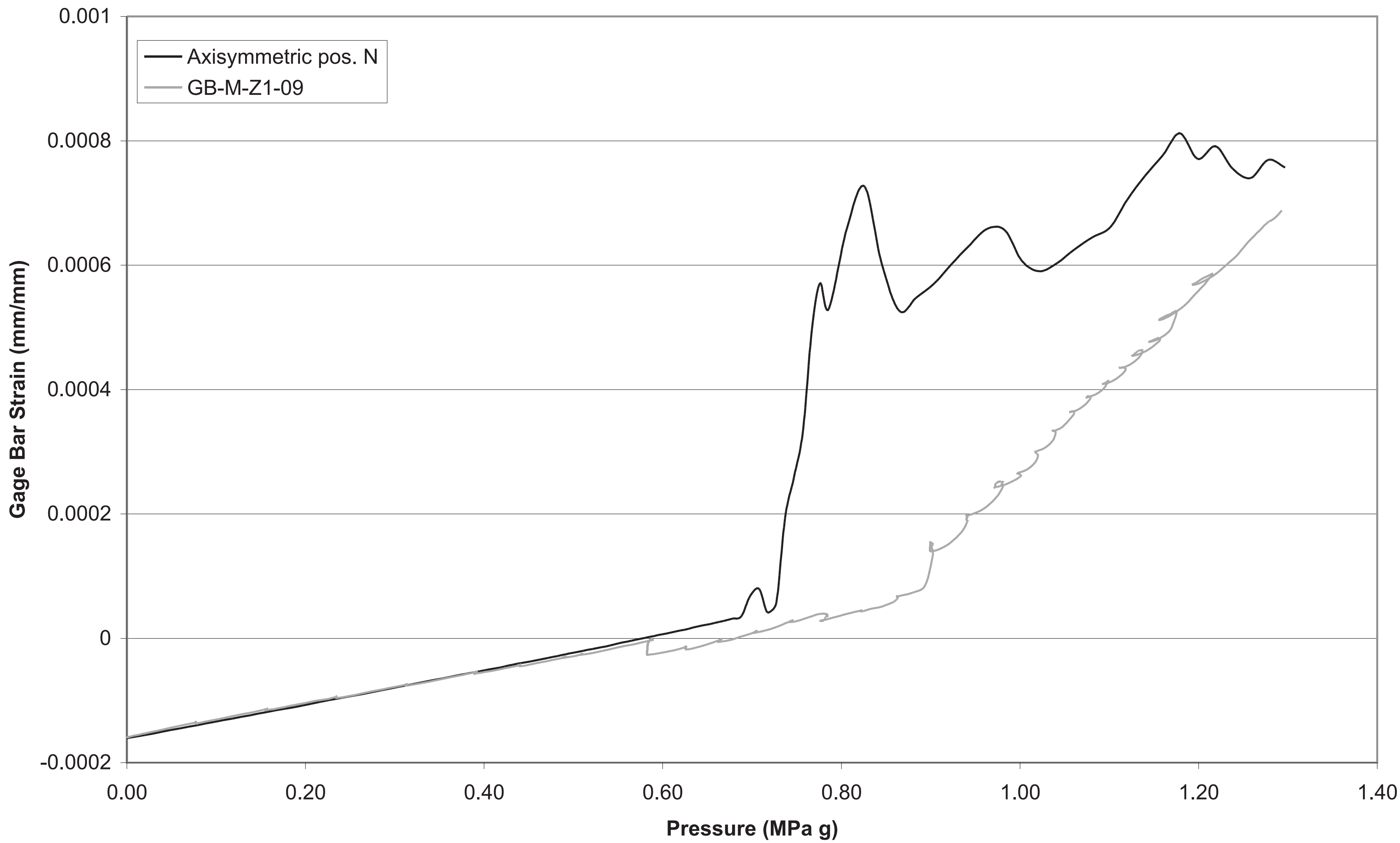

Figure 4-37. 1999 Pretest Analysis vs. LST at Wall Base Gage Bar Position N

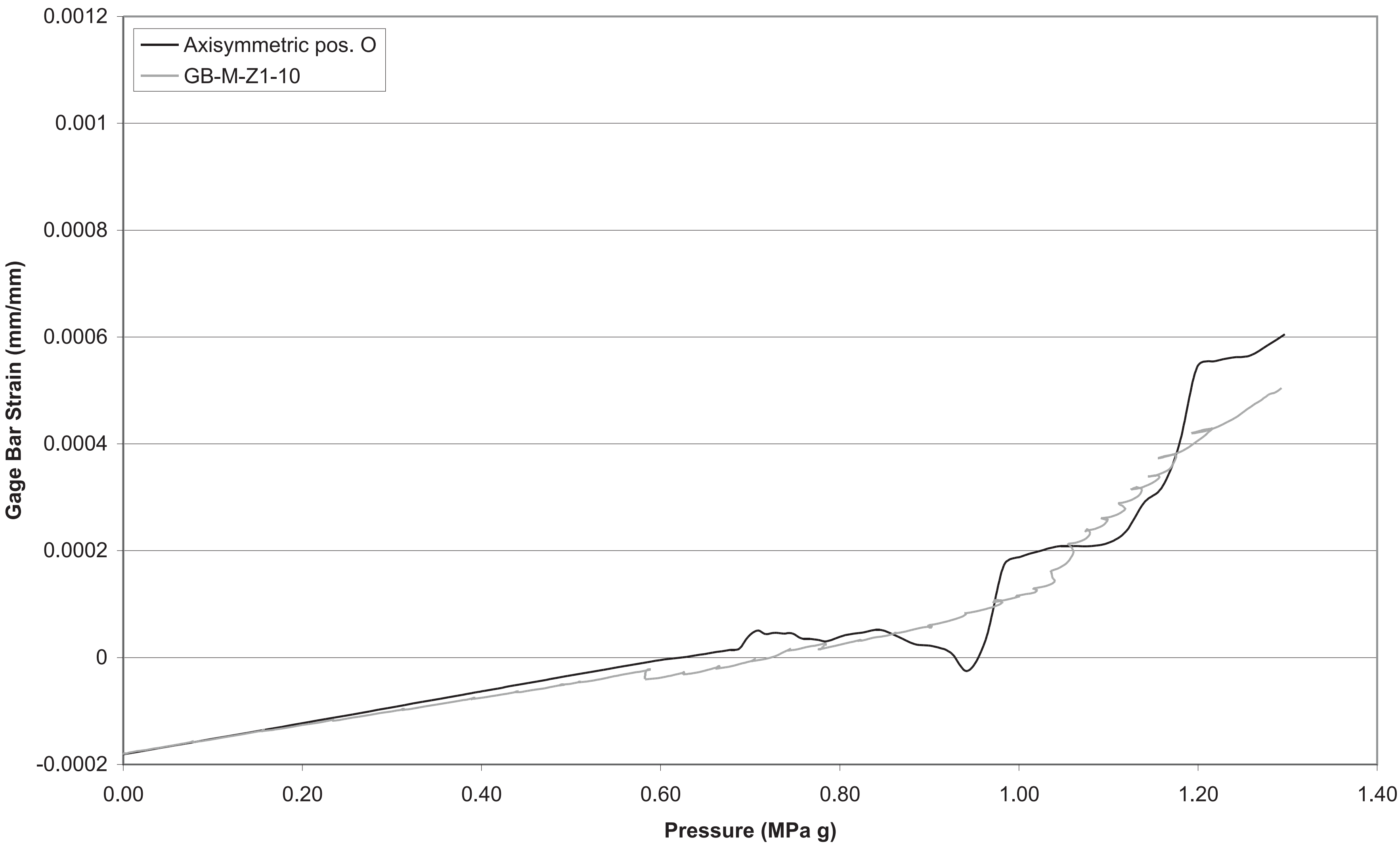

Figure 4-38. 1999 Pretest Analysis vs. LST at Wall Base Gage Bar Position O

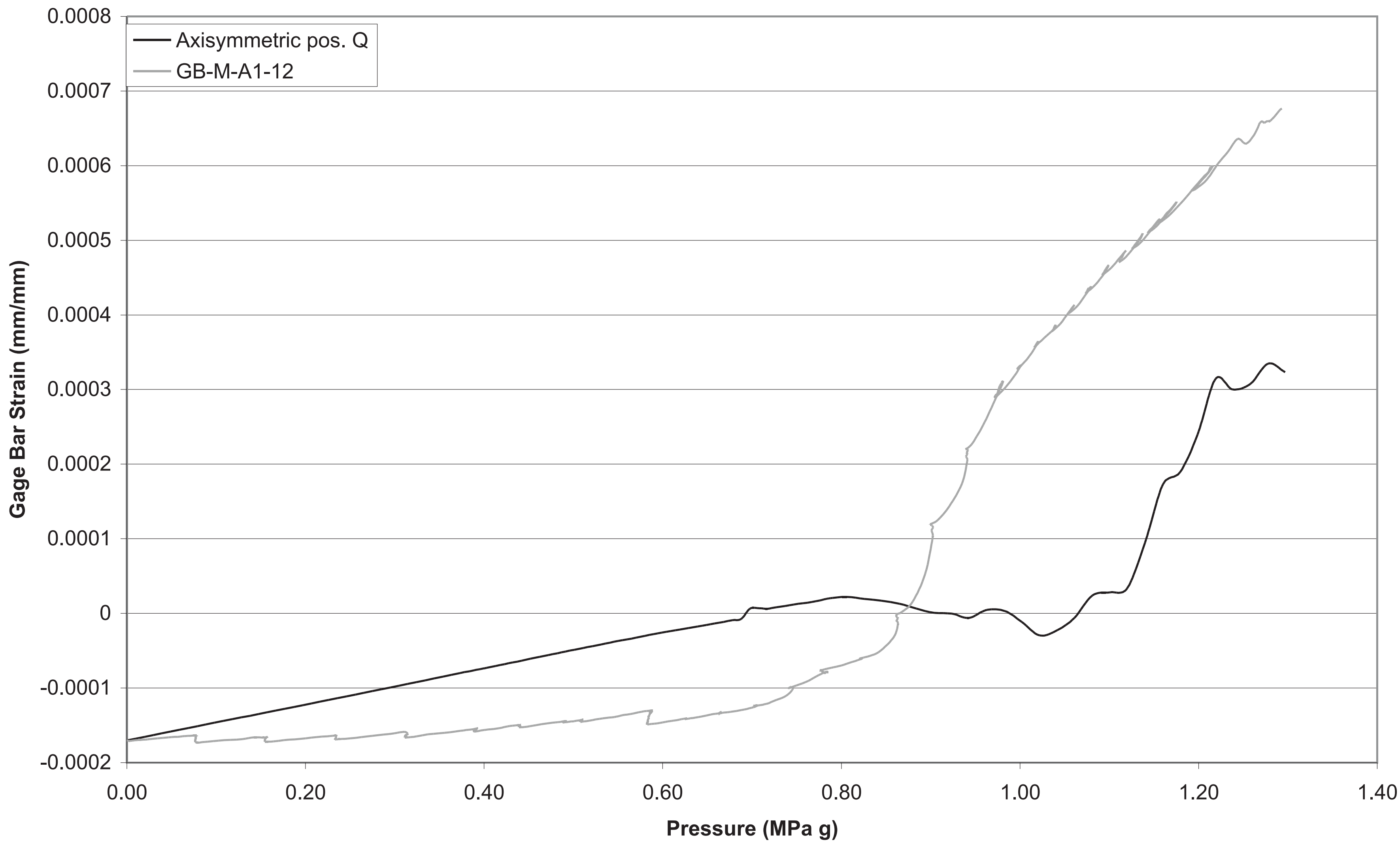

Figure 4-39. 1999 Pretest Analysis vs. LST at Wall Base Gage Bar Position Q

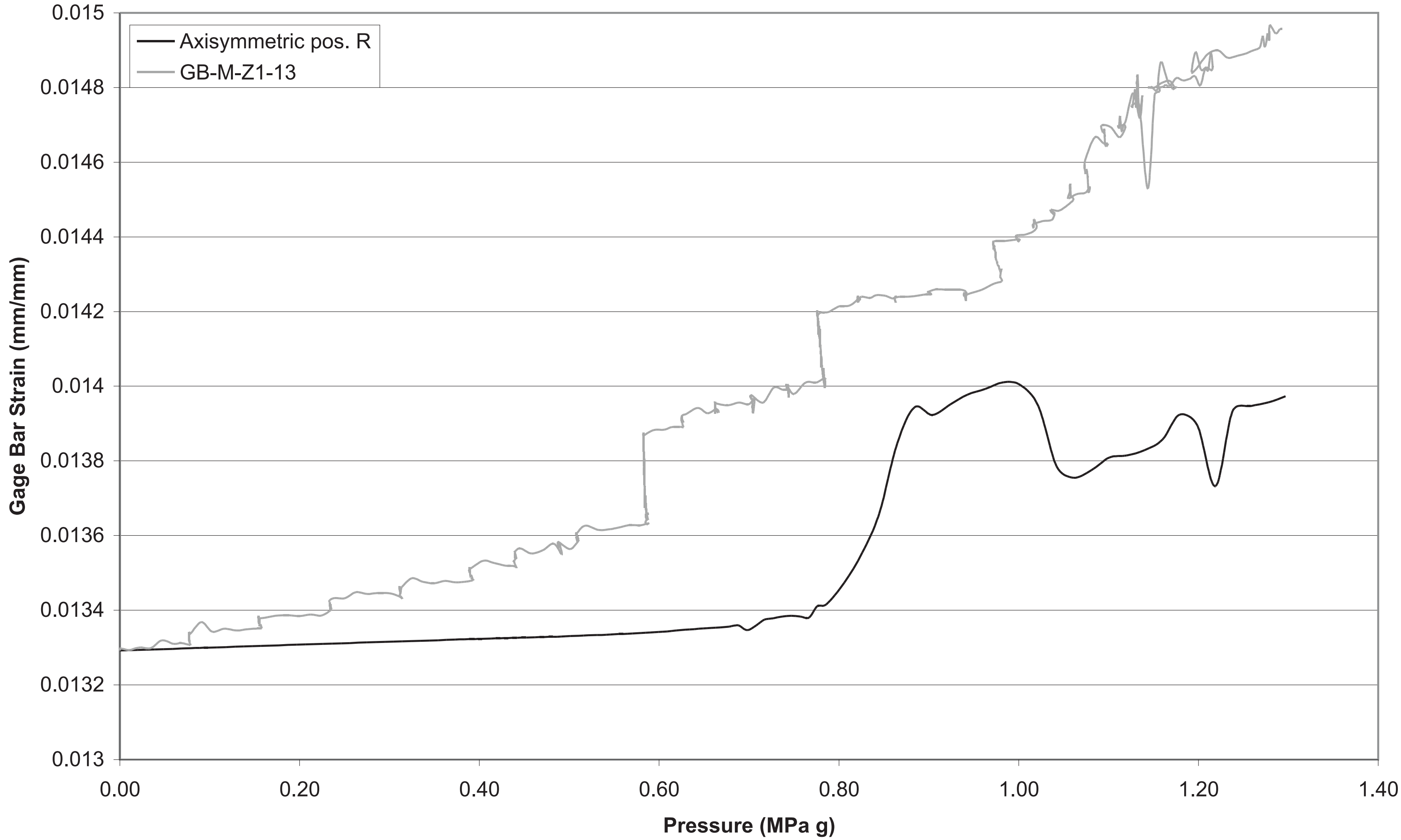

Figure 4-40. 1999 Pretest Analysis vs. LST at Wall Base Gage Bar Position R

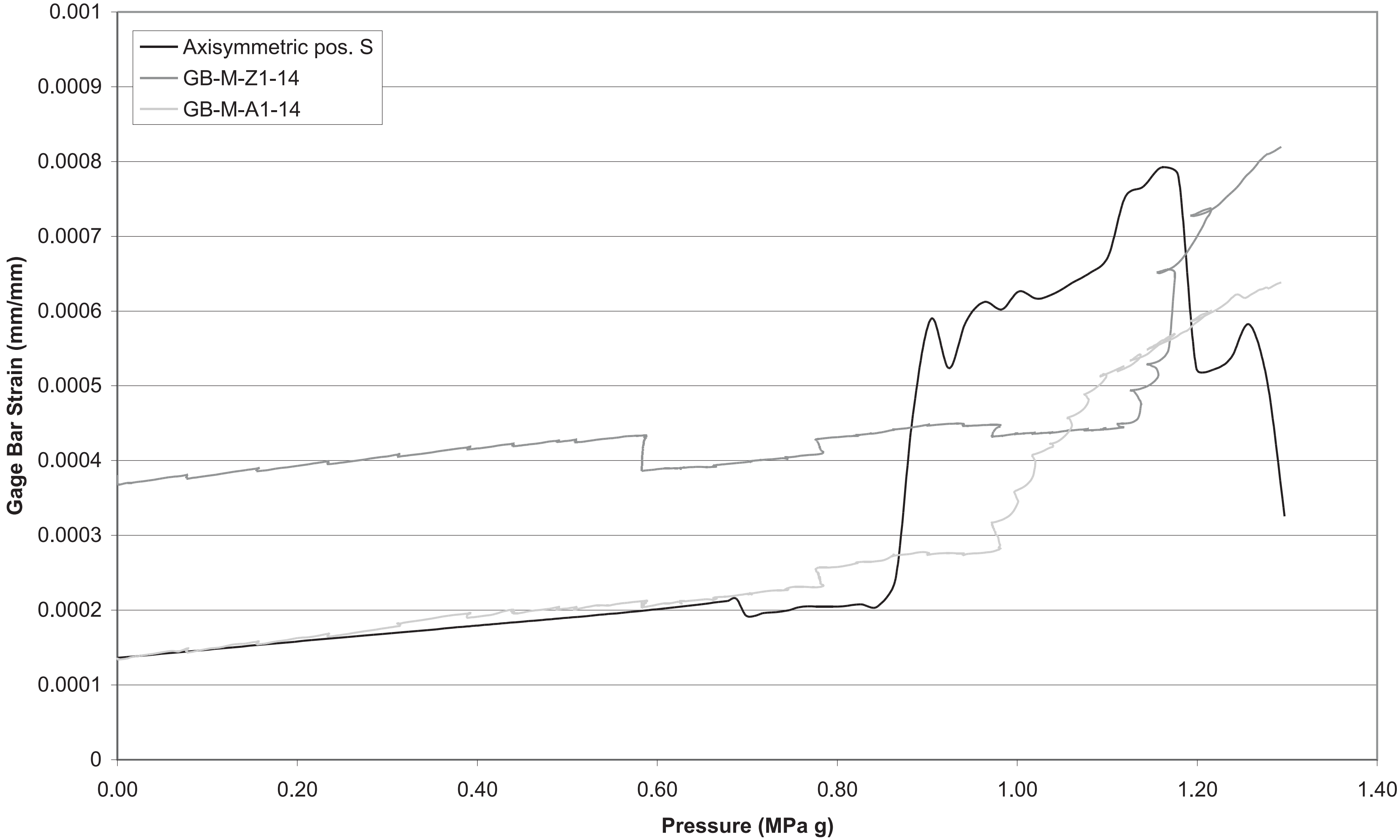

Figure 4-41. 1999 Pretest Analysis vs. LST at Wall Base Gage Bar Position S

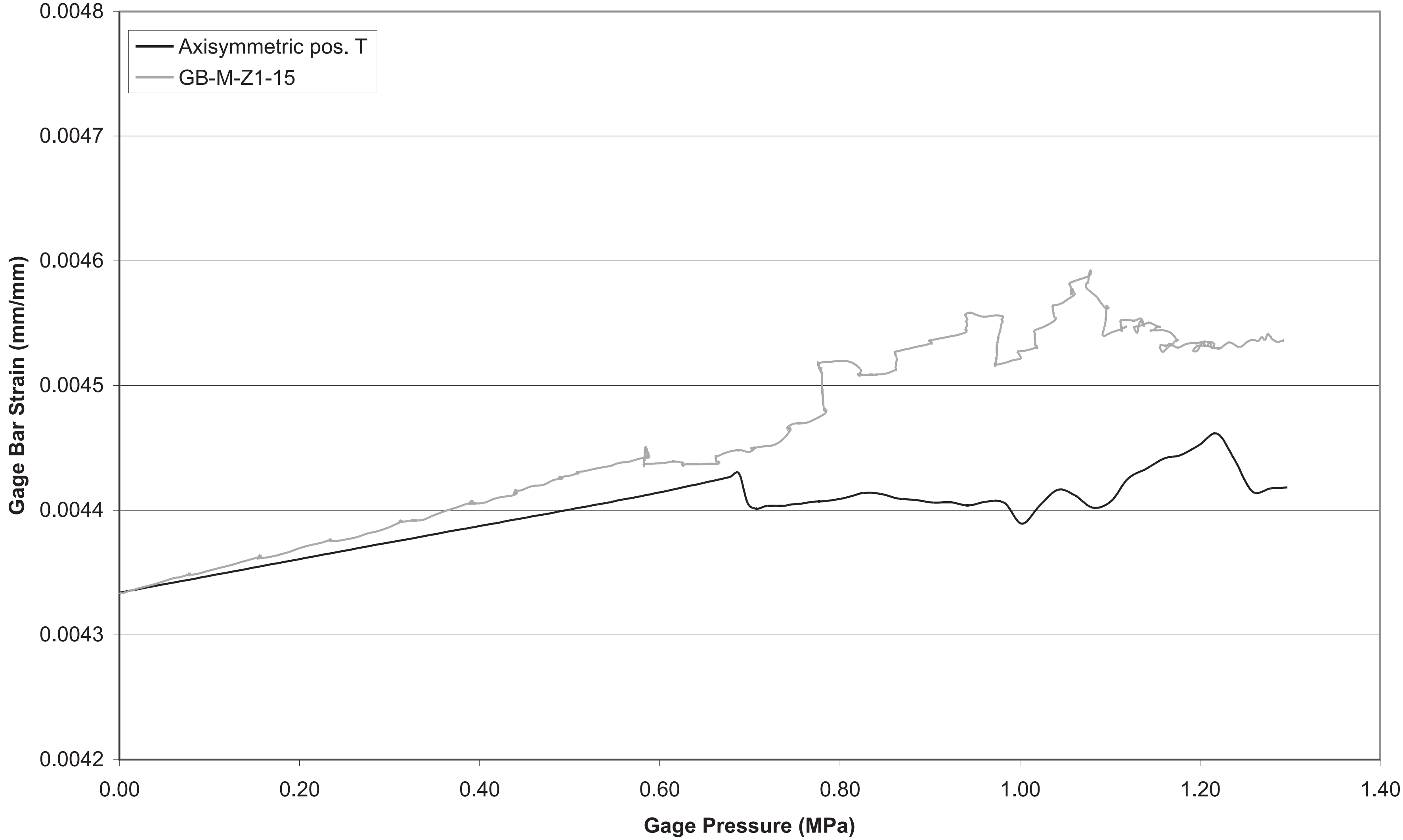

Figure 4-42. 1999 Pretest Analysis vs. LST at Wall Base Gage Bar Position T

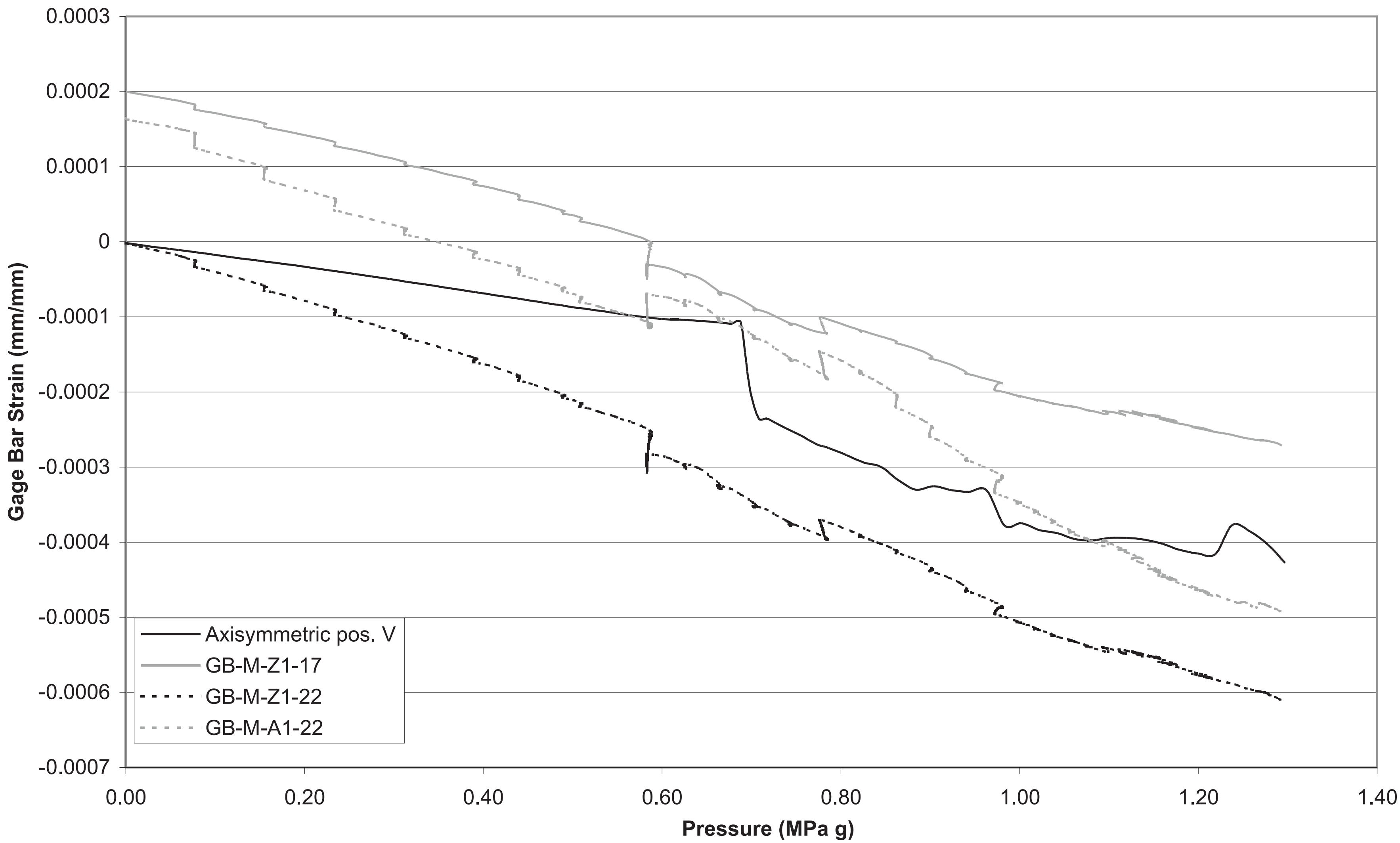

Figure 4-43. 1999 Pretest Analysis vs. LST at Wall Base Gage Bar Position V

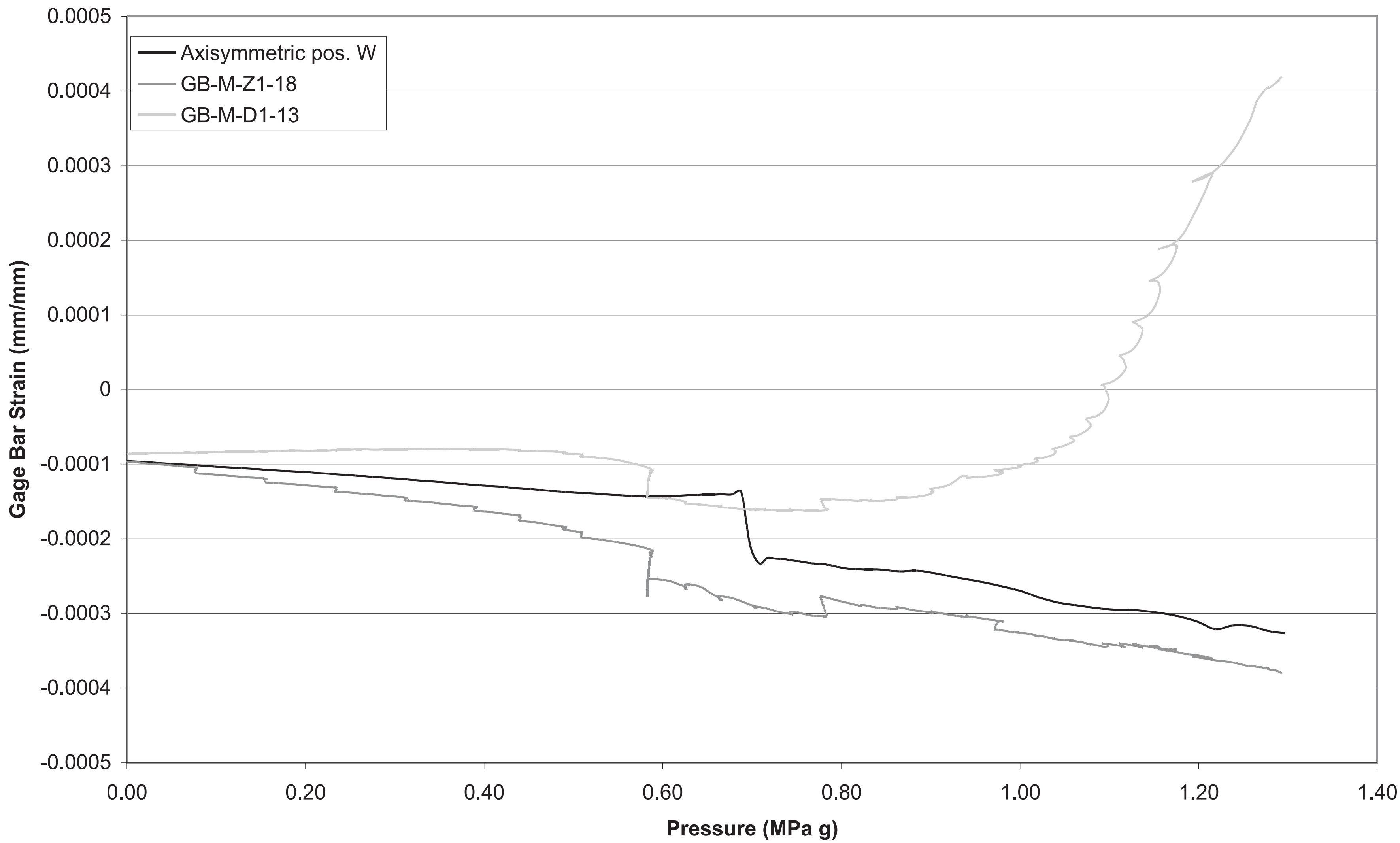

Figure 4-44. 1999 Pretest Analysis vs. LST at Wall Base Gage Bar Position W

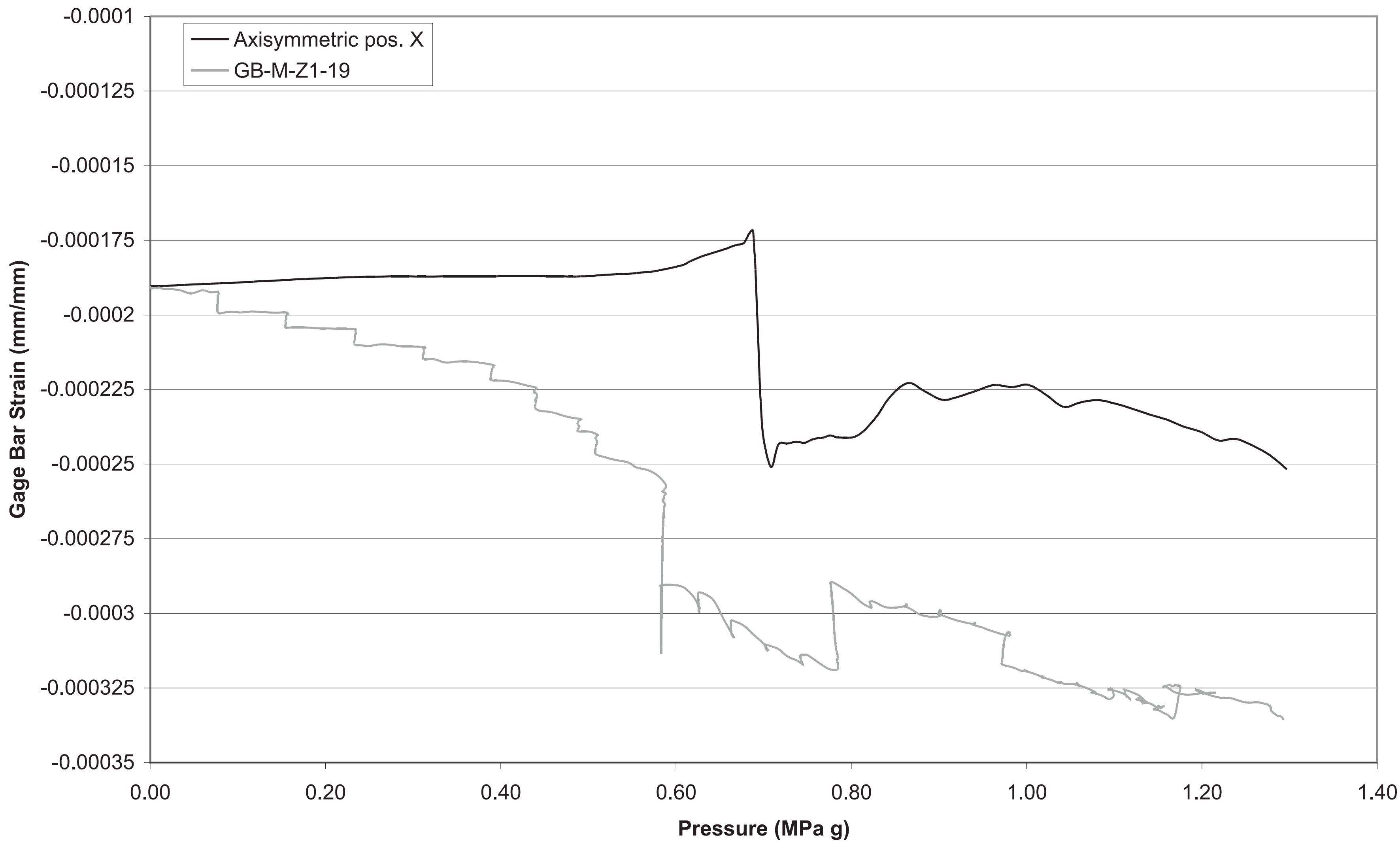

Figure 4-45. 1999 Pretest Analysis vs. LST at Wall Base Gage Bar Position X

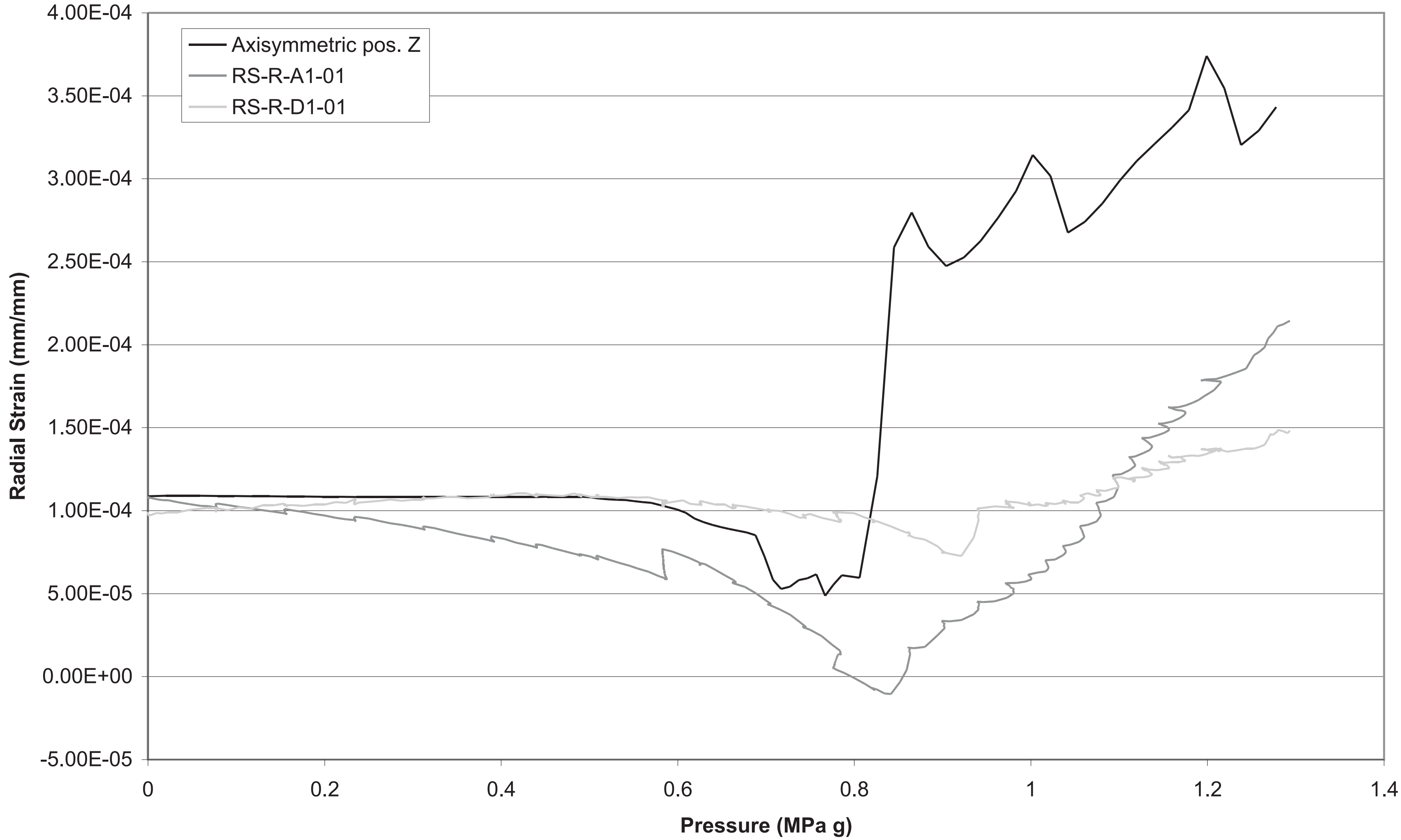

Figure 4-46. 1999 Pretest Analysis vs. LST at Wall Base Radial Stirrup Position Z

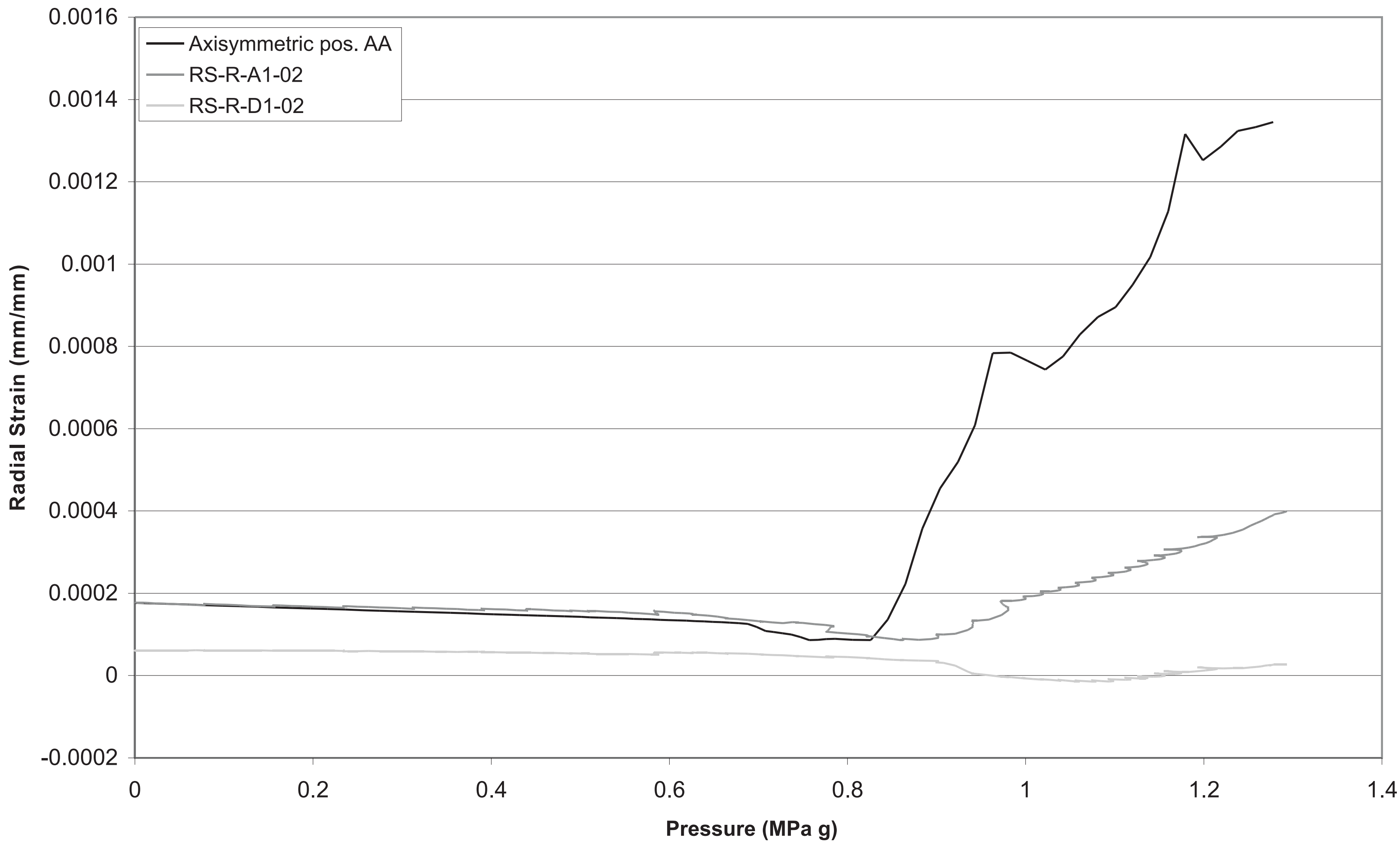

Figure 4-47. 1999 Pretest Analysis vs. LST at Wall Base Radial Stirrup Position AA

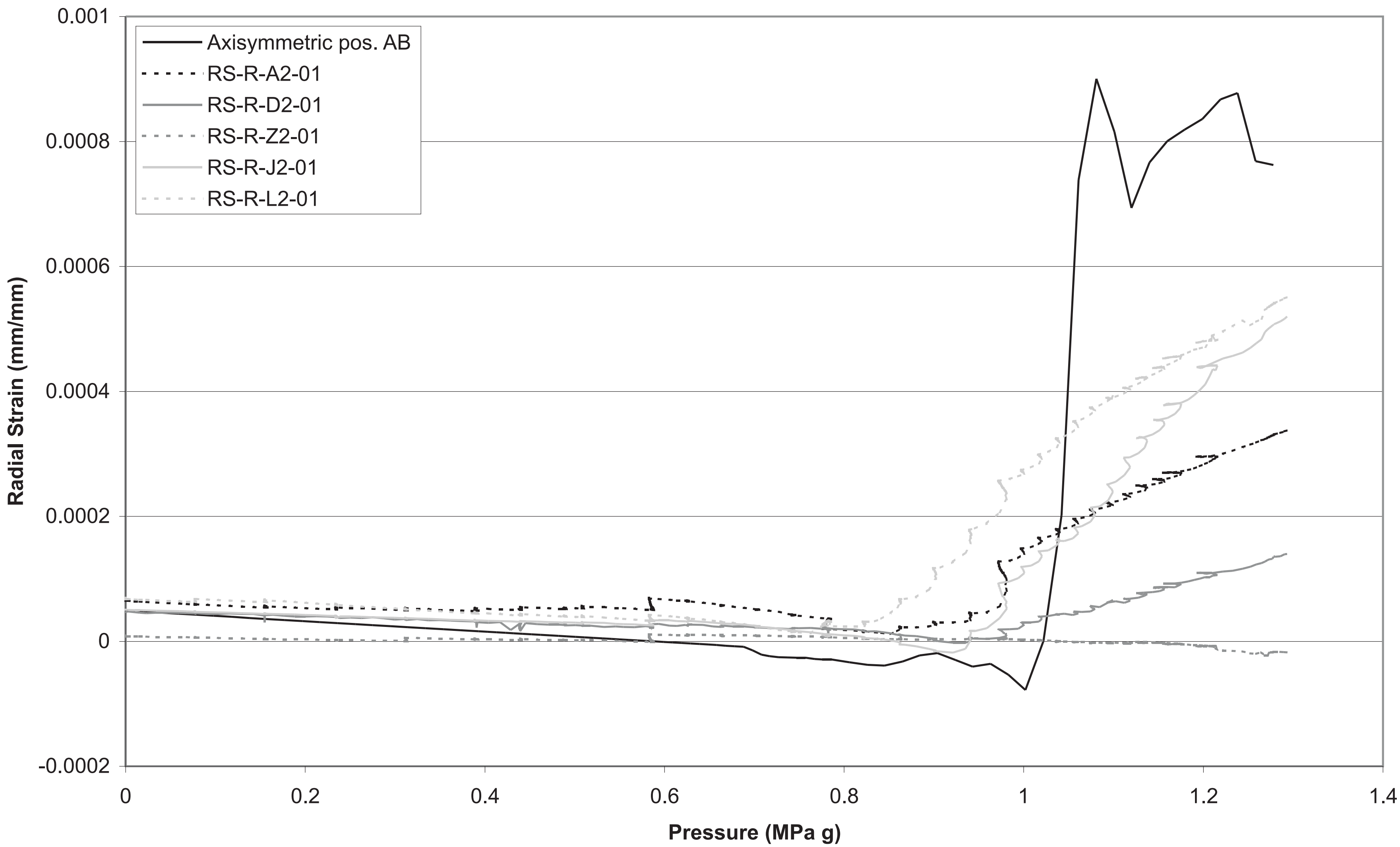

Figure 4-48. 1999 Pretest Analysis vs. LST at Wall Base Radial Stirrup Position AB

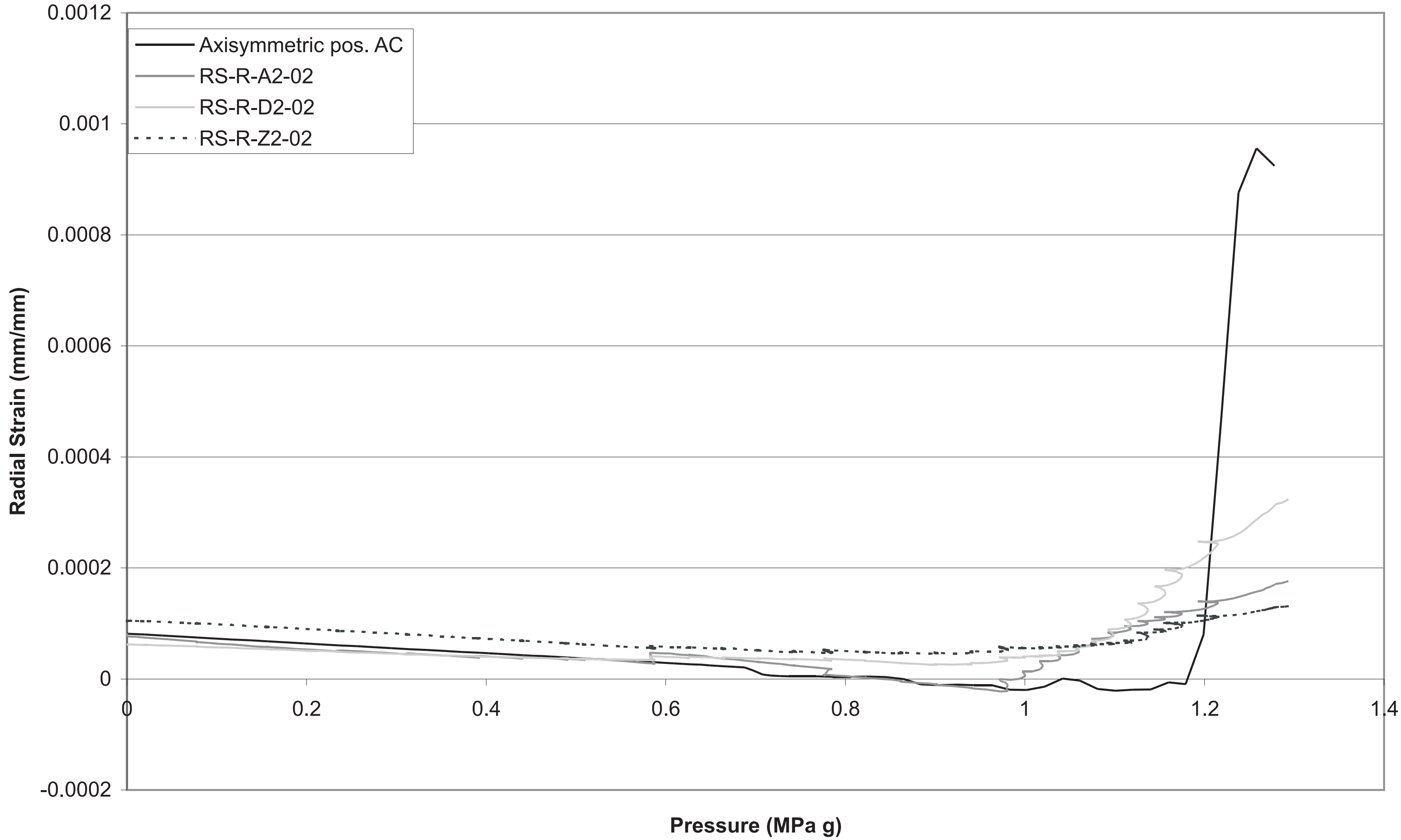

Figure 4-49. 1999 Pretest Analysis vs. LST at Wall Base Radial Stirrup Position AC

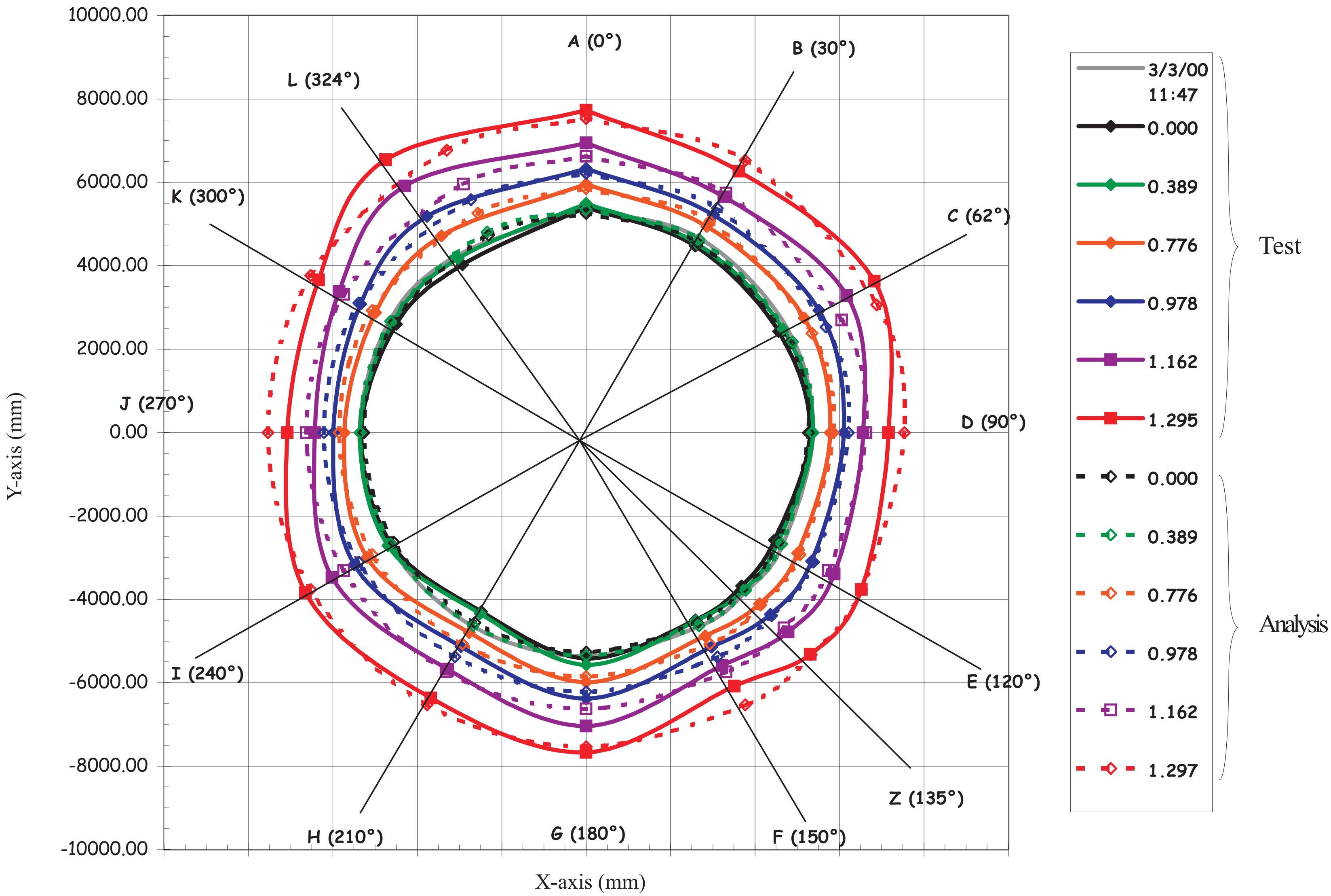

Figure 4-50. PCCV LST - Deformation @ El 4680 (5) × 100
Compared to Axisymmetric Pretest Analysis

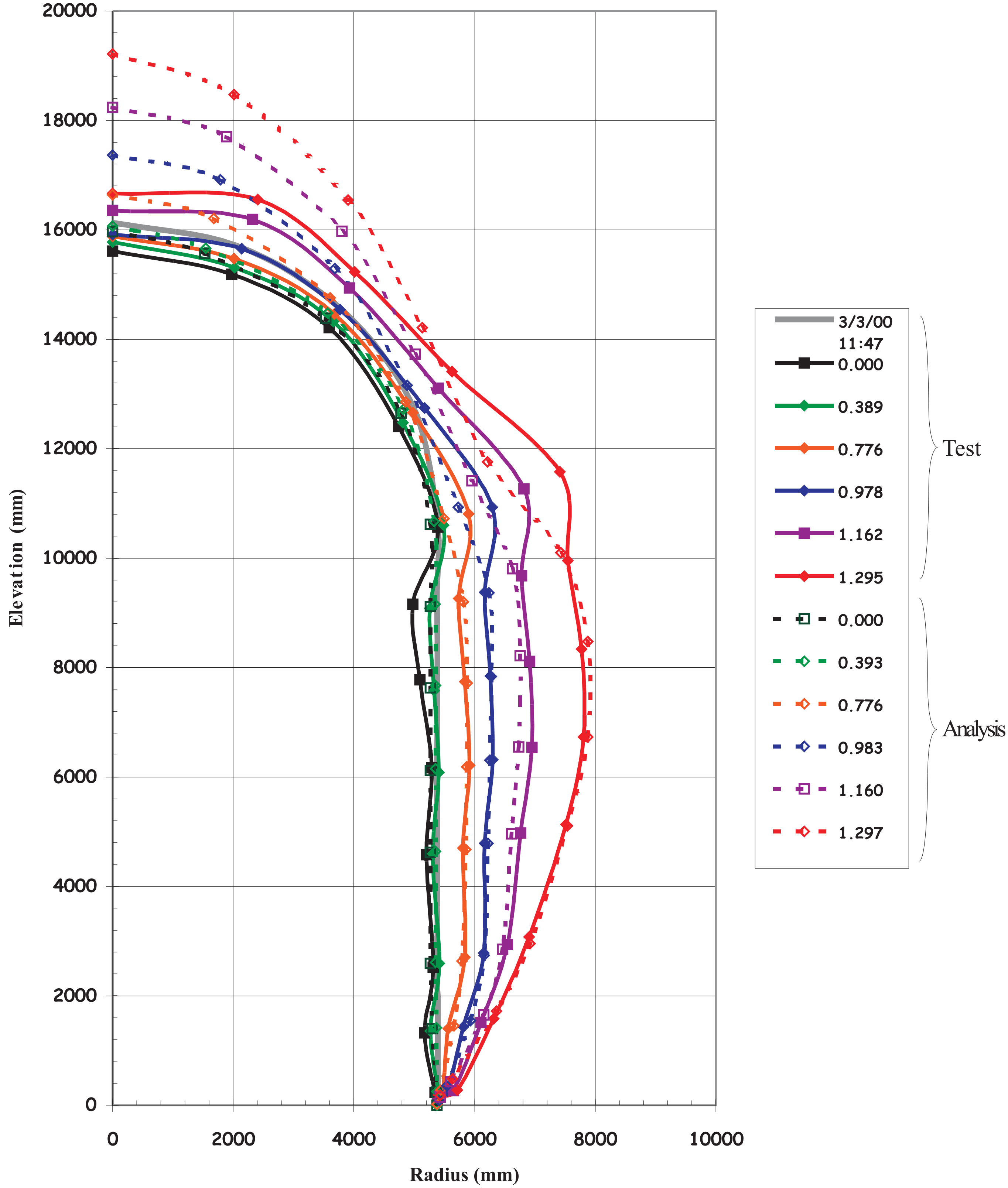

Figure 4-51. PCCV LST - Deformation @ Azimuth 135 (Z) × 100
Compared to Axisymmetric Pretest Analysis

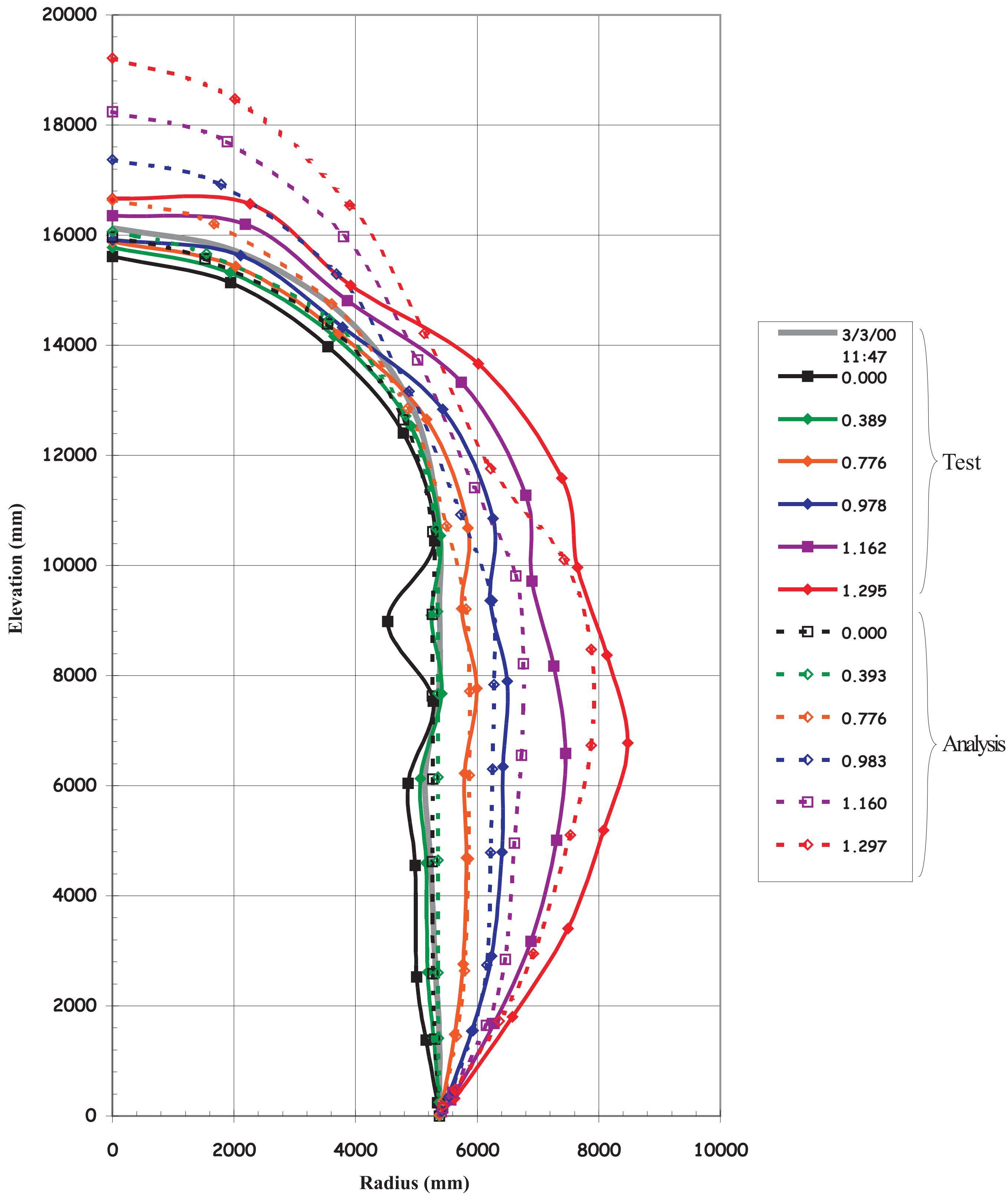

Figure 4-52. PCCV LST - Deformation @ Azimuth 324 (L) × 100
Compared to Axisymmetric Pretest Analysis

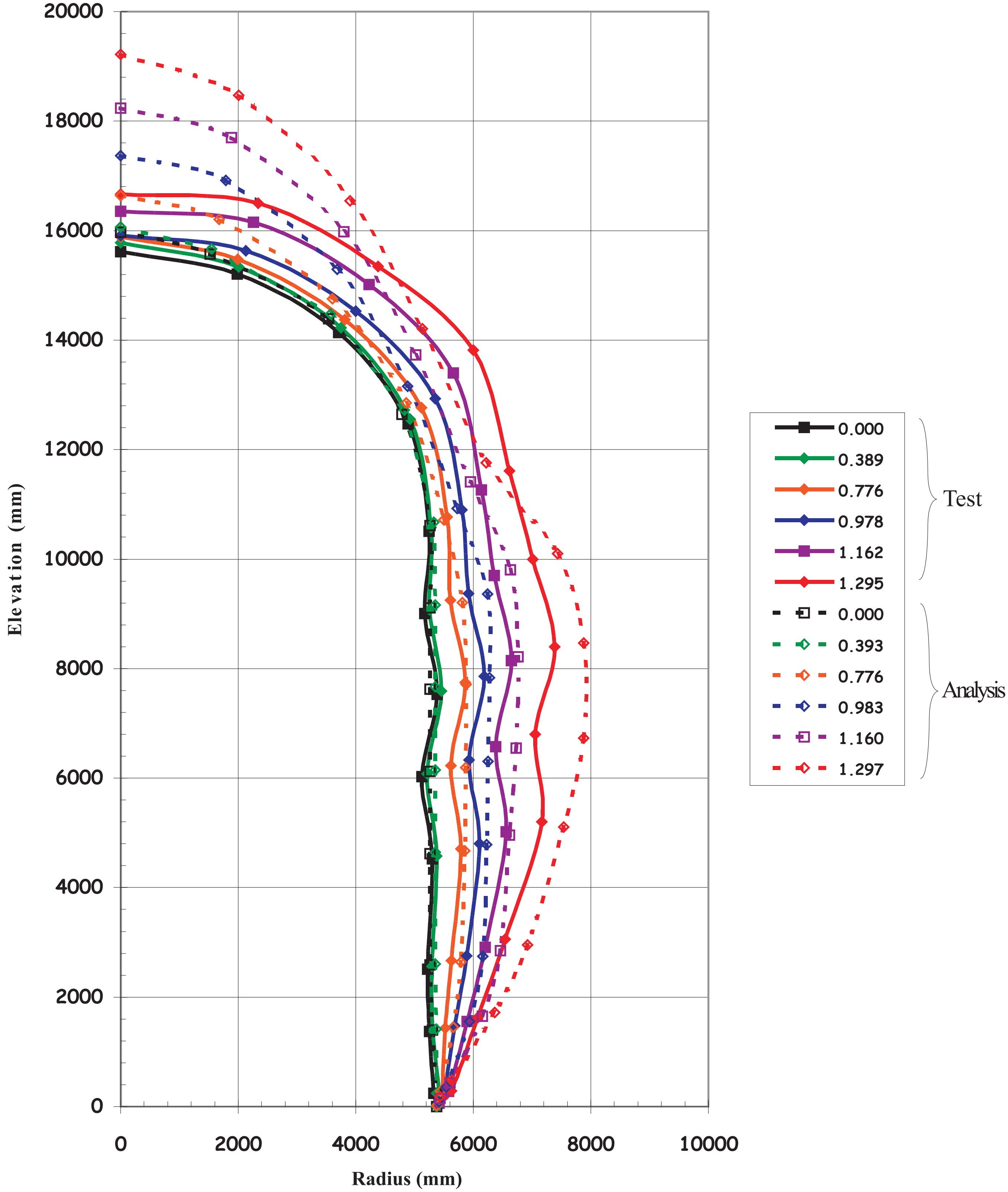

Figure 4-53. PCCV LST - Deformation @ Azimuth 90 (D) × 100
Compared to Axisymmetric Pretest Analysis

5.0 GLOBAL AXISYMMETRIC ANALYSIS

5.1 Overview of Pretest Model

The pretest axisymmetric model represents the 135 degree azimuth, which was assumed to be typical of a "free-field" azimuth, away from buttresses or penetrations. Figure 5-1 illustrates the model. The ABAQUS [5] general purpose finite element program Version 5.8-15, along with the ANACAP-U [4] concrete and steel constitutive modeling program, were used for all pretest analyses [1]. Tendons and their prestressing were modeled to replicate expected tendon stress-strain behavior and friction effects; however, axisymmetric modeling does not allow tendon slip modeling for the hoop tendons, only for the vertical tendons. The pretest axisymmetric grid had 12 elements through the wall thickness near the basemat. The concrete and liner were represented with 8-node quadrilateral elements (ABAQUS CAX8R) and 3-node axisymmetric shell elements, respectively. The total number of elements used was 2009.

The reinforcement in the structure was represented with ABAQUS rebar subelements. These subelement stiffnesses are overlaid onto the parent concrete elements in which they reside, but do not have separate degrees of freedom, and so have strain compatibility with the concrete. The rebar stress-strain behavior is evaluated separately from the concrete, however. The bottom of the model was supported by nonlinear contact springs, with "zero" resistance to uplift and very high compression stiffness. The subgrade stiffness was not considered.

One complex aspect of the pretest analysis models (both global and local) was the tendon modeling. Significant effort was exercised in the tendon representation in order to:

1. Calculate the tendon stress distribution throughout the pressurization sequence, including the effects of friction;
2. Calculate the displacements of the concrete wall correctly, since this drives the liner, thereby driving the prediction of liner strain concentrations.

The vertical tendons were modeled with 144 truss elements (with friction ties to adjacent concrete nodes) and 36 axisymmetric shell elements. Axisymmetric shells were used in the dome to represent the smeared hoop and vertical components of the hairpin tendons. This avoided the mathematical difficulty of terminating tendon elements at the dome apex with a finite cross-section area but zero radius. Hoop tendons were modeled as rebars, so they were always bonded to the concrete. The model was prestressed with the ABAQUS *INITIAL STRESS command in conjunction with the *PRESTRESS HOLD option (for the hoop tendons) that allowed the model stresses to equilibrate, while forcing the hoop tendon stresses to remain at predetermined levels.

Pressure load was applied to all interior model surfaces over 161 increments. The ABAQUS feature DIRECT=NOSTOP was used with five iterations per load step. The five iterations ensure that materials in the plastic range stay on a yield surface, but the "NOSTOP" parameter allows advancement of the solution before achieving full force convergence, which is difficult to achieve in cracked concrete elements. Instead of achieving force convergence, the displacement convergence at each increment was monitored to ensure the quality of the solution.

Some results of the axisymmetric analysis are plotted in Figures 5-2, 5-3, and 5-4. As in Chapter 4, results of both the 1999 (pretest round-robin submittal) and the 2000 pretest analysis are plotted. The primary difference in the two analyses is the vertical tendon prestressing–the 2000 analysis introduces large friction losses into the straight run of vertical tendon. These figures show displacements versus pressure at several points on the model. The vertical grid lines on the pressure history plots represent multiples of design pressure, Pd = 0.39 MPa. A comparison of these results to the test were provided in Chapter 4. For radial response, different critical milestones can also be noted by the changes in curve slope. Cylinder cracking coincides with the slope jump in the curves at about 1.7 Pd. Progressive yielding of steel elements corresponds to the gradually increasing slope of the displacement curves.

The two primary damage locations predicted by the axisymmetric analyses were the cylinder midheight and the wall-basemat juncture. The largest strains tended to occur near the inner corner of the wall-basemat juncture, in the concrete near the liner anchor embedment. The pretest study of potential shear failure at the wall-basemat juncture showed that while wall-basemat outer surface concrete crushing (compressive stress reaching f_c') was predicted to occur by 3.2 Pd, a through-wall shear failure was not likely until at least 4.0 Pd. Other failure modes were judged to be more likely prior to reaching this pressure. This prediction appears to have been borne out by the test. Note that, although no evidence of "crushing" was observed on the outside surface of the cylinder wall-base, f_c' may have been reached as predicted by analysis. Visible evidence of crushing would only occur at compressive strains that are much larger than the -0.0025 required to reach stress of f_c'. Strains of about 0.005 would be necessary for visible spalling to occur.

5.2 Changes to Pretest Model

While the predicted radial expansion behavior of the cylinder was accurate (within ~4%) with the pretest model, as outlined in Chapter 4, the basemat uplift and dome vertical displacement were significantly overpredicted. A posttest analysis effort was undertaken by making changes to the axisymmetric model to calibrate to the test. Initially, the following changes were made strictly to assess the sensitivity to these changes:

1. 10% additional prestress was added to the vertical tendons,
2. 10% additional vertical prestress area was added to the dome, and
3. Very thorough check of basemat rebar input was conducted.

Initial posttest analyses were run with ABAQUS Version 5.8-15. Results of these initial sensitivity analyses for vertical tendon prestress showed some promise in getting closer to the test measurements. However, early in 2001, the authors started using ABAQUS Version 5.8-18 in an effort to ensure that all of the PCCV analysis work would be upwardly transportable to new versions of ABAQUS. When this version transfer was made, a significant program bug was found in 5.8-18 (and 5.8-21) related to the use of prestress hold and small deflection theory. (Note that small deflection theory was used in conjunction with the tendon friction modeling strategy adopted for the curved portions of tendons.) This bug was finally resolved by ceasing to use the prestress hold option. Currently, Version 5.8-18 for all analyses is used, but without prestress hold, by increasing the prestress by trial and error to account for elastic shortening. Confirmation that the new strategy and new version can now replicate the pretest results is provided in Figures 5-2, 5-3, and 5-4. This is a significant finding and change in solution strategy for the conduct of containment analysis using ABAQUS.

Once this bug was resolved, global model calibration was continued and consisted of the following steps.

1. Basemat rebar checking was completed, and checked out ok.
2. A basemat spring sensitivity study was conducted.

The basemat spring study began by a two order of magnitude softening of the support spring compression stiffness. This produced very little change in results. Then a hand calculation of the supporting soil stiffness (as transmitted through the mudmat) was performed and incorporated into the model. The weight of the PCCV model (including the instrumentation frame) was calculated to be approximately

$$W = 4{,}800 \text{ kips}.$$

A stiffness along the bottom of the basemat was assumed based on a total dead load deflection of 0.1 inch (2.5 mm). This is based on an assumption of typical subgrade properties working in conjunction with the 15-cm-thick concrete mudmat. Then the basemat spring stiffnesses were distributed based on tributary area following the 1/6:2/3:1/6 rule for isoparametric elements with mid-side nodes. This produced vertical uplift displacements that were less than the pretest analysis, but still much larger than the test measurements. As a sensitivity check, one order of magnitude softening and stiffening of the compressive springs was introduced and analyzed. The results of the basemat compression spring sensitivity evaluation are summarized below.

- Pretest solution was based on an "essentially" rigid base with zero tensile resistance.

- Adjusting the *distribution* of forces on the underside of the basemat by assigning stiffness according to tributary areas achieved minor reduction in uplift and more rational distribution of support forces, but the compression stiffness assumed was still very stiff. This means that even small basemat flexure or bulging is manifested as uplift, i.e., the bulging is reacted against a rigid surface.

- Trying softer stiffnesses to account for soil behavior tends to increase basemat flexure, but this is compensated by the "starting point" of uplift, i.e., the negative displacement due to dead load before pressurization. The results of the foundation stiffness sensitivity cases are plotted in Figures 5-5, 5-6, and 5-7.

Through this foundation sensitivity study, insights have emerged that, in the authors' opinion, explain the basemat displacement phenomena and why the basemat uplift measurements showed essentially zero uplift. The basemat underside pressure for the final two axisymmetric analyses are plotted in Figures 5-8 and 5-9, and a deformed shape for the final posttest case is plotted in Figure 5-10. With the refined foundation spring modeling, the absolute (without rezeroing or adjusting for dead load) displacements of the center of the basemat and the outer edge of the basemat are plotted in Figure 5-11. This shows that under deadload, the basemat settles downward roughly uniformly by about –2.54 mm. This is a direct result of the foundation stiffness assignment based on engineering judgment. During pressurization, however, the center and edge displace very differently. As the basemat flexes, the contact pattern shrinks (as shown in Figures 5-8 to 5-10) so the weight of the model is distributed over a smaller area and settles deeper into the soil (i.e., more downward displacement occurs). At the edge, however, the displacement begins rising until finally, at about 2.5 Pd, it becomes positive. It is reasonable to assume (as drawn in Figure 5-10) that the mudmat, which is several orders of magnitude more flexible than the basemat, will follow the dished shape of the basemat. All parts of the mudmat are likely to elastically rebound as bottom surface pressures decrease at the outer radii. This elastic rebounding will continue until the absolute displacement crosses zero, the point where the soil was stress-free prior to constructing the model. This theory explains how, even with some appreciable basemat flexure, the mudmat could remain in contact with the basemat at relatively high pressures, and thus register virtually zero displacement measurement. Late in the LST, the outer edge of the basemat might have begun to uplift slightly, but without detailed soil stiffness measurements this would be very difficult to predict. It is even possible that the outer edge of the mudmat could have lifted slightly simply due to kinematics (as shown in Figure 5-10), but this too was impossible to measure. Note that all of the displacements associated with this basemat flexure phenomenon are very small (~2 mm).

The final foundation stiffnesses used in the posttest analysis were judged reasonable, forming the basis of the final axisymmetric analyses. In the revised comparison to SOL #1, the analysis result was plotted as zero when the result was negative, and positive when it crossed the axis. Per the preceding discussion, this result represents the stress/force neutral point of the supporting soil prior to constructing the model and the point after which the mudmat might stop following the underside of the basemat.

The last set of modeling changes dealt with the dome. In the final posttest analysis, the stressing of the vertical tendons was kept the same as in the 1999 analysis (no friction along the straight portion) because it agreed best with measured and observed behavior. The dome tendon strategy, however, was modified. The change was based on the observation that the nonaxisymmetric geometry of the "hairpin" tendons, at azimuths such as 135 degrees, leads to contributions from both sets of hairpin tendons. Both sets intersect the 135-degree r-z plane at 45 degrees. Thus it was deduced that the effective thickness for the shell used to model the vertical tendons is actually 2cos (45 degrees) times the thickness used in the pretest analysis. The final posttest analyses reflect this change, i.e., a 41% increase in dome tendon area, which provided improved correlation to the test.

5.3 Results and Comparisons

The displacement profiles at the 135 degree azimuth that were compared to the pretest analysis are recompared to the final posttest analysis in Figure 5-12. All of the axisymmetric analysis results are then recompared to the test in Figures 5-13 through 5-23. The LST converted and temperature corrected data is plotted along with a posttest analysis using the 1999 model with modified basemat "soil" springs, added dome tendon thickness, and a set of curves labeled "Final Posttest." The final posttest analysis is the same as the "1999-Soil-Mod-5-Dome," but with updated material properties to match those used immediately prior to the test. Both curves are provided for comparison. For most of the data locations, the most up-to-date material properties provide the closest correlation. This is especially true of the radial displacement plots, SOLs 2 through 6.

All of the wall-base juncture comparisons are replotted with the final posttest analysis in Figures 5-24 through 5-46.

The plots and discussion in this section provide an explanation of basemat uplift behavior, and dome vertical displacement correlation is improved, but is still overpredicted by analysis. Prediction of radial displacement at the springline (SOL 7) is also low by about a factor of 2, but all other behavior comparisons show generally good correlation.

5.4 Conclusions on Global Analysis

The conclusions reached about the global axisymmetric analyses performed for the project and discussed in Chapter 4 and 5 are summarized below.

- Pretest Analysis: Radial displacements were generally well predicted by global axisymmetric analysis, but dome and vertical displacements were significantly overpredicted.

- Posttest Analysis: uplift and displacement predictions were significantly improved by softening and redistributing soil basemat springs according to tributary area. Dome displacements were improved by thickening the dome meridional tendon representation due to the rectilinear hairpin layout.

- The behavior predictions were improved by using no vertical tendon friction in the cylinder.

- Wall-base juncture behavior was well predicted by the detailed wall-base juncture (axisymmetric) modeling, and by the pretest analysis, but was further improved in the final posttest analysis.

- Analysis with the 5.8 series versions of ABAQUS should not use the prestress hold option. In general, a trial-and-error method for choosing prestress levels that equilibrate to the desired levels has proven reliable.

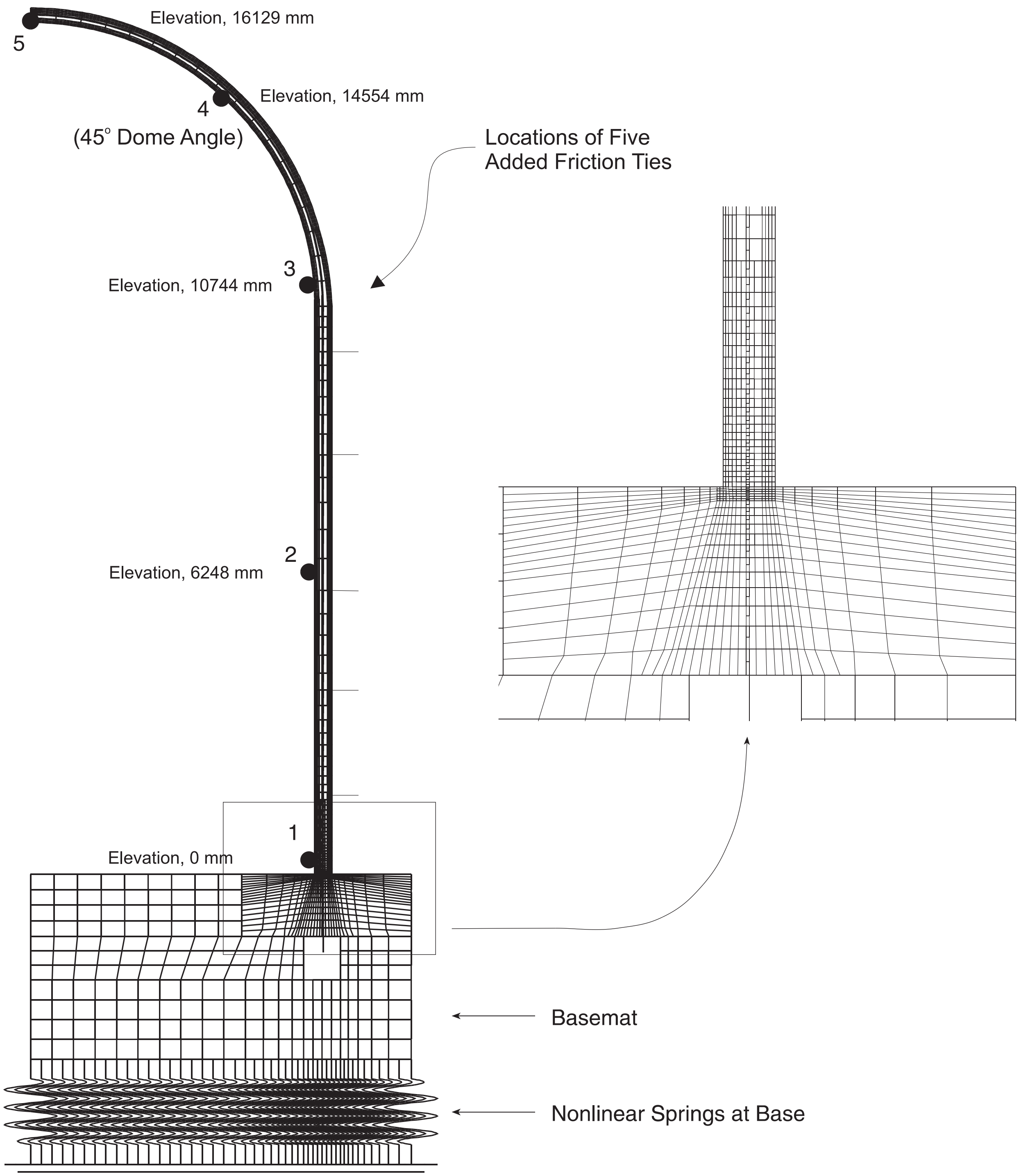

Figure 5-1. Axisymmetric Model of PCCV and Locations for Plotted Output

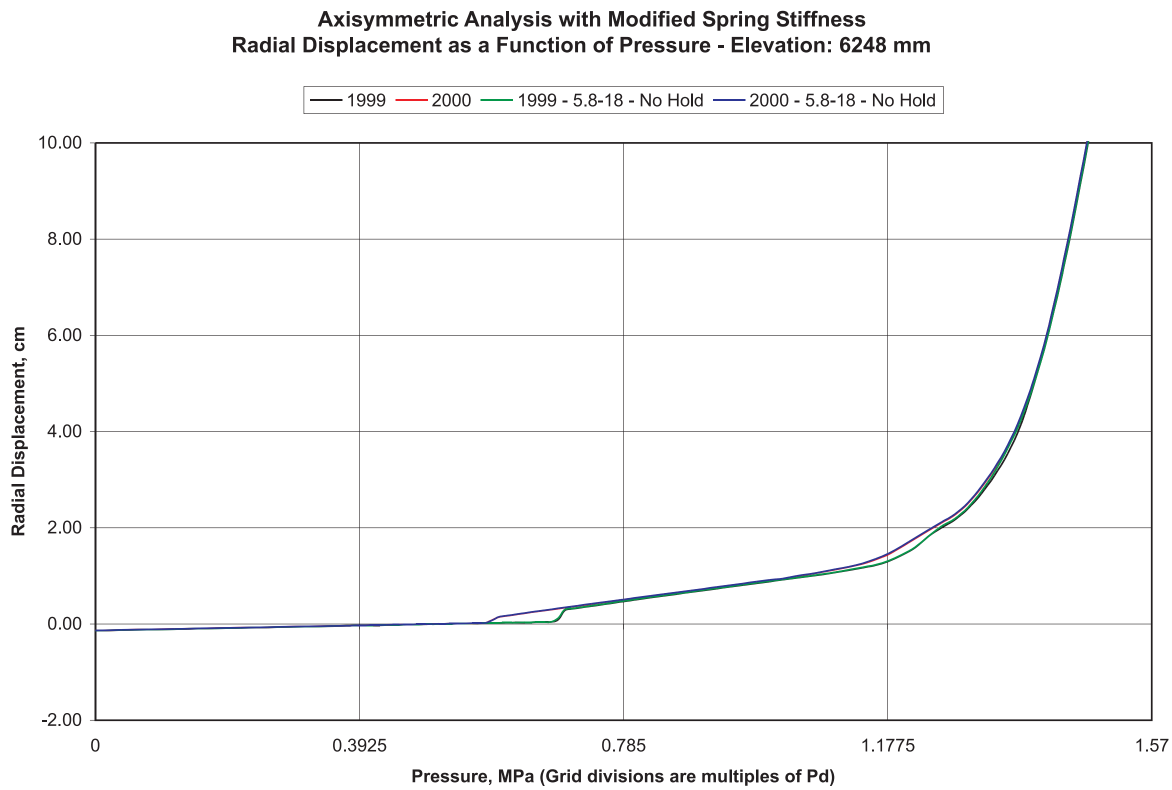

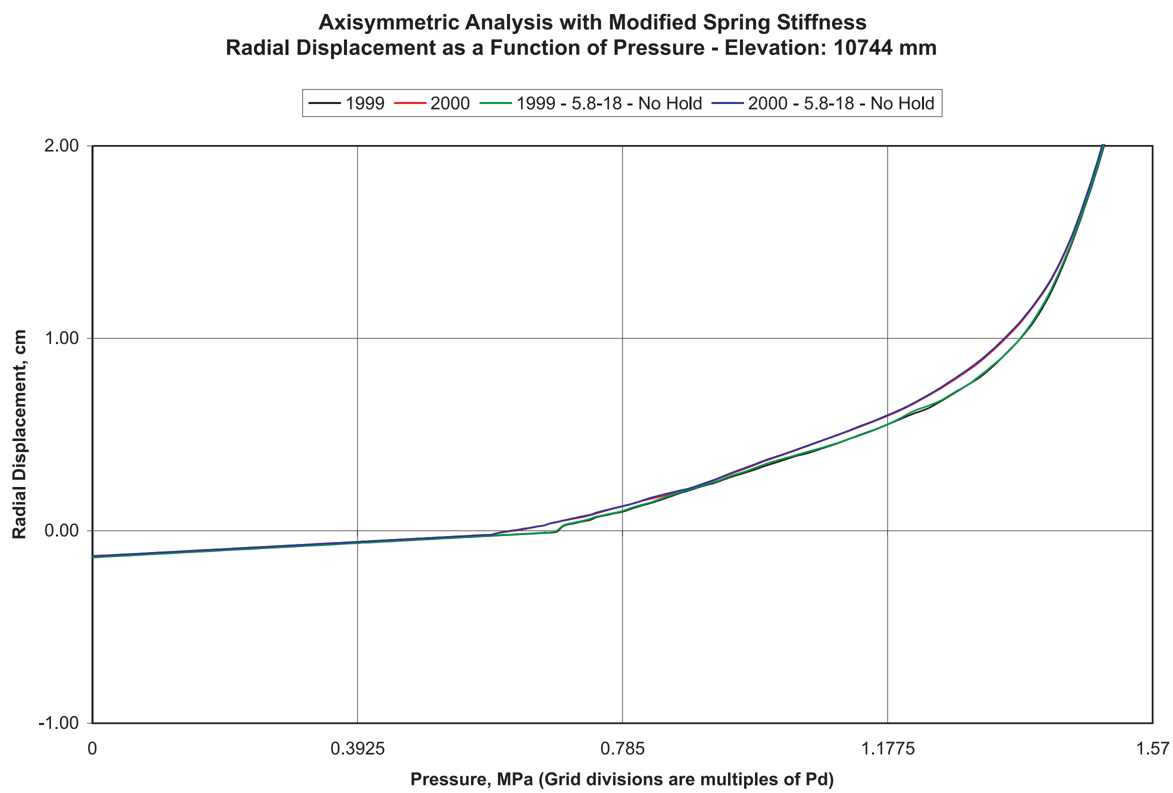

Figure 5-2. Radial Displacements Comparison of Pretest and Posttest Analysis using Different ABAQUS Versions and No Prestress Hold

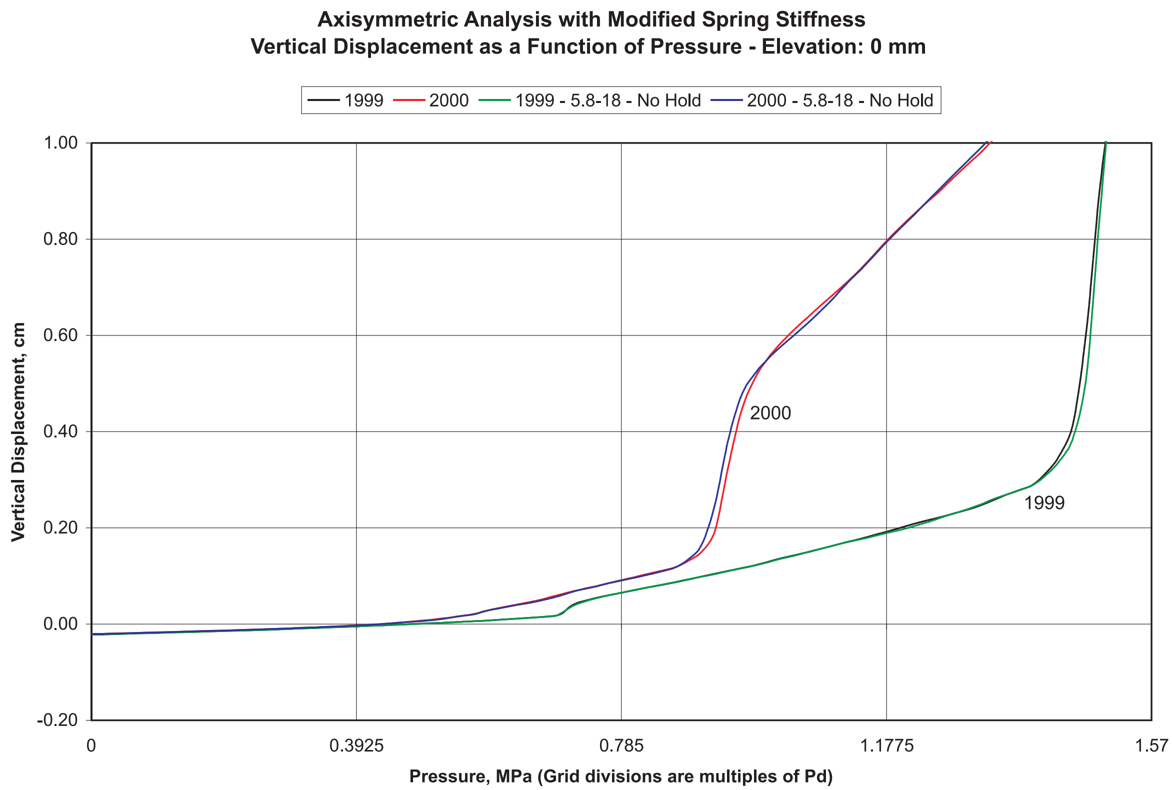

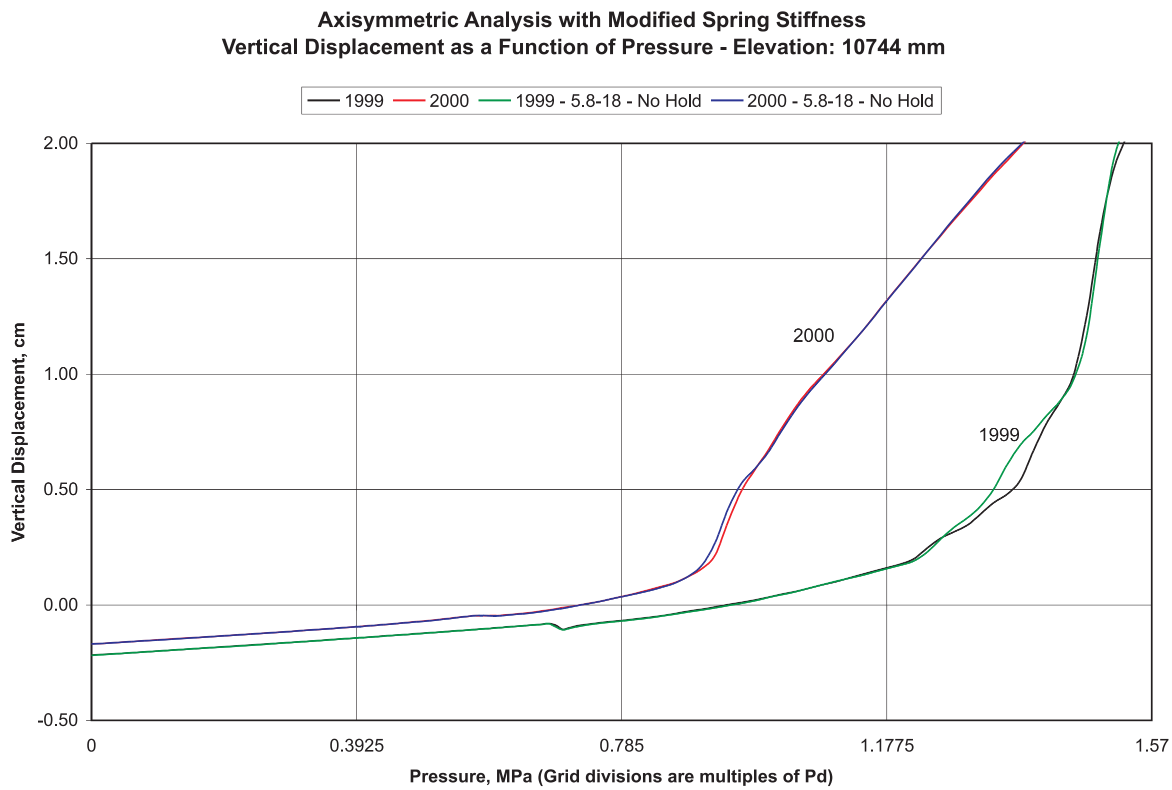

Figure 5-3. Vertical Displacements Comparison of Pretest and Posttest Analysis using Different ABAQUS Versions and No Prestress Hold

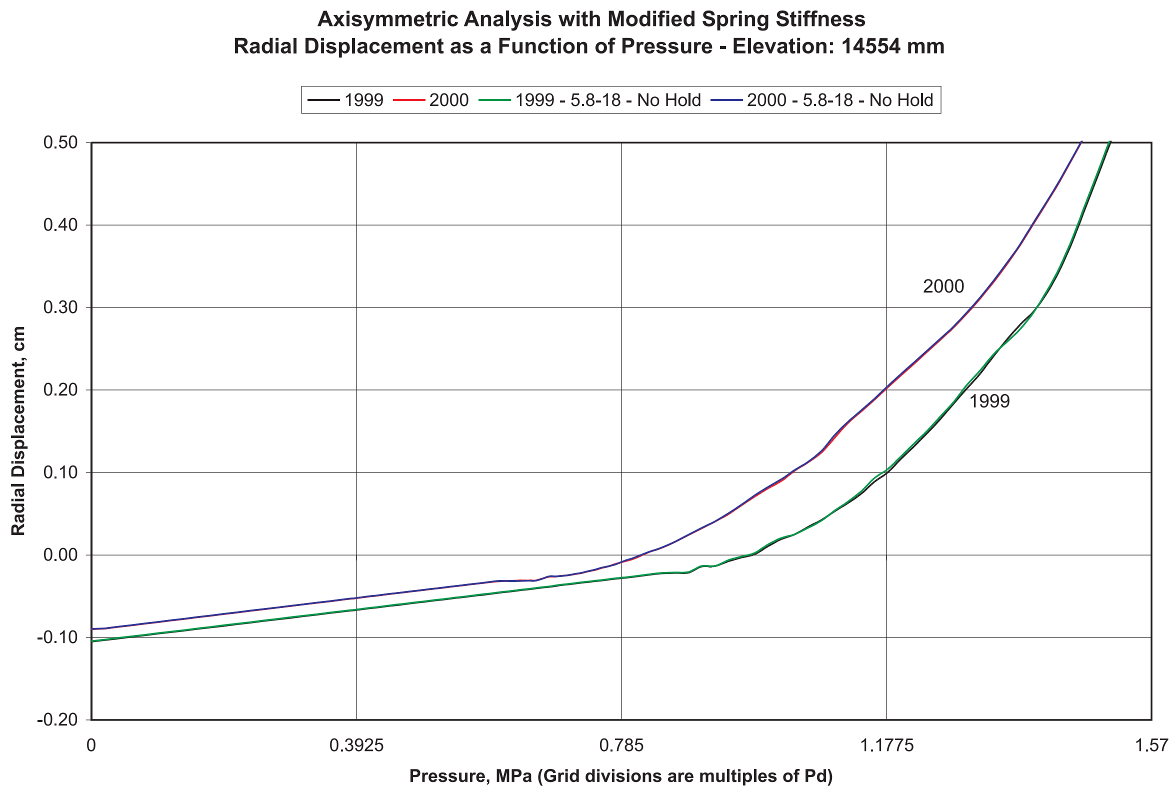

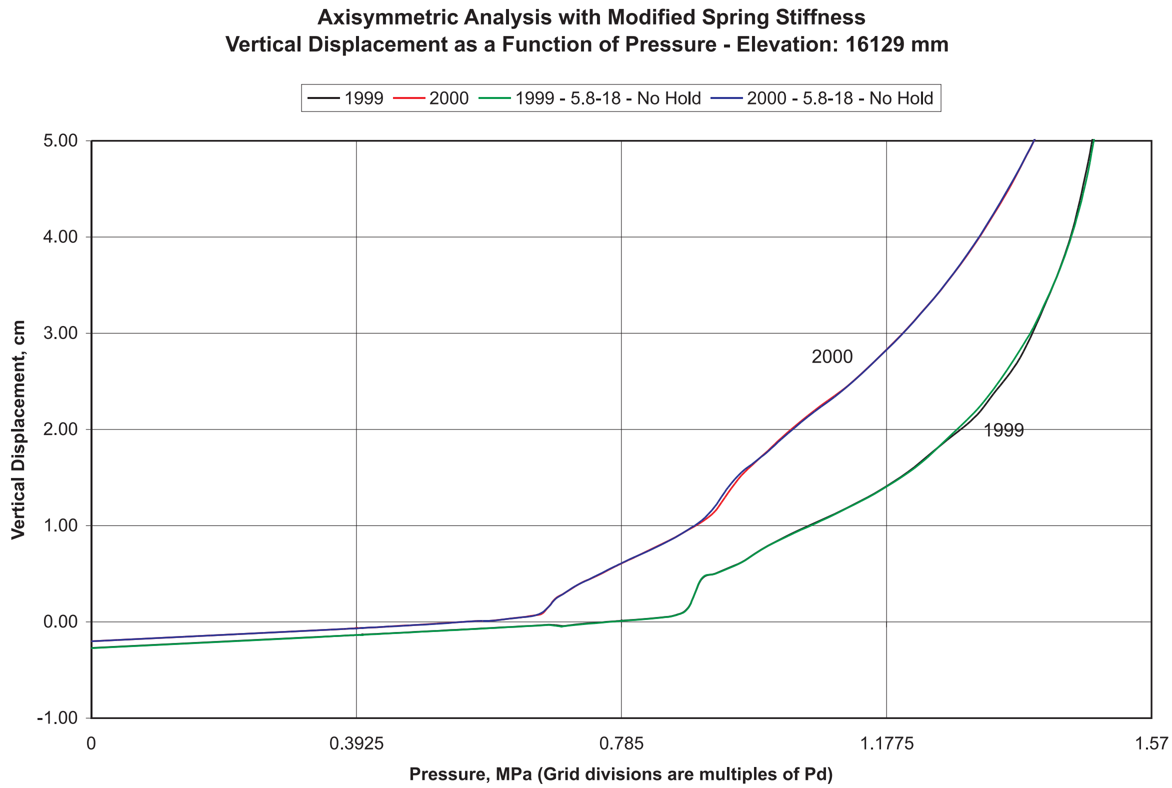

Figure 5-4. Dome Displacements Comparison of Pretest and Posttest Analysis using Different ABAQUS Versions and No Prestress Hold

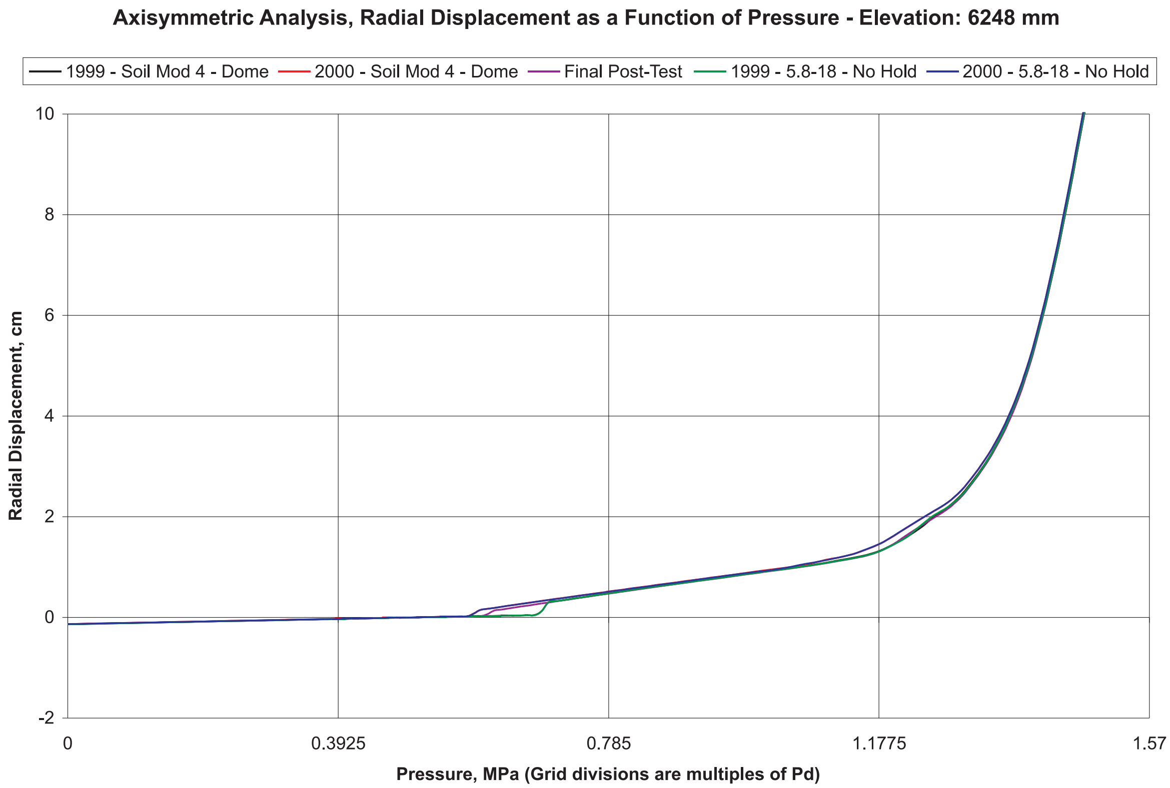

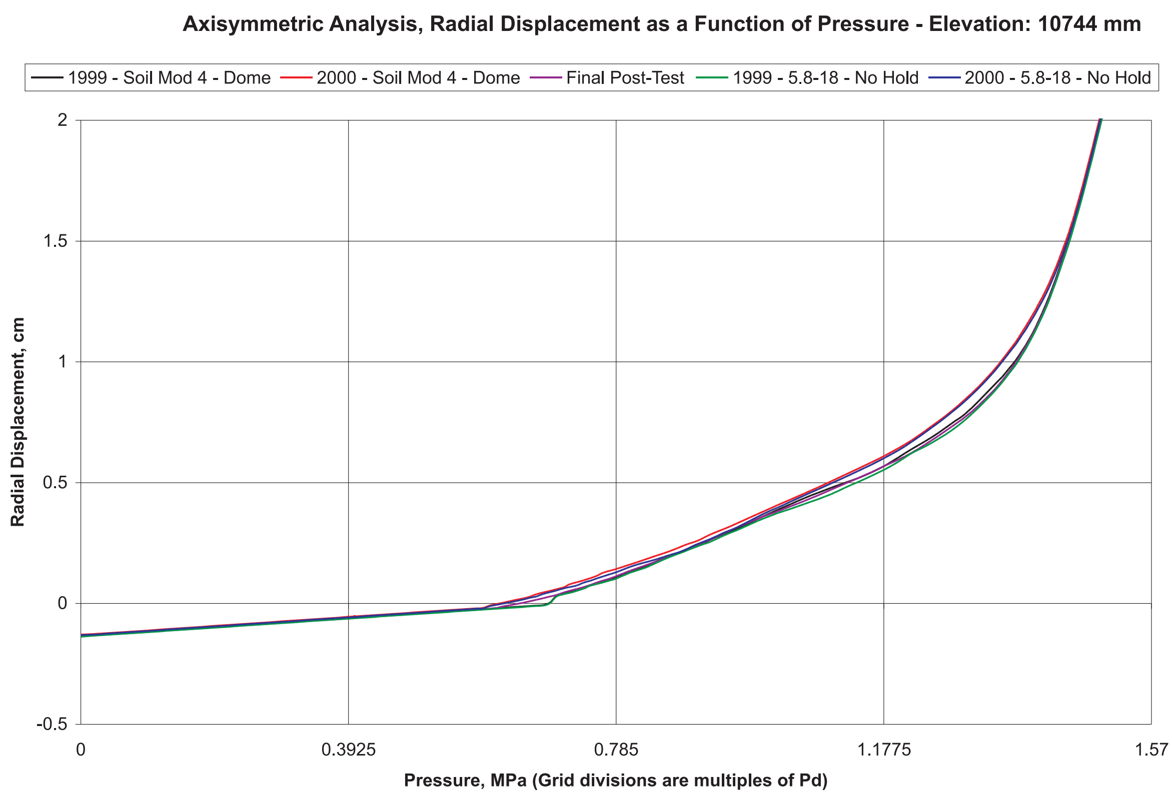

Figure 5-5. Radial Displacements Comparison of Pretest and Posttest Analysis using Different ABAQUS Versions and No Prestress Hold

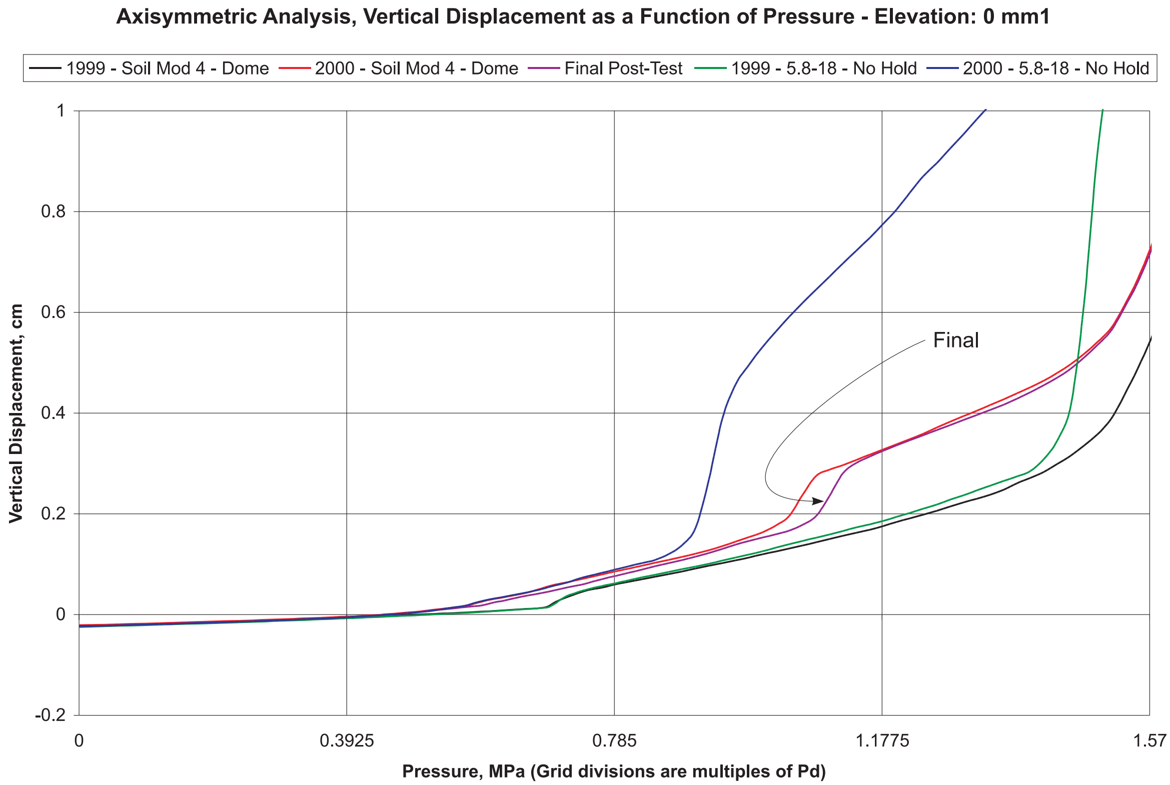

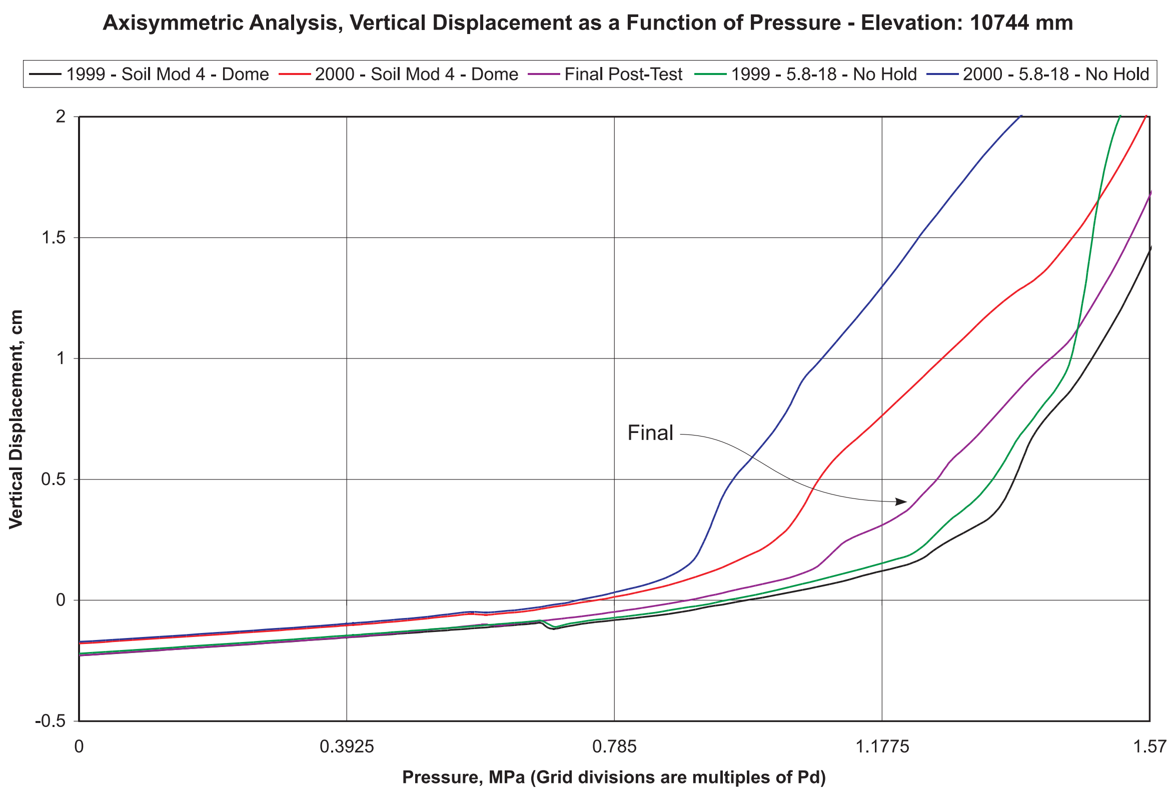

Figure 5-6. Vertical Displacements Comparison of Pretest and Posttest Analysis using Different ABAQUS Versions and No Prestress Hold

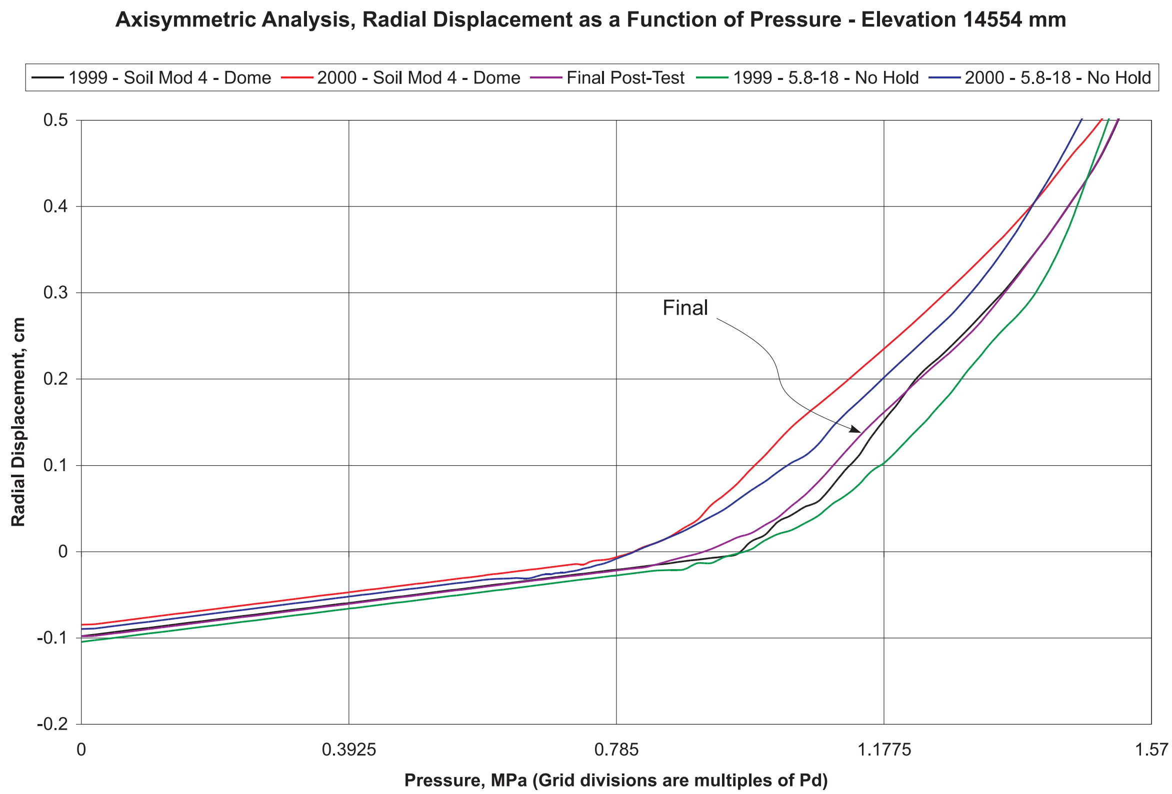

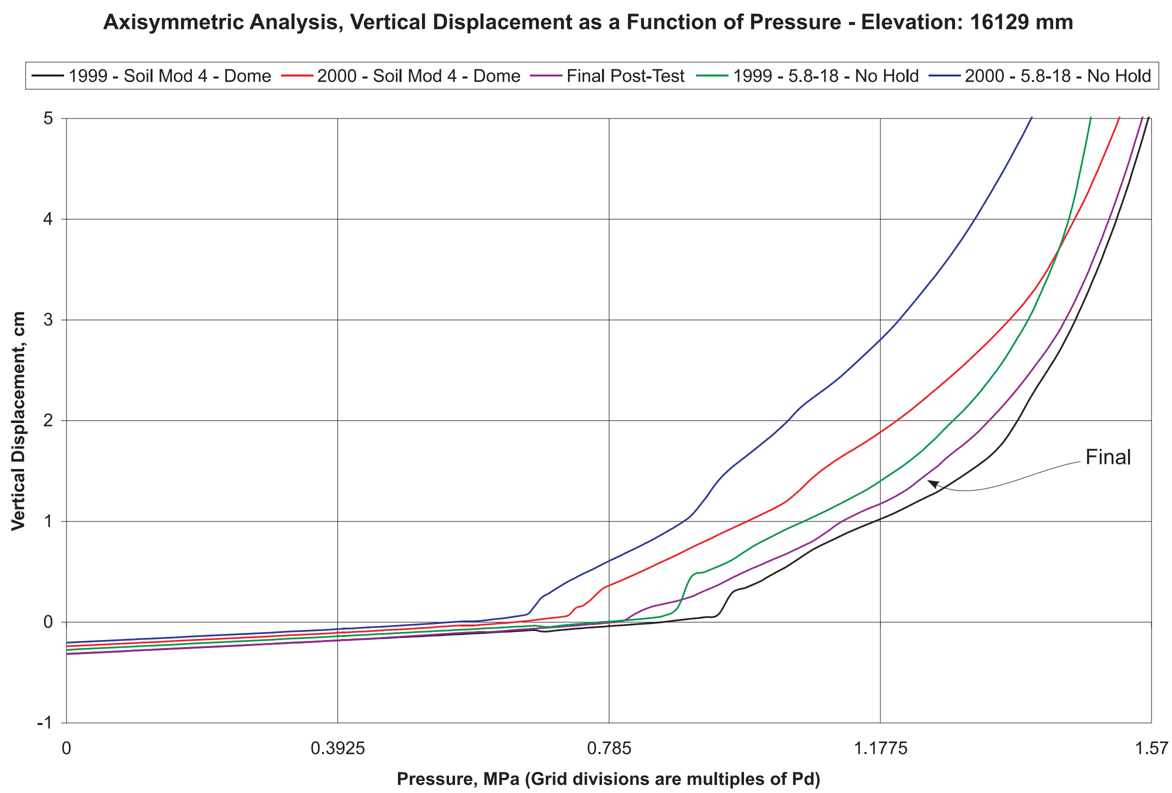

Figure 5-7. Dome Displacements Comparison of Pretest and Posttest Analysis using Different ABAQUS Versions and No Prestress Hold

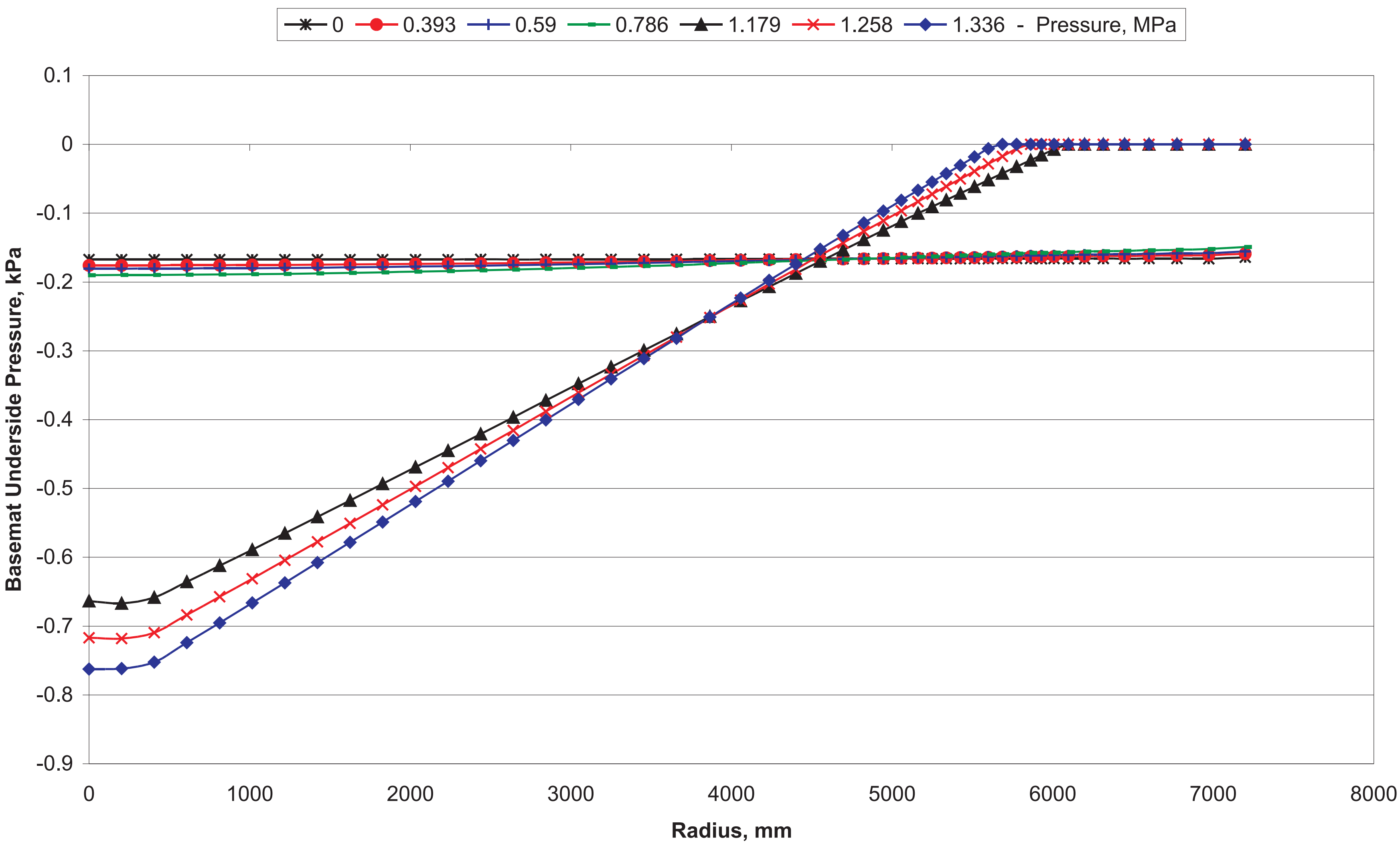

Figure 5-8. Basemat Underside Pressure versus Radius, 1999 Analysis with Final Soil Springs and Dome

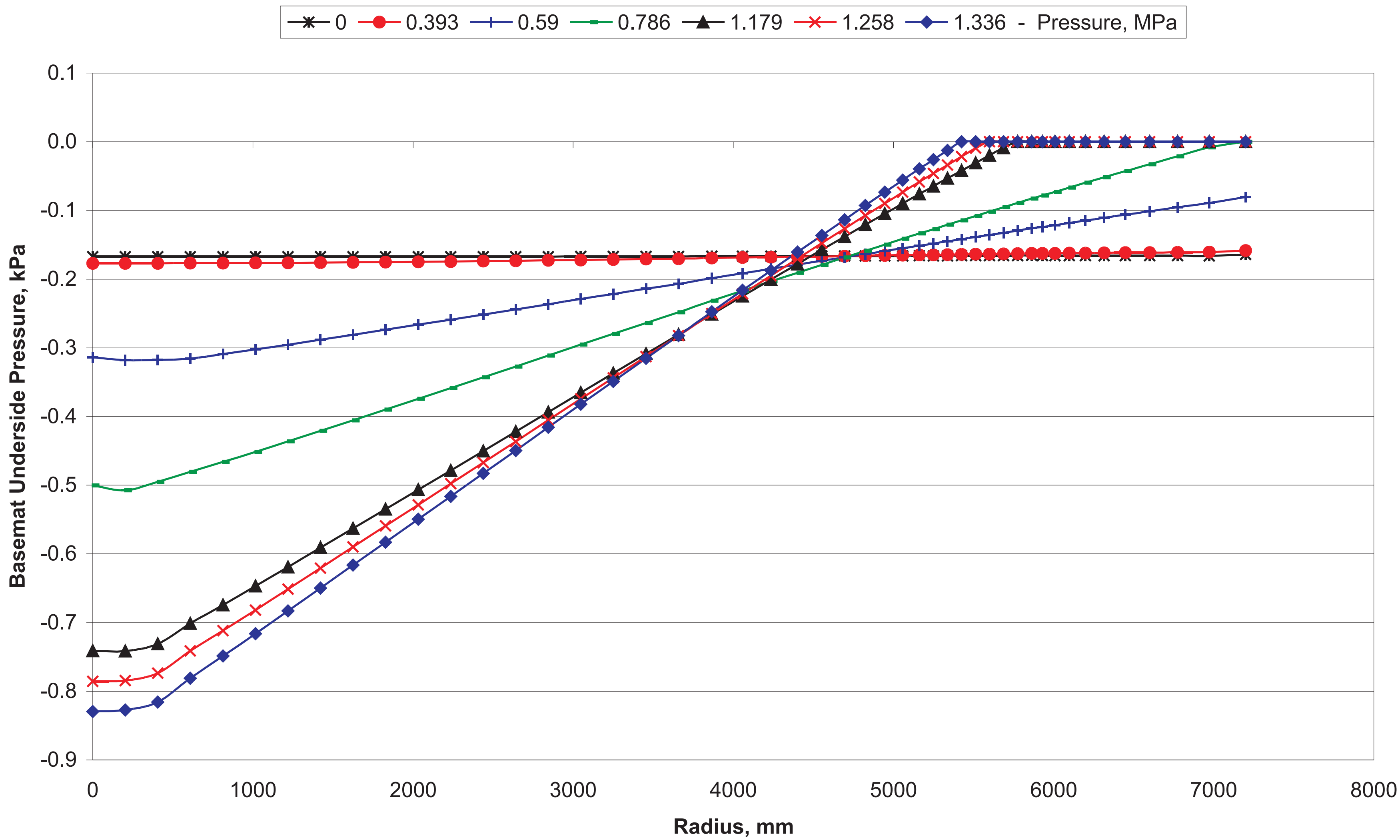

Figure 5-9. Basemat Underside Pressure versus Radius,
2000 Analysis with Final Soil Springs and Dome, and No Straight Tendon Friction

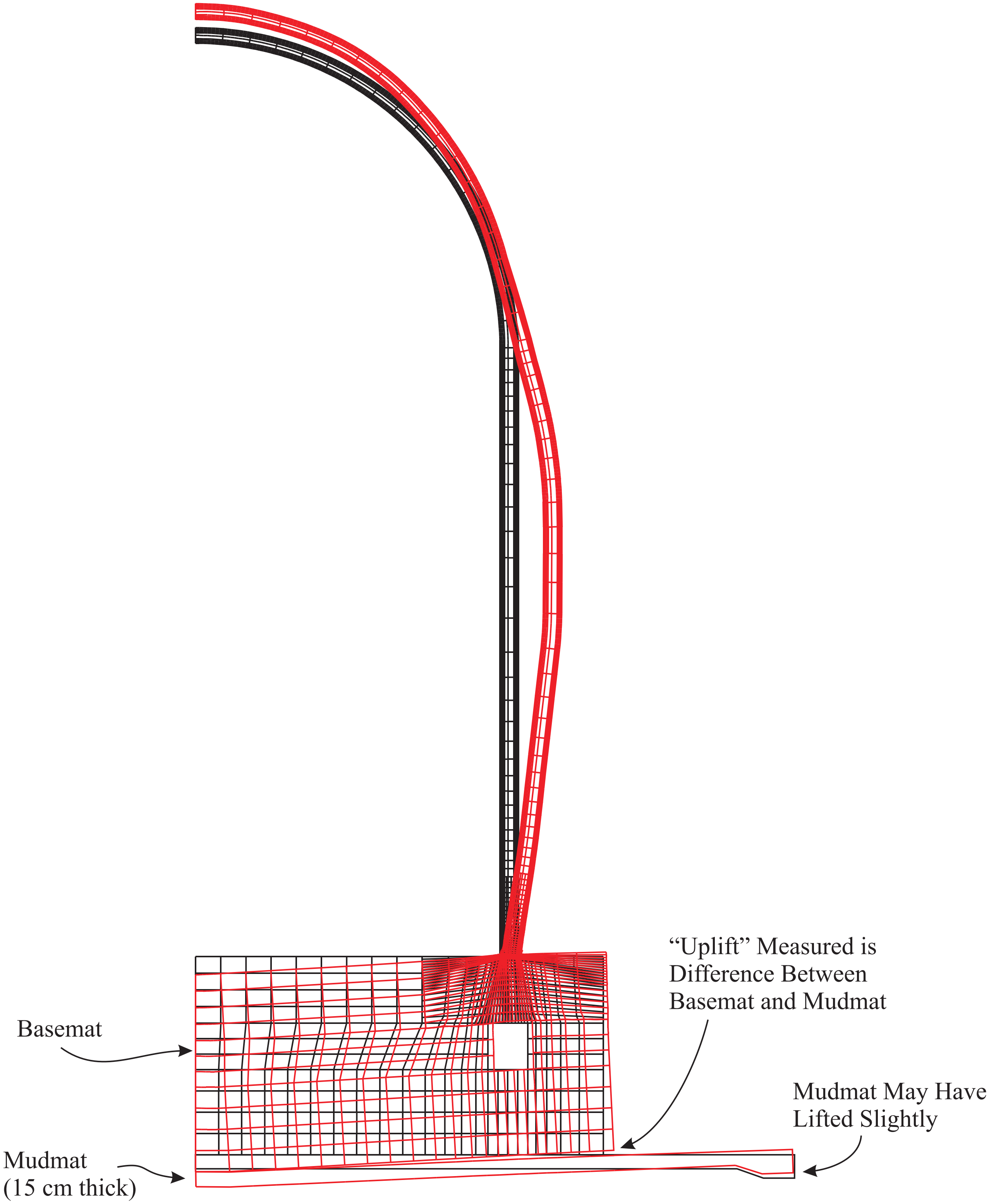

Figure 5-10. Illustration of Basemat/Mudmat Uplift

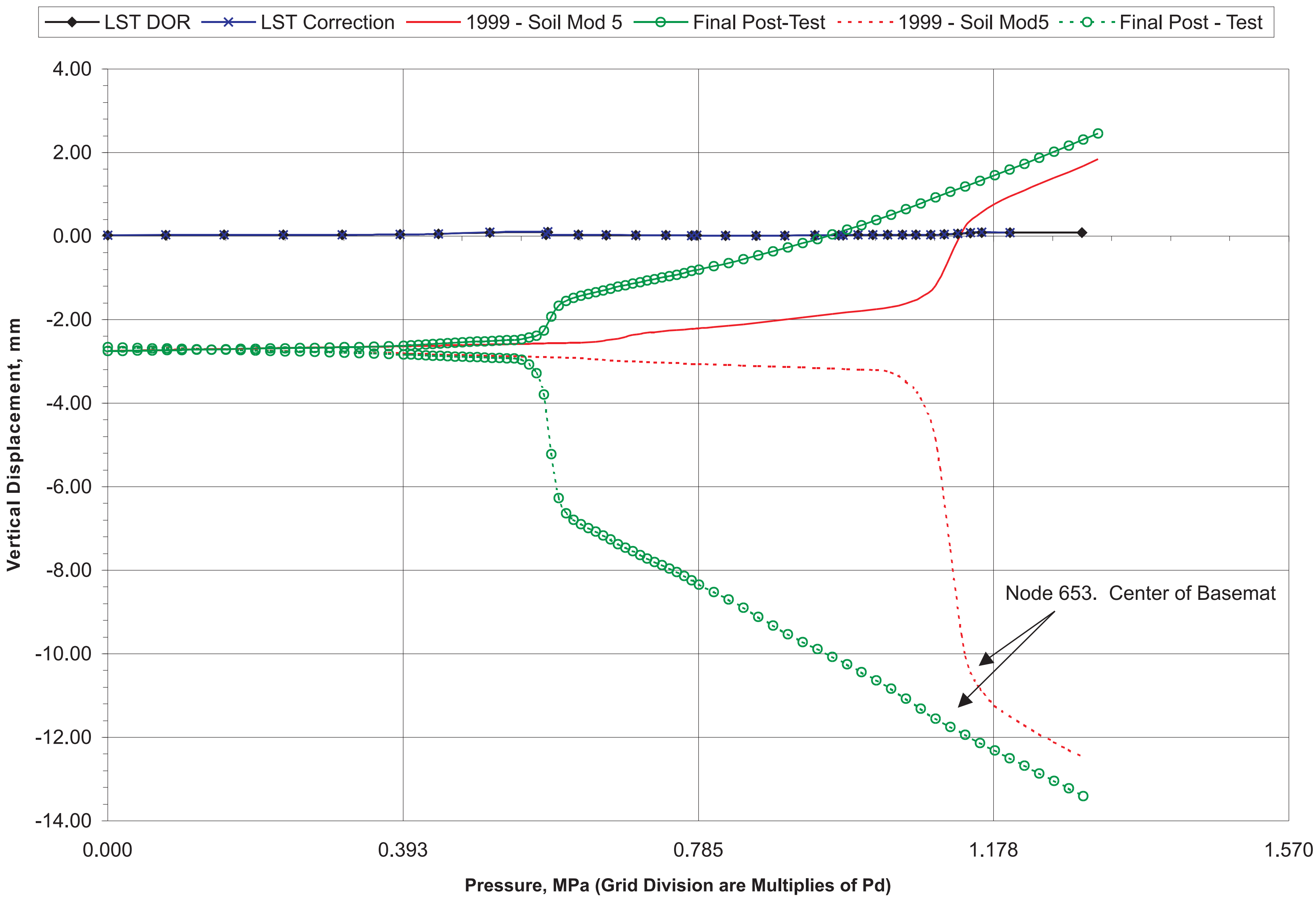

Figure 5-11. Standard Output Location #1. Azimuth: 135 Degrees, Elevation: 0.00 Meters, Top of Basemat

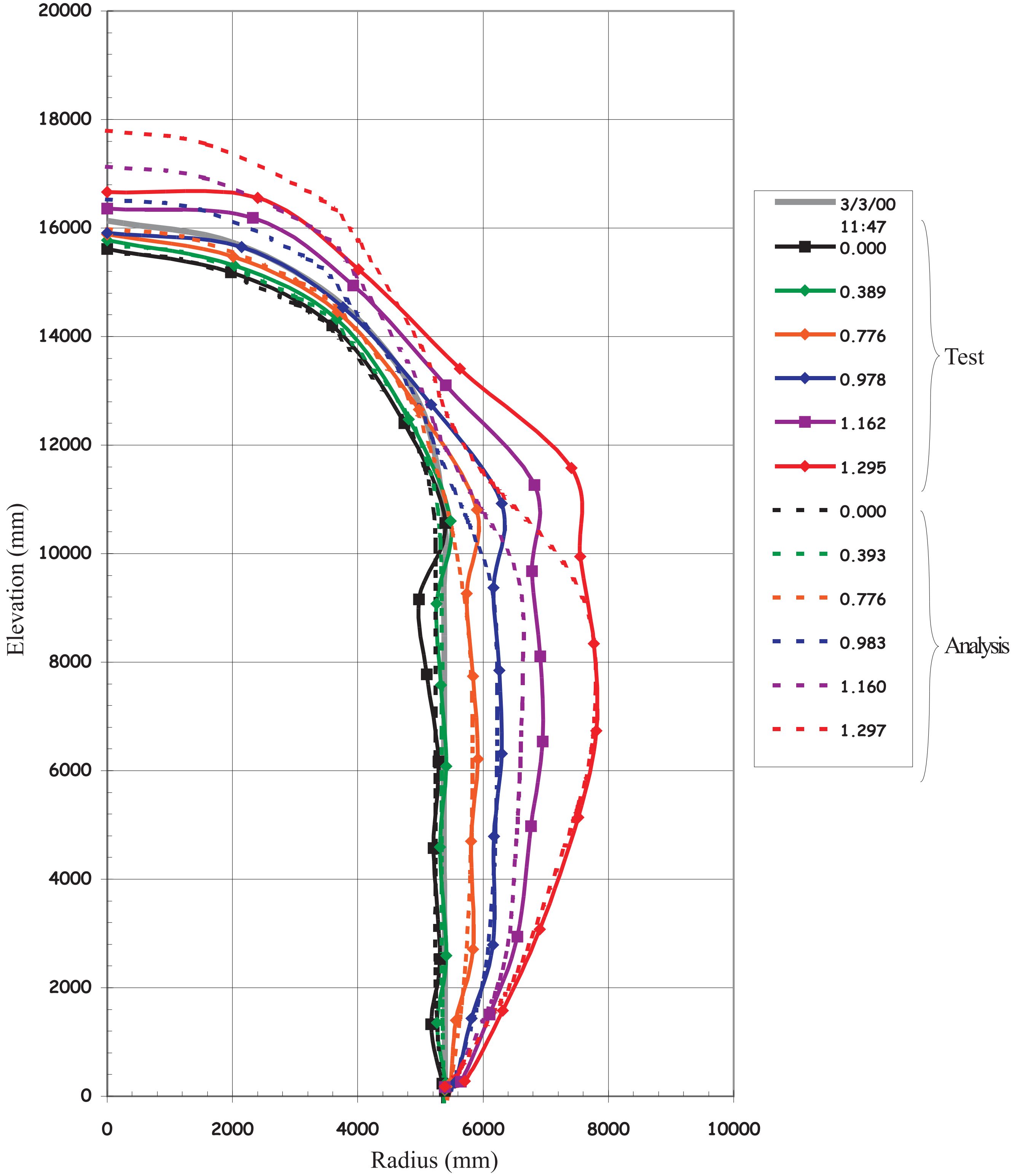

Figure 5-12. PCCV LST - Deformation @ Azimuth 135 (Z) × 100
Compared to Axisymmetric Final Posttest Analysis

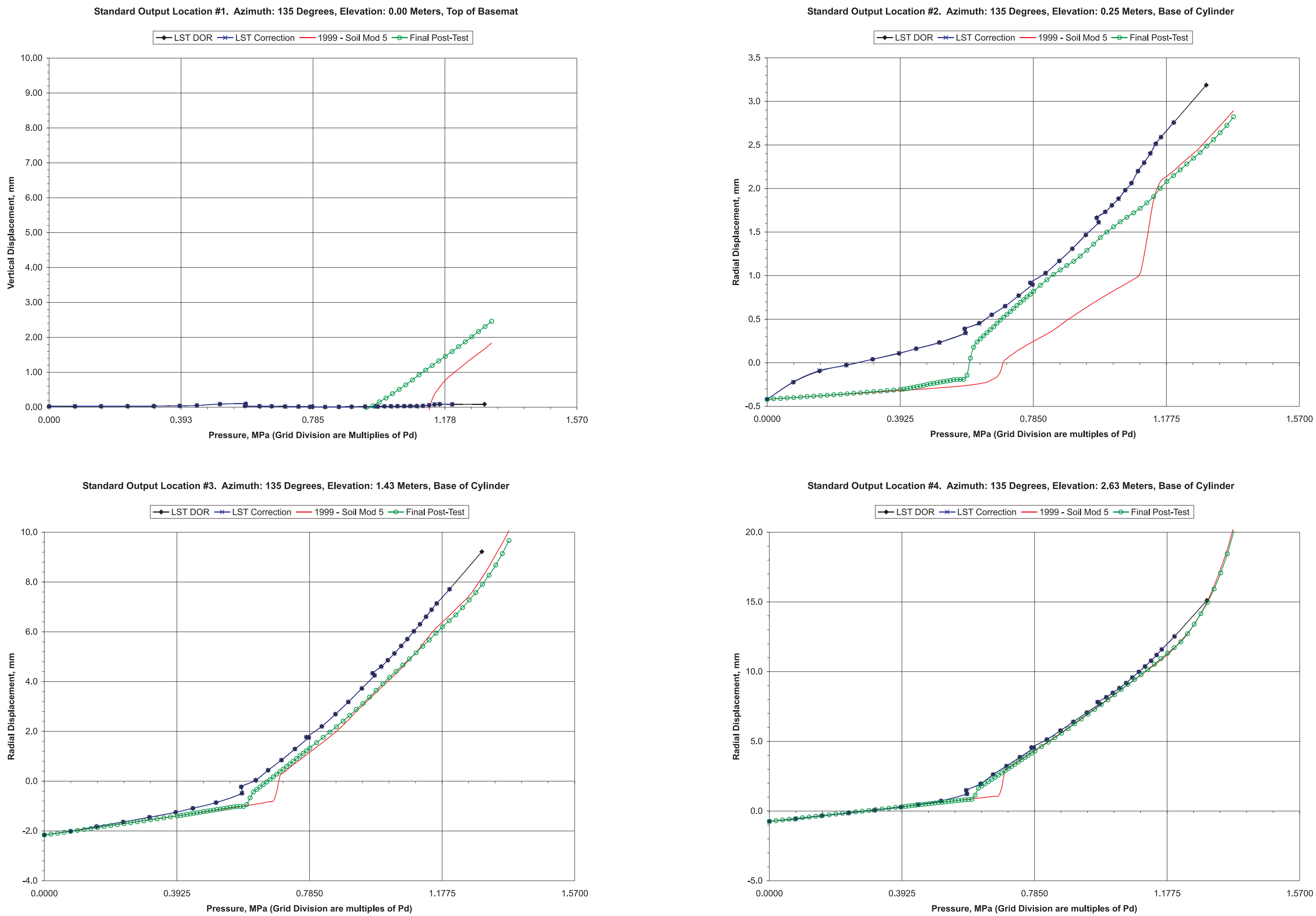

Figure 5-13. Comparisons at Standard Output Location 1, 2, 3, and 4

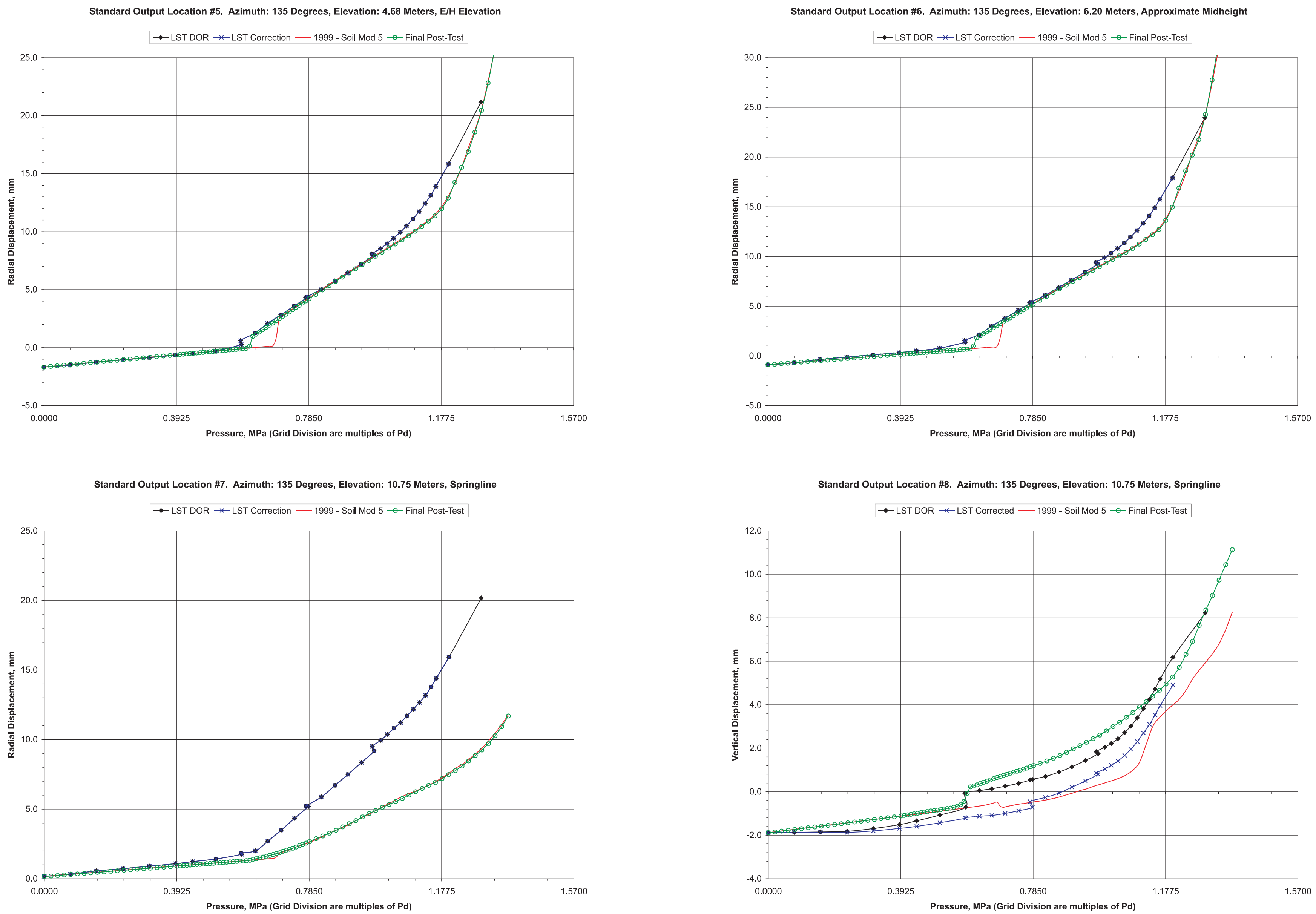

Figure 5-14. Comparisons at Standard Output Location 5, 6, 7, and 8

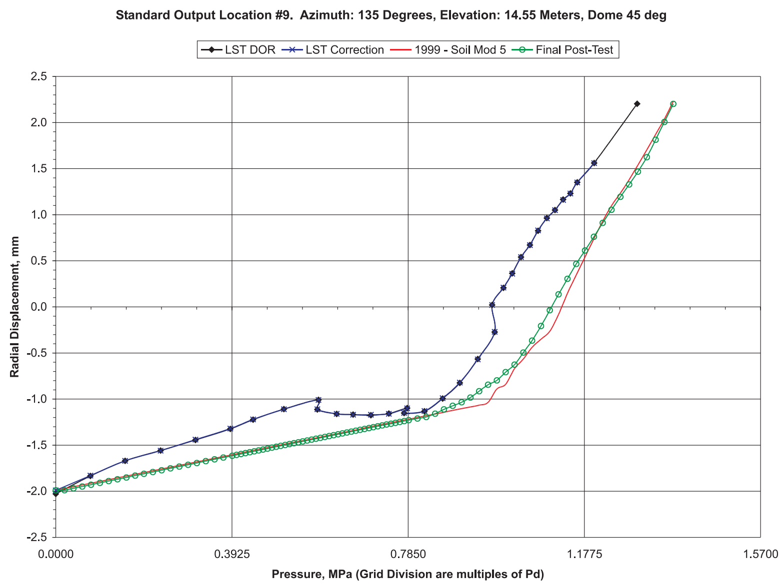

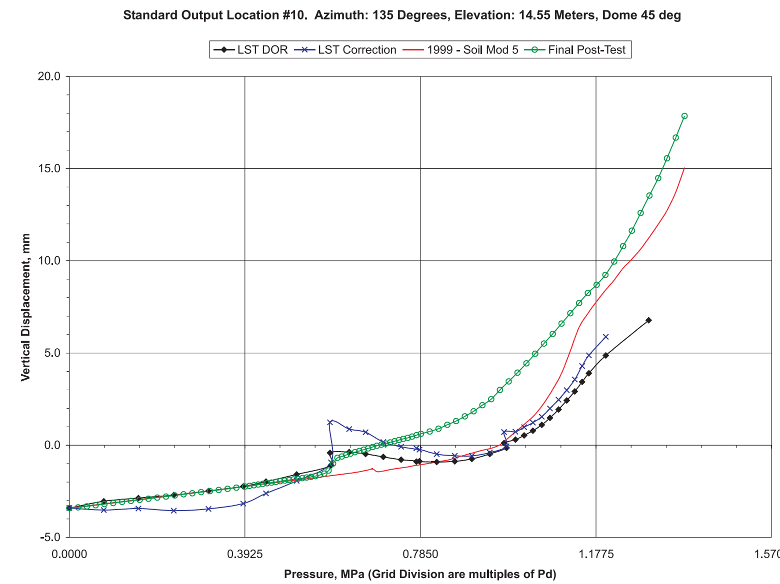

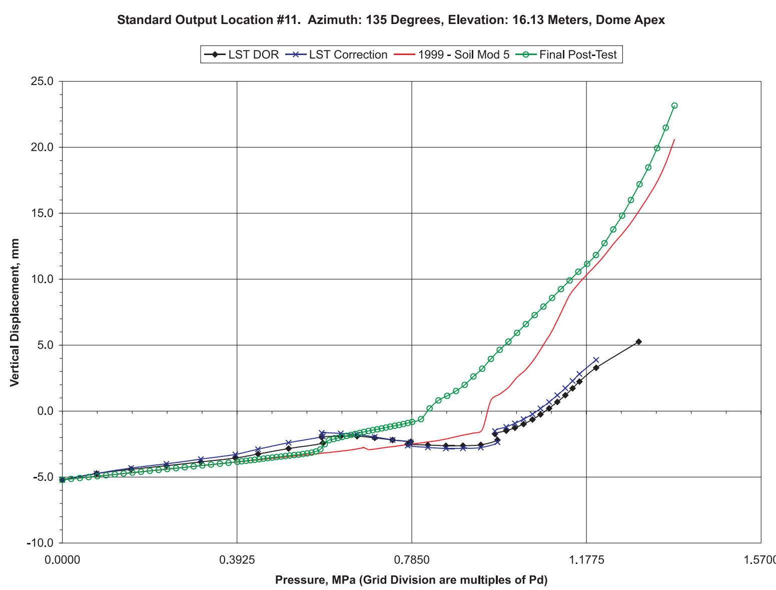

Figure 5-15. Comparisons at Standard Output Location 9, 10, and 11

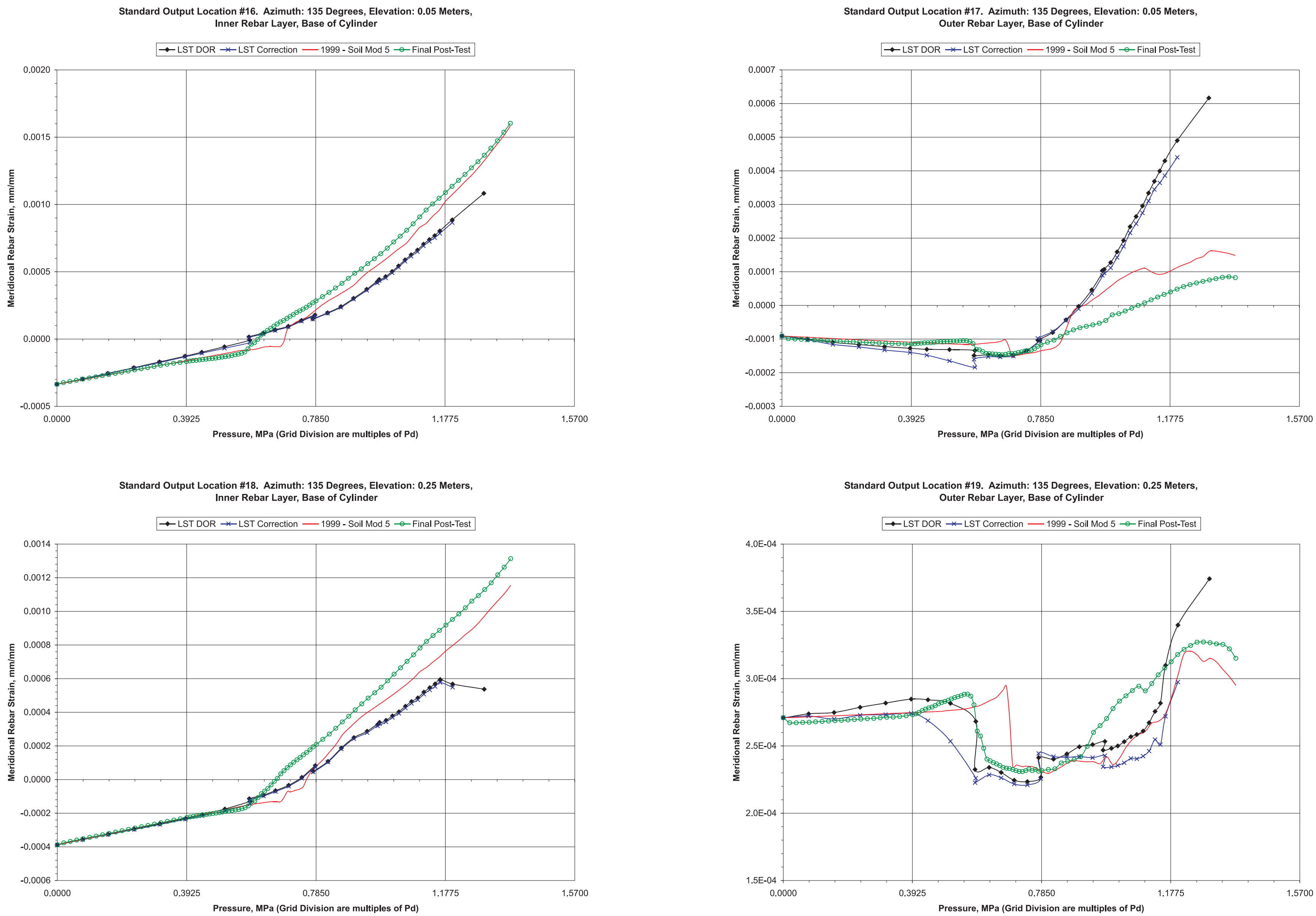

Figure 5-16. Comparisons at Standard Output Location 16, 17, 18, and 19

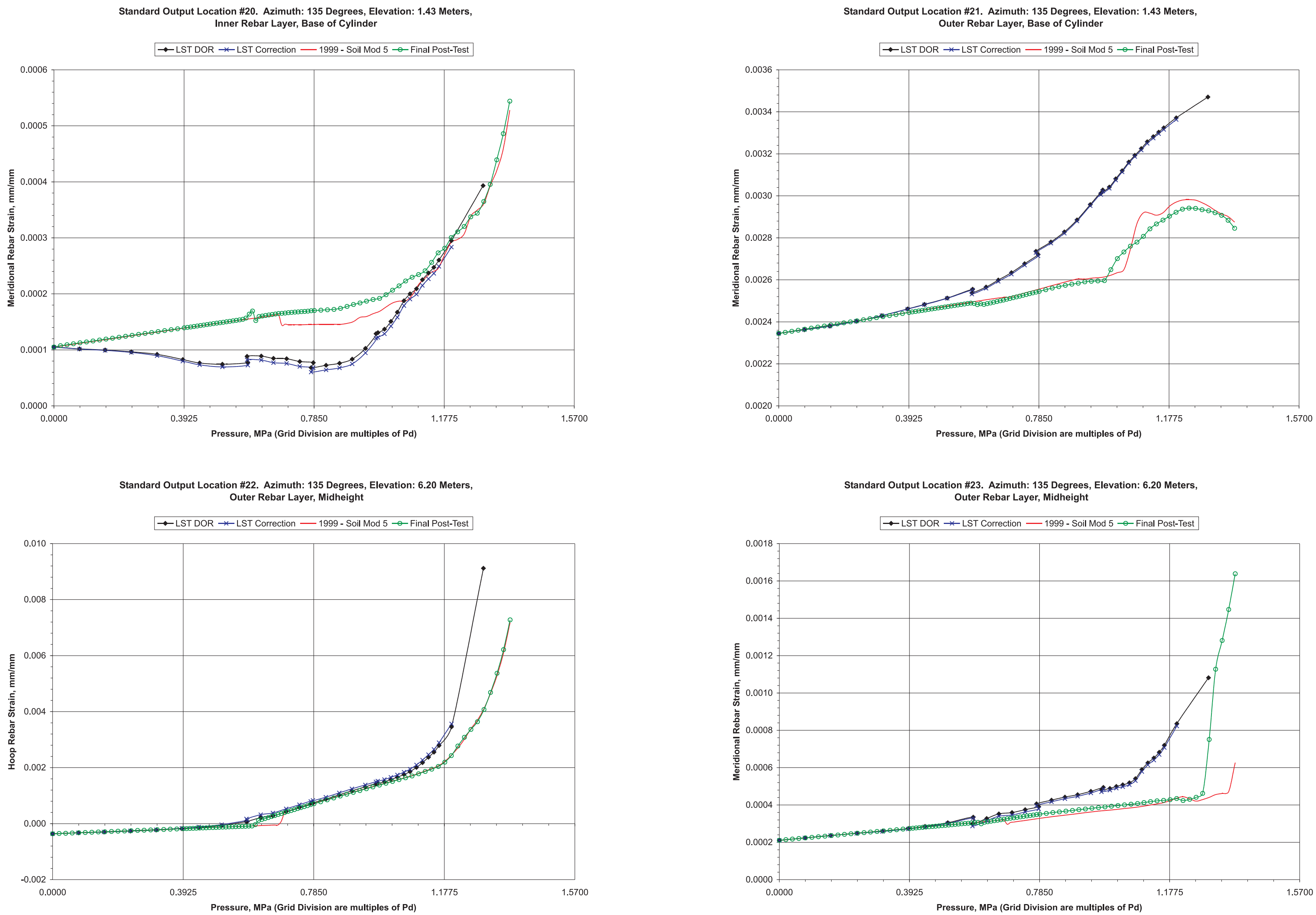

Figure 5-17. Comparisons at Standard Output Location 20, 21, 22, and 23

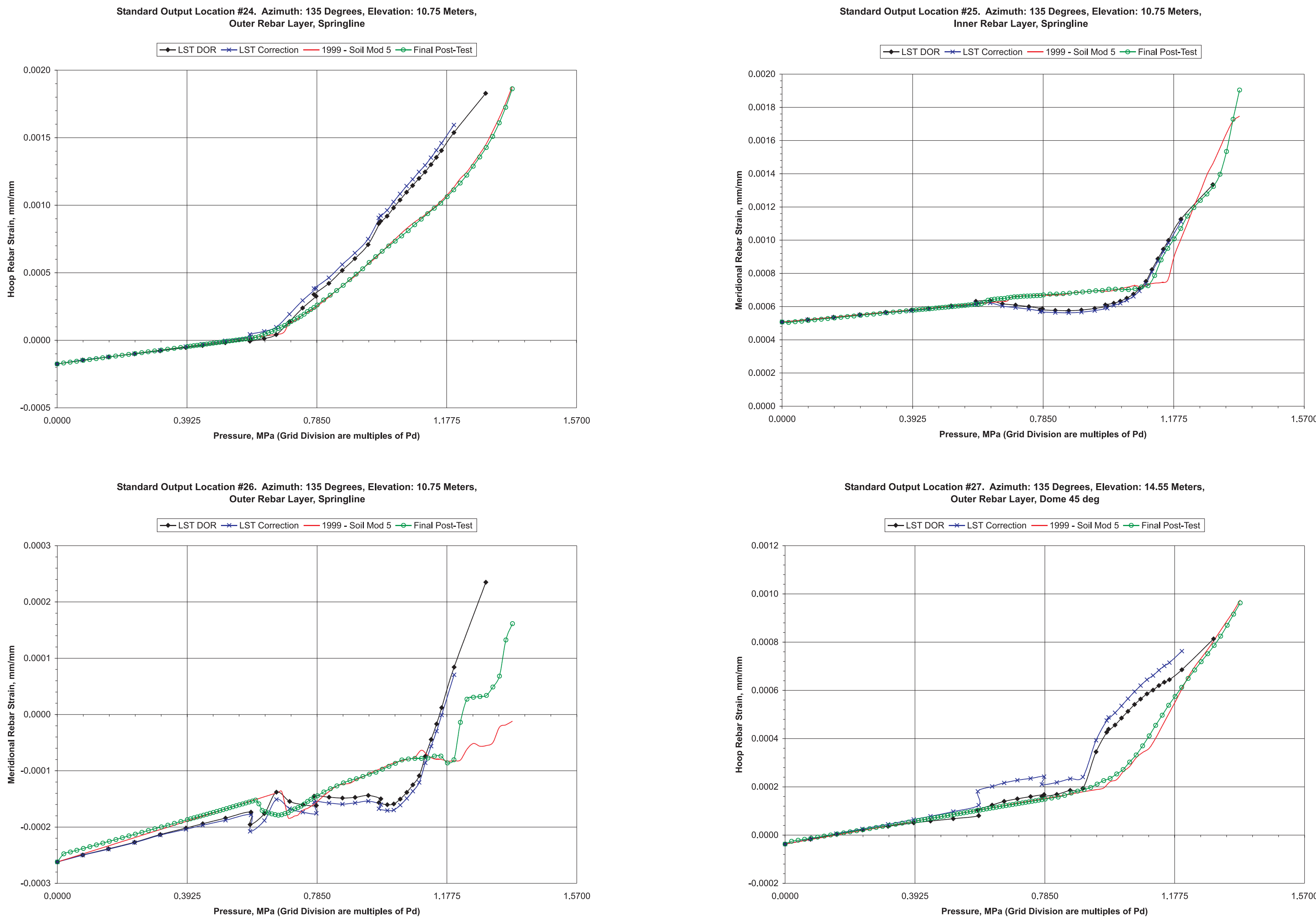

Figure 5-18. Comparisons at Standard Output Location 24, 25, 26, and 27

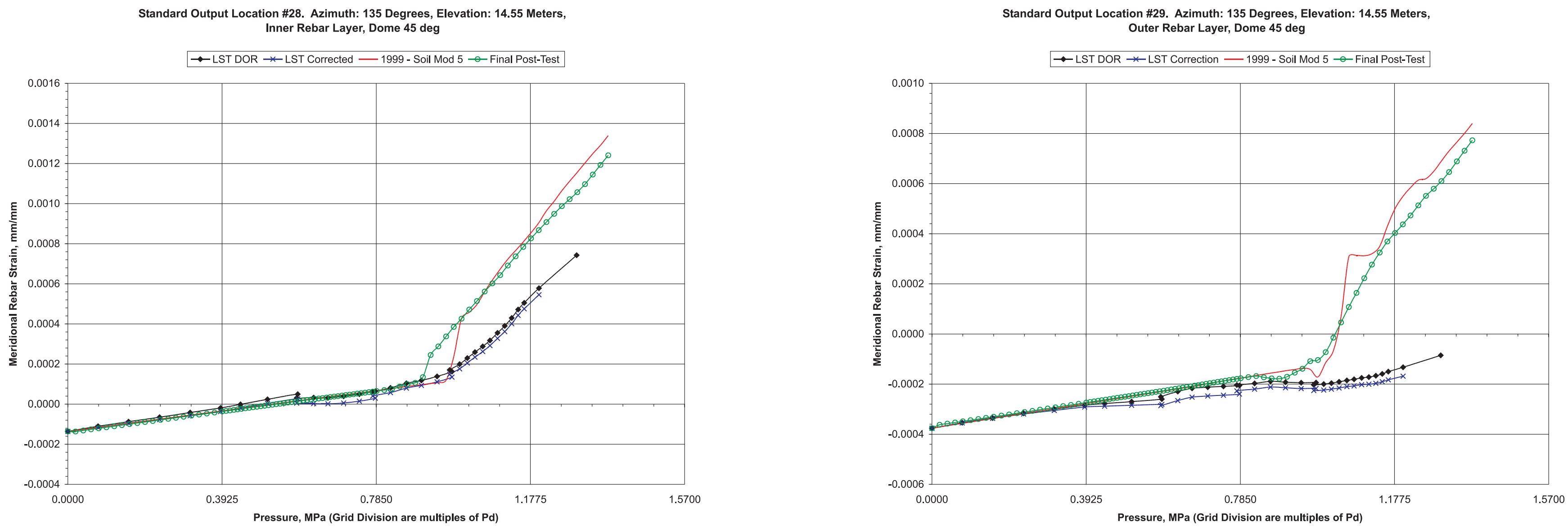

Figure 5-19. Comparisons at Standard Output Location 28 and 29

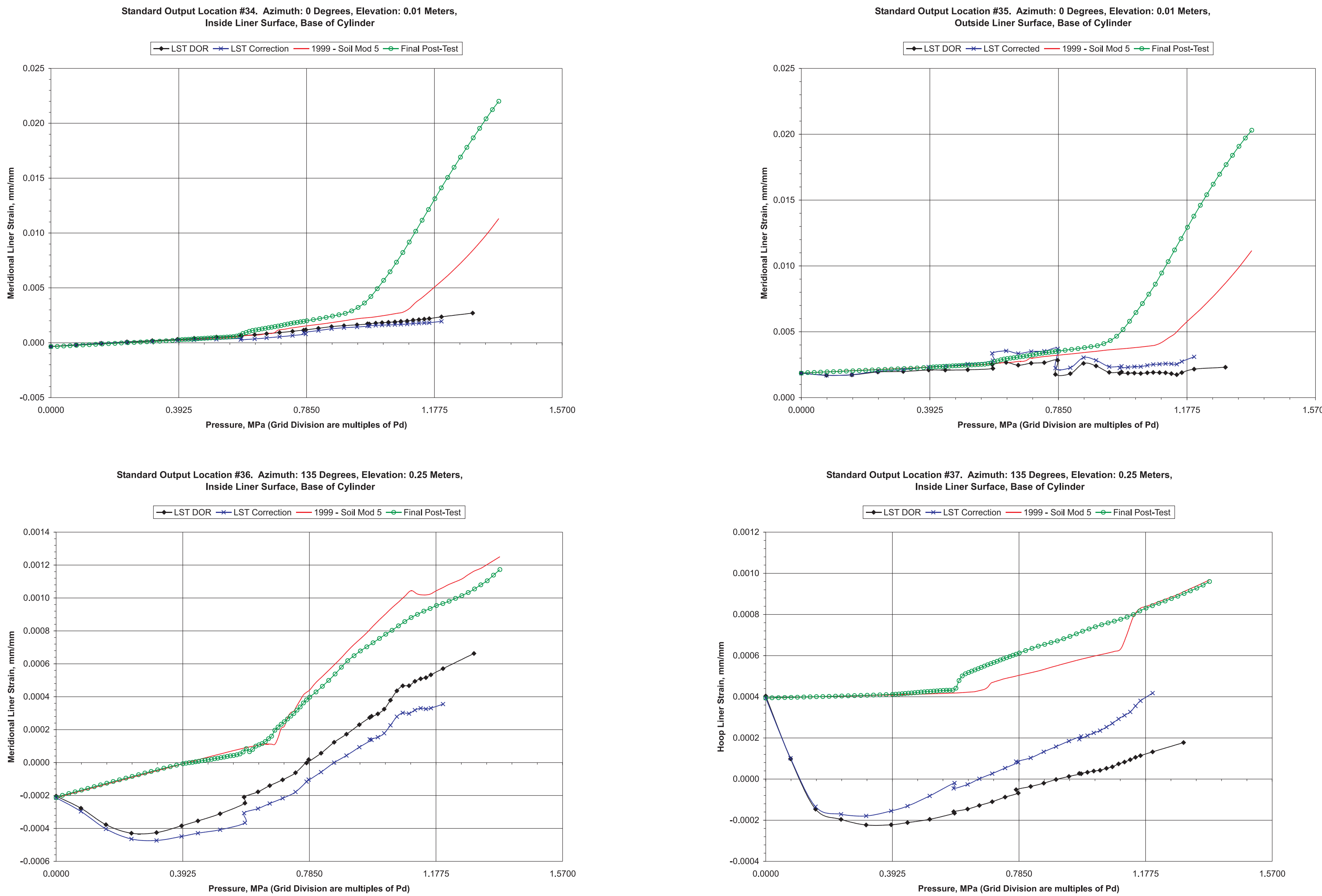

Figure 5-20. Comparisons at Standard Output Location 34, 35, 36, and 37

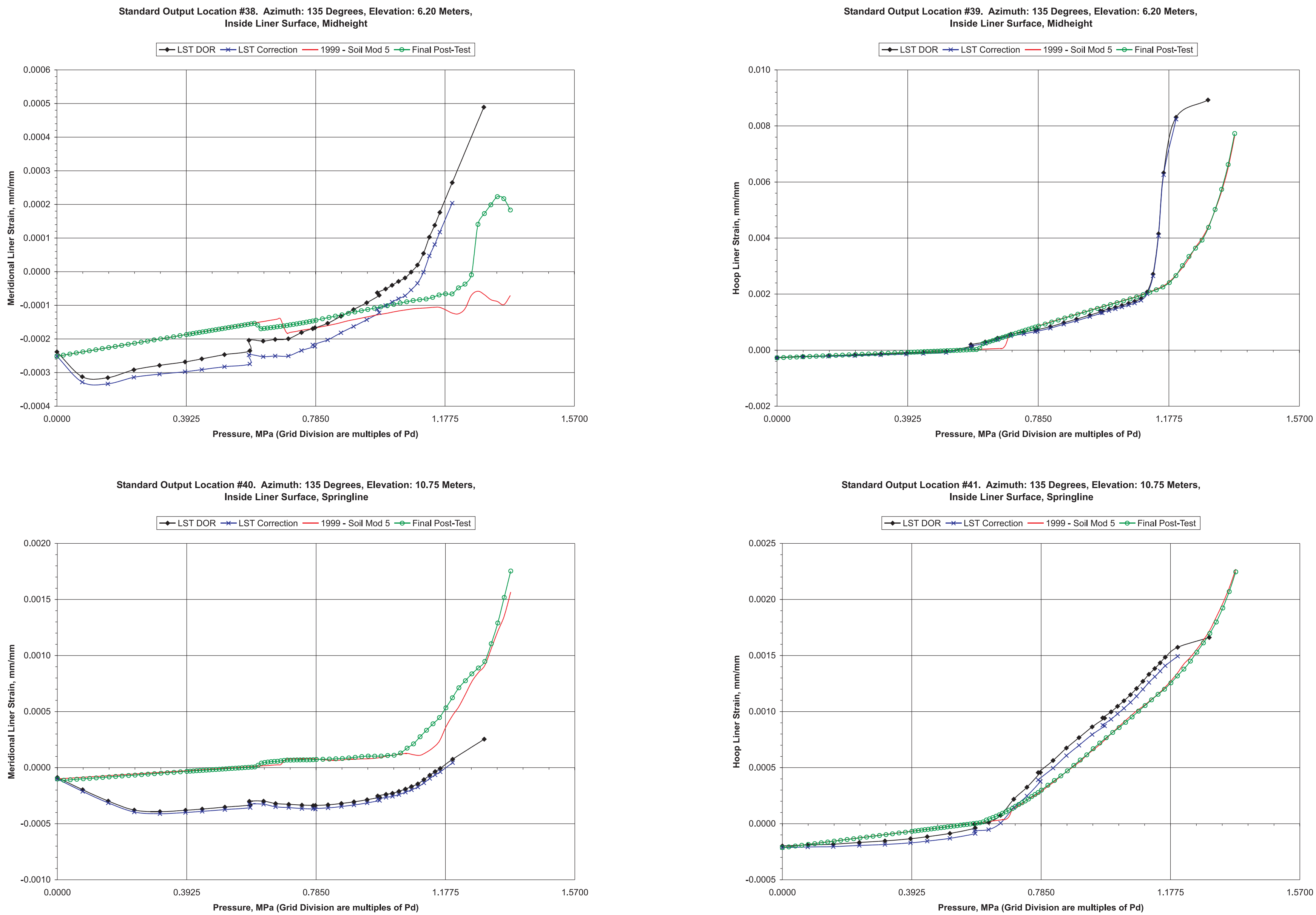

Figure 5-21. Comparisons at Standard Output Location 38, 39, 40, and 41

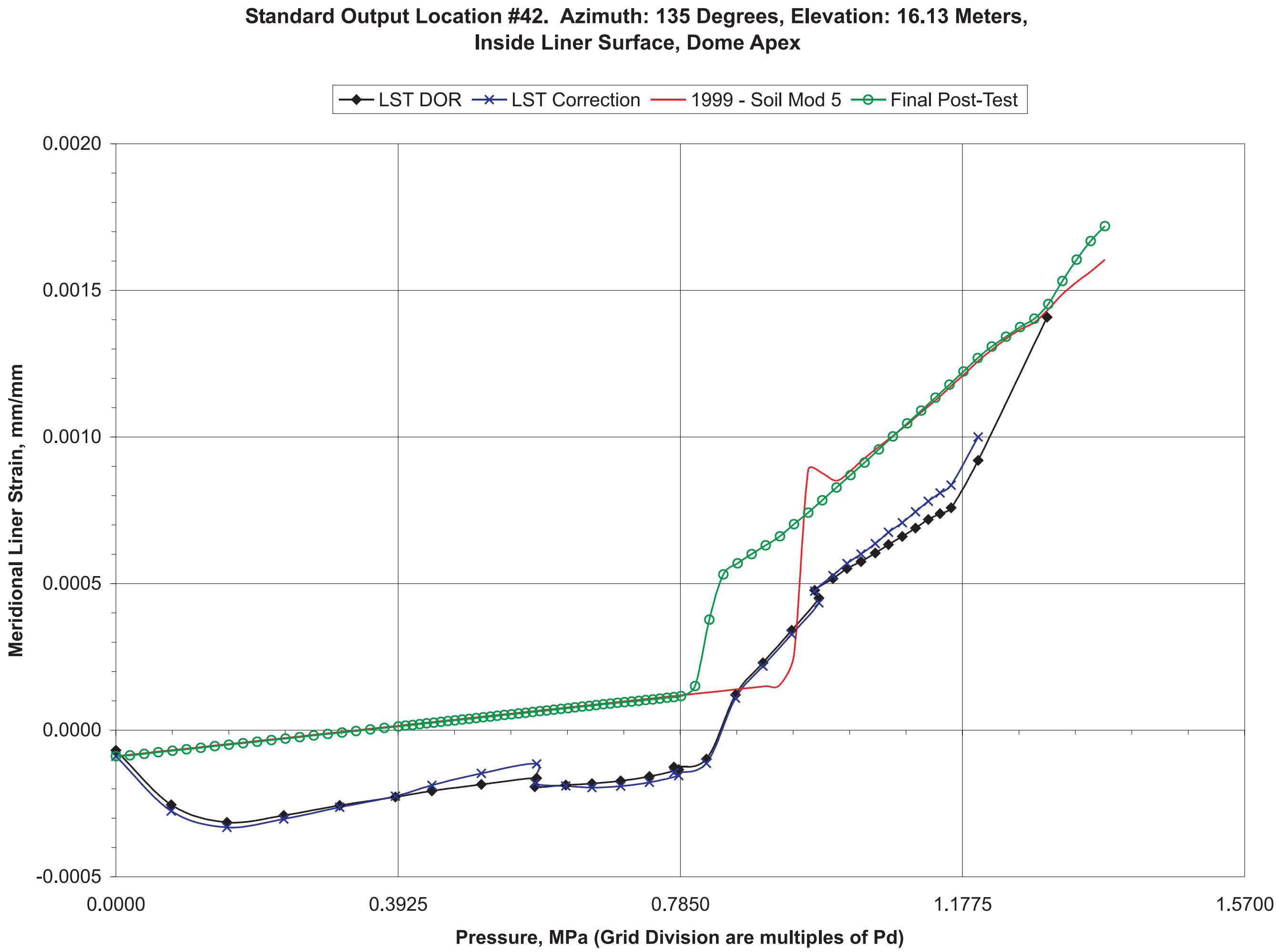

Figure 5-22. Comparisons at Standard Output Location 42

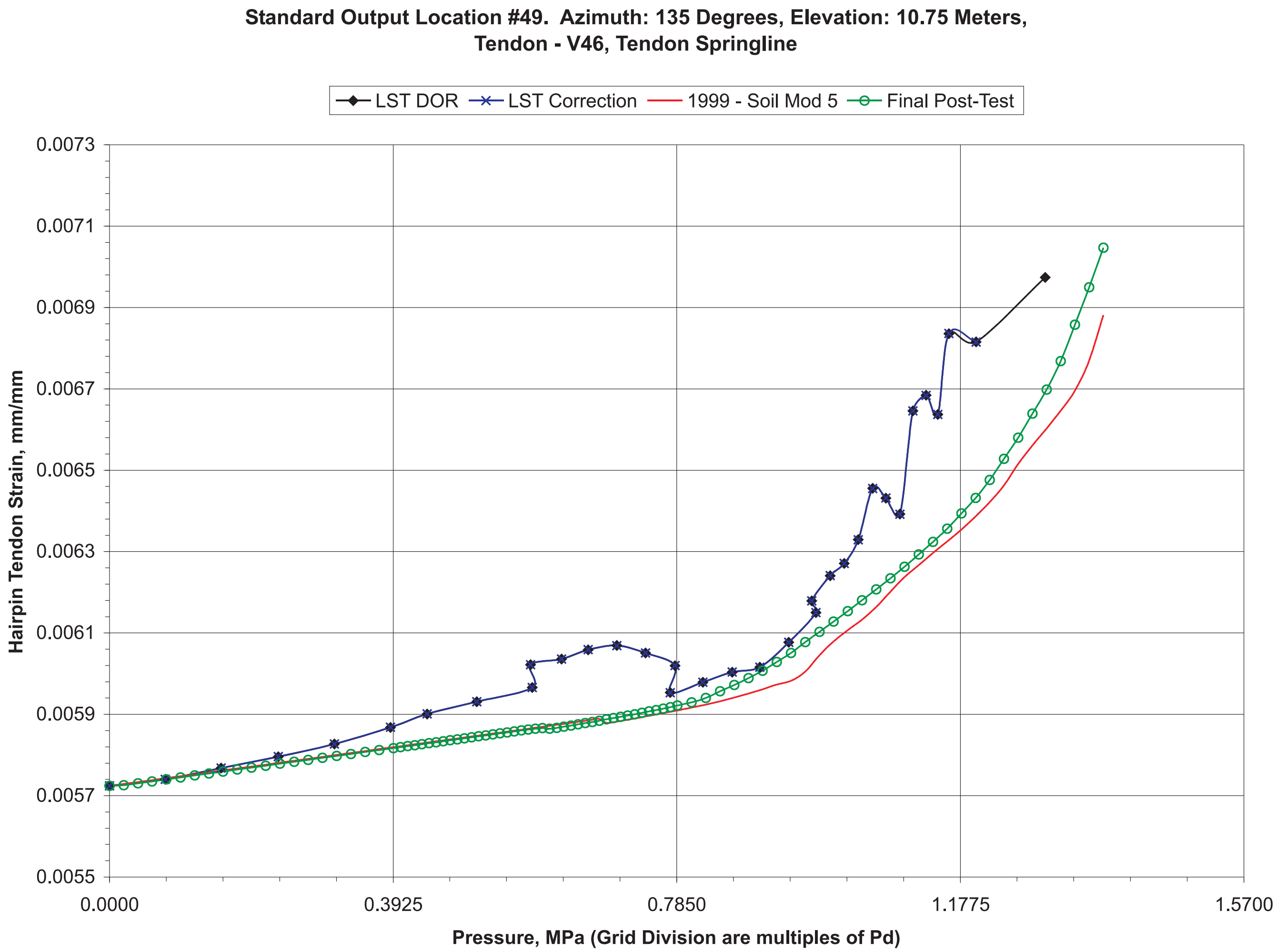

Figure 5-23. Comparisons at Standard Output Location 49

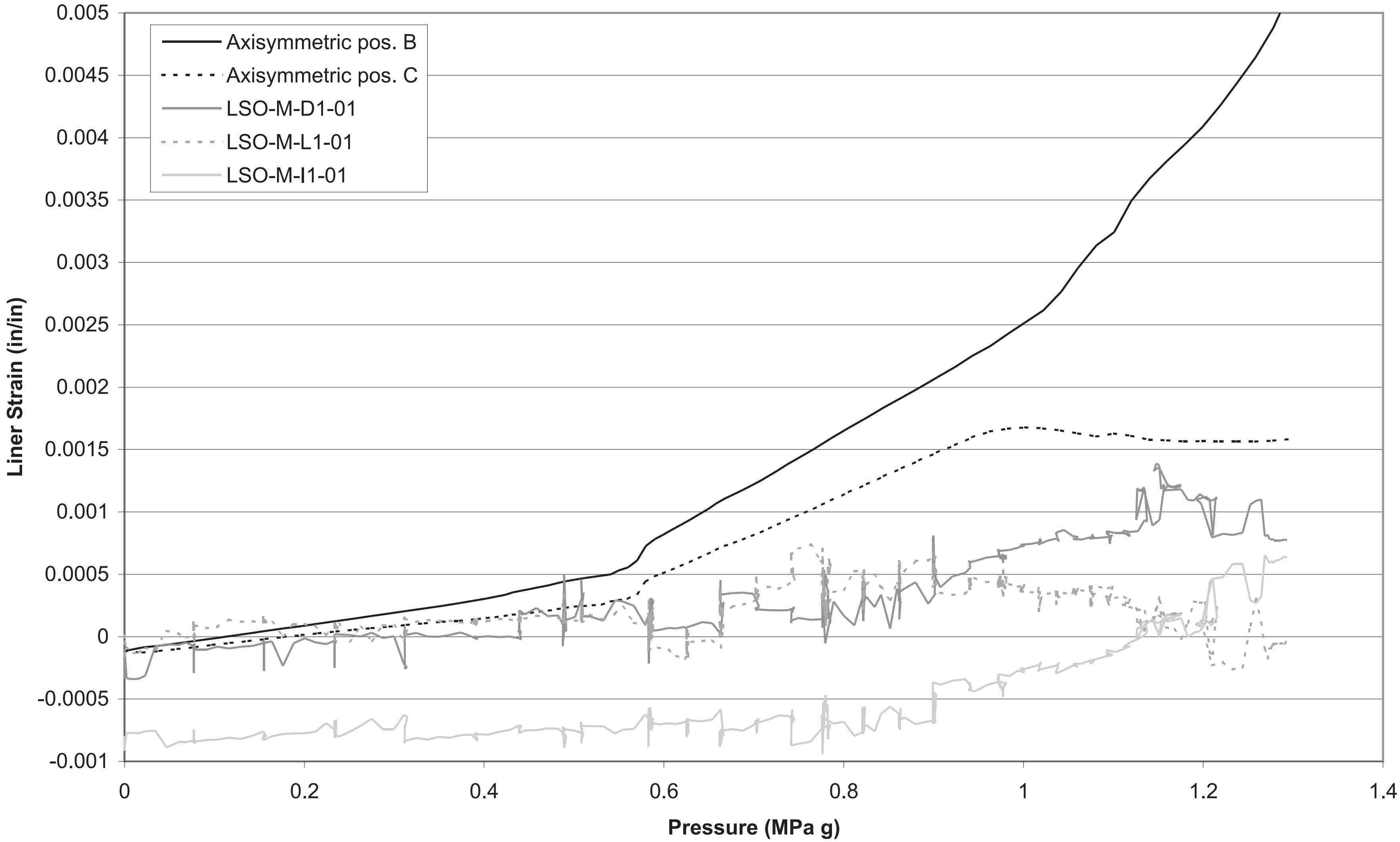

Figure 5-24. Final Posttest Analysis Vs. LST at Wall Base Liner Position B-C

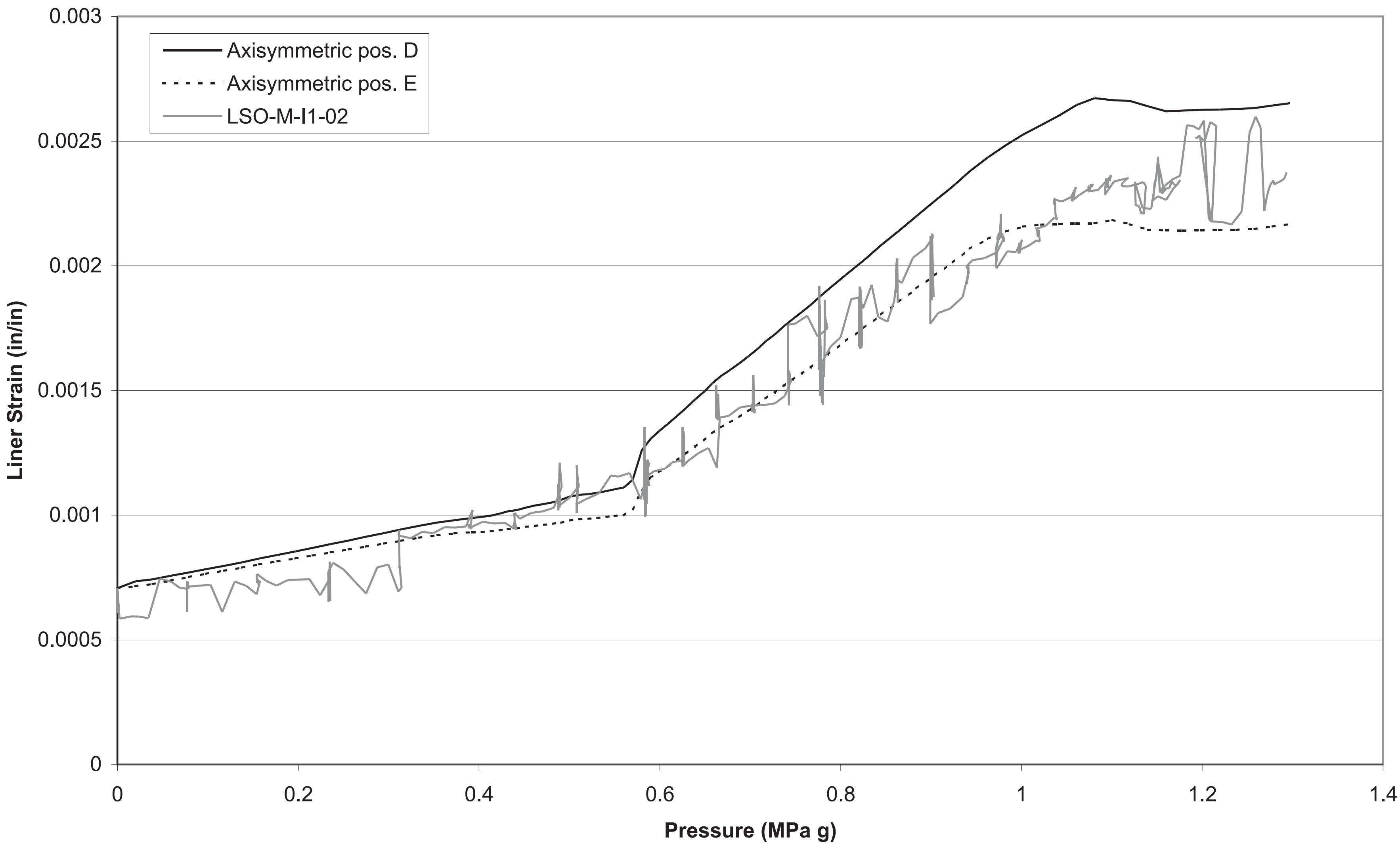

Figure 5-25. Final Posttest Analysis Vs. LST at Wall Base Liner Position D-E

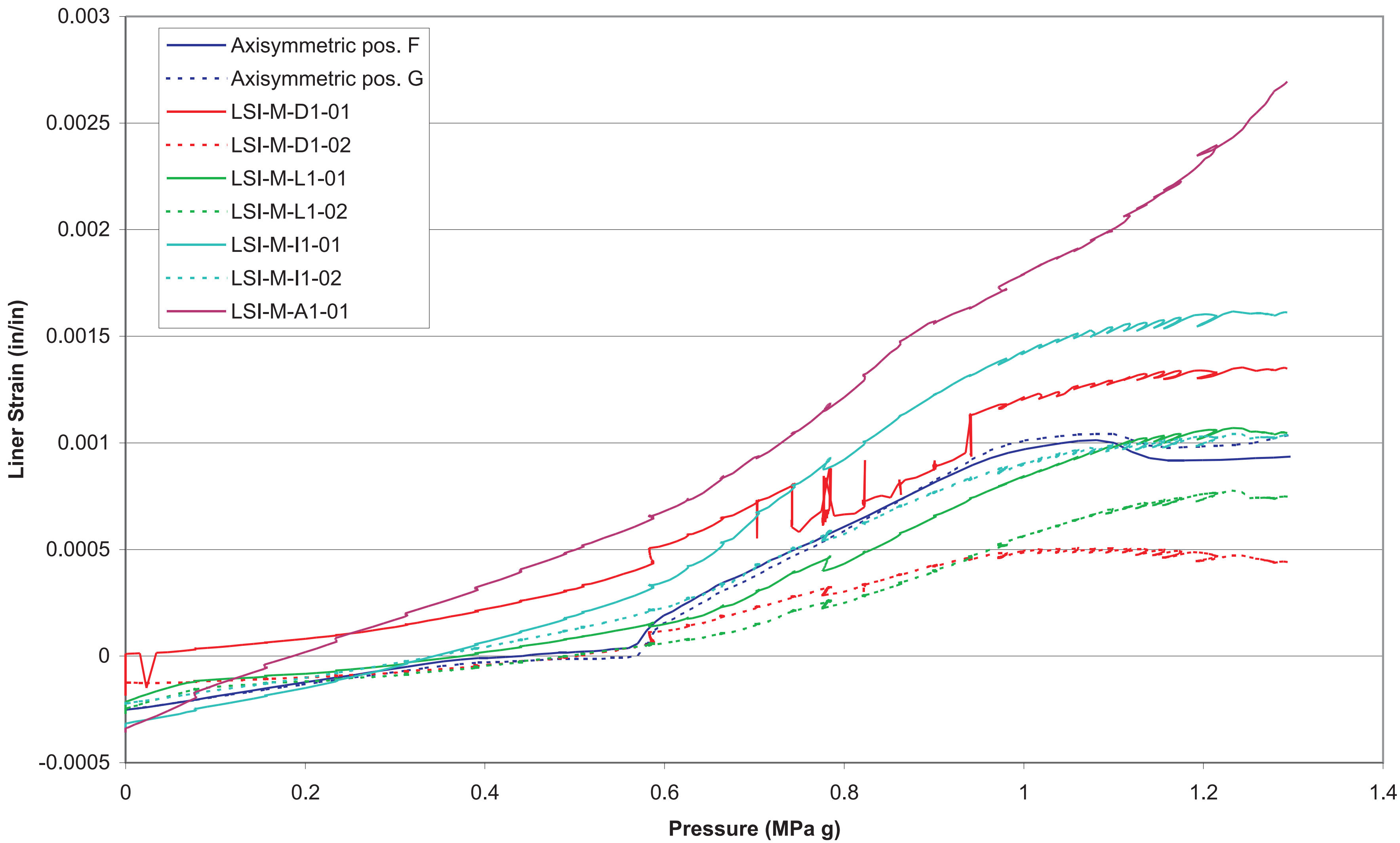

Figure 5-26. Final Posttest Analysis Vs. LST at Wall Base Liner Position F-G

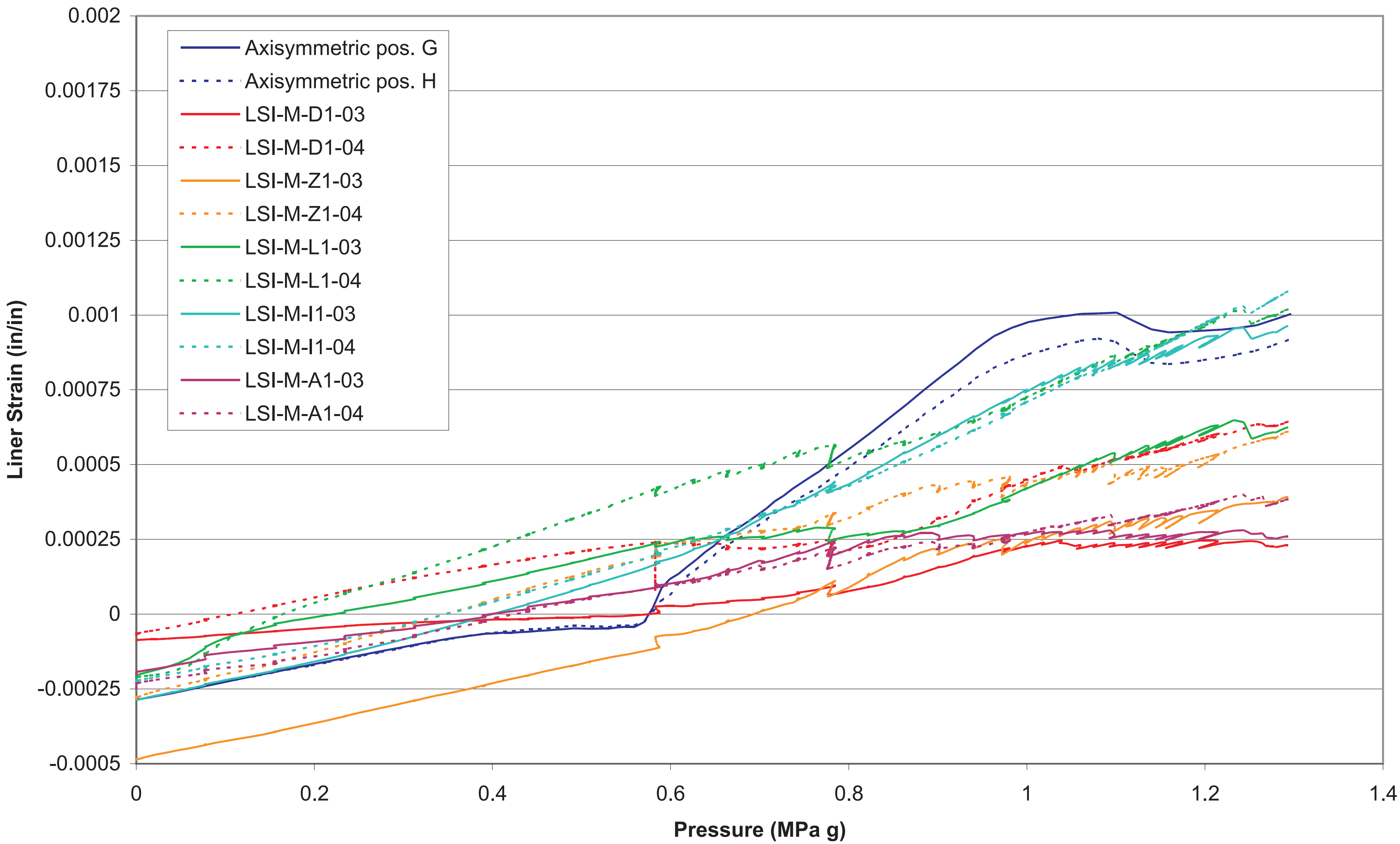

Figure 5-27. Final Posttest Analysis Vs. LST at Wall Base Liner Position G-H

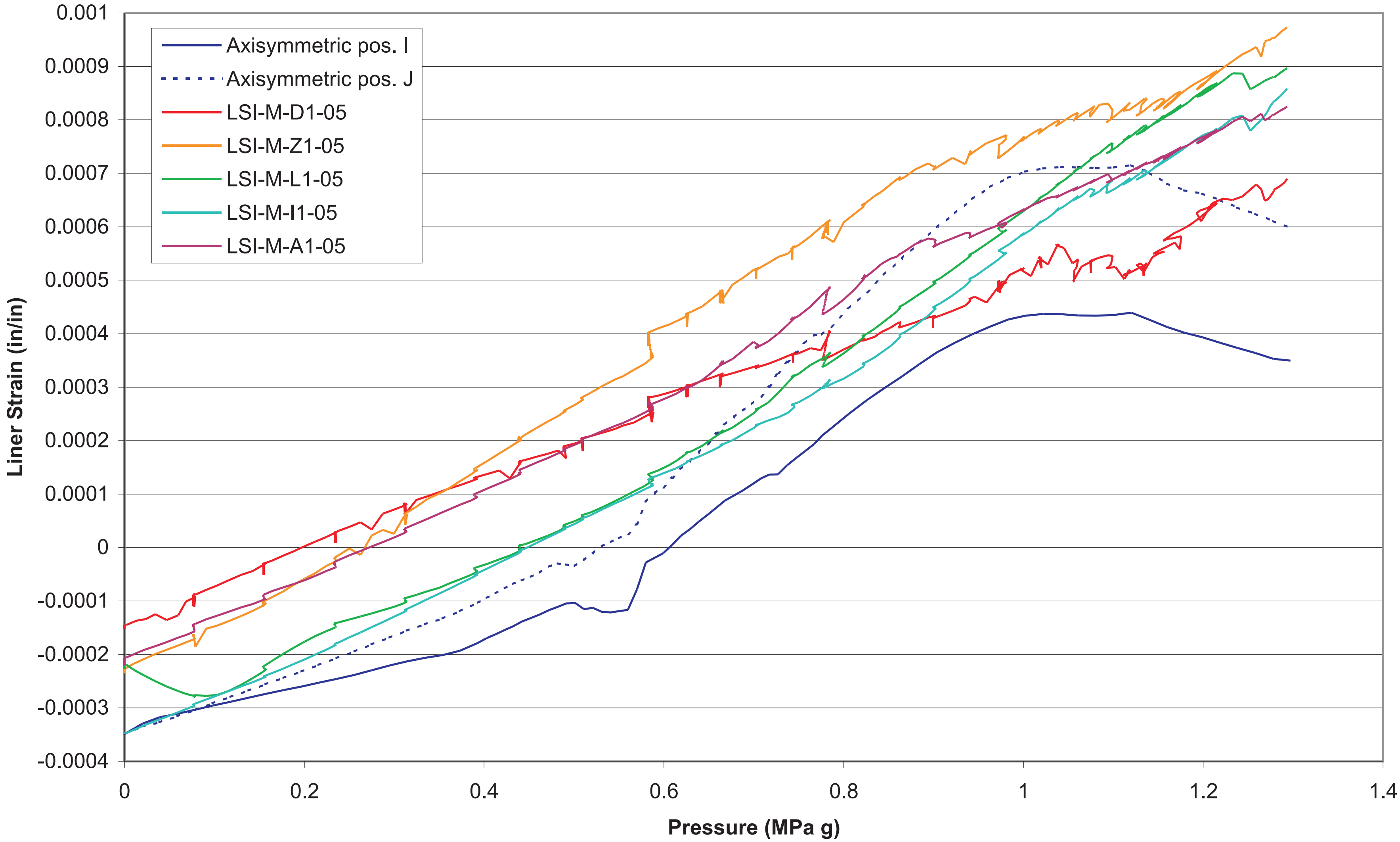

Figure 5-28. Final Posttest Analysis Vs. LST at Wall Base Liner Position I-J

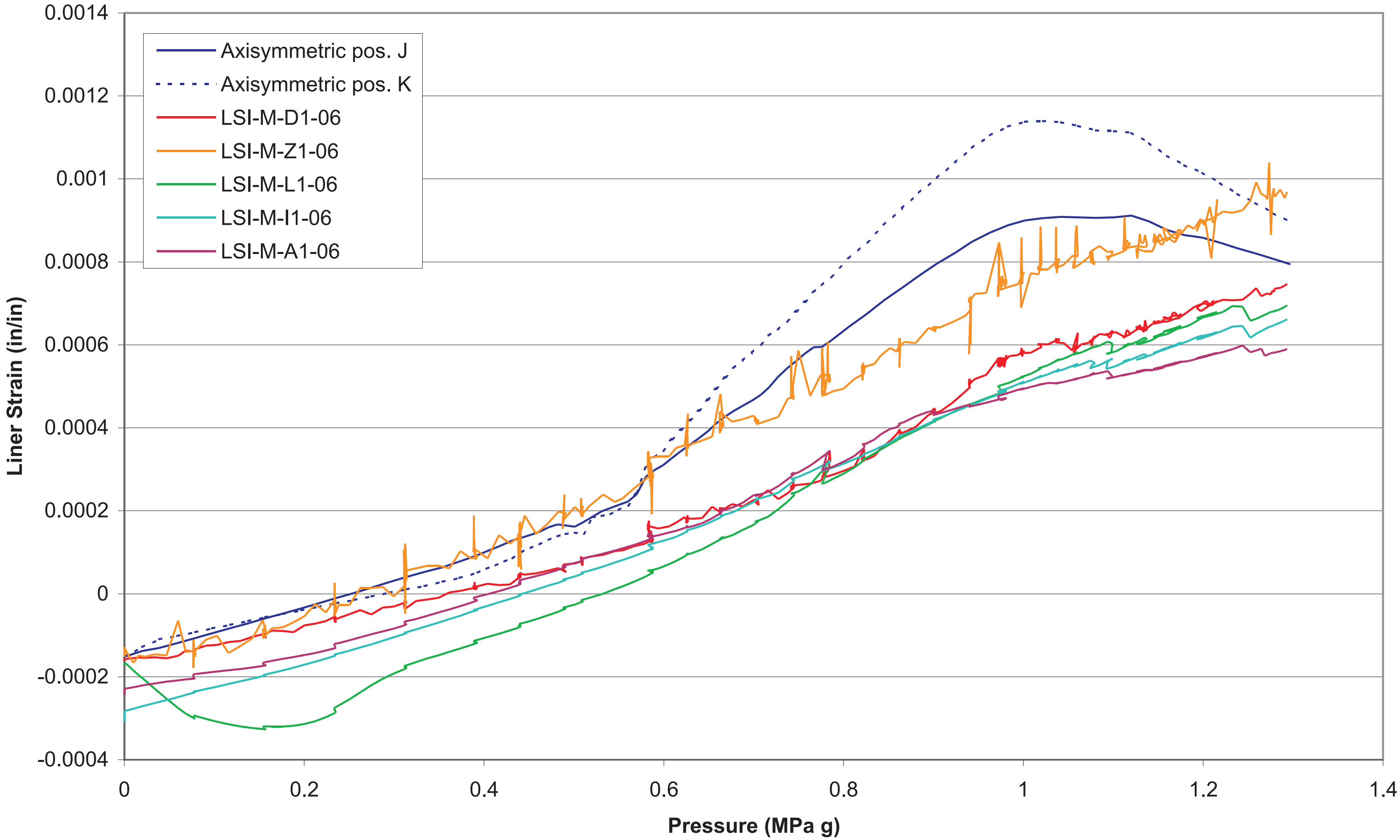

Figure 5-29. Final Posttest Analysis Vs. LST at Wall Base Liner Position J-K

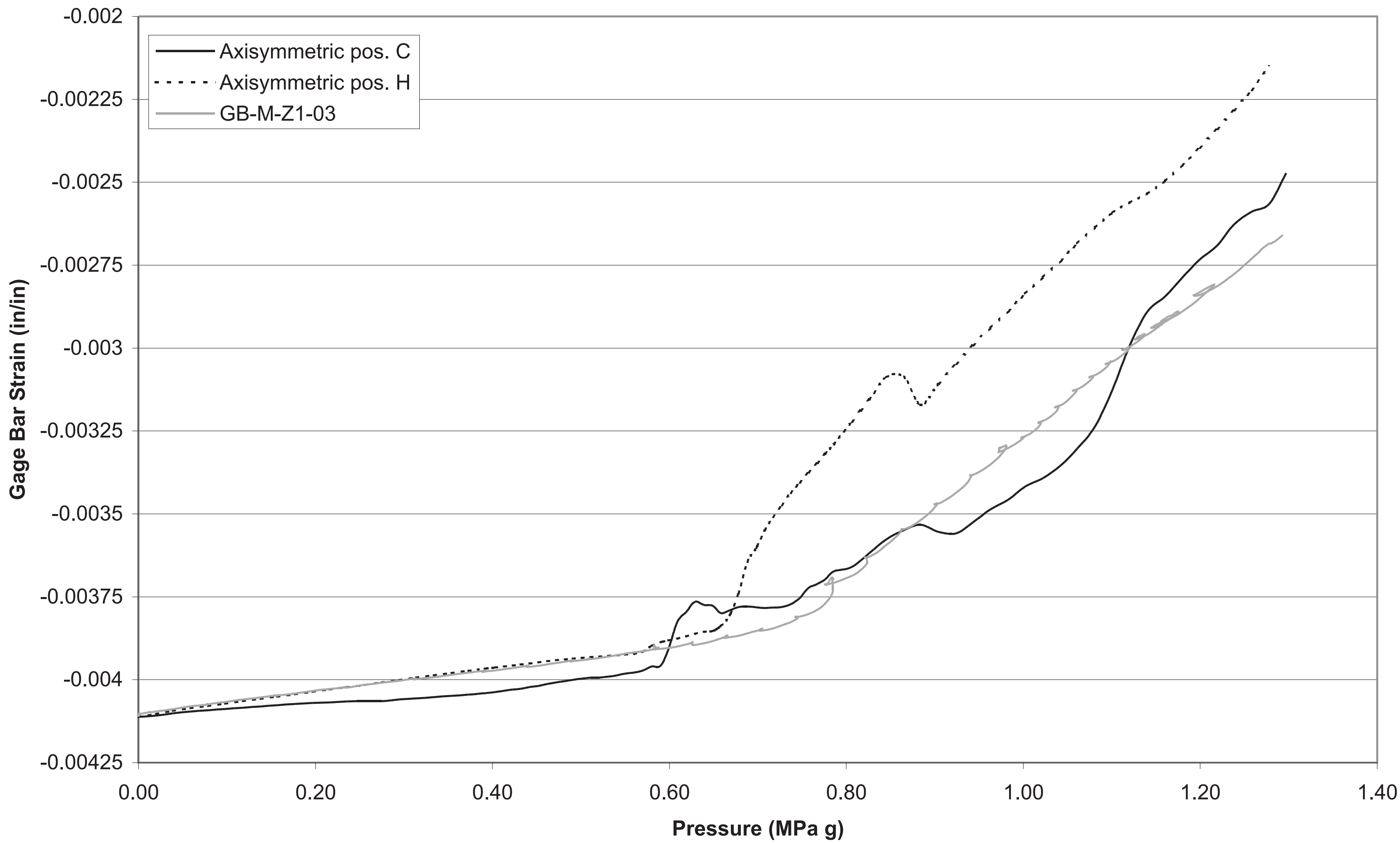

Figure 5-30. Final Posttest Analysis Vs. LST at Wall Base Gage Bar Position C-H

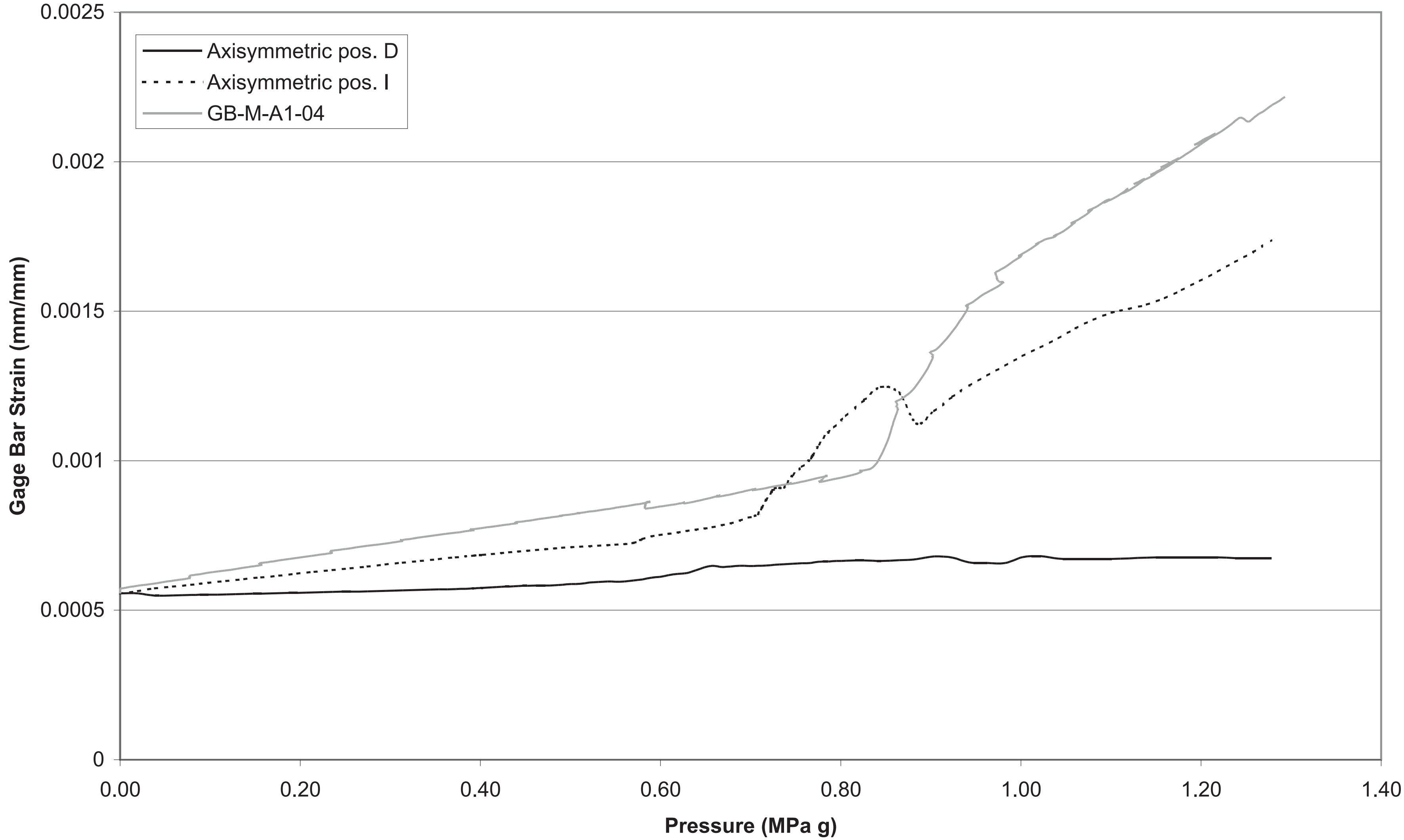

Figure 5-31. Final Posttest Analysis Vs. LST at Wall Base Gage Bar Position D-I

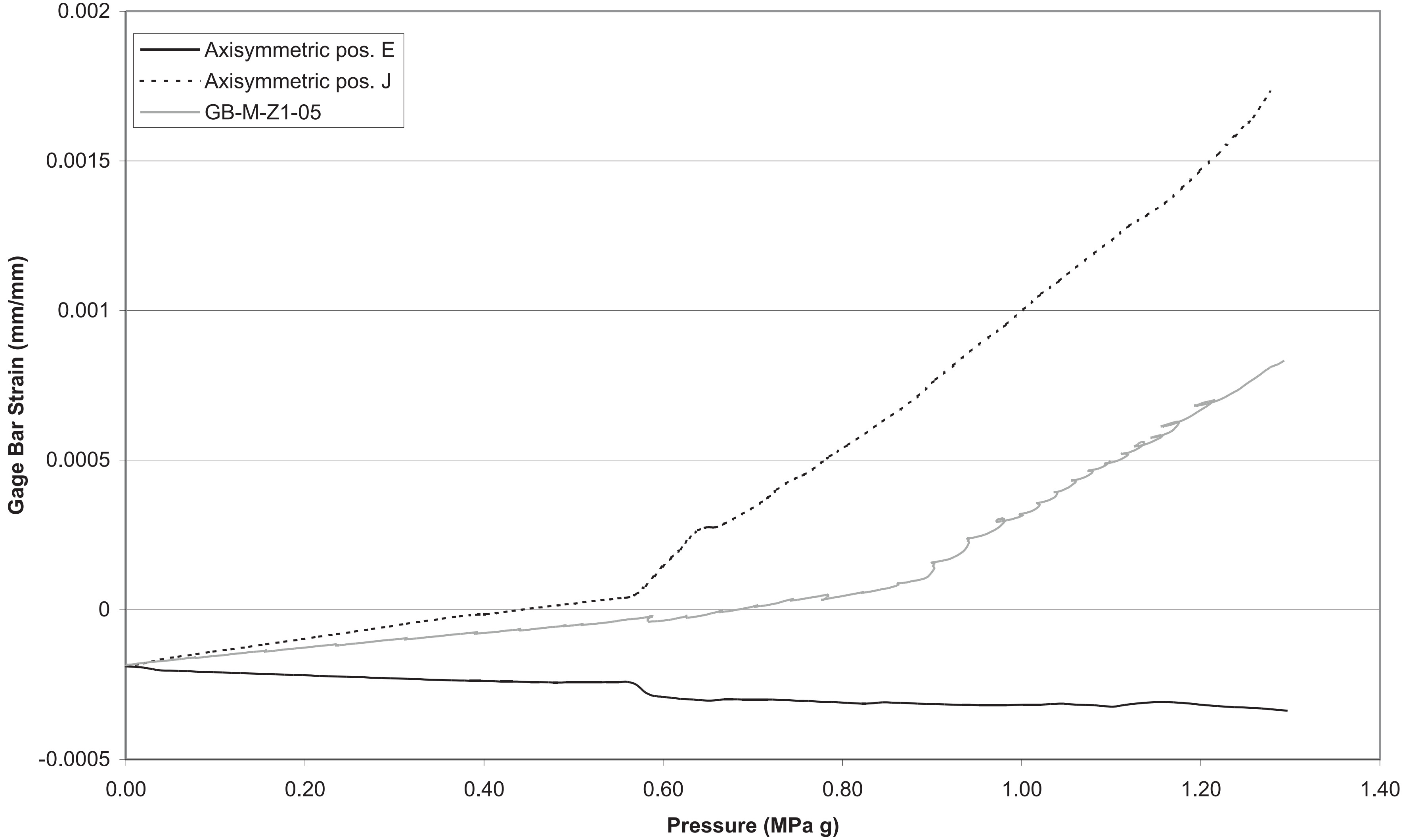

Figure 5-32. Final Posttest Analysis Vs. LST at Wall Base Gage Bar Position E-J

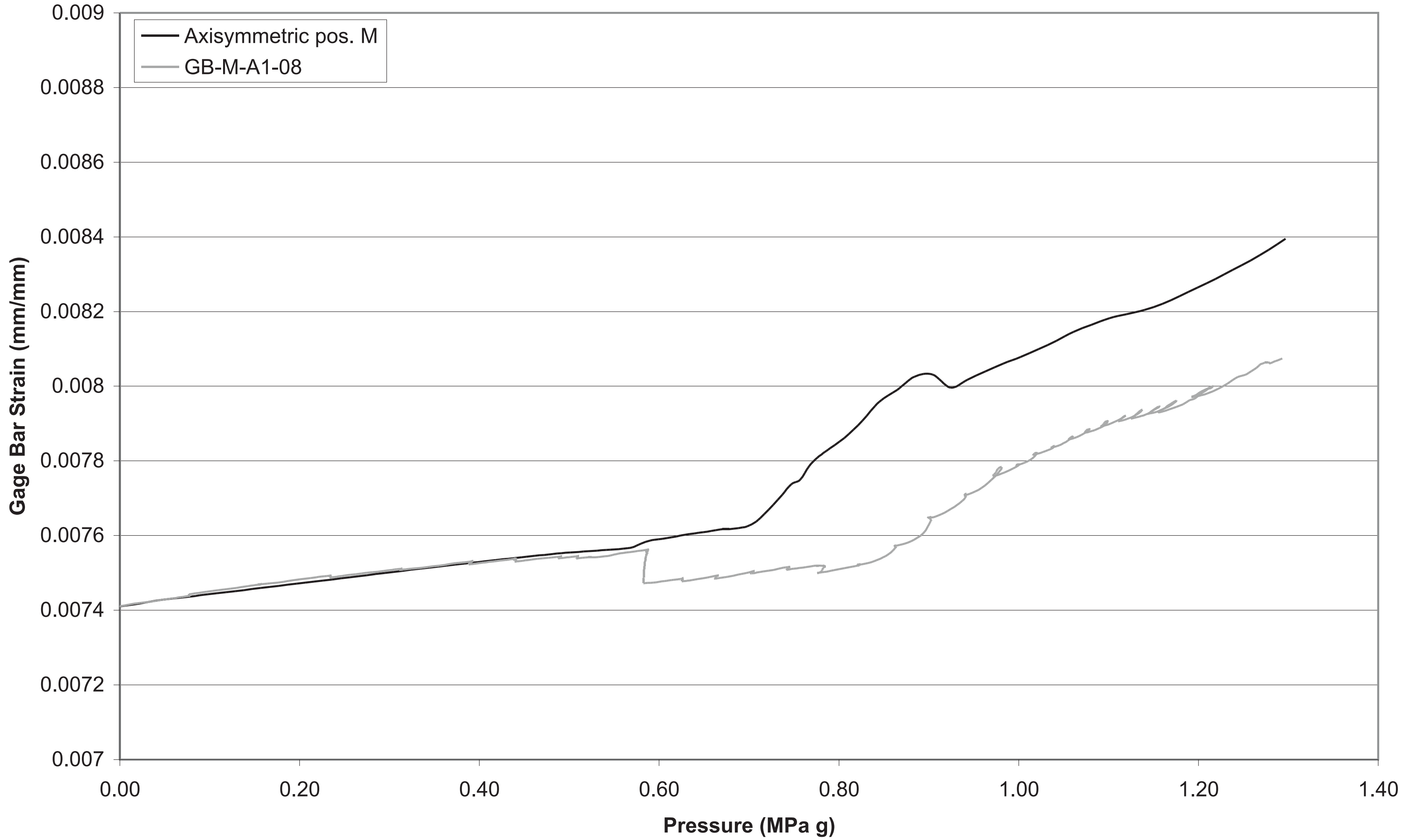

Figure 5-33. Final Pos-test Analysis Vs. LST at Wall Base Gage Bar Position M

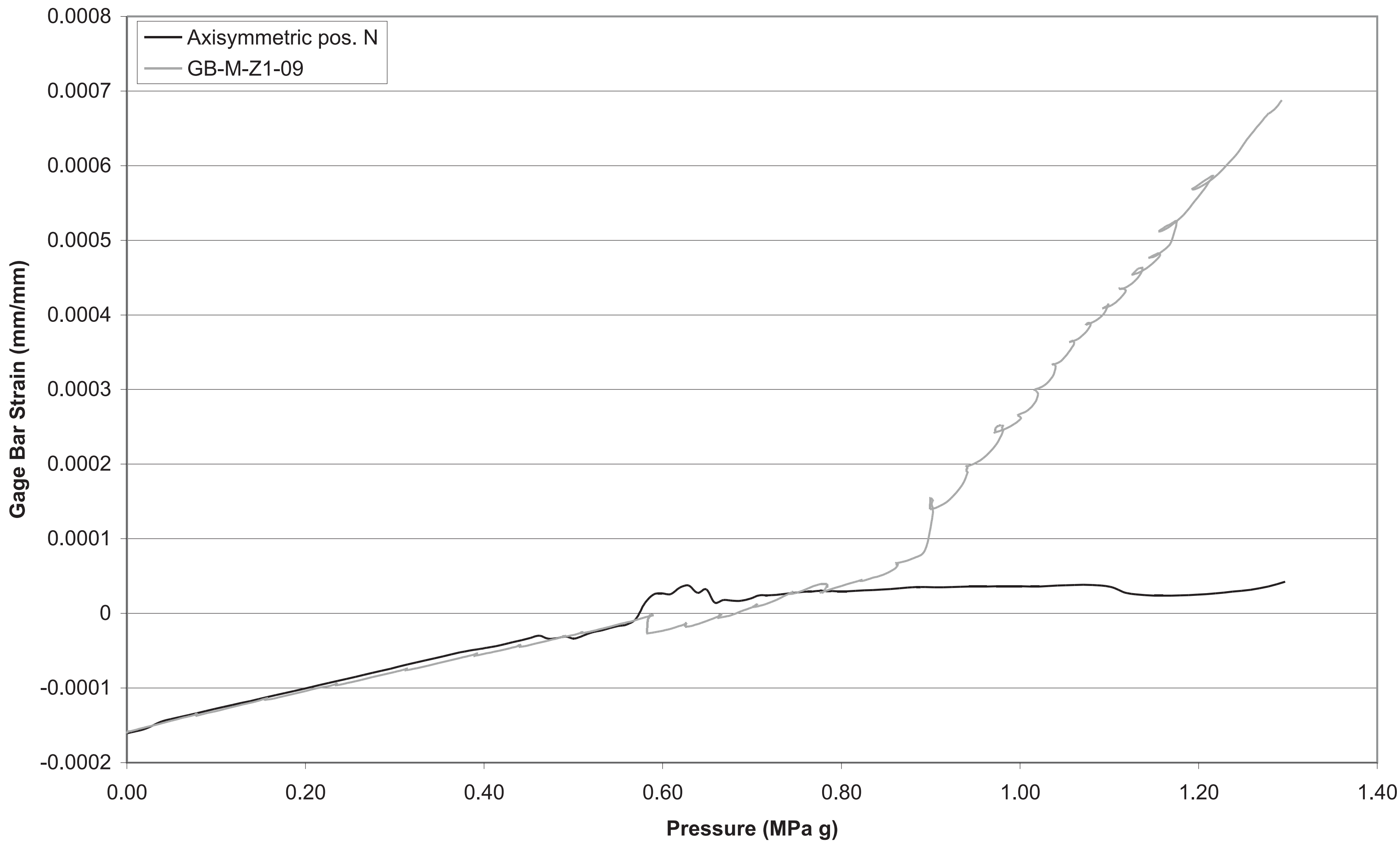

Figure 5-34. Final Posttest Analysis Vs. LST at Wall Base Gage Bar Position N

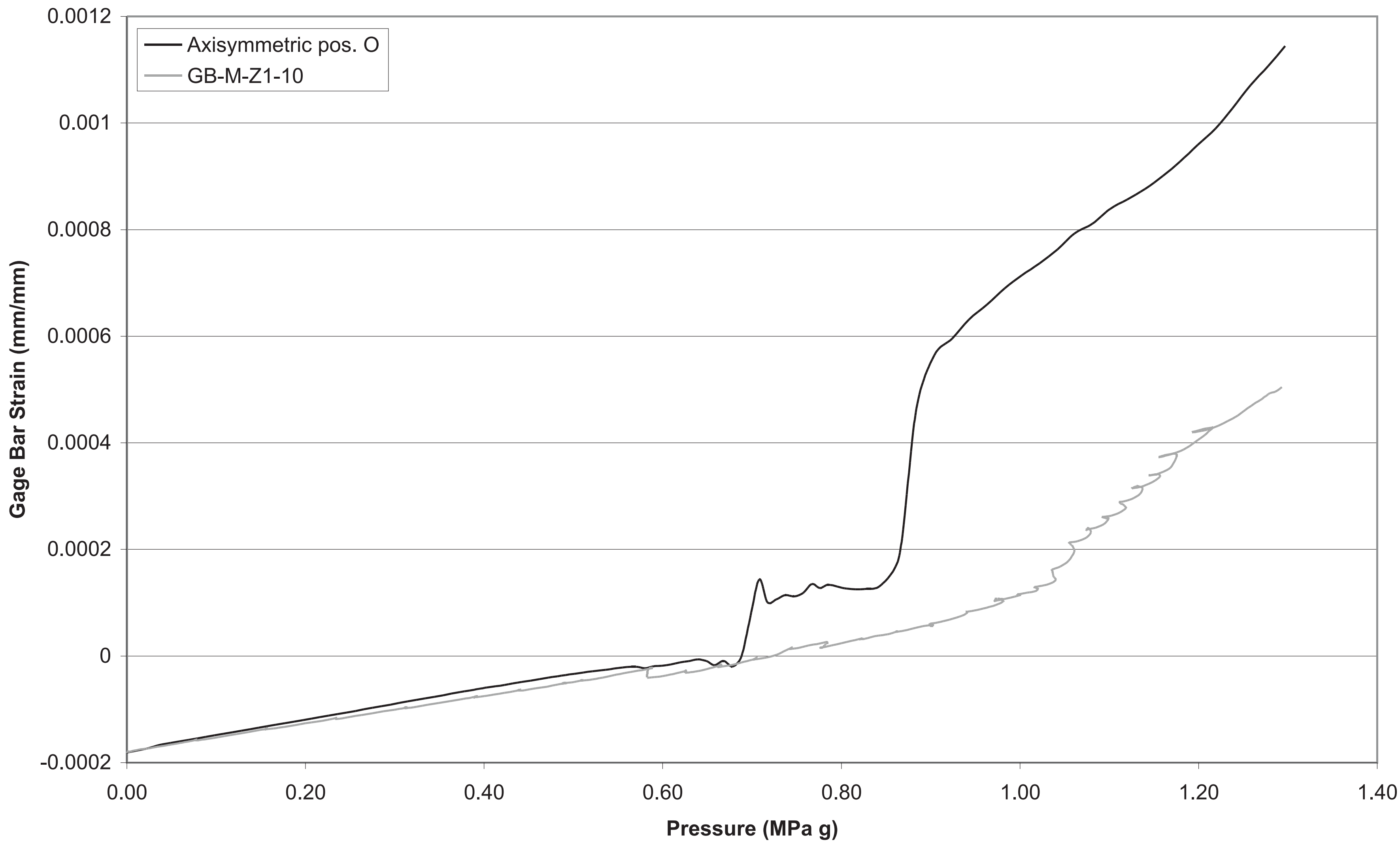

Figure 5-35. Final Posttest Analysis Vs. LST at Wall Base Gage Bar Position O

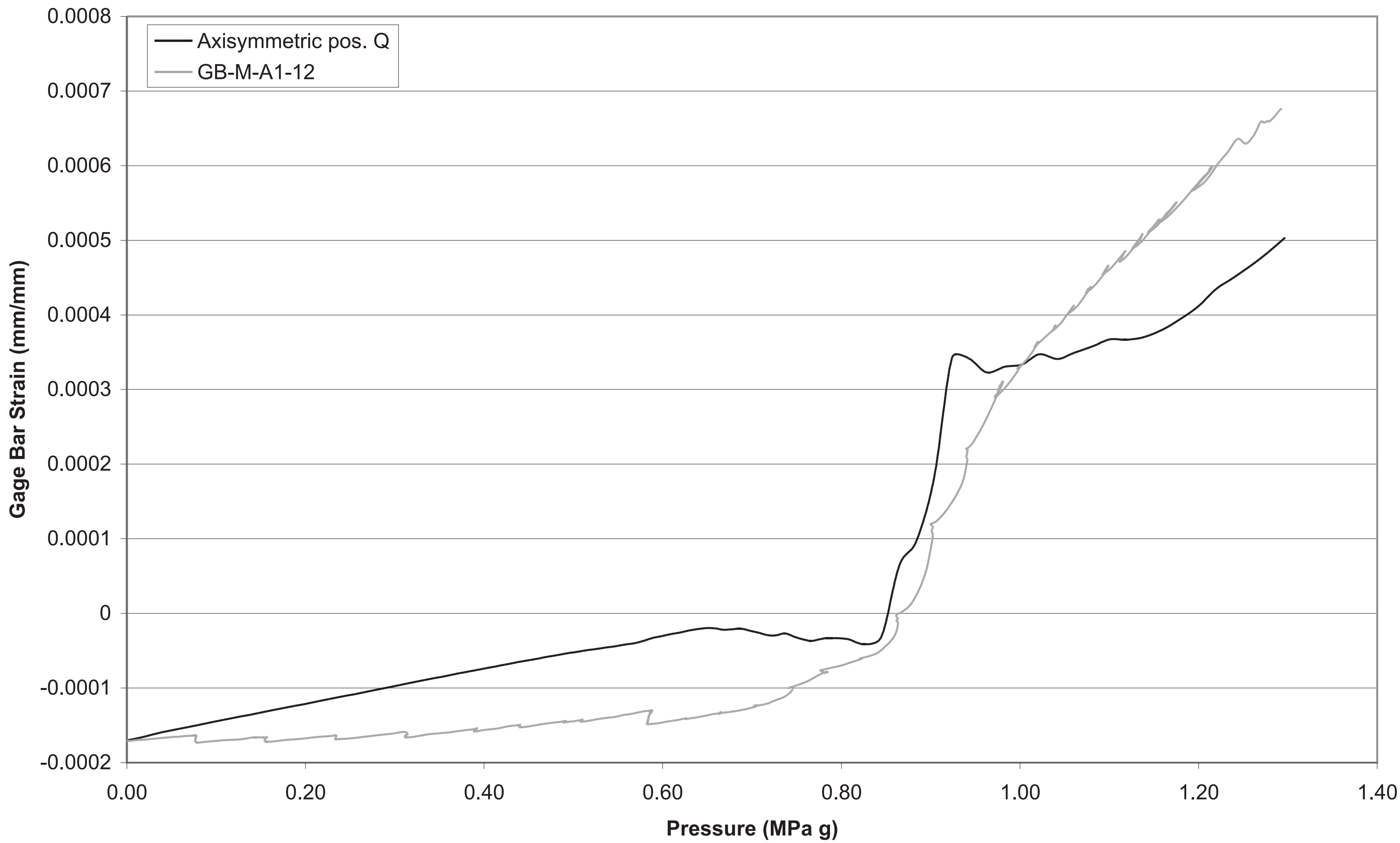

Figure 5-36. Final Posttest Analysis Vs. LST at Wall Base Gage Bar Position Q

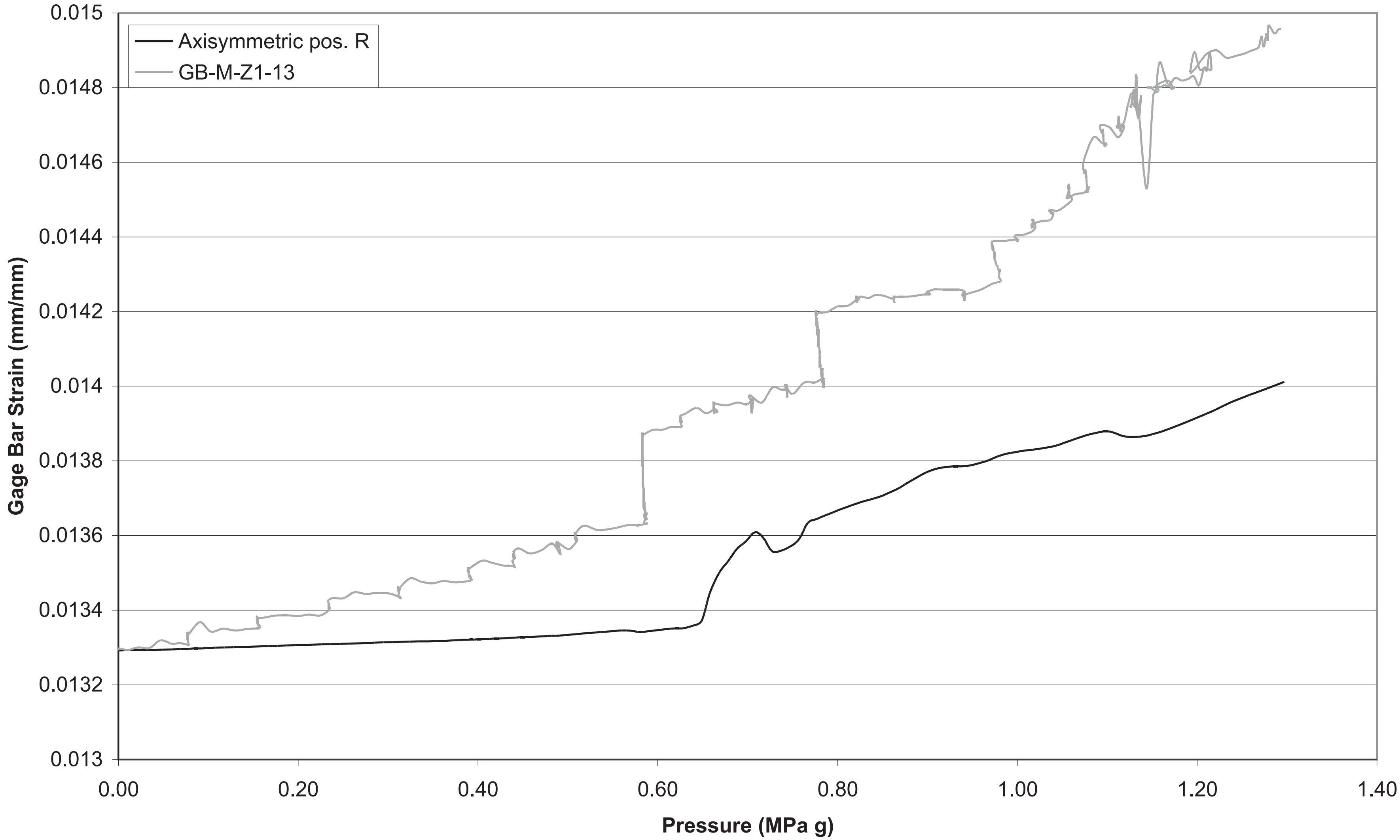

Figure 5-37. Final Posttest Analysis Vs. LST at Wall Base Gage Bar Position R

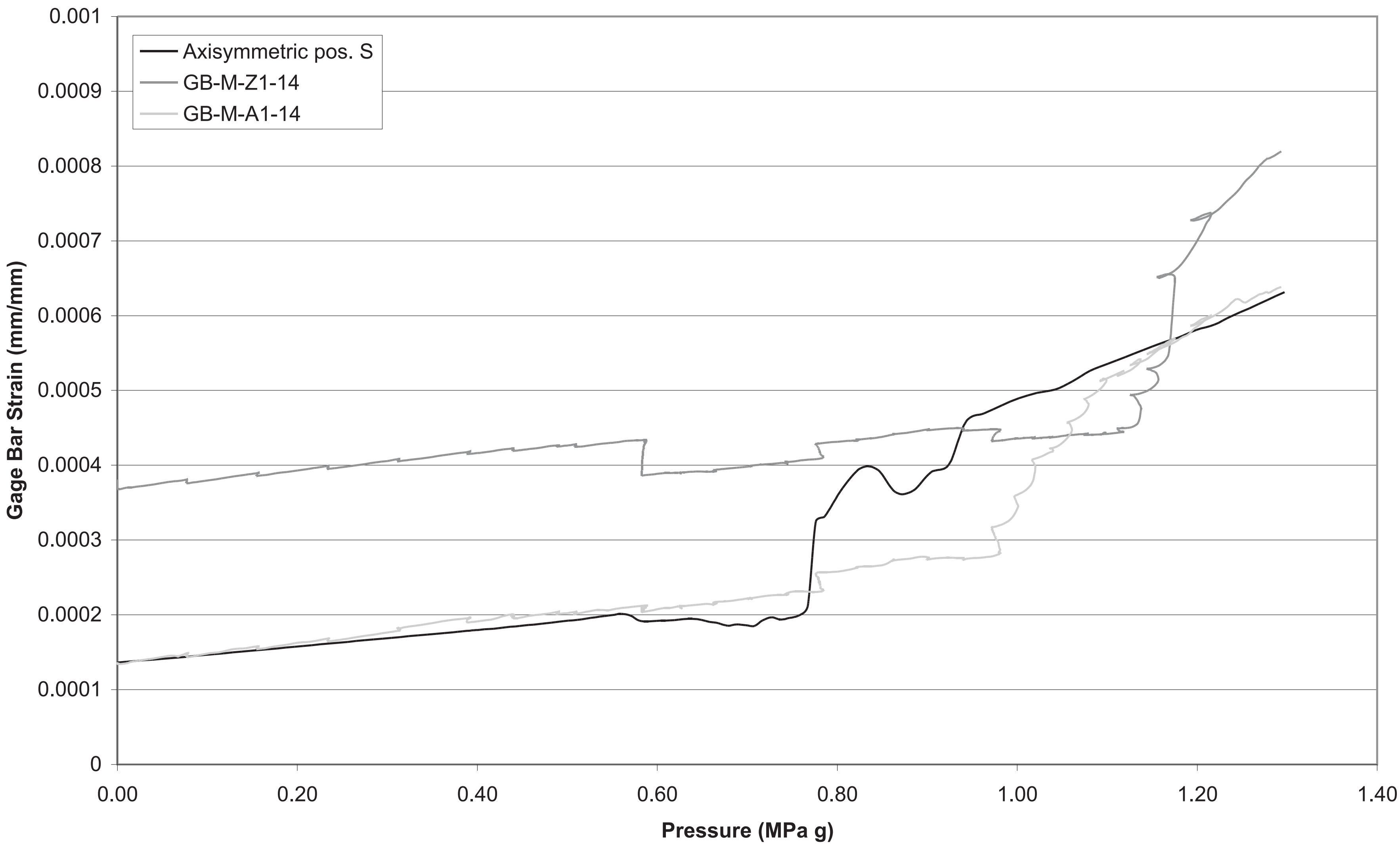

Figure 5-38. Final Posttest Analysis Vs. LST at Wall Base Gage Bar Position S

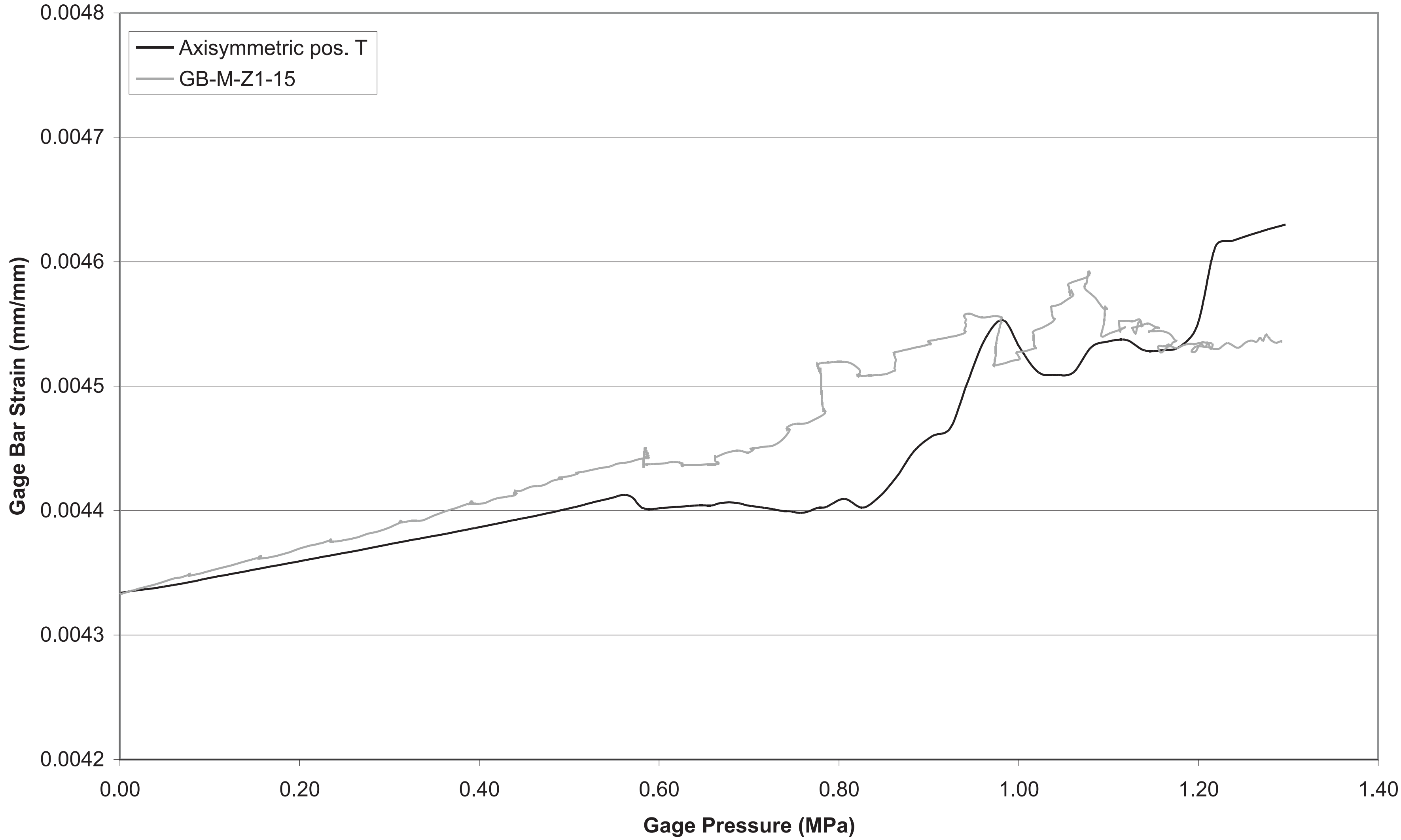

Figure 5-39. Final Posttest Analysis Vs. LST at Wall Base Gage Bar Position T

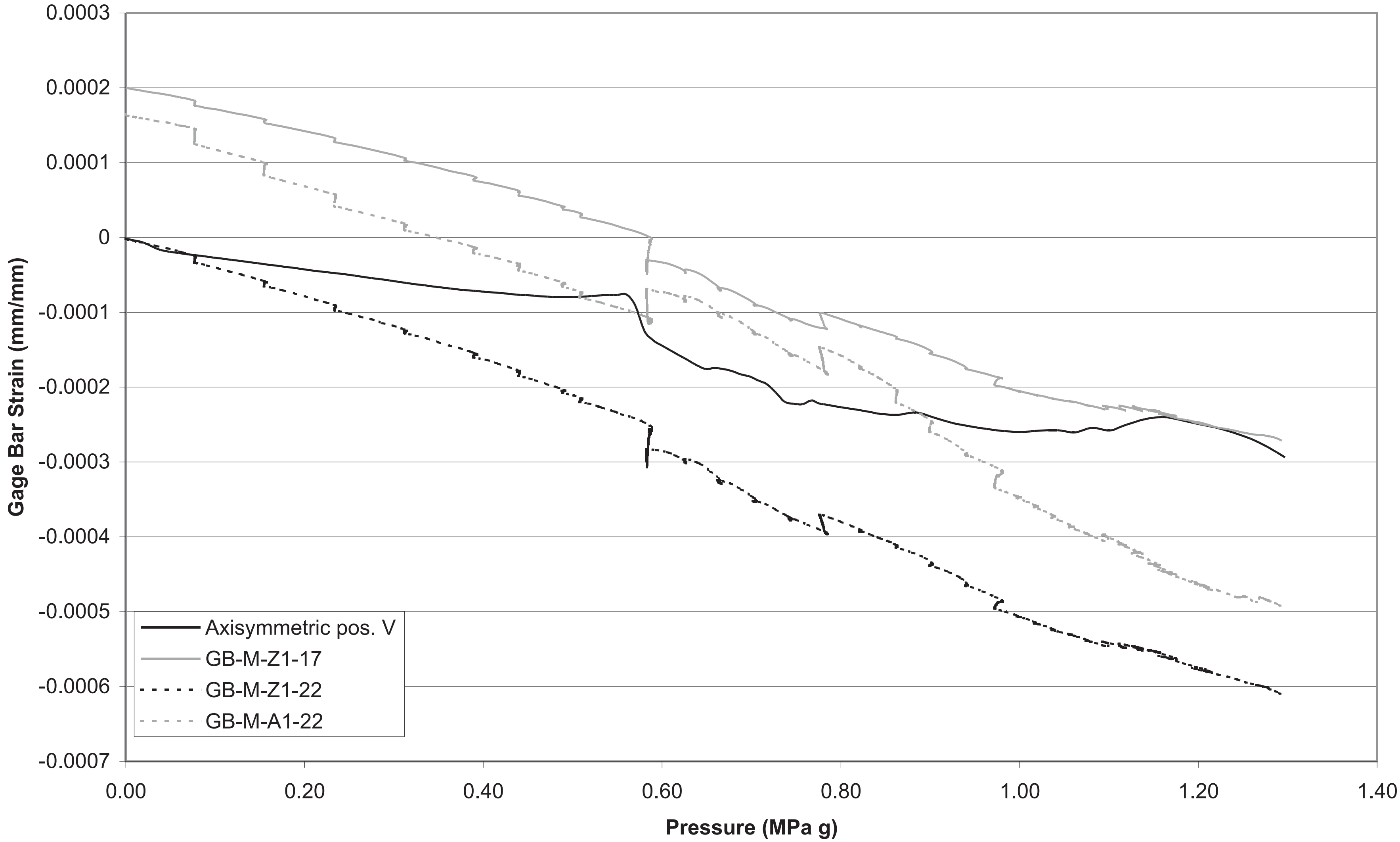

Figure 5-40. Final Posttest Analysis Vs. LST at Wall Base Gage Bar Position V

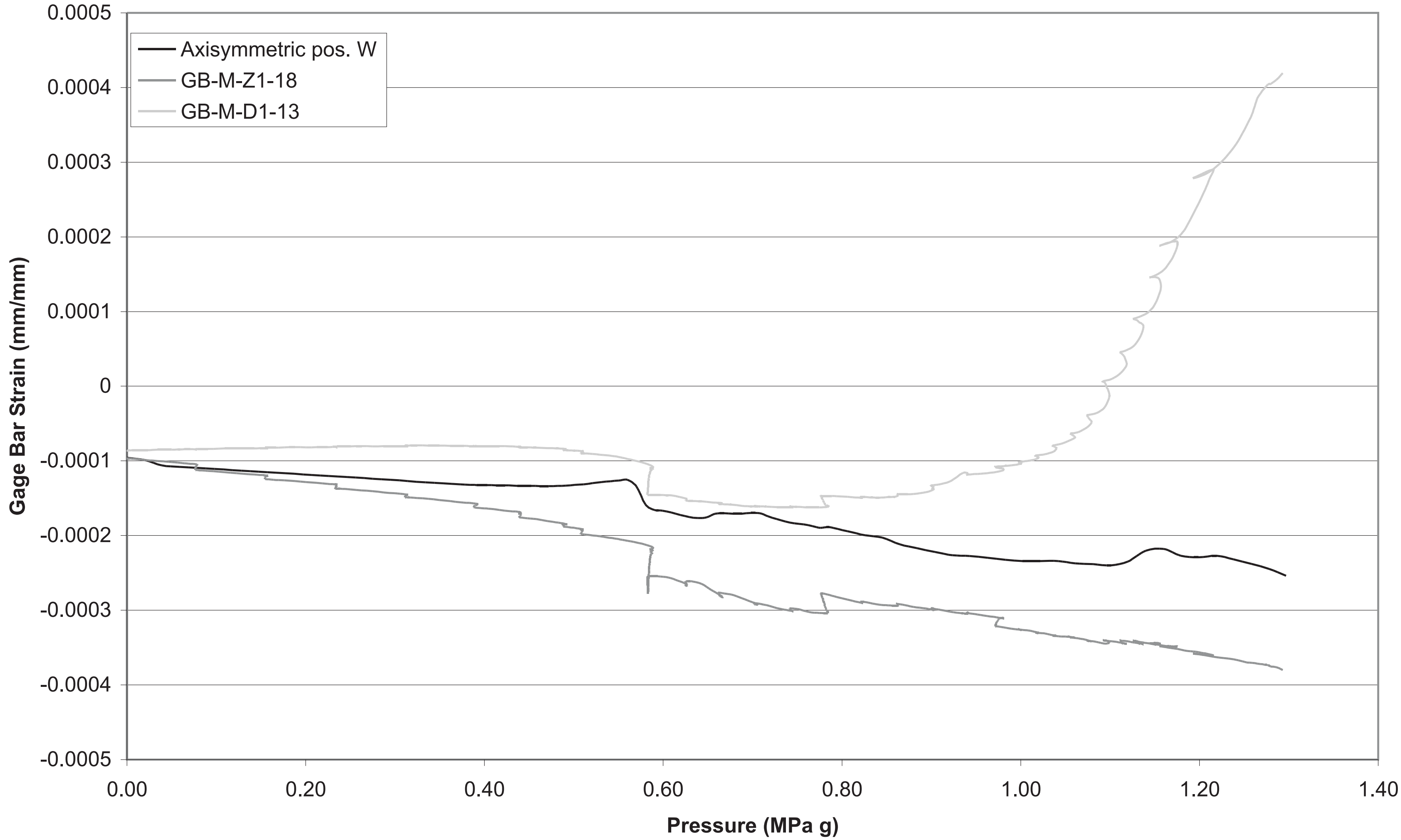

Figure 5-41. Final Posttest Analysis Vs. LST at Wall Base Gage Bar Position W

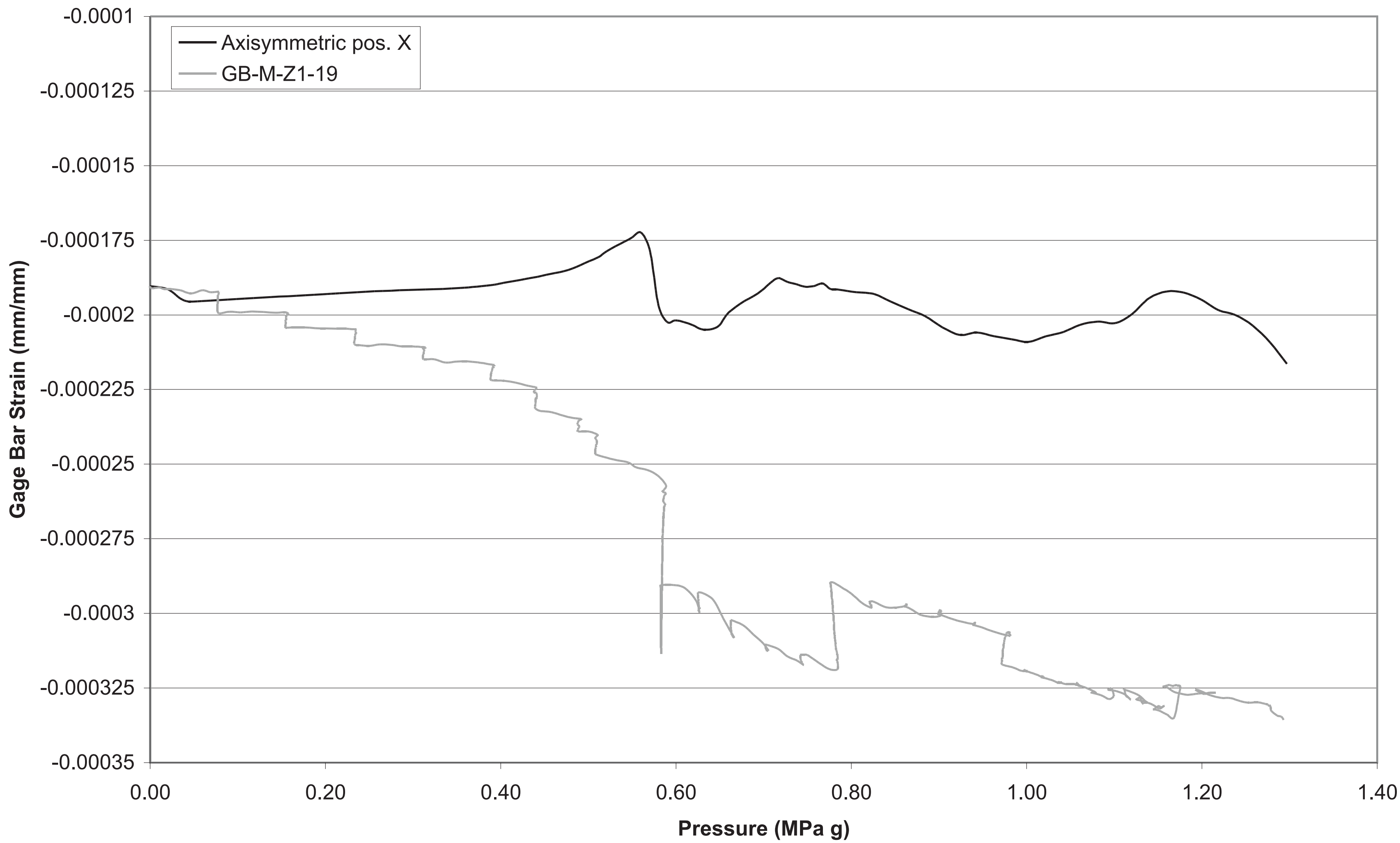

Figure 5-42. Final Posttest Analysis Vs. LST at Wall Base Gage Bar Position X

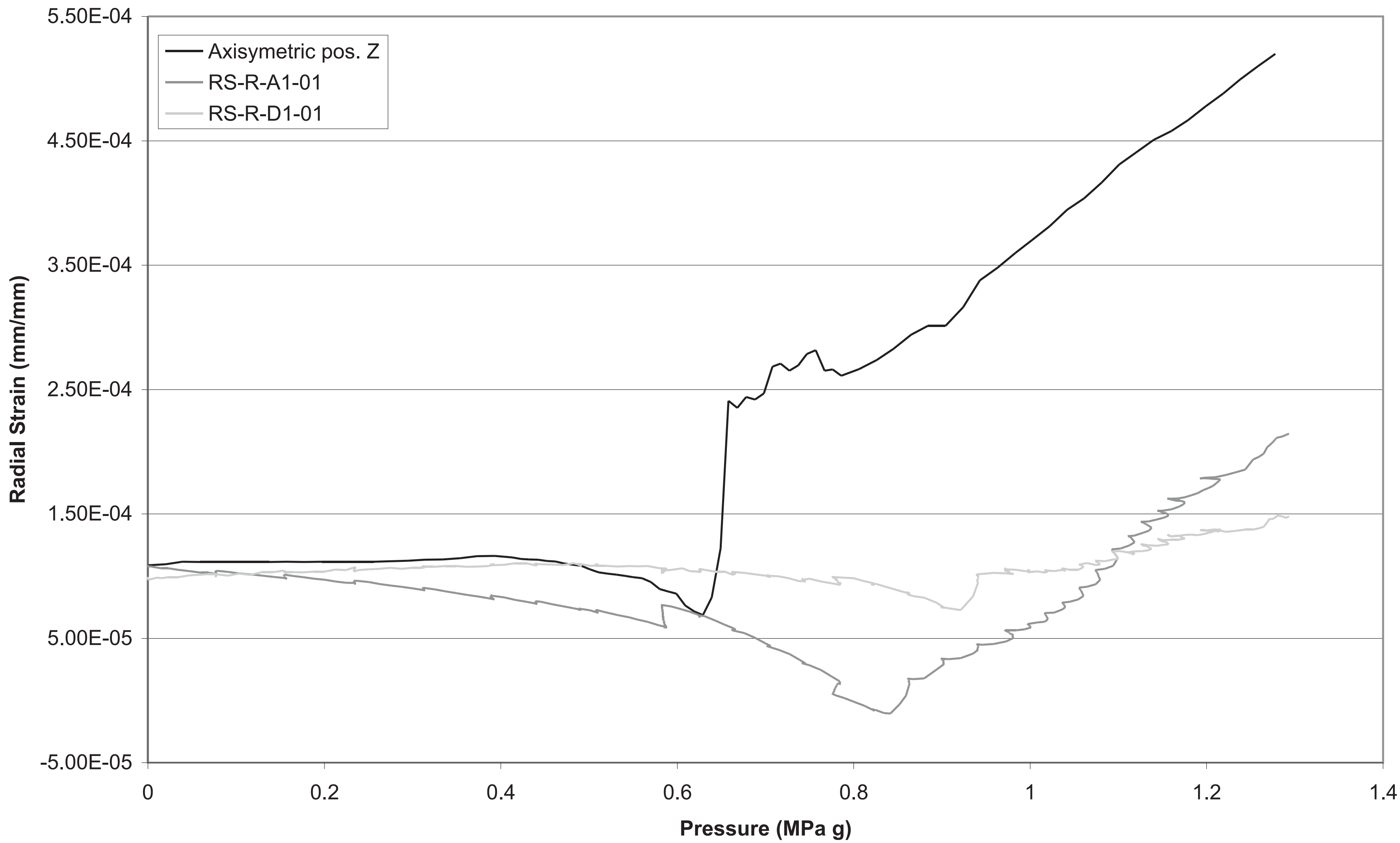

Figure 5-43. Final Posttest Analysis Vs. LST at Wall Base Radial Stirrup Position Z

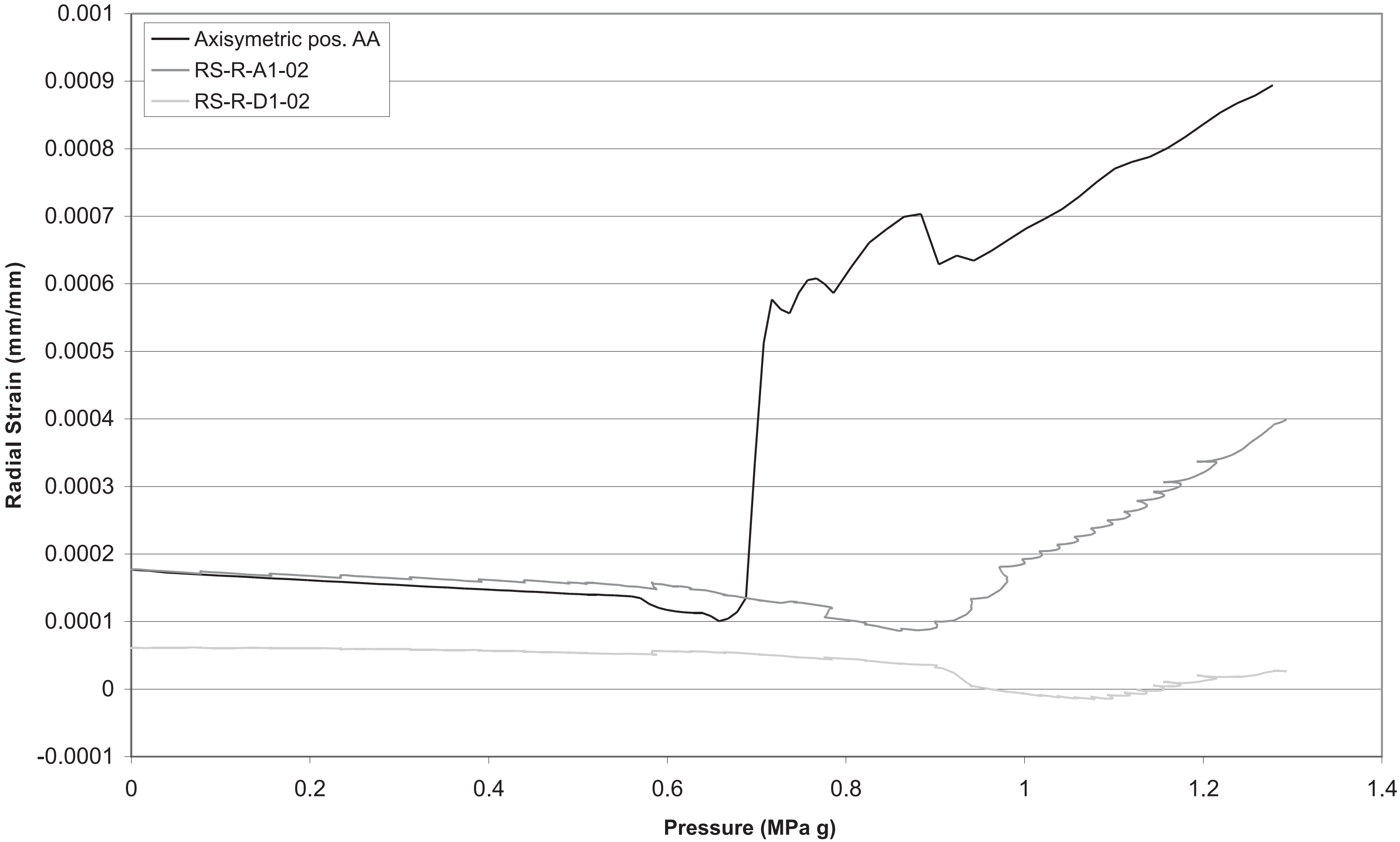

Figure 5-44. Final Posttest Analysis Vs. LST at Wall Base Radial Stirrup Position AA

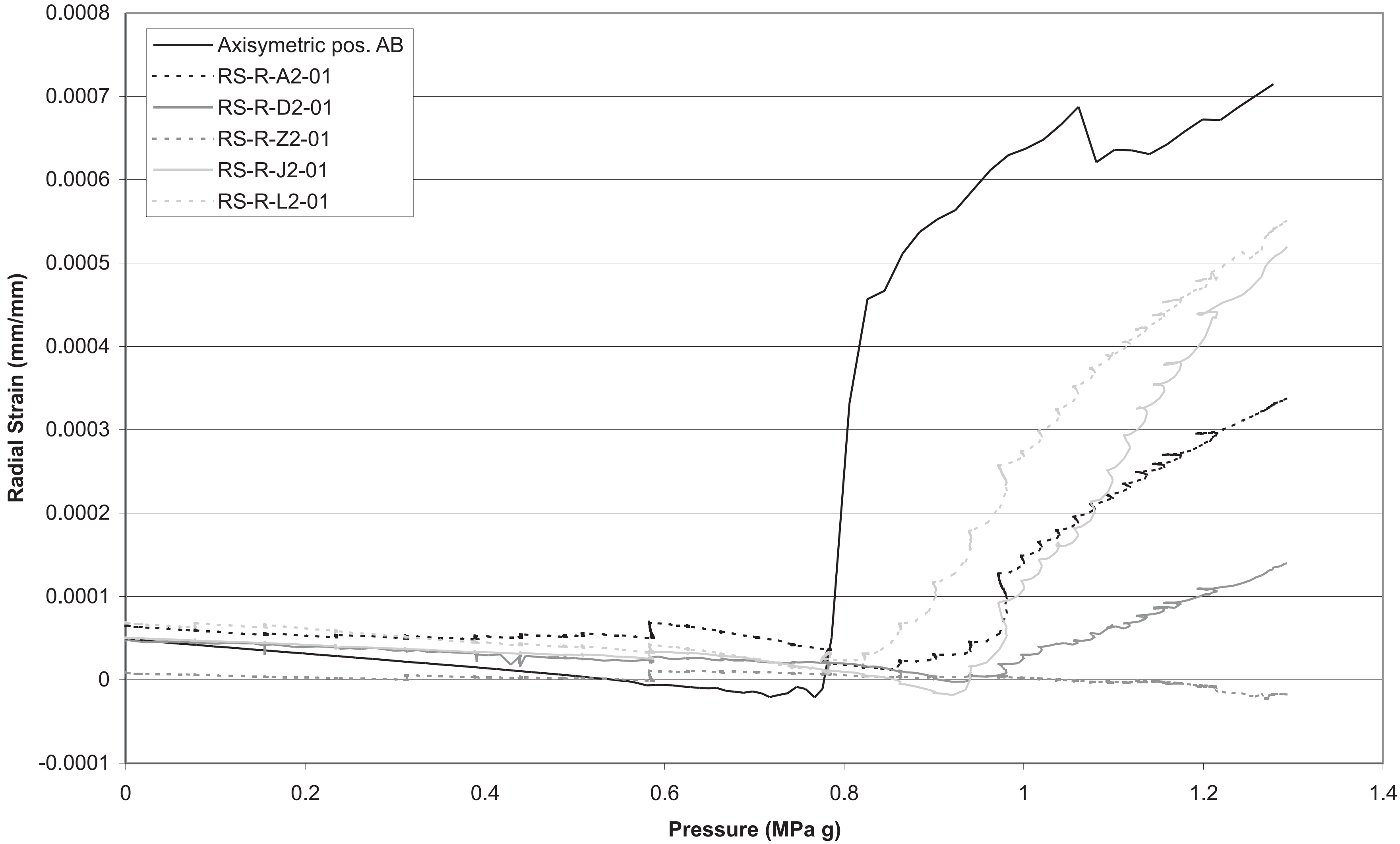

Figure 5-45. Final Posttest Analysis Vs. LST at Wall Base Radial Stirrup Position AB

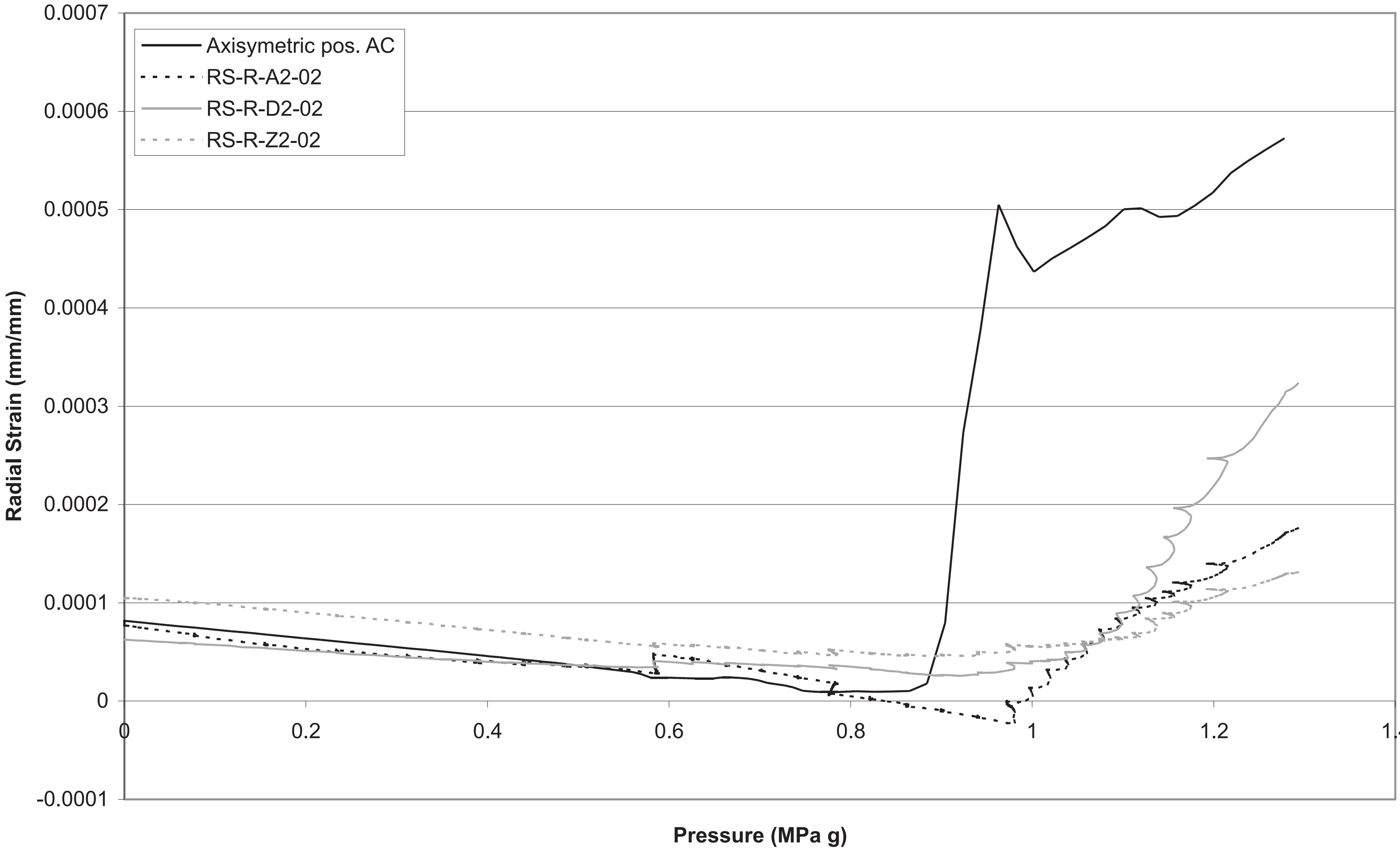

Figure 5-46. Final Posttest Analysis Vs. LST at Wall Base Radial Stirrup Position AC

6.0 3DCM MODEL POSTTEST ANALYSIS

6.1 Overview of Pretest Model and Focus of Posttest Analysis

The 3DCM model is a detailed representation of a horizontal slice through the PCCV cylinder that extends from elev. 4.67 m to elev. 8.96 m, and extends 360 degrees circumferentially, as shown in Figure 6-1. For modeling convenience, the centerline elevations of the E/H, A/L, and M/S were assumed to be the same (requiring only a few centimeters upward and downward adjustment of these centerlines from their true location). The penetrations, therefore, were represented in vertical half-symmetry. Both buttresses were modeled. The liner was explicitly modeled with shell elements; liner anchors were modeled with beam elements; and rebar was modeled one-for-one with rebar subelements. The liner grid density was not as fine as for the individual local models, so the 3DCM model was not used to predict peak local liner strains. The grid was considered fine enough, however, to represent the stiffness and yielding behavior of the liner in order to predict displacement versus pressure histories at the boundaries of local models. A more detailed description of the 3DCM model, its objectives, and pretest results can be found in [1]. Some results of the final pretest 3DCM model were shown in Chapter 2.

The modeling of the hoop and vertical tendons in the 3DCM is analogous to that described for the axisymmetric model meridional dome tendons. Each tendon was modeled with a truss element and friction truss-ties to adjacent concrete nodes, as shown in Figure 6-2. The tie elements have a length equal to the radius of the tendon ducts. When the tendon is curved, the truss ties are oriented at an angle of arctan(0.21), because the coefficient of angular friction used in the model design and assumed for its behavior was 0.21. By assigning this system of tendon elements small displacement theory, the friction truss-ties always transmit the exact amount of theoretical angular friction force from the tendon to the concrete. When the tendon segment being tied is straight, the tie element is oriented perpendicular to the tendon (no friction). Thus, wobble friction along straight runs of tendon is not modeled directly. Wobble friction was considered, however, in estimating tendon stresses at the boundaries of the models. Anchor set losses were simulated by reversing the orientation of the friction truss elements over the anchor set loss zone. The length of this zone was predetermined from design calculations to be 37.5 degrees from the buttress centerline, as shown in Figure 2-14.

Because the model and tendons deform during prestress equilibration, the anchor stress application required several trial iterations to achieve the desired anchor force on all tendons at the end of the prestress loading step. The hoop tendon anchor force was applied at both ends of the tendons. The vertical tendon stresses (1341 MPa) were applied to the tendon element tails at the bottom of the model. The target stress for vertical tendons away from penetrations was the design stress. The target stress for vertical tendons with any path deviation caused by penetrations was reduced from the design stress by the angular friction loss encountered between the base of the PCCV wall (Elev. 0) and the base of the 3DCM model. This theoretical loss along portions outside the 3DCM model was performed by hand calculation.

After prestressing, pressure was applied to the model. The distribution of stress and strain in the hoop tendons of the 3DCM pretest model was shown in Chapter 2. By 3.0 Pd, strains in the hoop tendon adjacent to the hatches reached 1.4%, while strains elsewhere were generally between 0.006 and 0.010. At 3.5 Pd, peak strains exceeded 5%, which is enough to rupture a tendon. Thus, if model pressurization were not precluded by a liner failure/leakage, the 3DCM model predicts 3.5 Pd as a structural limit state. (Note that this is lower than that predicted by 2D (axisymmetric analysis alone.)

Important observations of the 3DCM model response and of comparisons to the LST follow.

1. The 3DCM model deforms radially outward significantly more than the test measurements and more than the axisymmetric analysis (as shown in Figures 2-17 and 2-18). (The 3DCM model exhibits on-set of global yielding at a lower pressure. Global yielding occurs over a broader range of pressure, and the post-yield behavior is softer than the axisymmetric model.)
2. At pressures lower than 3.0 Pd, the buttresses (90 and 270 degrees) actually displace radially more than most other azimuths. This trend reverses itself beyond 3.0 Pd, but at $P < 3.0$ Pd, the trend is clearly at odds with test observation.

3. As shown in Figures 6-3 through 6-6, while the 3DCM model provided a good simulation of the tendon stress distribution at the test's initial conditions, as pressure increased, different stress redistribution occurred in the tendons than was simulated by the analysis.

Addressing these three differences between the 3DCM model and the LST observations became the primary focus of the 3DCM posttest analysis work.

6.2 Analysis of Special Models to Derive 3DCM Buttress Springs

In looking for modeling assumptions that would cause the observed variances with the LST, the first observation was that the buttresses above and below the 3DCM model boundaries have meridonal bending stiffness not represented in the analysis boundary conditions. A reasonably simple way to account for this would be to derive equivalent spring properties and then apply radial spring elements, as shown in Figure 6-2. The global axisymmetric models were used for this purpose, as shown in Figures 6-7 and 6-8.

The derivation was performed by adding a 2D plane stress representation of a buttress to the axisymmetric model. The model was then cut at the appropriate 3DCM model horizontal boundary. Zero rotation boundary conditions were applied at the cut boundary, and horizontal and vertical tendon prestress was maintained as in the full axisymmetric models. A horizontal displacement was then applied to the cut boundary, as shown in Figures 6-7 and 6-8. Separate models were analyzed with and without the buttress present and the force versus displacement results were plotted and differenced, as shown in the Figures 6-7 and 6-8. The difference results become the force versus deflection properties assigned to the buttress springs. The force versus deflection in Figure 6-7 shows a force plateau reached beyond displacement of about 1.3 mm (0.005 inches). The spring force-displacement curves were defined to large displacements.

The displacement results with this buttress spring change are plotted later in the chapter.

6.3 Posttest Tendon Modeling (and Intermediate Results)

The next and only other modeling assumption at significant variance with observed test behavior was the tendon modeling, especially the representation of friction. A lengthy study and series of analyses focused on this phenomenon. This chapter discusses and presents results for run numbers 4, 5, 6, 7, and 9 from that study.

The 3DCM tendon modeling was reviewed in detail and a first change was implemented based on the observation that from the tendon tangent points 5 degrees from the buttress edge to the tendon anchor point, the tendons were not previously tied to the concrete mesh (i.e., they were assumed frictionless). The situation is shown in Figure 6-9. The pretest modeling approach was consistent with the 1999 axisymmetric modeling assumption that straight tendon runs do not require friction modeling. Moreover, in the pretest work, this distance was short enough that direct tendon-to-concrete contact was not required. With hindsight from the test, however, it was observed that at higher pressures, the tendon nodes in this region passed through the concrete mesh, which, of course, cannot occur in the structure, except for small readjustments of the tendon location within the tendon duct.

Figure 6-9 shows the remedy. These straight segments were still assumed frictionless, but were simply tied to the concrete with perpendicular truss elements. Moving past several preliminary investigative analyses, the change depicted in Figure 6-9 was named 3DCM Model 4. 3DCM Model 5 simply added the previously described buttress springs. Results of Models 4 and 5 are provided in Figures 6-10 through 6-19. These figures show improvements over the pretest analysis, but still have significant differences from the test.

The focus of the posttest effort then returned to the tendon friction modeling methodology. Significant insights into the behavior of the tendons were provided by the tendon force (and strain) test measurements shown previously in Figures 6-3 to 6-6. The locations of these tendons on the 3DCM (H35, H53, H67, and H68) are shown in Figure 6-20. The symbols plotted on the tendon for the profile plots are a combination of the load cells (force) and wire strain gage (strain converted to force) measurements. The "Tensmeg" data was not used. The strain gage data was converted to force by first converting the strain gage measurements to axial strain (according to formulae described in [6] which account for the pitch of the individual wires in the tendon strands), then converting to stress using average tendon stress-strain data, and finally multiplying by the nominal area of the tendon, 3.393 cm^2 (0.525 in^2), to get force. These calculations were prepared by SNL.

Tendon H35 shows good agreement with initial analytical stress distributions, but most of the data for H35 is at the tendon ends. Tendons H53, H67, and H68, which have some good data interior from the ends, again show good agreement with initial stress distribution, but significant differences as pressurization builds. This tends to validate the initial approach to tendon friction modeling. (Note that in the tendon modeling approach the correct stress distribution is achieved by only applying stress at the anchorage; no initial stress is applied interior to the ends of the tendon).

Two important observations can be made about the hoop tendon behavior as pressure increases.

1. When pressure reaches the pressure to overcome prestress, P = 0.59 MPa (see discussion in [1] for the pressure calculation), tendon stress distributions begin to change from the classical angular friction design assumption to an approximately uniform distribution. This change occurs between approximately 1.5 Pd and 2.5 Pd; then the stress distributions stay fairly uniform at most higher pressures.

2. The apparent strain increases in the tendons corresponding to the force/strain gage readings are significantly larger (e.g. 0.48% versus 0.36% for H53) than the strain that corresponds purely to radial expansion. This can only be explained by force redistribution associated with sliding. Thus, the position of the tendon relative to the concrete must be allowed to change after initial prestress in order to adequately simulate tendon behavior during overpressurization.

These observations led to some extensive changes and studies of the tendon friction modeling. It was understood throughout the project that tendon friction may be quite complex, and that it may even dynamically change with pressure, but the tools to model such behavior were limited. The analysis strategies that were investigated were chosen to, at the very least, bracket the observed LST behavior. The analyses presented herein are as follows.

Model 6. (Shown in Figure 6-21). Apply prestress. Then, by using the ABAQUS *MODEL CHANGE capability, fix the tendon nodes at their initially deformed position relative to the concrete. In other words, start from classical design prestress with friction and then grout (bond) the tendons.

Model 7. (Shown in Figure 6-22). Based on observation 1 (above), perform run 5 (the run with only buttress springs added) up to P = 1.5 Pd (0.59 MPa), then model change all friction elements to non-friction elements (truss ties aligned perpendicular to the tendons). In other words, at P = 1.5 Pd, perfectly unbond the tendons.

Model 9. (Shown in Figure 6-23). Try a case with some aspects of run 6 *and* 7. After prestress, keep the initial friction elements, but add a new set of friction elements in the reverse orientation so that if points on the tendon move in the reverse direction from that of initial prestress, they will experience reverse direction friction in the process.

To simplify the friction study, anchor set losses were approximated more simply than in the pretest analysis. The same anchor set azimuth was used as before, but the friction was removed along the anchor set zone, so that tendon stress became constant over the anchor set zone. The initial tendon stress profile for all three runs (6, 7, and 9) are shown in Figures 6-24, 6-25, and 6-26, respectively. This approximation was deemed reasonable to study the more global effects of varying friction treatment along the remaining path of the tendons.

6.4 Posttest Results and Comparisons

The results of the different tendon friction bounding cases are plotted in Figures 6-27 through 6-54. Figures 6-38 to 6-54 demonstrate the effects on tendon stress in the different tendon friction simulations.

Considering run 6 with essentially bonded tendons (Figures 6-27 to 6-30), the "free-field" azimuth (135 and 180 degrees) agree well with the axisymmetric analysis and the test behavior, while the radial displacement of the E/H is overpredicted. The buttress radial displacement is also more in line with the test.

Considering run 7 with essentially unbonded tendons (after P = 1.5 Pd), the E/H displacement prediction is very good, but the 180 degrees and other nearby azimuths are significantly overpredicted.

Run 9 with two-direction friction behaves closer to run 6, the bonded case, but here the tendons are not bonded – their sliding just meets friction resistance in either direction. Although the E/H radial displacement is still somewhat overpredicted, run 9 is the best representation of tendon friction possible without resorting to a contact-surface type of tendon-to-concrete friction simulation.

6.5 Conclusions on 3DCM Analysis and Tendon Behavior

The posttest 3DCM models provide a bracketed simulation of the tendon friction behavior and the radial displacement patterns that occurred in the test. The comparisons that help form conclusions on tendon modeling and behavior are the replotting of the tendon stress distributions shown in Figures 6-3 through 6-6 for the posttest analysis. This is done in Figures 6-46 through 6-56. Runs 6, 7, and 9 are shown for each case. The following summarizes the additional observations provided by these figures.

The effects of friction are most clearly shown for the H35 tendon, which sweeps around all of the penetrations. Run 6 shows the most pronounced friction effects, run 9 shows a little less, and run 7 shows uniform distribution after 1.5 Pd.

In general, the tendon friction simulation runs 6, 7, and 9 show progressively better agreement with test measurements, with run 9 showing quite good agreement at the anchors and at most points interior to the tendon ends. (Consider tendon H68, for example, Figure 6-56. At 3.0 Pd, the analysis force distribution passes almost directly through the test data points. Note that the top curve is for 3.5 Pd – it would be reasonable to roughly interpolate between 3.0 Pd and 3.5 Pd to estimate the 3.3 Pd curve.)

Based on these and the other observations in this chapter, the results of run 9 are used to drive the M/S (and estimated F/W) penetrations posttest analysis.

Finally, in regards to tendon friction behavior, the test measurements and analytical evidence support the conclusion that tendon friction is important to the tendon behavior, but traditional friction design formulas that predict tendon stress distribution begin to break down once pressurization exceeds the pressure that overcomes prestress (in this case, roughly 1.5 Pd). Some parts of the tendon are forced to slide relative to the duct in the reverse direction of travel from that during prestressing. Under this action, angular friction properties probably still hold, but the direction of friction forces are opposite to the direction of travel. The best calculation methods recommended to account for this are, in descending order of preference, 1) an advanced contact friction surface between the tendons and the concrete (not manageable for the current problem size and complexity); 2) preset friction ties applied in one direction during prestressing and added in the other direction during pressurization (3DCM Model 9); and 3) if neither of these methods are practical within the scope of the calculation, start with an average stress level (using a friction loss design formula), but assume uniform stress distribution in the tendons throughout pressurization, i.e., an unbonded tendon assumption, and finally 4) same as 3, but using a bonded tendon assumption. For method 4, however, this can lead to a premature prediction of tendon rupture, because the tendon strain increments during pressurization will match the hoop strain increments of the vessel wall one-to-one, and this was not observed during the PCCV LST.

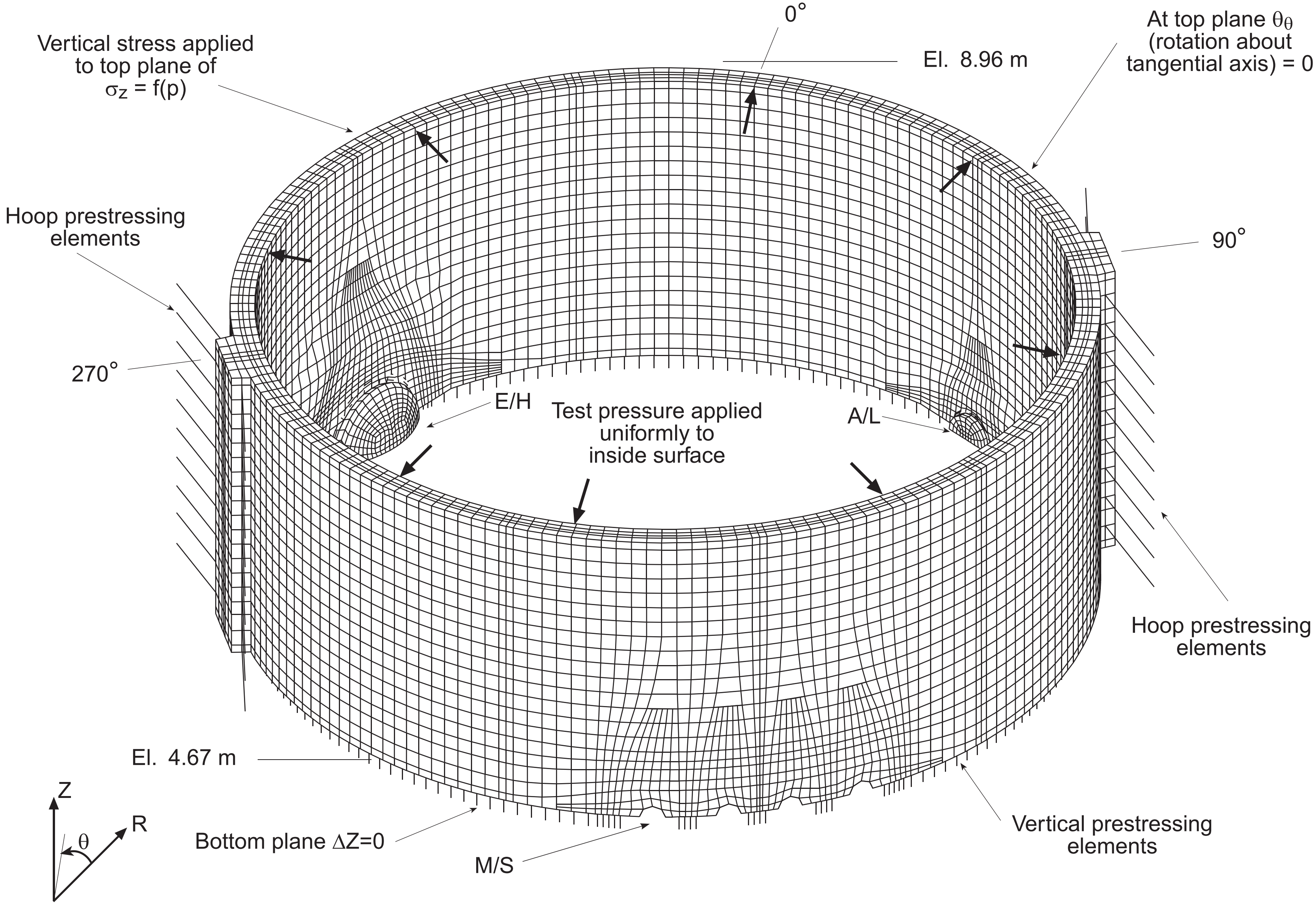

Figure 6-1. 3DCM Model Vertical Boundary Conditions

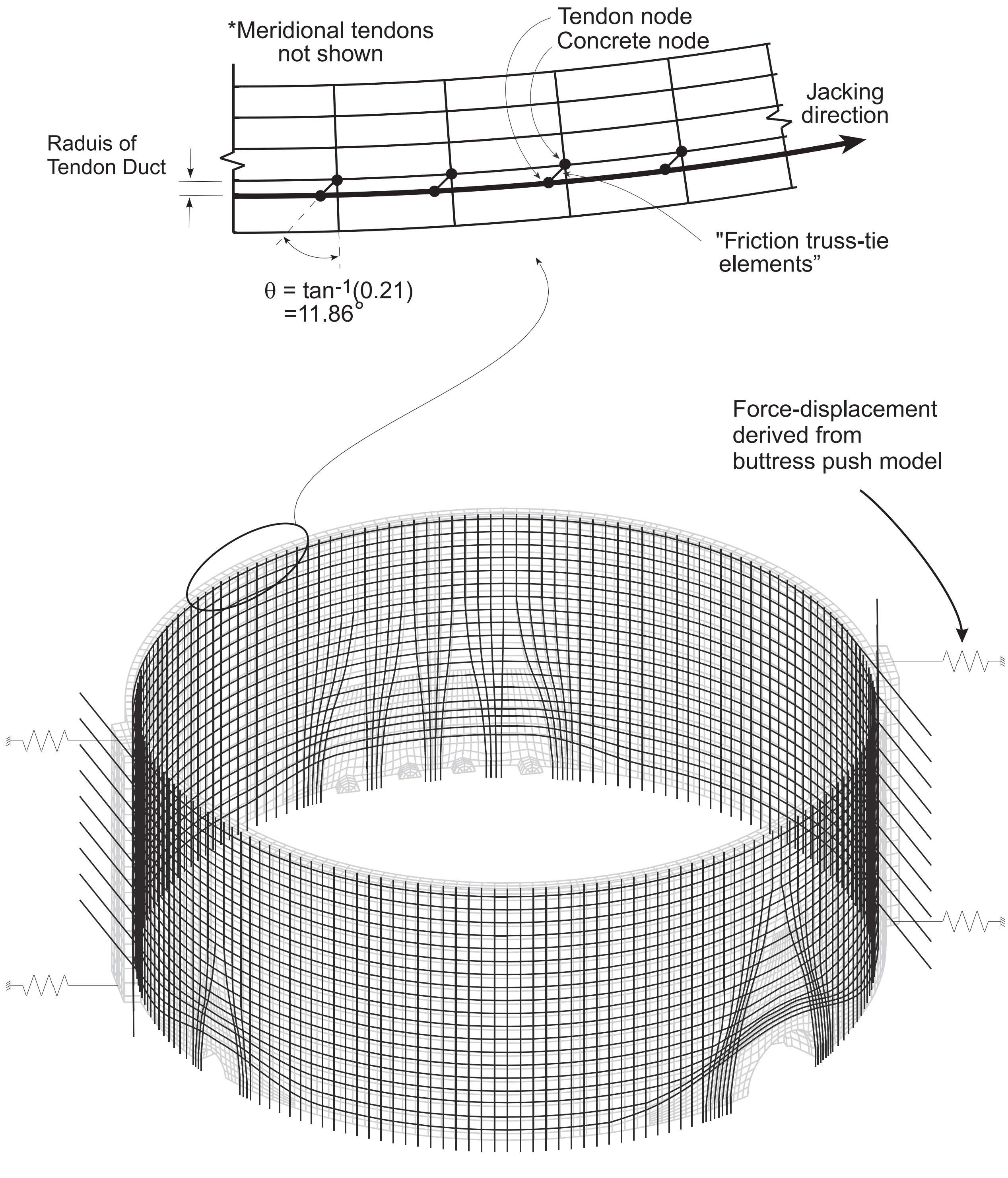

Figure 6-2. Isometric View of 3DCM Tendon Modeling and Added Buttress Springs

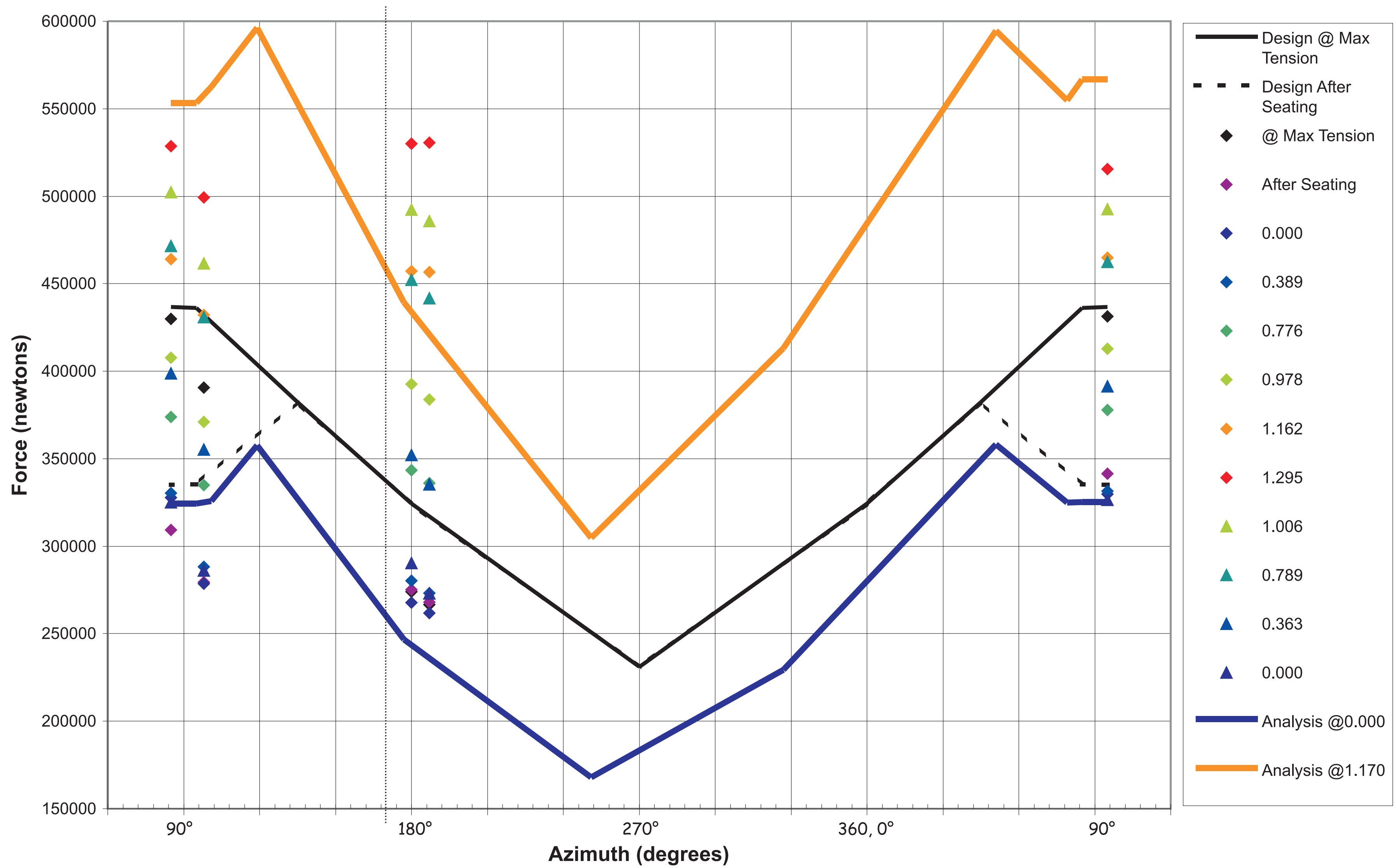

Figure 6-3. H35 Tendon Force Comparisons to Pretest

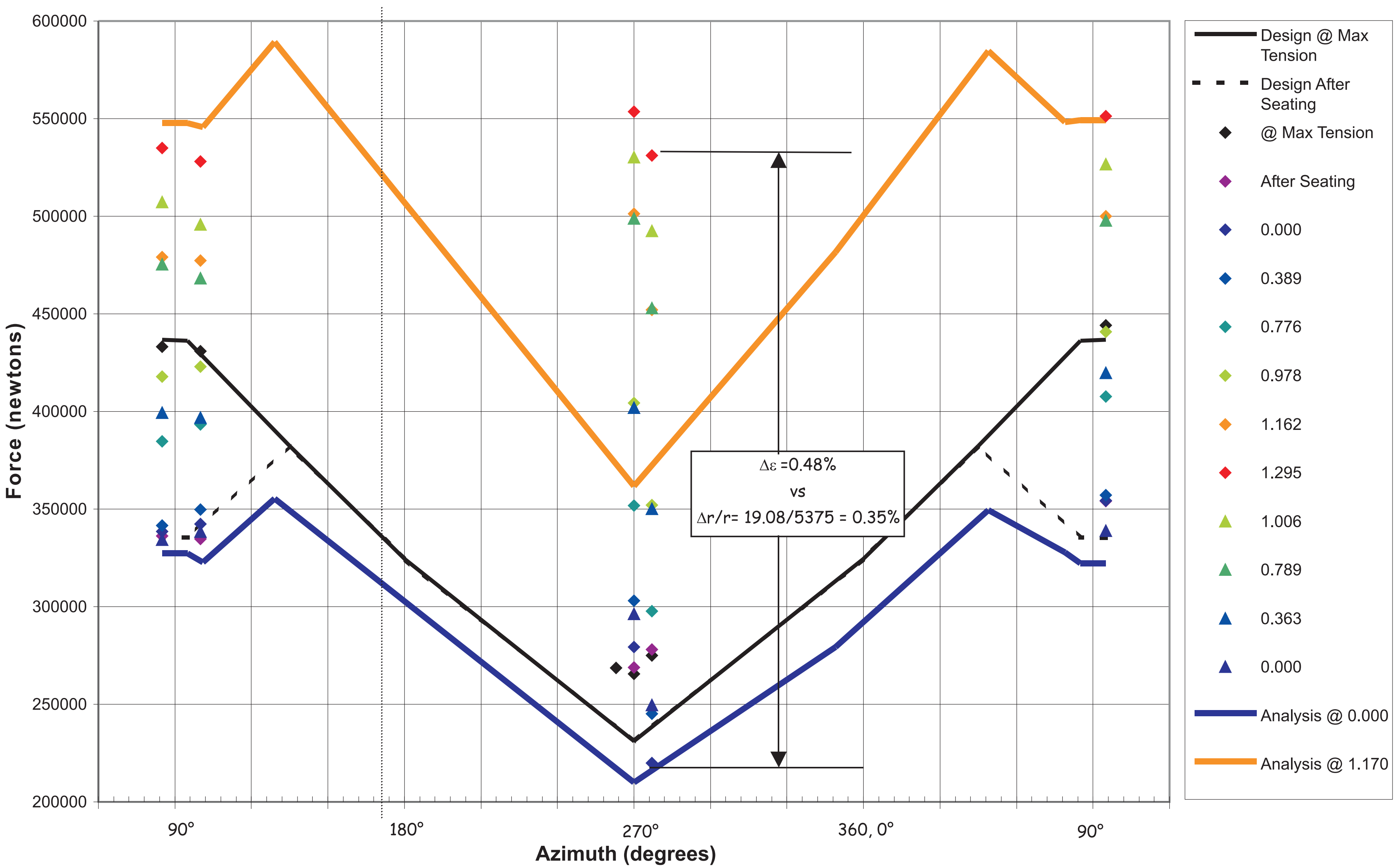

Figure 6-4. H53 Tendon Force Comparisons to Pretest

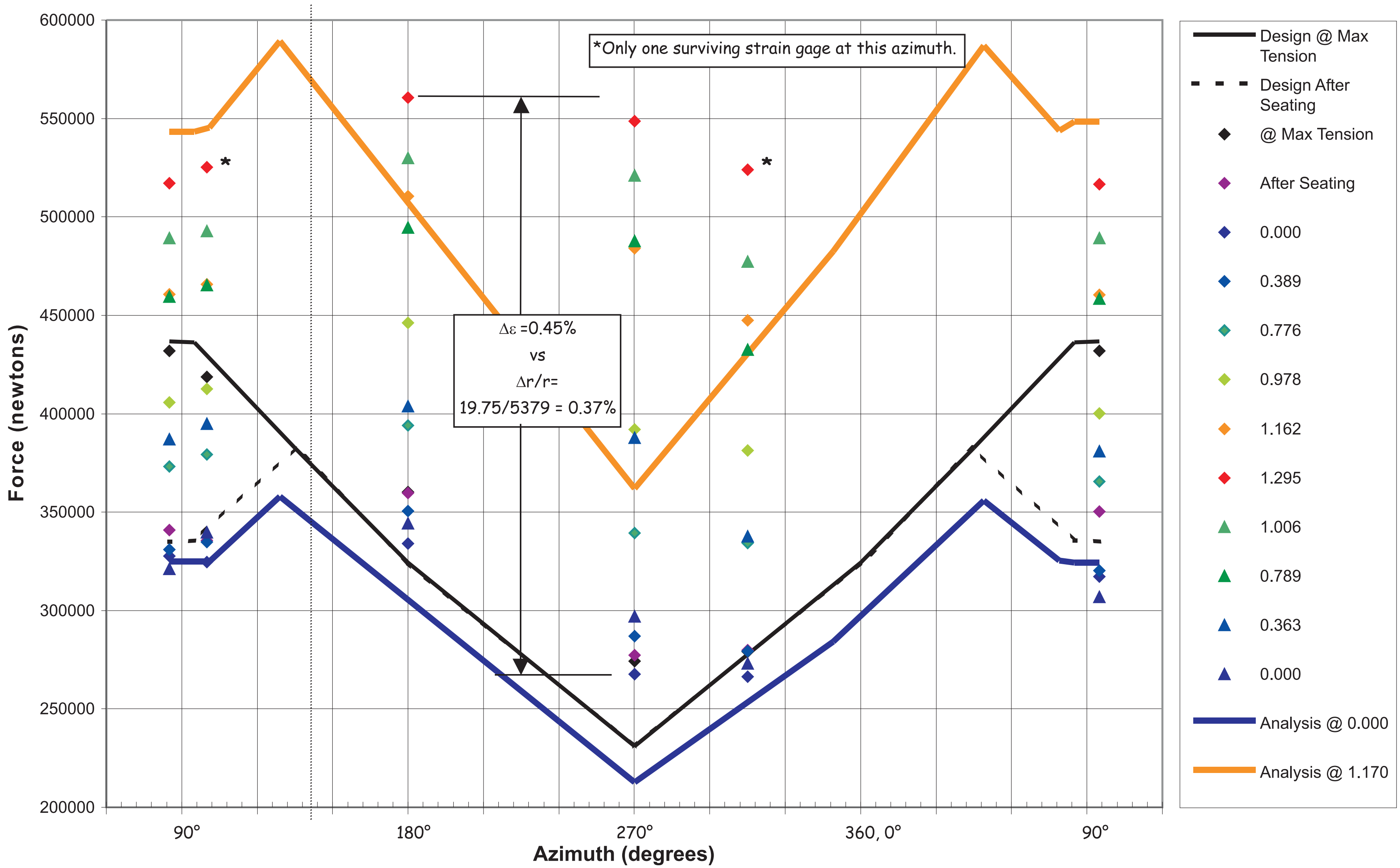

Figure 6-5. H67 Tendon Force Comparisons to Pretest

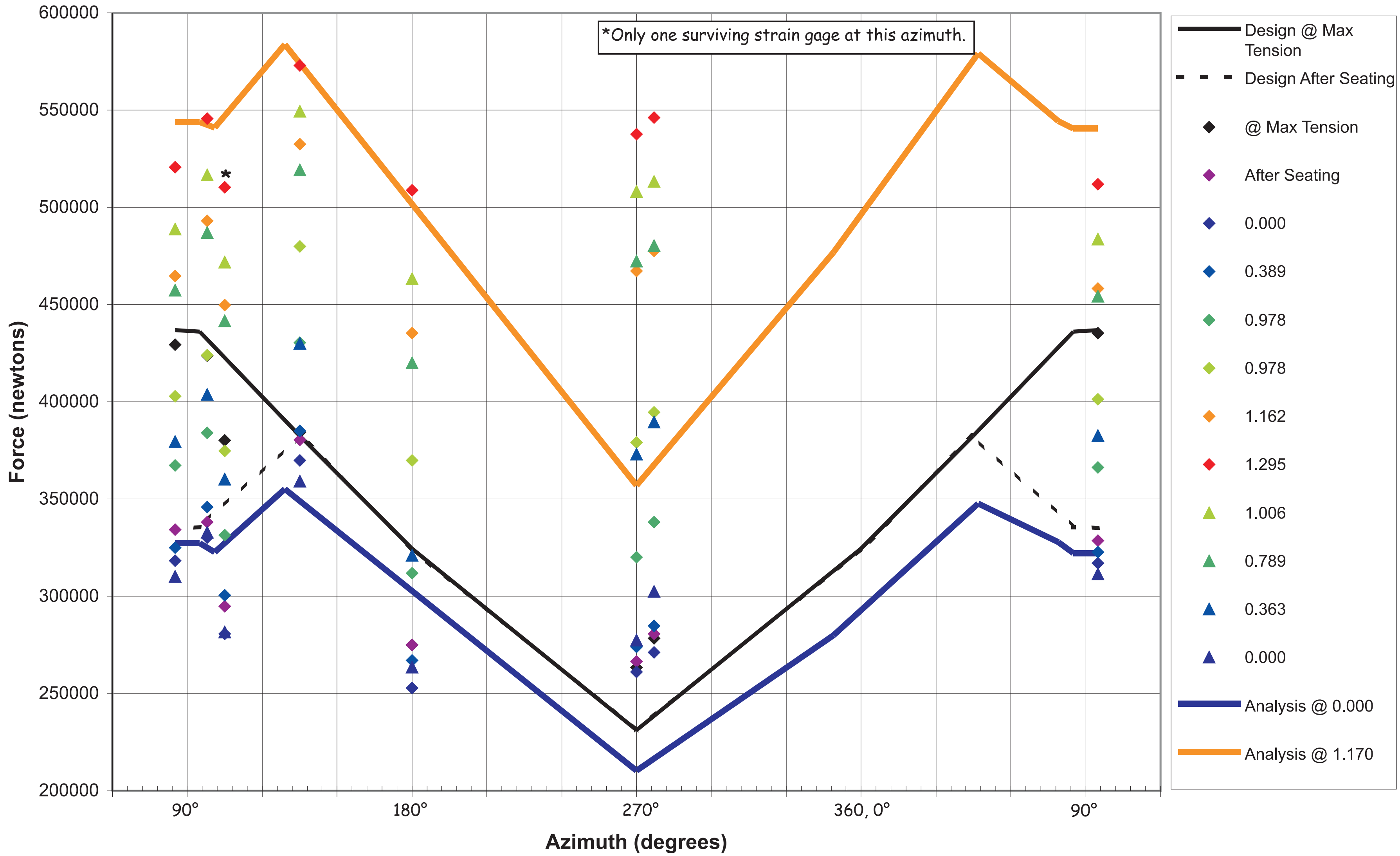

Figure 6-6. H68 Tendon Force Comparisons to Pretest

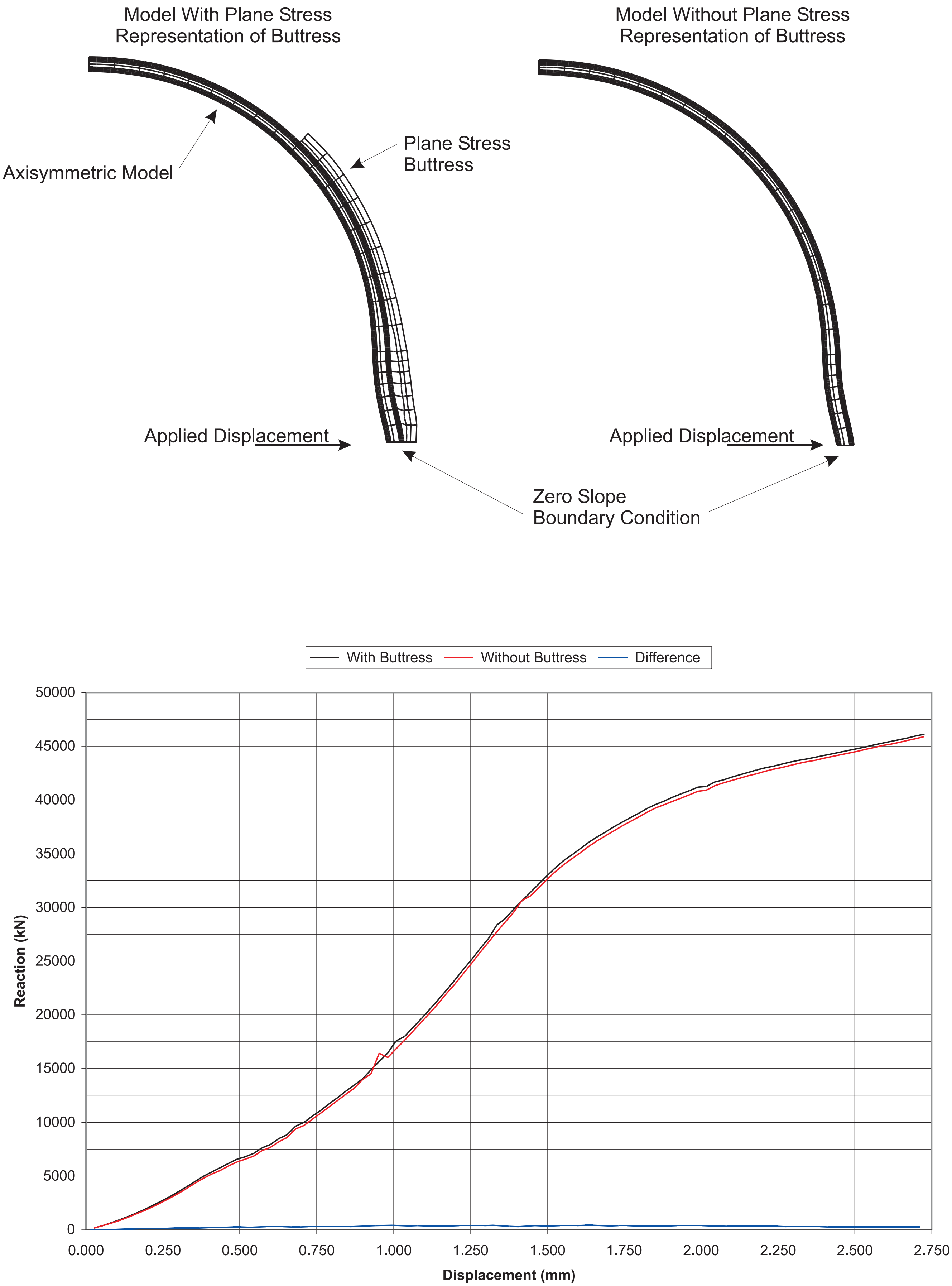

Figure 6-7. Definition of Upper 3DCM Buttress Radial Spring Properties by Axisymmetric Analysis

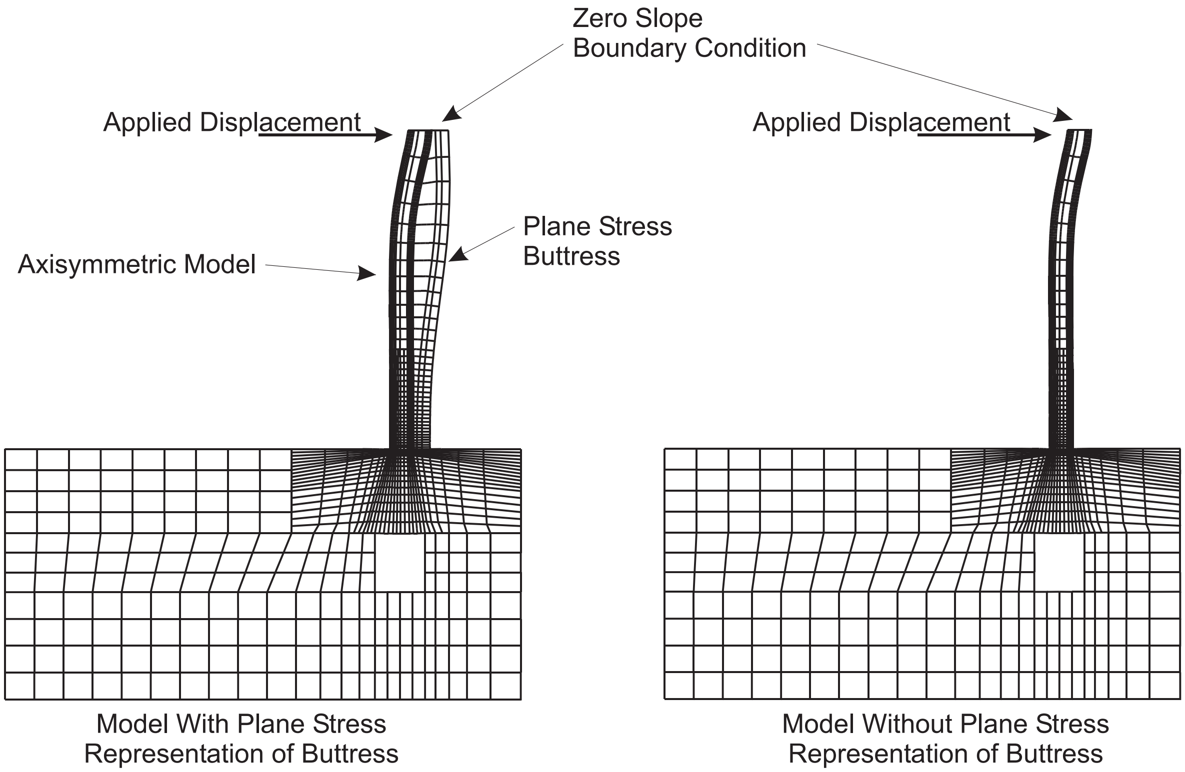

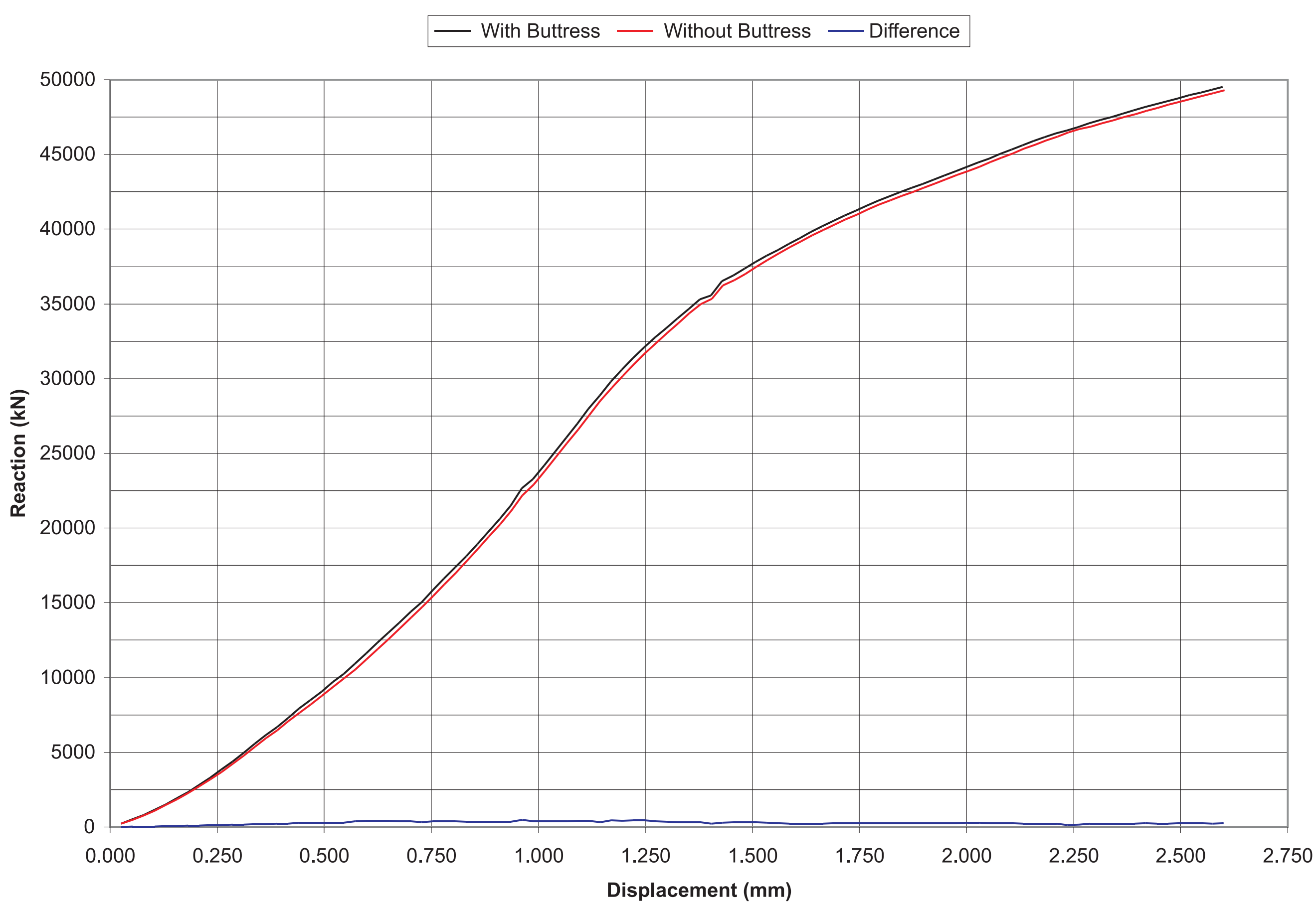

Figure 6-8. Definition of Lower 3DCM Buttress Radial Spring Properties by Axisymmetric Analysis

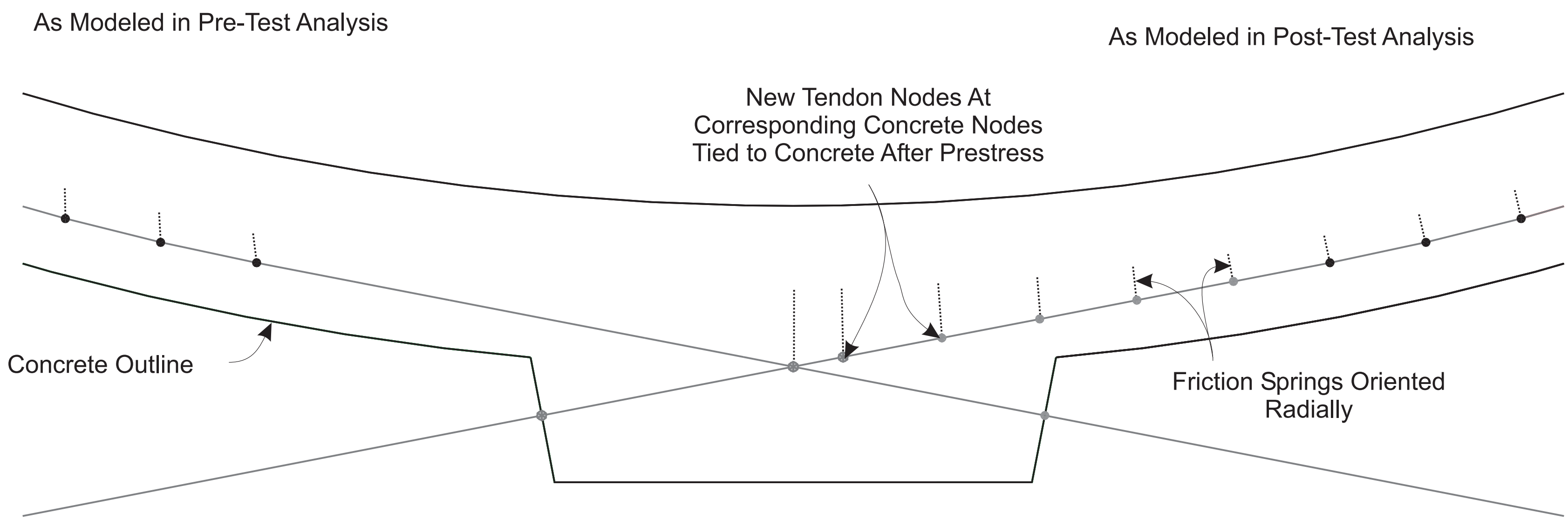

Figure 6-9. Addition of Tendon Ties in Straight Run of Tendons Between Tangent Points and Anchorages

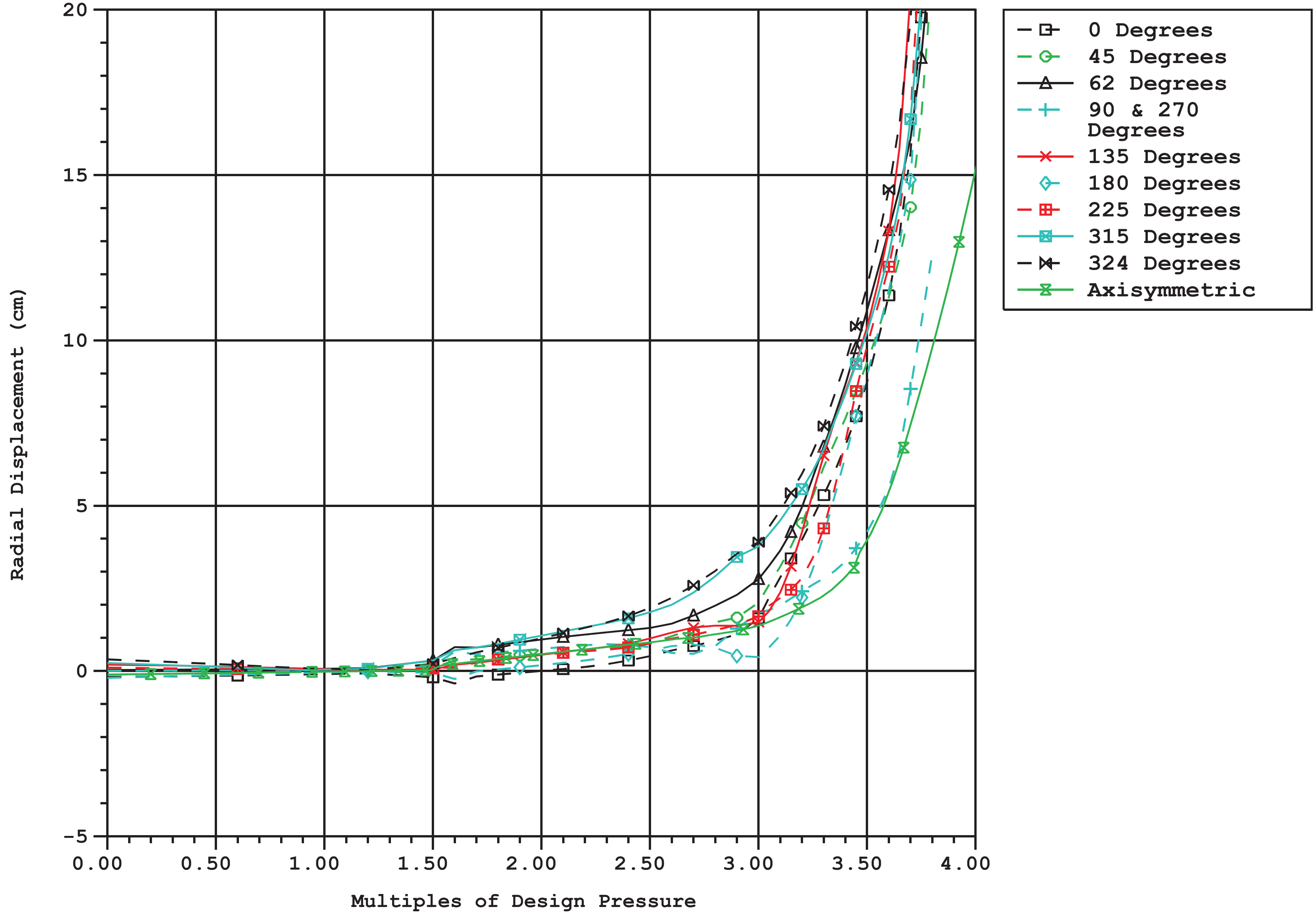

Figure 6-10. Radial Displacement at Elevation 4.7M, 3DCM Run 4 Compared to Axisymmetric

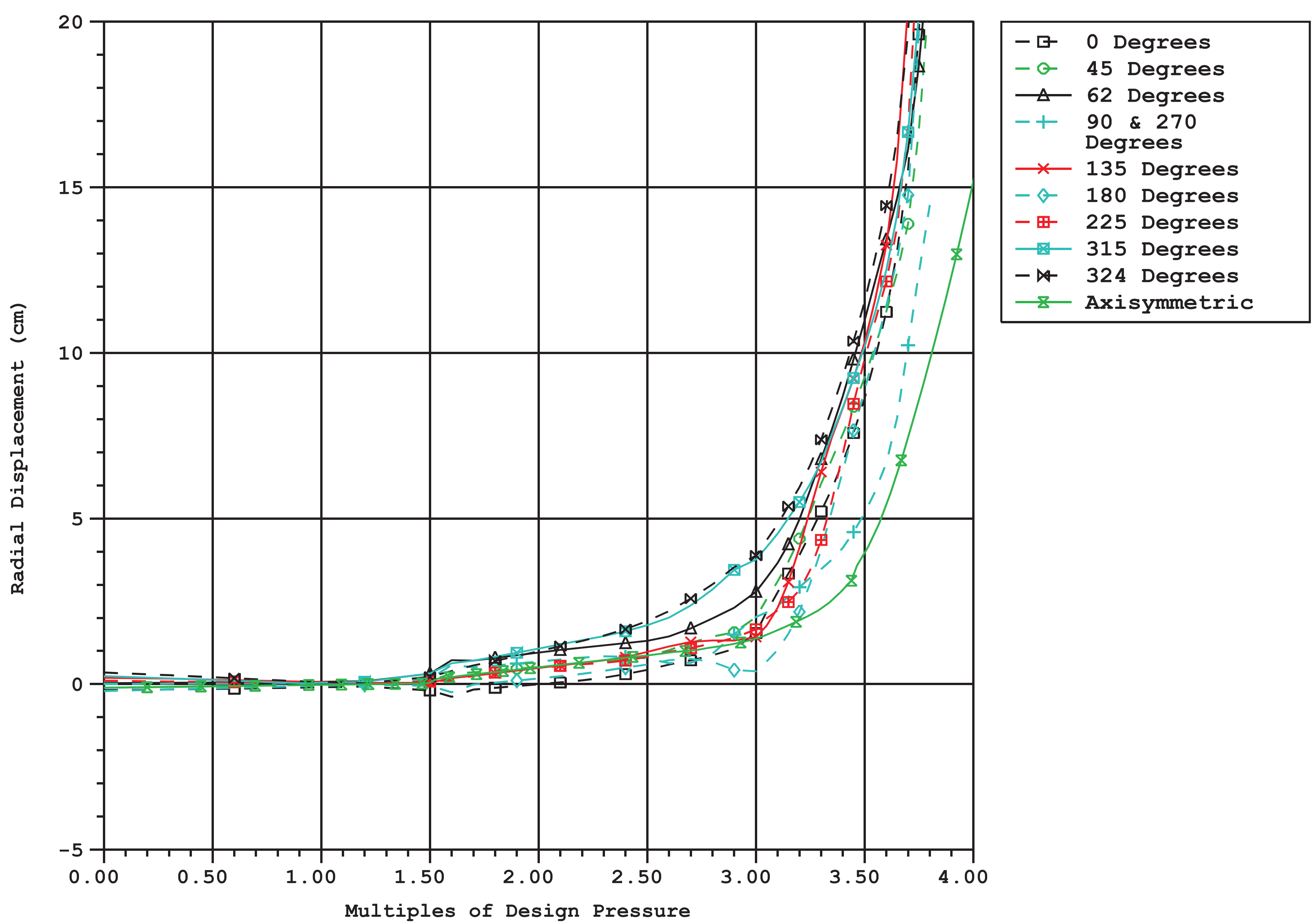

Figure 6-11. Radial Displacement at Elevation 4.7M, 3DCM Run 5 Compared to Axisymmetric

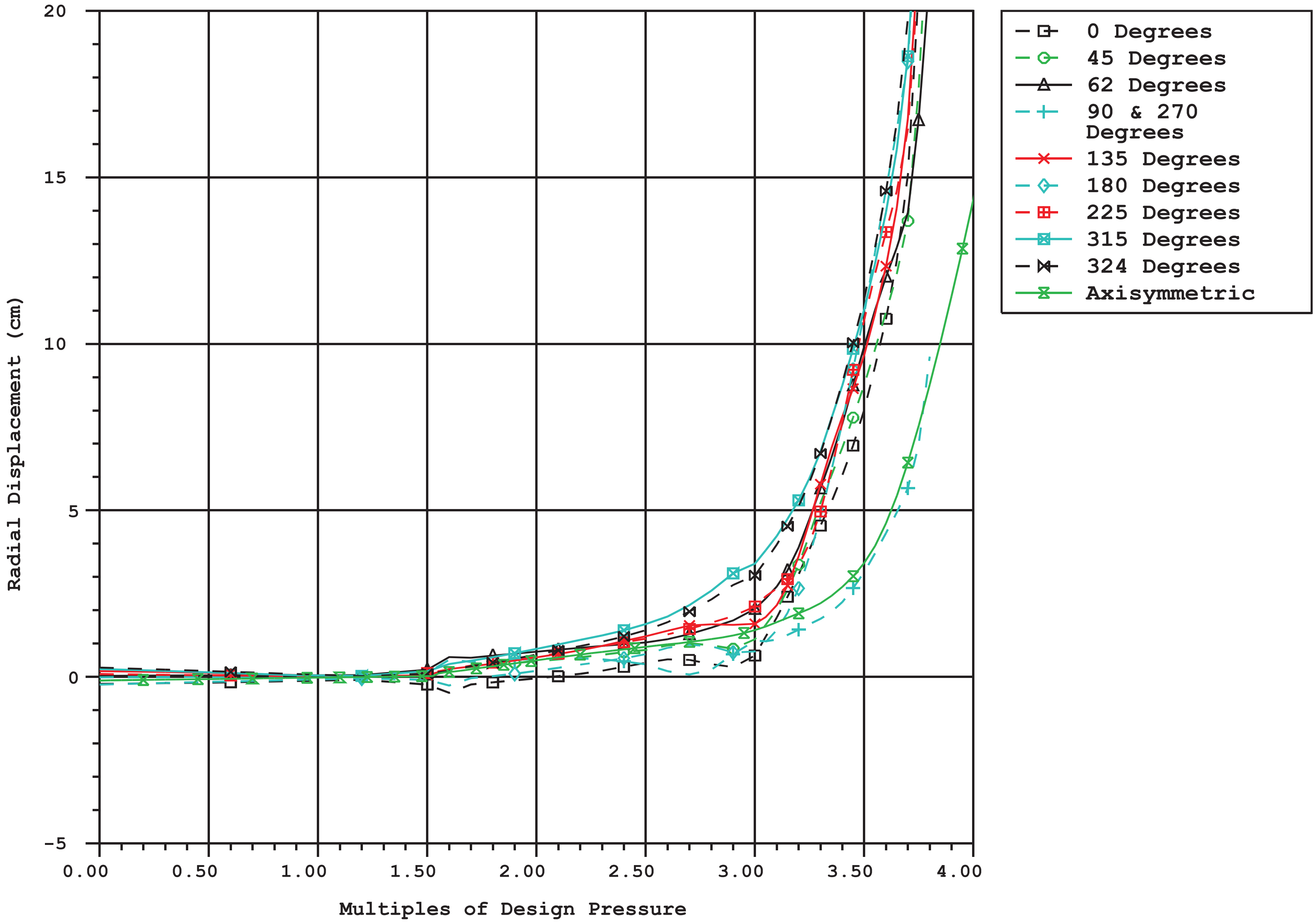

Figure 6-12. Radial Displacement at Elevation 8.9M, 3DCM Run 4 Compared to Axisymmetric

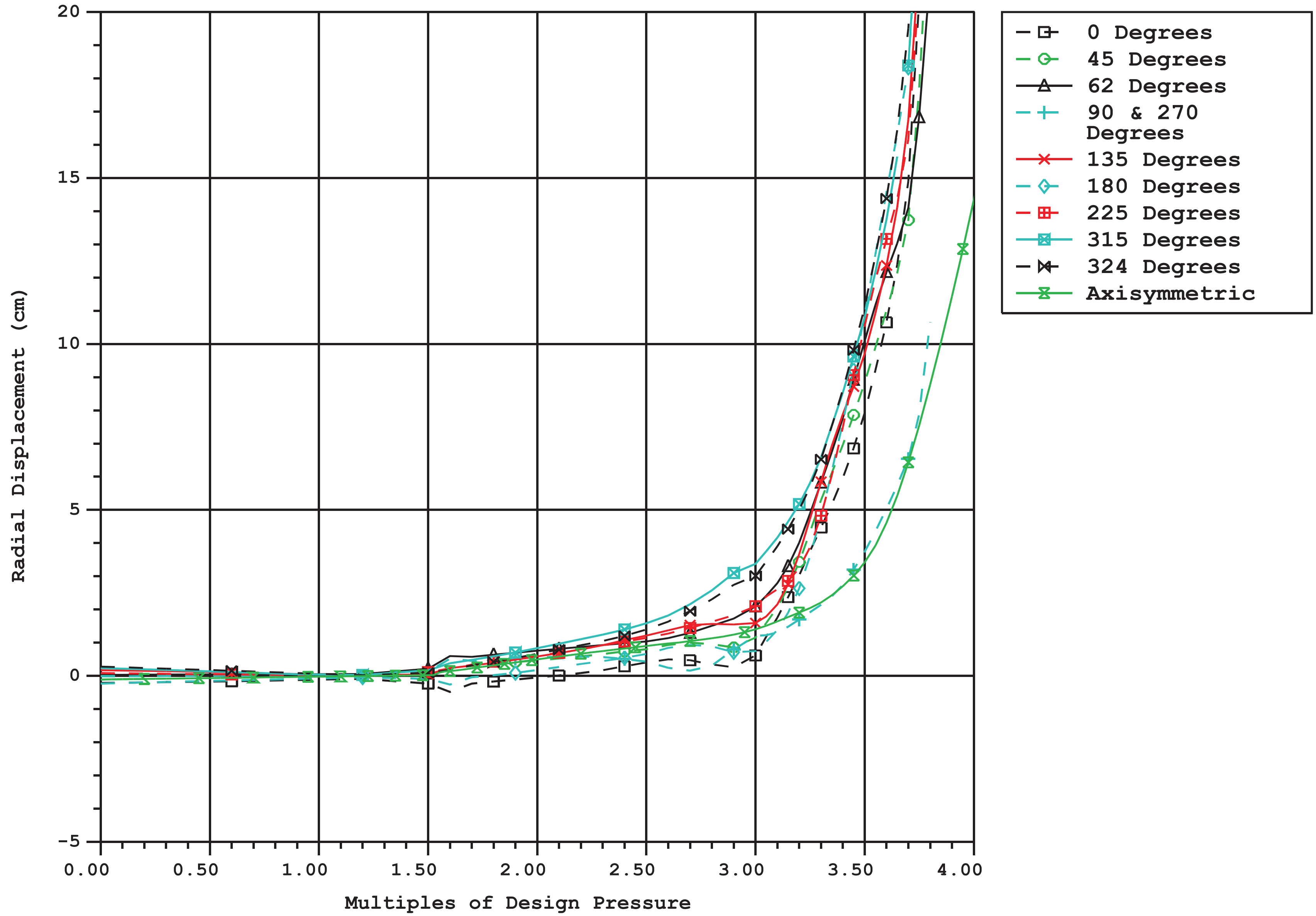

Figure 6-13. Radial Displacement at Elevation 8.9M, 3DCM Run 5 Compared to Axisymmetric

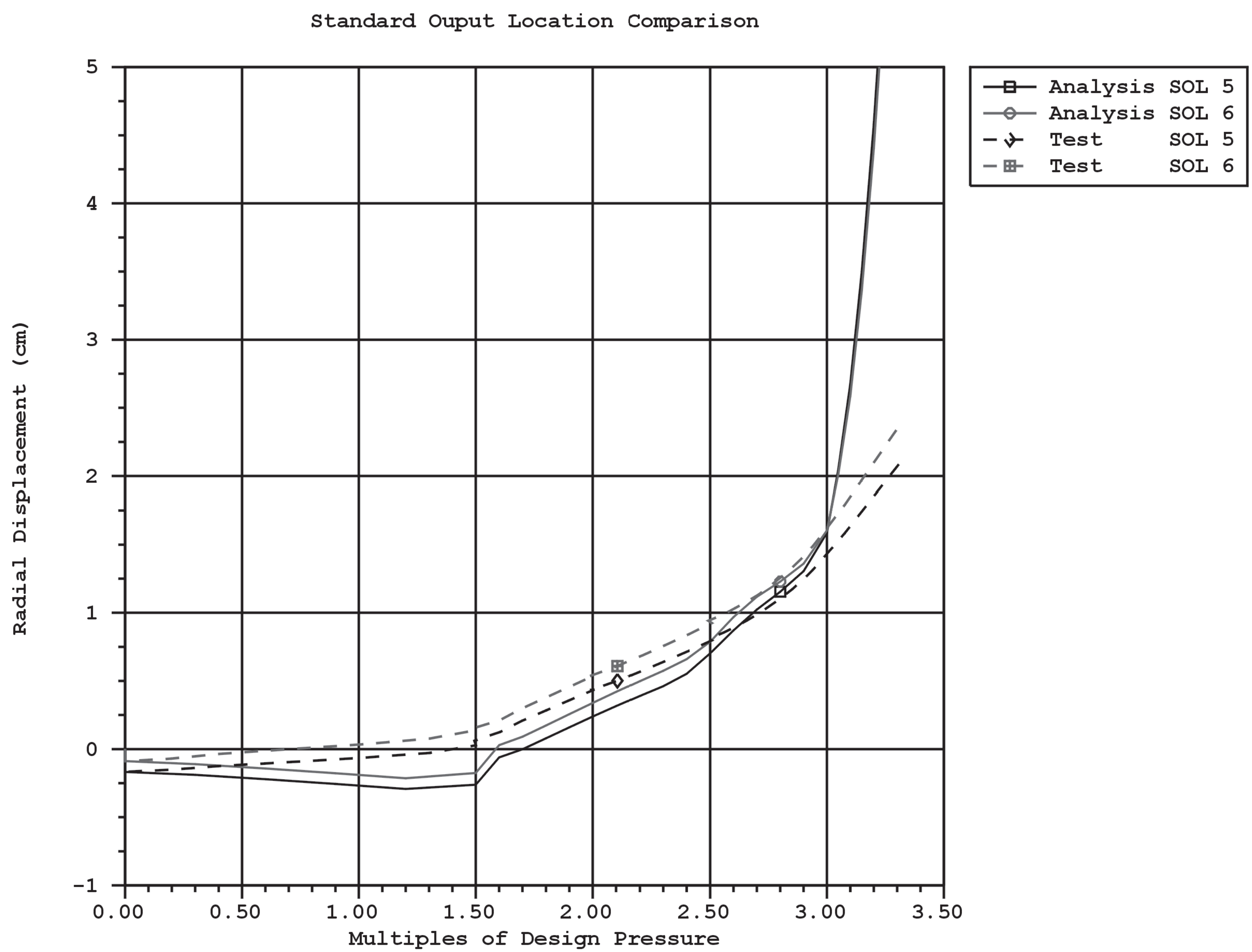

Figure 6-14. Comparison of Run 4 SOL 5 and 6 (Radial Displacement at 135 Degrees, 4.7M, 6.2M)

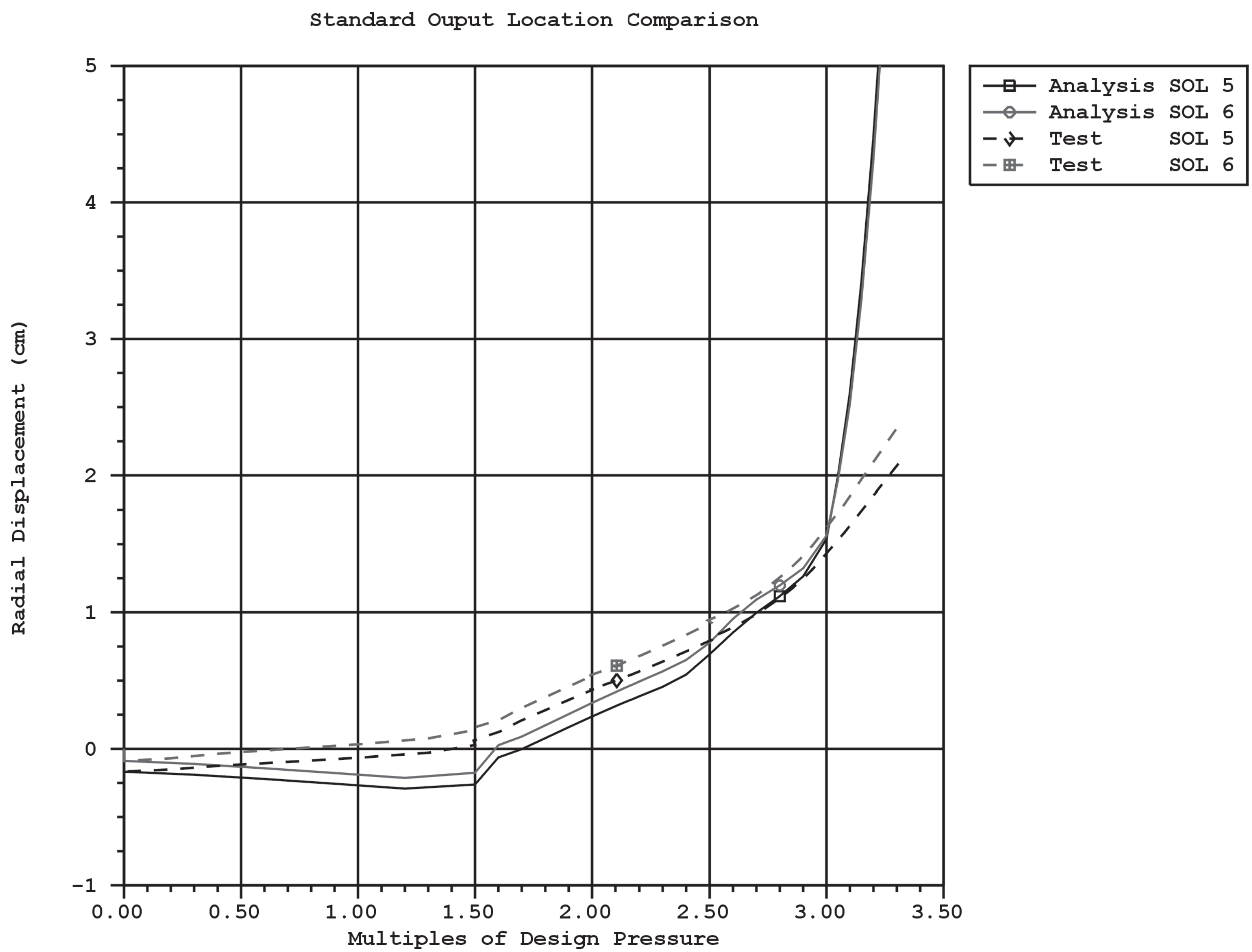

Figure 6-15. Comparison of Run 5 SOL 5 and 6 (Radial Displacement at 135 Degrees, 4.7M, 6.2M)

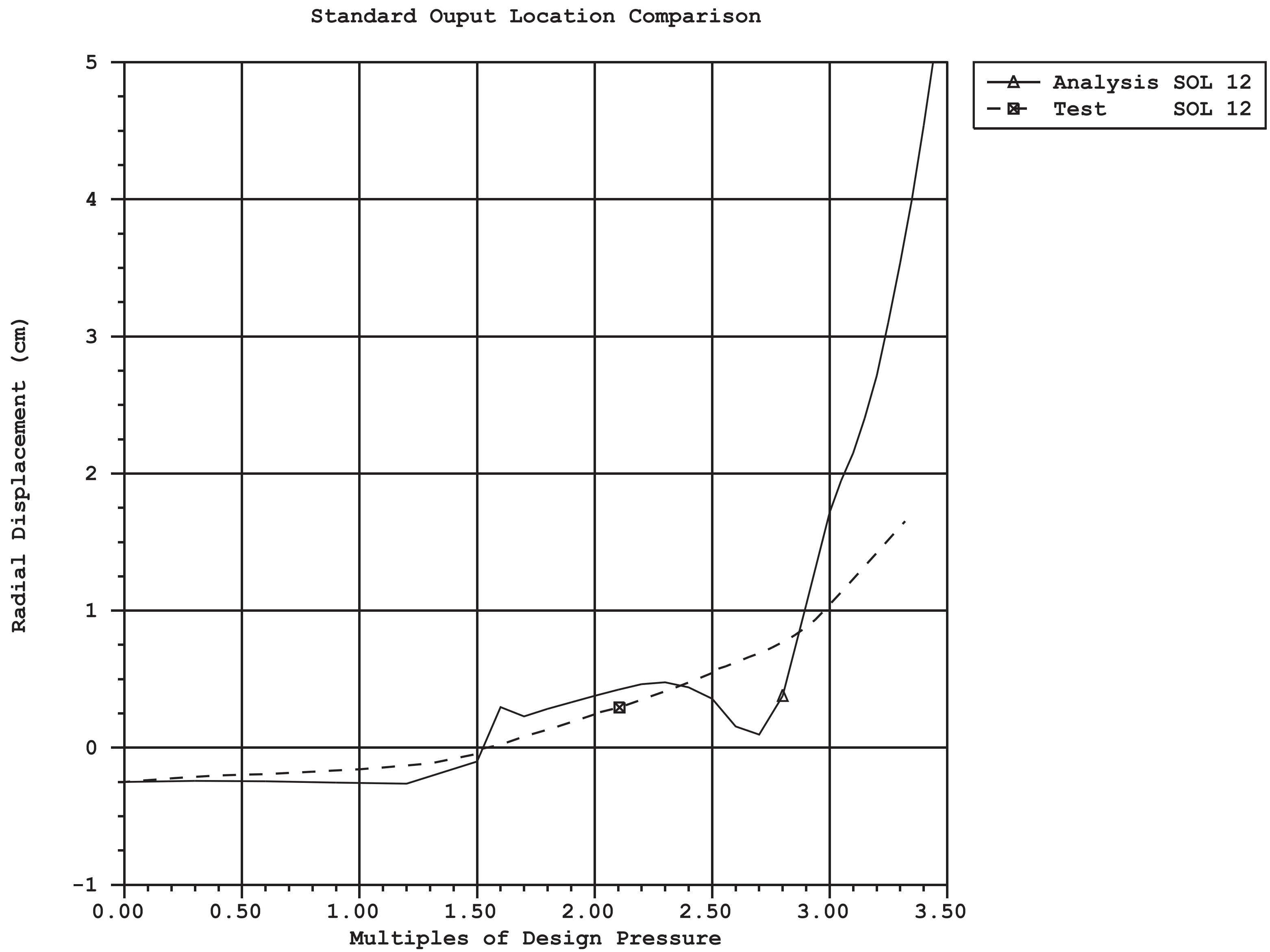

Figure 6-16. Comparison of Run 4 SOL 12 (Radial Displacement at 90 Degrees Butress, 6.2M)

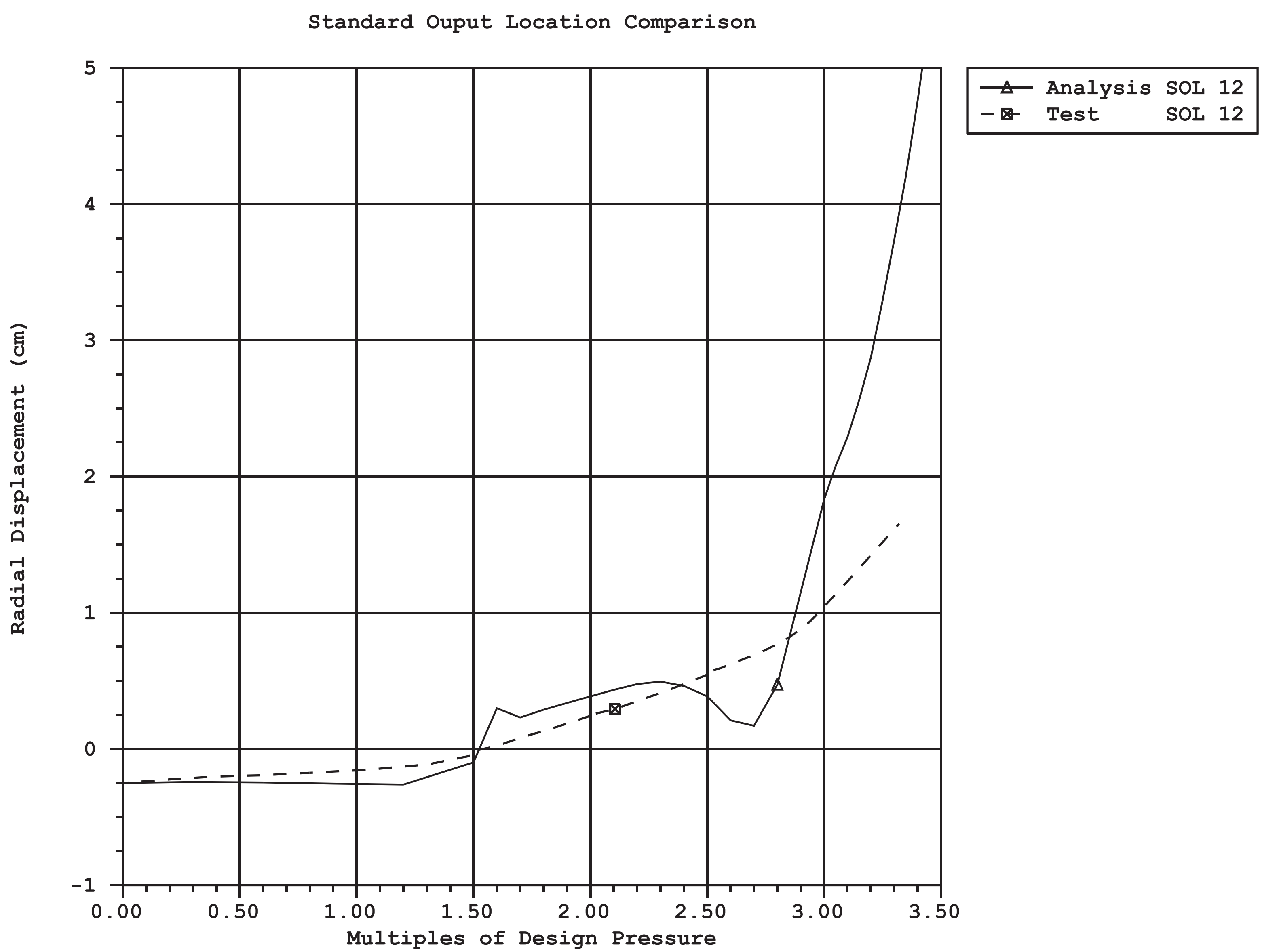

Figure 6-17. Comparison of Run 5 SOL 12 (Radial Displacement at 90 Degrees Butress, 6.2M)

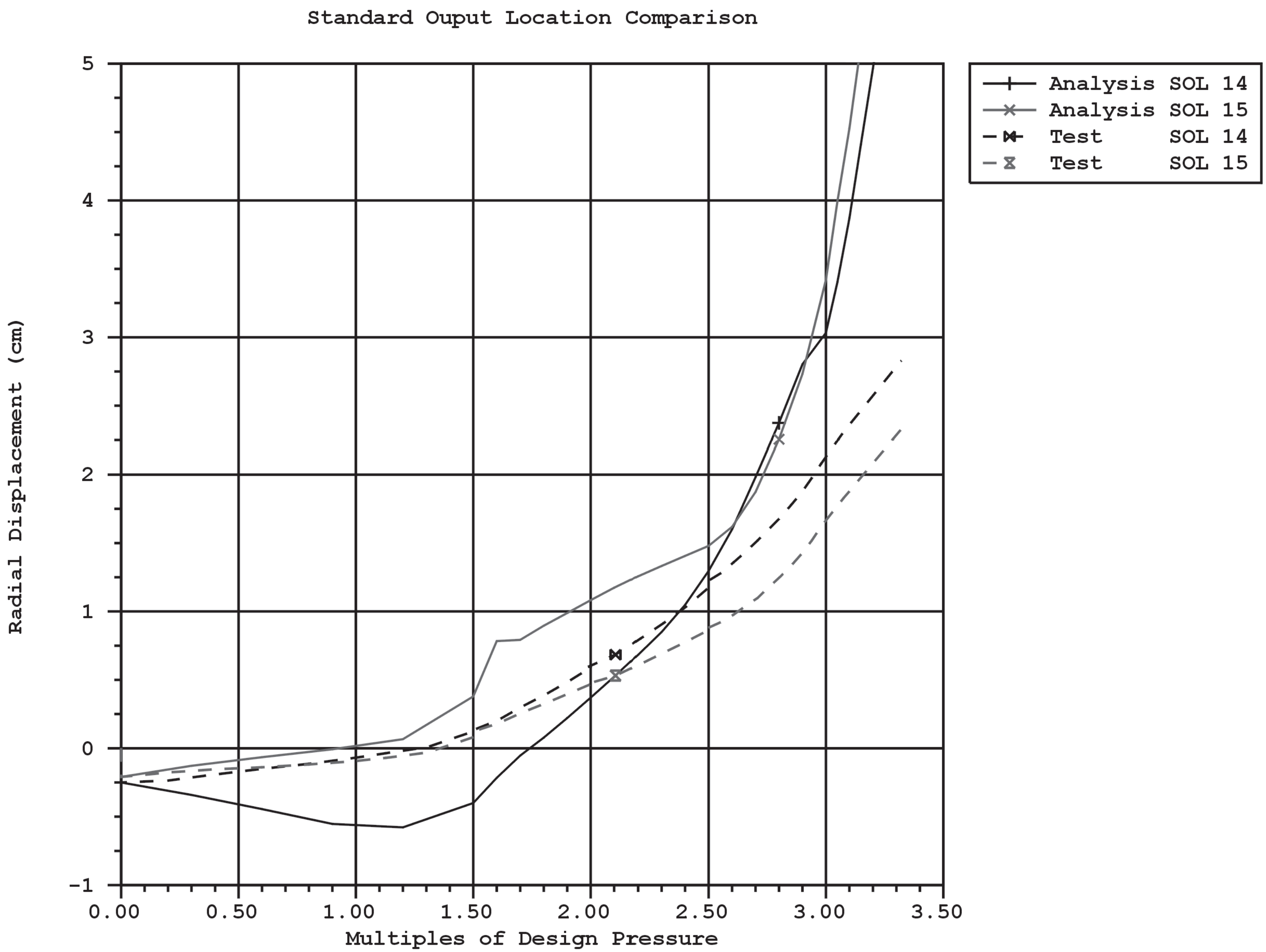

Figure 6-18. Comparison of Run 4 SOL 14 and 15 (Radial Displacement at E/H and A/L)

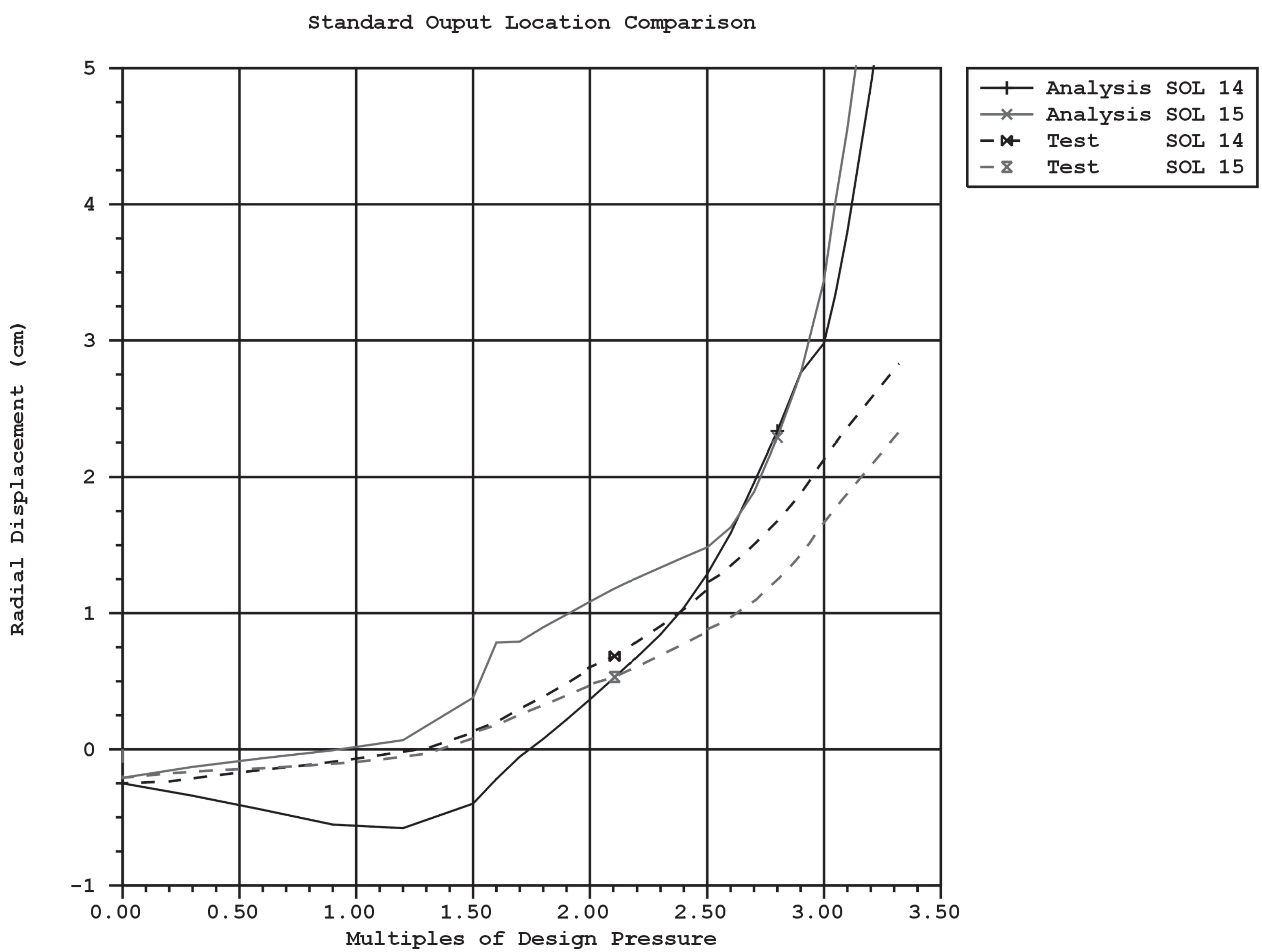

Figure 6-19. Comparison of Run 5 SOL 14 and 15 (Radial Displacement at E/H and A/L)

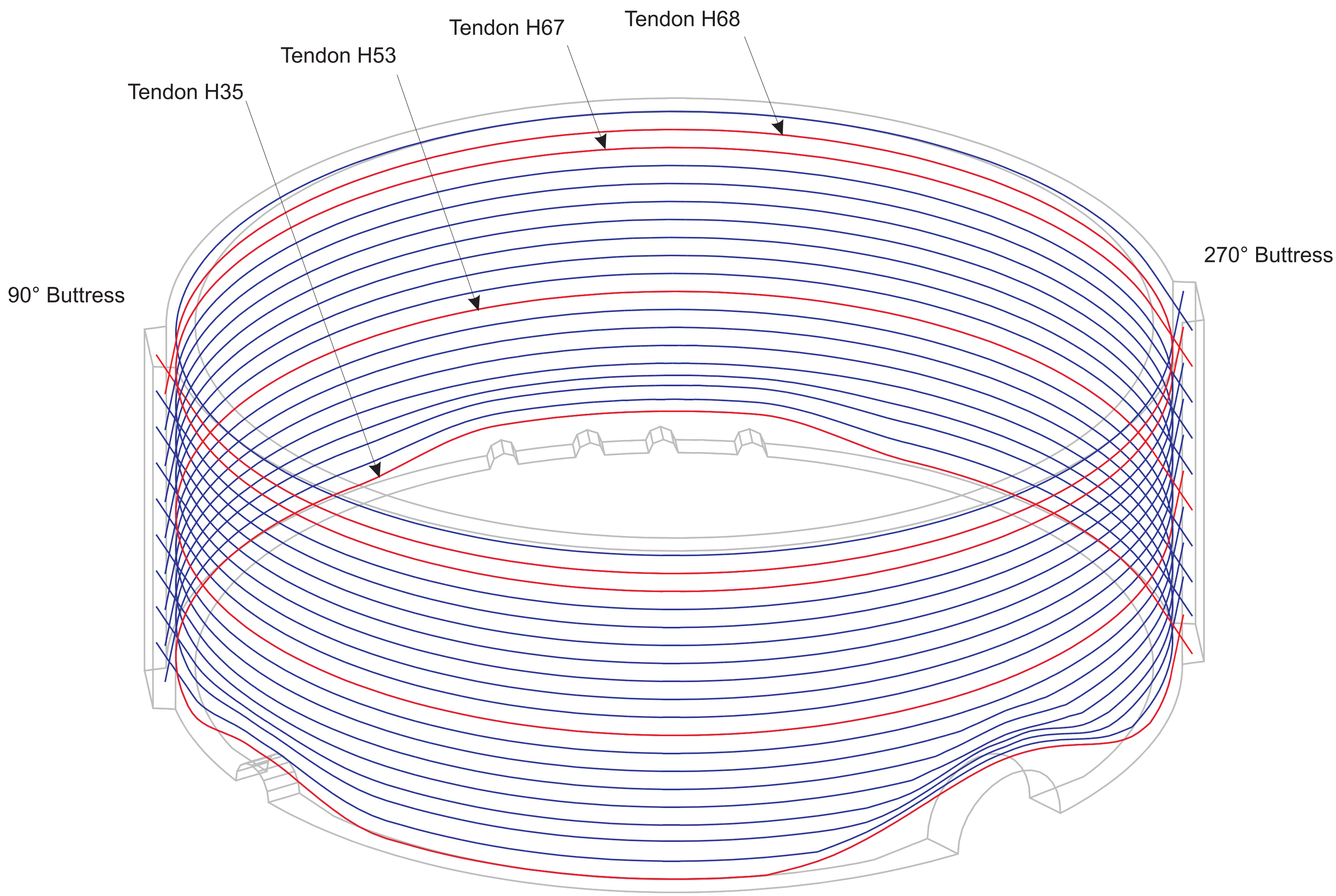

Figure 6-20. Location of Instrumented Tendons H35, H53, H67, and H68

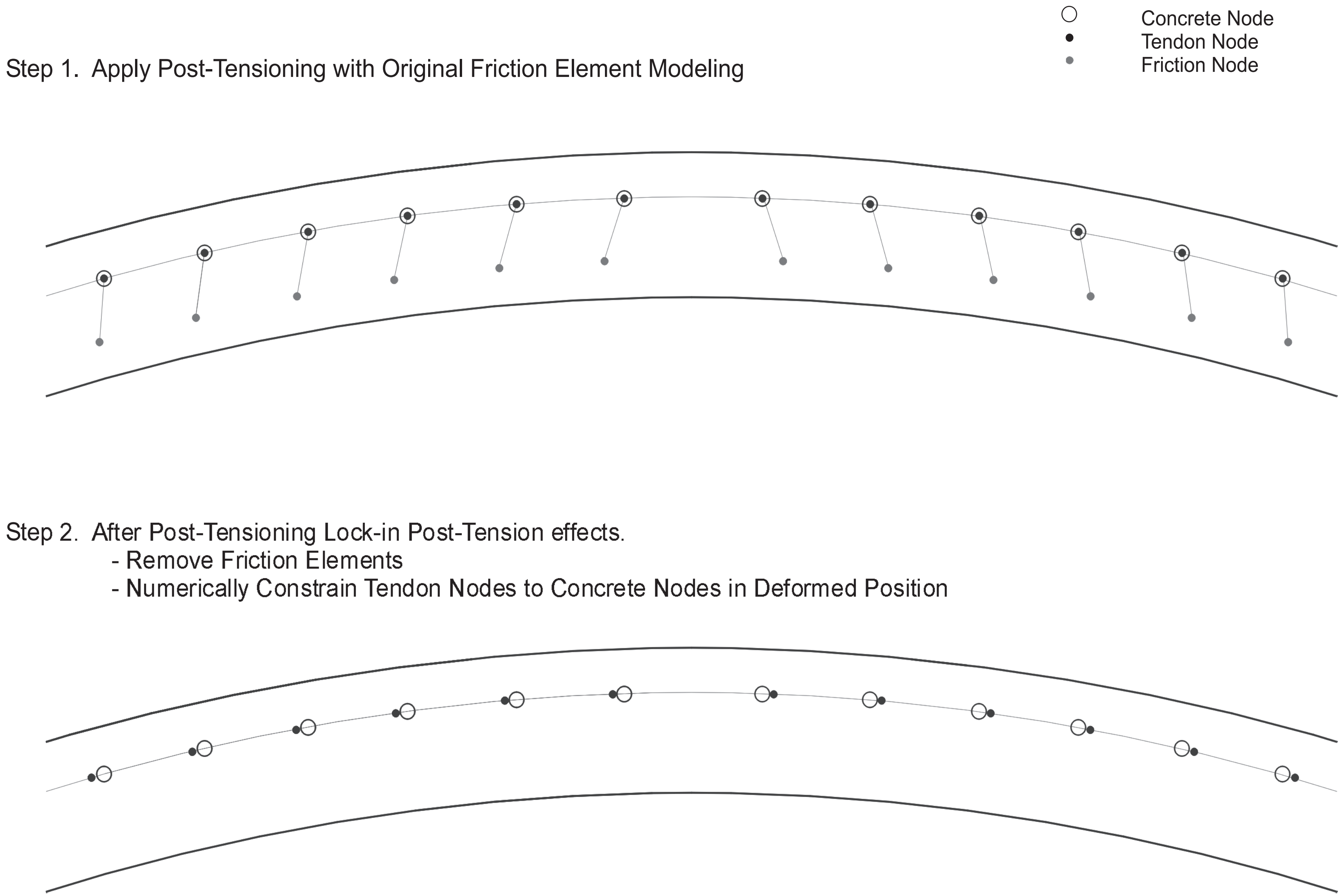

Figure 6-21. Tendon Friction Modeling Schematic for Run 6

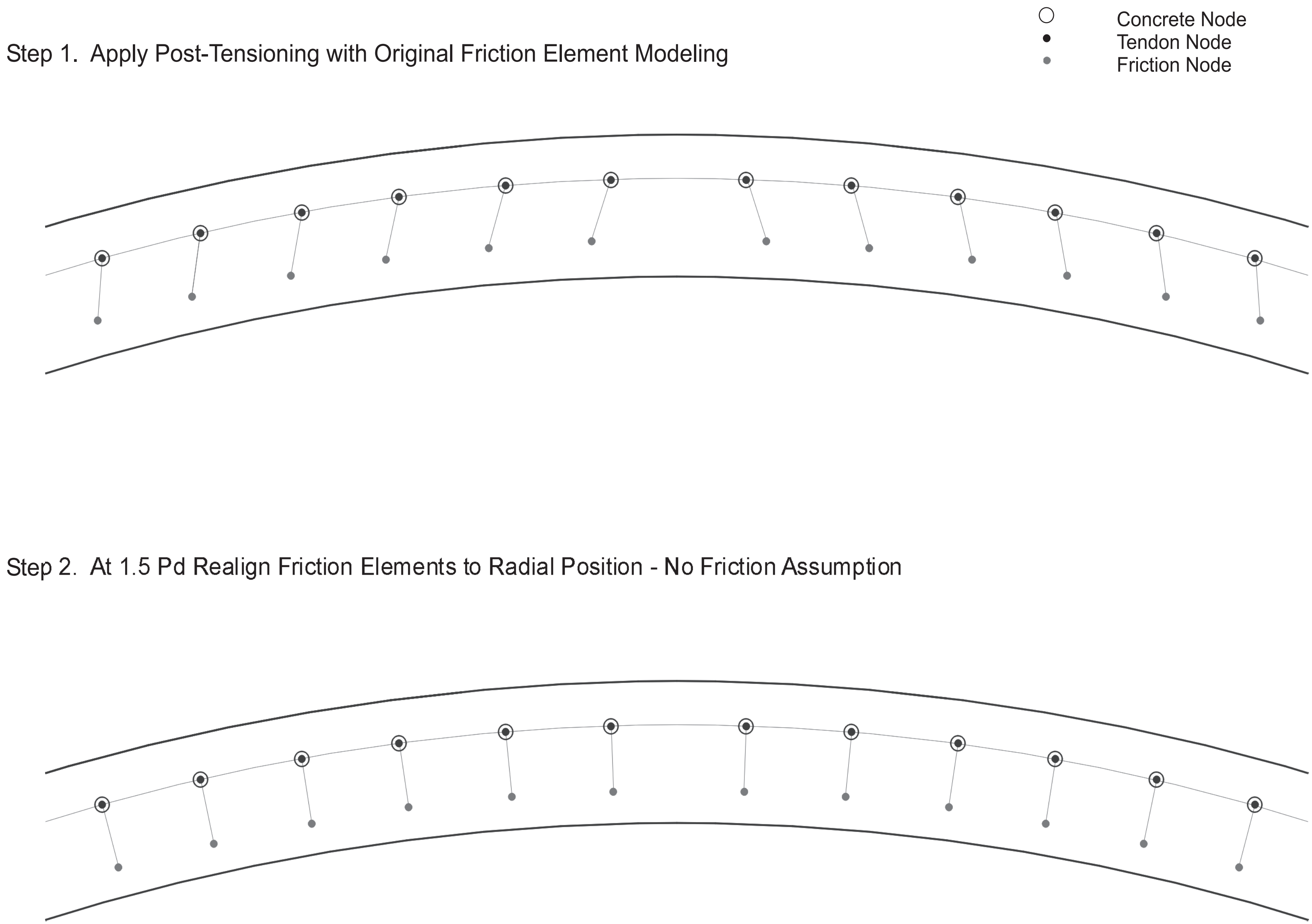

Figure 6-22. Tendon Friction Modeling Schematic for Run 7

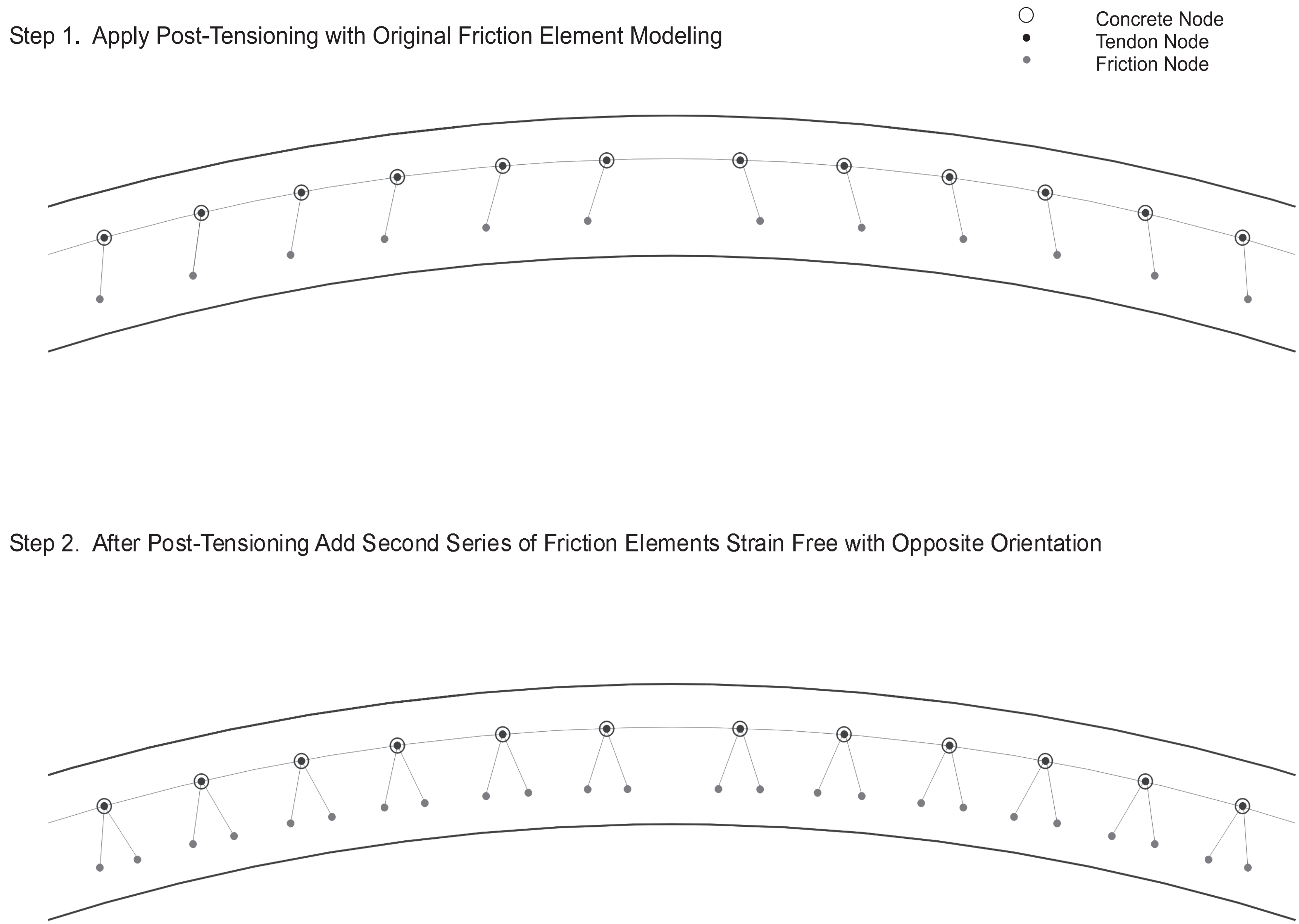

Figure 6-23. Tendon Friction Modeling Schematic for Run 9

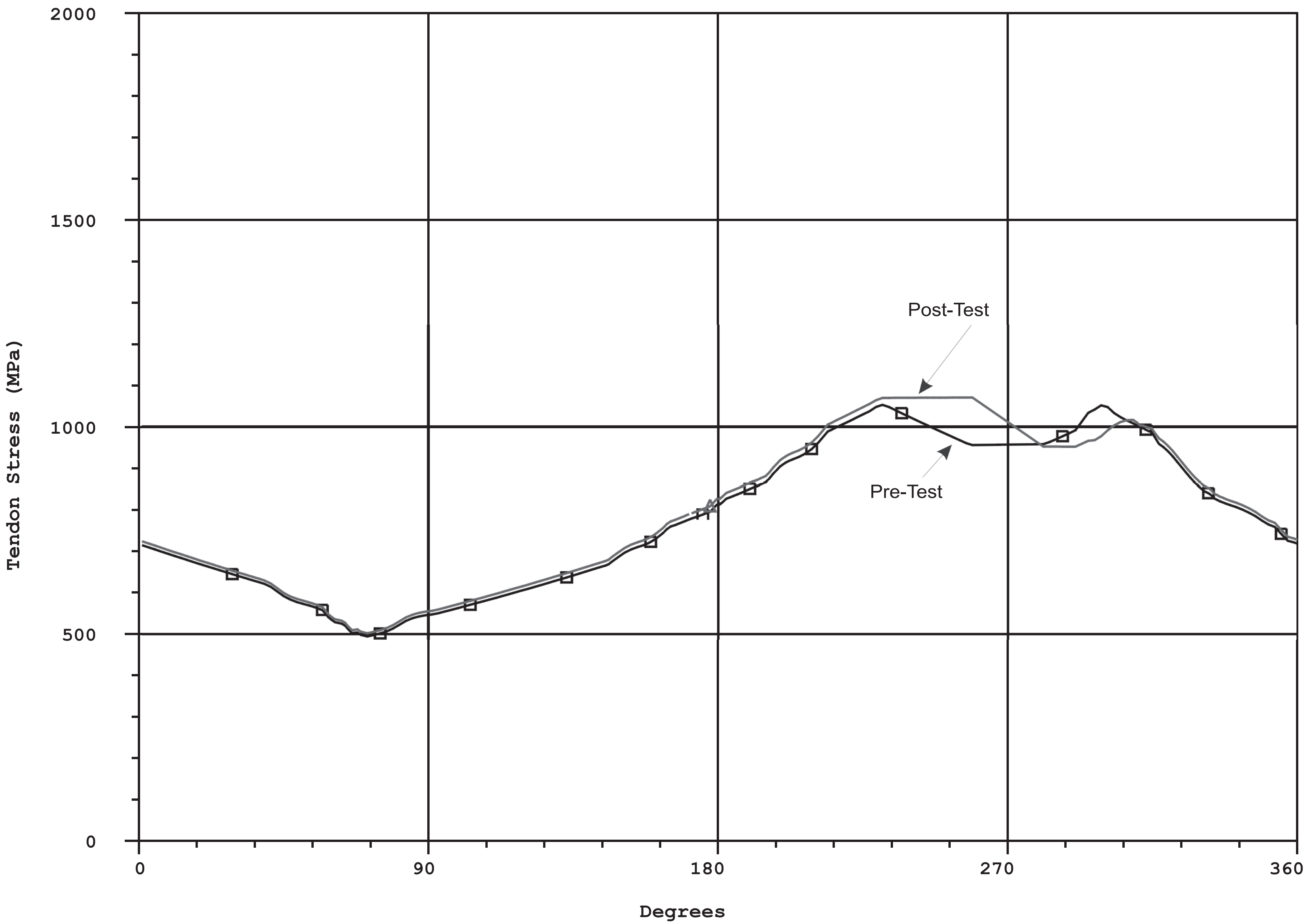

Figure 6-24. Changes to Anchor Set Prestress for Posttest 3DCM Study, Tendon H35

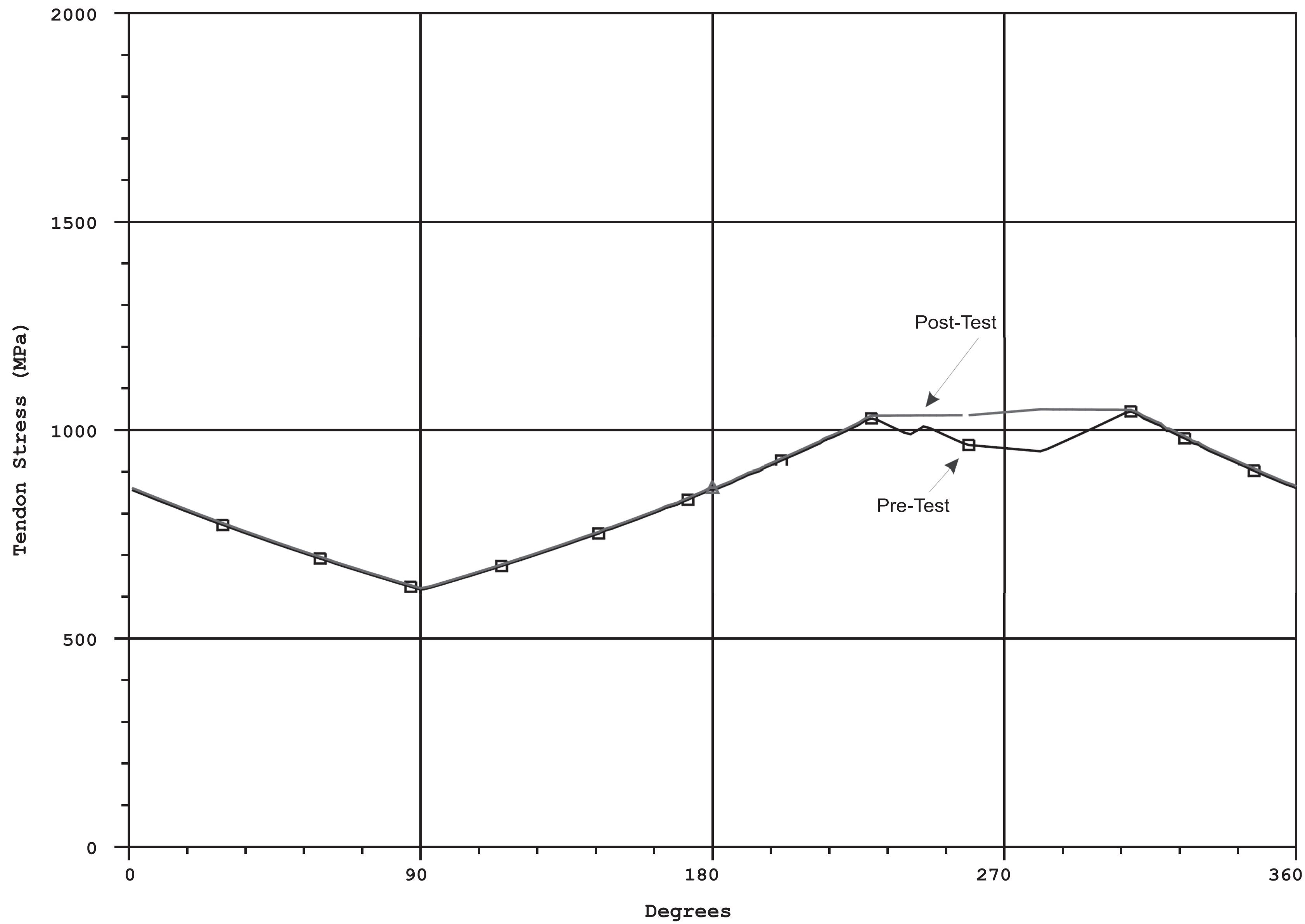

Figure 6-25. Changes to Anchor Set Prestress for Posttest 3DCM Study, Tendon H53

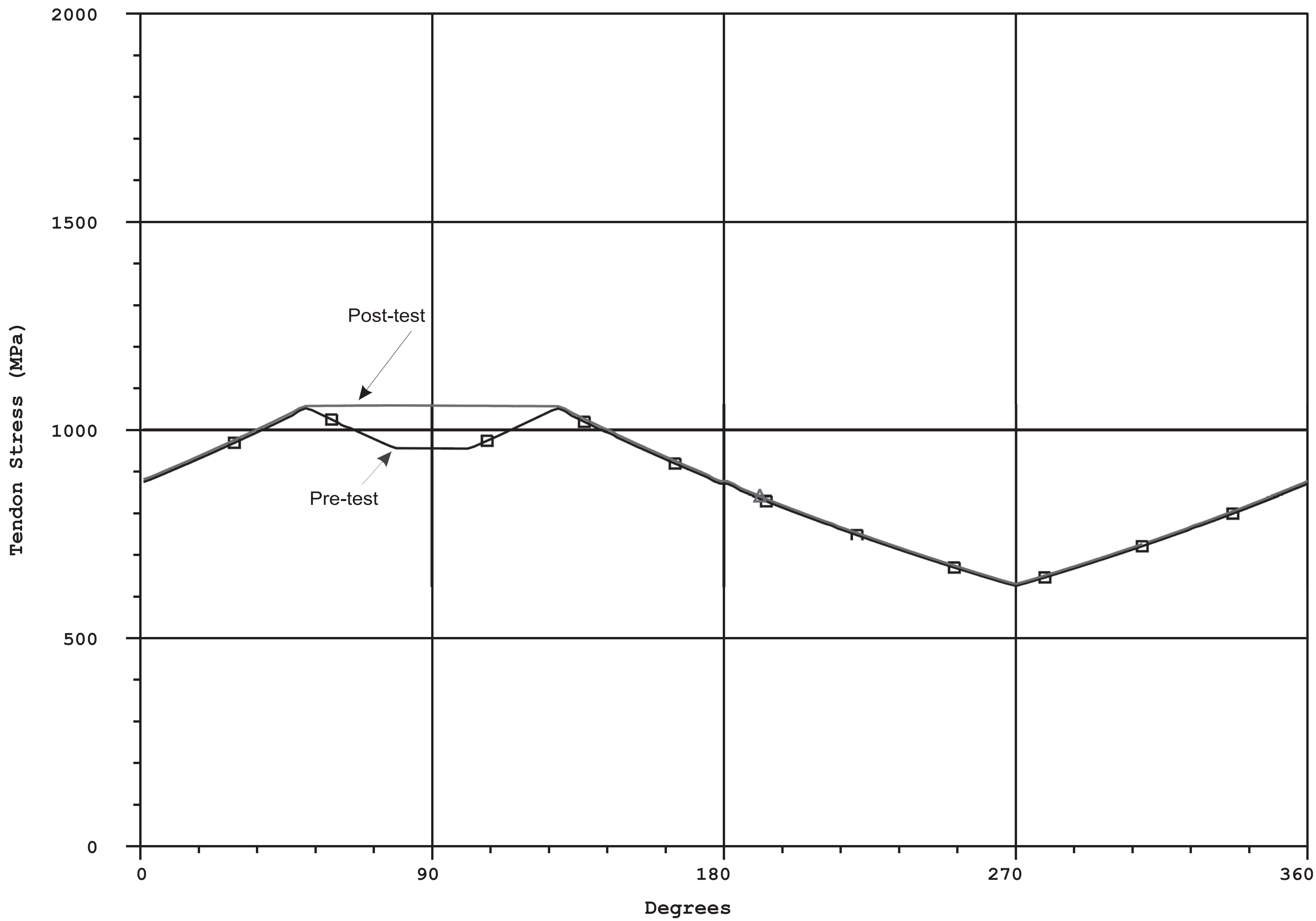

Figure 6-26. Changes to Anchor Set Prestress for Posttest 3DCM Study, Tendon H68

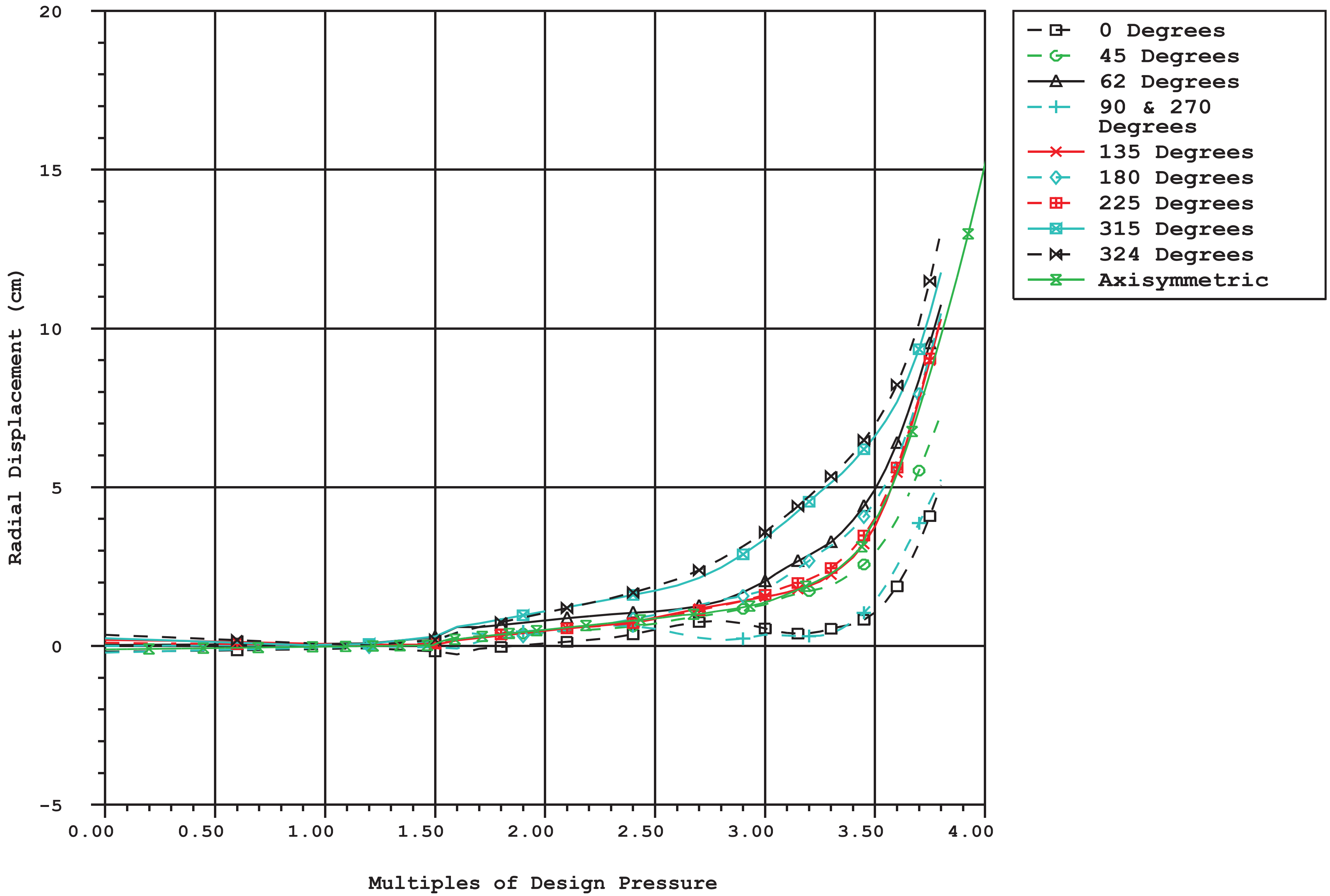

Figure 6-27. Radial Displacement at Elev. 4.7M, Posttest 3DCM Run 6 (Tendons "Bonded" After Prestressing) Compared to Axisymmetric

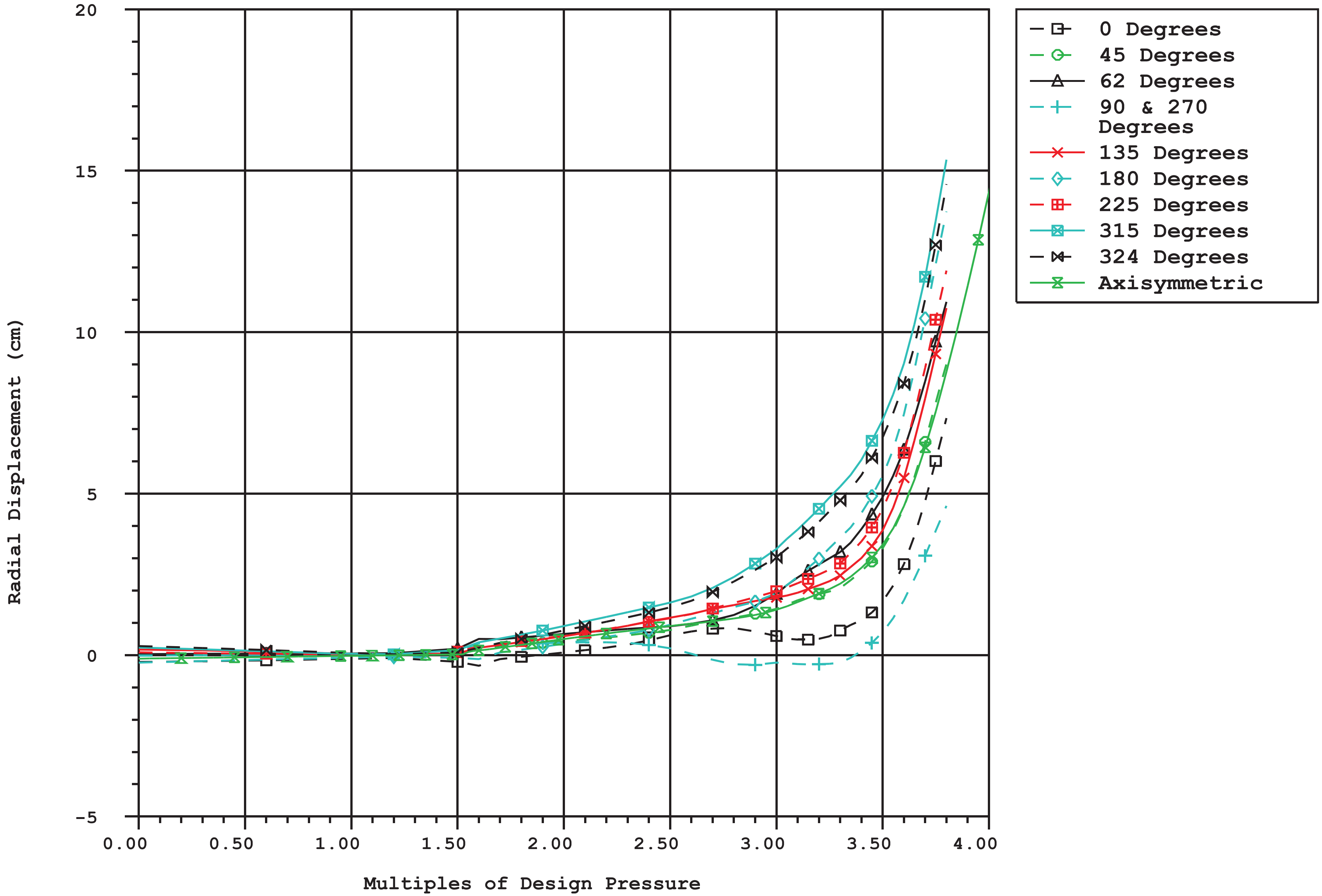

Figure 6-28. Radial Displacement at Elev. 6.2M, Posttest 3DCM Run 6 Compared to Axisymmetric

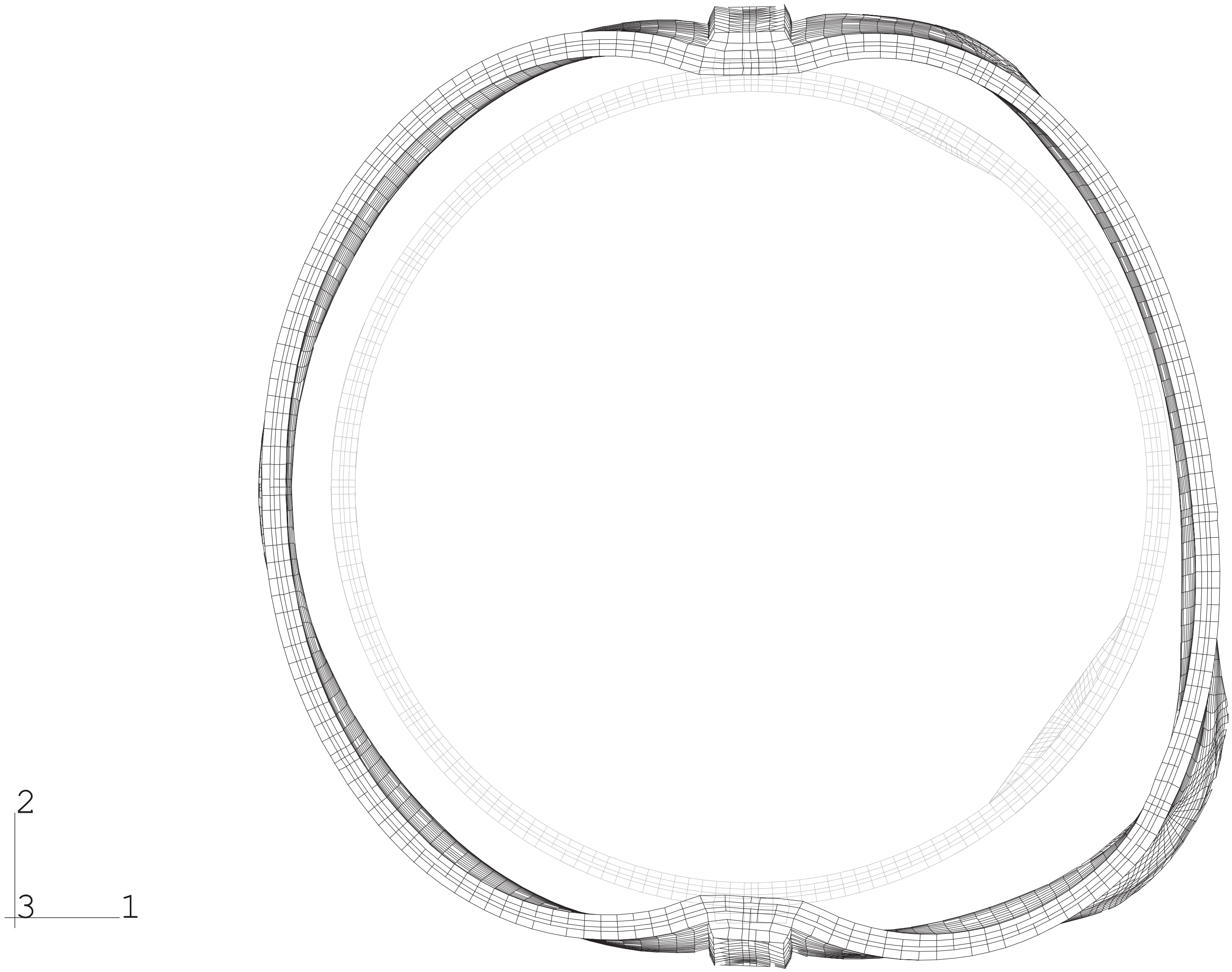

Figure 6-29. 3DCM Posttest Deformed Shape at P = 2.5Pd, Run 6 (mag. Factor = 100×)

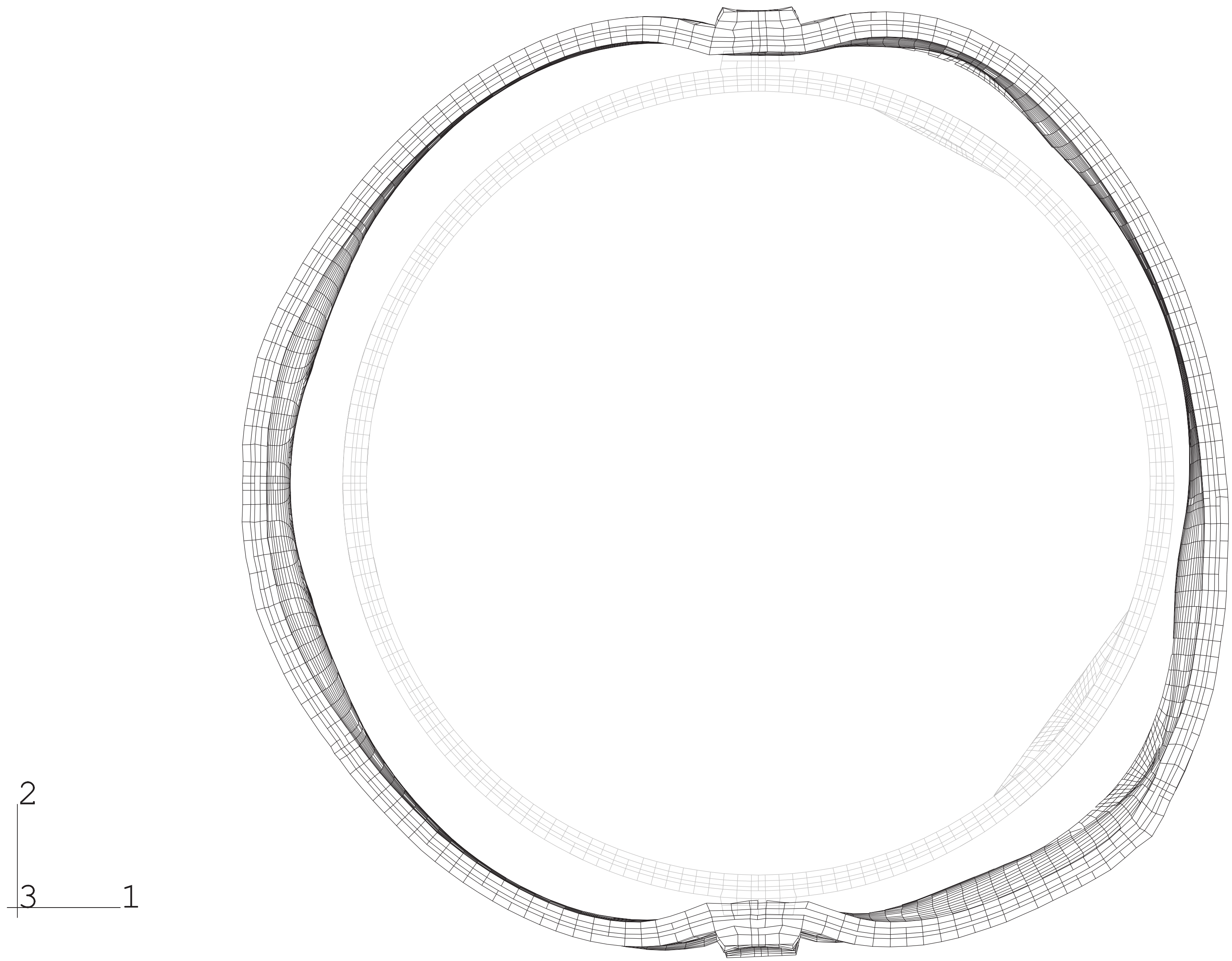

Figure 6-30. 3DCM Posttest Deformed Shape at P = 3.8Pd, Run 6 (mag. Factor = 10×)

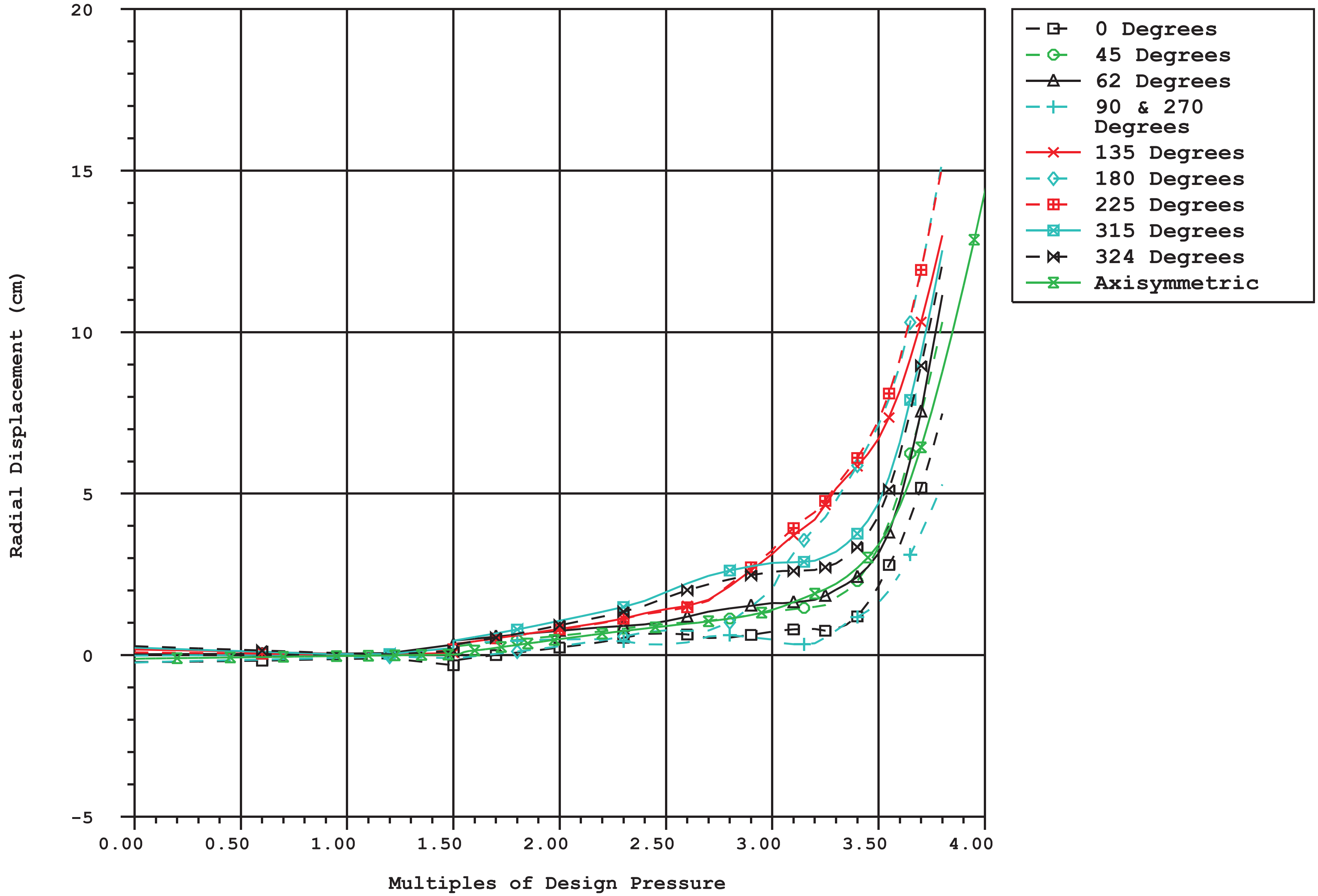

Figure 6-31. Radial Displacement at Elev. 6.2M, Posttest 3DCM Run 7 (No Friction After Prestress is Overcome) Compared to Axisymmetric

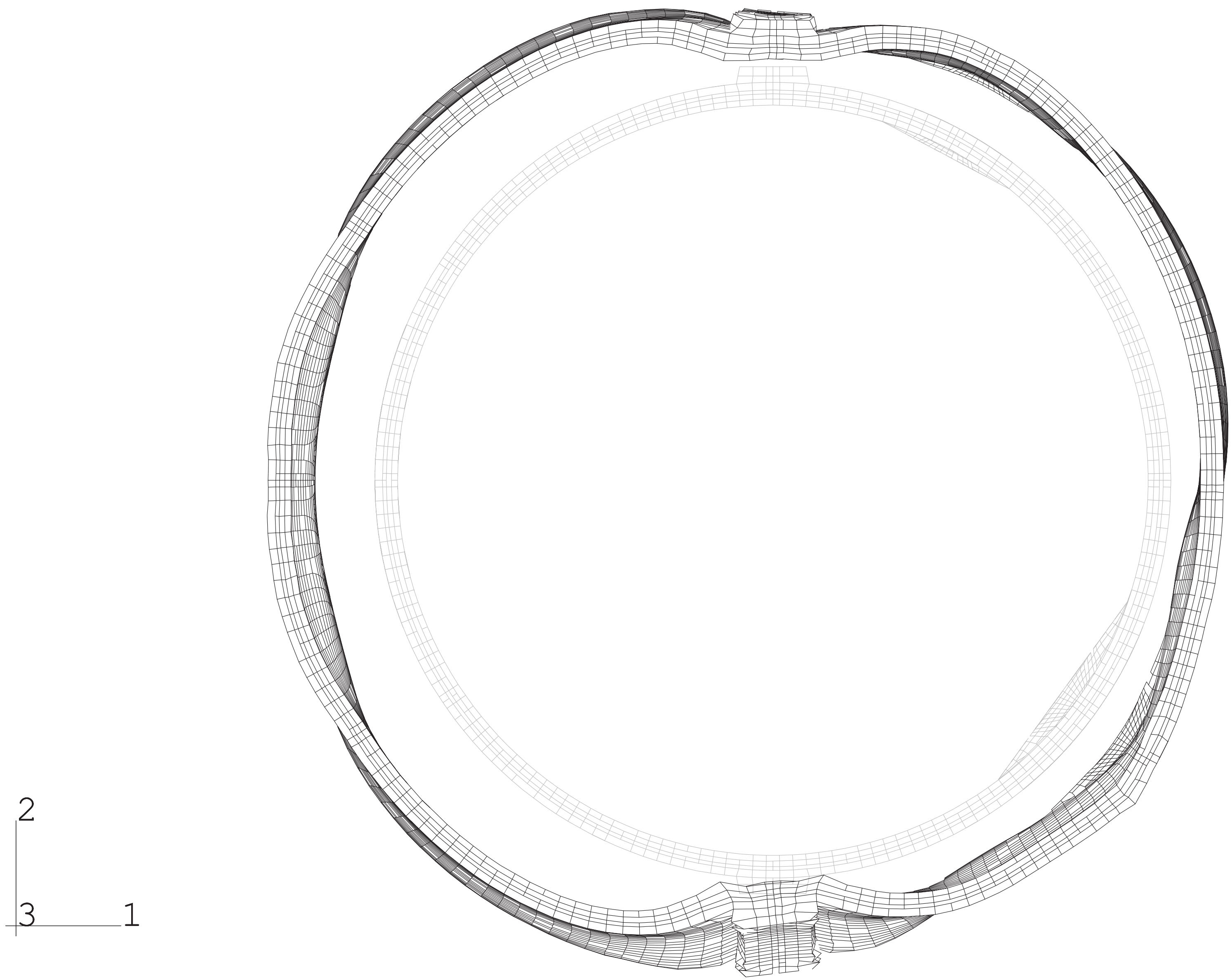

Figure 6-32. 3DCM Posttest Deformed Shape at P = 2.0 Pd, Run 7 (mag. Factor = 100×)

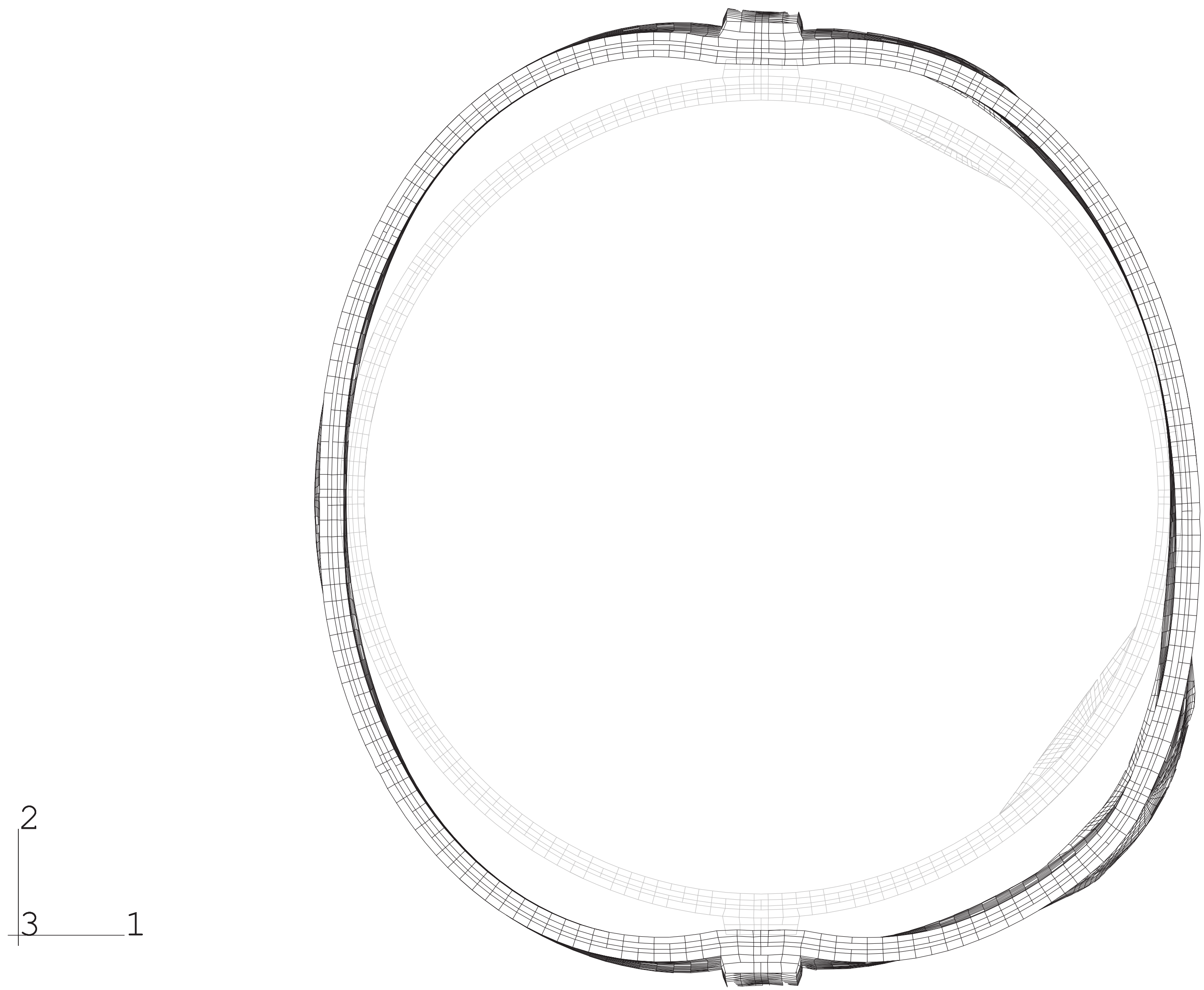

Figure 6-33. 3DCM Posttest Deformed Shape at P = 3.8 Pd, Run 7 (mag. Factor = 10×)

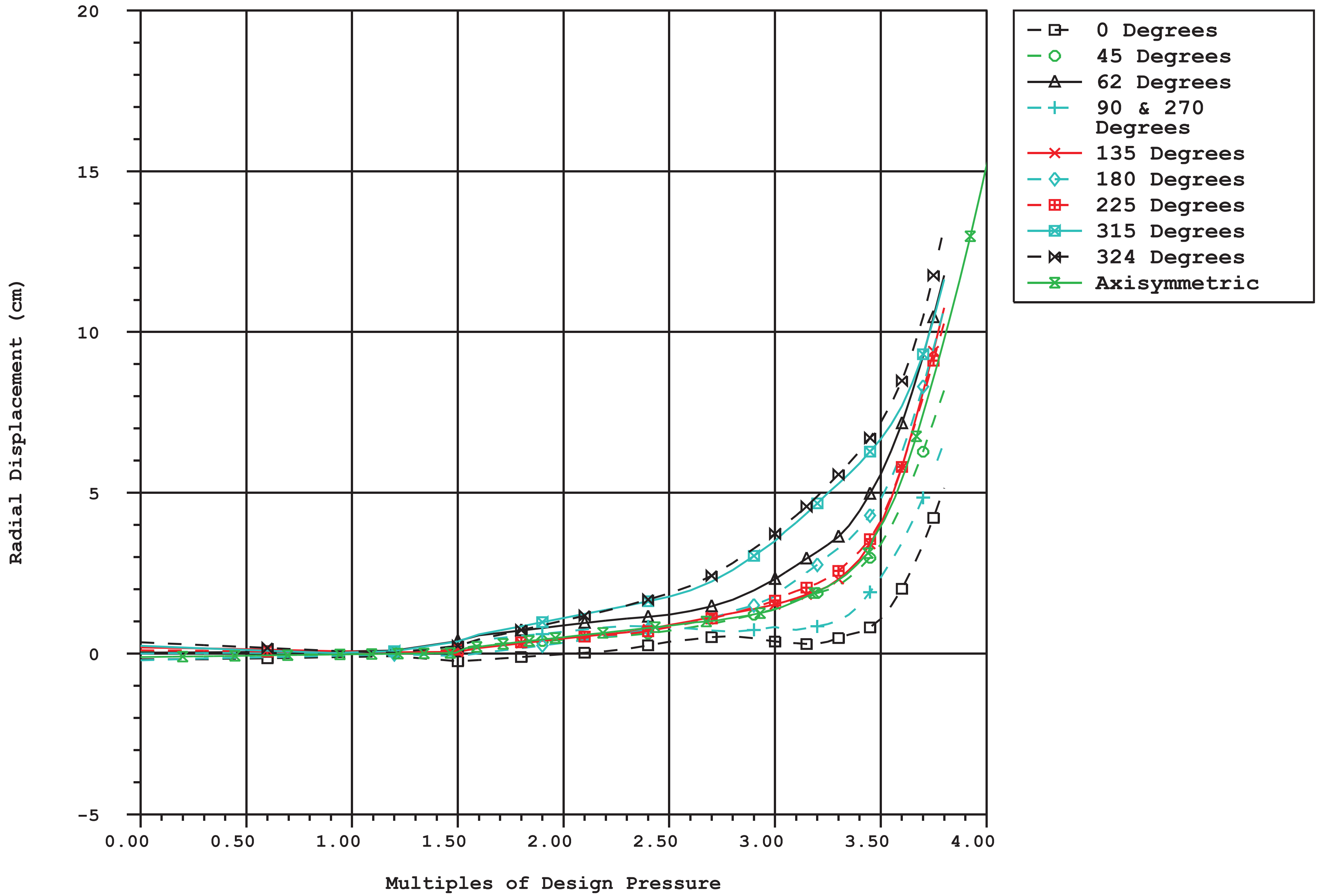

Figure 6-34. Radial Displacement at Elev. 4.7M, Posttest 3DCM Run 9
(Bi-directional Friction) Compared to Axisymmetric

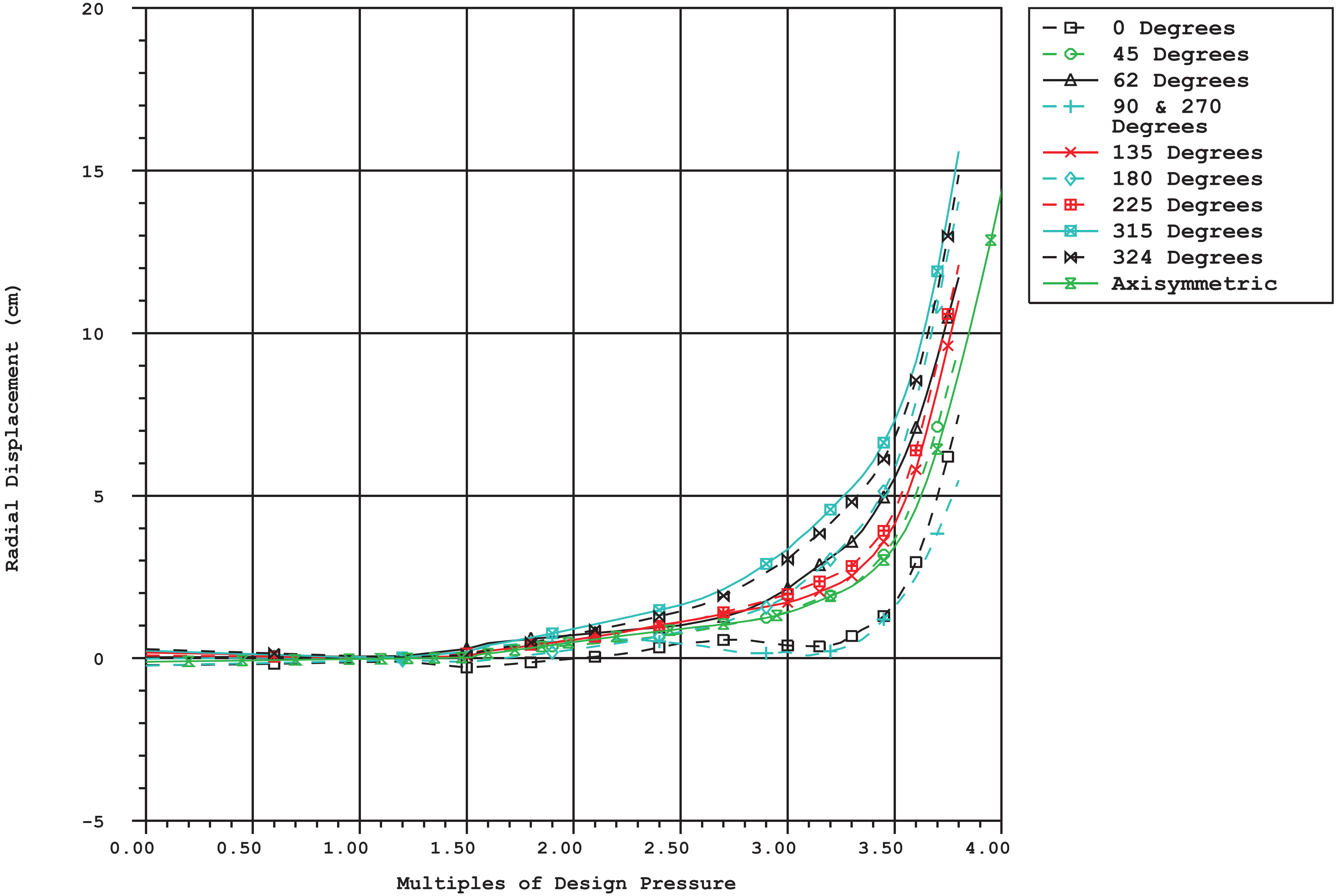

Figure 6-35. Radial Displacement at Elev. 6.2M, Posttest 3DCM Run 9 Compared to Axisymmetric

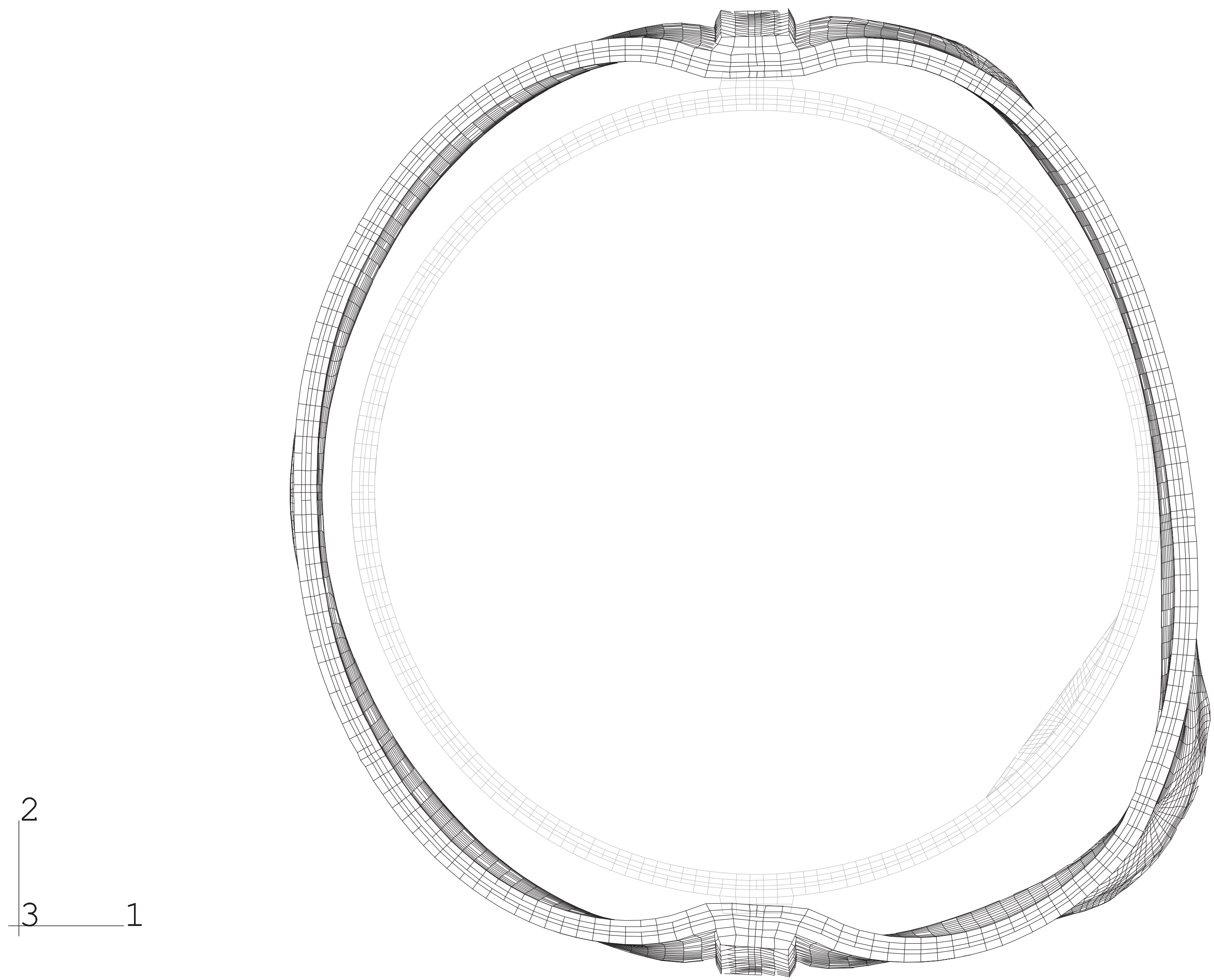

Figure 6-36. 3DCM Posttest Deformed Shape at P = 2.5 Pd, Run 9 (mag. Factor = 100×)

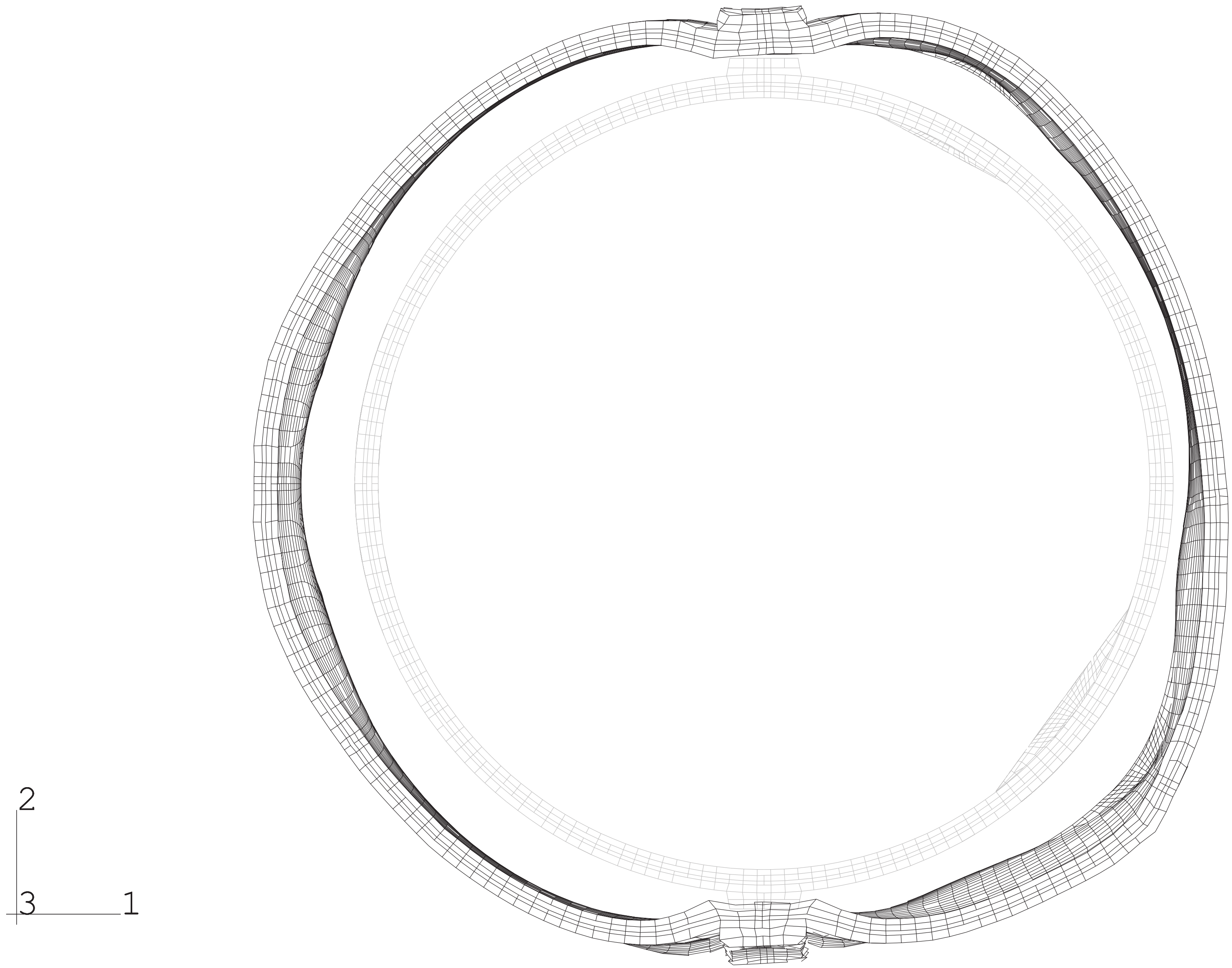

Figure 6-37. 3DCM Posttest Deformed Shape at P = 3.8 Pd, Run 9 (mag. Factor = 10×)

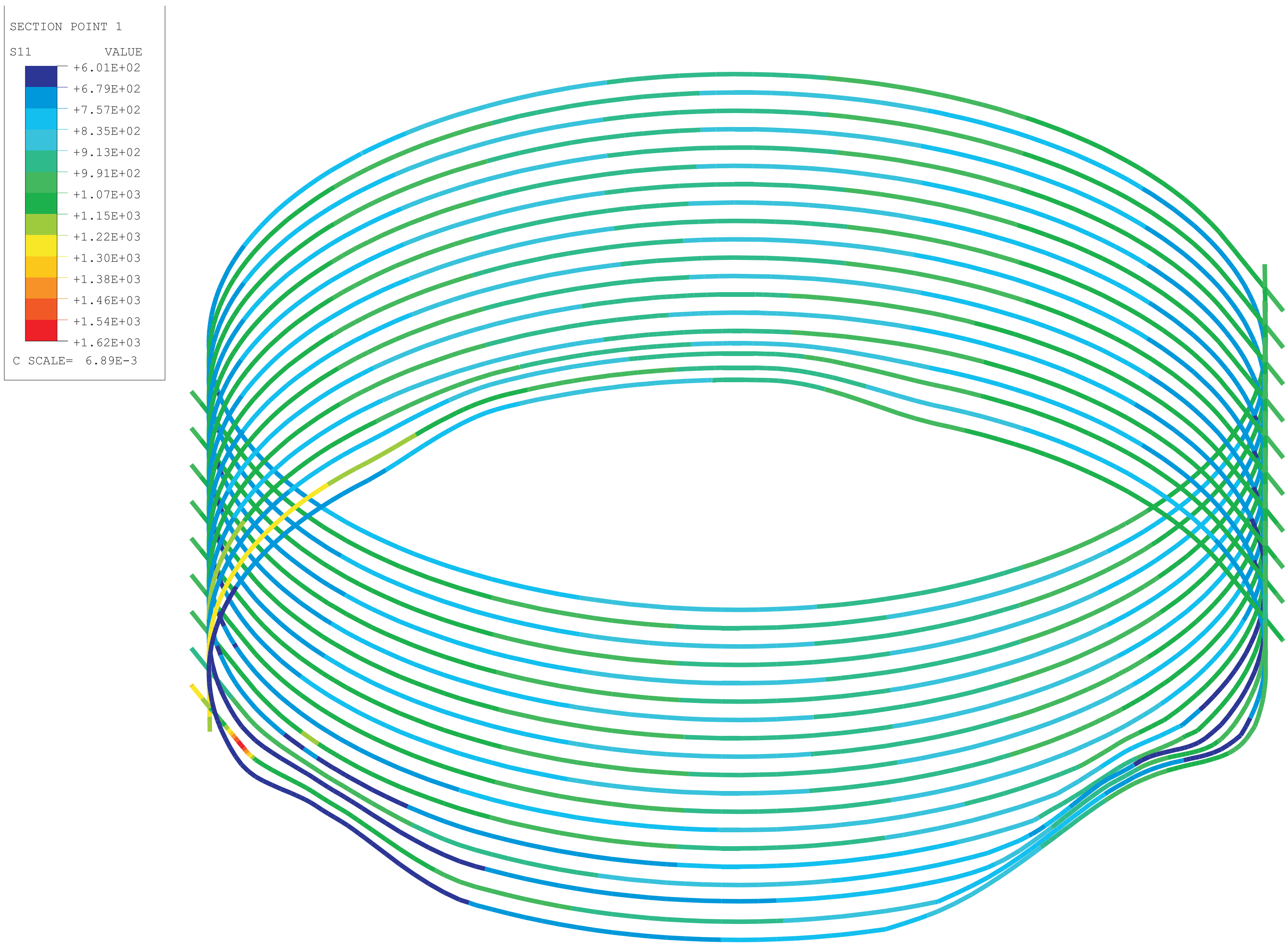

Figure 6-38. 3DCM Posttest Tendon Stress Contours at P = 1.5 Pd, Run 6

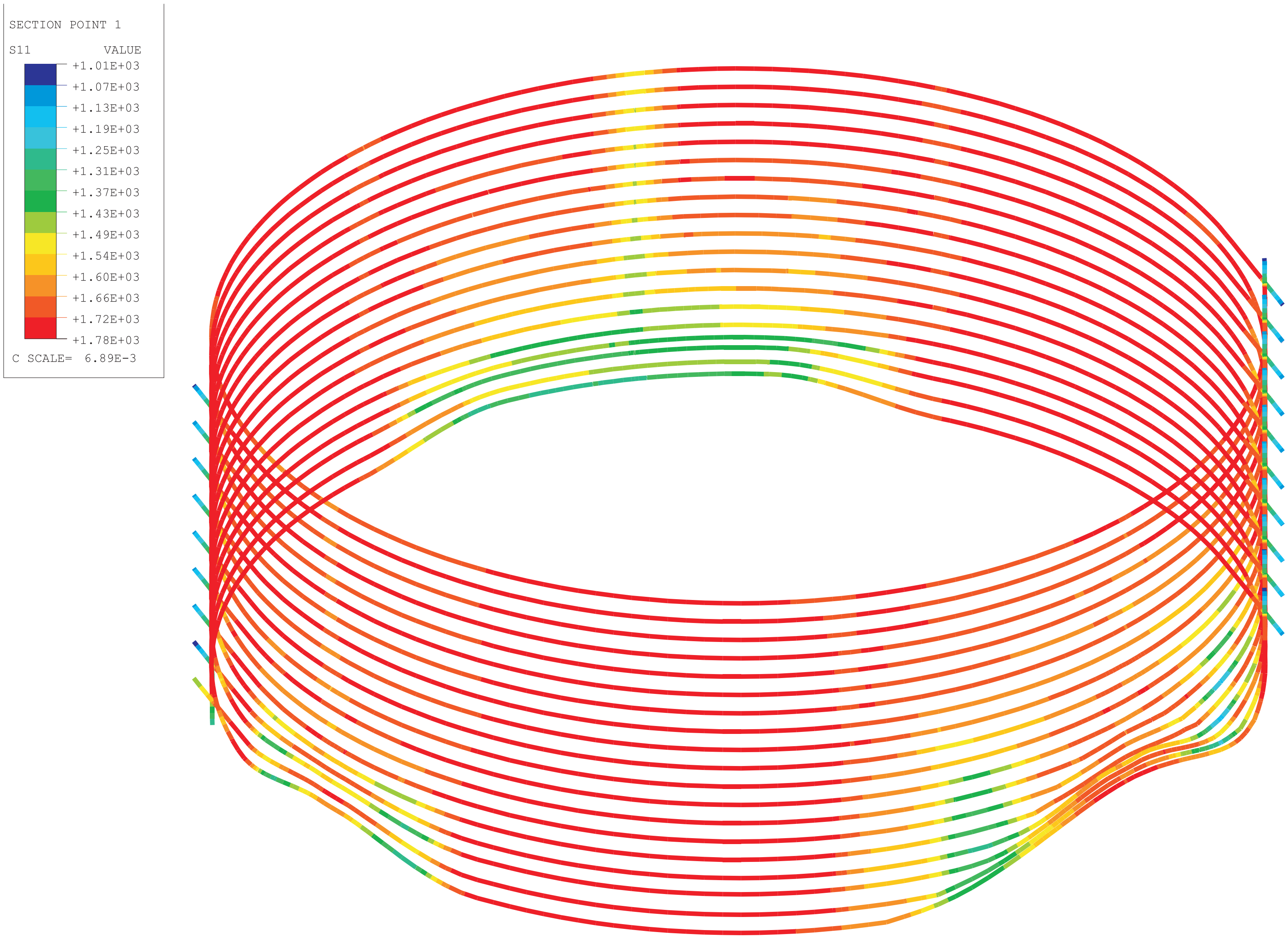

Figure 6-39. 3DCM Posttest Tendon Stress Contours at P = 3.5 Pd, Run 6

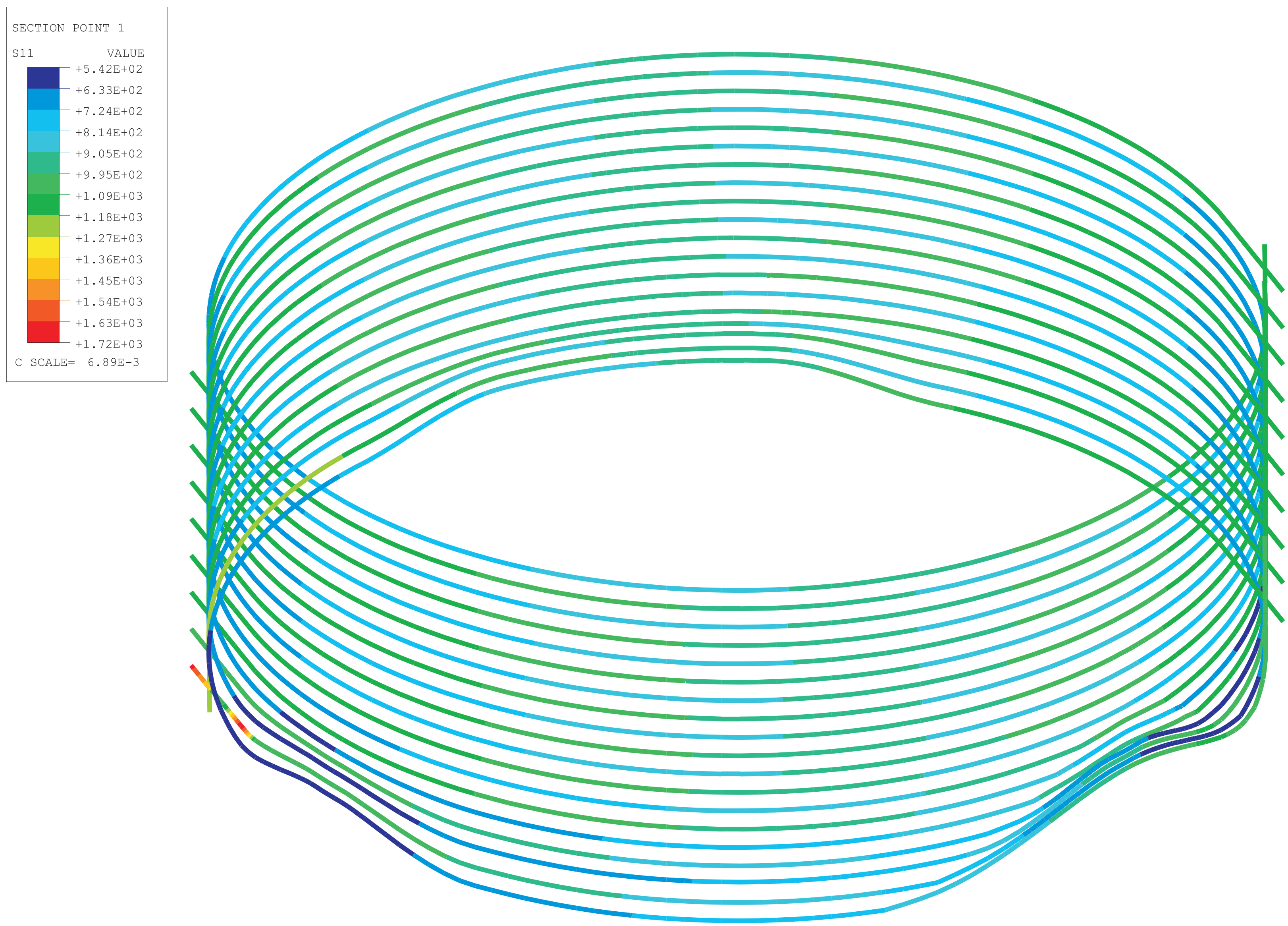

Figure 6-40. 3DCM Posttest Tendon Stress Contours at P = 1.5 Pd, Run 7, Before Friction Element Modeling Modification

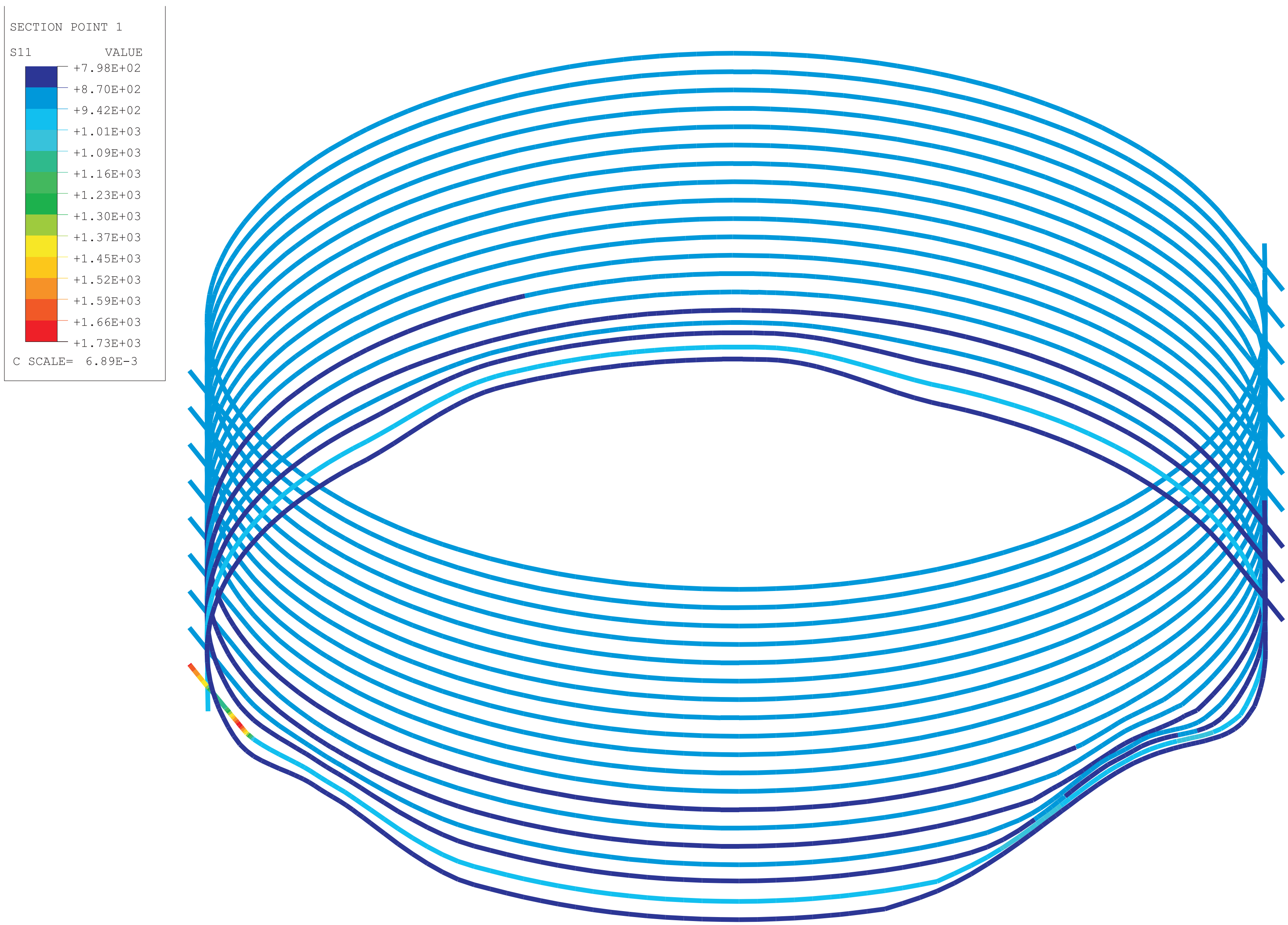

Figure 6-41. 3DCM Posttest Tendon Stress Contours at P = 1.5 Pd, Run 7, After Friction Element Modeling Modification

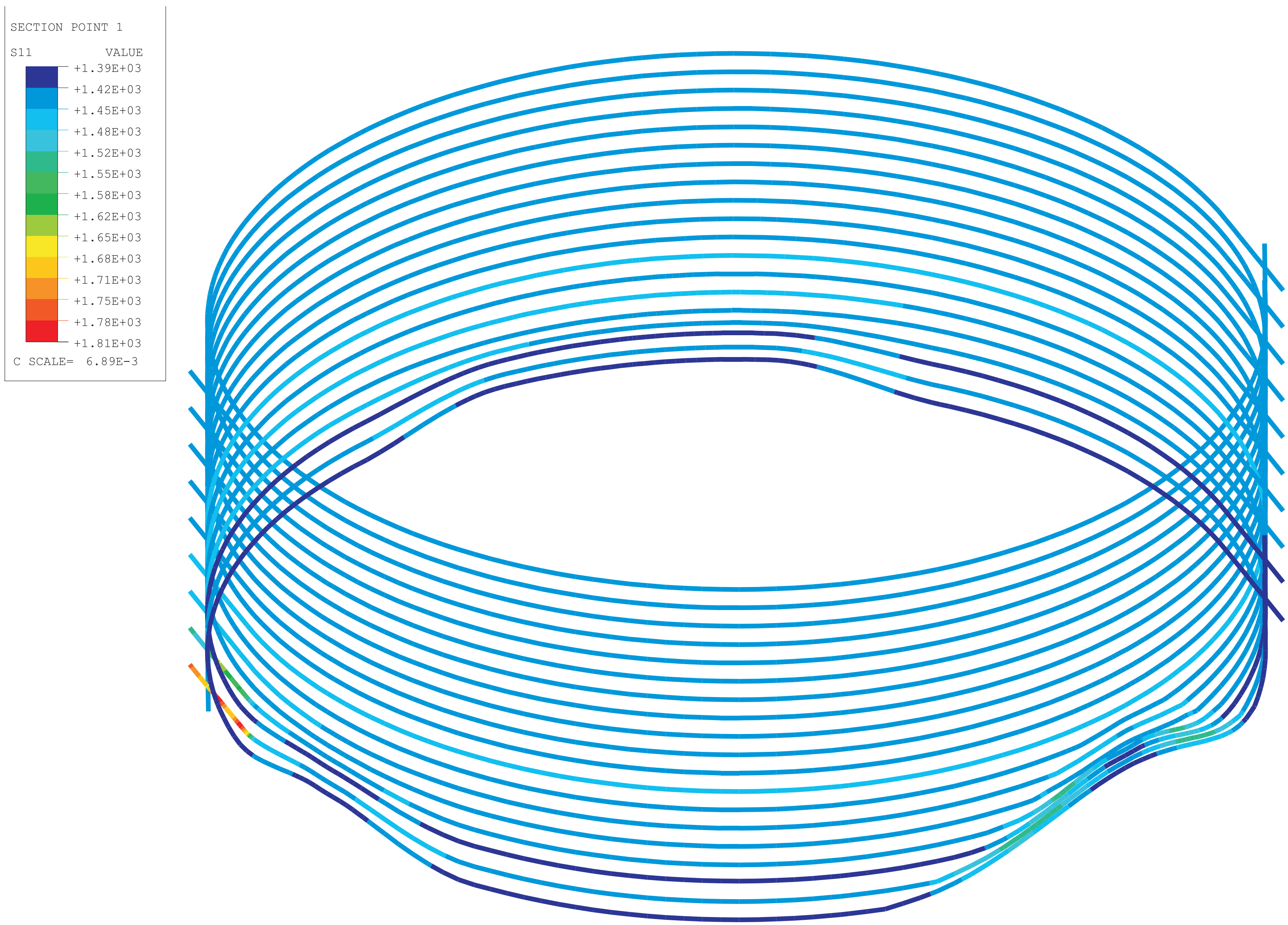

Figure 6-42. 3DCM Posttest Tendon Stress Contours at P = 3.5 Pd, Run 7

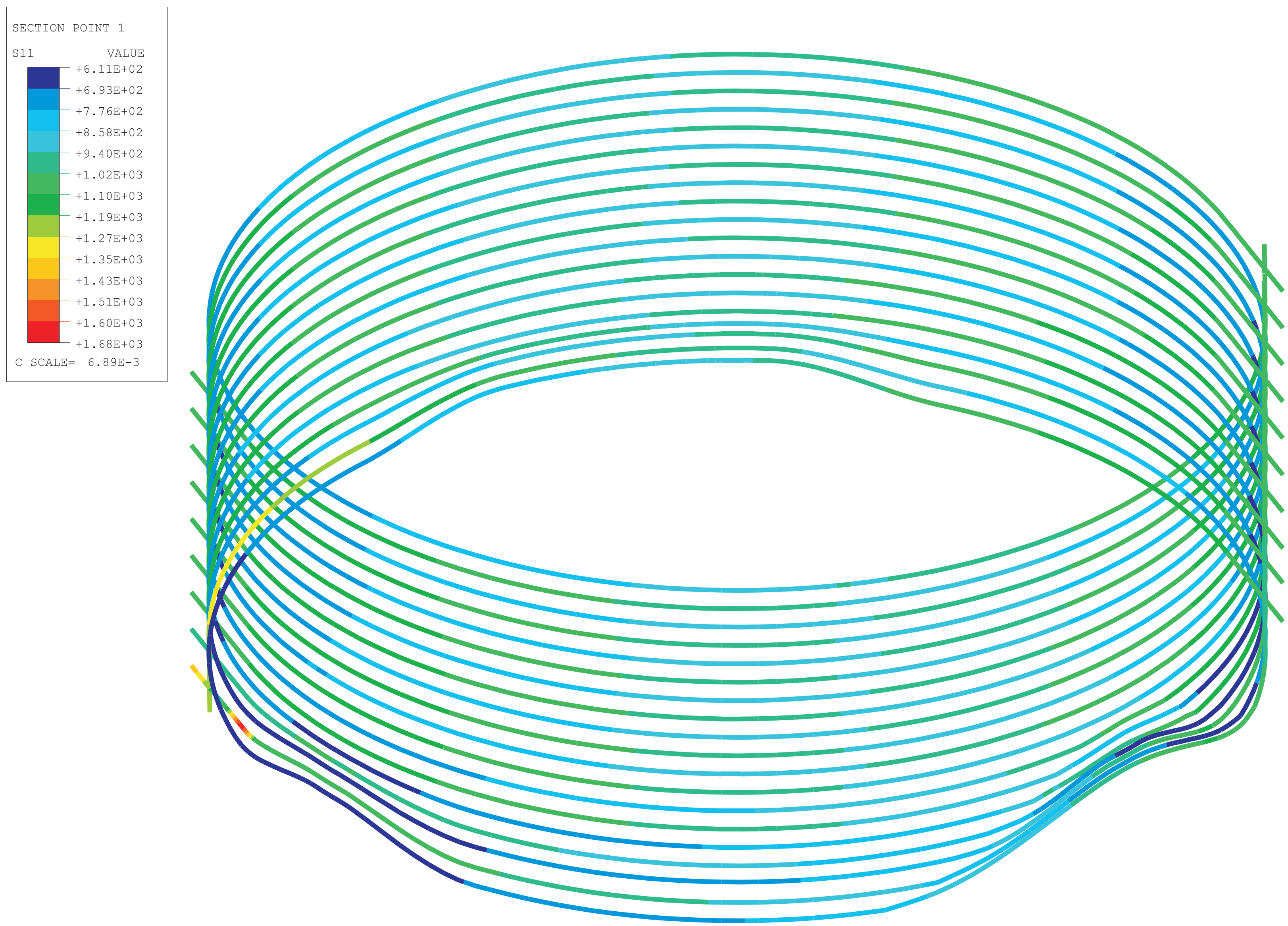

Figure 6-43. 3DCM Posttest Tendon Stress Contours at P = 1.5 Pd, Run 9

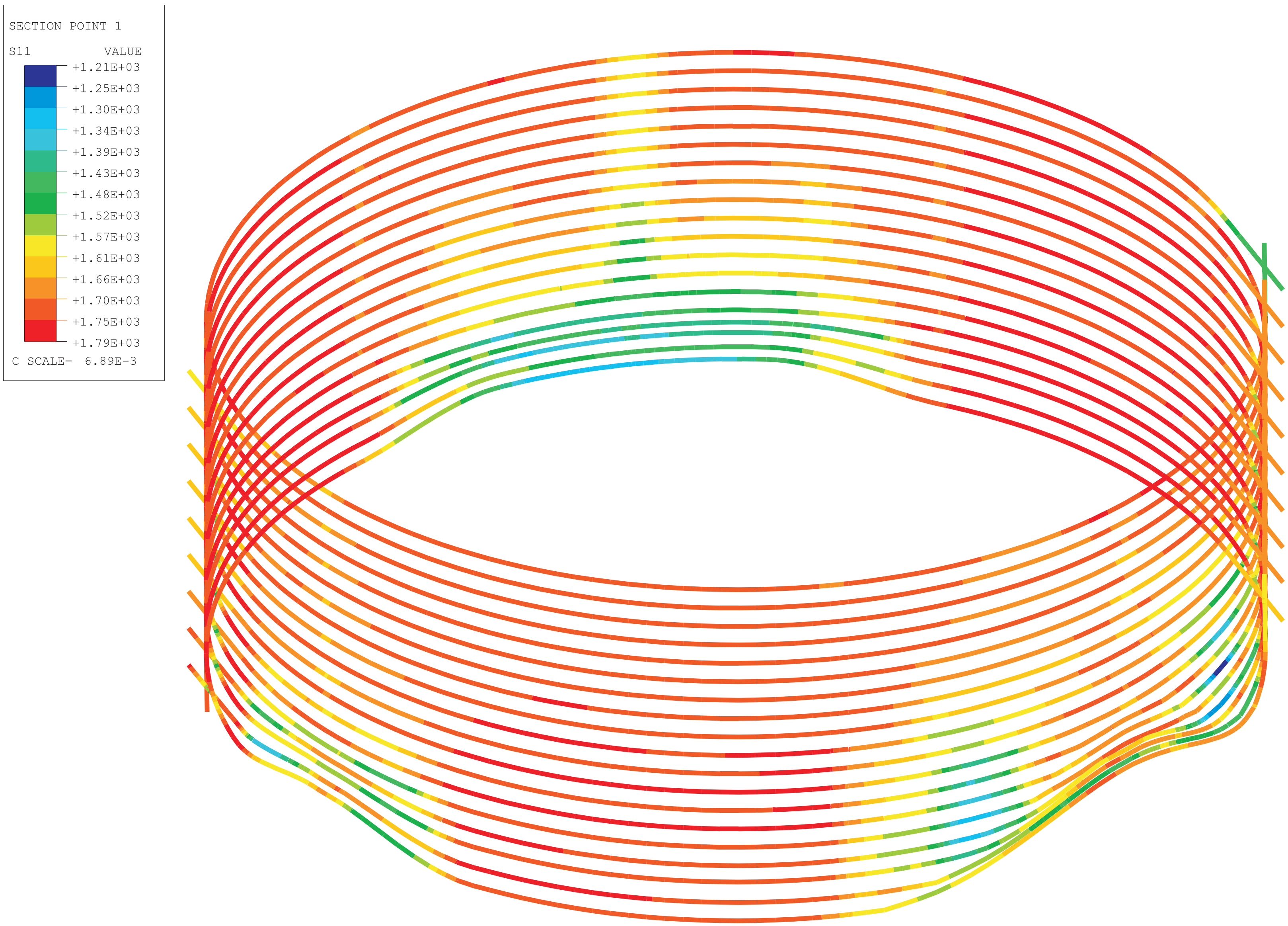

Figure 6-44. 3DCM Posttest Tendon Stress Contours at P = 3.5 Pd, Run 9

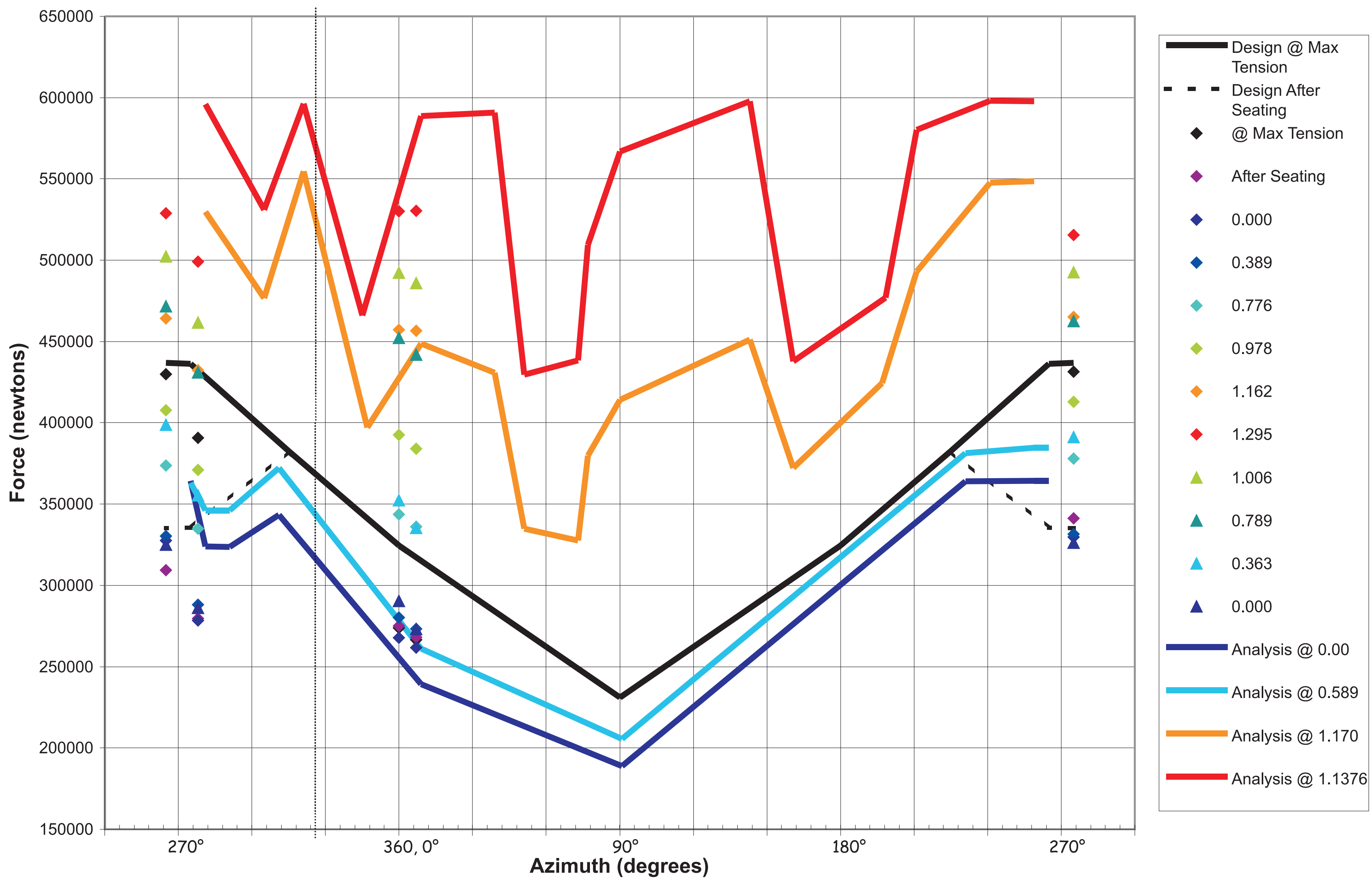

Figure 6-45. H35 Hoop Tendon Force Comparisons to Posttest Run #6

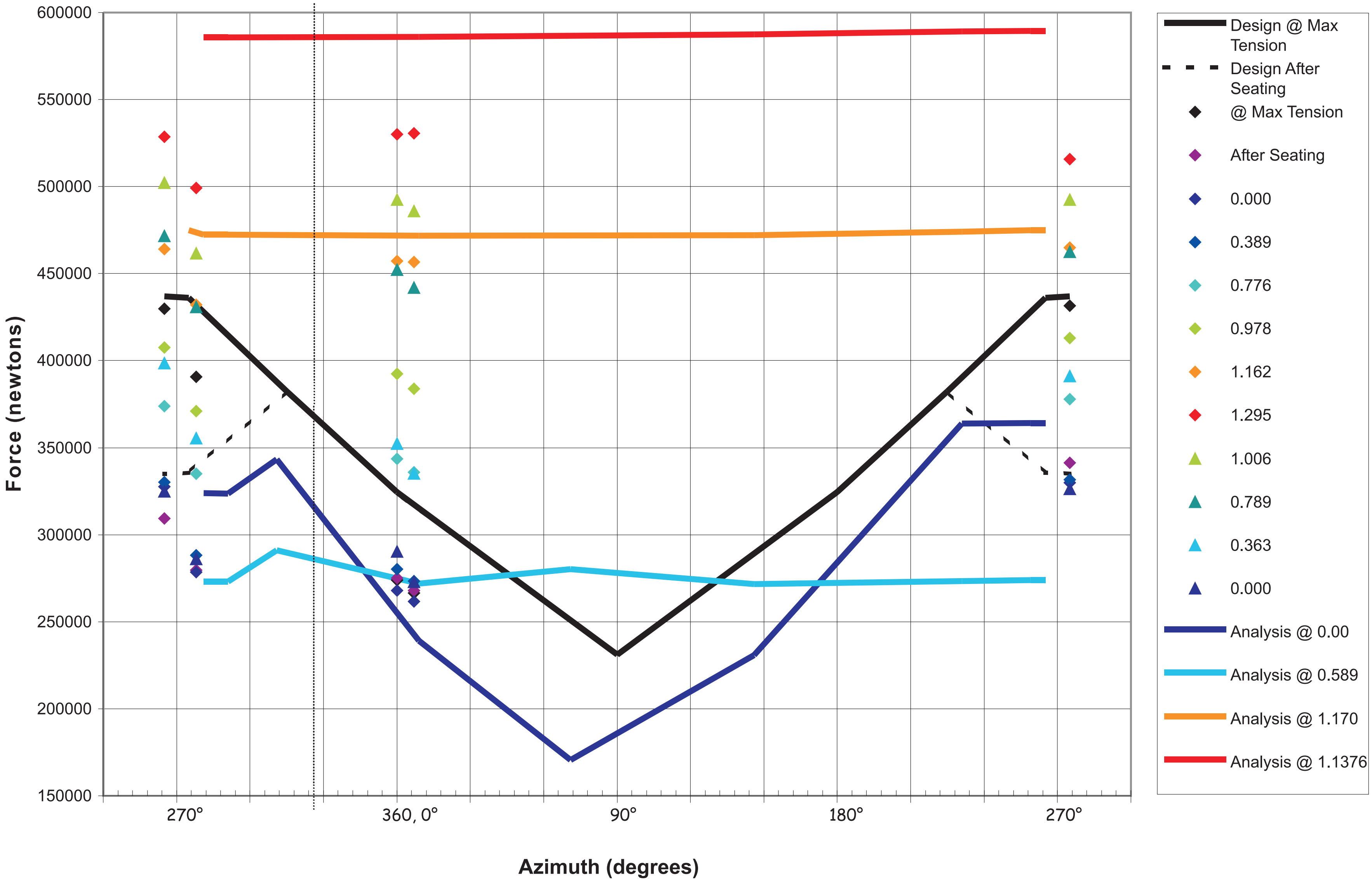

Figure 6-46. H35 Hoop Tendon Force Comparisons to Posttest Run #7

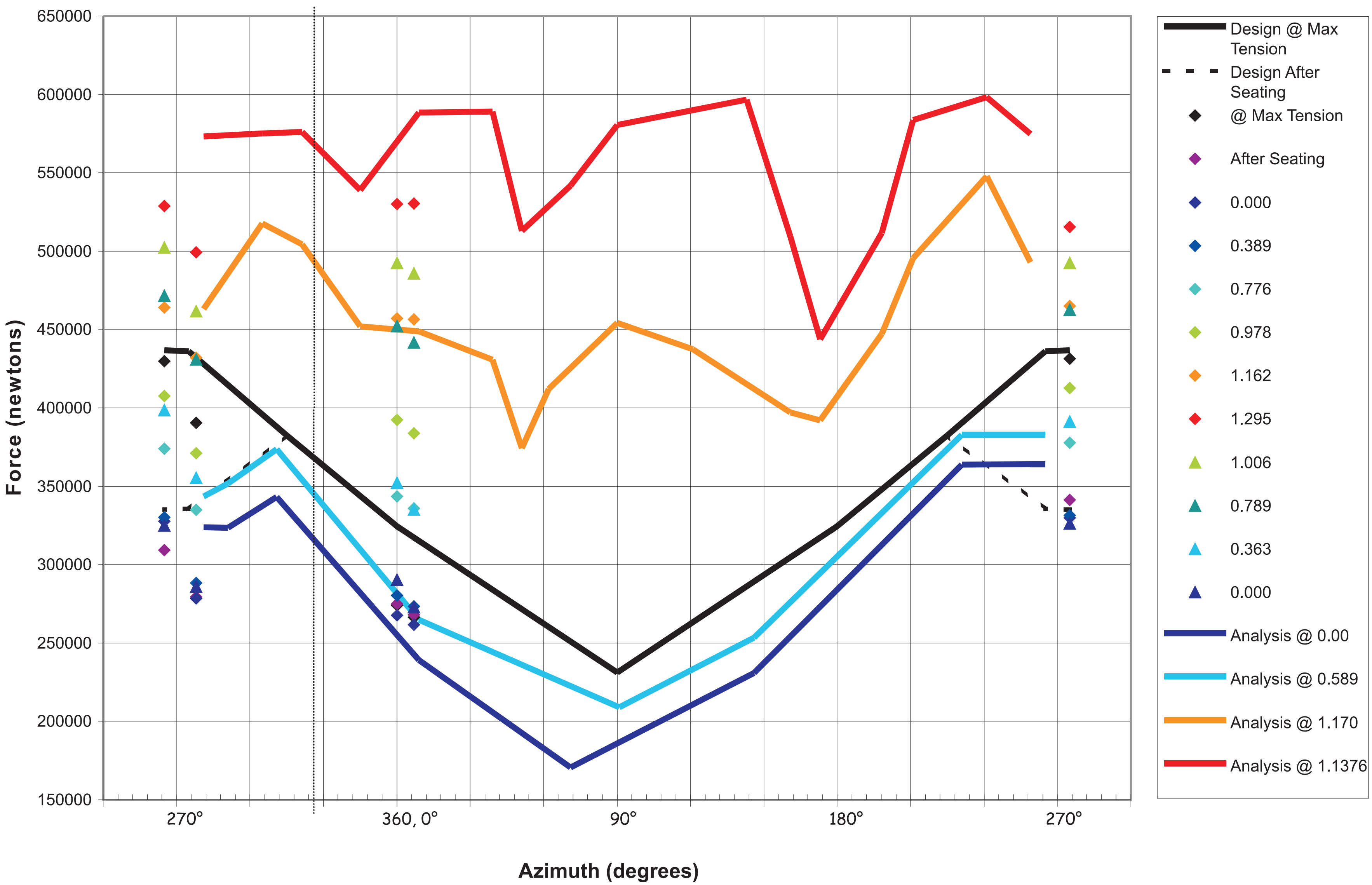

Figure 6-47. H35 Hoop Tendon Force Comparisons to Posttest Run #9

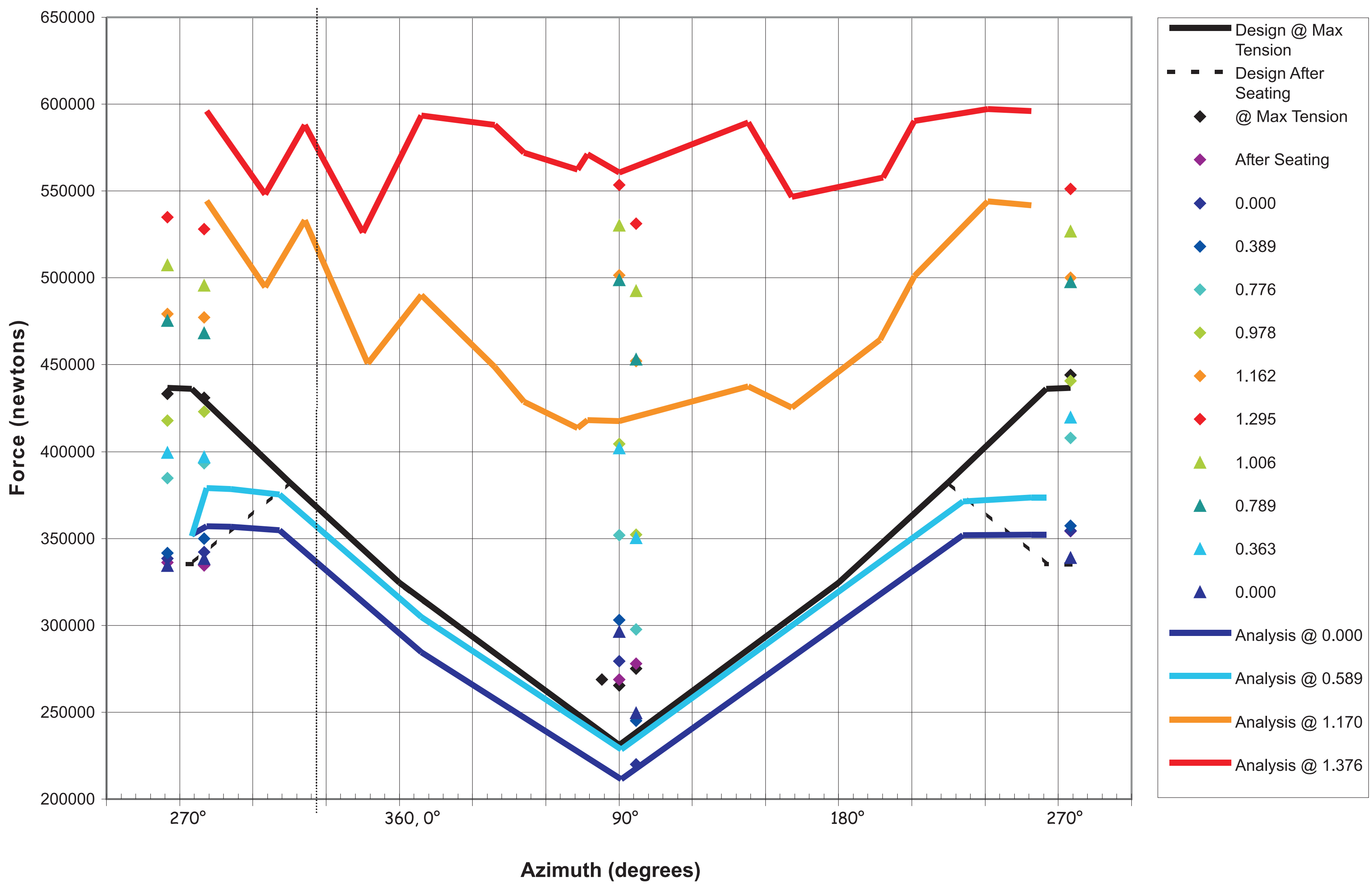

Figure 6-48. H53 Hoop Tendon Force Comparisons to Posttest Run #6

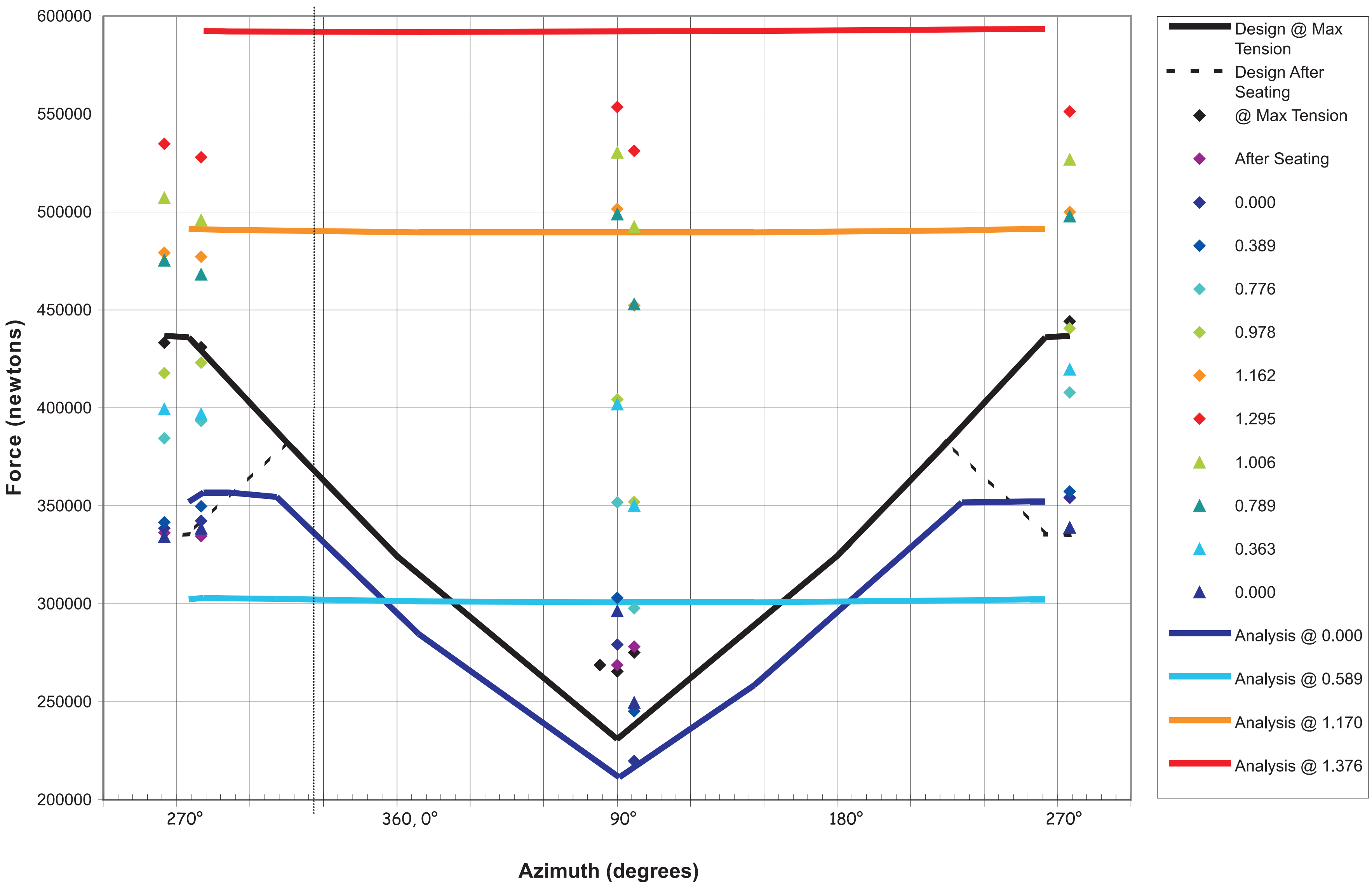

Figure 6-49. H53 Hoop Tendon Force Comparisons to Posttest Run #7

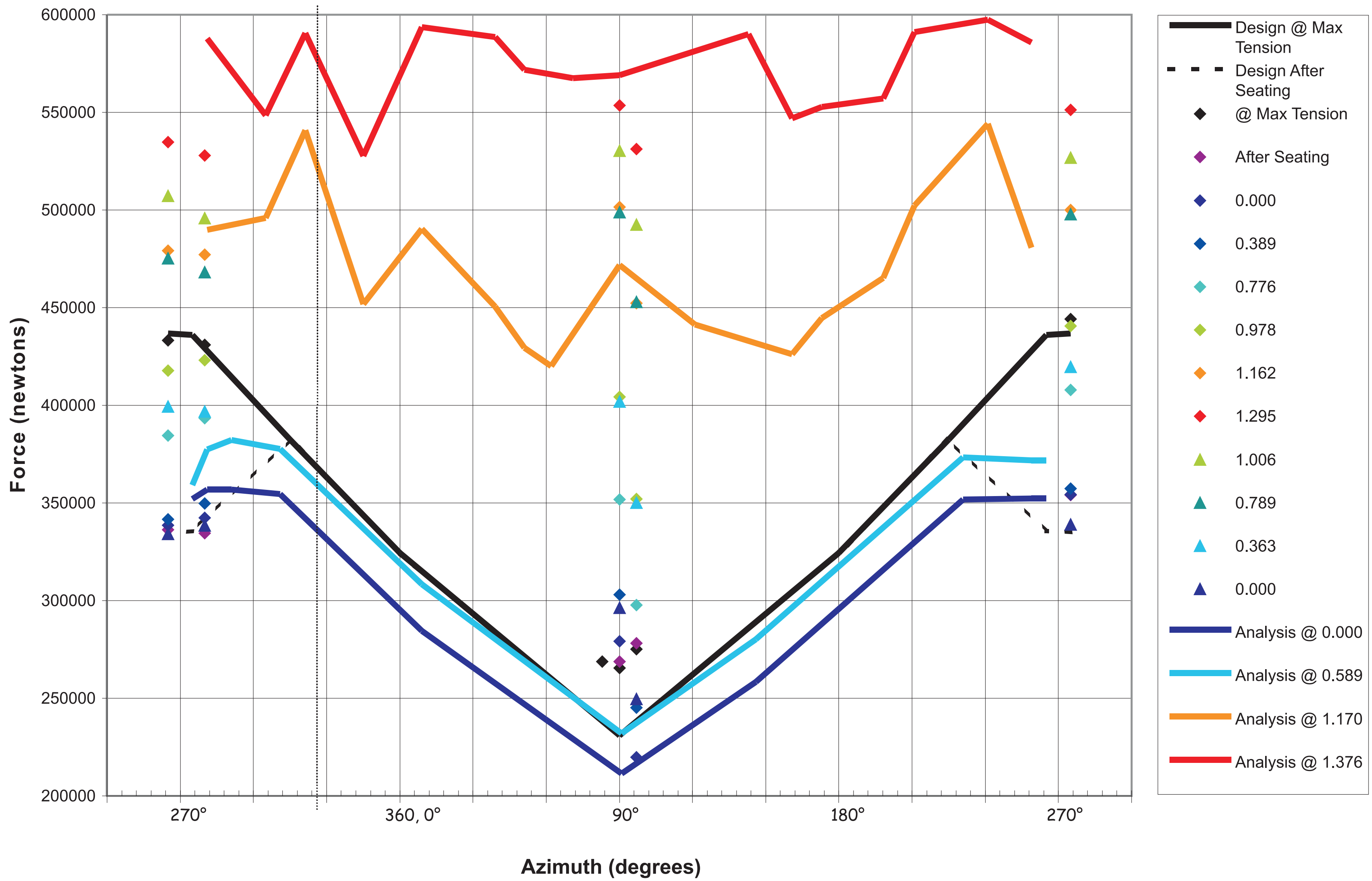

Figure 6-50. H53 Hoop Tendon Force Comparisons to Posttest Run #9

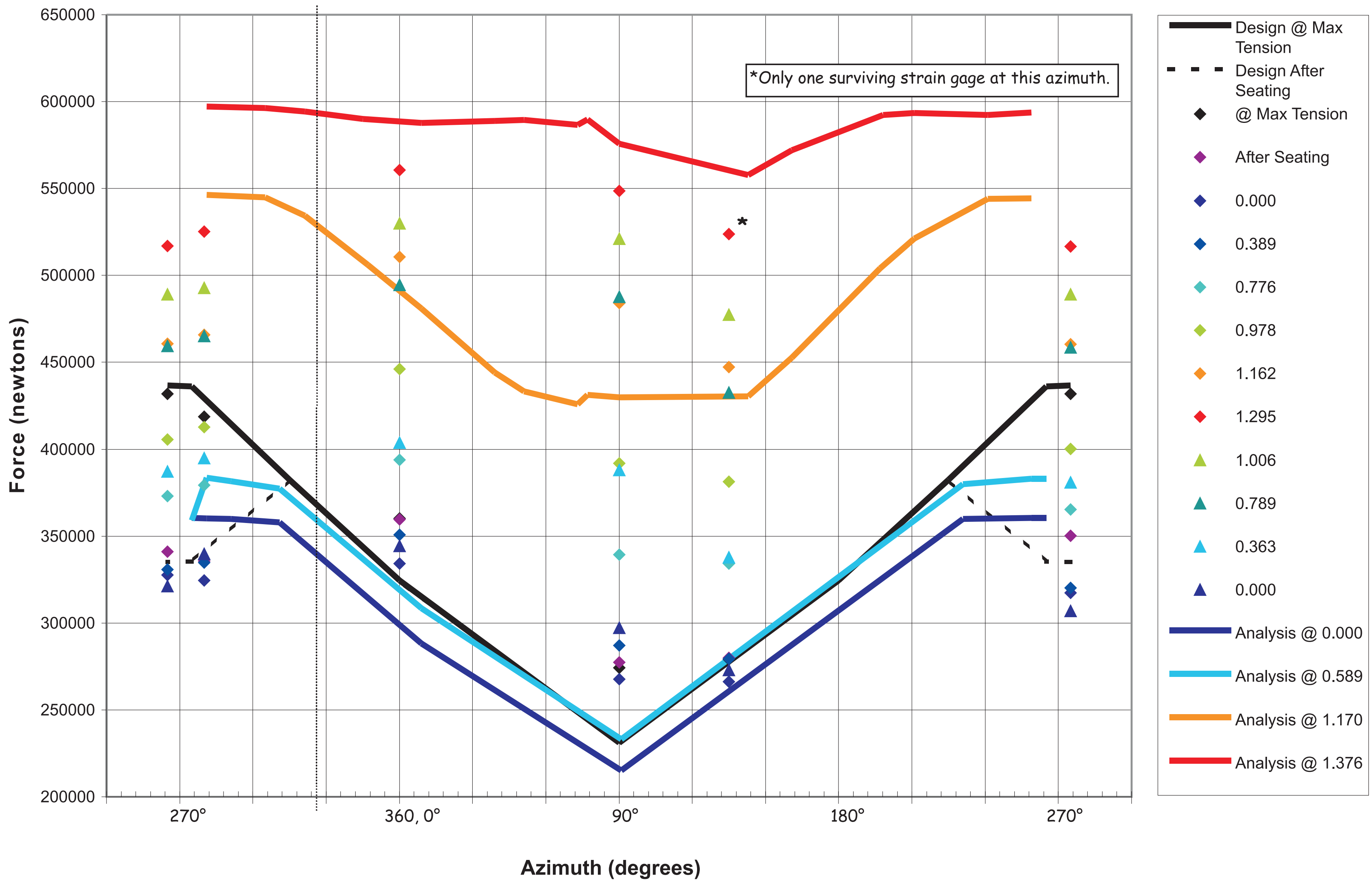

Figure 6-51. H67 Hoop Tendon Force Comparisons to Posttest Run #6

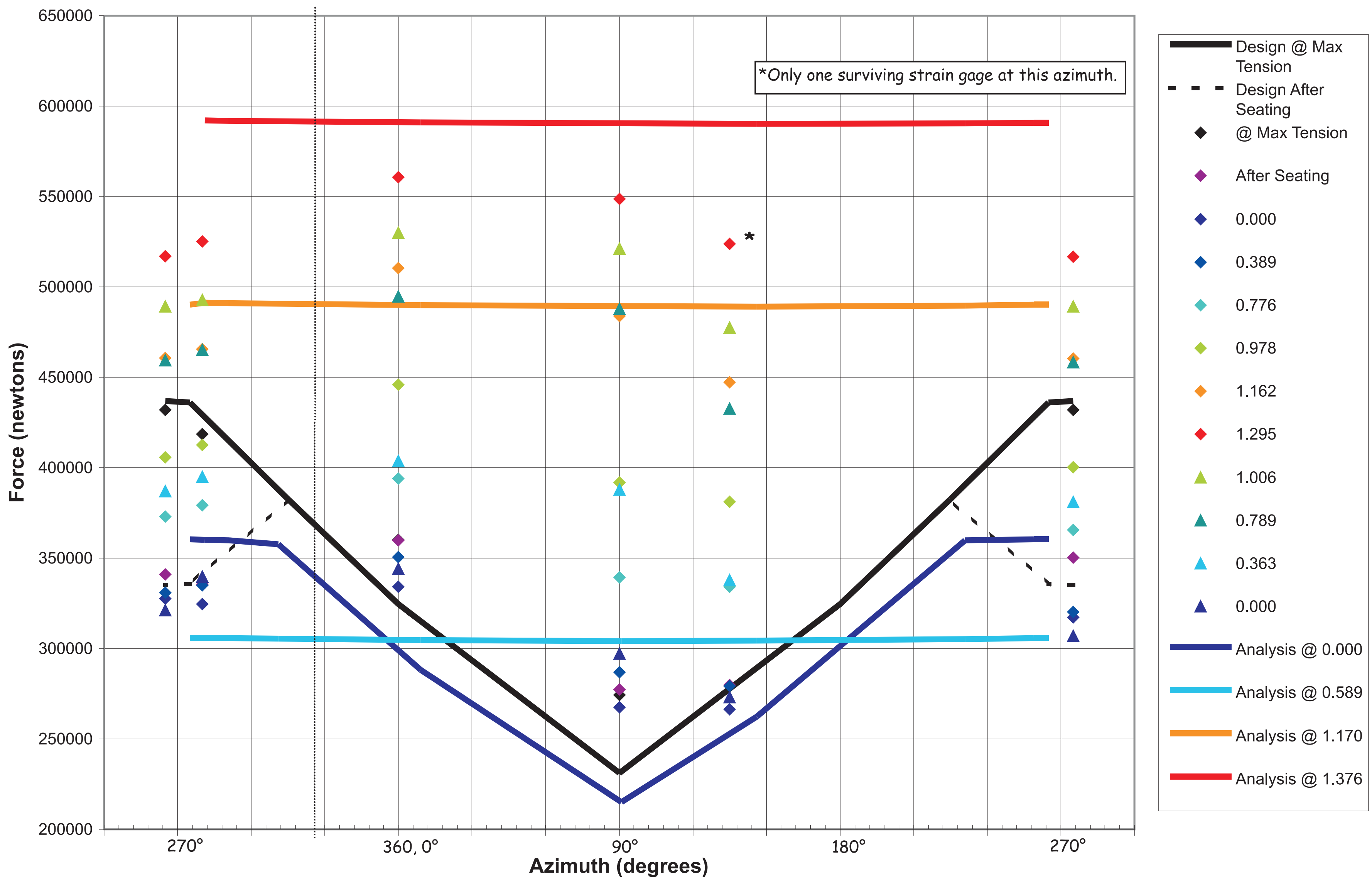

Figure 6-52. H67 Hoop Tendon Force Comparisons to Posttest Run #7

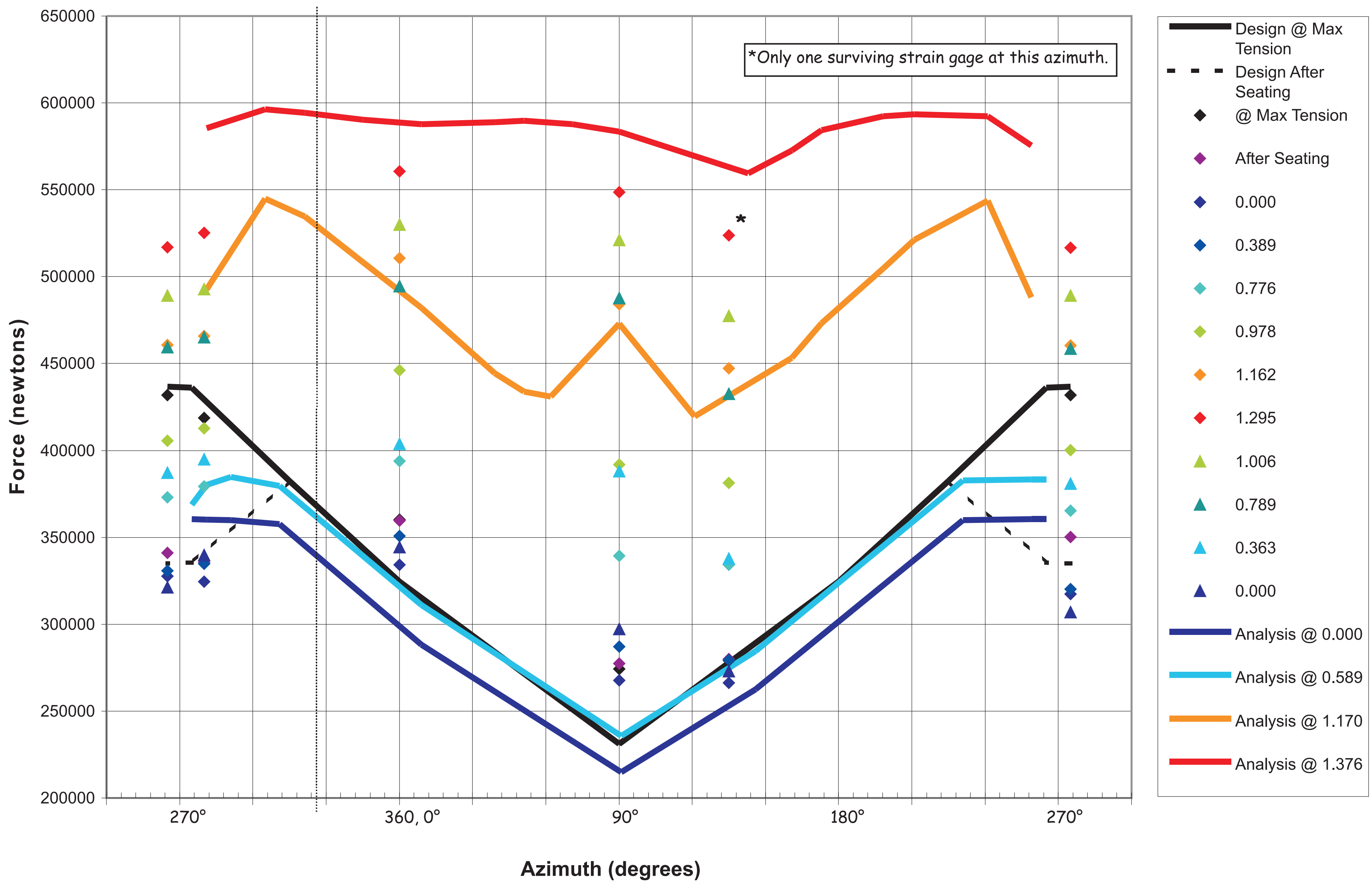

Figure 6-53. H67 Hoop Tendon Force Comparisons to Posttest Run #9

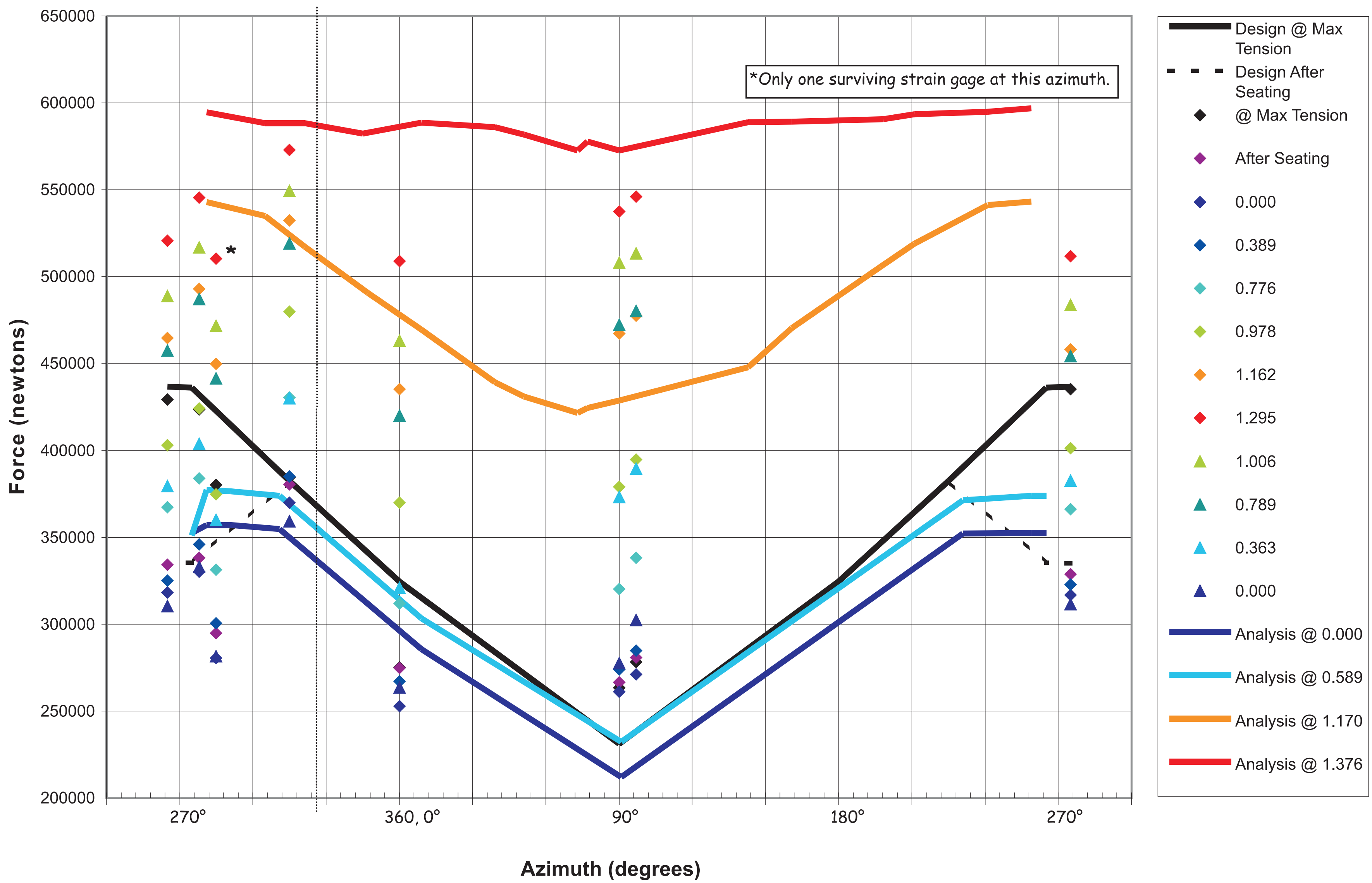

Figure 6-54. H68 Hoop Tendon Force Comparisons to Posttest Run #6

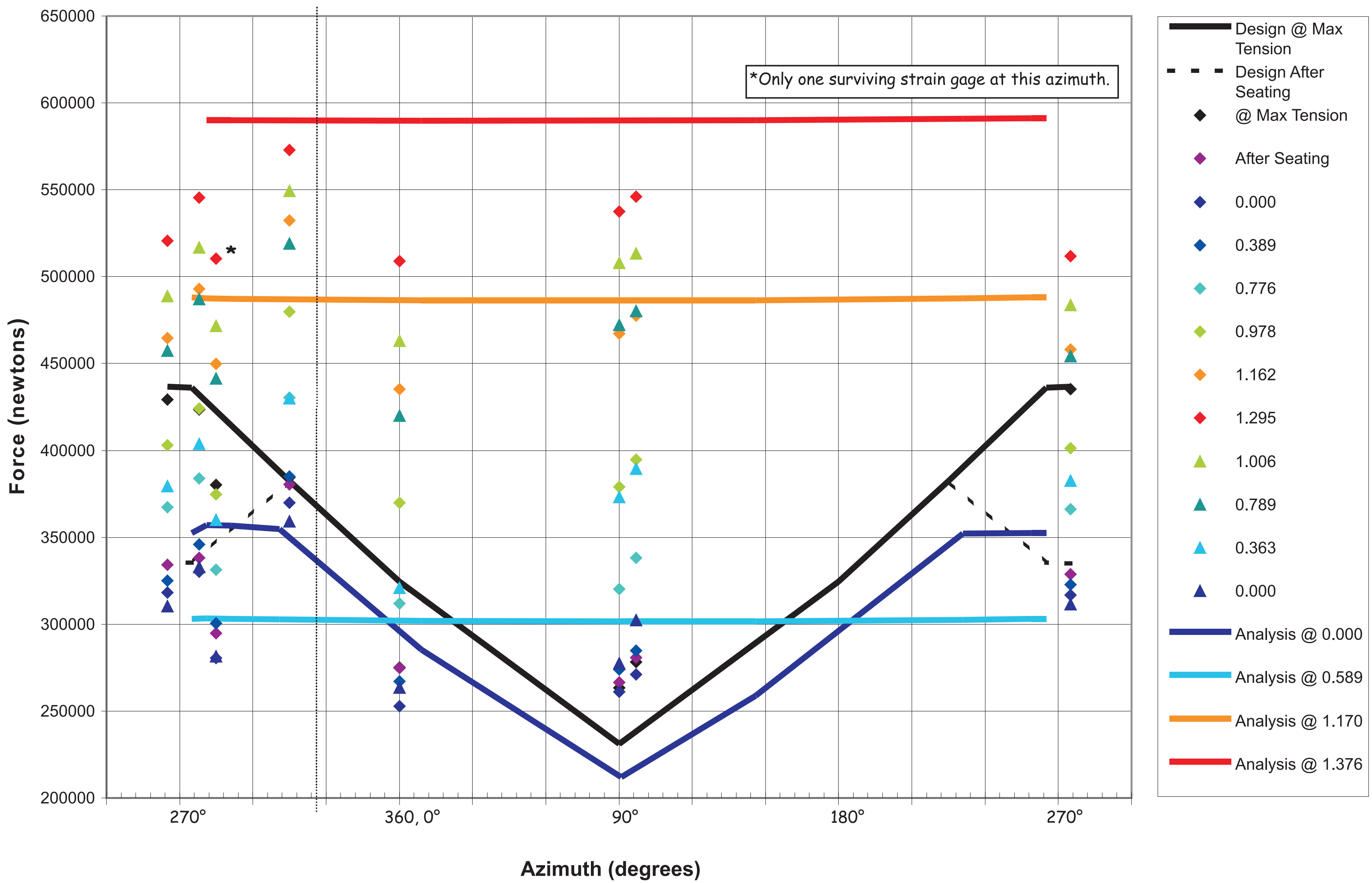

Figure 6-55. H68 Hoop Tendon Force Comparisons to Posttest Run #7

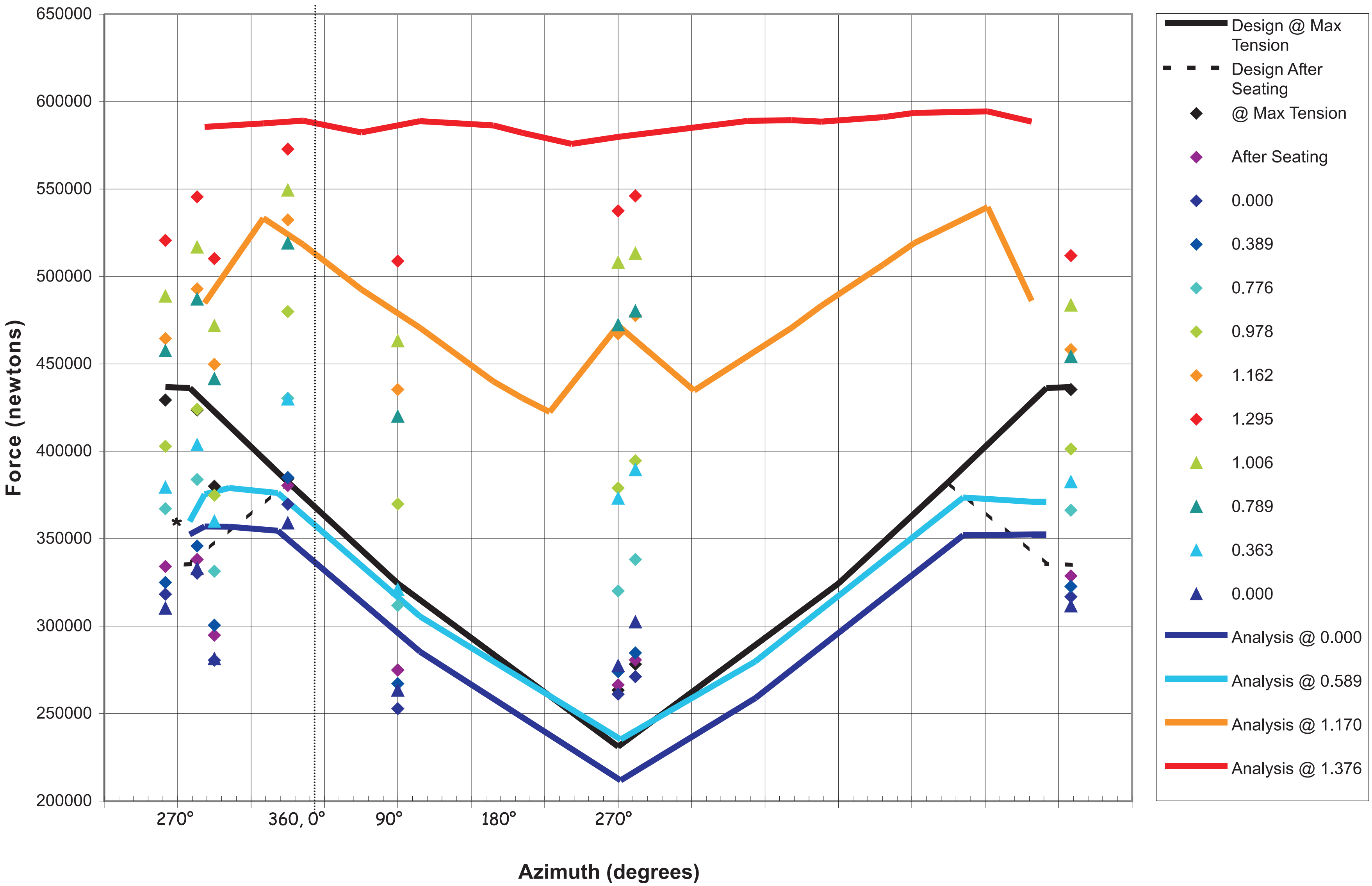

Figure 6-56. H68 Hoop Tendon Force Comparisons to Posttest Run #9

7.0 REVISED LOCAL PENETRATION POSTTEST MODEL ANALYSES

7.1 Overview of Pretest Local Models

The concrete and liner model for the pretest analysis E/H study is illustrated in Figure 7-1. The grid was developed by generating a concrete mesh based on the tendon layout and then joining the embedded edges of the T-anchor webs to the concrete mesh with the ABAQUS *SURFACE attachment command. The upper quadrant around the hatch was selected for modeling in order to have a local model completely encompassed by the 3DCM model. Five layers of concrete elements through the wall thickness were used, and the liner was modeled with shell elements so that liner bending and membrane behavior could be studied. The method of connecting the liner to the concrete (shown in Figure 7-2) was an important assumption, one that has been studied in the posttest analyses. In the pretest analysis, the liner had no bond or friction with the concrete, other than tying the T-anchor webs to the concrete. Rebar in the concrete wall was modeled with rebar subelements, and tendons were modeled explicitly with truss elements and friction truss-tie elements, as previously described.

The local E/H analyses results were reported as a function of pressure, and adjusted so the average hoop strains at the boundary matched the average hoop strains in the 3DCM model at the same location and pressure. Pretest E/H analysis revealed elevated liner strains 1) near hoop stiffeners that terminate near the 3:00 position of the edge of the insert plate, as indicated in Figure 7-3; 2) locally near the termination of vertical stiffeners; and 3) at the juncture to the wall embossment. Strains near the vertical stiffener exceed 16% at 3.2 Pd, which became the most probable failure pressure and failure location predicted for the PCCV model.

The A/L is the second-largest penetration in the PCCV model, located at the 62 degree azimuth at elevation 4.525 m. As with the E/H, there are liner connection and anchorage details near the A/L that cause large strain concentrations; this makes the region near the A/L another candidate for a liner tearing failure mode. It was modeled and analyzed in a similar fashion as the E/H.

The M/S is the third-largest penetration group, consisting of a group of four penetrations located at the 180 degree azimuth. (The F/W penetration group is similar to M/S penetration in geometry. However, since it is at a lower elevation at the same azimuth as the M/S, and was therefore assumed to see lower near-field strains, it was not explicitly modeled. The results of the M/S analysis should be applicable to the F/W penetration as well, however.) As with the E/H, there are liner connection and anchorage details near the M/S that cause strain concentrations, making the region near the M/S another candidate for liner tearing failure. The local M/S 3D model is illustrated in Figure 7-4. The modeling details for the local M/S model are similar to those developed for the E/H model. The liner-anchor interaction (shear force deflection behavior of the anchors) is modeled identically to the E/H, as is the method of attaching the liner/anchor mesh to the concrete mesh.

Unlike the E/H and A/L models, which were given symmetry boundary conditions on both vertical boundary planes, the M/S model was directly loaded with displacement versus pressure histories at every node along the boundaries of the model. These pressure histories (different at every node and in all three degrees of freedom) were obtained directly from the 3DCM model. The end result of the average hoop strain correlation approach used for the E/H and A/L is believed to be nearly the same as the direct application of displacements to nodes used in the M/S model. Some liner strain results for the pretest analysis of the M/S are shown in Figure 7-5. The "hot spots" for this region are near the vertical T-anchor terminations and the thickened insert plate surrounding the penetration group. Peak strains at 3. 2 Pd are only about 3%, and these were generally lower than those predicted for the E/H.

7.2 E/H Model Posttest Analysis

As reported in the test-to-analysis comparisons of Chapter 4, liner strains in the vicinity of the E/H penetration collar were much lower than predicted by analysis. Since these predicted high-strain locations were fundamental to the failure predictions, significant effort was conducted toward reevaluating and reanalyzing the E/H model after the test.

Since the highest measured strains in the E/H region were observed on the side away from the buttress, the E/H model was converted to a 3D concrete and liner model for the upper quadrant around the E/H opening between azimuth 18 degrees and 324 degrees for posttest evaluation. This model was developed and modified from a similar E/H local model with buttress that was used in the pretest analysis. Figure 7-6 illustrates the finite element model and boundary conditions used in the posttest analyses. Unlike the pretest analysis, the radial displacement at the bottom boundary of the model (elev. 15.34 feet) was not specified according to results from axisymmetric analysis and only vertical displacement was applied (fixed) at the boundary. Figures 7-7 and 7-8 plot the rebar, tendon and liner details around the E/H opening.

In the search to understand the sources of differences between the local E/H predictions and the test observations, a number of changes were introduced into the posttest analysis:

1. The buttress was removed and the model shifted to the other side of the hatch;

2. Rebars were regenerated (this was necessary to extend the model to 18 degrees, but a few refinements were also made);

3. The liner was made continuous at azimuth 18 degrees, removing a discontinuity that had been present at the edge of the pretest model;

4. A circular cross section (CIRC) for tendon beams was used instead of the pipe cross section previously used;

5. A pressure (stress) boundary condition was applied at the top boundary. This was incorrectly applied in the pretest analysis:

6. The orientation of friction truss-ties were adjusted for hoop tendons that are straight in elevation view (i.e. the tendons that are not wrapped around the E/H opening). This change was based on the observation that tendon friction behavior at high pressure did not necessarily follow the friction orientation set at the beginning of the analysis (i.e., the friction orientation assumed in design); the friction was essentially set to zero for these portions of tendons; and

7. The tendons were all pulled at the 18 degree azimuth edge of the model because of difficulties encountered at the 324 degree boundary. Tendon strains at the 324 degree symmetry plane were unrealistic until this change was made.

The posttest model with these changes was referred to as Model A.

With this set of changes (and the calibration provided from the LST) the posttest E/H model's hoop expansion behavior correlates well with global displacement behavior. The adjustment to the pressure function required in the pretest analysis to match average hoop strains between the E/H and 3DCM is no longer needed, and the overall confidence in the predictive aspects of the model has been significantly improved.

7.3 E/H Posttest Results and Comparisons

Results of the basic E/H posttest model (Model A) are plotted in Figures 7-9 through 7-16. Comparing these plots to those of the pretest analysis report [1] shows a uniform displaced shape and deformation pattern that agrees better with the test. In other words, adjustments to the pressure scale for matching hoop displacements were no longer needed. At pressure beyond 3.5 Pd, liner and tendon strains grew larger and tendons reached strains approaching rupture in the zone between 0 degrees and 6 degrees azimuth. This was caused by a discontinuity in wall reinforcement. (The percentage of hoop reinforcement decreases in this region between the free-field percentage and the extra added around the E/H.) A high strain zone also exists just above the E/H. The liner strains near the E/H collar, though significantly lower than in the pretest analysis, were still elevated and show similarities to the pretest analysis, which, based on the LST strain measurements, is a generally incorrect prediction. The strains near the edge of the embossment are also generally lower than what was measured in the test. The authors have proposed a hypothesis for each of these observations, which were tested by the following variations of posttest analysis shown in Table 7-1.

Table 7-1. Variations of Posttest Analysis

Model	Liner/Concrete Friction Bond	Precrack at Edge of Embossment
A	No	No
B	Yes	No
C	No	Yes

Hypothesis 1: In the PCCV tests, the liner in the E/H area had a high degree of bond-friction with concrete, preventing slippage of the liner relative to the concrete; relative slippage is required for elevated strains to develop near local discontinuities like T-anchors and stiffeners.

Hypothesis 2: Formation of a major crack near the edge of the E/H embossment further concentrated the liner strains at the edge of the embossment. (Posttest inspection revealed the presence of a large void in the concrete behind the liner at this location and a significant crack was also observed on the outside surface of the concrete at this location.)

The hypotheses are examined in Cases B and C. Case B uses the contact surface sticking/friction capability in ABAQUS. Contact with friction bonding properties were assigned to the liner-concrete interaction surface for Case B. The results of Case B are plotted in Figures 7-17 through 7-22. They show that by preventing relative slip between liner and concrete, the overall behavior of the system (concrete strains, tendon strains, liner strains away from the hatch) remains the same, but the elevated strains close to the collar are completely eliminated.

The results of Case C are plotted in Figures 7-23 through 7-29. The ANACAP-U pre-cracking algorithm was used to introduce pre-cracking along the edge of the embossment. According to the liner strain results, however, the pre-cracking has only a minor effect on liner strain localization. Based on this result, investigating this phenomena may require a discrete crack approach, where a double row of concrete nodes along the embossment are introduced and allowed to open.

Thus, Hypothesis 1 has been clearly demonstrated to be true. Smeared crack analysis, however, has been unable to demonstrate Hypothesis 2.

The liner areas near the E/H that have hoop stiffener splices (rat-holes), some of which exhibited tears, are shown in Figures 7-30 and 7-31. To further investigate Hypothesis 2, and to develop a model that even more closely simulates what occurred in the test, two more analyses were performed, as shown in Table 7-2.

Table 7-2. Additional Analyses for Hypothesis 2

Cases	Liner/Concrete Friction Bond	Precrack at Edge of Embossment
D	Yes	Yes
E	Yes	Yes-Discrete Crack

The first (Case D) is an extension of the previous analysis series; namely, the liner/concrete friction bond was applied to the pre-cracked case (directed crack at element integration points). The liner strain results of this case are summarized in Figure 7-32, 7-33, and 7-34. The results are similar to Case C, except that now the liner strain concentrations near the Hatch collar insert plate are (for the most part) eliminated, as they were in Case B.

In the final case (Case E), the integration point directed crack is reduced to one row of elements and a discrete crack is formed by adding double rows of nodes along an assumed crack line, as shown in Figure 7-35. The double row of nodes could not be extended all the way through the wall section because it would interrupt the modeling of the reinforcement (modeled with subelements within the concrete elements). However, just "unzipping" the first element layer (which has no reinforcement) to simulate a discrete crack partway through the wall thickness was found to create a liner elevated strain phenomenon.

The results of Case E are illustrated in Figures 7-36 through 7-39, at pressures of 2.8, 3.0, 3.2, 3.5, and 3.6 Pd. At this point, a mild strain concentration emerged at the edge of the wall embossment. The peak strain predictions of this wall embossment edge are listed in Table 7-3.

Table 7-3. Peak Strains Calculated at Edge of Wall Embossment, E/H

Pressure	Peak Strain at Wall Embossment	Rat-Hole Strain Concentration		e_{peak} Pristine	e_{peak} w/Grinding
		Pristine	With Grinding		
2.8 Pd	0.0036	45	59	0.16	0.21
3.0 Pd	0.0047	"	"	0.21	0.28
3.2 Pd	0.0053	"	"	0.24	0.31

Note from Figures 7-30 and 7-31 that the mild strain concentration simulated in E/H Model Case E coincides with rat-hole weld seam details. Numerous tears occurred at these details (see Figure 1-5). Based on the results of the detailed liner rat-hole (weld-seam) analysis (Chapter 8), the additional strain concentration associated with these local details is approximately 45 for a pristine rat-hole detail and about 59 for locations with severe (~40% reduction in thickness) local liner thinning by grinding from the weld repairs. (These strain concentrations would be applied to free-field liner strains away from all discontinuities). As reported in [8], there was extensive liner thinning at most of these tear locations. The tears at the edge of the embossment can be explained by magnifying the strains calculated in the E/H analysis by the strain concentration factors from Chapter 8. This calculation is shown in Table 7-3. It shows that with discrete crack modeling and local rat-hole modeling, a liner tear would be predicted to occur as early as 2.8 Pd. Based on the evidence provided by liner strain gages and acoustic monitoring, one of the tears along this embossment edge may have even occurred as early as 2.5 Pd.

The posttest E/H study thus presents a modeling strategy with results that correlate well with the LST measurements and observations. A somewhat higher strain prediction might be possible if a discrete crack (separate rows of nodes) were propagated all the way through the concrete wall, but this would require a complete change in rebar modeling strategy to (a discrete element representation of rebar) - one that is probably not practical even for very detailed analytical evaluations of containments.

7.4 M/S Model Posttest Analysis

The M/S penetration consists of a group of four penetrations located at the 180 degree azimuth. As with the other penetrations, there are liner connection and anchorage details near the M/S that cause strain concentrations, making the region near the M/S another candidate for liner tearing failure. The local M/S 3D model is illustrated in Figure 7-4. The liner-anchor interaction (shear force deflection behavior of the anchors) is modeled identically to the E/H, as is the method of attaching the liner/anchor mesh to the concrete mesh. Unlike the E/H and A/L models, however, the M/S model was loaded directly with displacement versus pressure histories at every node along the boundaries of the model, plus internal pressure. These pressure histories (different at every node and in all three degrees of freedom) were obtained directly from the 3DCM model. Some liner strain results for the pretest analysis of the M/S were shown in Figure 7-5. The hot spots for this region are near the vertical T-anchor terminations and the thickened insert plate surrounding the penetration group.

The posttest analysis effort for the M/S penetration began with detailed checking of model geometry, but no changes to the M/S model were found to be necessary, other than updating the applied displacement versus pressure histories. These displacement histories were obtained from 3DCM posttest Model 9, the final 3DCM analysis which gave radial displacement history at the 180 degree azimuth, agreeing well with the test results.

Posttest analysis strain contour results are shown in Figures 7-40 through 7-44. The figures show a little larger strains than in the pretest analysis but still not large enough for a liner tearing prediction. At 3.3 Pd (the end of the LST), the strains around the edge of the liner insert collar are between 2% and 3%. As shown in Section 7.5, this agrees fairly well with liner strain measurements taken during the LST.

After studying the F/W geometry in the posttest phase of the project, it was determined that a F/W penetration model would essentially consist of a scaled-down version of the M/S model, with the same displacement histories applied. Because of the similarities between the M/S penetration model and an F/W model, the posttest studies did not analyze the F/W model. Instead, the results of the posttest M/S model analysis were assumed to represent the F/W penetrations, as well. Comparisons to test measurements at both the M/S and F/W locations are made in Section 7.5.

7.5 M/S and F/W Results and Comparisons with the Test

Figure 7-45 shows the M/S penetration geometry and the strain concentration locations predicted in the pretest work. Similar conditions exist at the F/W penetrations, as shown in Figure 7-46. An additional concentration location not specifically called out in Figure 7-45 is the liner-to-collar transition at the 3:00 and 9:00 positions of the penetration group (using a clock-face analogy). All of these strain concentration locations were well-instrumented for the LST, as shown in Figure 7-47. The figure also shows where tears were observed, and highlights gages at strain concentration locations that are compared to analysis. Strain versus pressure histories for all of the M/S and F/W liner strain gages are plotted in Figures 7-48 and 7-49. It is interesting to note the wide variation in peak strain measurements, even at locations that are theoretically identical; for example, locations 4 and 14 at the 9:00 and 3:00 positions of the M/S. Gage 14 measures twice as much as 4, even though nominal geometric conditions are the same. Of course, there are many contributing factors to these differences, most significantly, variations in as-built conditions–slight variations in liner thickness (due to manufacturing and weld repair grinding) from one side to the other, gage placement relative to the collar/weld, material properties (including welding heat effects), etc. Also note that many of the highest liner strains recorded anywhere on the model during the LST are near the M/S (e.g., 4.6% for gage 19) and the F/W (e.g., 6.4% for Gage 33).

Finally, it is worth noting that the highest strain measurements can, but do not always, correspond to tear locations. Examples supporting this are:

Gages 40 and 41, which are close to the long tear (tear 3) at the F/W, have relatively low strains. Gage 40, in particular, shows evidence of rising strain prior to tear occurrence; then, starting at about 2.9 Pd, declining strain from stress relief caused by the tear.

Gage 33, on the other hand, may have been located near the tip of the crack of tear 3. Gage 33 shows quite low strain up to 3.1 Pd and then a sudden jump. This supports a hypothesis that tear 3 initiated at a pressure of 2.9 Pd at the 7:30 o'clock position (midpoint of the tear) and then between 2.9 Pd and 3.1 Pd, the tear ran along a band of equally high strain (as evidenced by analysis) around the perimeter of the thickened collar and up to nearly the 9 o'clock position. When it reached that position, Gage 33 shot up due to localized crack tip effects.

Figure 7-50 shows the locations extracted from the local penetration analysis to compare liner strains with the M/S and F/W measurements. The locations are labeled A, B, C, and D. Figures 7-51 through 7-54 compare the M/S and F/W liner strain gages that correspond to these locations. These figures show that the posttest analysis of the M/S penetrations captures the strains measured in the LST quite well for both the M/S and F/W penetrations. Note that the free-field hoop strains near the F/W are 10% - 15% lower than at the M/S (based on measured radial displacement), explaining why measured strains near the M/S were initially larger than near the F/W. It is likely, however, that the occurrence of tears at the F/W versus non-tears at the M/S is due to the more extensive weld repair in the F/W area.

7.6 Conclusions on Local Penetrations Analysis

Liner strains measured in the vicinity of the E/H penetration collar were much lower than predicted by pretest analysis. Since the predicted high strain locations were fundamental to the failure predictions, significant effort was made to reanalyze the E/H model after the test. With a set of changes that included conversion of the model to the other side of the hatch (away from the buttress) and a correction to the vertical stress boundary condition, posttest E/H model's hoop expansion behavior correlated much better with measured global displacement behavior. The hoop deformation correlation-to-pressure function introduced in the pretest work was no longer needed.

Two hypotheses were developed and subsequently proven by the posttest analyses.

Hypothesis 1: The liner in the E/H area had a high degree of bond-friction with concrete, preventing slippage of the liner relative to the concrete; relative slippage is required for elevated strains to develop near local discontinuities like T-anchors and stiffeners.

Hypothesis 2: Formation of a major crack near the edge of the E/H embossment further concentrated the liner strains at the edge of the embossment.

The hypotheses were examined by several analysis cases. They showed that by preventing relative slip between liner and concrete, the overall behavior of the system (concrete strains, tendon strains, liner strains away from the hatch) remained the same, but the elevated strains close to the collar were eliminated. In the final case, integration point directed cracks were introduced to one row of elements and a discrete crack was formed by adding double rows of nodes along an assumed crack line. The double row of nodes was not extended all the way through the wall section due to difficulties with modeling reinforcement. However, just unzipping the first element layer to simulate a discrete crack partway through the wall thickness created a liner elevated strain phenomenon. The mild strain concentration that was simulated in Case E coincides, in location, with rat-hole weld seam details, and in the LST, numerous tears occurred at these details. Based on results of detailed liner rat-hole (weld-seam) analysis (Chapter 8), the additional strain concentration associated with these details is enough to make a tear prediction at the edge of the embossment. This shows that with discrete crack modeling and local rat-hole modeling, a liner tear could have been predicted to occur as early as 2.8 Pd. Based on the evidence provided by liner strain gages and acoustic monitoring, one of the tears along this embossment edge may have even occurred as early as 2.5 Pd. The posttest E/H study thus presents a modeling strategy with results that correlate well with the LST measurements and observations. A somewhat higher strain prediction might be possible if a discrete crack (separate rows of nodes) were propagated all the way through the concrete wall, but this would require a change in rebar modeling strategy–one that is probably not practical even for very detailed analytical evaluations of containments.

The M/S and F/W penetration hot spots (both analysis and LST observations) occurred near the vertical T-anchor terminations and the thickened insert plate surrounding the penetration group, e.g. at the 3:00 and 9:00 positions. For the posttest analysis effort, no changes to the M/S model were necessary, other than updating the applied displacement versus pressure histories that were obtained from 3DCM posttest Model 9, the final 3DCM analysis, which gave radial displacement history at the 180 degree azimuth, agreeing well with the test results. After studying the F/W geometry in the posttest phase of the project, it was determined that the F/W penetration model was so similar to the M/S penetration model that it was not necessary to pursue analysis of the F/W model; the posttest M/S model analysis was assumed to represent the F/W penetrations, as well.

Several noteworthy observations could be made from the well-instrumented M/S and F/W locations that are relevant to penetration response prediction and evaluation.

1. Many of the highest strains recorded during the LST are near the M/S (e.g., 4.6% for Gage 19) and the F/W (e.g., 6.4% for Gage 33).

2. There is a wide variation in peak strain measurements, even at locations that are theoretically identical. Of course, there are many contributing factors to these differences: slight variations in liner thickness (due to manufacturing and weld repair grinding), gage position relative to the collar/weld, material properties (including welding heat effects), etc.

3. The highest strain measurements can, but do not always, correspond to tear locations. Examples supporting this are:

    A. Gage 40, near the long tear (tear 3) at the F/W, shows evidence of rising strain prior to tear occurrence; then, starting at 2.9 Pd, declining strain due to the stress relief caused by the tear.

B. Gage 33, on the other hand, located near the crack tip, shows quite low strain up to 3.1 Pd and then a sudden jump. This supports a hypothesis that tear 3 initiated at a pressure of 2.9 Pd at about the 7:30 position (midpoint of the tear) and then between 2.9 Pd and 3.1 Pd, the tear ran along a band of equally high strain (as evidenced by analysis) around the perimeter of the thickened collar and up to the 9:00 position, at which time Gage 33 shot up due to localized crack tip effects.

Plots comparing the analysis to the M/S and F/W liner strain gages show that the posttest analysis of the M/S penetrations captures the strains measured in the LST quite well for both the M/S and F/W penetrations.

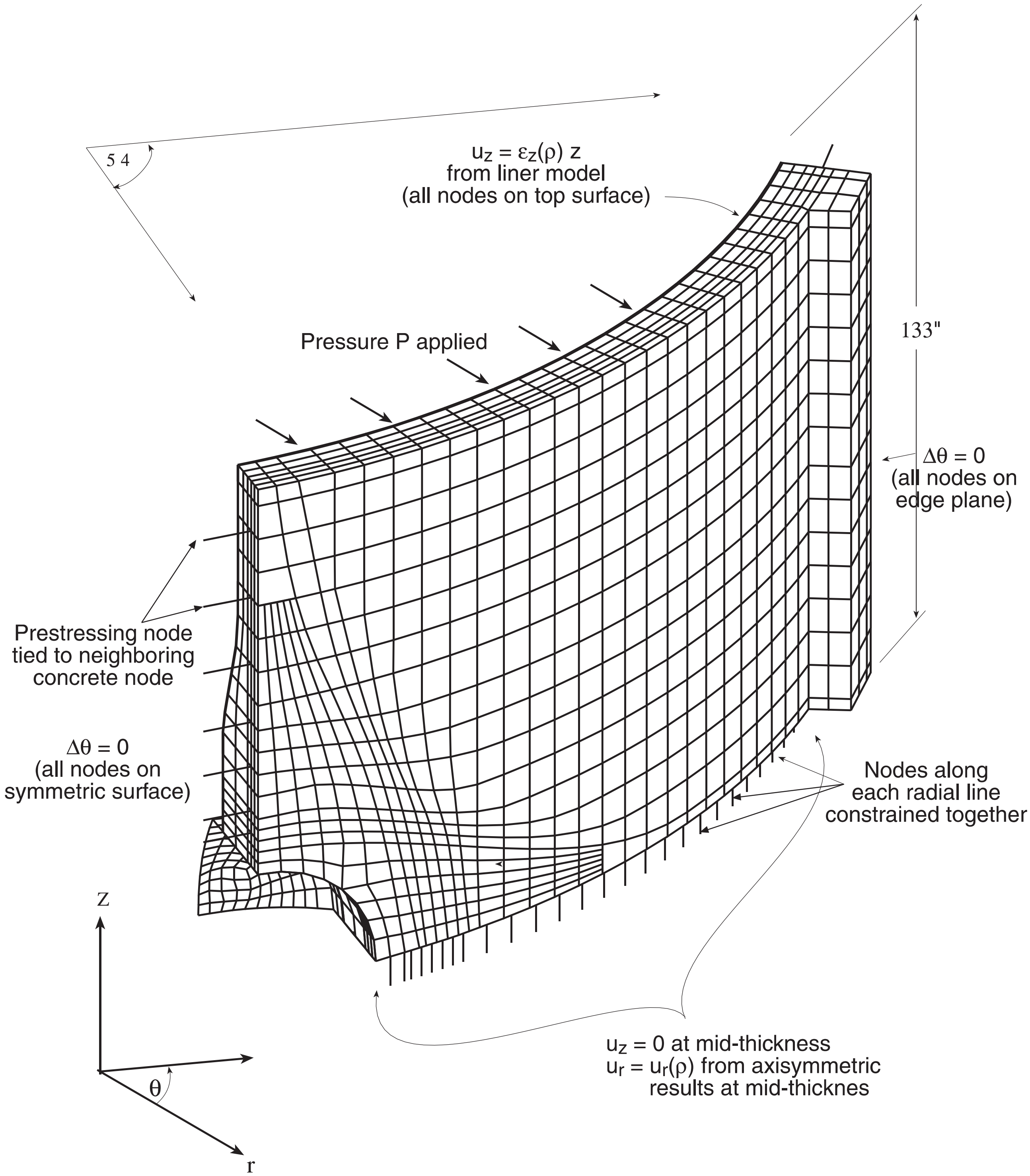

Figure 7-1. Boundary Conditions and Geometry for 3D E/H Model Used in Pretest Analysis [1]

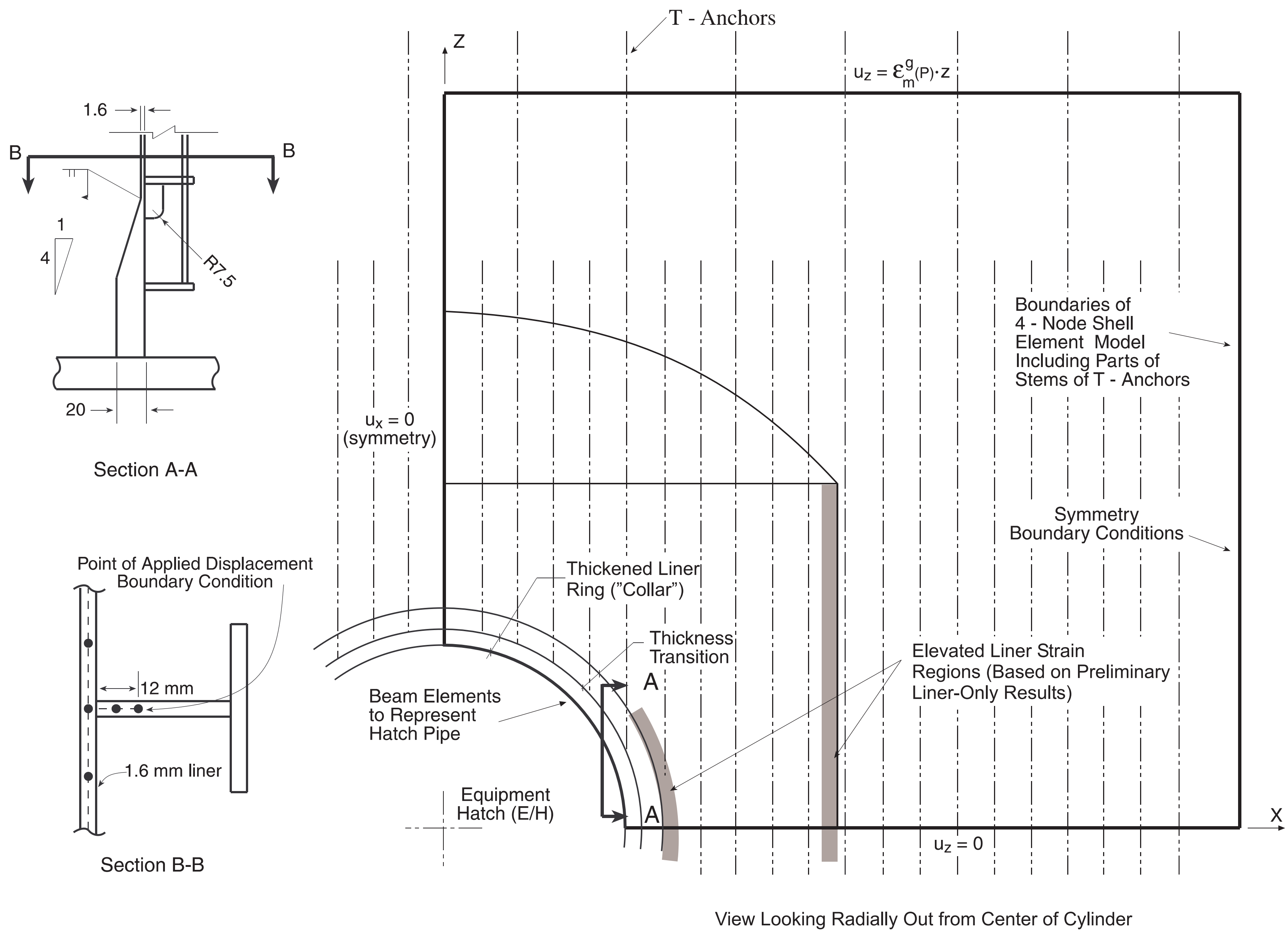

Figure 7-2. Additional Details of Pretest E/H Model (View from Inside PCCV Looking Out Radially)

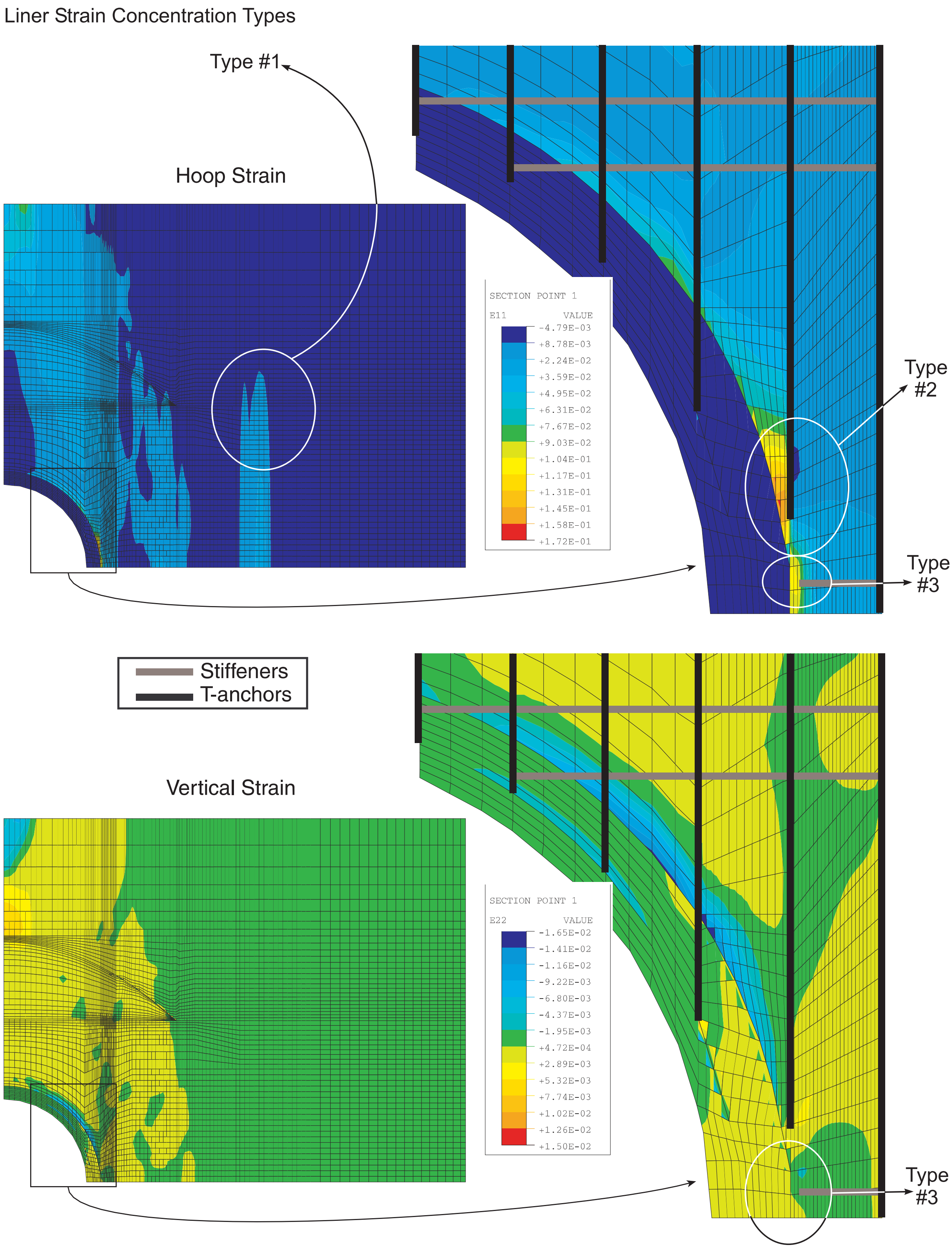

Figure 7-3. Liner Contour Strain Plots at P = 3.2 Pd for E/H from Pretest Analysis [1]

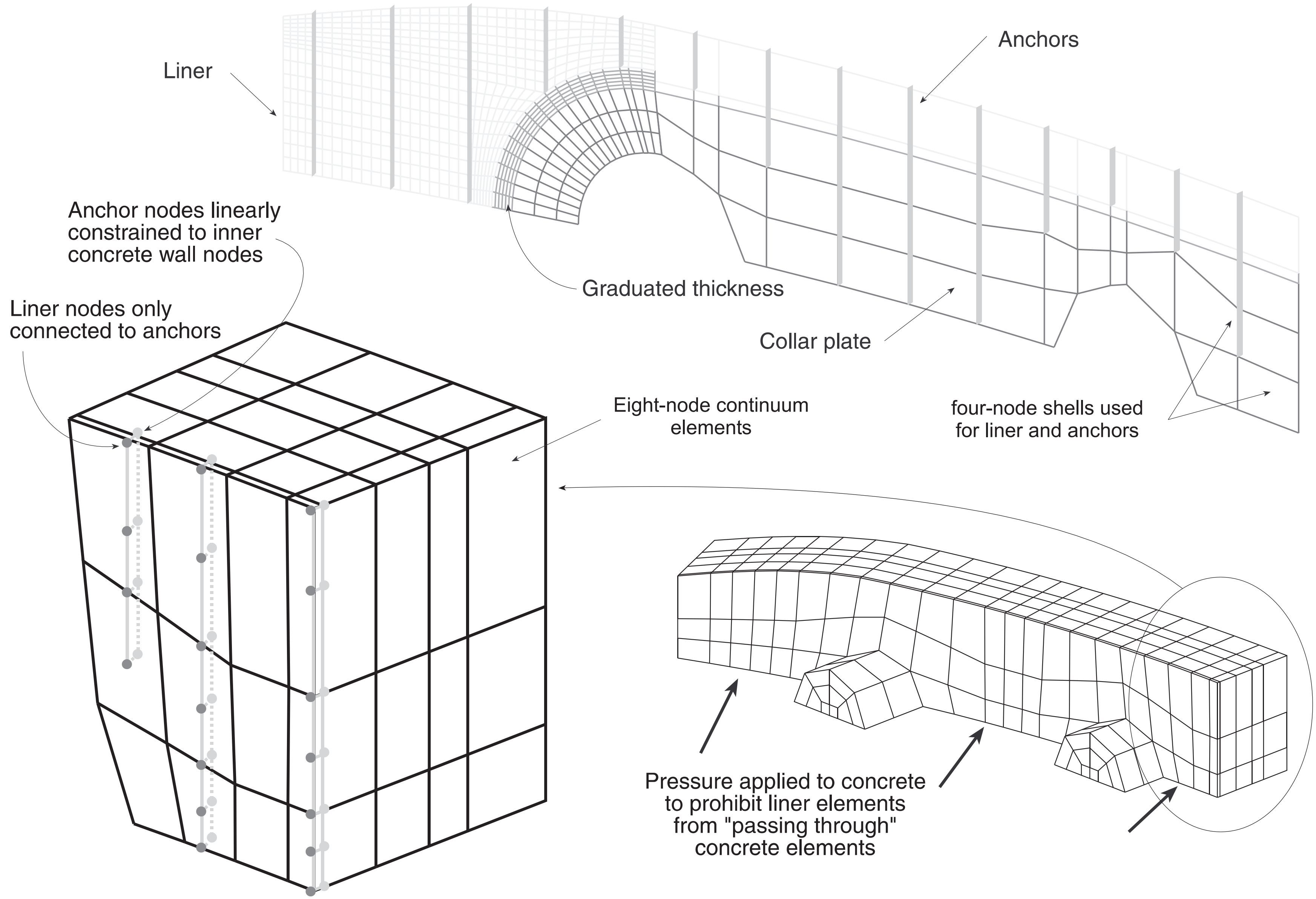

Figure 7-4. M/S Local Model Liner Details from Pretest Analysis

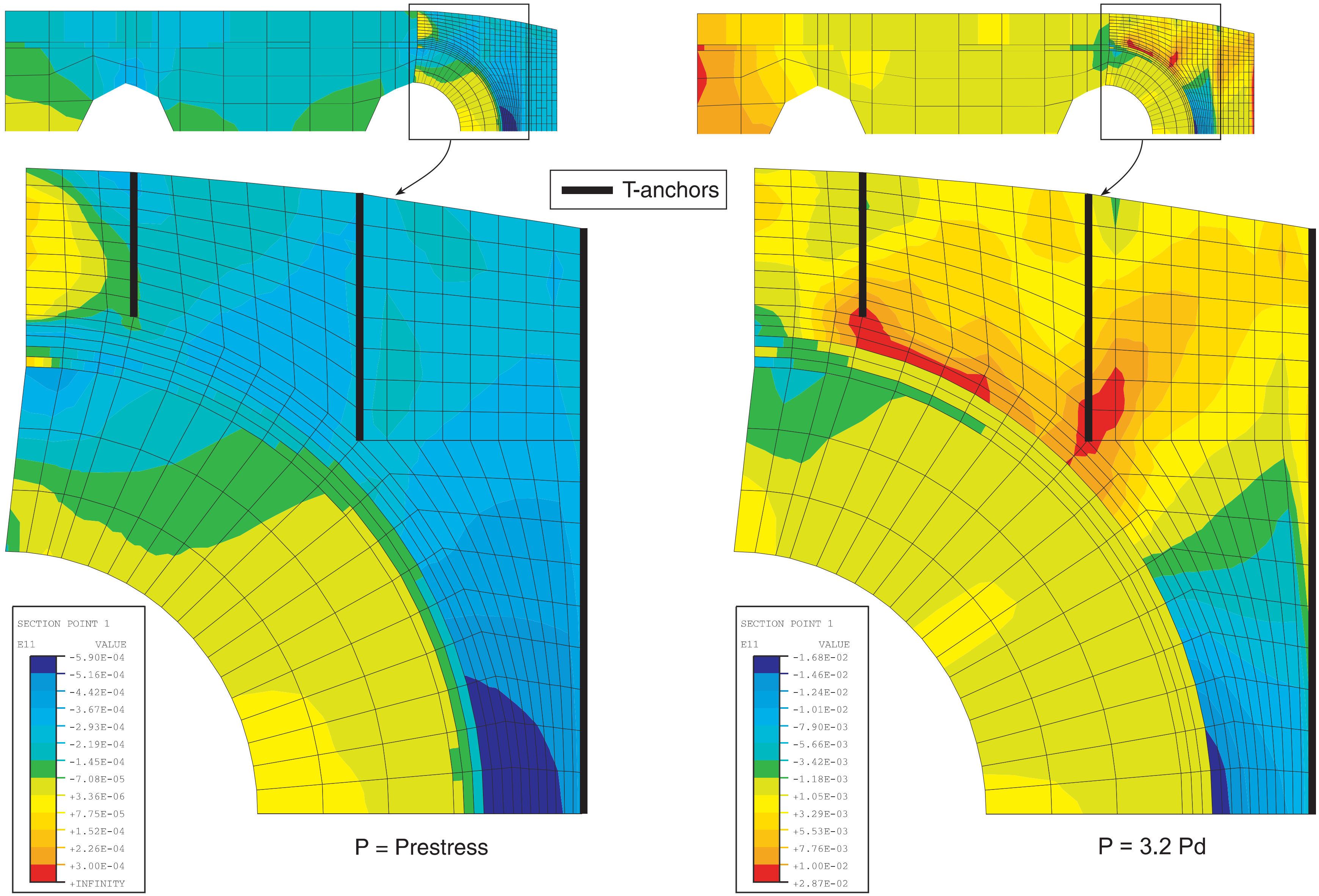

Figure 7-5. Liner Contour Hoop Strain Plots from Pretest M/S Model Analysis

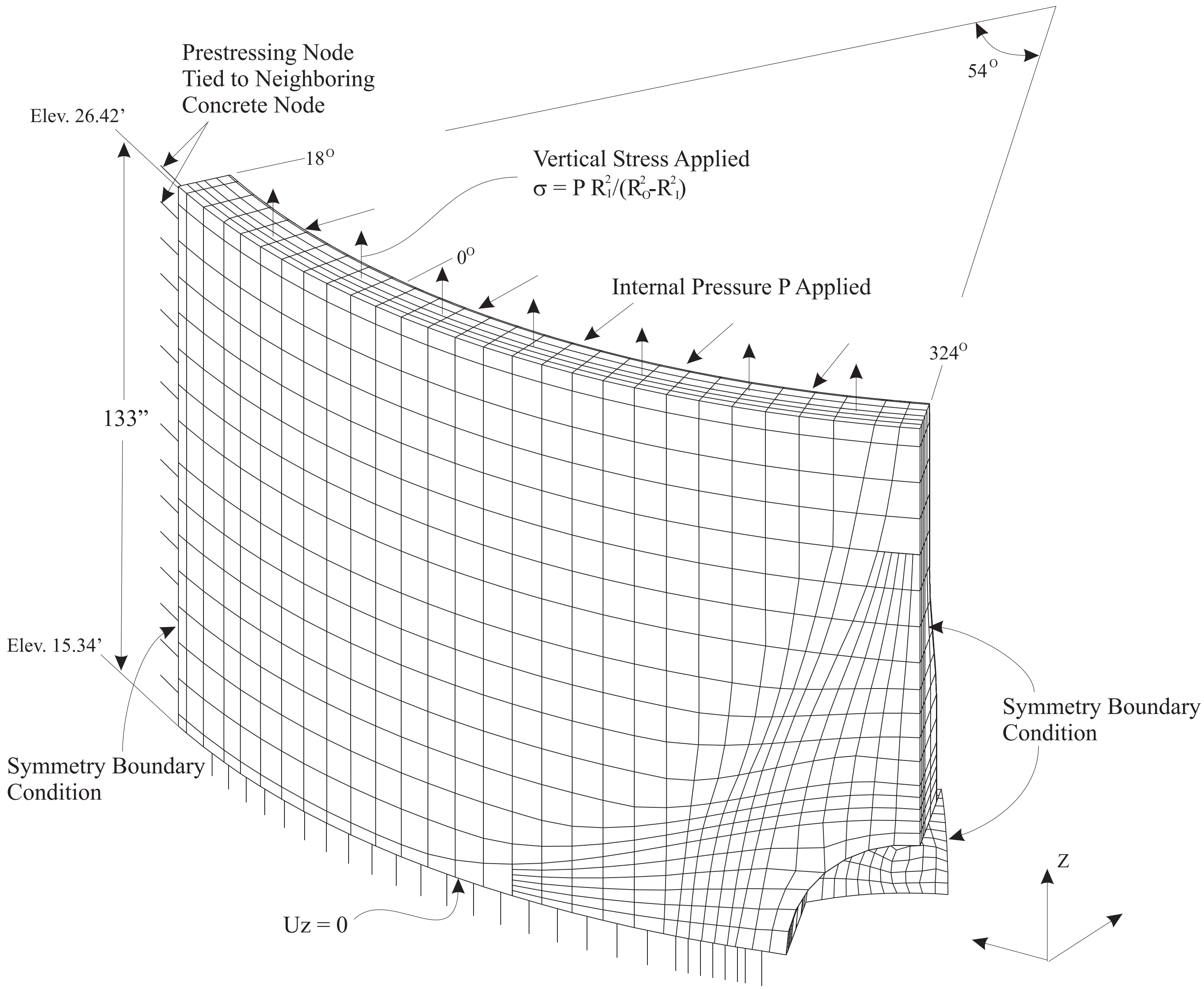

Figure 7-6. Finite Element Mesh and Boundary Conditions for 3D E/H Model

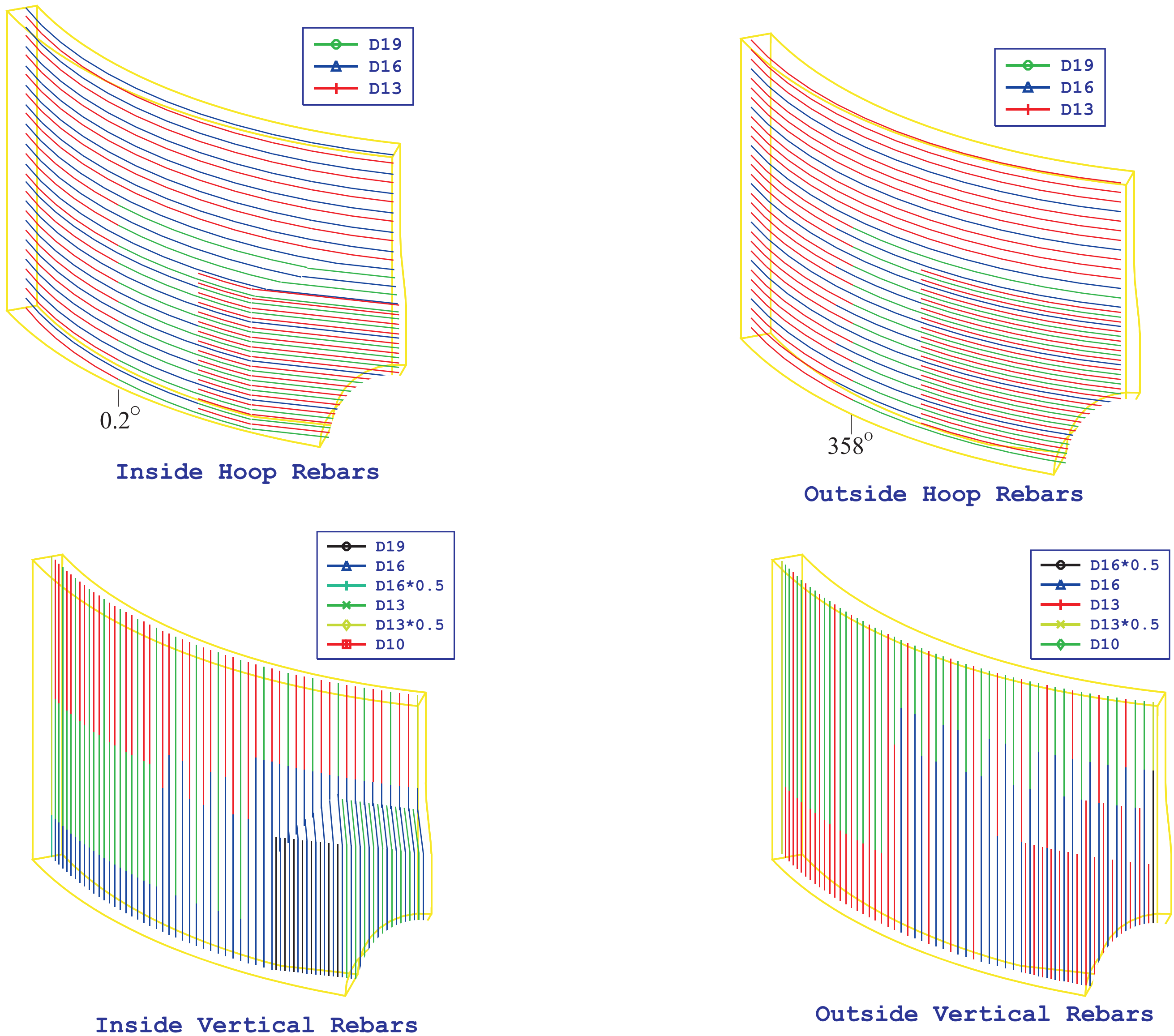

Figure 7-7. Schematic of Hoop and Vertical Rebars in E/H Region

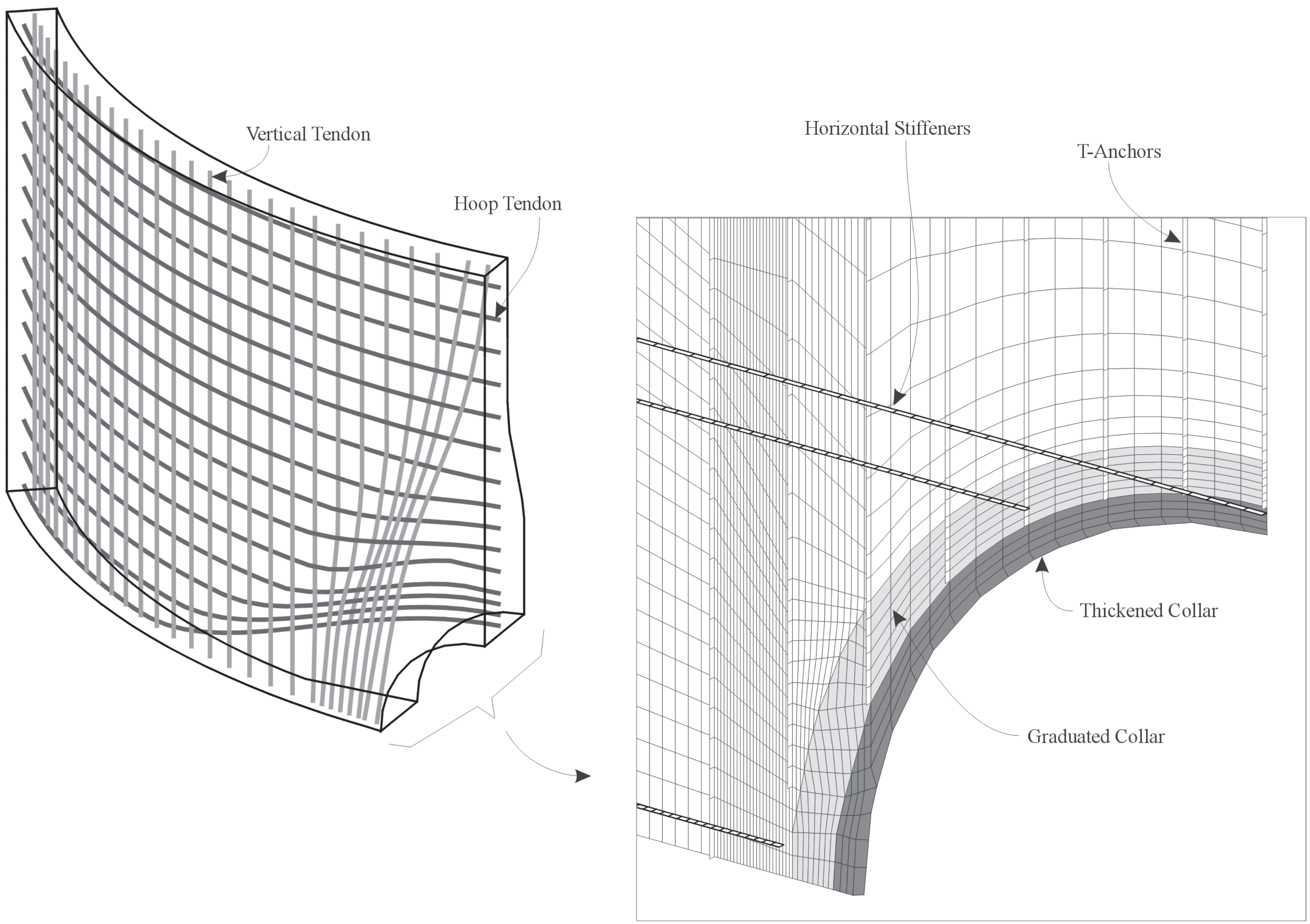

Figure 7-8. E/H Finite Element Model Including Tendons, Liner, Anchors, and Stiffeners

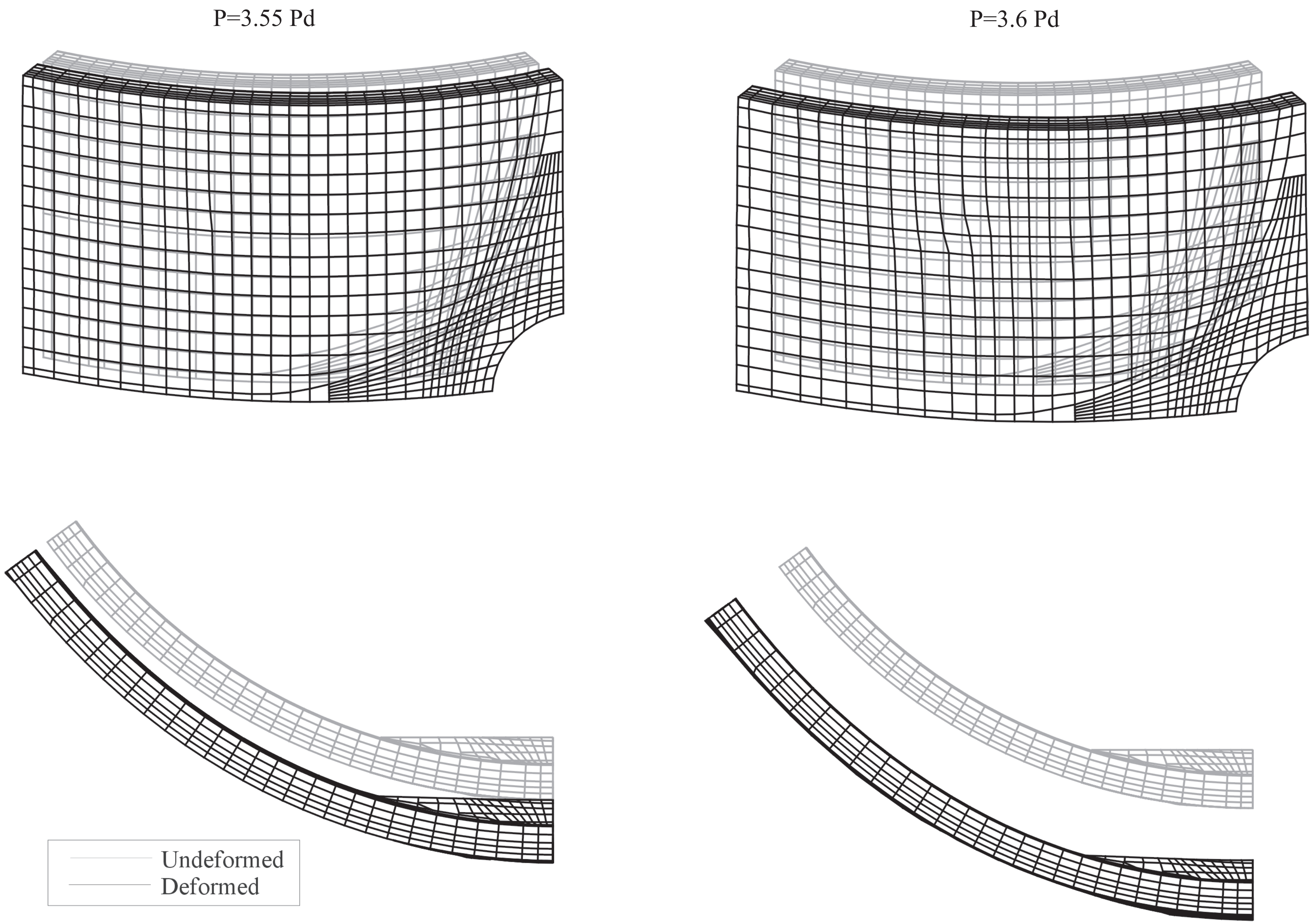

Figure 7-9. Deformed Shape of E/H Mode, Case A (Magnification Factor = 10)

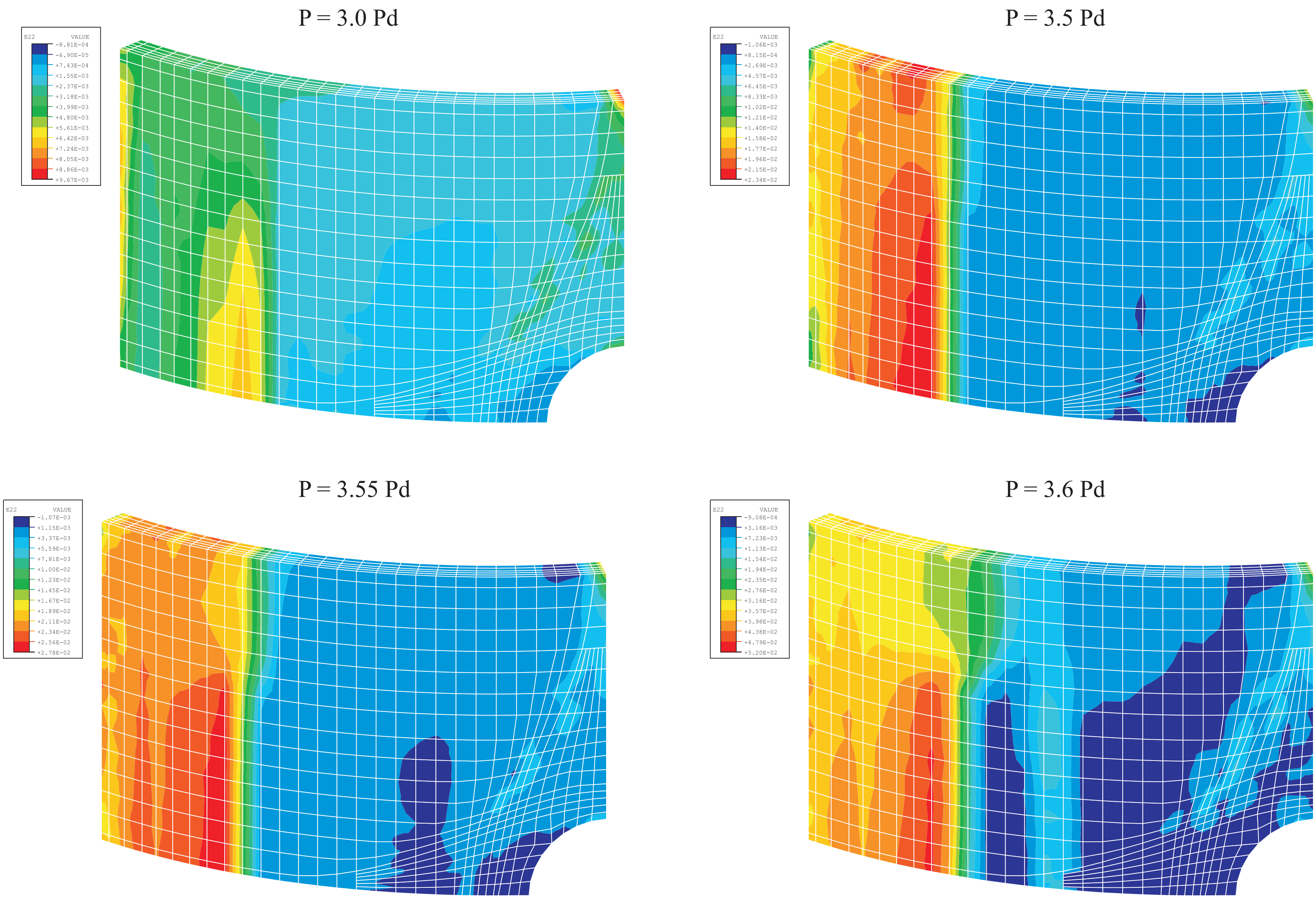

Figure 7-10. Concrete Hoop Strain Contours, Posttest Analysis Case A

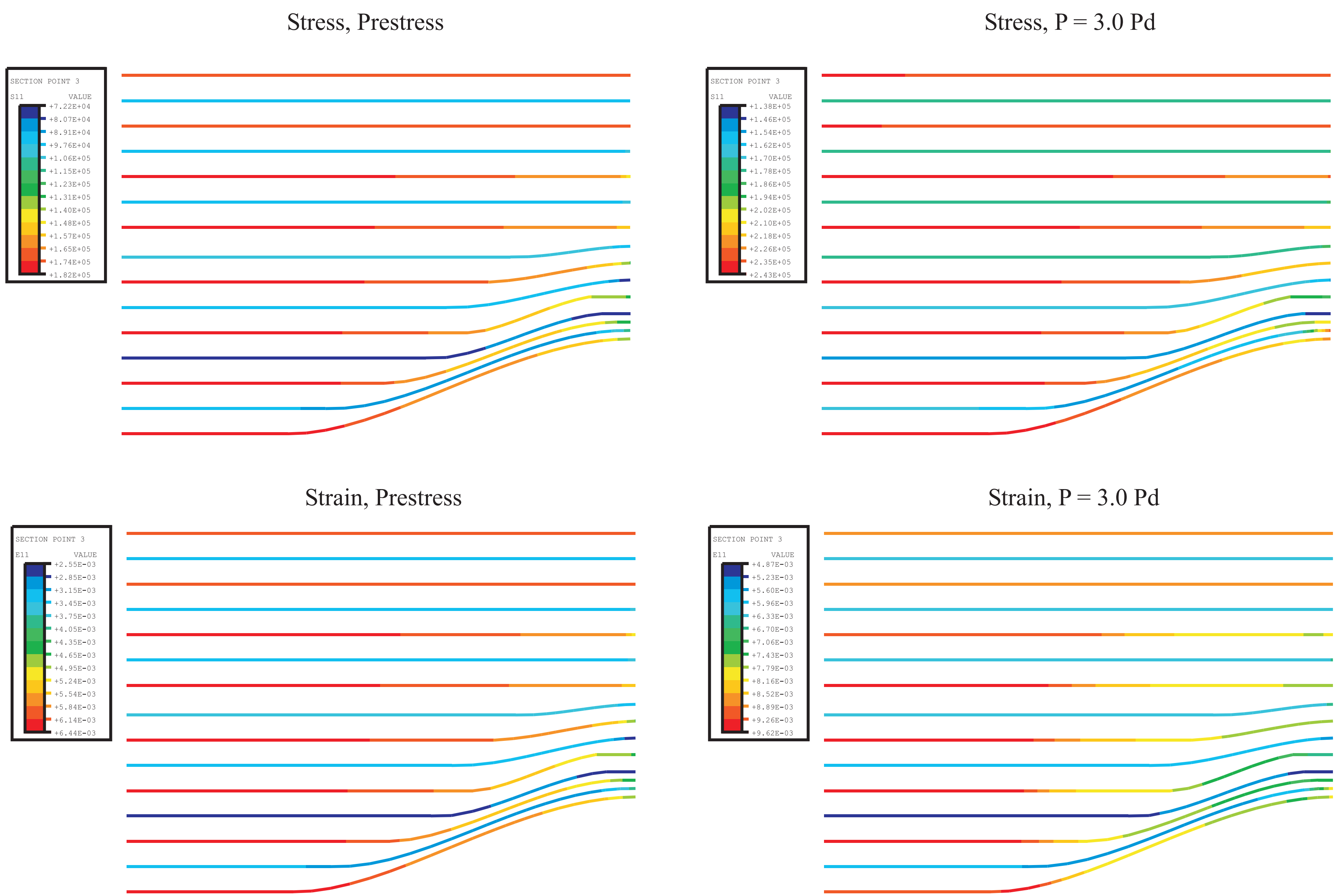

Figure 7-11. Hoop Tendon Stresses and Strains, Posttest Analysis Case A, at Prestress and at 3.0 Pd
(Stresses in psi; multiply by 0.00690 for MPa)

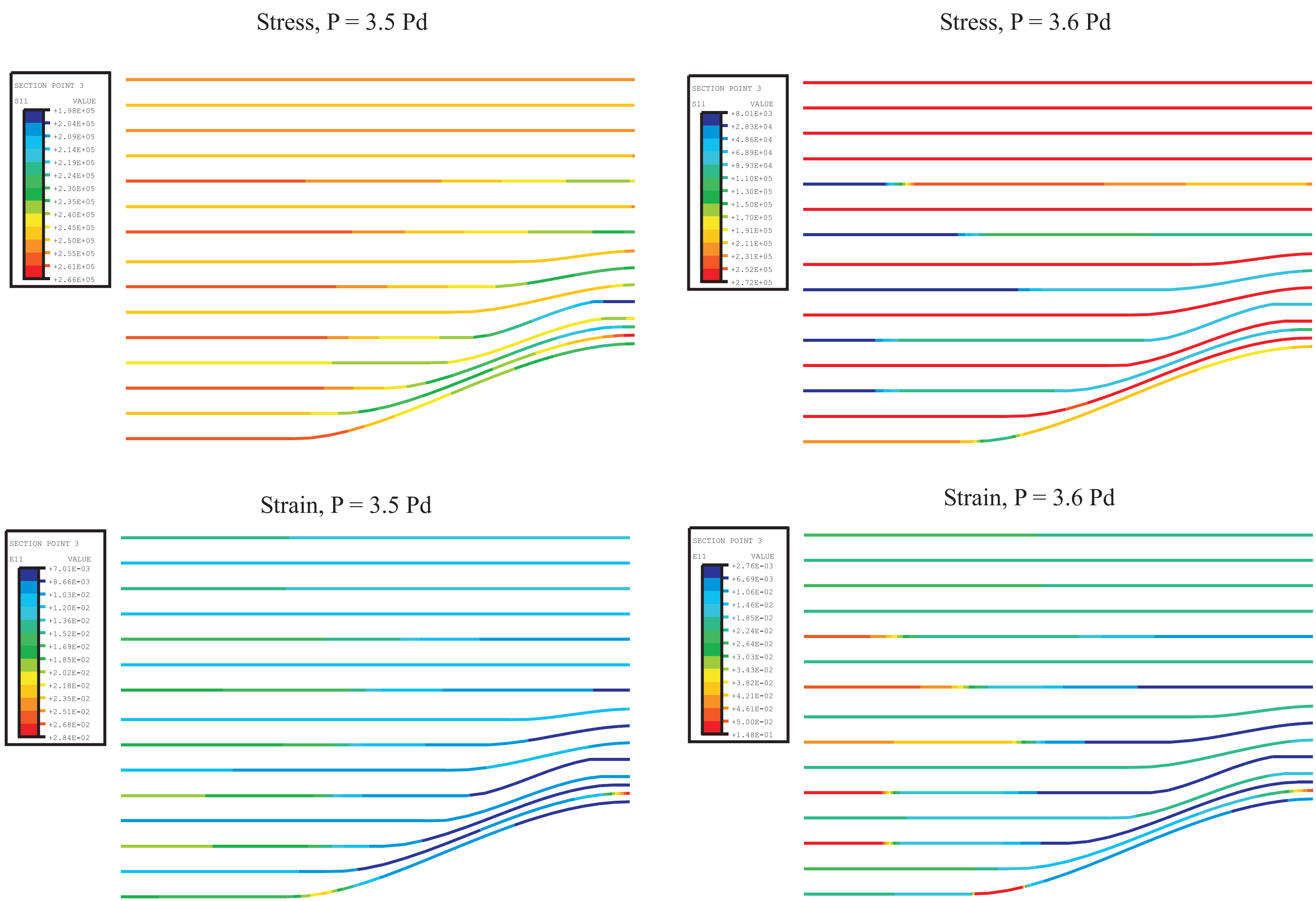

Figure 7-12. Hoop Tendon Stresses and Strains, Posttest Analysis Case A, at 3.5 Pd and 3.6 Pd
(Stresses in psi; multiply by 0.00690 for MPa)

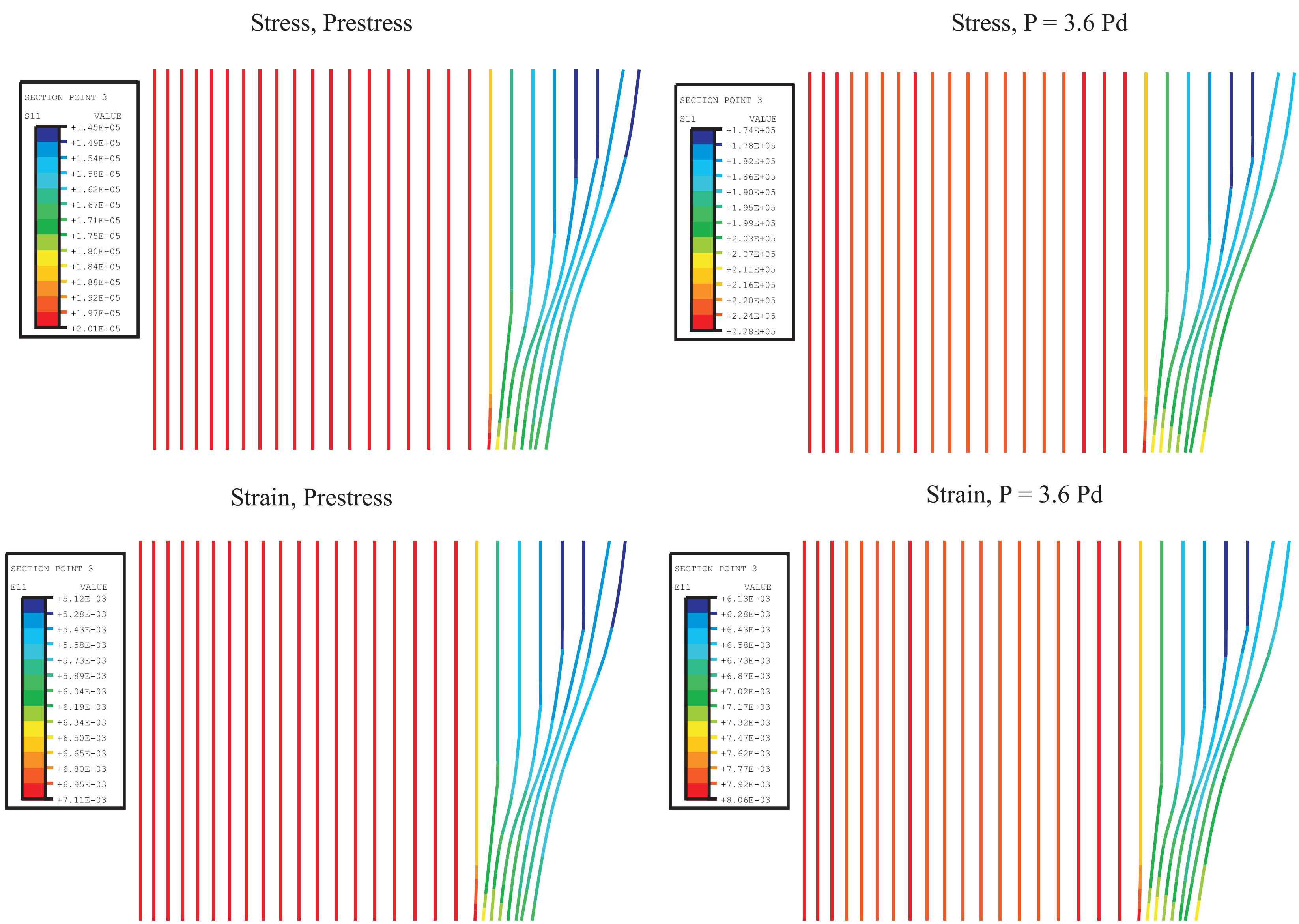

Figure 7-13. Vertical Tendon Stresses and Strains, Posttest Analysis Case A, at Prestress and 3.6 Pd
(Stresses in psi; Multiply by 0.00690 for MPa)

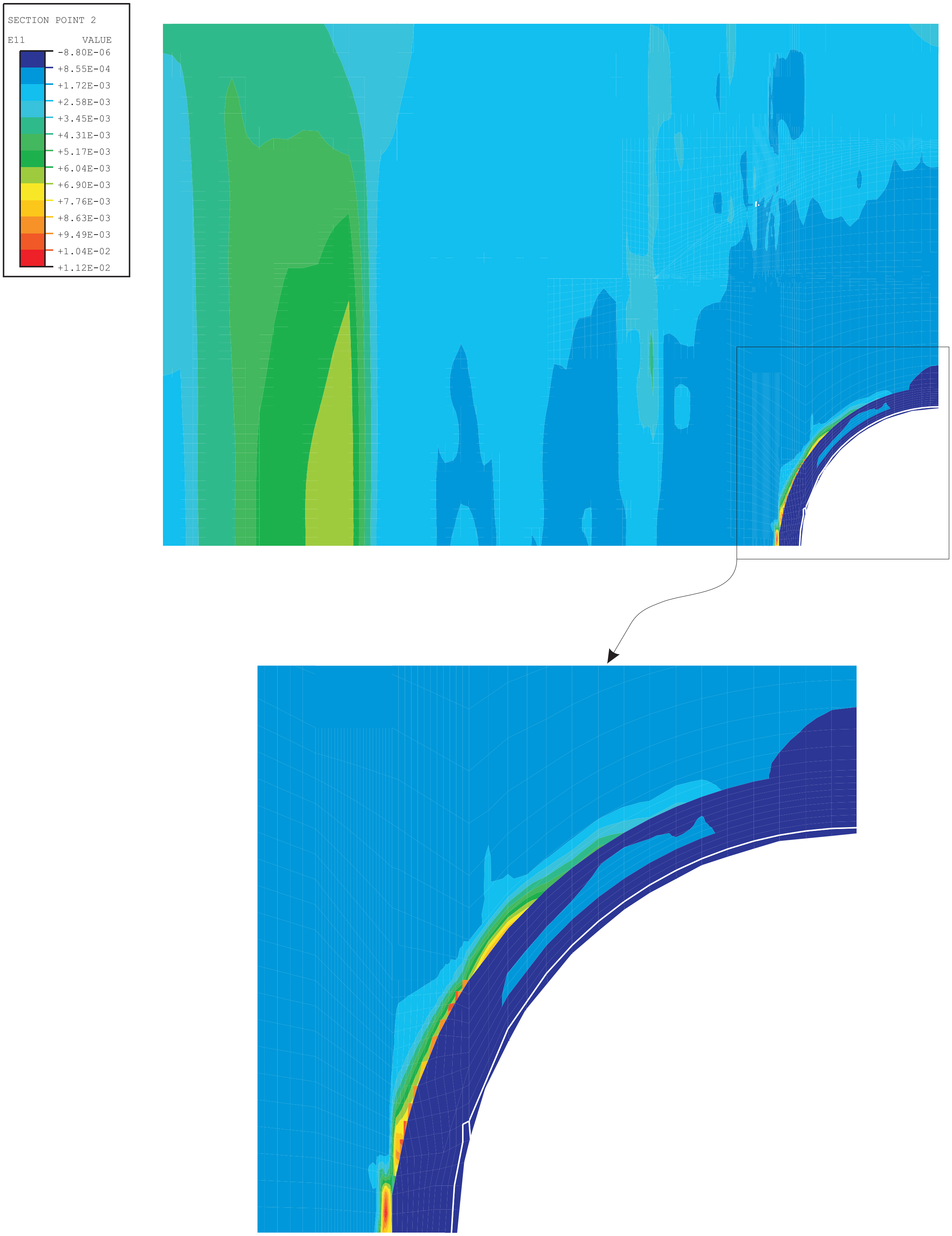

Figure 7-14. Liner Hoop Strains, Posttest Analysis Case A, at 3.0 Pd

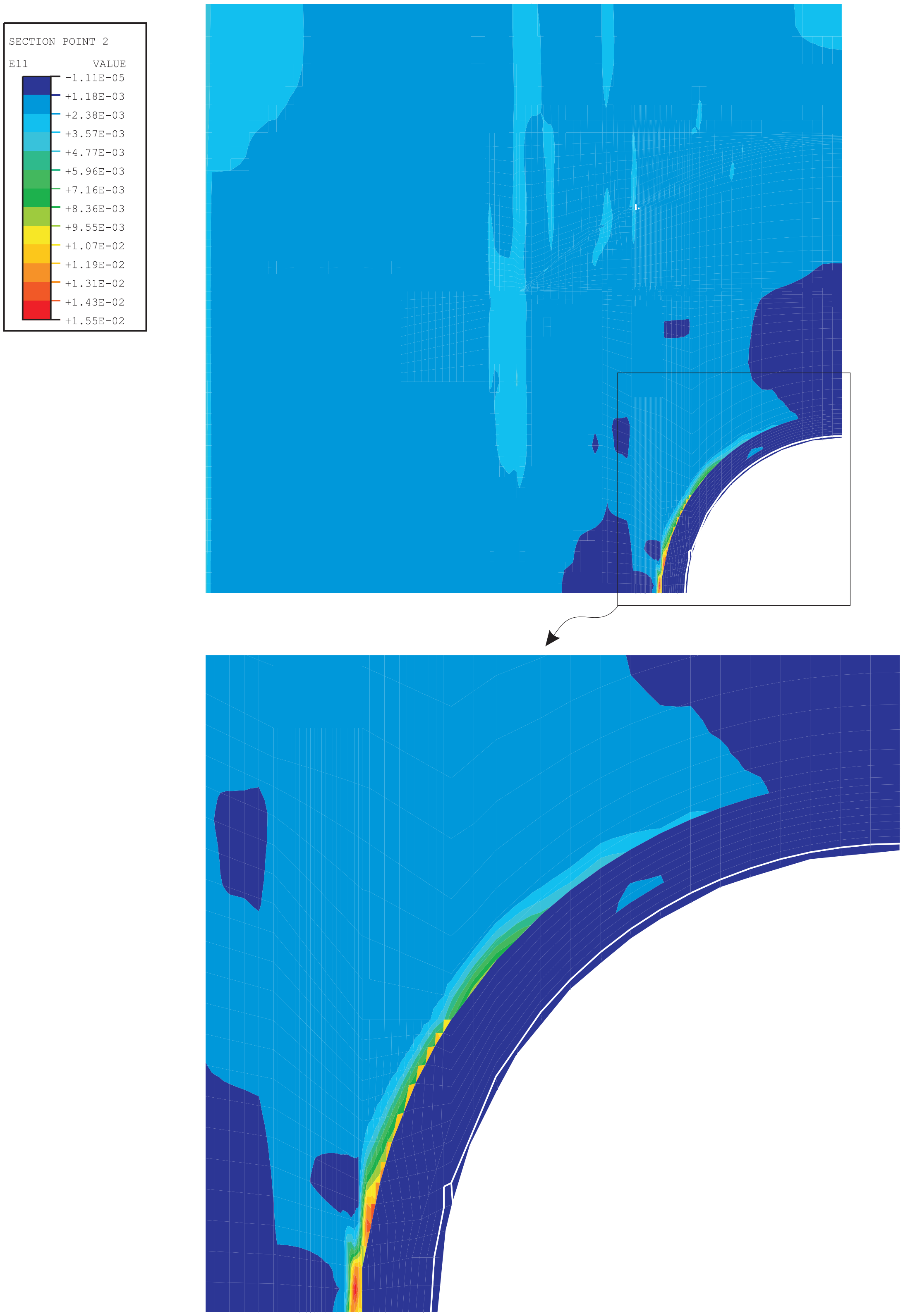

Figure 7-15. Liner Hoop Strains, Posttest Analysis Case A, at 3.2 Pd

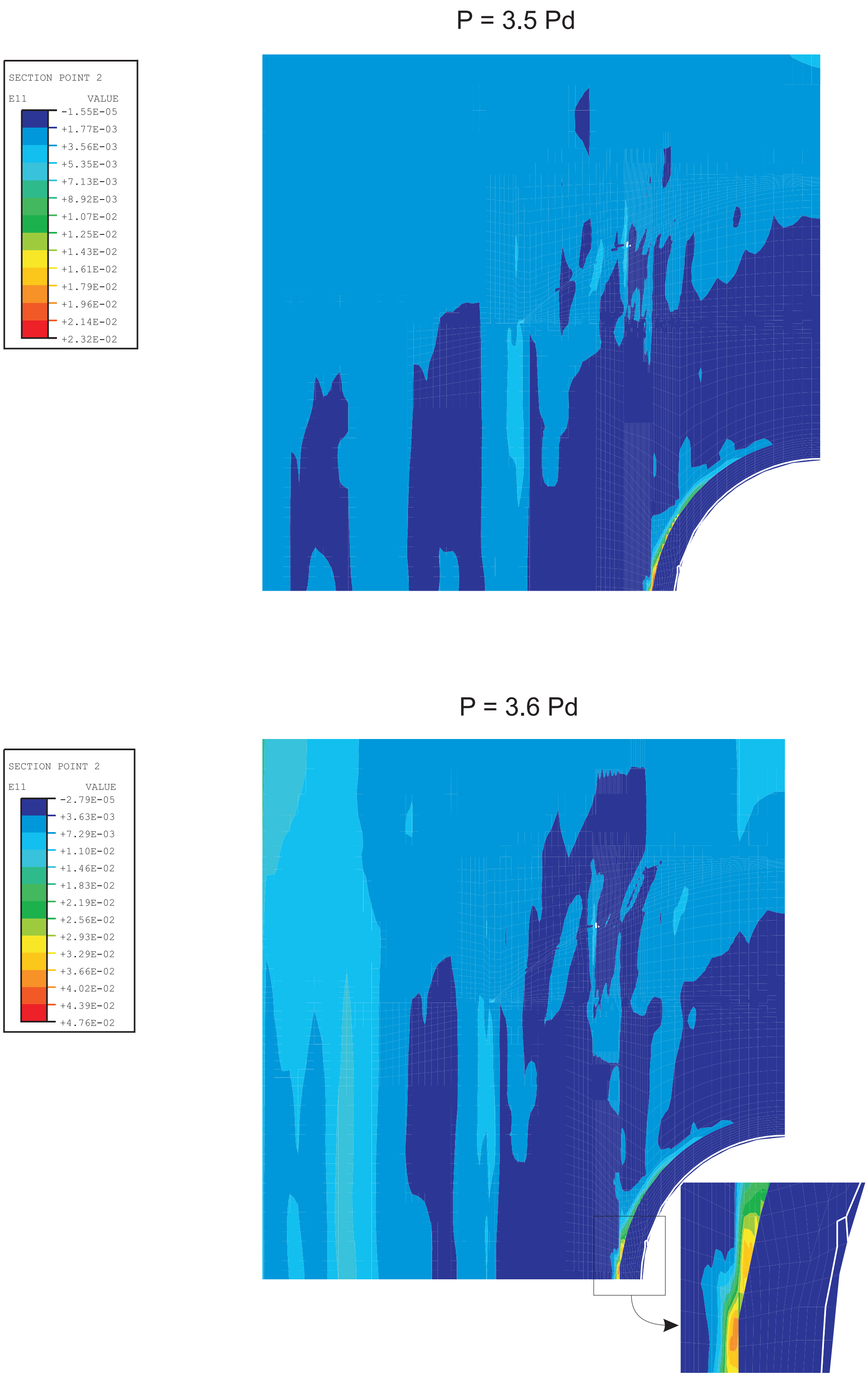

Figure 7-16. Liner Hoop Strains, Posttest Analysis Case A, at 3.5 Pd and 3.6 Pd

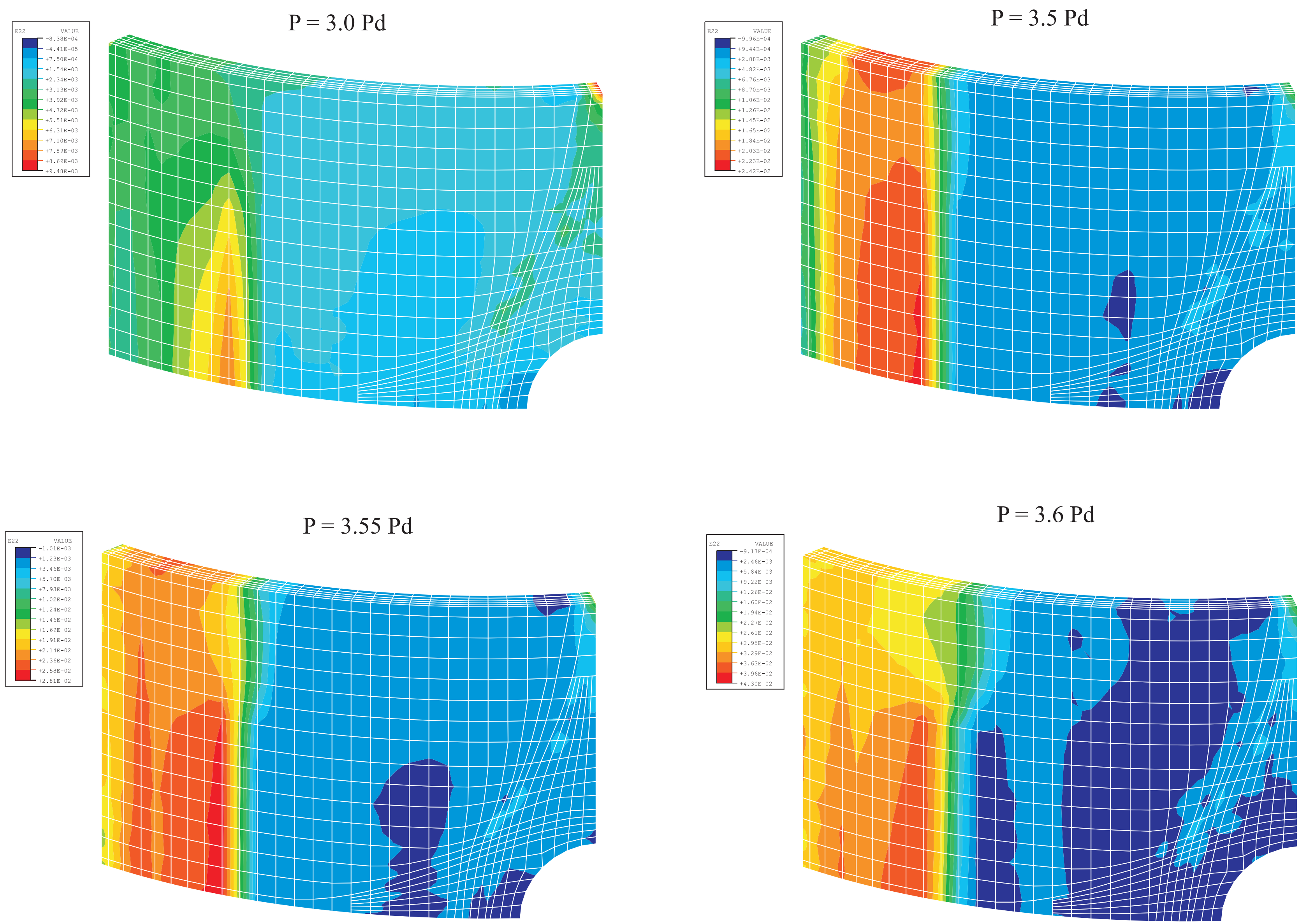

Figure 7-17. Concrete Hoop Strain Contours, Posttest Analysis Case B

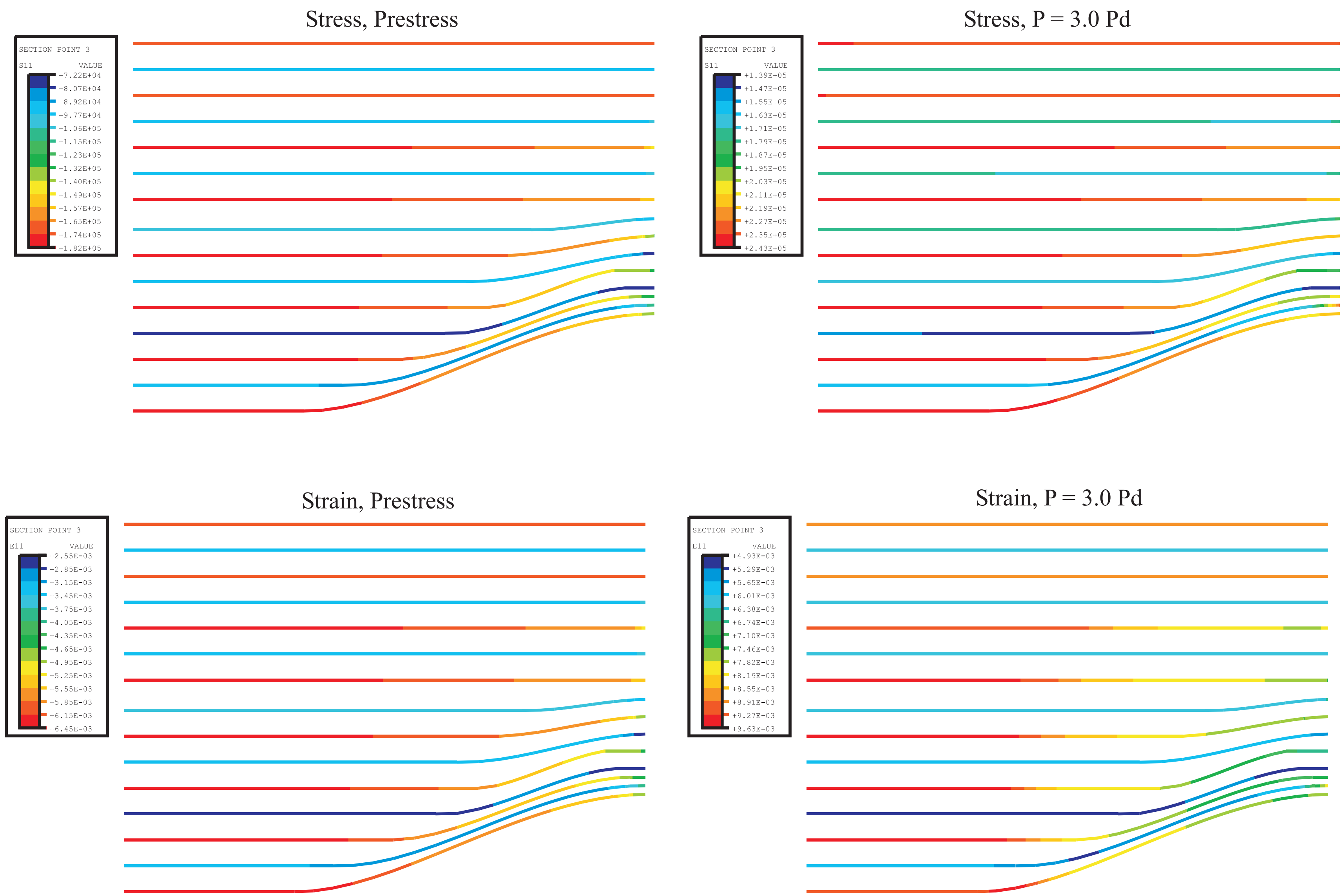

Figure 7-18. Hoop Tendon Stresses and Strains, Posttest Analysis Case B, at Prestress and 3.0 Pd
(Stresses in psi; Multiply by 0.00690 for MPa)

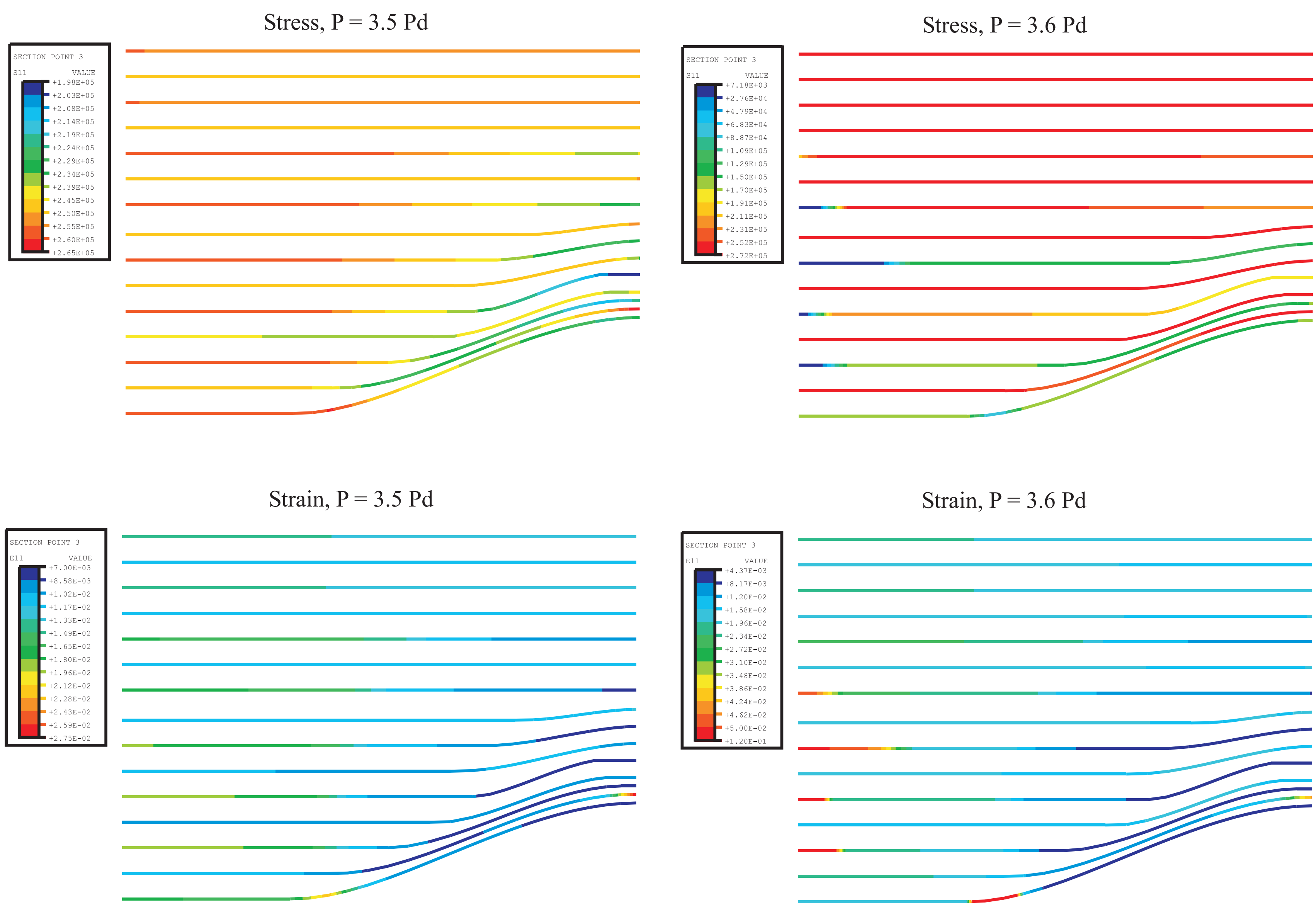

Figure 7-19. Hoop Tendon Stresses and Strains, Posttest Analysis Case B, at 3.5 Pd and 3.6 Pd
(Stresses in psi; Multiply by 0.00690 for MPa)

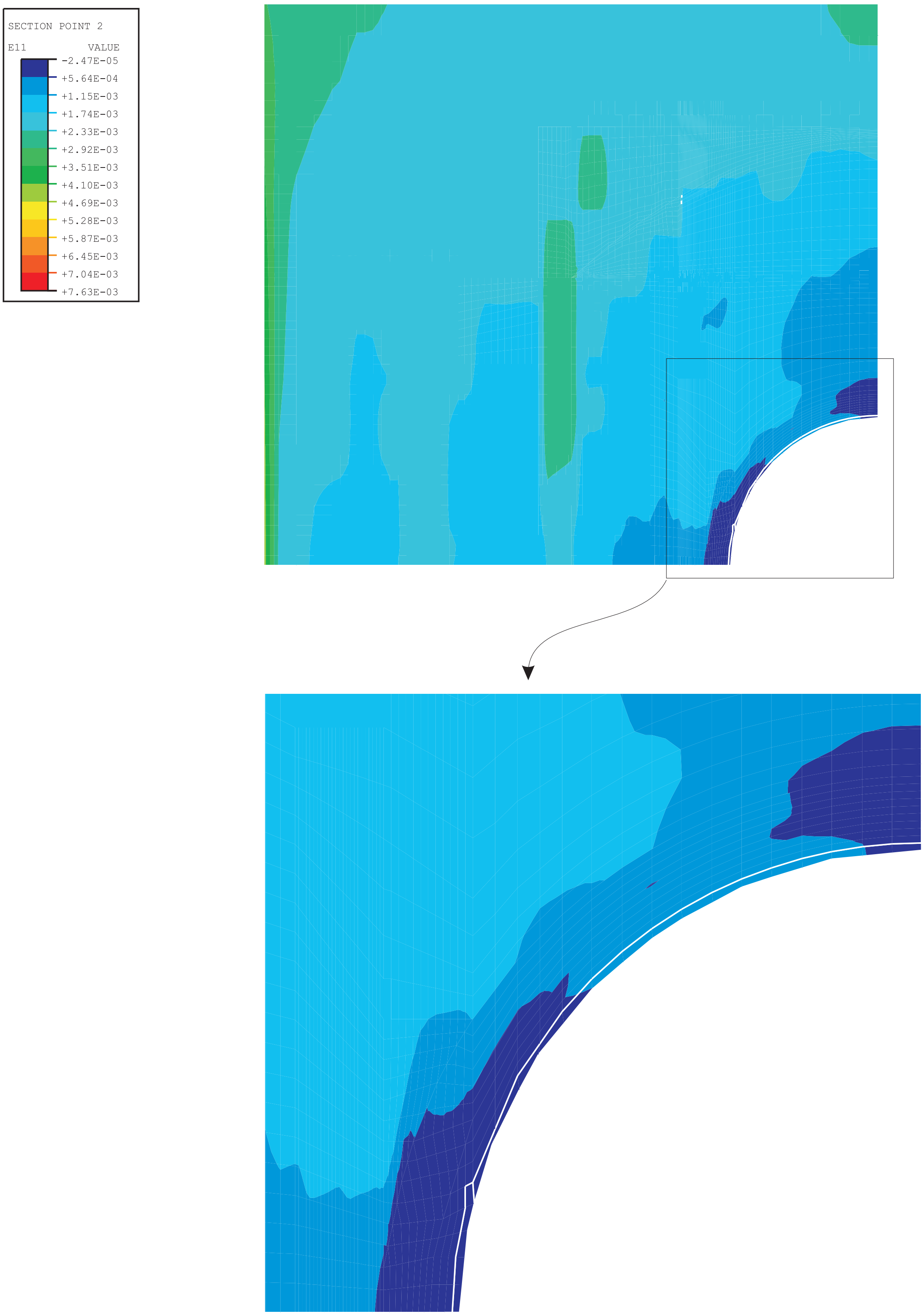

Figure 7-20. Liner Hoop Strains, Posttest Analysis Case B, at 3.0 Pd

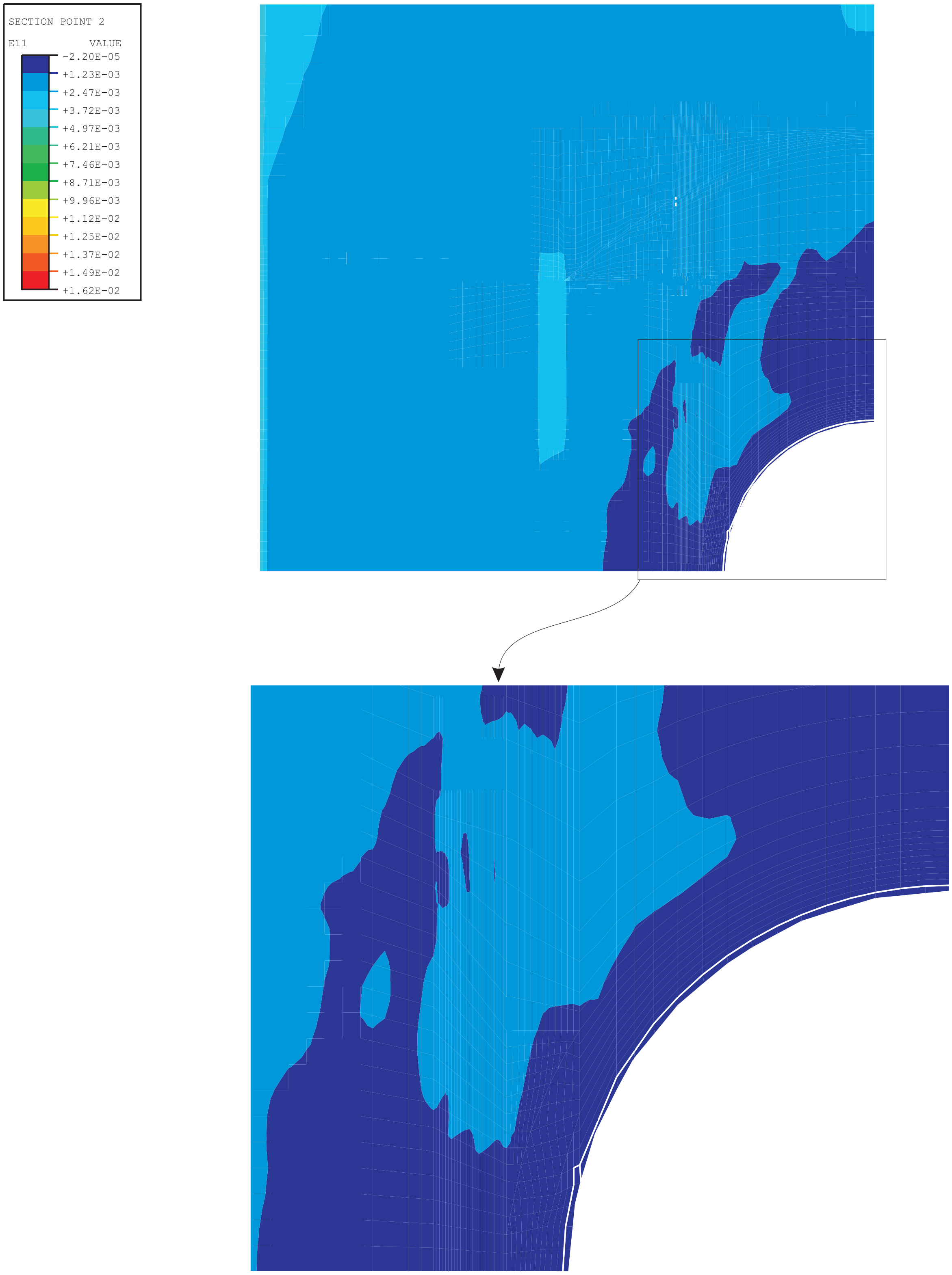

Figure 7-21. Liner Hoop Strains, Posttest Analysis Case B, at 3.2 Pd

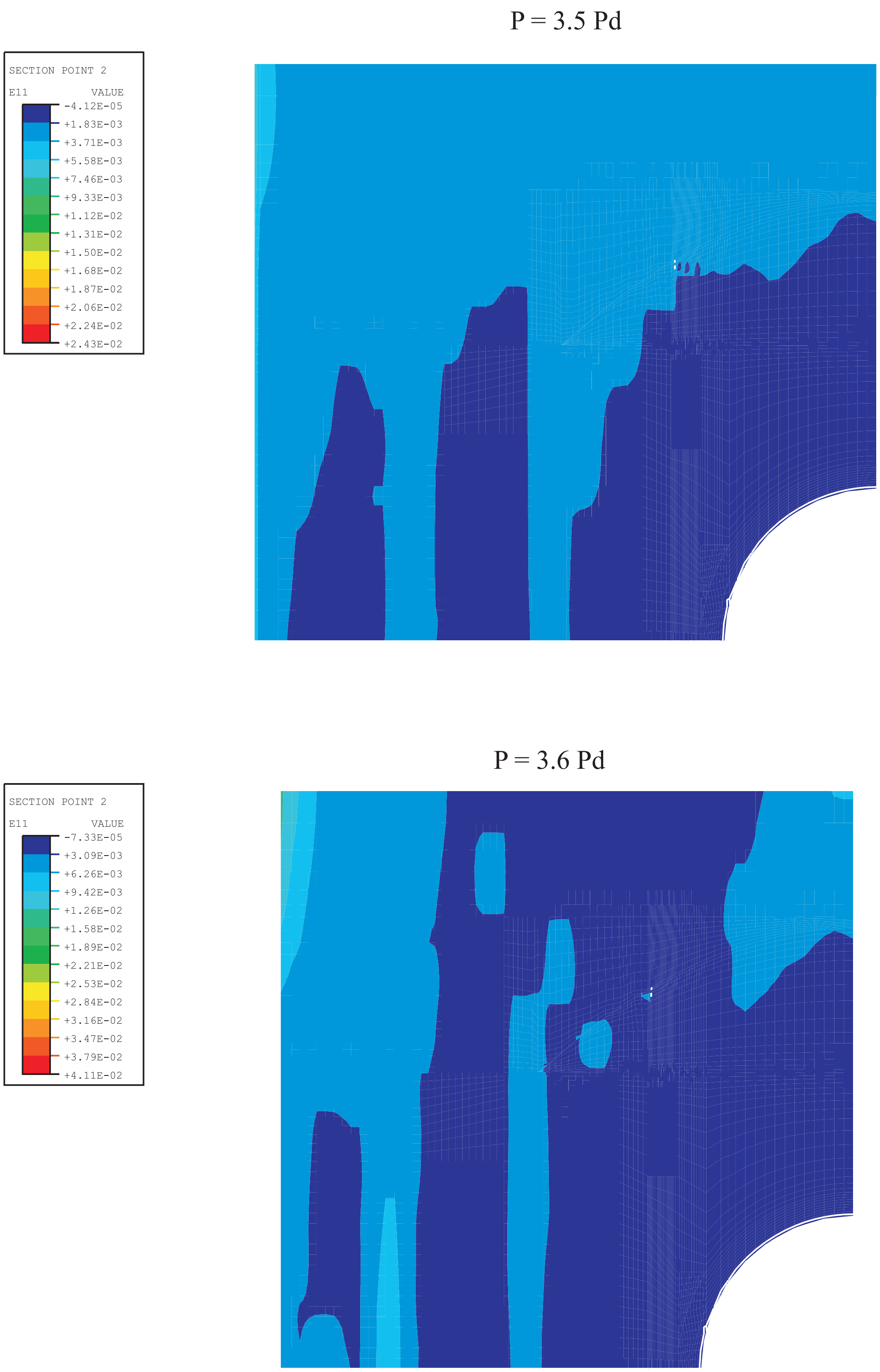

Figure 7-22. Liner Hoop Strains, Posttest Analysis Case B, at 3.5 Pd and 3.6 Pd

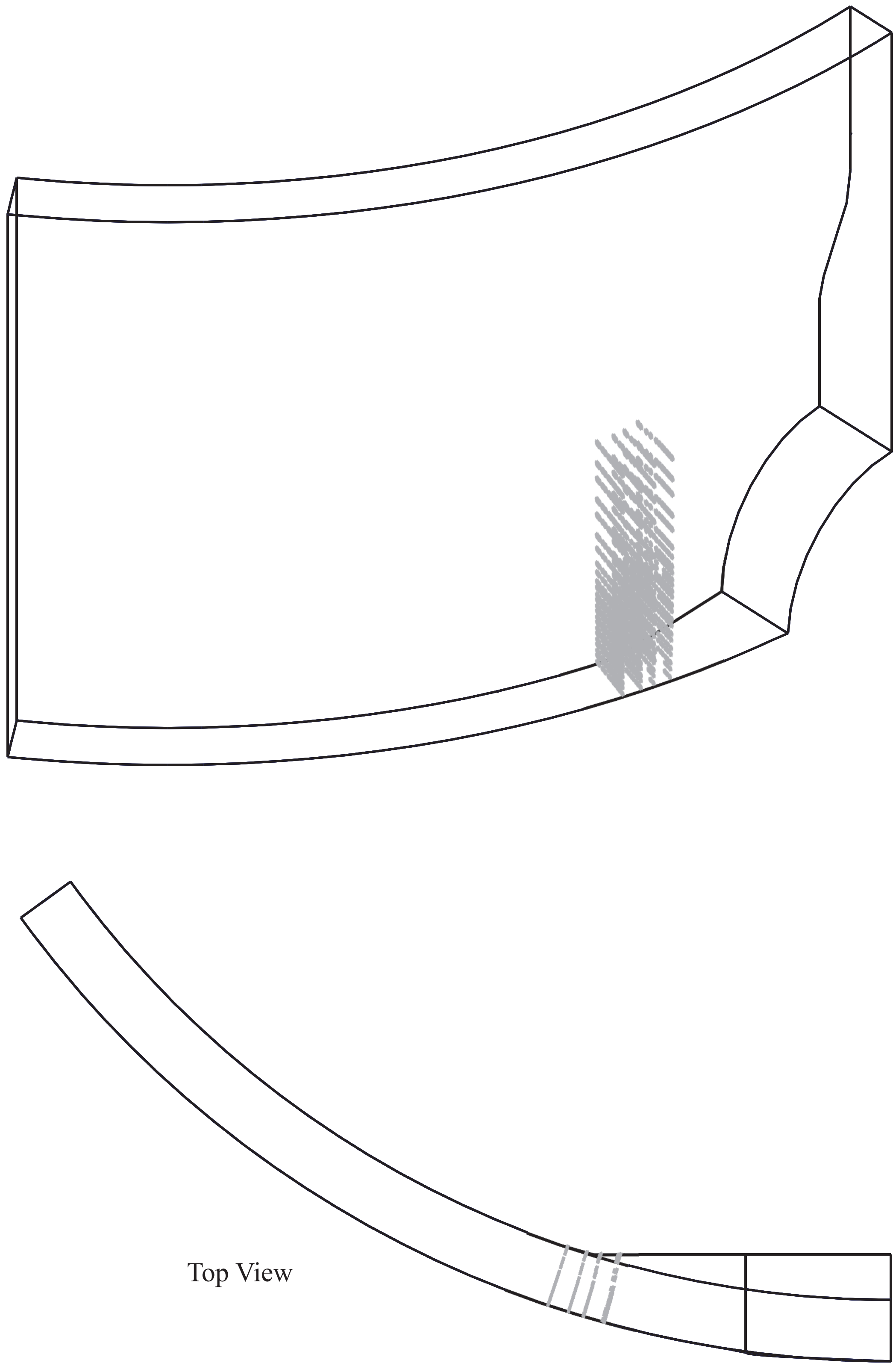

Figure 7-23. Pre-Cracking along Edge of E/H Embossment

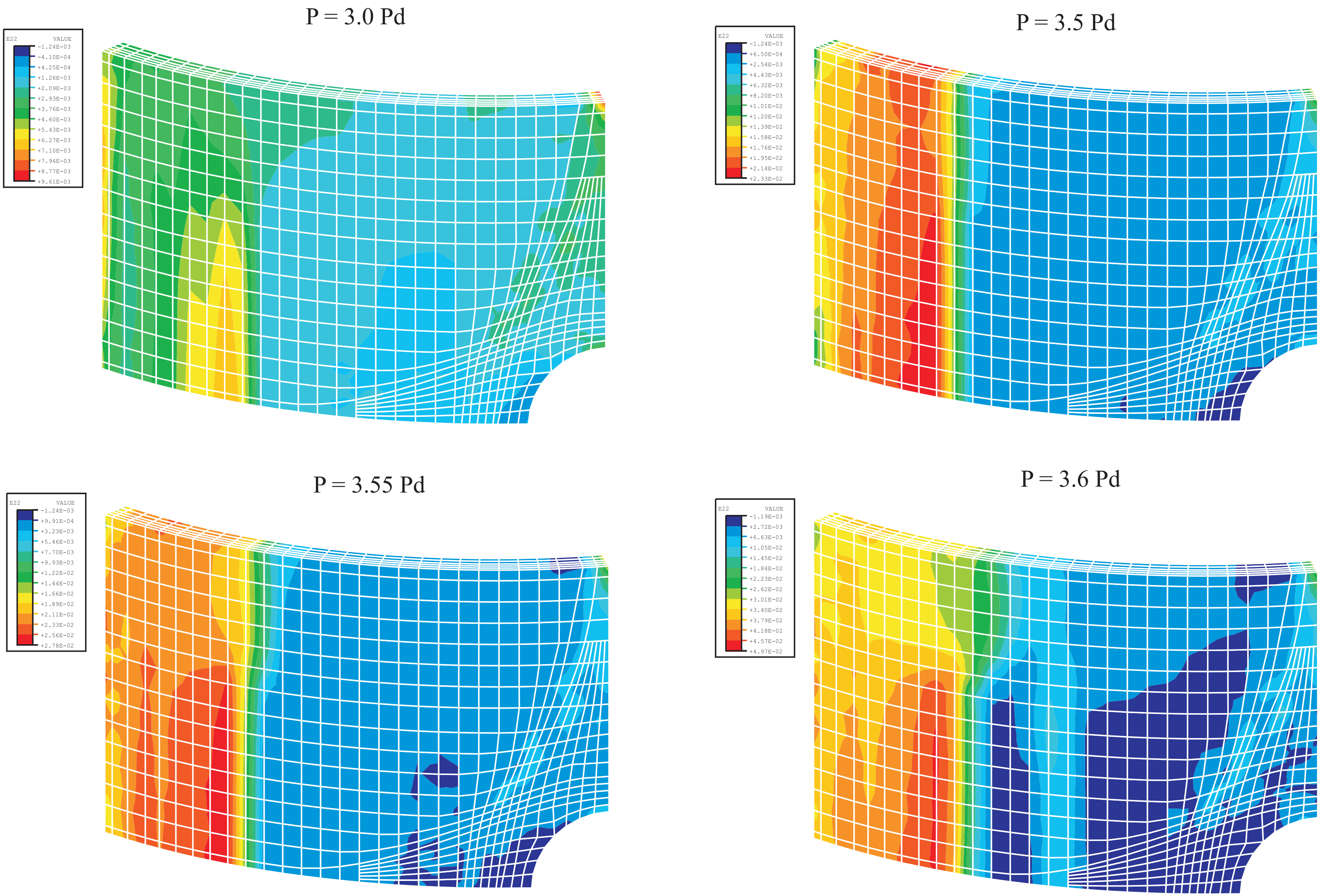

Figure 7-24. Concrete Hoop Strain Contours, Posttest Analysis Case C

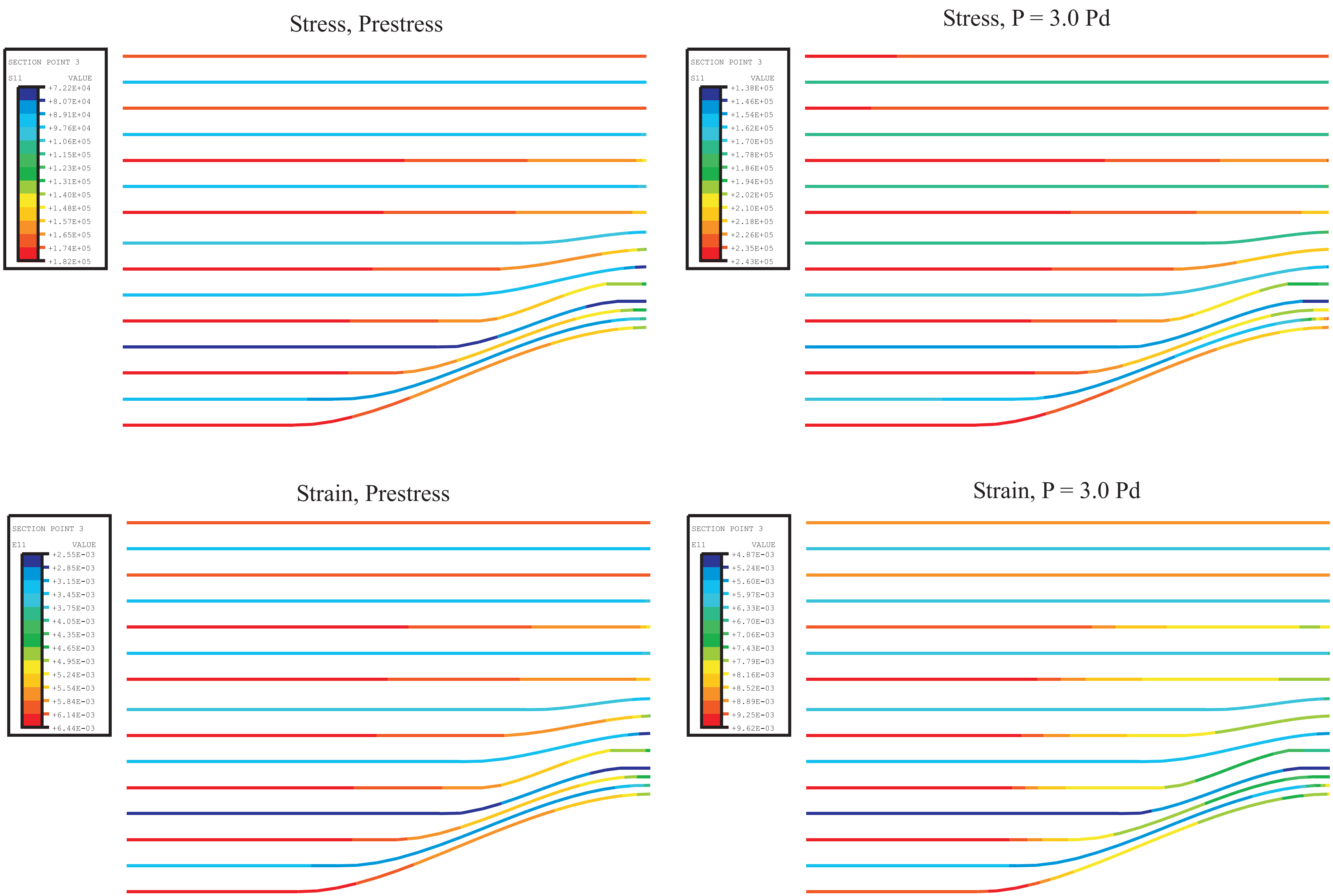

Figure 7-25. Hoop Tendon Stresses and Strains, Posttest Analysis Case C, at Prestress and 3.0 Pd
(Stresses in psi; Multiply by 0.00690 for MPa)

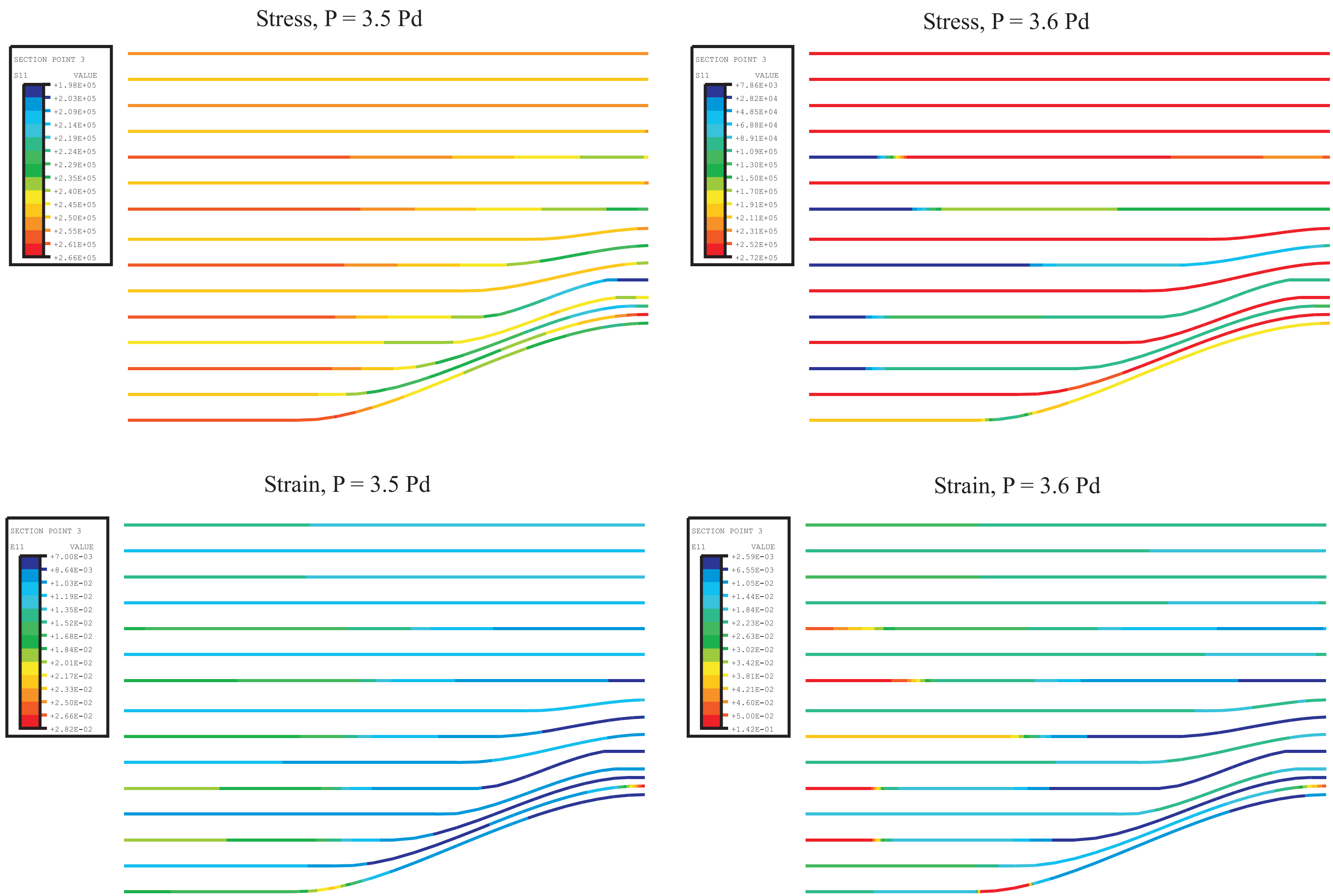

Figure 7-26. Hoop Tendon Stresses and Strains, Posttest Analysis Case C, at 3.5 Pd and 3.6 Pd
(Stresses in psi; Multiply by 0.00690 for MPa)

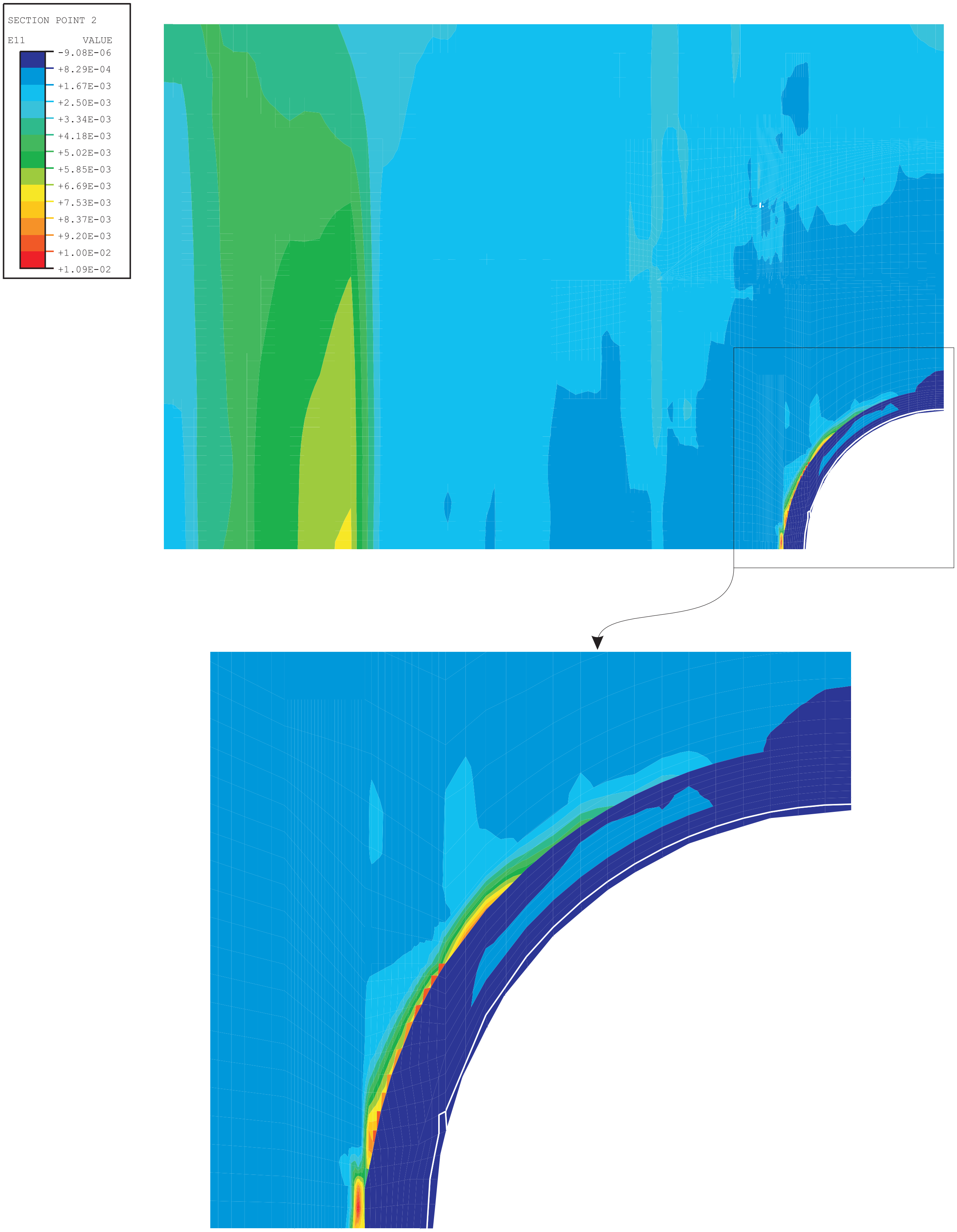

Figure 7-27. Liner Hoop Strains, Posttest Analysis Case C, at 3.0 Pd

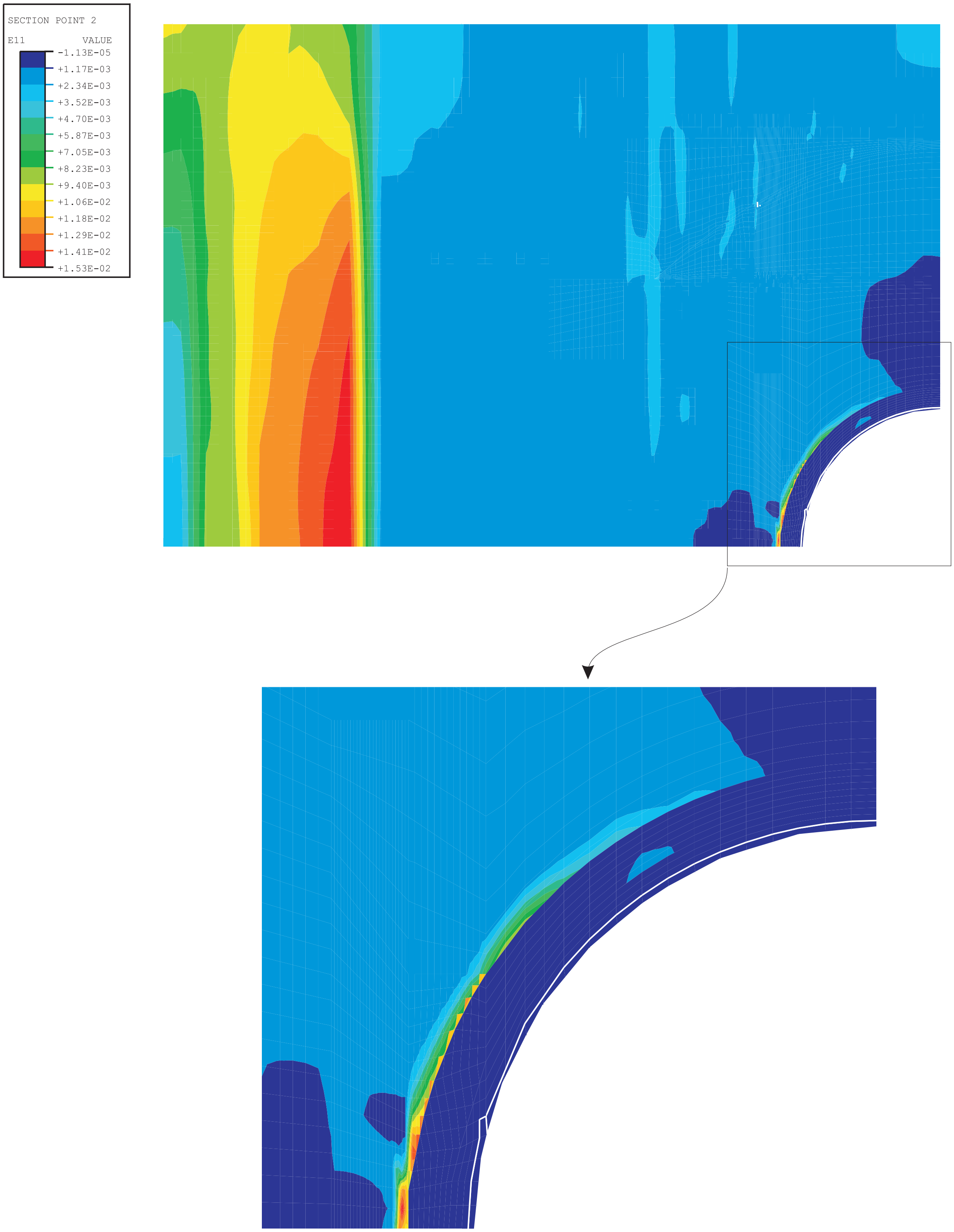

Figure 7-28. Liner Hoop Strains, Posttest Analysis Case C, at 3.2 Pd

P = 3.5 Pd

P = 3.6 Pd

Figure 7-29. Liner Hoop Strains, Posttest Analysis Case C, at 3.5 Pd and 3.6 Pd

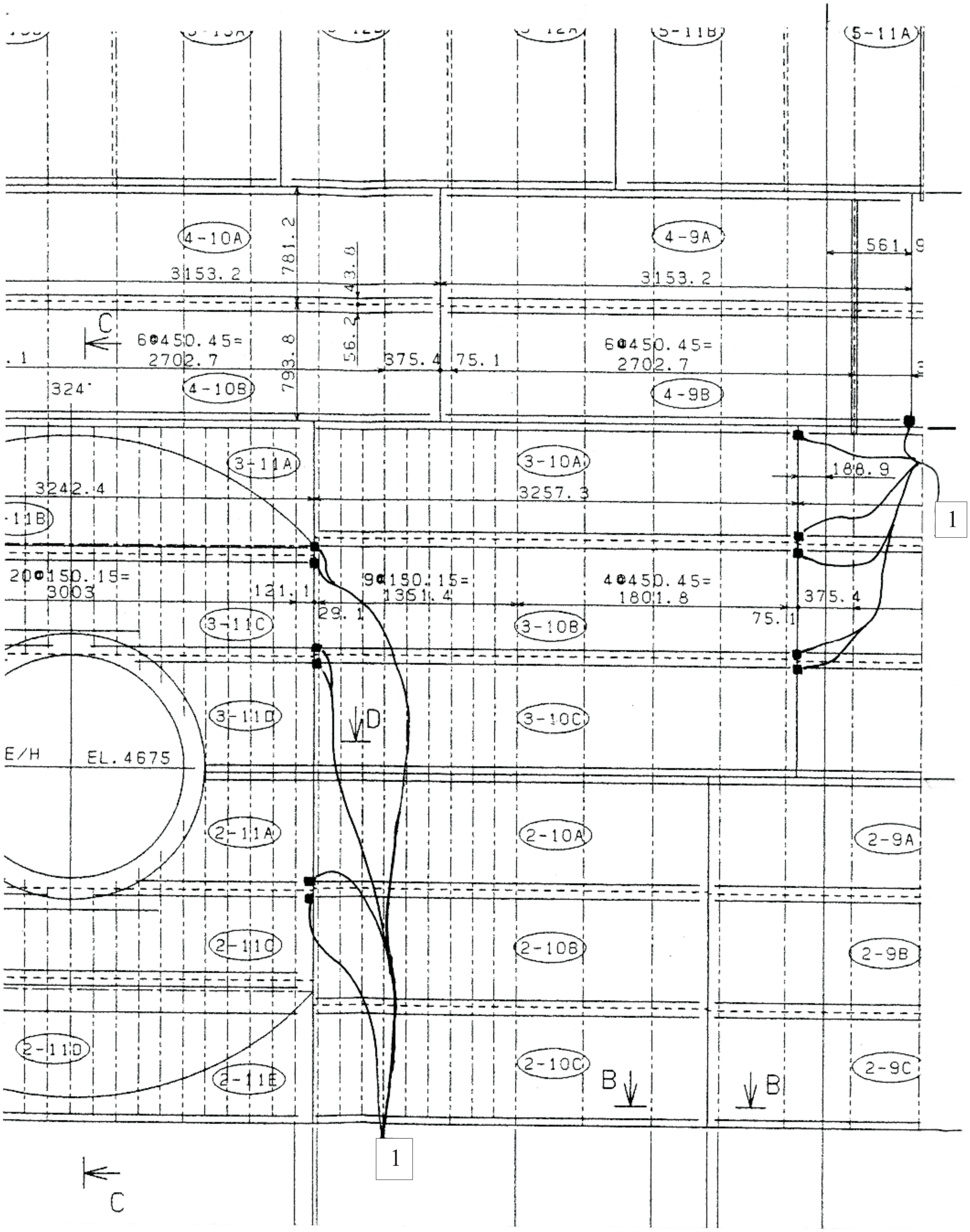

Figure 7-30. Strain Concentration Type 1 Near 270 Degrees Buttress and Near E/H

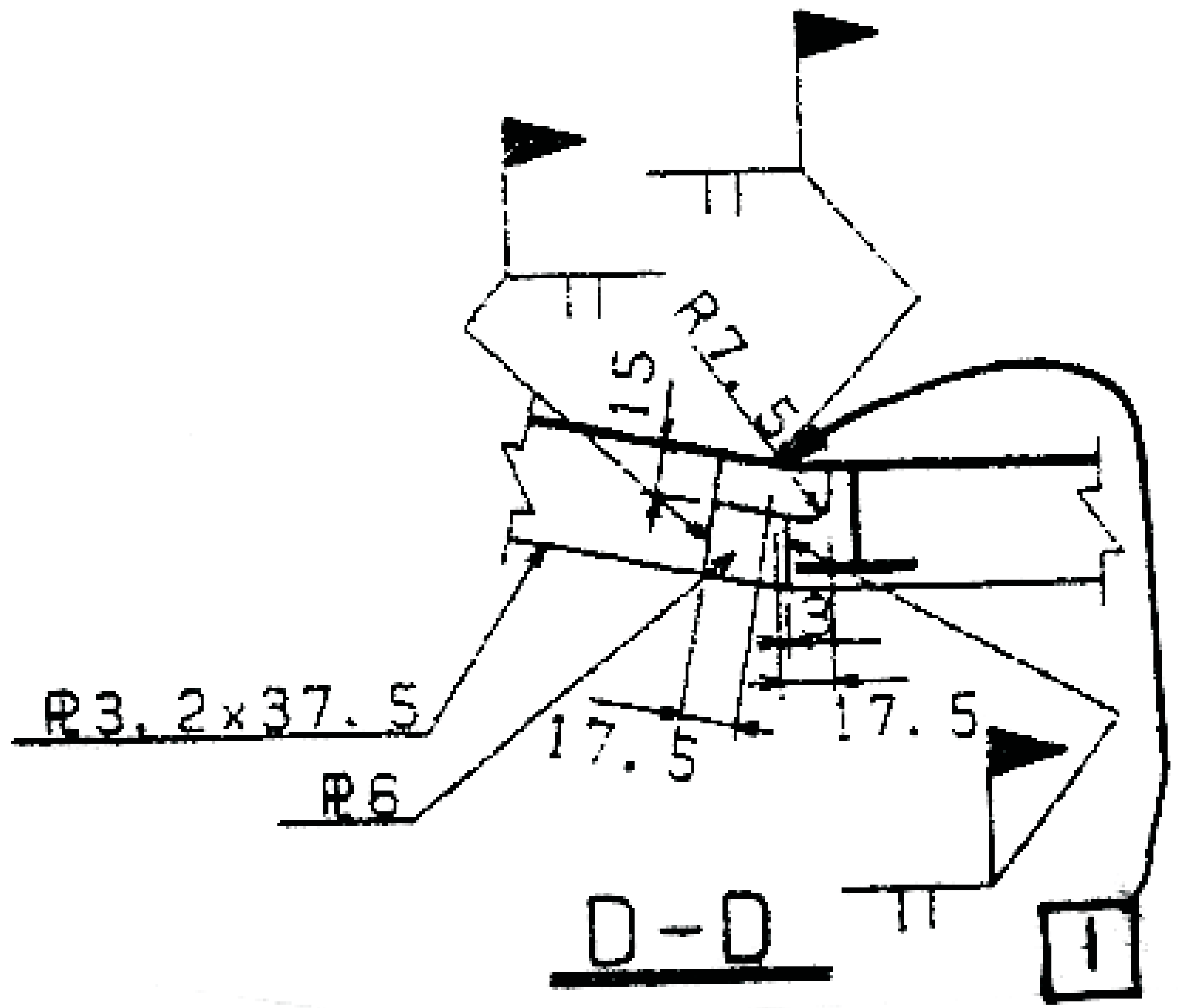

Figure 7-31. Liner Strain Concentration Rat-Hole Detail

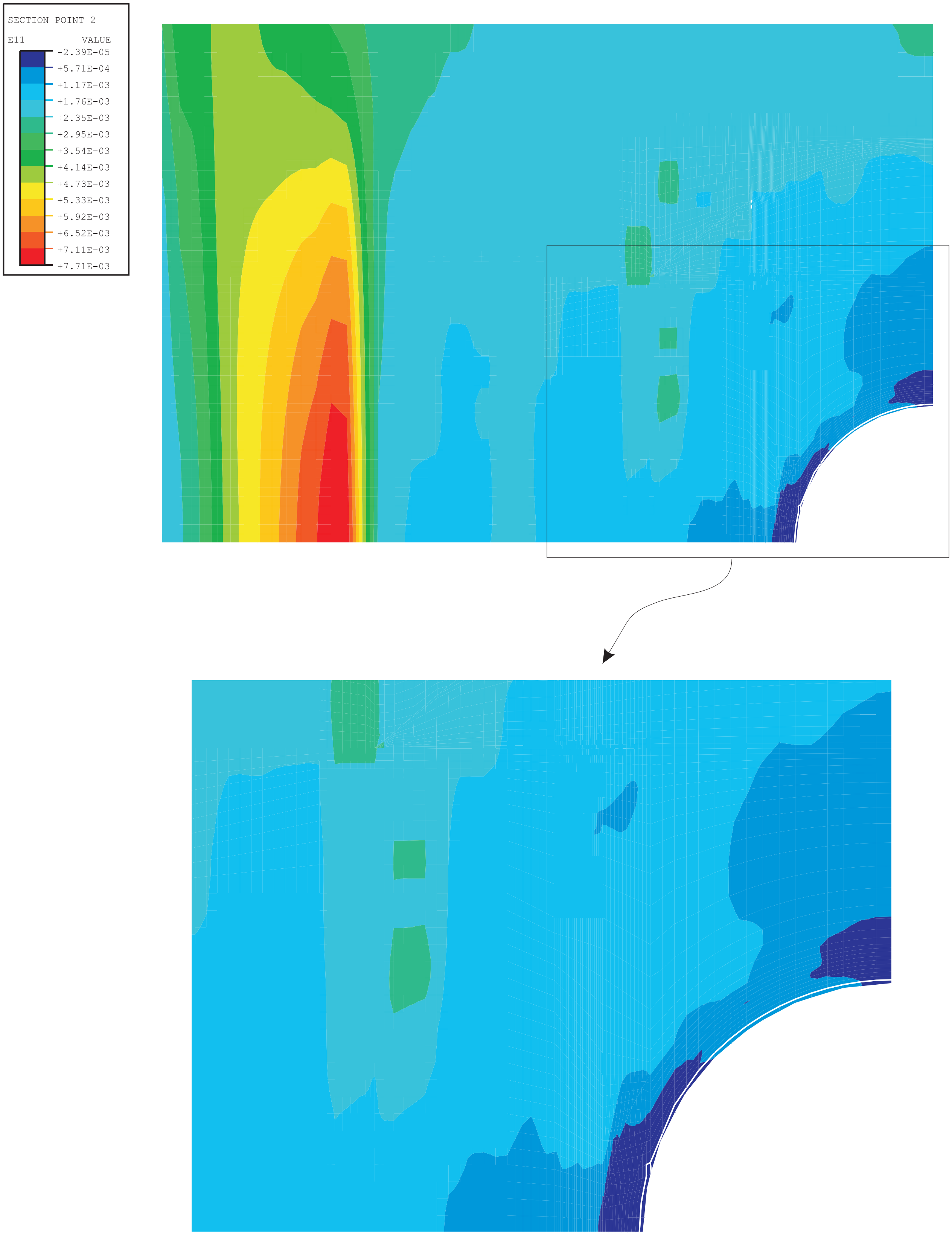

Figure 7-32. Liner Hoop Strains, Posttest Analysis Case D, at 3.0 Pd

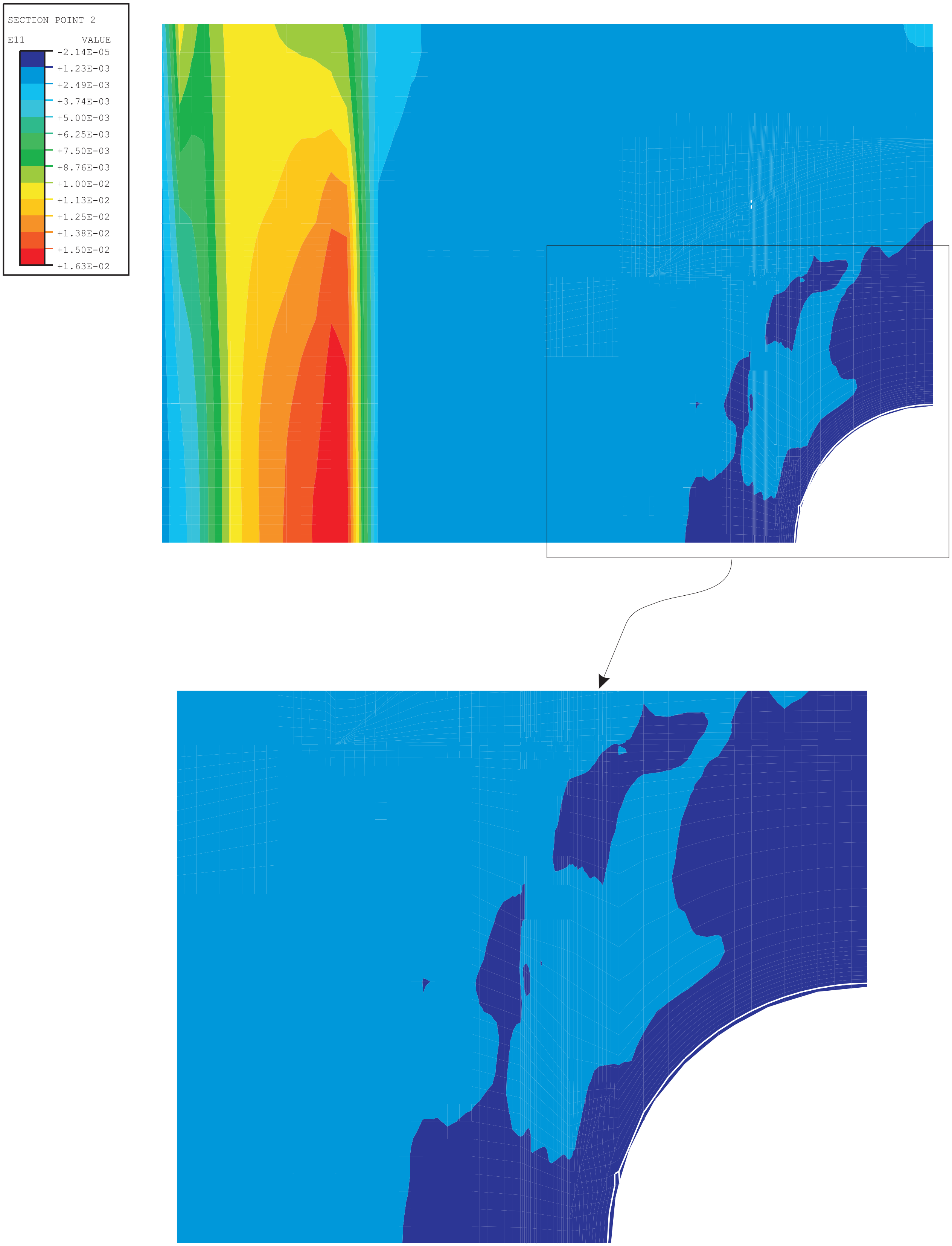

Figure 7-33. Liner Hoop Strains, Posttest Analysis Case D, at 3.2 Pd

P = 3.5 Pd

P = 3.6 Pd

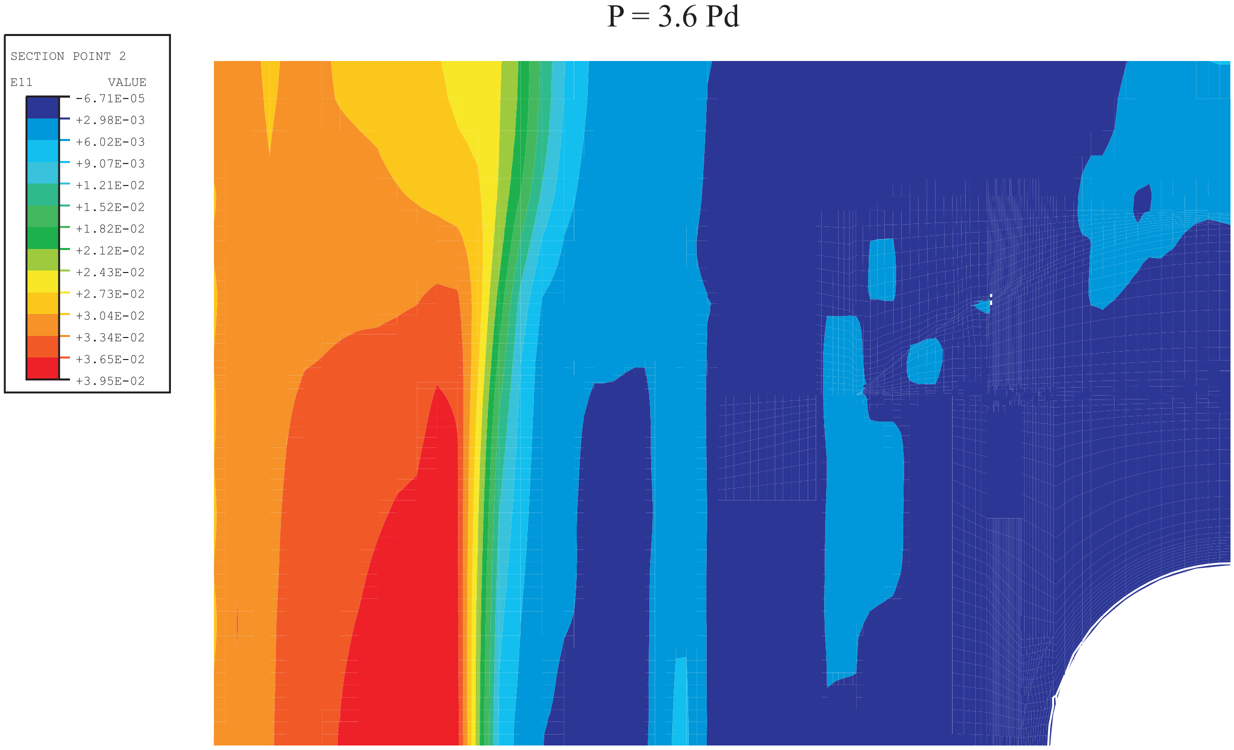

Figure 7-34. Liner Hoop Strains, Posttest Analysis Case D, at 3.5 Pd and 3.6 Pd

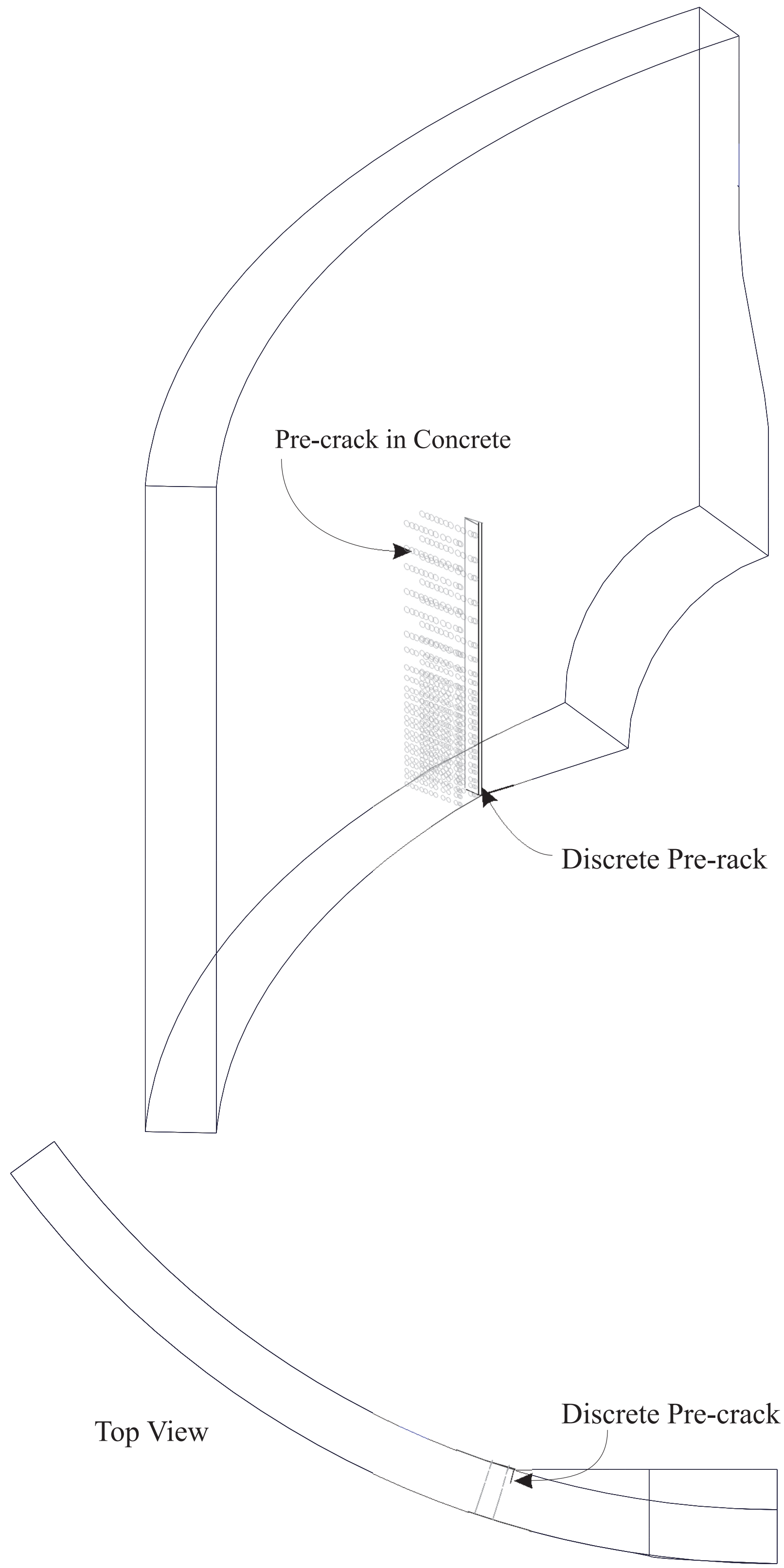

Figure 7-35. Illustration of Case E, Discrete Pre-Crack

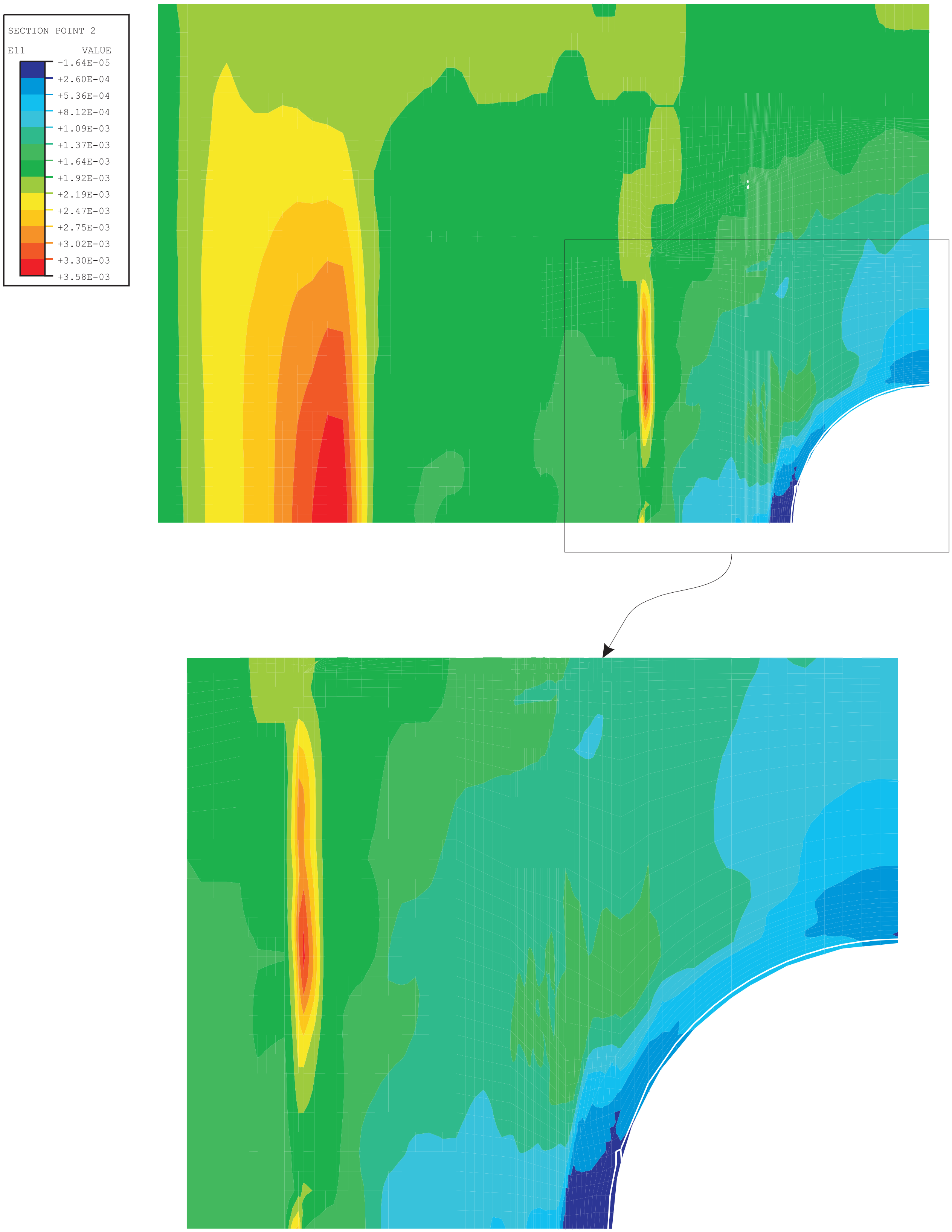

Figure 7-36. Liner Hoop Strains, Posttest Analysis Case E, at 2.8 Pd

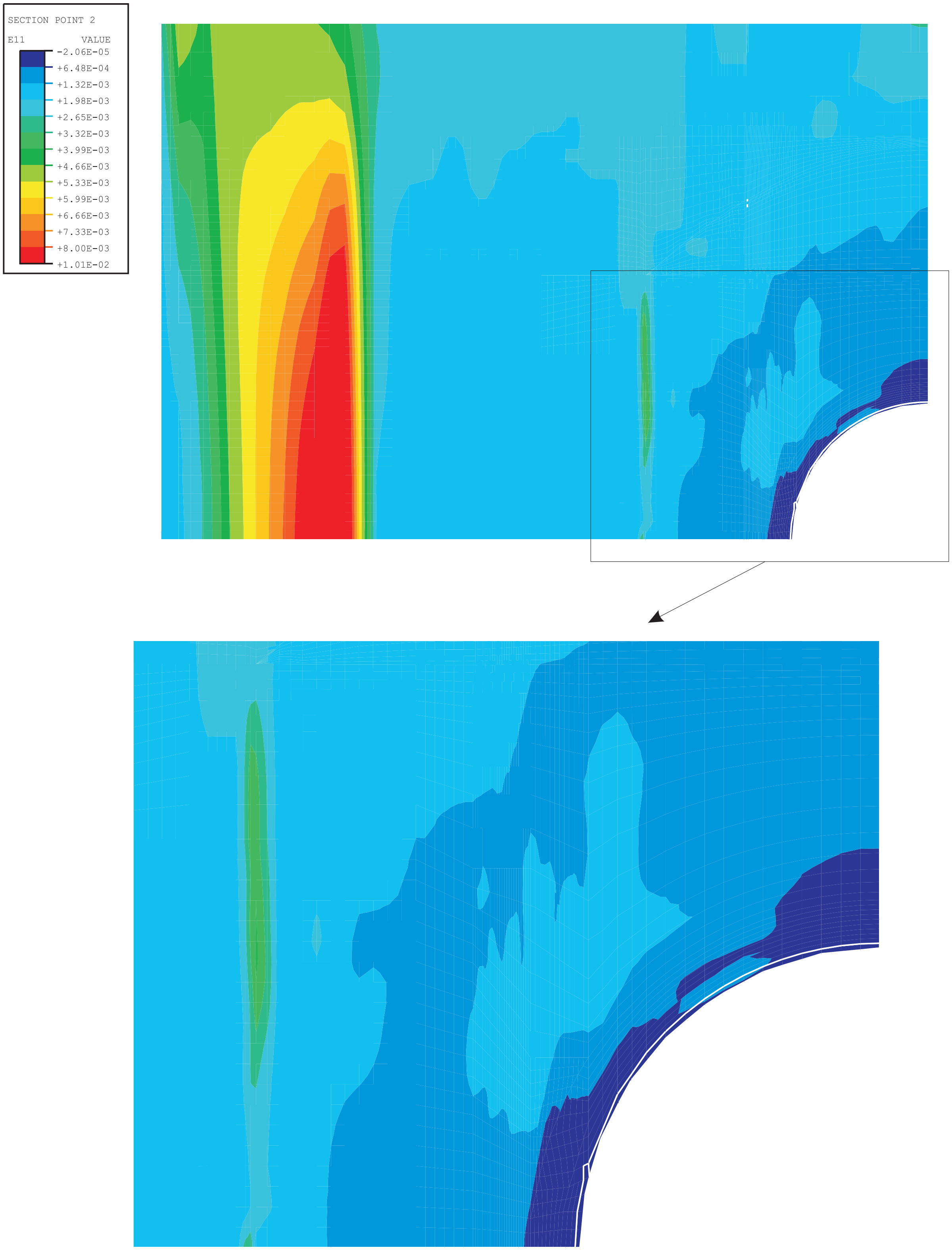

Figure 7-37. Liner Hoop Strains, Posttest Analysis Case E, at 3.0 Pd

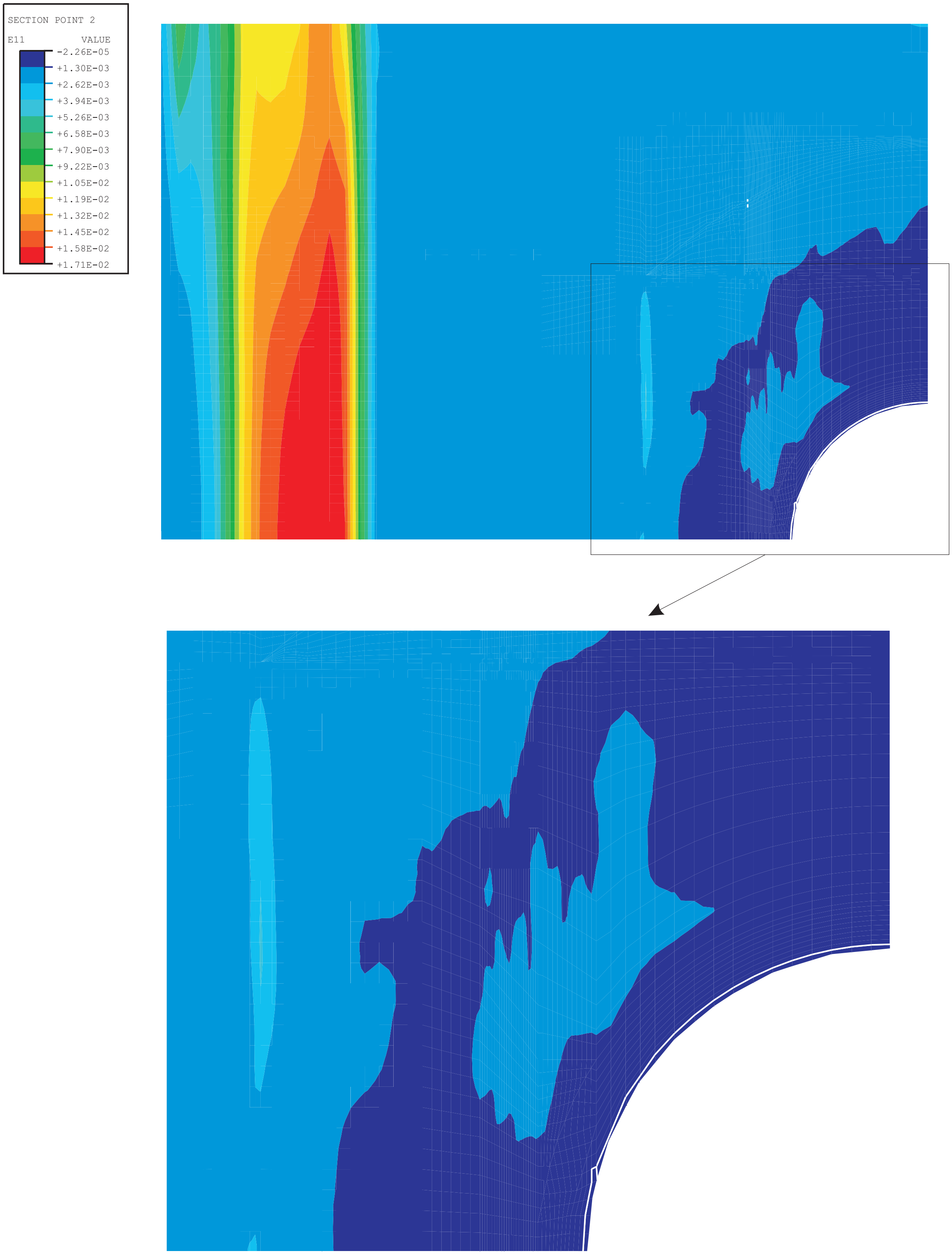

Figure 7-38. Liner Hoop Strains, Posttest Analysis Case E, at 3.2 Pd

P = 3.5 Pd

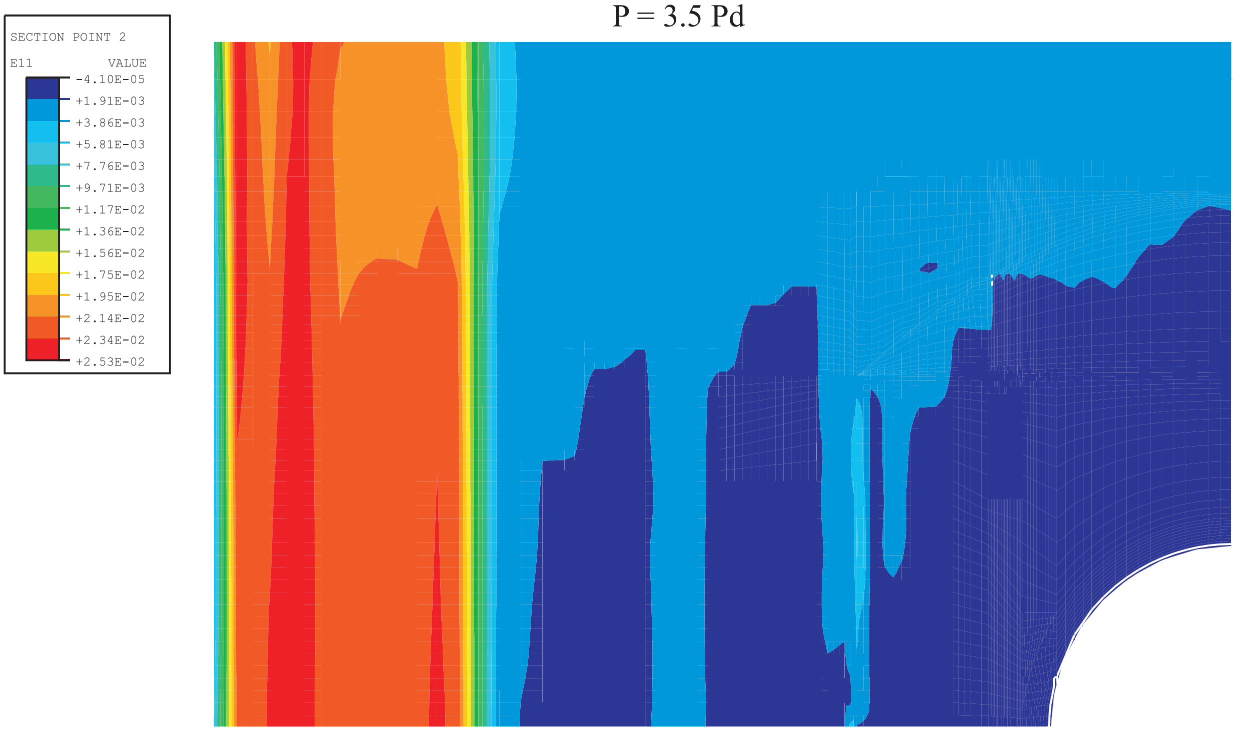

P = 3.6 Pd

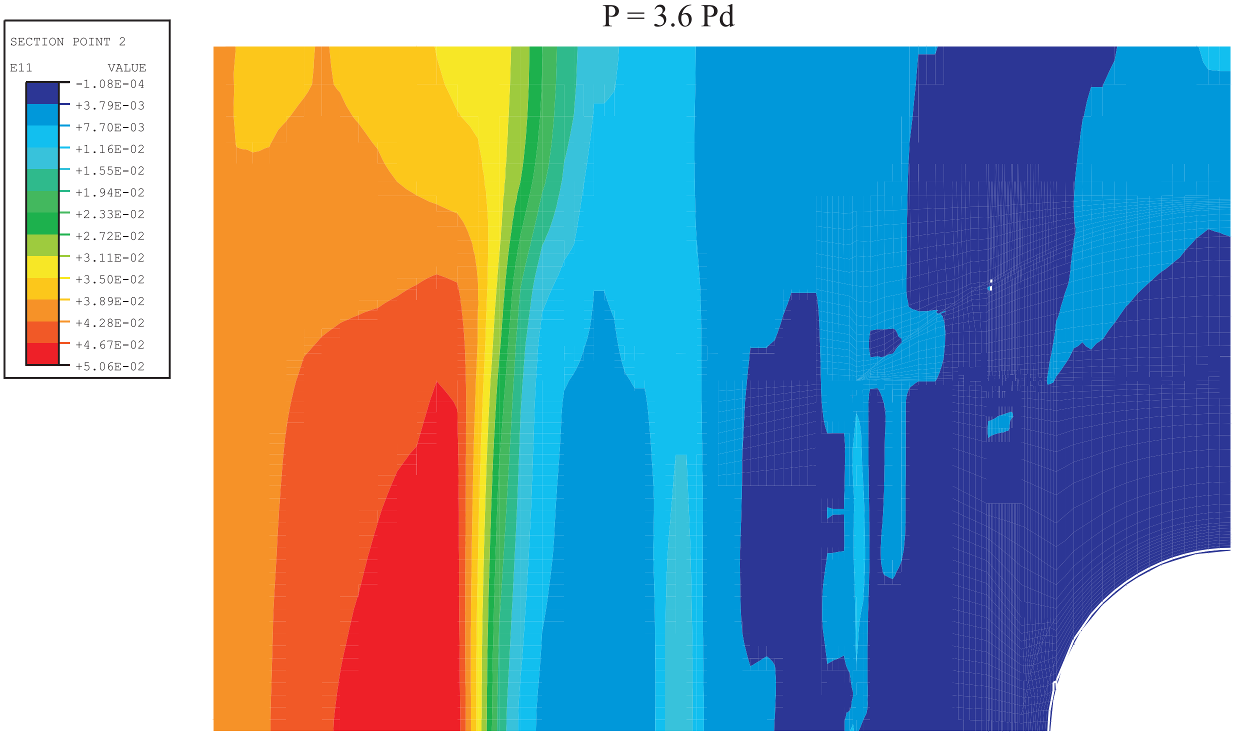

Figure 7-39. Liner Hoop Strains, Posttest Analysis Case E, at 3.5 Pd and 3.6 Pd

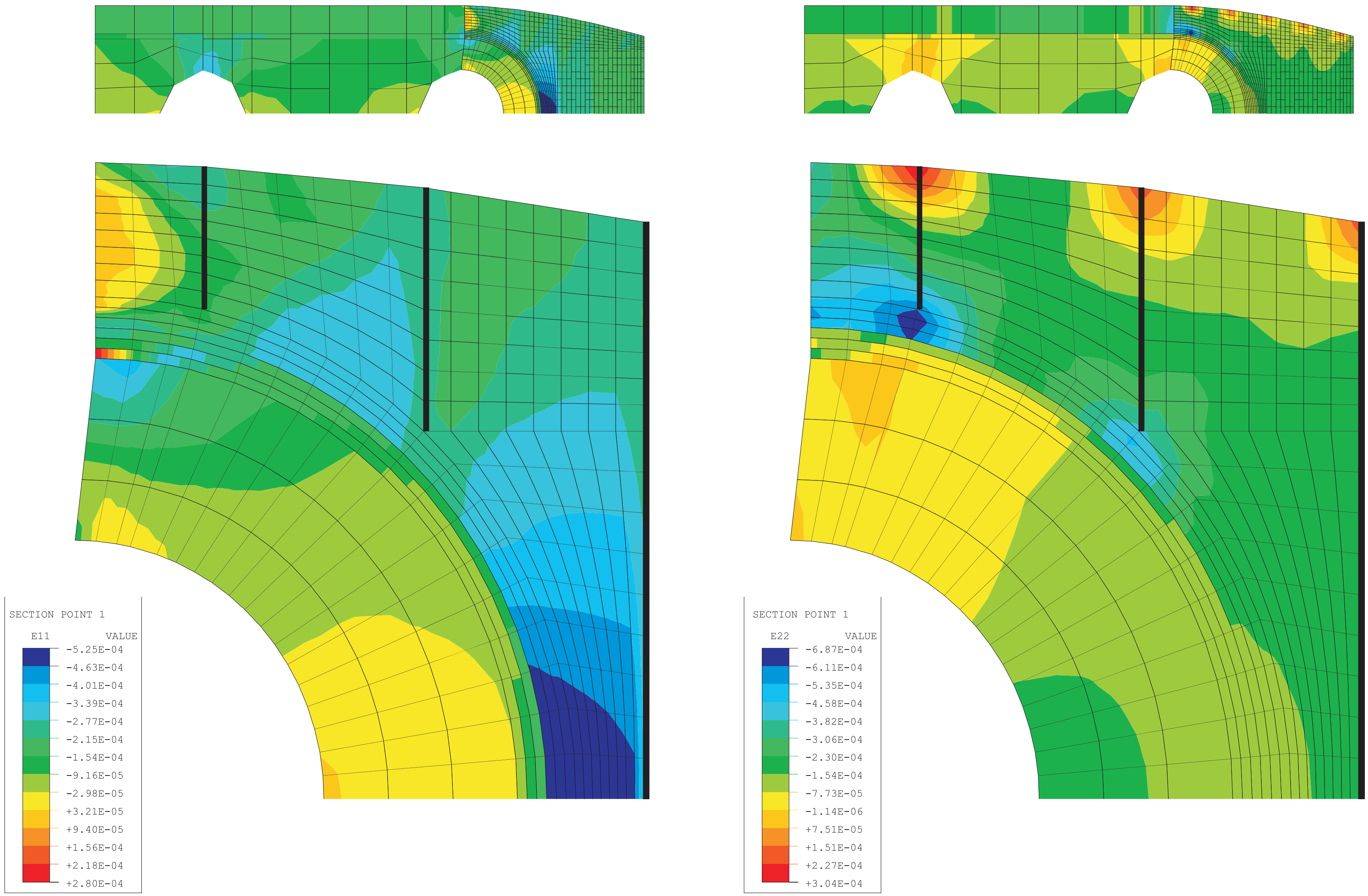

Figure 7-40. Hoop (Left) and Meridional (Right) Strains for Posttest M/S Analysis at Prestress

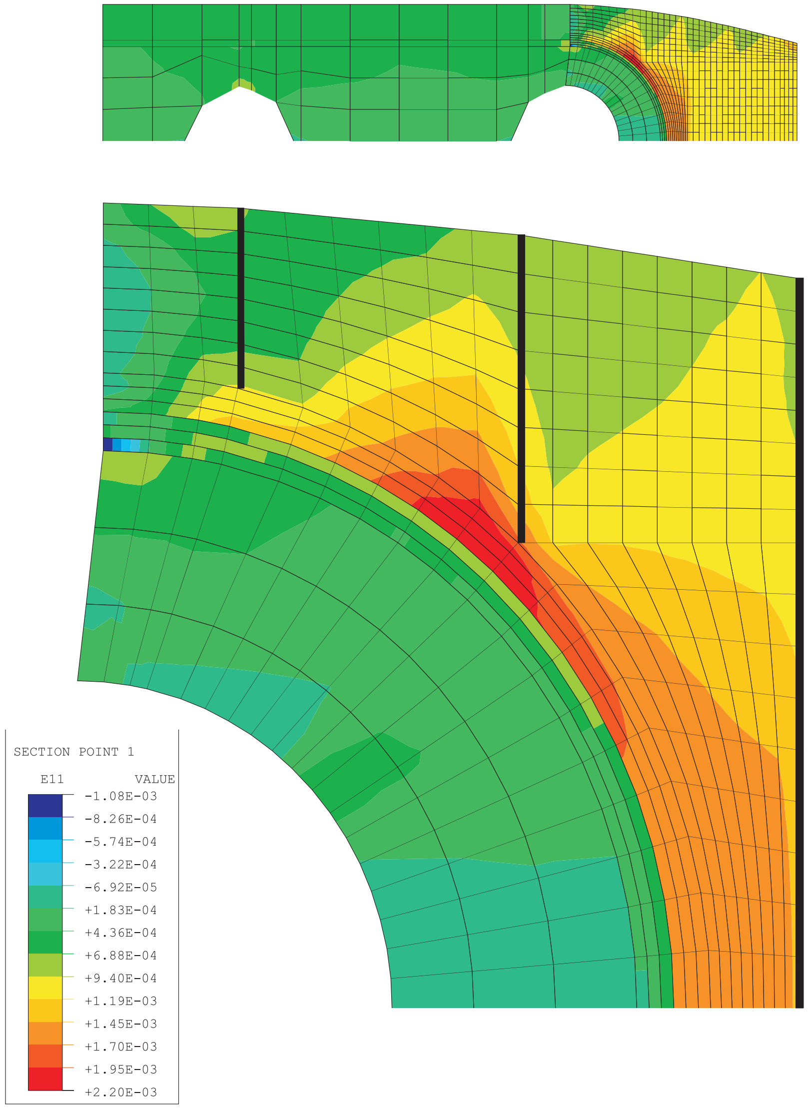

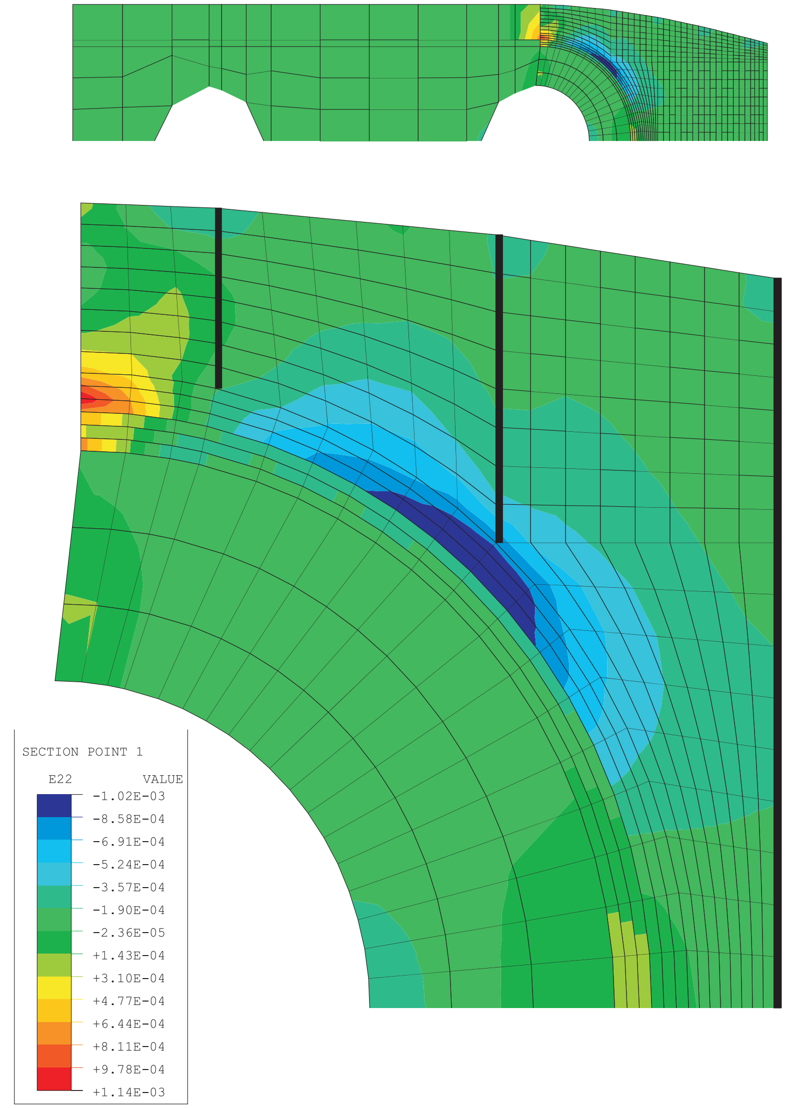

Figure 7-41. Hoop (Left) and Meridional (Right) Strains for Posttest M/S Analysis at P = 2.0 Pd

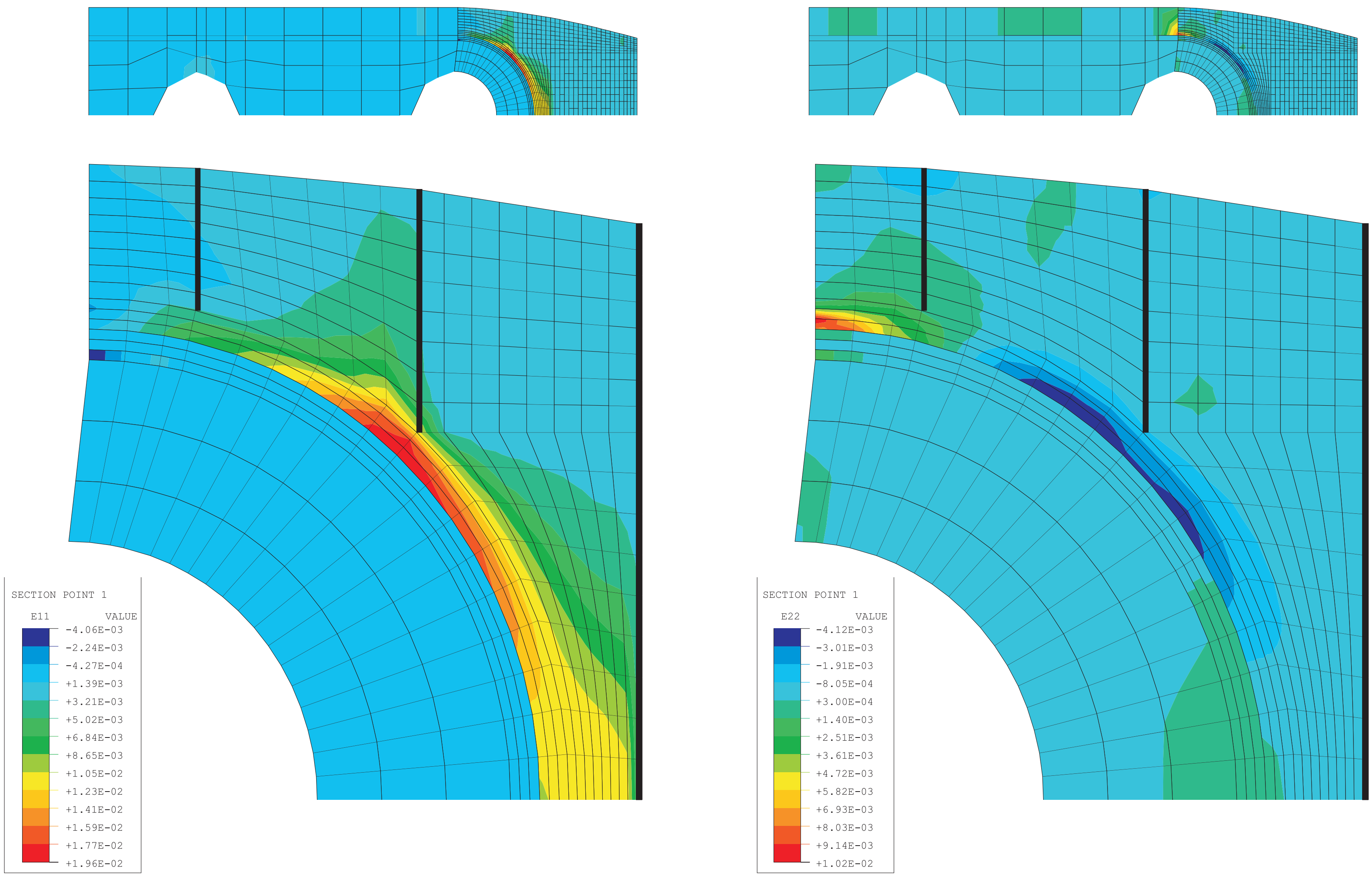

Figure 7-42. Hoop (Left) and Meridional (Right) Strains for Posttest M/S Analysis at P = 3.0 Pd

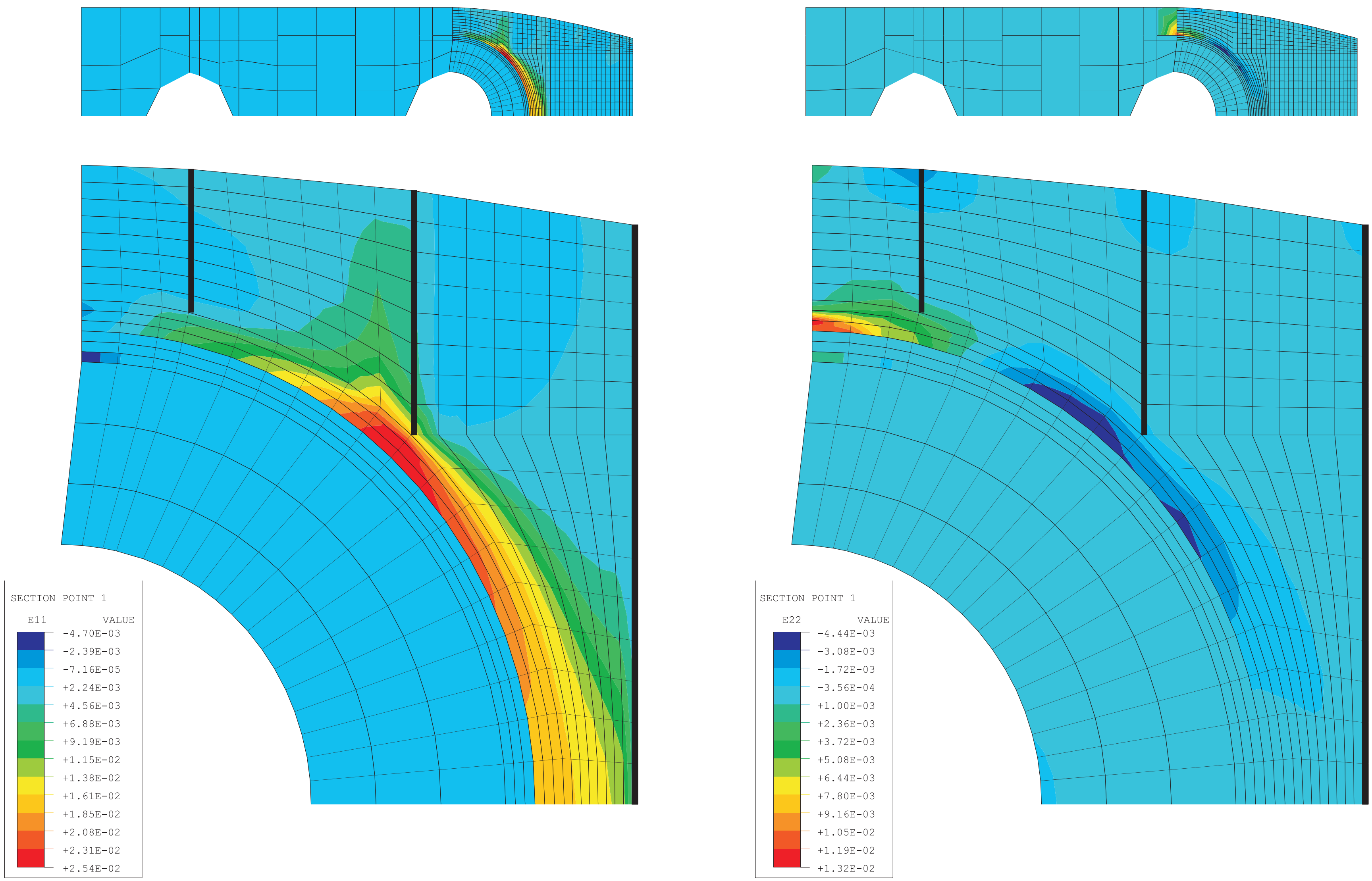

Figure 7-43. Hoop (Left) and Meridional (Right) Strains for Posttest M/S Analysis at P = 3.3 Pd

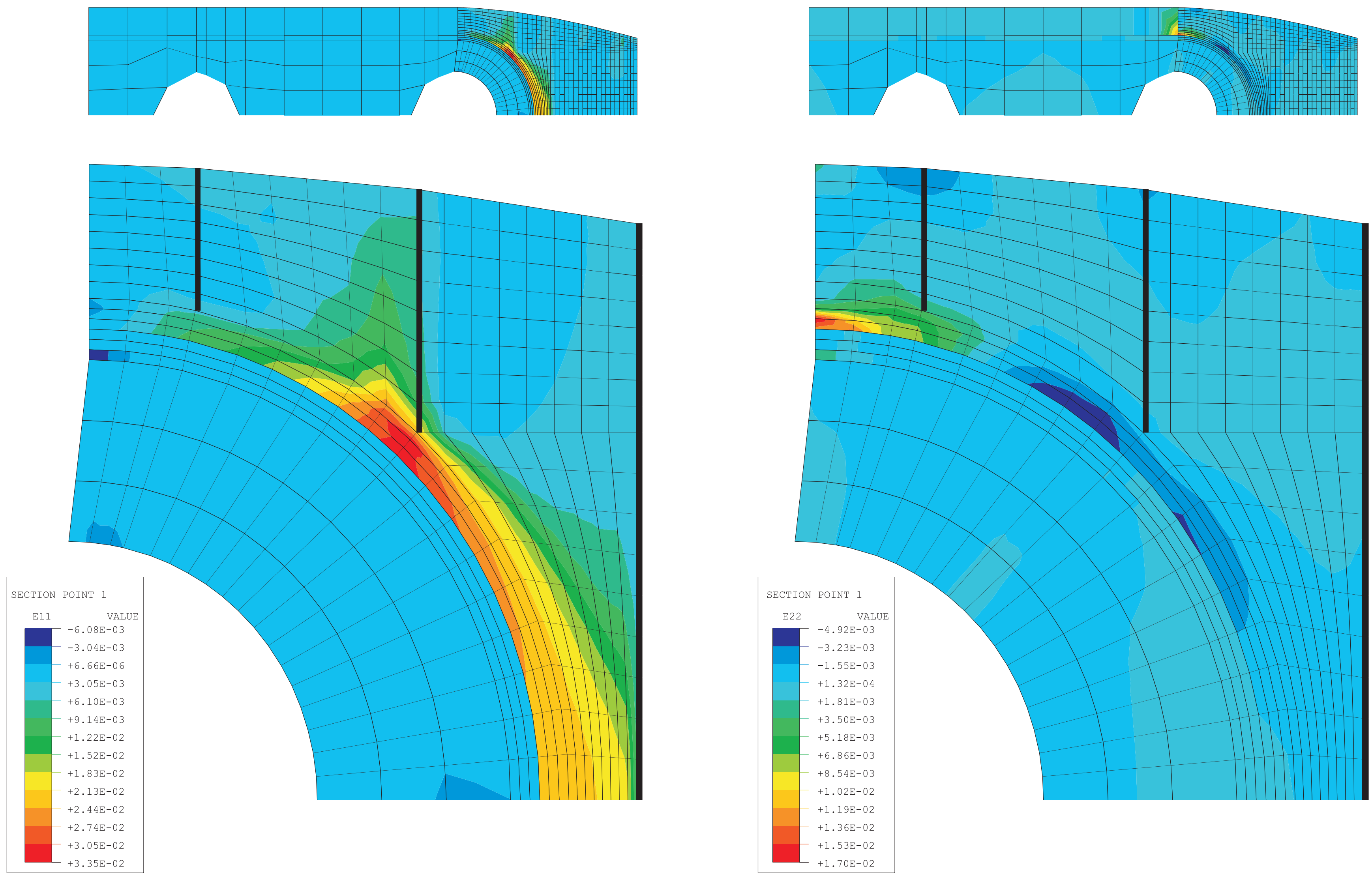

Figure 7-44. Hoop (Left) and Meridional (Right) Strains for Posttest M/S Analysis at P = 3.5 Pd

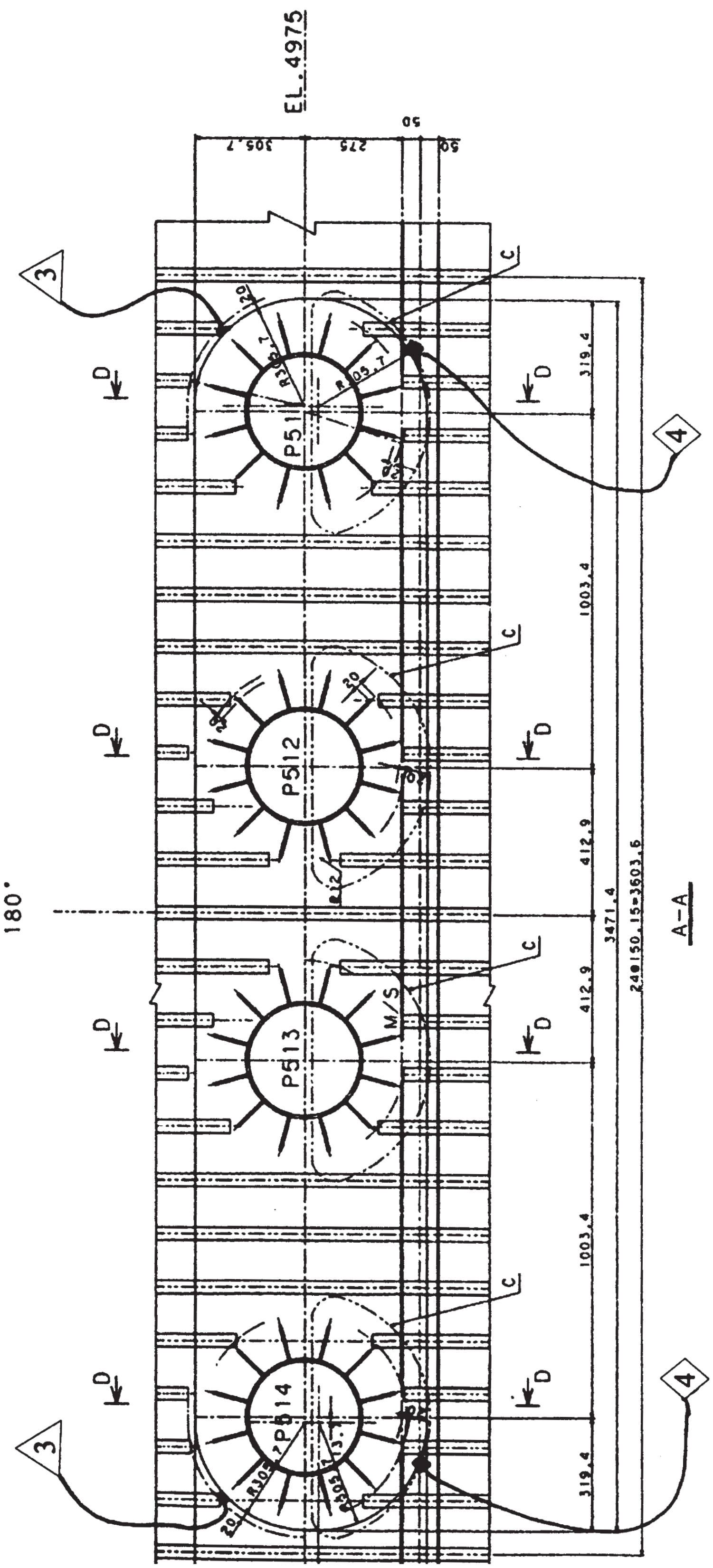

Figure 7-45. Strain Concentration Type 3 and 4 Near M/S Penetrations

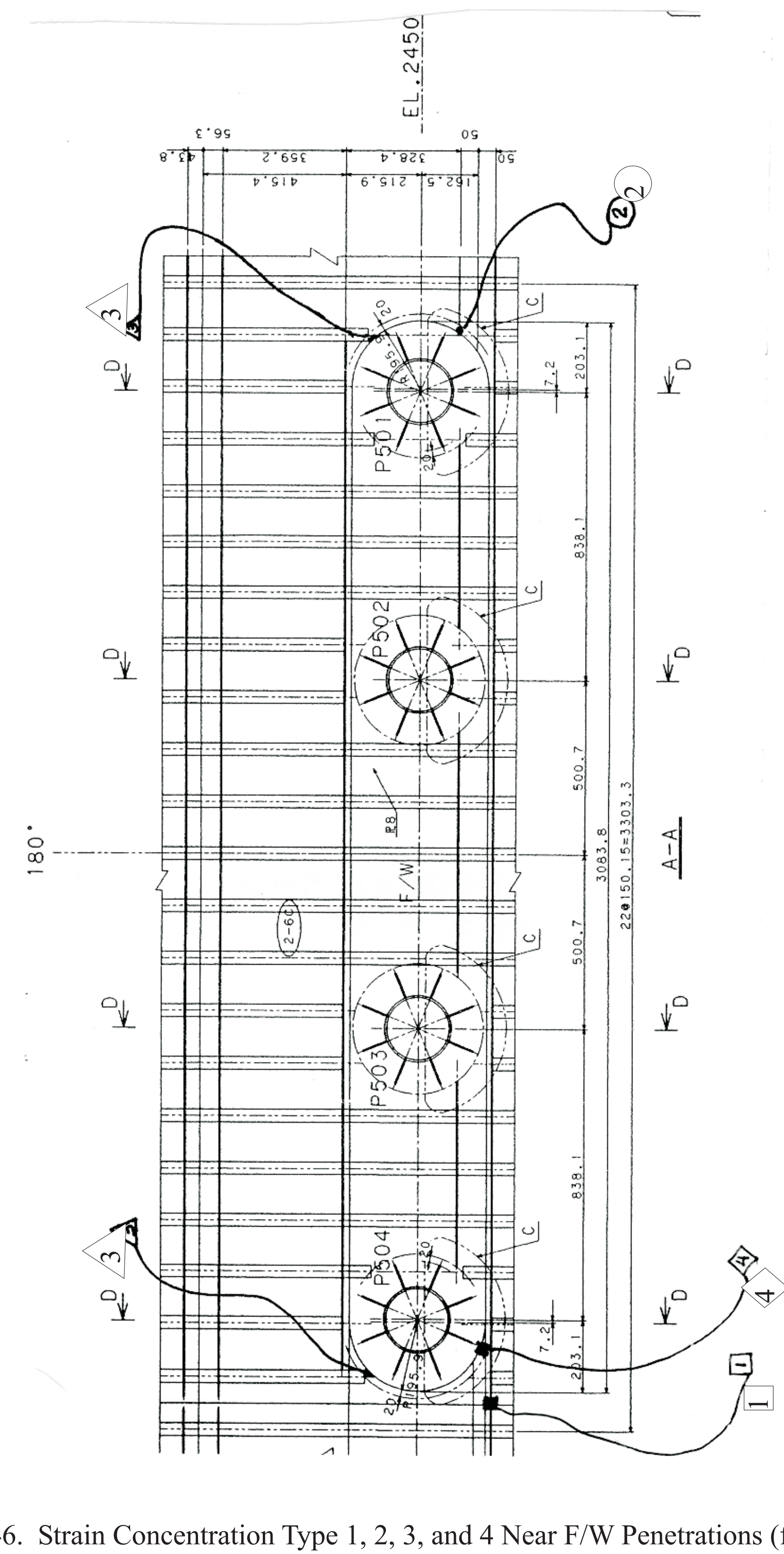

Figure 7-46. Strain Concentration Type 1, 2, 3, and 4 Near F/W Penetrations (from [1])

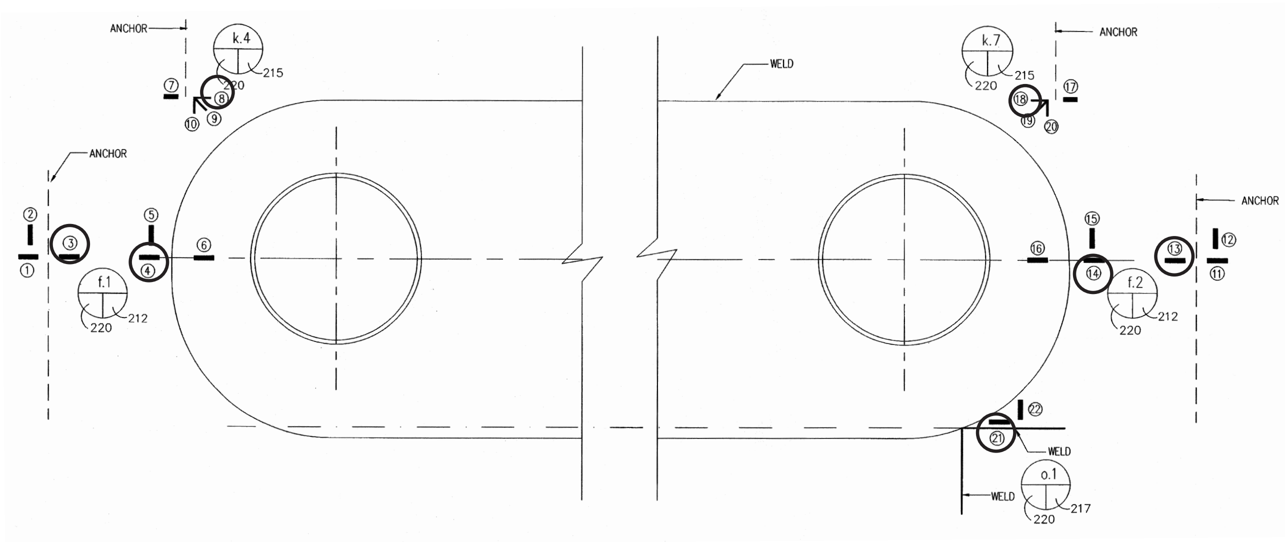

M/S - Inside View

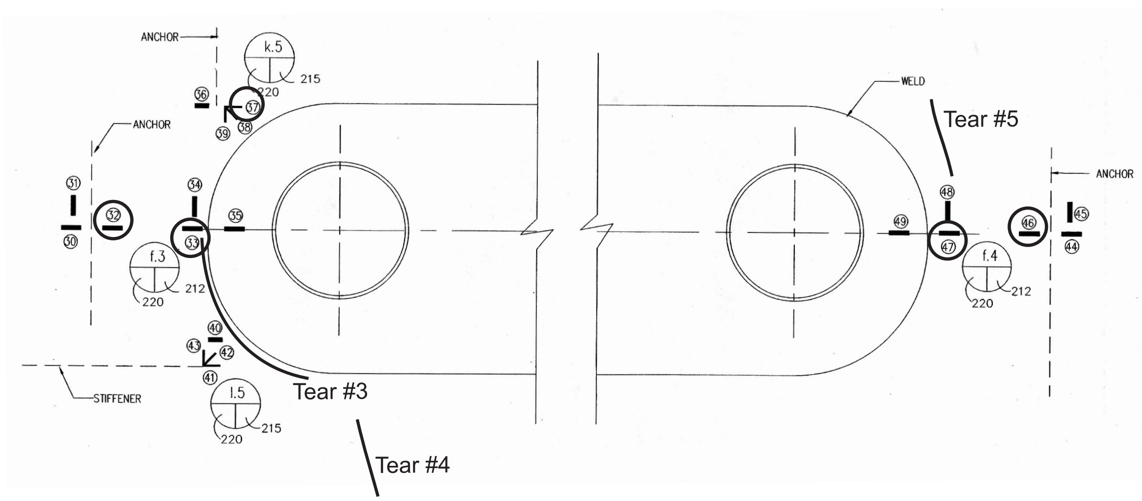

F/W - Inside View

Figure 7-47. Strain Gage Locations Near the M/S and F/W Penetrations

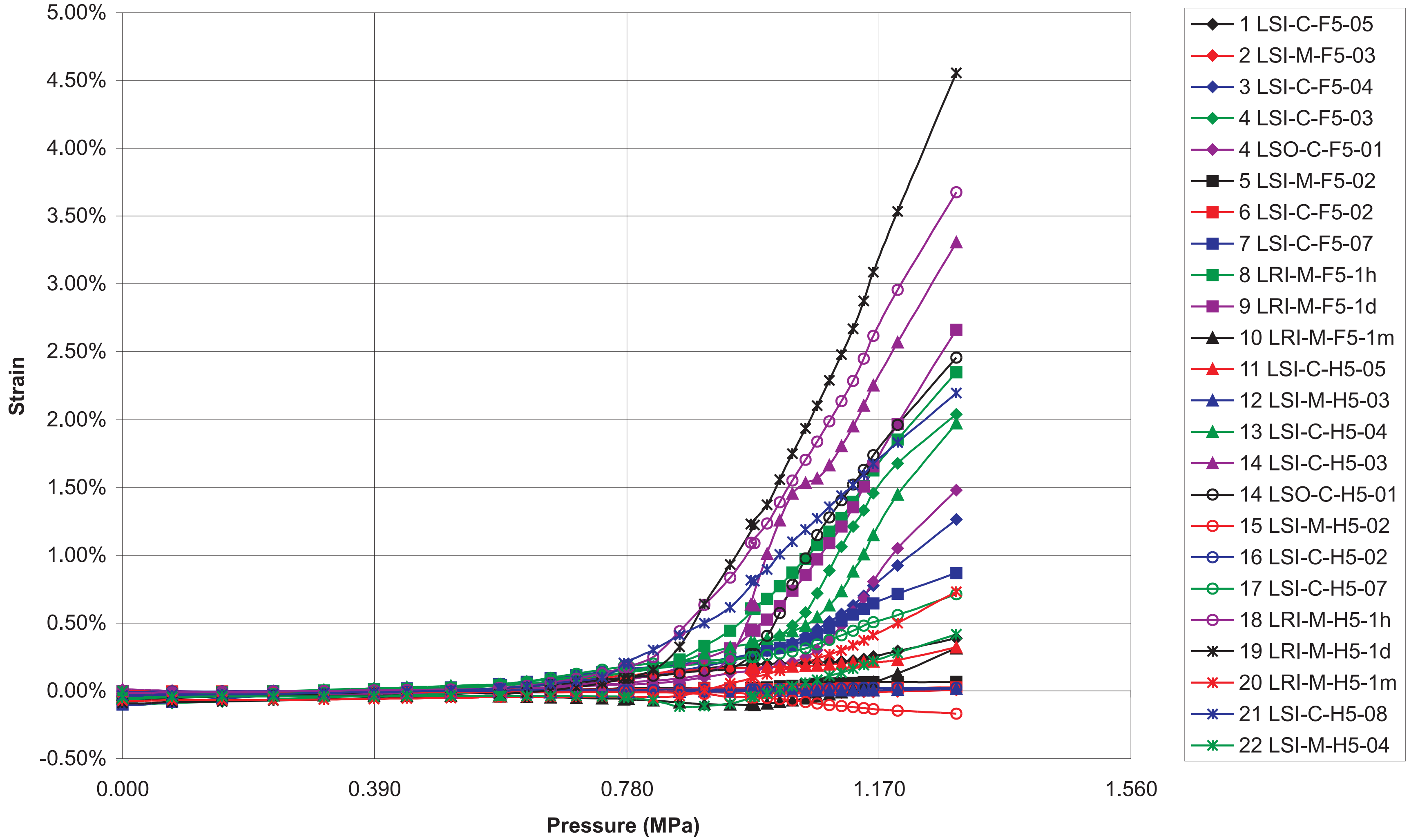

Figure 7-48. Liner Strain Histories Measured by the Gages Near the M/S Penetrations

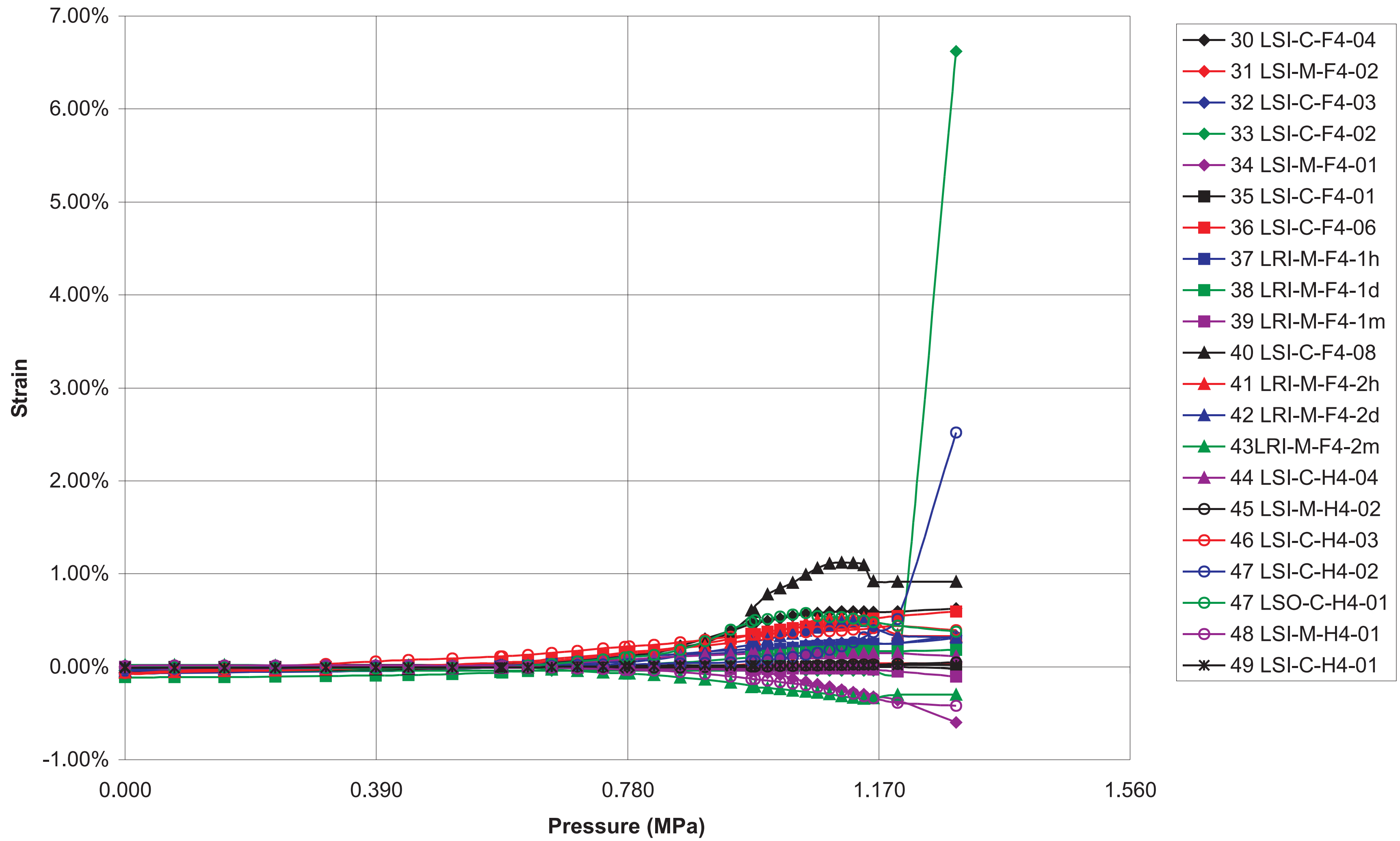

Figure 7-49. Linear Strain Histories Measured by the Gages Near the F/W Penetrations

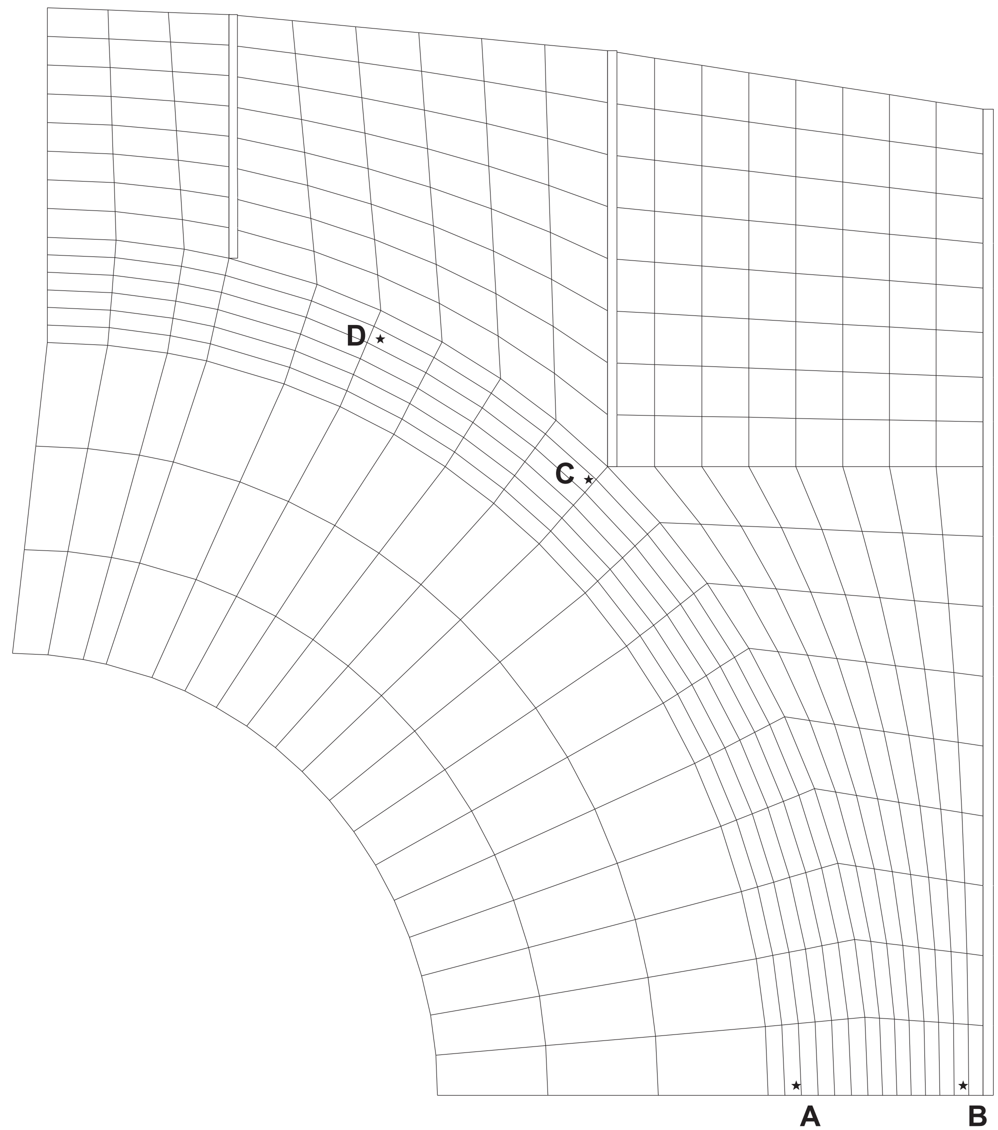

Figure 7-50. Liner Strain Locations for Comparing Analysis to M/S and F/W Gage Measurements

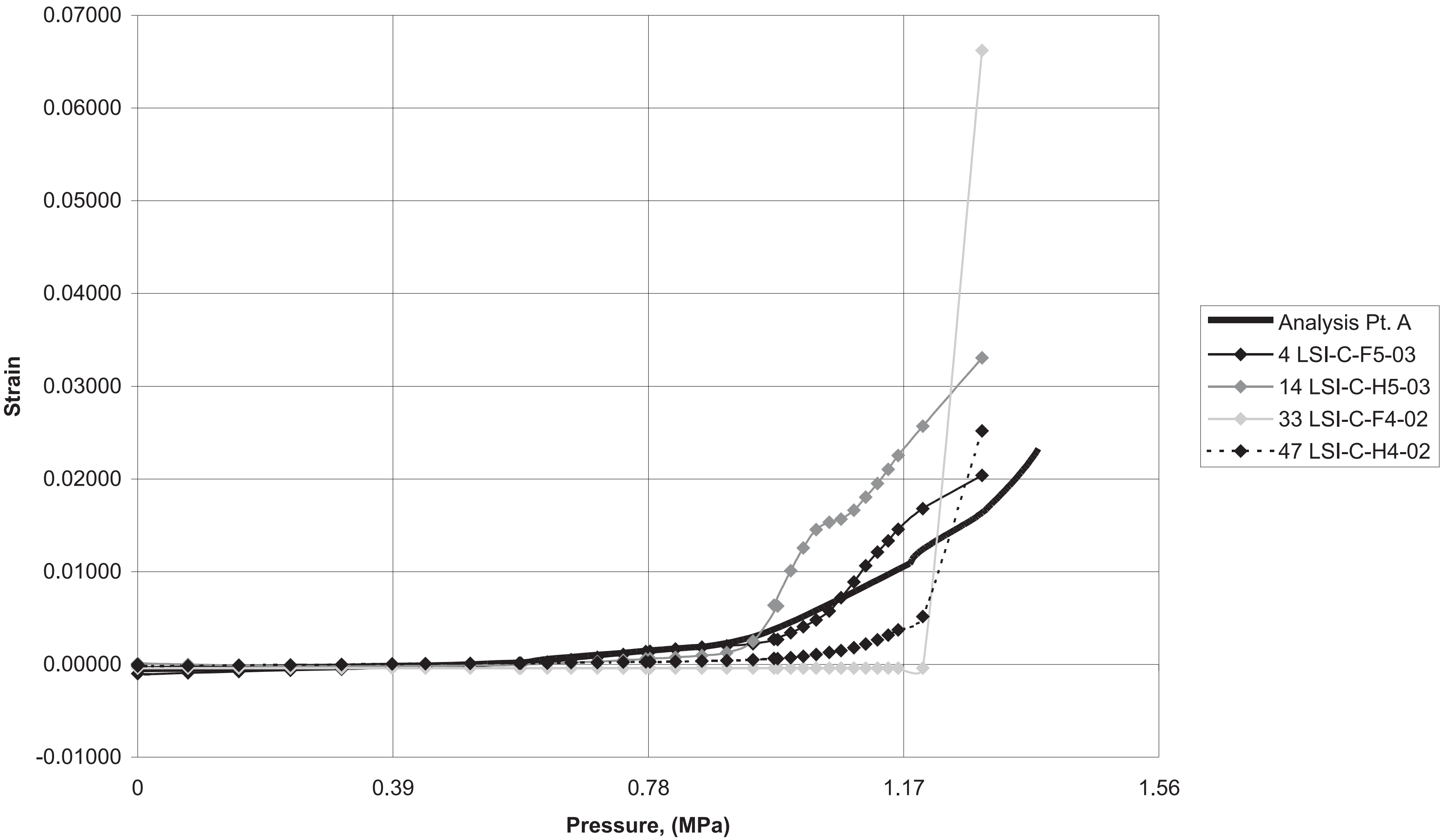

Figure 7-51. M/S and F/W Test vs. Analysis Linear Strain Comparisons at Location "A," Near Collar Insert, 3:00, 9:00 Position

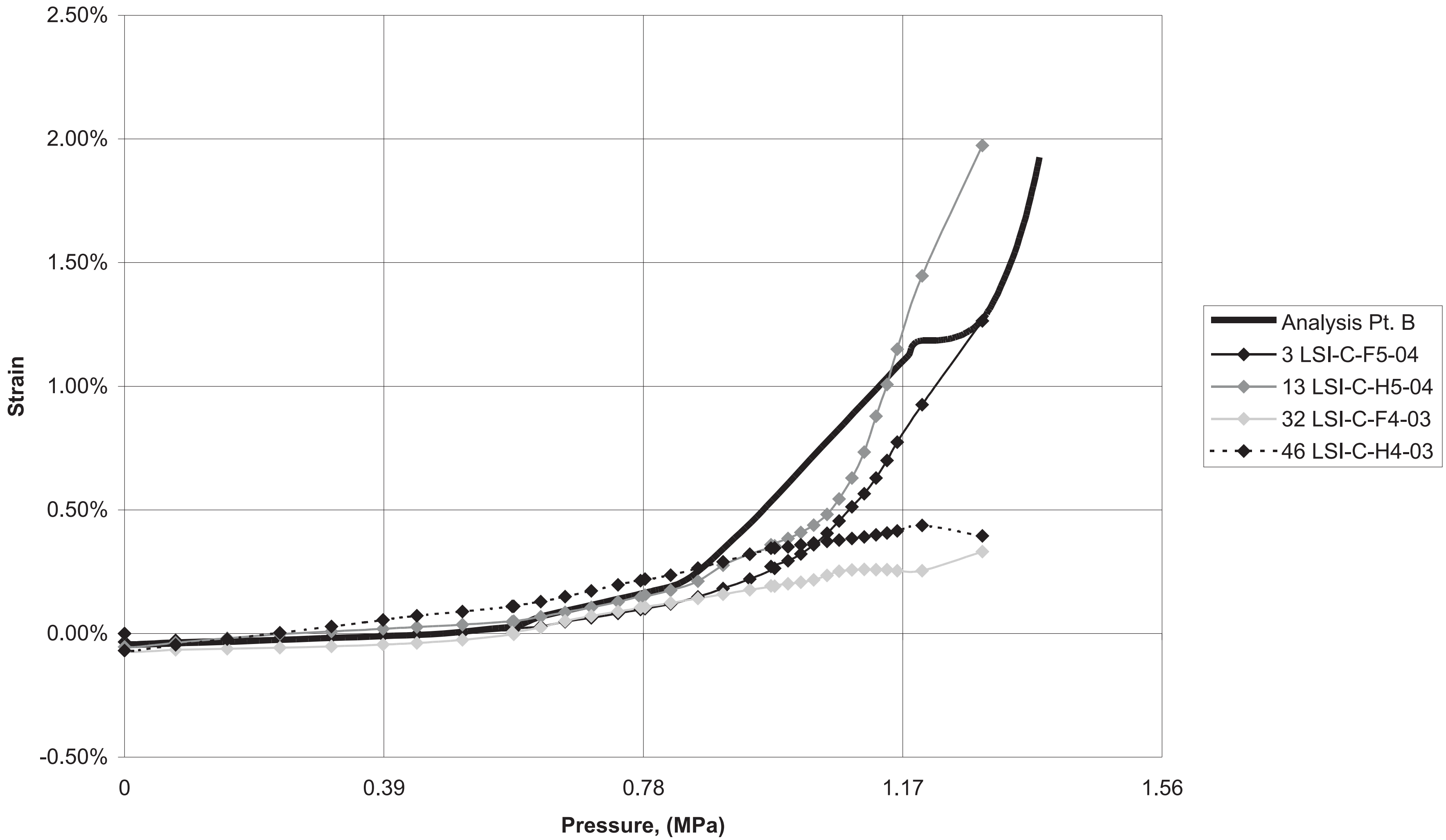

Figure 7-52. M/S and F/W Test vs. Analysis Linear Strain Comparisons at Location "B," Near T-Anchor, 3:00, 9:00 Position

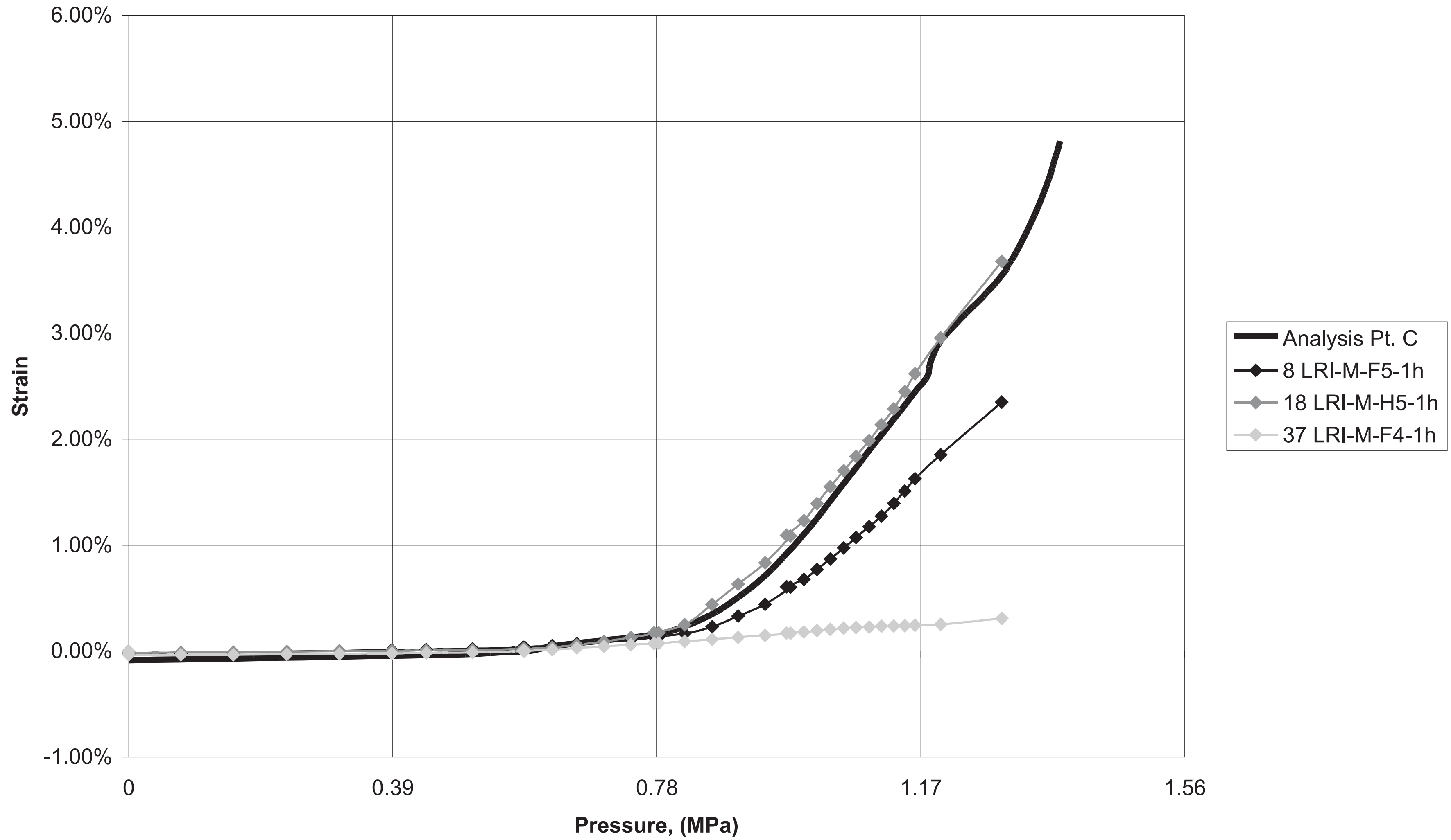

Figure 7-53. M/S and F/W Test vs. Analysis Linear Strain Comparisons at Location "C," Near T-Anchor, 3:00, 9:00 Position

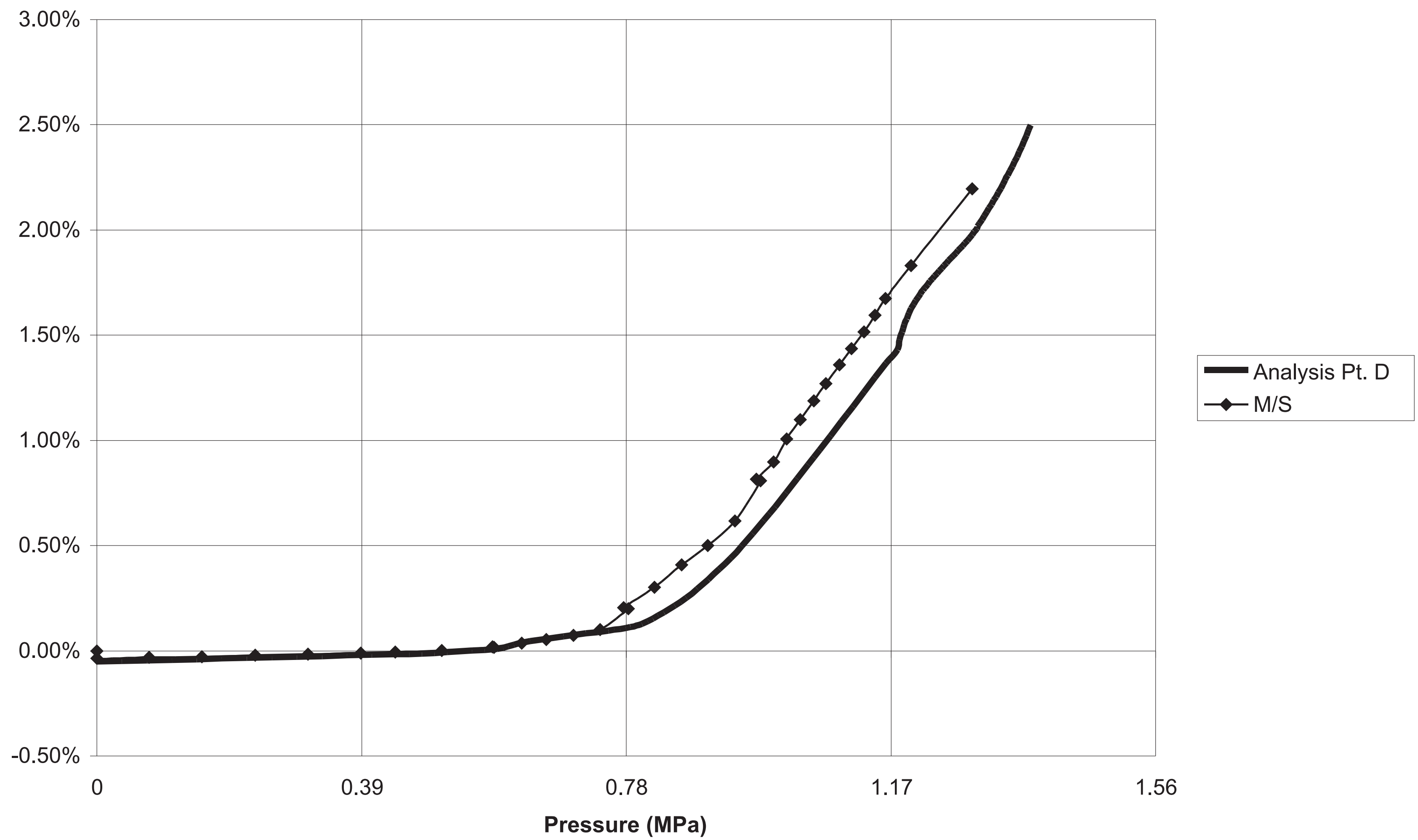

Figure 7-54. M/S Test vs. Analysis Linear Strain Comparisons at Location "D," Near Weld-Corner, 3:00, 9:00 Position.

8.0 LINER SEAM AND "RAT-HOLE" DETAIL ANALYSIS

8.1 Objectives of New Models

The PCCV model exhibited 16 distinct locations at which liner tears occurred. These locations are illustrated in Figure 8-1. In the pretest analysis report [1], the predicted elevated liner strain locations were categorized as Location Types 1 through 5.

1. Vertical weld seams intercepted by a horizontal stiffener and interrupted by rat-hole;
2. The termination points of vertical T-anchors near penetrations;
3. The termination points of horizontal stiffeners near penetrations;
4. Weld-connection points of multiple acute-angled liner pieces;
5. The wall-liner/basemat-liner connection.

Of these five, liner tears at the first three location types were predicted as likely to occur and Location 2 was identified as the most likely. However, all of the 16 tear locations observed were near weld seams, with some variation in the presence or configuration of a rat-hole. Furthermore, by comparing the "before and after" photos taken by SNL (Reference [8] with a typical tear, tear 16, shown in Figure 8-2), it is observed that liner welding irregularities were present at almost all of the tear locations. These irregularities included points of extensive repair, such as grinding, points of discontinuous or missing back-up bars, or points with weld and liner seam fit-up irregular geometry. Locations where a seam and rat-hole existed and high strains were measured, but a tear did not occur (e.g., at Location D-7, located just below where tear 16 occurred), further prove the importance of the welding details to the occurrence of liner tearing.

The liner weld irregularities have been well documented by the findings of [8], and are summarized as follows.

- Visual observation showed extensive grinding and weld repair in the liner welds where most of the tears occurred. Ultrasonic measurements showed substantial reductions in thickness near these tears. Measurements showed ~23% thickness reduction in many locations, and more (up to 40% in a few locations). (Several instances were found in which the liner adjacent to repair welds had been completely ground through and subsequently repair welded.)

- Localized plastic deformation occurred in association with many of the vertical field welds, particularly in the vicinity of the tears. No evidence of brittle fracture was seen.

- Photos of the back side of the liner revealed irregularities (missing segments of back-up bars, discontinuities in horizontal stiffeners) associated with a number of the tears.

- Mechanical testing showed only small strain localization in the weld heat affected zones — much less than observed in the liner base metal. Ultimate strength (~72 ksi) was not degraded by welding.

- No evidence was found of material problems that could account for the premature tearing of the liner. Only one tear (1) was associated with a weld defect. This was a lack-of-fusion defect, not porosity in the fusion zone.

- Metallography showed that nearly all of the tear areas had been ground at least 23%, both in preparation for repair welding and following repair welding. The report [8] concluded that most of the tears can be attributed to this excessive grinding.

- Some free-field tears were caused or exacerbated by back-side discontinuities in back-up bars and horizontal stiffeners. Some were also caused or exacerbated by back-side discontinuities (such as stiffeners) that served to localize plastic strain in these areas.

These observations, however, leave many unanswered questions about quantifying the effects of welding irregularities and distinguishing these from the strain concentration effects that are solely related to geometry.

In defining the objectives for posttest study of the liner tear locations, it is important that the study be aligned with the overall objectives of the containment research program; namely, to develop, refine, and validate analytical methods for predicting the overpressure behavior of containments. In other words, local analysis of the liner tear areas should not just model a detail where a tear occurred and see if the calculated high strains locations agree with the tear location, but should use the liner strain measurement data to refine and validate the methodology for modeling such locations. This, hopefully, will result in improved methods, and improved confidence in methods, for analyzing such details in full-scale containments. Further, by studying behavior with and without back-up bars, analytical support can be added to the test result conclusions already emerging from the SNL research about the importance of continuous back-up bar design code requirements. With these objectives in mind, the steps (and objectives) followed for this portion of the posttest analysis effort were as follows.

1. Analyze a "Type 1" liner strain concentration location at a group of liner strain gages to calibrate the finite element modeling to the strain measurements. The locations selected as typical were D-7 – near a typical vertical-seam/horizontal-stiffener-rathole – and tear 16, just a little above location D-7. Location D-7 is typical of rat-hole locations where significantly elevated strains occurred (some were measured), but no tears occurred. Tear 16 has some unique aspects, but part of the tear is typical of a number of tear geometries. The mesh is liner-only, without concrete.

2. Perform mesh-size and material property sensitivity analysis for calibrating to strain gage measurements to develop conclusions and guidelines for future modeling of similar details in full-scale containments. The material sensitivity analyses include the introduction of variation of stress-strain-curve assumptions for liner base metal, weld material, and heat-affected-zone material. It also includes differences in thickness from those of the nominal design, which were observed/measured on the as-built model. Input for these material property assumptions was obtained from SNL's metallurgical examination report [8].

3. Provide comparison to strain gage measurements.

4. Analyze with and without back-up bars.

5. Develop conclusions about the utility of local liner-only modeling for examining these type of details, and about the effects of liner base metal grinding, HAZ material property variation, and back-up bar discontinuities on the liner's propensity to tear.

8.2 Description of Computational Grids

The basic computational grid for the liner seam studies is shown in Figures 8-3 and 8-4. The grid consists of 4-node shell elements with reduced integration (ABAQUS S4R elements), and thicknesses assigned as described later in this chapter. Where unaffected by grinding, the as-measured thickness of 1.8 mm was used. Guidance for the thickness assignments was taken from SNL's posttest thickness measurements reported in [8]. The grids extend across one "span" between T-anchors, or 450 mm, on the assumption that between T-anchors, the liner is relatively free to locally strain and deform irrespective of the concrete backing. These grids also ignore the curvature of the PCCV wall, and so are flat.

The boundary conditions applied to the grids are a pinned condition at the left edge of the mesh and an applied x-displacement at the right edge.

The height of the model is 300 mm with hoop stiffeners at the 1/3 points. The lower stiffener has a rat-hole cutout at the midpoint. This mesh provides inherent comparisons between free-field liner behavior, liner vertical and horizontal seams without stiffeners, and a vertical seam with stiffener/rat-hole. It also specifically models the condition at Location D-7, and by adding various flaws (described later), it can be made to simulate tear 16 and other rat-hole locations, with or without back-up bars.

All edges of the grids have fixed conditions for out-of-plane deformations and rotational degrees of freedom. Horizontal (hoop) and vertical (meridional) displacements are fixed along the left and bottom edges, respectively. The grids are loaded in displacement control horizontally and vertically along the right and top edges. Loading in both the hoop and meridional directions simulates the bi-axial states of stress developed in the actual containment liner. The load history applied was derived from LST data. The applied vertical displacement was calculated from the liner meridional strain, measured at gage LSI-M-Z6-01, multiplied by the model height, 300 mm. The history of liner meridional strain and the best-fit curve used for the model is shown in Figure 8-5. The horizontal displacement history was derived from the radial displacement, measured at gage DT-R-Z5-01. The radial displacement was converted to hoop strain by dividing by the radius, 5373 mm, and then multiplying by the mesh width, 450.4 mm. Figure 8-6 shows the radial displacement history and the best-fit curve used for the analysis.

The model (and most of its variations) was loaded from an equivalent internal pressure of 0.55 MPa (80 psig) up to the end of the LST, 1.30 MPa 1(87.9 psig) or 3.3 Pd. The starting pressure was chosen as the point where the internal pressure overcomes the initial containment prestressing when the hoop strain is approximately zero. Table 8-1 lists the measured liner strain and displacement and the converted data for the displacement boundary conditions. Temperature correction was not applied. Two of the parameter runs (the ones most closely replicating Location D-7), were then run beyond 3.3 Pd to see when a tear might have occurred if the LST had proceeded to higher pressure.

Table 8-1. Liner Model Displacement Loading Boundary Conditions (for LST)

Pressure MPa	Radial Disp. mm (estimated)	Meridional Strain (estimated)	Δ horizontal (mm)	Δ vertical (mm)
0.55	-0.35	-0.00023	-0.0305	-0.0711
85.0	0.43	-0.00022	0.0014	-0.0026
90.0	1.14	-0.00021	0.0038	-0.0025
95.0	1.87	-0.00020	0.0062	-0.0024
100.0	2.58	-0.00019	0.0085	-0.0023
105.0	3.25	-0.00018	0.0107	-0.0022
110.0	3.90	-0.00017	0.0129	-0.0020
115.0	4.53	-0.00016	0.0149	-0.0019
120.0	5.17	-0.00015	0.0171	-0.0018
125.0	5.77	-0.00014	0.0190	-0.0016
130.0	6.40	-0.00012	0.0211	-0.0015
135.0	7.08	-0.00010	0.0234	-0.0012
140.0	7.77	-0.00008	0.0256	-0.0010
145.0	8.54	-0.00006	0.0282	-0.0007
150.0	9.35	-0.00004	0.0308	-0.0004
155.0	10.30	-0.00001	0.0340	-0.0002
160.0	11.27	0.00002	0.0375	0.0003
165.0	12.60	0.00010	0.0416	0.0011
170.0	14.00	0.00017	0.0462	0.0020
175.0	15.65	0.00024	0.0516	0.0028
180.0	17.50	0.00032	0.0577	0.0038
185.0	19.70	0.00042	0.0650	0.0050
187.9	21.15	0.00048	0.0698	0.0057

8.3 Mesh Sensitivity Study

Three variations of the mesh refinement were investigated in the initial parameter study. Figures 8-7 – 8-9 show the finite element grids used as the baseline, coarse, and fine models, respectively. The coarse mesh has approximately half the refinement of the baseline model and the fine mesh has approximately double the refinement. The number of nodes, elements, and degrees of freedom for each model are summarized in Table 8-2.

Table 8-2. Liner Model, Mesh Sensitivity, Model Statistics

Model	Coarse	Baseline	Fine
Number of Nodes	11011	20724	33391
Number of Elements	10428	19960	32436
Number of D. O. F.	64956	123006	198720
Percent Difference, Baseline	-47%		62%

Maximum principal strain contour plots of the liner for the baseline, coarse, and fine models are shown in Figures 8-10 – 8-12 at the end of the analysis, approximately 187.9 psig. The local contour plots of the liner in the stiffener cutout location have equal widths and heights between the three different grids. The dimensions with respect to the weld centerline and the stiffener centerline are shown on each plot. These results show similar response with strain concentrations developing at the reentrant corners of the rat-hole and liner. As expected, the peak strains at the concentration vary somewhat, with the largest strain calculated for the finest mesh. The peak strains at the reentrant corner are 7.1%, 10.2%, and 13.0% for the coarse, baseline, and fine grids, respectively.

To more accurately compare the sensitivity of the mesh refinement, strains at locations away from the concentration were extracted. Figures 8-13 and 8-14 show plots of the principal strain history for the three models at locations approximately 5 mm and 1.2 mm below the stiffener reentrant corner. These comparisons show a significant change in strain histories between the course mesh and baseline mesh, but much closer comparison between baseline and fine. Figures 8-15 and 8-16 show strain profiles in line with the stiffener, moving across the rat-hole. To compare strains at the same geometric positions, two integration points of the fine mesh were averaged to provide data comparisons at a single point of the baseline mesh. This shows that by simple averaging of strains across a single element, the fine and baseline meshes produce roughly the same results. Thus it was concluded, in the analyst's opinion, that the baseline mesh descritization is of adequate size for the liner tear study. Note that the fundamental element dimension (hoop direction) for the baseline mesh was 0.8 mm, a little less than half of the liner thickness, and about half of the reduced liner thickness.

8.4 Material and Geometry Variations

The next phase of the liner tear study conducted analyses to assess the effects of material and geometry variations. The first variation was to implement varying material properties near the weld areas. This included assignment of different material properties to the base metal, HAZ, and weld fusion zone (WFZ) regions of the model. The second variation only modified the material in the WFZ. This is expected to show that strain localization develops predominately at softer HAZ, as opposed to the discontinuity immediately adjacent to the WFZ. The final phase incorporated geometry modifications to the model near the weld lines. This included thinning elements and varying the extent of thinning in the vicinity of the welds due to grinding. The geometry modifications were coupled with modified material properties ranging from uniform to including variations of base metal, HAZ, and WFZ regions. The material and geometry variations were based on data contained in the SNL metallurgical analysis report [7]. The material property parameters from [7] are summarized in Table 8-3.

Description of the variations introduced for the parameter study are provided below, listed in Table 8-4, and illustrated in Figure 8-17. The material variations were introduced by shifting the entire plastic portion of the stress-strain curve up or down by the ratio of the UTS listed in Table 8-3 to the UTS of the base metal listed in Table 8-3.

8.4.1 Mesh Sensitivity Study

1. Baseline Mesh
2. Coarse Mesh
3. Fine Mesh

All subsequent models use the baseline mesh.

Table 8-3. Microhardnesses of Zones Surrounding Welds (from Reg. [8])

Zone	Avg. Hardness*	Std. Dev.	UTS (ksi)**	UTS (MPa)**
Base metal	160	6.9	74.5	515
Fine-grained HAZ	151	4.3	71	490
Med-grained HAZ	154	3.4	72	495
Coarse HAZ	164	6.8	76.5	525
Fusion Zone	180	11.4	84	580
Recrystallized fusion zone	173	5.9	80.5	550

* Vickers hardness, 100 gram load

** Ultimate Tensile Strength (UTS) estimates. Reference [8] notes that UTS estimates are based on conversion tables for hardness tests made with much heavier loads. As a result, the estimated UTS values should be taken only as approximations; they are useful primarily for comparing the expected relative strengths of the various regions, not the absolute strengths.

8.4.2 Material Variation

1. Varying material, base metal, fine, medium, coarse HAZ regions, and fusion zones.

2. Varying material, base metal, and fusion zones. No HAZ material variation.

8.4.3 Geometry and Material Variation

1. Varying material, base metal, fine, medium, coarse HAZ regions, and fusion zones. Grinding from base to horizontal seam weld, Extent +/- 10mm either side of vertical seam weld, 20% thickness reduction.

2. Varying material, base metal, fine, medium, coarse HAZ regions, and fusion zones. Grinding from base to horizontal seam weld, Extent +/- 20 mm either side of vertical seam weld, 20% thickness reduction.

3. Varying material, base metal, and fusion zones. Grinding from base to horizontal seam weld, Extent +/-10 mm either side of vertical seam weld, 20% thickness reduction.

4. Varying material, base metal, and fusion zones. Grinding from base to horizontal seam weld, Extent +/-20 mm either side of vertical seam weld, 20% thickness reduction.

5. Varying material, base metal, fine, medium, coarse HAZ regions, and fusion zones. Grinding from base to horizontal seam weld, Extent +/- 10mm either side of vertical seam weld, 40% thickness reduction.

6. Varying material, base metal, fine, medium, coarse HAZ regions, and fusion zones. Grinding from base to horizontal seam weld, Extent +/- 20 mm either side of vertical seam weld, 40% thickness reduction.

7. Varying material, base metal, and fusion zones. Grinding from base to horizontal seam weld, Extent +/- mm either side of vertical seam weld, 40% thickness reduction.

8. Varying material, base metal, and fusion zones. Grinding from base to horizontal seam weld, extent +/- 20 mm either side of vertical seam weld, 40% thickness reduction.

8.5 Results and Comparisons with Test

The spatial distributions of stresses and strains at a pressure of 188 psig (3.3 Pd) for the baseline plus the first 10 parameter cases (Cases 1 and 4 through 13) are shown in Figures 8-18 through 8-39. Each set provides horizontal

Table 8-4. Sensitivity Study Parameters

Analysis	Overgrinding	Base Metal			Fine Grained HAZ			Medium Grained HAZ			Coarse Grained HAZ			Fusion Zone		
	Width	K	σ_y	t	K	σ_y	t	K	σ_y	t	K	σ_y	t	K	σ_y	t
	(mm)		(ksi)	(mm)		(ksi)	(mm)		(ksi)	(mm)		(ksi)	(mm)		(ksi)	(mm)
b-01	0.0	1.00	54.56	1.80	1.00	54.56	1.80	1.00	54.56	1.80	1.00	54.56	1.80	1.00	54.56	1.80
b-02*	0.0	1.00	54.56	1.80	1.00	54.56	1.80	1.00	54.56	1.80	1.00	54.56	1.80	1.00	54.56	1.80
b-03**	0.0	1.00	54.56	1.80	1.00	54.56	1.80	1.00	54.56	1.80	1.00	54.56	1.80	1.00	54.56	1.80
b-04***	0.0	1.00	54.56	1.80	0.95	51.83	1.80	0.97	52.92	1.80	1.03	56.20	1.80	1.13	61.65	1.80
b-05	0.0	1.00	54.56	1.80	1.00	54.56	1.80	1.00	54.56	1.80	1.00	54.56	1.80	1.13	61.65	1.80
b-06	10.0	1.00	54.56	1.44	0.95	51.83	1.44	0.97	52.92	1.44	1.03	56.20	1.44	1.13	61.65	1.80
b-07	20.0	1.00	54.56	1.44	0.95	51.83	1.44	0.97	52.92	1.44	1.03	56.20	1.44	1.13	61.65	1.80
b-08	10.0	1.00	54.56	1.44	1.00	54.56	1.44	1.00	54.56	1.44	1.00	54.56	1.44	1.13	61.65	1.80
b-09	20.0	1.00	54.56	1.44	1.00	54.56	1.44	1.00	54.56	1.44	1.00	54.56	1.44	1.13	61.65	1.80
b-10	10.0	1.00	54.56	0.99	0.95	51.83	0.99	0.97	52.92	0.99	1.03	56.20	0.99	1.13	61.65	1.80
b-11	20.0	1.00	54.56	0.99	0.95	51.83	0.99	0.97	52.92	0.99	1.03	56.20	0.99	1.13	61.65	1.80
b-12	10.0	1.00	54.56	0.99	1.00	54.56	0.99	1.00	54.56	0.99	1.00	54.56	0.99	1.13	61.65	1.80
b-13	20.0	1.00	54.56	0.99	1.00	54.56	0.99	1.00	54.56	0.99	1.00	54.56	0.99	1.13	61.65	1.80
c-03	With back-up bars and Tear 16 modeling (missing short section of back-up bar on horiz. weld seam															
c-04	With back-up bars and Tear 16 modeling variation (added "over" liner grinding only at missing horiz. back-up bar)															
c-05	With back-up bars and Tear 16 modeling															
c-06	With back-up bars; no Tear 16 modeling															
c-07	With back-up bars, and additional grinding only at "Tear 16"; no missing back-up bar															

* 2 is coarse mesh
** 3 is fine mesh
*** 4 is baseline mesh (best estimate case)

(hoop) stress, vertical (meridional) stress, and Von Mises stress, and the analogous strain components. The figures illustrate competing strain concentrations and provide evidence of the variety of conditions that probably existed in the PCCV model (both at the tear locations and at similar details that didn't tear). It is clear from Figures 8-18 through 8-25 (Cases 1, 4, 5, 6) that the cases with unmodified thicknesses all develop their highest strains near the stiffener edge, not next to the weld. Further, for Cases 1 and 4, the end of the analyses (which corresponds to 3.3 Pd and the end of the LST) show peak strains lower than the tearing threshold. (Depending on the biaxiality of stress, the tearing threshold is calculated to be approximately 20%. The liner tearing criteria is covered in detail in the pretest analysis report, and not repeated here.) The baseline case peak effective plastic strain reaches only 11.4%, so for a "perfectly" constructed detail, the model analyzed here does not predict a tear. When the best estimated HAZ and fusion zone material strengths are introduced (Case 4), some strain elevation moves into the fine HAZ, but it is not as large as the strain at the stiffener edges and the peak strain (18.7%) is still just below the strain that would indicate occurrence of a tear. This agrees with the observed behavior at locations like D-7.

When only the fusion zone strength is elevated, (Case 5), the level of strain concentration at the stiffener edges is intensified, and strains reach 21%, which is likely a tear condition. Since this was not observed in the test at locations without grinding related thickness reductions, it is probably not a realistic case; i.e., the best estimate material property adjustments appear necessary to achieve the most realistic behavior prediction.

When 20% thickness reductions are introduced (Cases 6 and 7) with best estimate weld zone strengths, the case with 20 mm of grinding width reaches its highest strains at the stiffener edge (max ε_{eff} = 17.8%), while the Case with 20 mm grinding width shows much more widely distributed elevated strains and also no fracture (max ε_{eff} = 12.2%). When only the grinding is introduced with no change to material properties (Cases 8 and 9), the high strain zone moves completely away from the stiffener ends and concentrates itself in the thinned area. But neither of these cases reach fracture.

In the last set of cases without back-up bars, 10 through 13, the thinning is 40%, and the highest elevated strains generally move into the thinned area. Cases 10 and 12 (23% and 20% strains) certainly fracture, while Case 11 and 13 (11% and 16% strains) do not. These Cases are particularly interesting, and in fact, for the tear locations that tore immediately adjacent to a vertical weld (Case 10), with its very focused band of high strain next to the fusion zone, appears to provide a good simulation of the tearing phenomena. All of these results are summarized in Table 8-5. This table also provides author's opinions as to whether the specific model variation captures observed behavior on the model, and where. These opinions are supported later in the discussion.

The next plot series, Figure 8-41 through 8-52, show horizontal (hoop) and vertical (meridional) strains at selected locations identified in Figure 8-40. The cases with modified material properties (4, 6, 7, 10, 11) are compared to the baseline on the left, and without modified material properties (5, 8, 9, 12, 13) are compared to the baseline on the right.

In order to draw conclusions about modeling such details, some comparisons with gage measurements are provided in Figures 8-54 through 8-58. In each plot, the gage name is provided, and the position numbers from the FE analysis are mapped in Figure 8-53. The gages are taken from various locations on the model that are all near vertical weld seams and rat-hole stiffener details: namely, at locations A5, K5, J5, D7, and Z5. A5 is near the edge of the E/H embossment that exhibited tears, and K5 is on the other side, which did not tear. J5 is near the 270° buttress, and D7 is near the 0° buttress. Z5 is near the 135 degree azimuth.

Fair correlation is obtained at position 2 (fine grained HAZ, near weld, in line with stiffener) with Cases 7 and 9. Case 10 agrees well below 3 Pd, but then turns up too quickly. Position 4 also shows fair correlation with several of the cases, and position 5 appears to agree with Cases 10 and 12.

8.6 Back-Up Bars and Additional Analyses

Since these models provide a reasonable representation of the actual liner behavior, a few models were extended to develop further insights. Because some locations (and some FE models that simulate them) clearly do not develop tears, the first model extension was to predict when these non-tear rat-hole details might have torn, had the LST proceeded to higher pressure. For this, Cases 1 and 4 were extended to higher pressure; of course, this was only a hypothetical simulation. Case1 was chosen because it is the baseline, and Case 4 was chosen as a best estimate simulation of pristine rat-hole details that did not tear, possibly similar to Locations D-7, Z-5, and J-5. The displacement versus pressure extension was made using the SFMT. Data from the SFMT at radial displacement gage DT-R-Z5-D1 was obtained and added to the LST data, as shown in Figure 8-59. The vertical boundary condition was created by a curve-fit extrapolation (Figure 8-60), because no liner strain measurements were taken in the SFMT.

The stress and strain contour results are plotted at 3.4 Pd and 3.6 Pd in Figures 8-61 and 8-68. They indicate a prediction that either case (with or without the HAZ material modifications) would tear prior to reaching 3.4 Pd. The tear, indicated by ε_{eff} = 26.3%, would occur next to the stiffener end. The strain histories of the element locations shown in Figure 8-40 for these extension runs are shown in Figures 8-69 through 8-76. These provide further evidence on which to base the prediction of tearing pressure, pegging it to between 3.37 and 3.4 Pd. These two cases are entitled Case 1b and 4b, because they use the same models as Case 1 and 4 – just pushed to higher pressure.

The next extension of the parametric study series added back-up bars and more specifically captured the details at tear 16. This set of changes is illustrated in Figure 8-77. The back-up bars are extra, separate elements. The back-up bar elements were only joined to the liner at the edges of the fusion zone, so they did not strengthen the liner in areas of liner thinning/grinding.

Tear 16 is of particular interest for this study because it encompasses three types of tear mechanisms along the path of the tear:

1. Across a horizontal seam where a short stretch of back-up bar was ground off (and with possible liner thinning caused by the grinding);

2. Along the HAZ next to a vertical seam; and

3. Next to the edge of the vertical back-up bar or next to the stiffener end inside the rat-hole.

Models C3, C4, C5, C6, and C7 capture possible variations of geometry that could influence these tearing mechanisms. The grinding and back-up bar versions are illustrated in Figure 8-77 and in Table 8-5. The stress strain contours for these models (at 3.3 Pd) are shown in Figures 8-78 through 8-87. Strain history plots versus pressure are also shown in Figures 8-89 through 8-94, the locations of which are shown in Figure 8-88.

As described previously, the conclusions of the studies are summarized in Table 8-5. The results are all tabulated at P=188 psig, 3.3 Pd. Many of the conclusions were based on comparisons to:

- Strain gage measurements,
- Physical measurements of liner ground thickness and HAZ characteristics obtained from [7], and
- Visual observations of tear geometry

The geometric locations of the gage groups are shown in Figures 8-95 through 8-98. Many detailed strain gage comparisons were developed at the pressure snapshots of 2.8 Pd and 3.3 Pd. Gage readings are compared to contour illustrations in Figures 8-99 through 8-114. These compare the gage readings for the five rat-hole gage groups directly on the same plots. Thus, one or more gage groups may agree well with a contour while other gage groups may not. The gage group's "agreement" is summarized in Table 8-5.

8.7 Conclusions of Liner Seam Analyses

The conclusions of the liner seam/rat-hole modeling study are summarized below.

- By comparison with strain gage measurements and posttest liner tear observations, some of the finite element liner-only meshes capture the strain concentrations in and around the rat-holes and liner welds reasonably well.

- Because of competing mechanisms (between the weld zone and the ends of stiffeners), making yield and ultimate strength adjustments to the HAZ material properties appears to be justified and necessary to correctly predict strain concentration location and intensity.

- Case C6 with back-up bars, nominal geometric properties, and best-estimate material properties is the best predictor of defect-free construction of rat-hole/weld-seam details, as probably occurred in the PCCV model at locations such as D7 and J5; however, even without back-up bars, Case 4, also provides reasonable simulation (and correlation with gages) at these locations.

- Case 10 appears to provide the best simulation of the behavior of tear occurrences in which severe liner thinning (due to weld repair grinding) was present and back-up bars were absent; these conditions existed at tears 7, 8, 10, 12, 13, 14, 15, and 16.

- Case C5 showed the highest strains of all the cases (with a peak over twice as high as Case 10) even though it is analogous to Case 10, with back-up bars added. This shows that in the presence of grinding-caused liner thinning, back-up bars may actually exacerbate the strain concentration in the HAZ. Note, however, that the peak strain in the HAZ was also strongly exacerbated by the presence of the tear 16 detail. This case appears to reasonably simulate the tears that occurred *with* back-up bars present, namely, tears 1, 2, 6, 9, 11, and 16. The severity of the strain in this case also shows that a tear ($\varepsilon_{eff} > 20\%$) at the geometry simulated would have been predicted to occur as early as 3.0 Pd.

- Cases C3 and C4 reasonably simulate tear 16. The lower strain concentration in these models also simulate other tears that appear to have formed at the ends of stiffeners: tears 3, 6, 7, 9, and 11.

- If a section of liner with a rat-hole/liner-seam detail such as that at tear locations 7, 12, 13, and 15 is subjected to additionally elevated strain (i.e. strain across the liner model that is larger than free-field global strain), a tear even earlier than 3.0 Pd can be justified. In practice, such a prediction could be approximated using a strain concentration factor approach. The strain concentration factors (K = peak ε_{eff} divided by global ε_{hoop}) implied by this liner seam study are as follows:

  ε_{hoop} = 21mm/5375mm = 0.00391

Case 4:	K = 48 (tear at stiffener end, no back-up bar)
Case C6:	K = 45 (tear at stiffener end, with back-up bar)
Case 10:	K = 59 (tear at HAZ, no back-up bar, and 40% thickness reduction due to grinding)
Case C4:	K = 91 (tear at tear 16, if a short segment of horizontal weld seam back-up bar is missing)

- Using the LST pressurization, the rat-hole/seam locations without defects, such as location D-7, still would have developed liner tears by a pressure of 3.4 Pd.

Table 8-5. Peak Effective Plastic Strains for Each Case

Case	Material	Grinding	Back-up Bars	Tear 16 Detail	Peak Strain at 188 psig (3.3 Pd)		Tear Predicted	Behavior Similar to:
					Location	Max. Effective Strain		
1	Nominal	No	No	--	Stiffener End	0.114	No	None
4	Heat-Adjacent	No	No	--	"	0.187	No	Yes-D7, Z5, A5, J5
5	Nominal+F.Z.	No	No	--	"	0.213	Yes	None
6	Heat-Adjacent	20% - 10mm	No	--	"	0.178	No	Yes-D7, K5
7	Heat-Adjacent	20% - 20mm	No	--	Stiffener End/Fine HAZ	0.122	No	Yes-D7, K5
8	Nominal+F.Z.	20% - 10mm	No	--	10mm from weld	0.121	No	Yes-D7, K5
9	Nominal+F.Z.	20% - 20mm	No	--	Stiffener End	0.164	No	None
10	Heat-Adjacent	40% - 10mm	No	--	Fine HAZ	0.231	Yes	Yes-tear 1,7,8,10, 12,13,14,15, 16
11	Heat-Adjacent	40% - 20mm	No	--	Stiffener End/Fine HAZ	0.107	No	Yes-K5, D7
12	Nominal+F.Z.	40%-10mm	No	--	10mm from weld	0.199	Yes	No
13	Nominal+F.Z	40% - 20mm	No	--	Stiffener End	0.157	No	Yes-K5, D7
C3	Heat-Adjacent	No	Yes	Yes	At tear 16 (and Stiffener End)	0.361	Yes/Yes	Yes-D7*, tear 3,6,7,9, 11,16
C4	Heat-Adjacent	No	Yes	Yes w/ grinding	Stiffener End (and tear 16)	0.354	Yes/Yes	Same as C3
C5	Heat-Adjacent	40% - 10mm	Yes	Yes w/ grinding	Fine HAZ (and tear 16)	0.567	Yes/Yes	Yes-D7*, tear 1,2,6,9, 11,16
C6	Heat-Adjacent	No	Yes	No	Stiffener End	0.175	No	Yes-D7, J5 A5
C7	Heat-Adjacent	No	Yes	No w/ Grinding	Stiffener End	0.299	Yes	Yes-tear 3,6,9,11

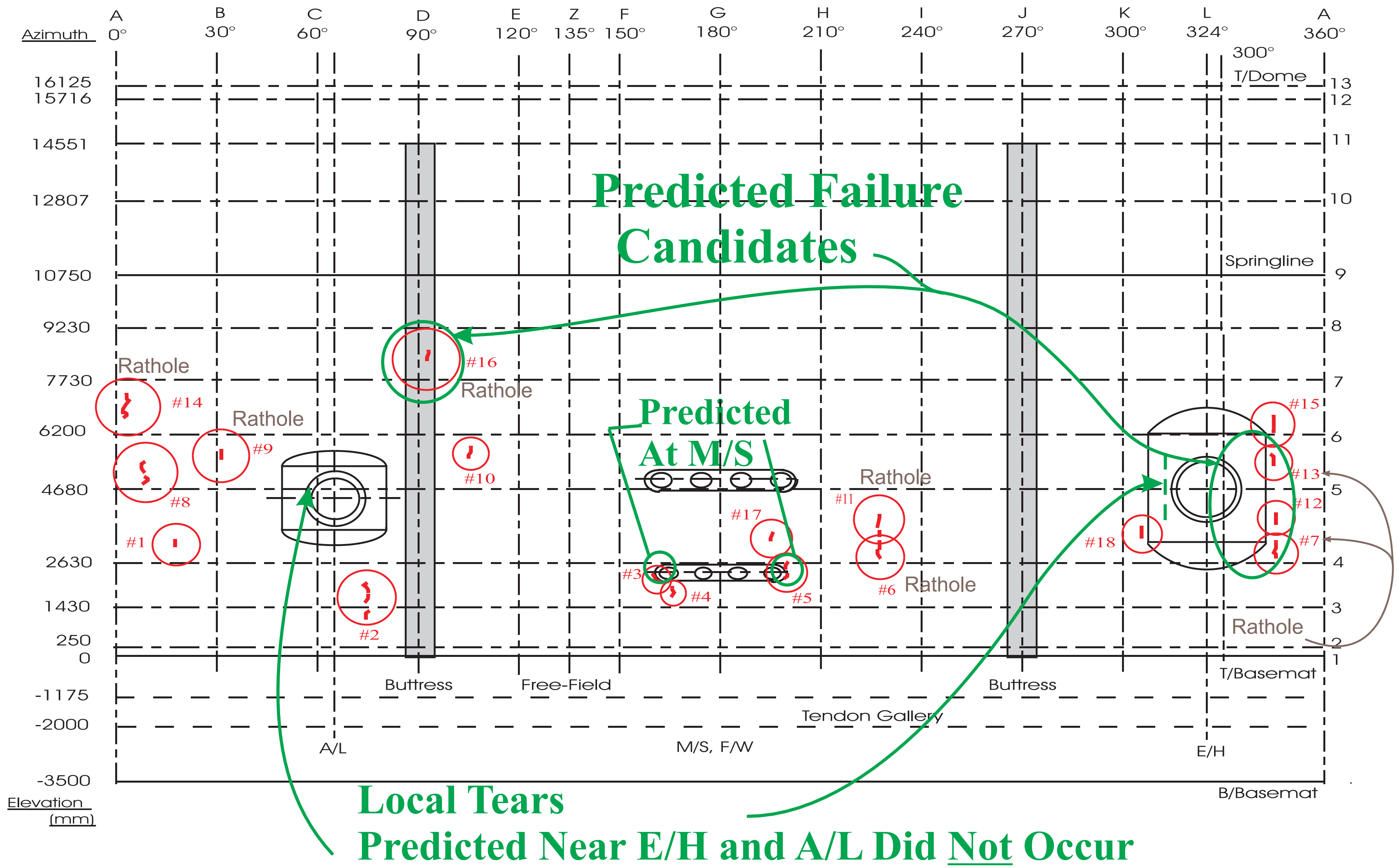

Figure 8-1. Liner Tears Observed in the 1:4 Scale PCCV LST

Liner Tear #16

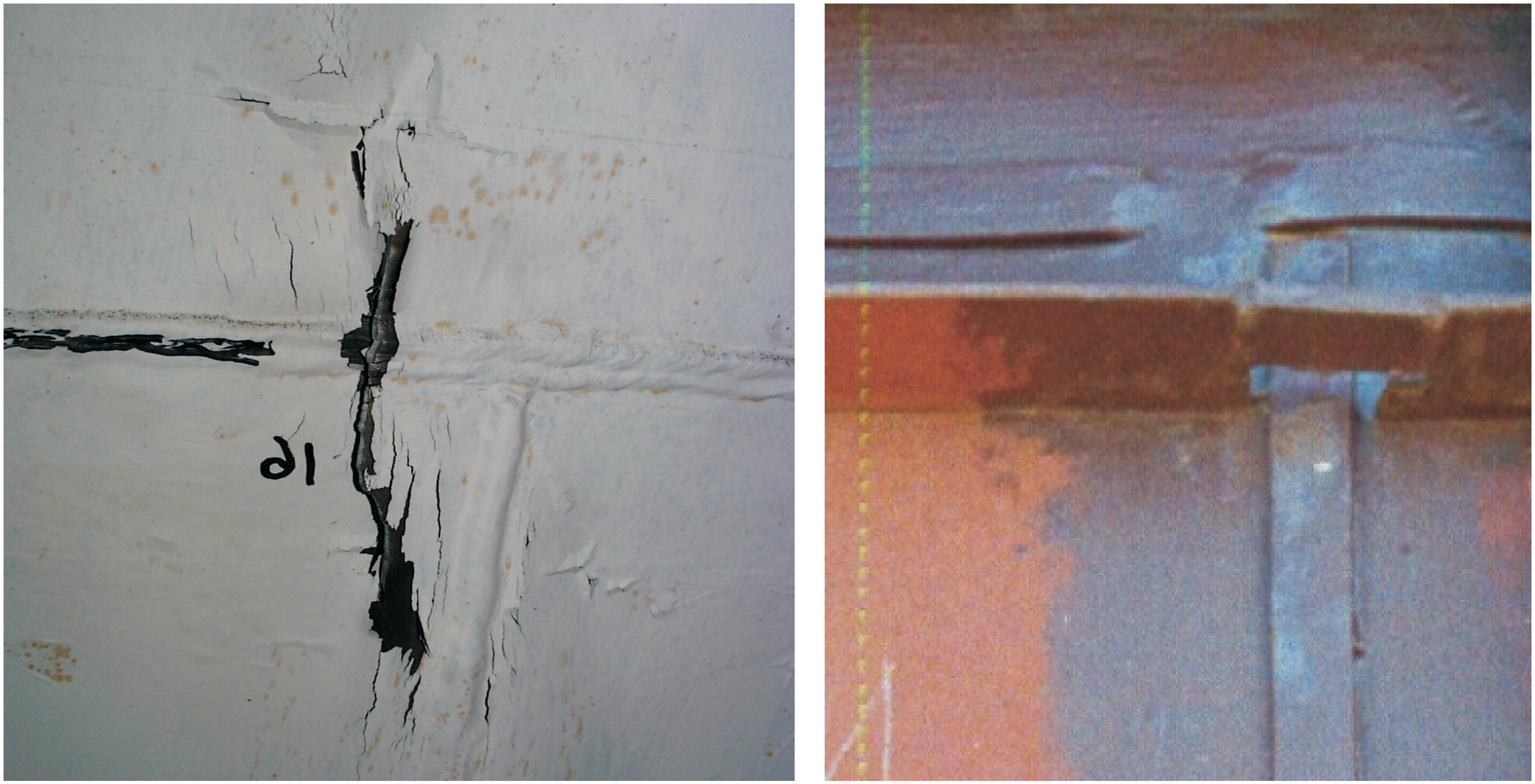

(Image reversed for comparison)

Figure 8-2. Photos of Typical Liner Tear, Inside Surface (Left), Concrete Side (Right)

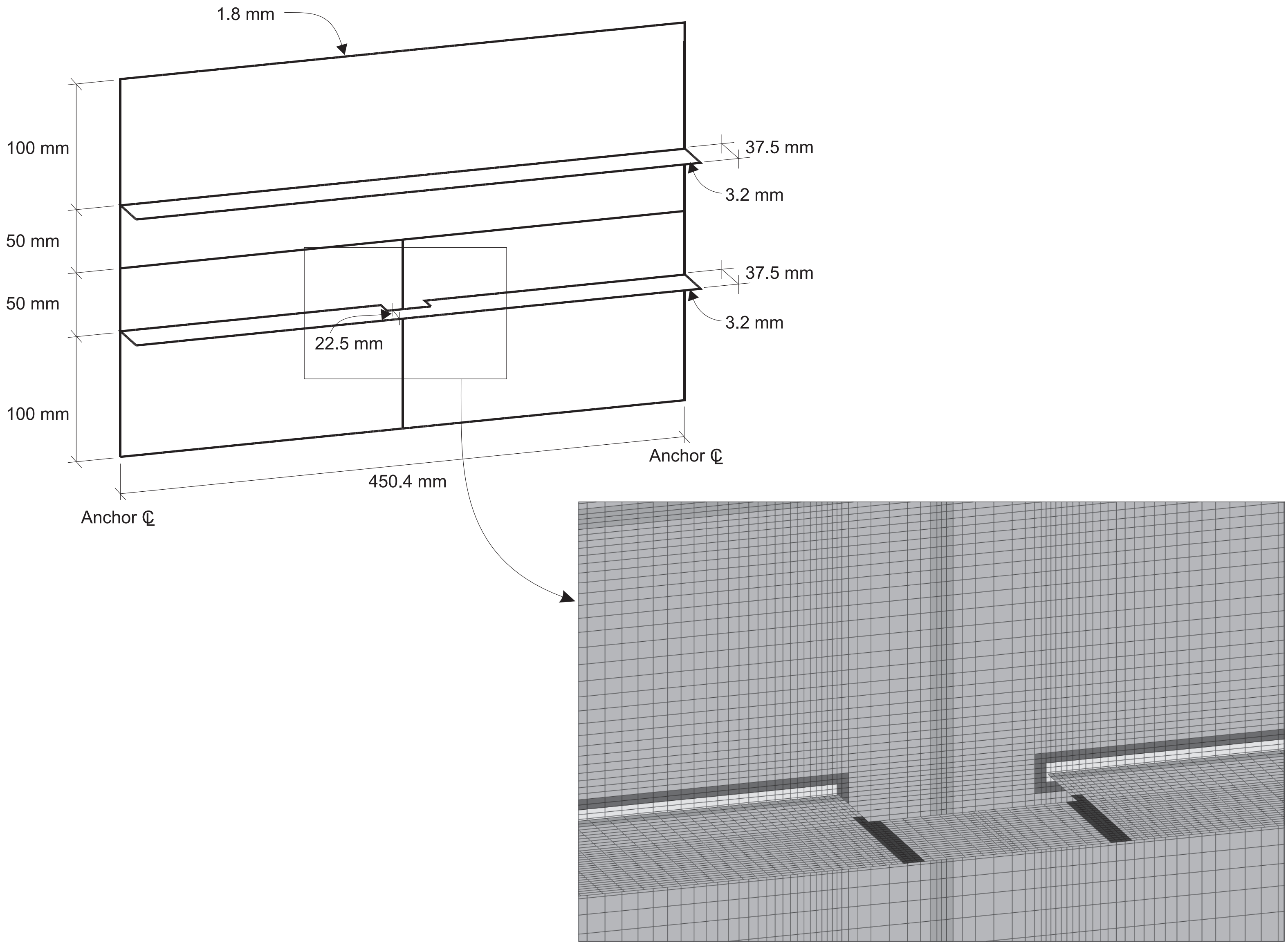

Figure 8-3. Liner Seam Model Geometric Details

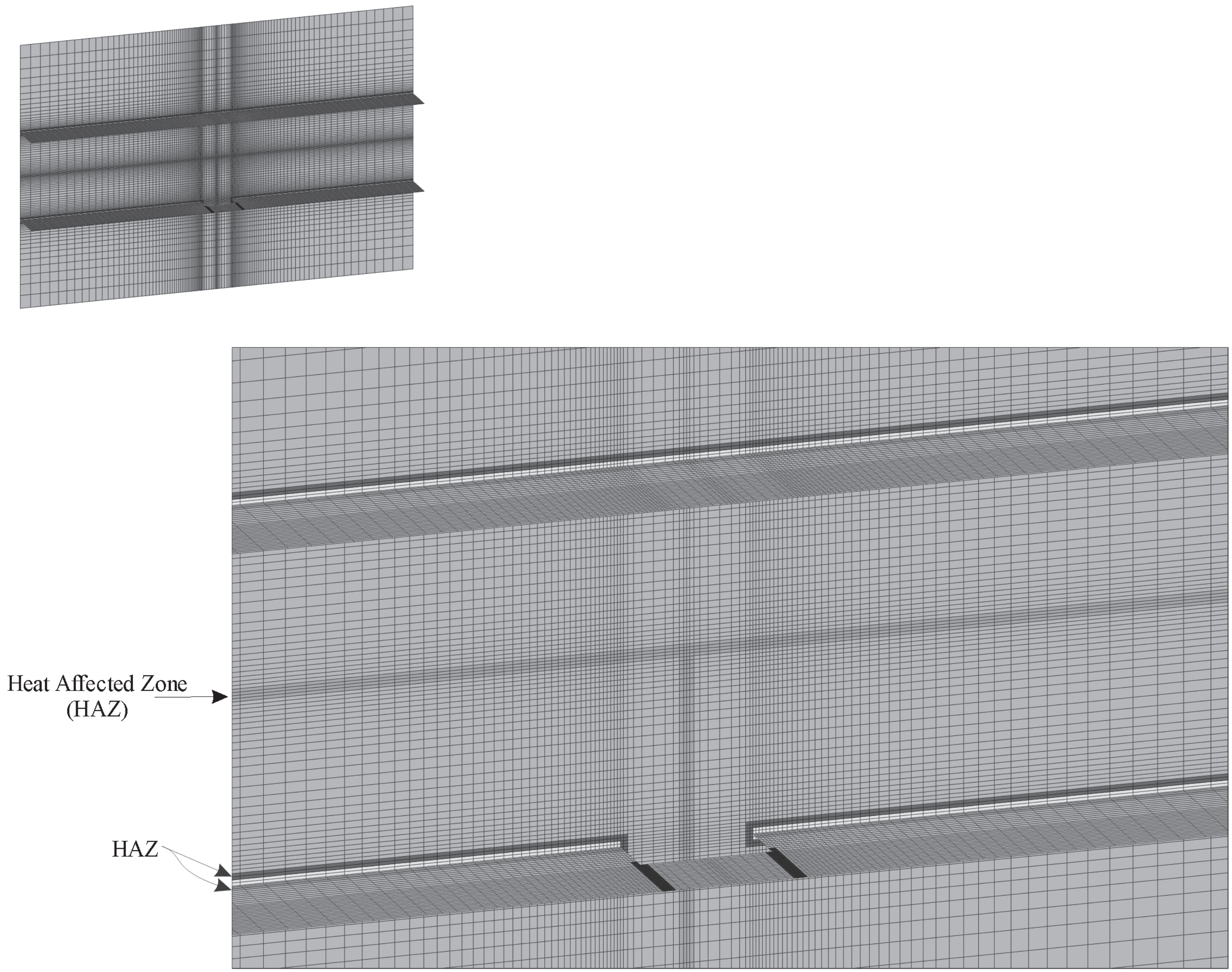

Figure 8-4. Liner Seam Model

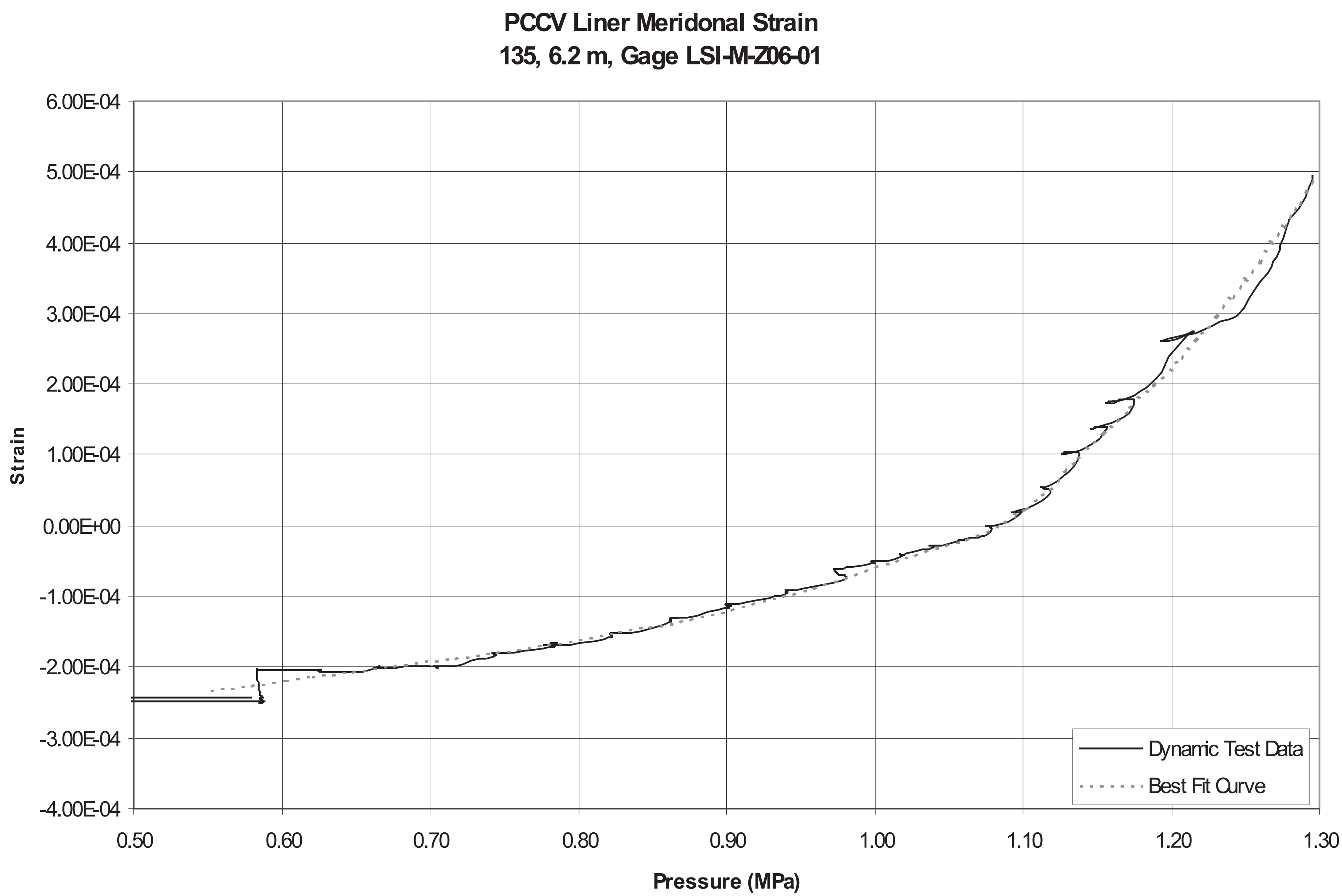

Figure 8-5. PCCV Liner Model 1, Posttest Analysis, Mesh Sensitivity, Measured Liner Meridian Strain at Gage LSI-M-Z6-01 with Best-Fit Curve Liner Model

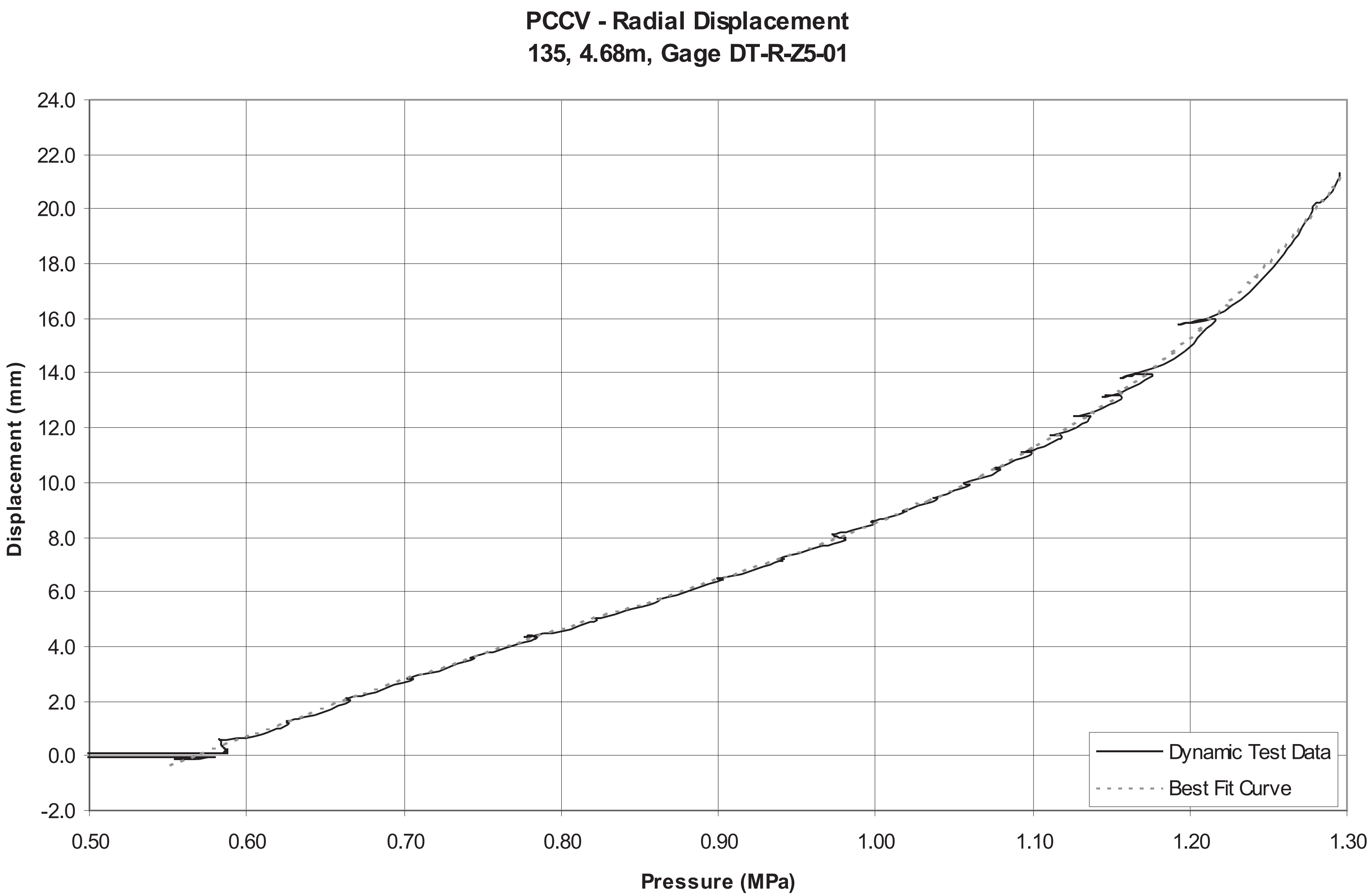

Figure 8-6. PCCV Liner Model 1, Posttest Analysis, Mesh Sensitivity, Measured Liner Radial Displacement at Gage DT-R-Z5-01 with Best-Fit Curve Liner Model

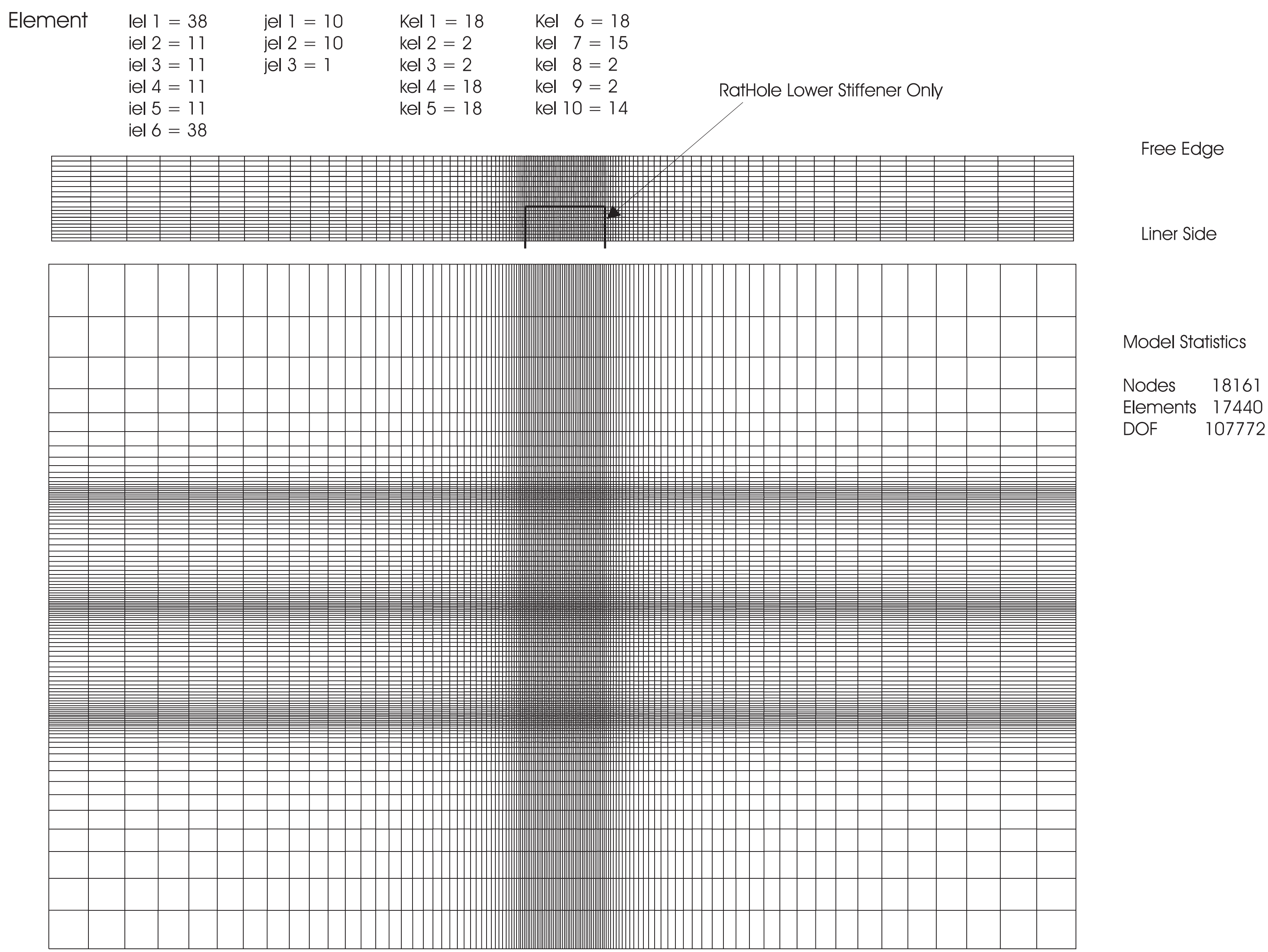

Figure 8-7. PCCV Liner Model 1, Posttest Analysis, Mesh Sensitivity - Baseline Mesh (Model 1)

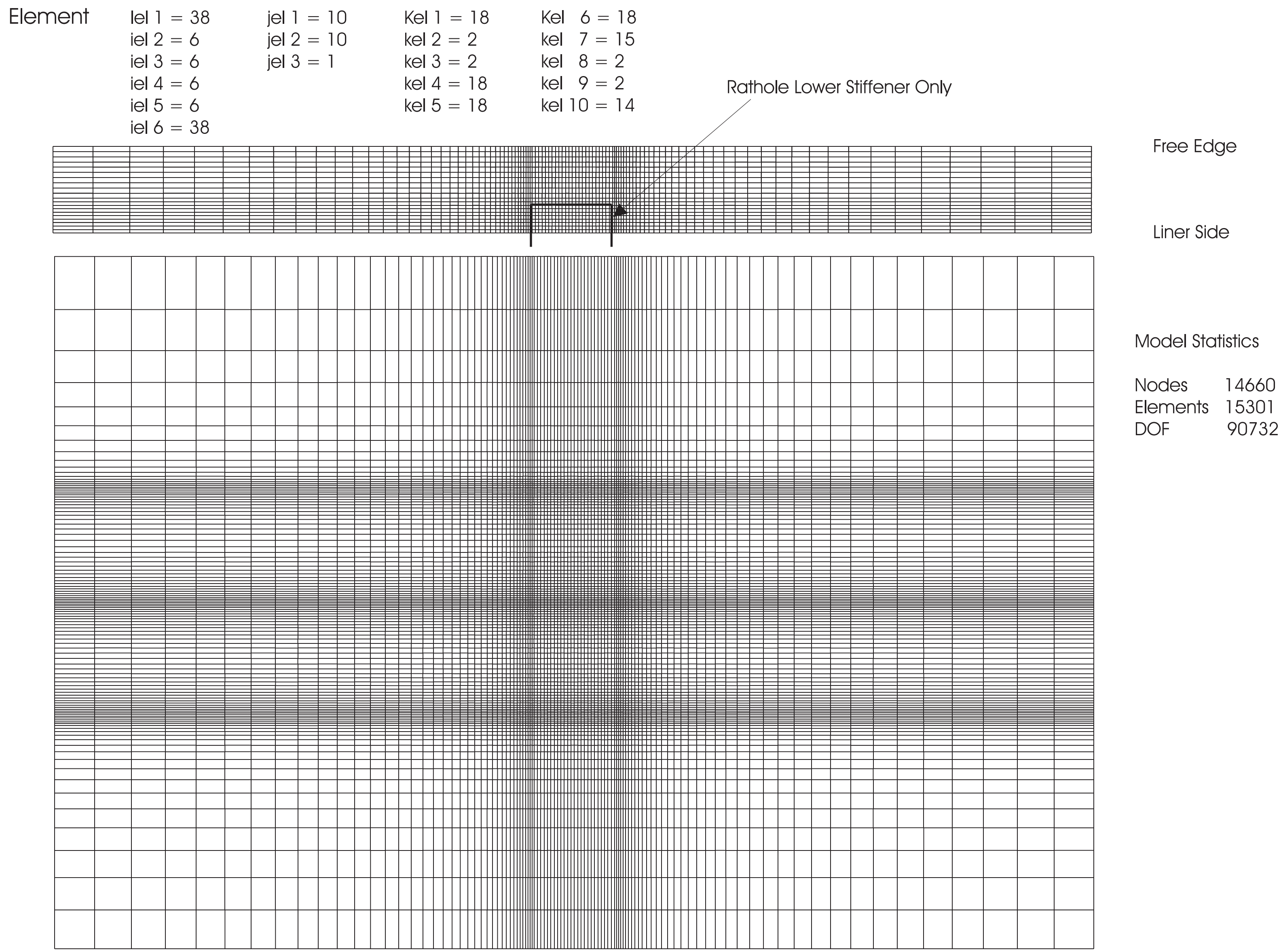

Figure 8-8. PCCV Liner Model 2, Posttest Analysis, Mesh Sensitivity - Coarse Mesh

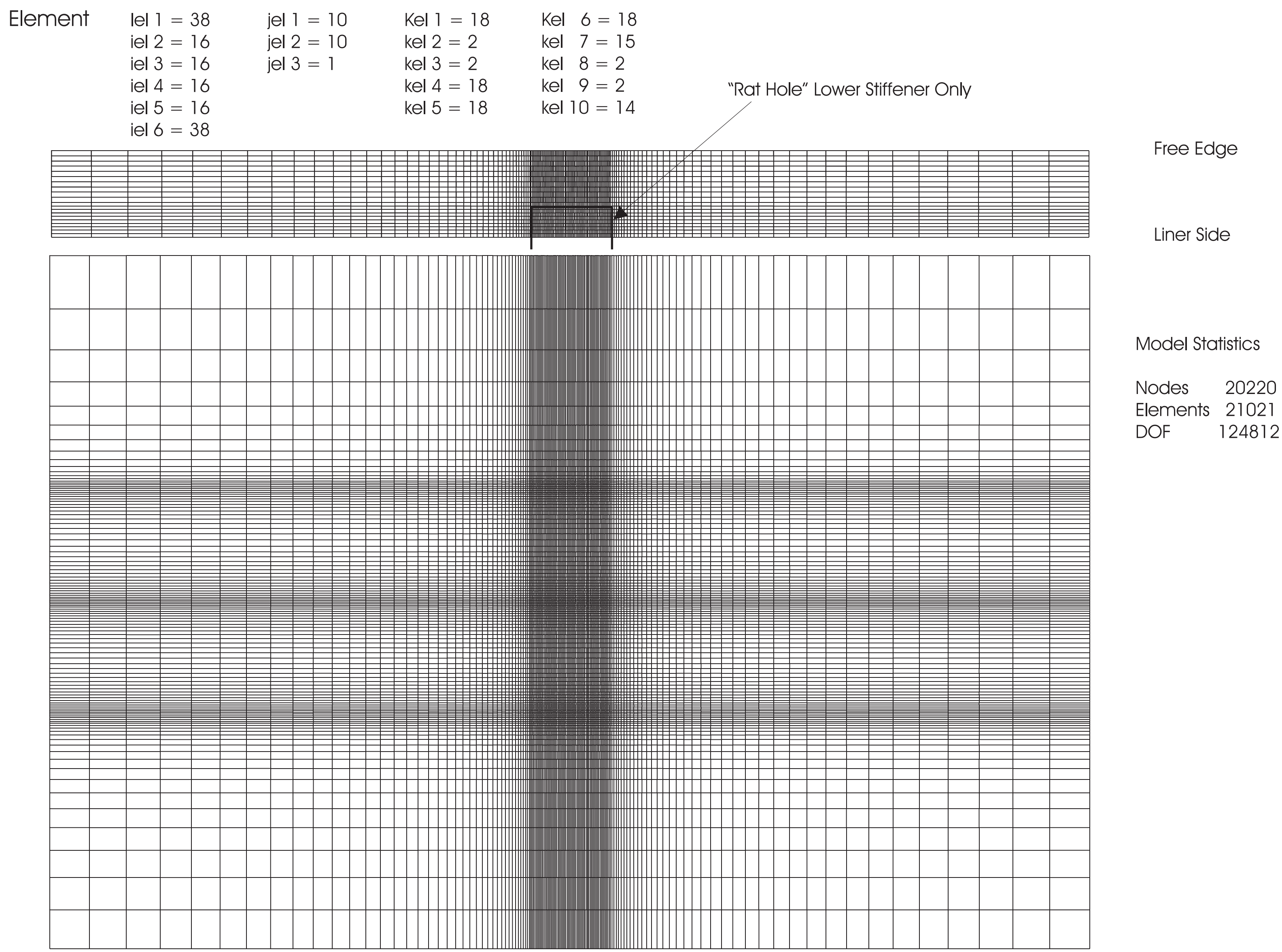

Figure 8-9. PCCV Liner Model 3, Posttest Analysis, Mesh Sensitivity - Fine Mesh

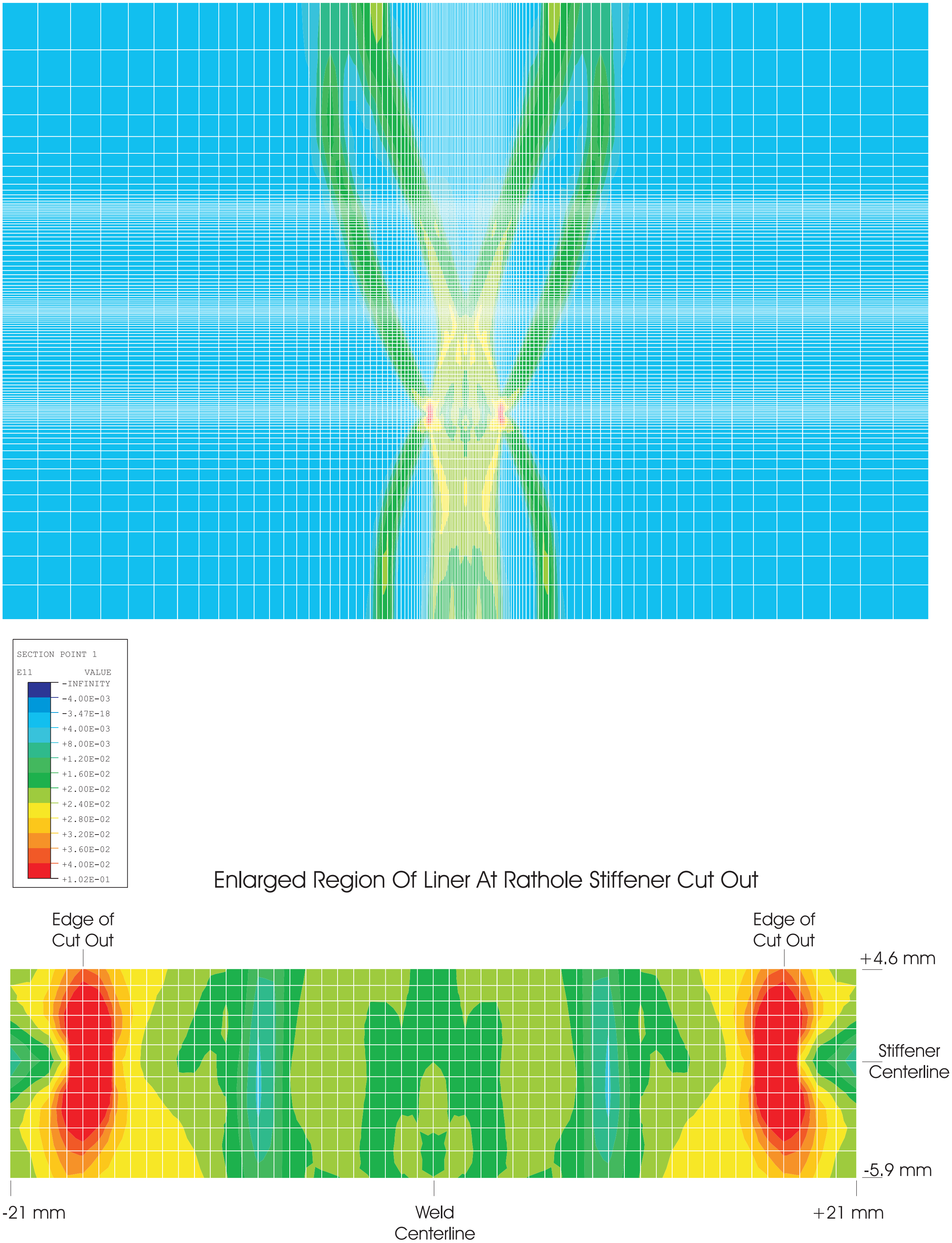

Figure 8-10. PCCV Liner Model 1, Posttest Analysis, Mesh Sensitivity, Baseline Mesh, Horizontal Strain Contour Plot At End of Analysis (1.3 MPa)

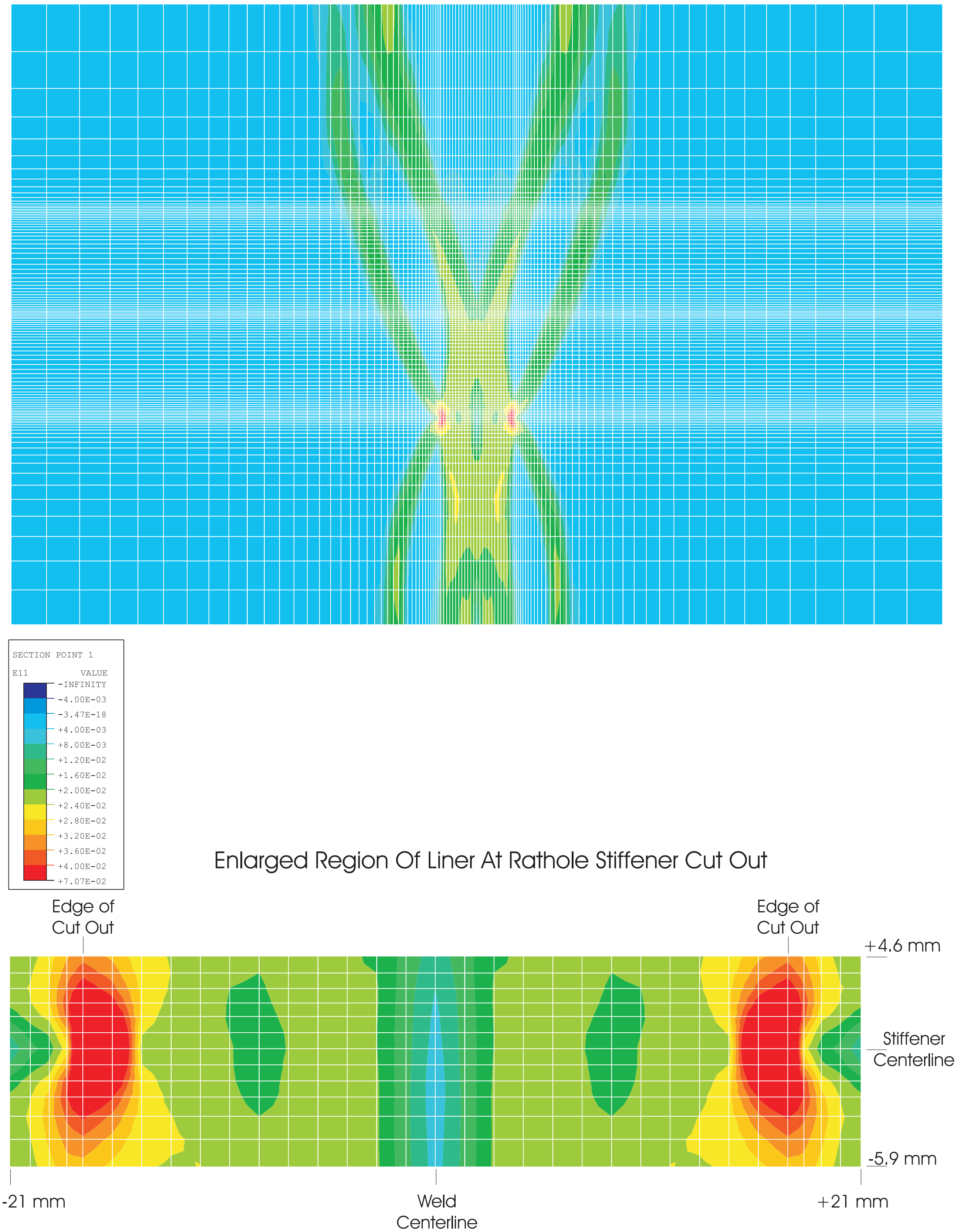

Figure 8-11. PCCV Liner Model 2, Posttest Analysis, Mesh Sensivity, Coarse Mesh, Horizontal Strain Contour Plot At End of Analysis (1.3 MPa)

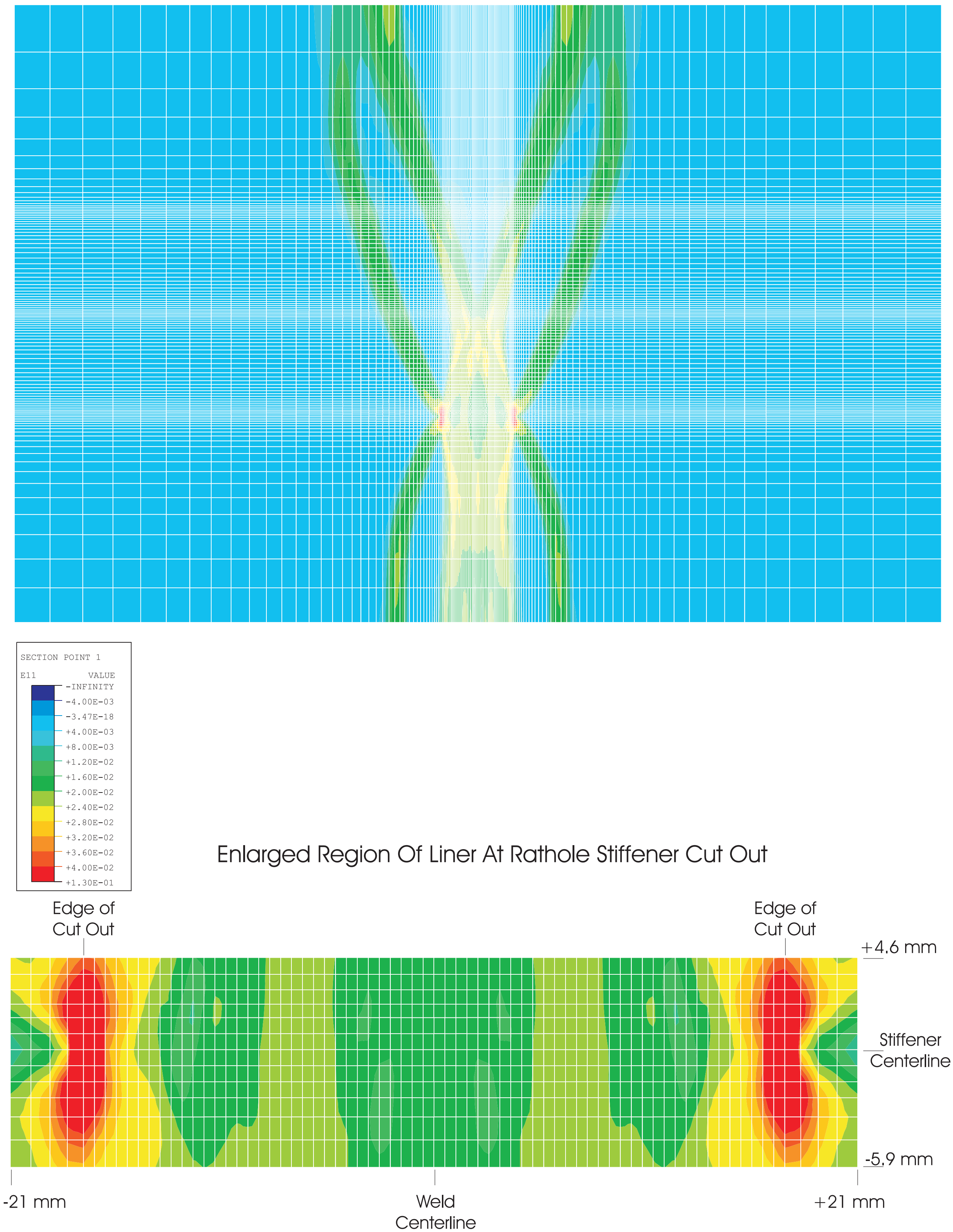

Figure 8-12. PCCV Liner Model 3, Posttest Analysis, Mesh Sensivity, Fine Mesh, Horizontal Strain Contour Plot At End of Analysis, (1.3 MPa)

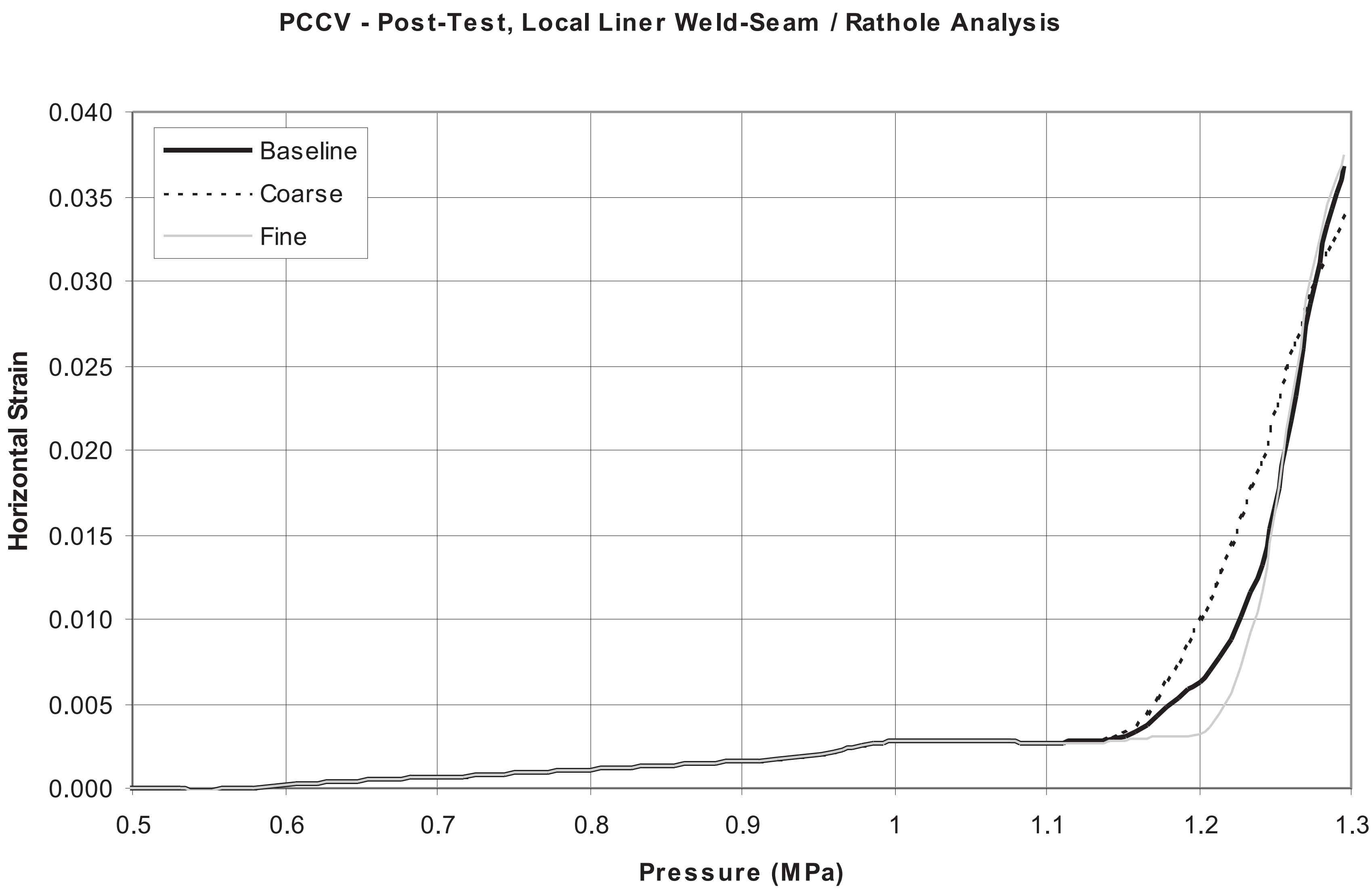

Figure 8-13. PCCV Liner Model, Posttest Analysis, Mesh Sensitivity, Comparison of Horizontal Strain, 5 mm Below Stiffener Reentrant Corner at Rat-Hole

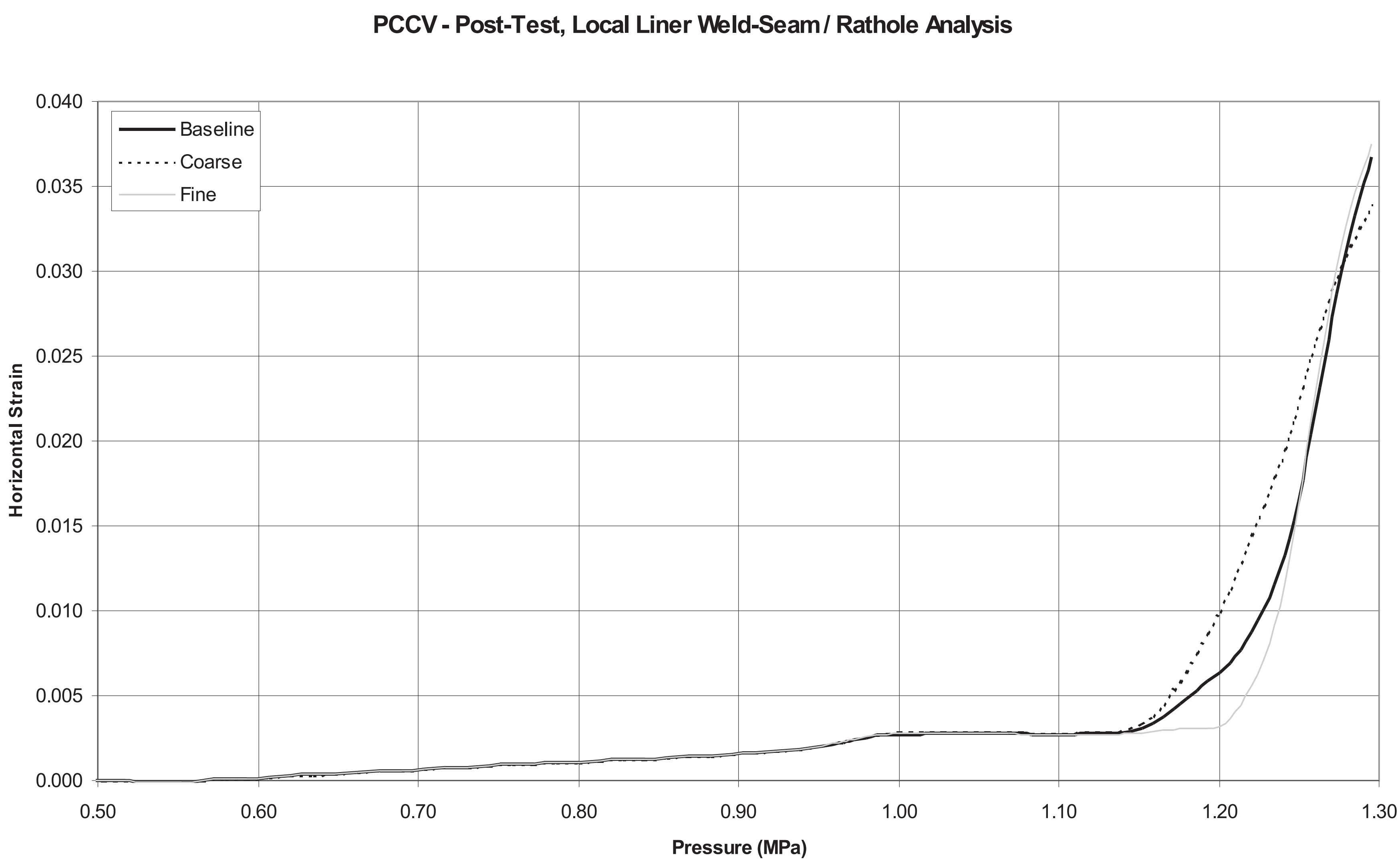

Figure 8-14. PCCV Liner Model, Posttest Analysis, Mesh Sensitivity, Comparison of Horizontal Strain, 1.2 mm Below Stiffener Reentrant Corner at Rat-Hole

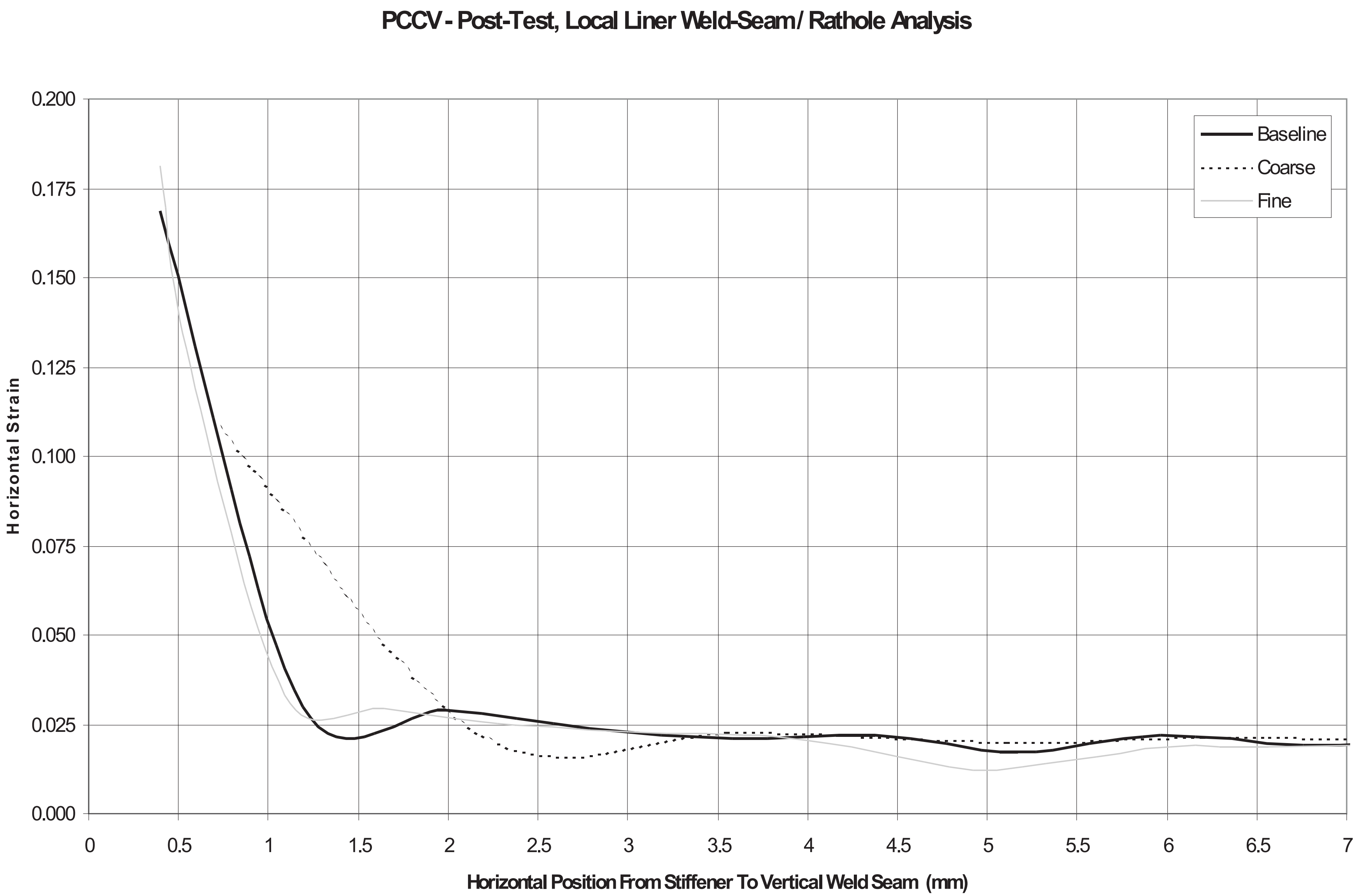

Figure 8-15. PCCV Liner Model, Posttest Analysis, Mesh Sensitivity, Comparison of Horizontal Strains, Horizontal Profile From Stiffener Towards Vertical Weld Seam at P = 1.3 MPa

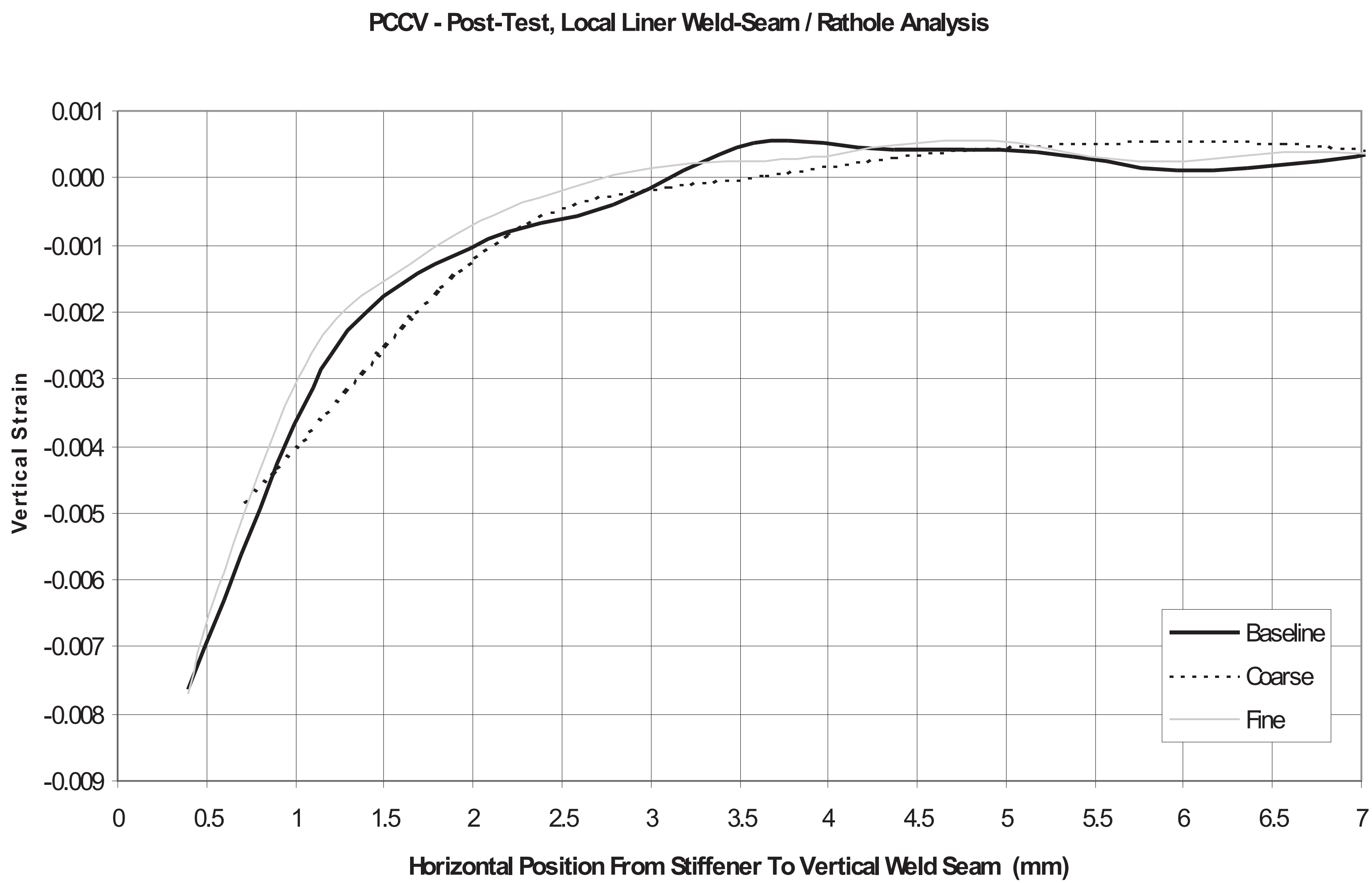

Figure 8-16. PCCV Liner Model, Posttest Analysis, Mesh Sensitivity, Comparison of Vertical Strains, Horizontal Profile from Stiffener Towards Vertical Weld Seam at P = 1.3 MPa

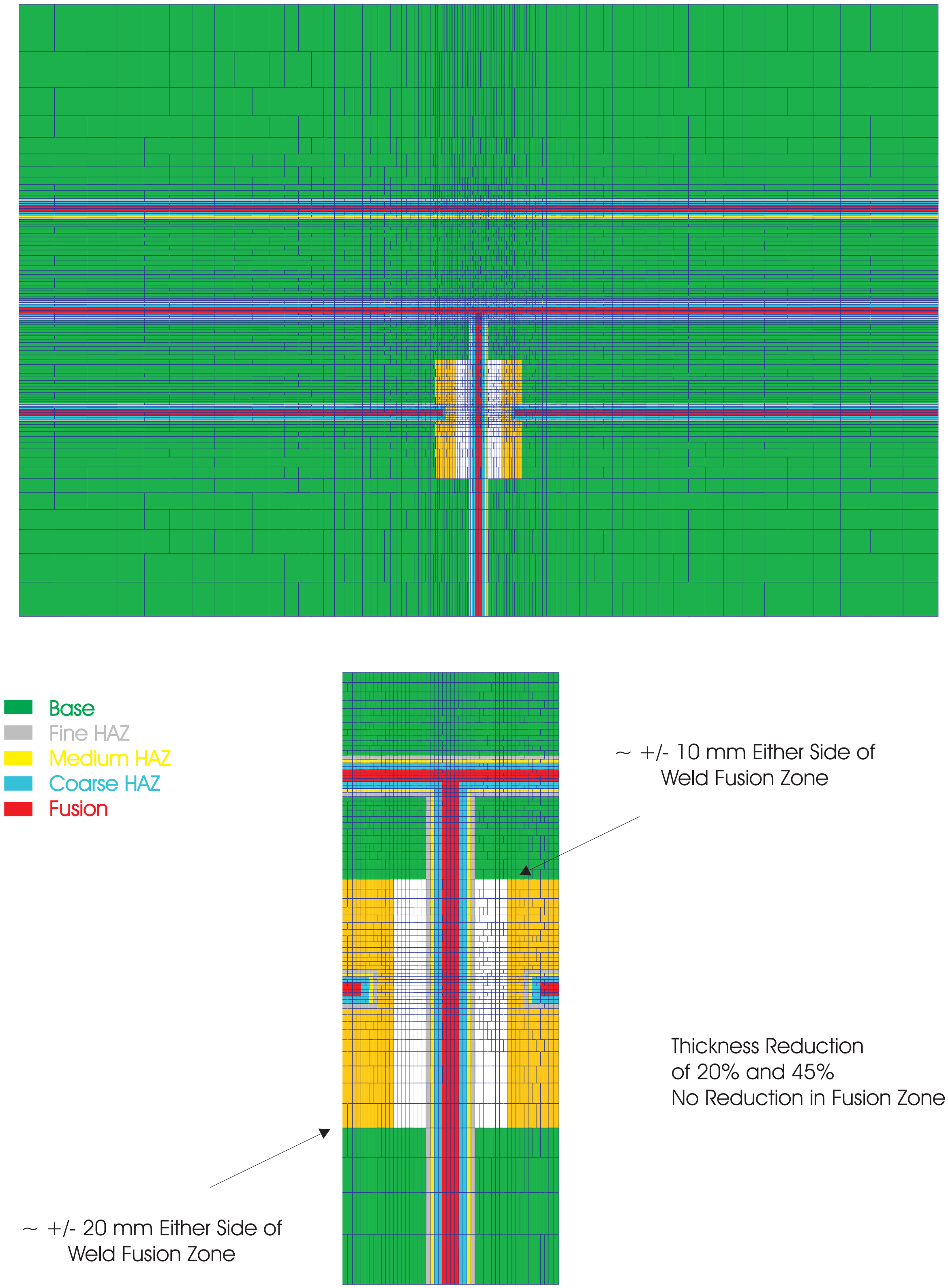

Figure 8-17. PCCV Liner Model, Posttest Analysis, Base, HAZ, and Fusion Regions, Extent of Thinning Zones

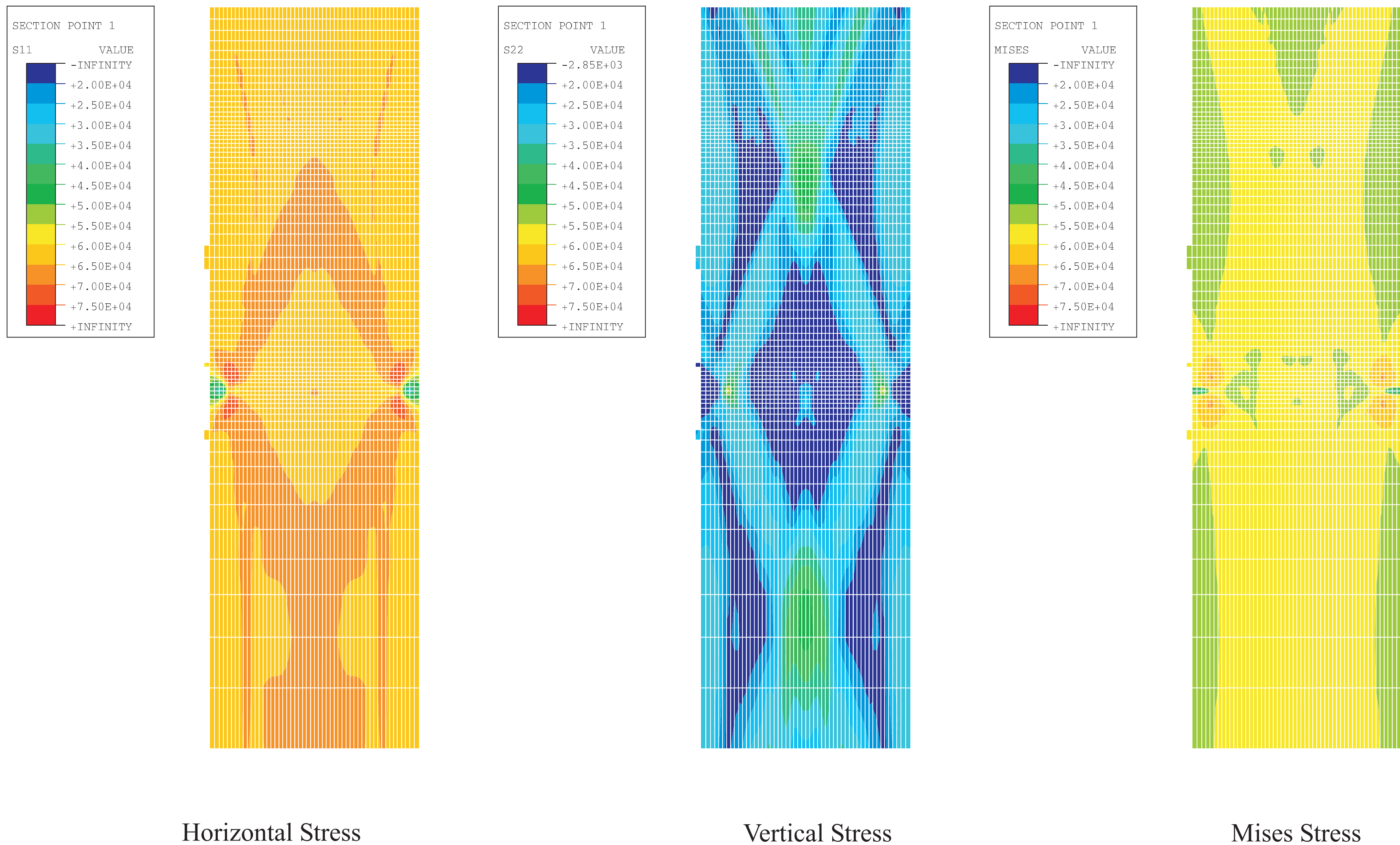

Figure 8-18. PCCV Liner Model, Posttest Analysis, Case 1, Stress Contour, at P = 3.3 Pd
(Stresses in psi; multiply by 0.00690 for MPa)

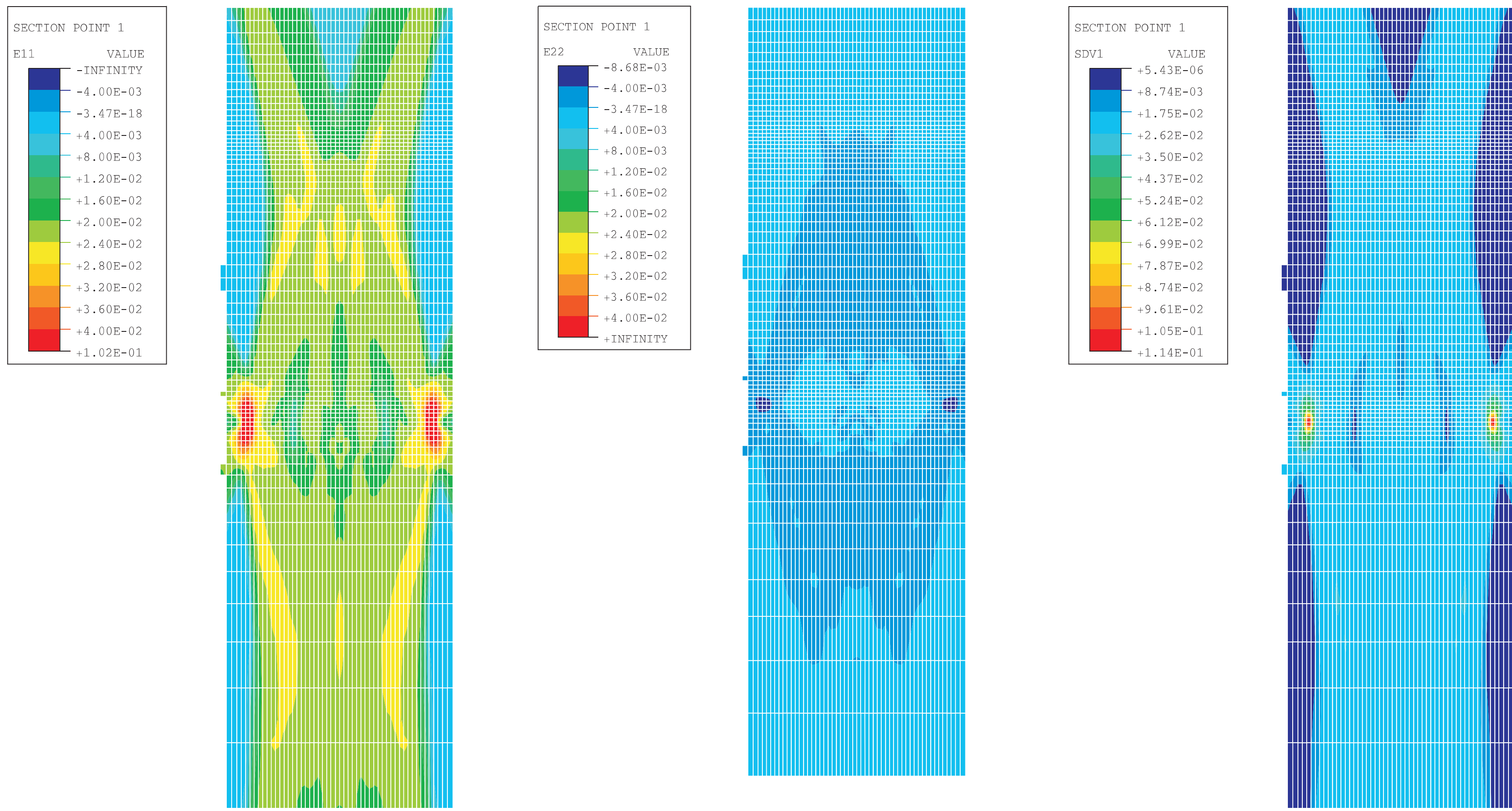

Horizontal Strain

Vertical Strain

Effective Plastic Strain

Figure 8-19. PCCV Liner Model, Posttest Analysis, Case 1, Strain Contour, at P = 3.3 Pd

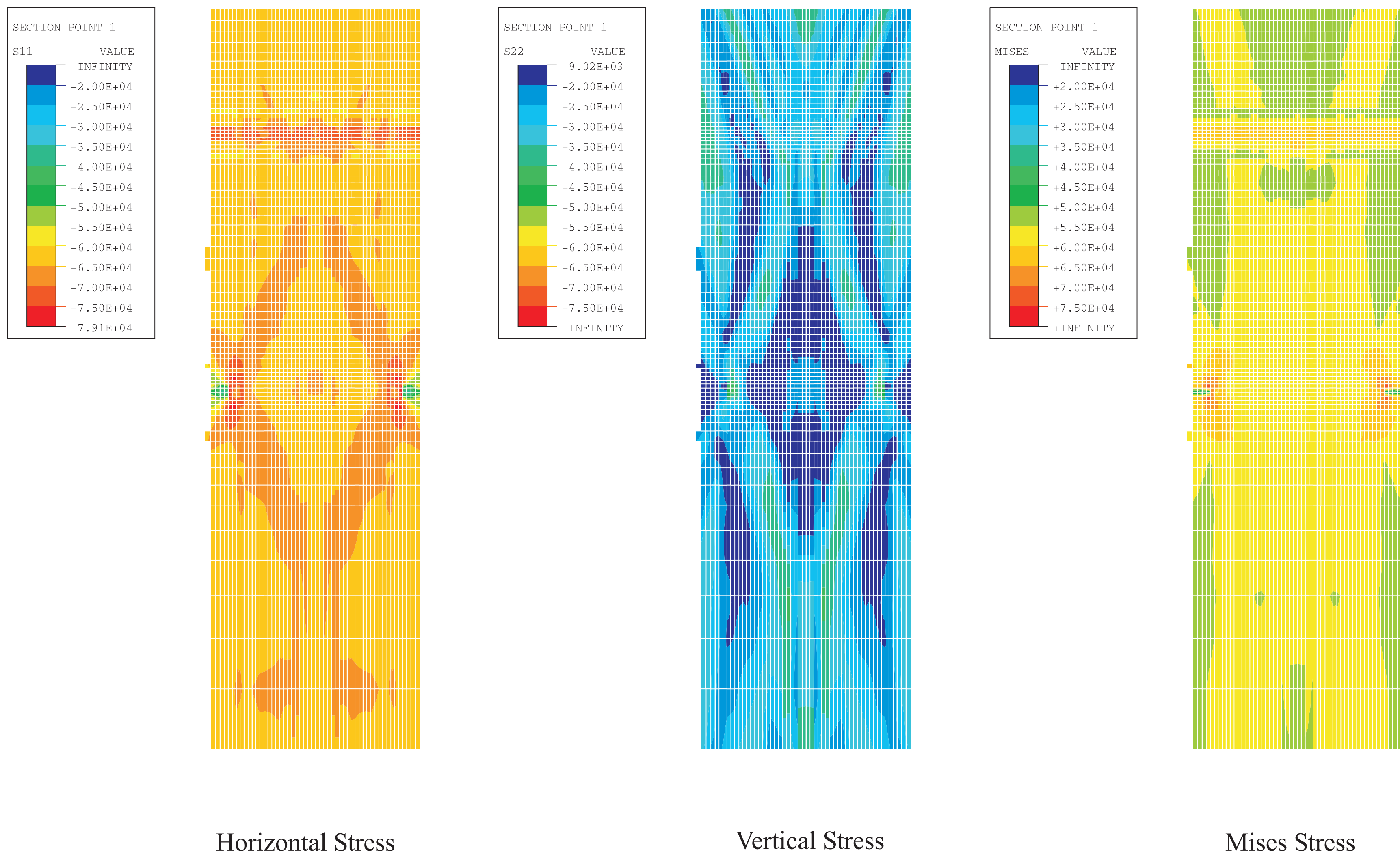

Figure 8-20. PCCV Liner Model, Posttest Analysis, Case 4, Stress Contour, at P = 3.3 Pd
(Stresses in psi; multiply by 0.00690 for MPa)

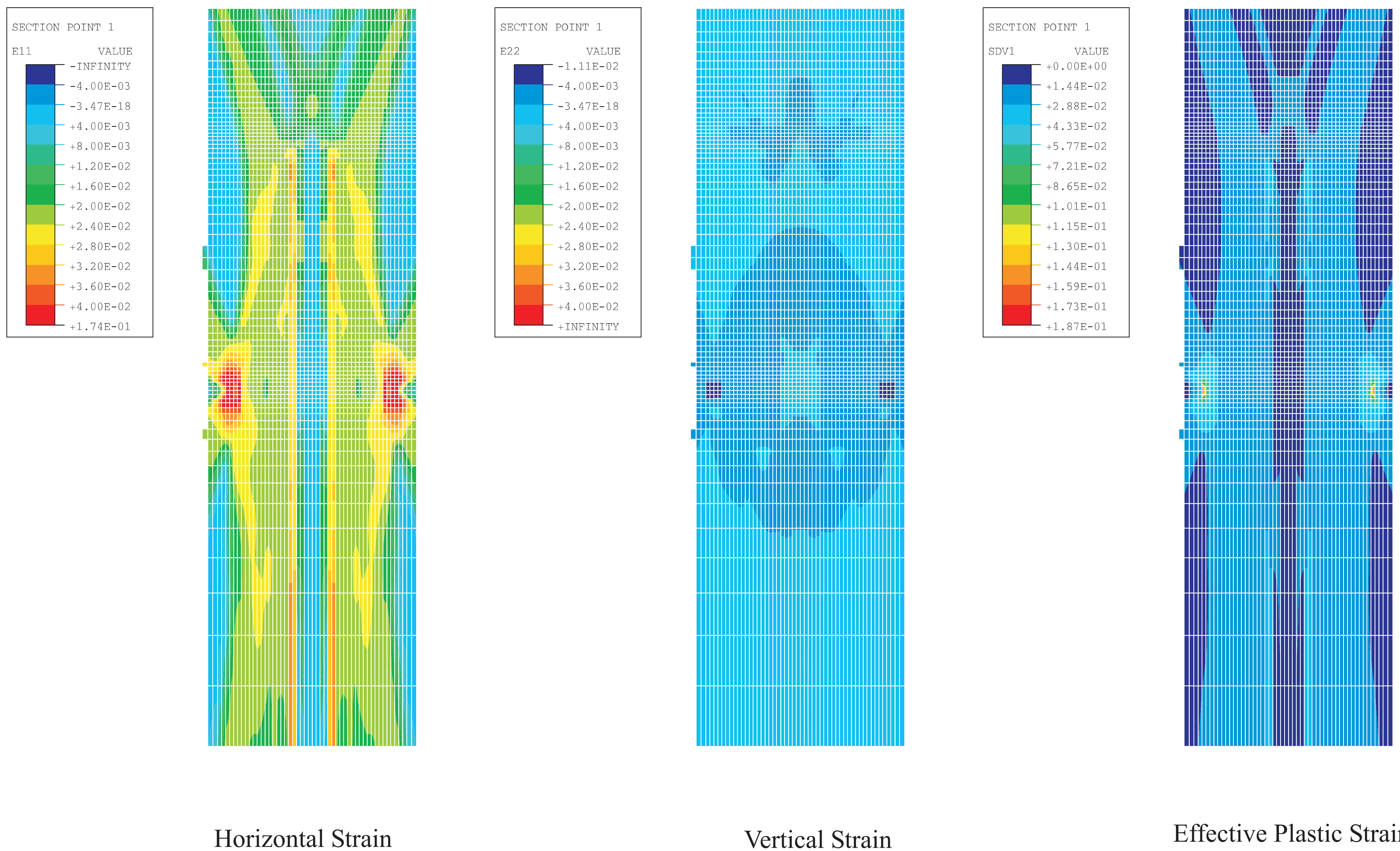

Figure 8-21. PCCV Liner Model, Posttest Analysis, Case 4, Strain Contour, at P = 3.3 Pd

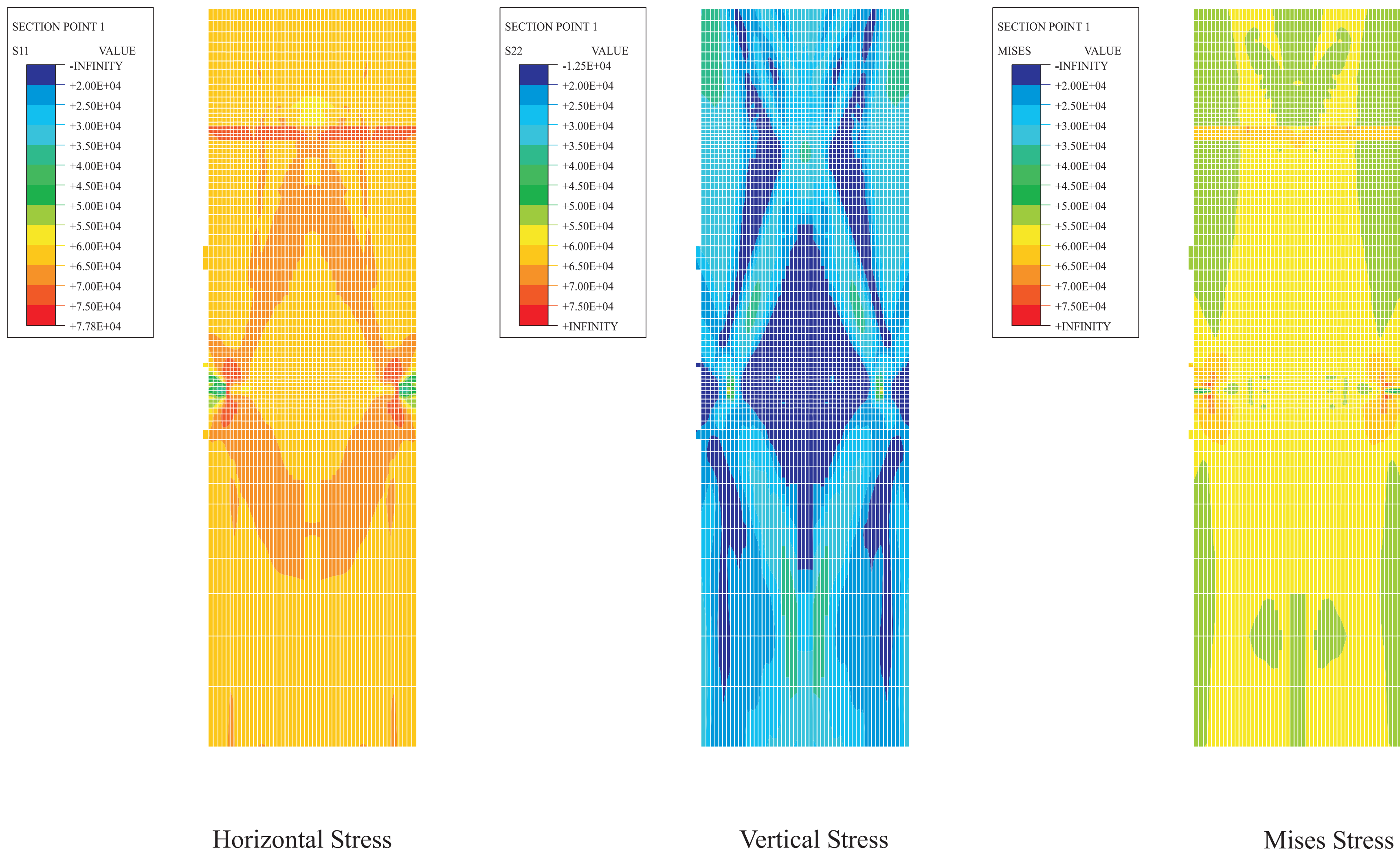

Figure 8-22. PCCV Liner Model, Posttest Analysis, Case 5, Stress Contour, at P = 3.3 Pd
(Stresses in psi; multiply by 0.00690 for MPa)

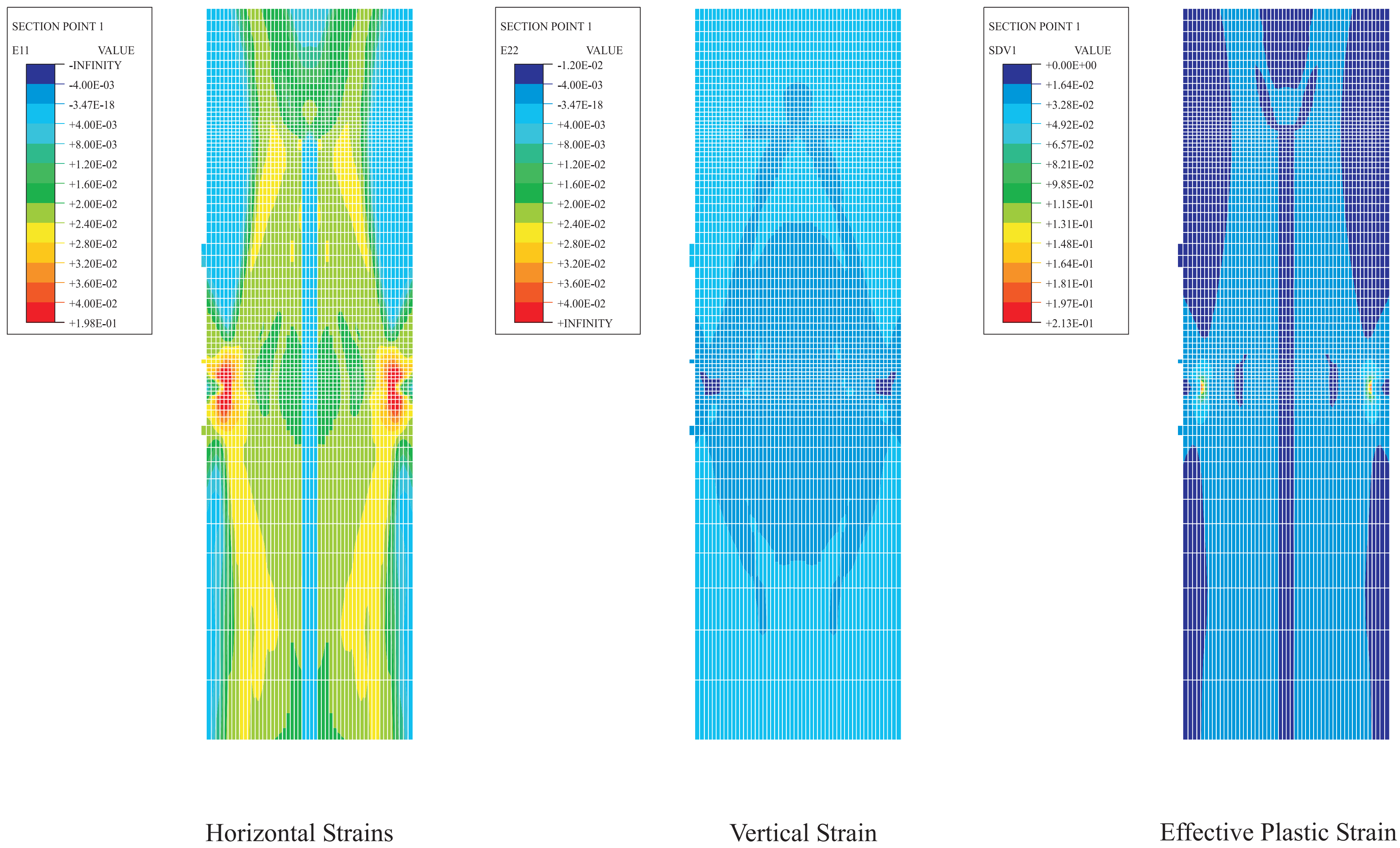

Figure 8-23. PCCV Liner Model, Posttest Analysis, Case 5, Stress Contour, at P = 3.3 Pd

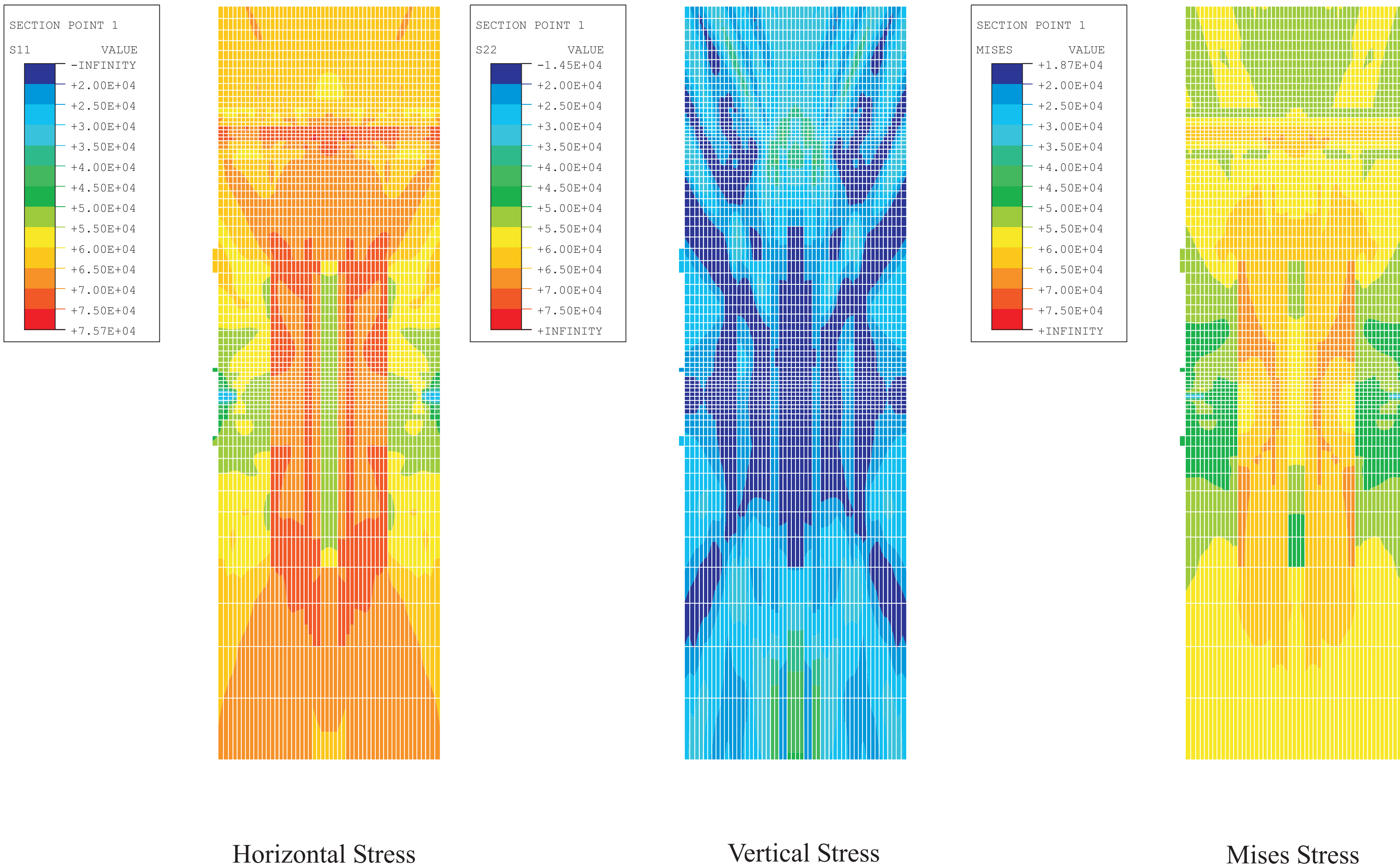

Figure 8-24. PCCV Liner Model, Posttest Analysis, Case 6, Stress Contour, at P = 3.3 Pd
(Stresses in psi; multiply by 0.00690 for MPa)

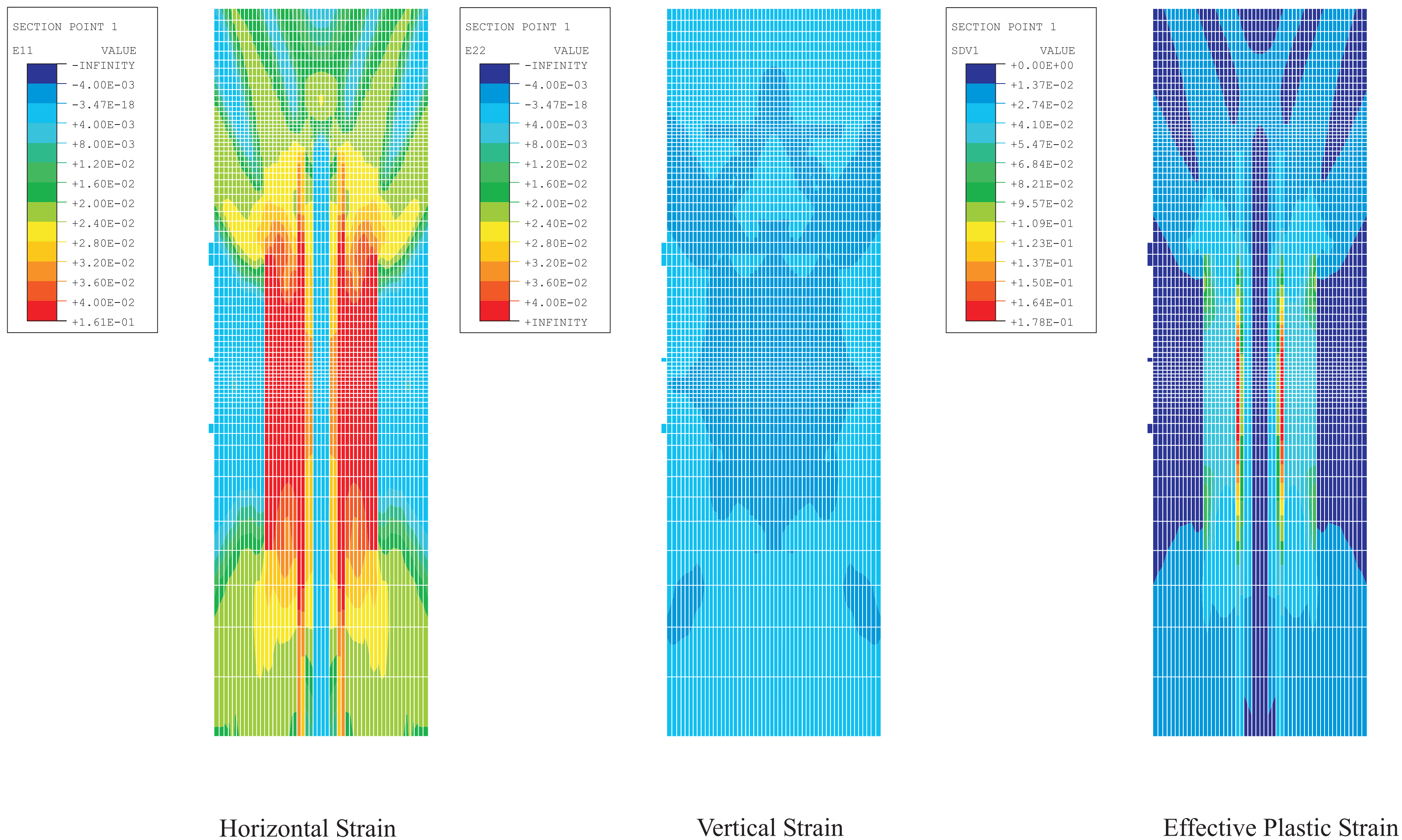

Figure 8-25. PCCV Liner Model, Posttest Analysis, Case 6, Strain Contour, at P = 3.3 Pd

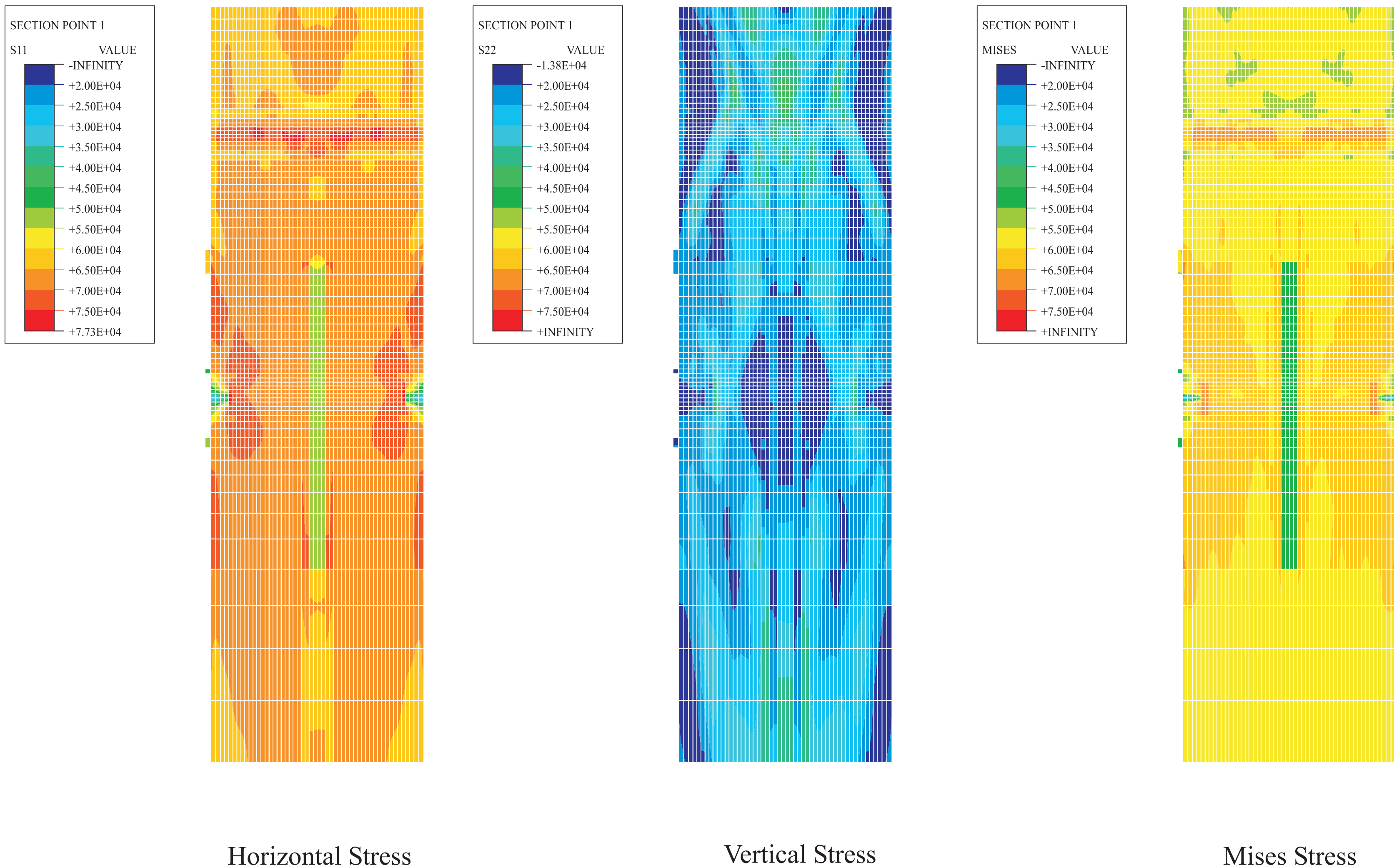

Figure 8-26. PCCV Liner Model, Posttest Analysis, Case 7, Stress Contour, at P = 3.3 Pd
(Stresses in psi; multiply by 0.00690 for MPa)

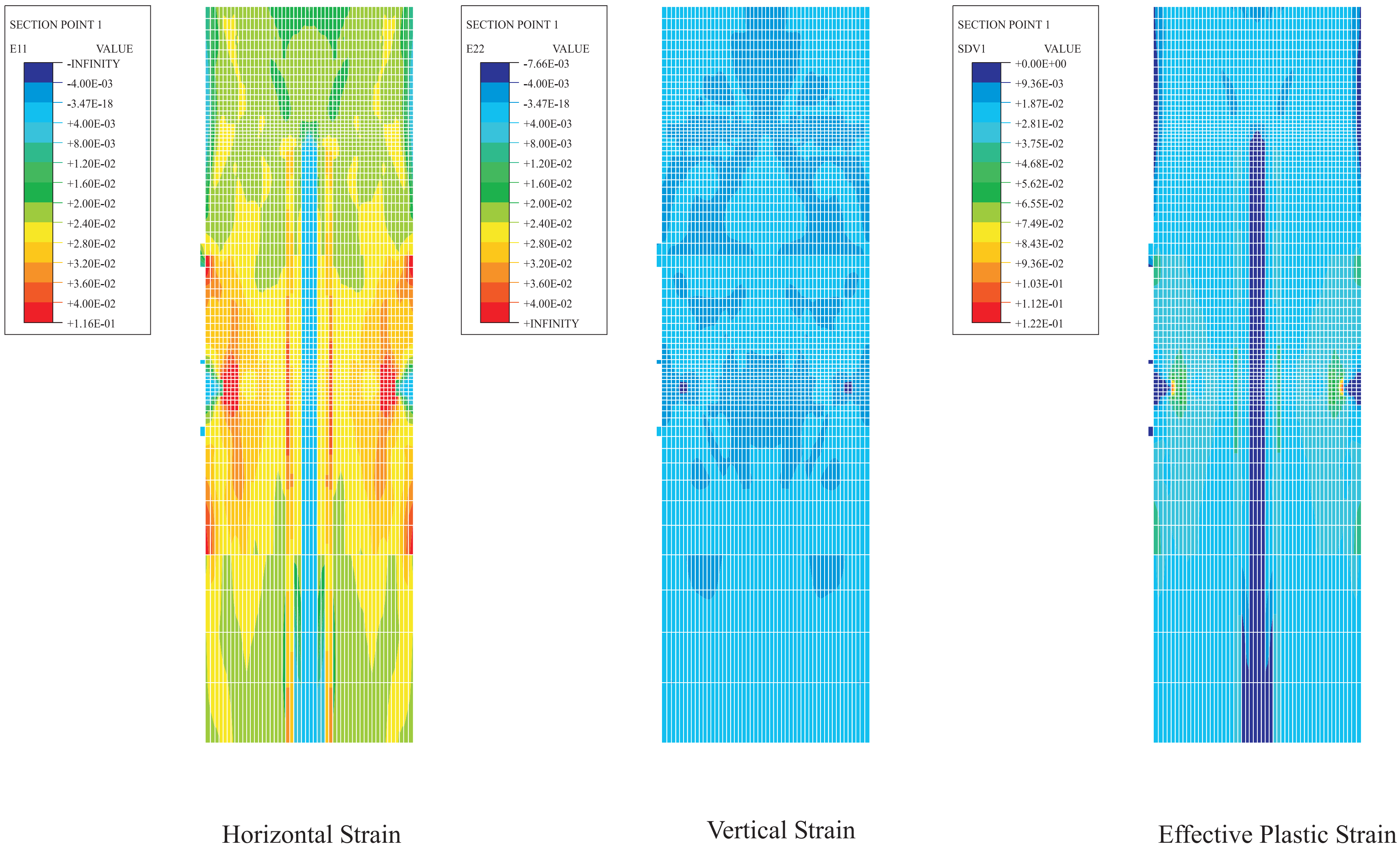

Figure 8-27. PCCV Liner Model, Posttest Analysis, Case 7, Stress Contour, at P = 3.3 Pd

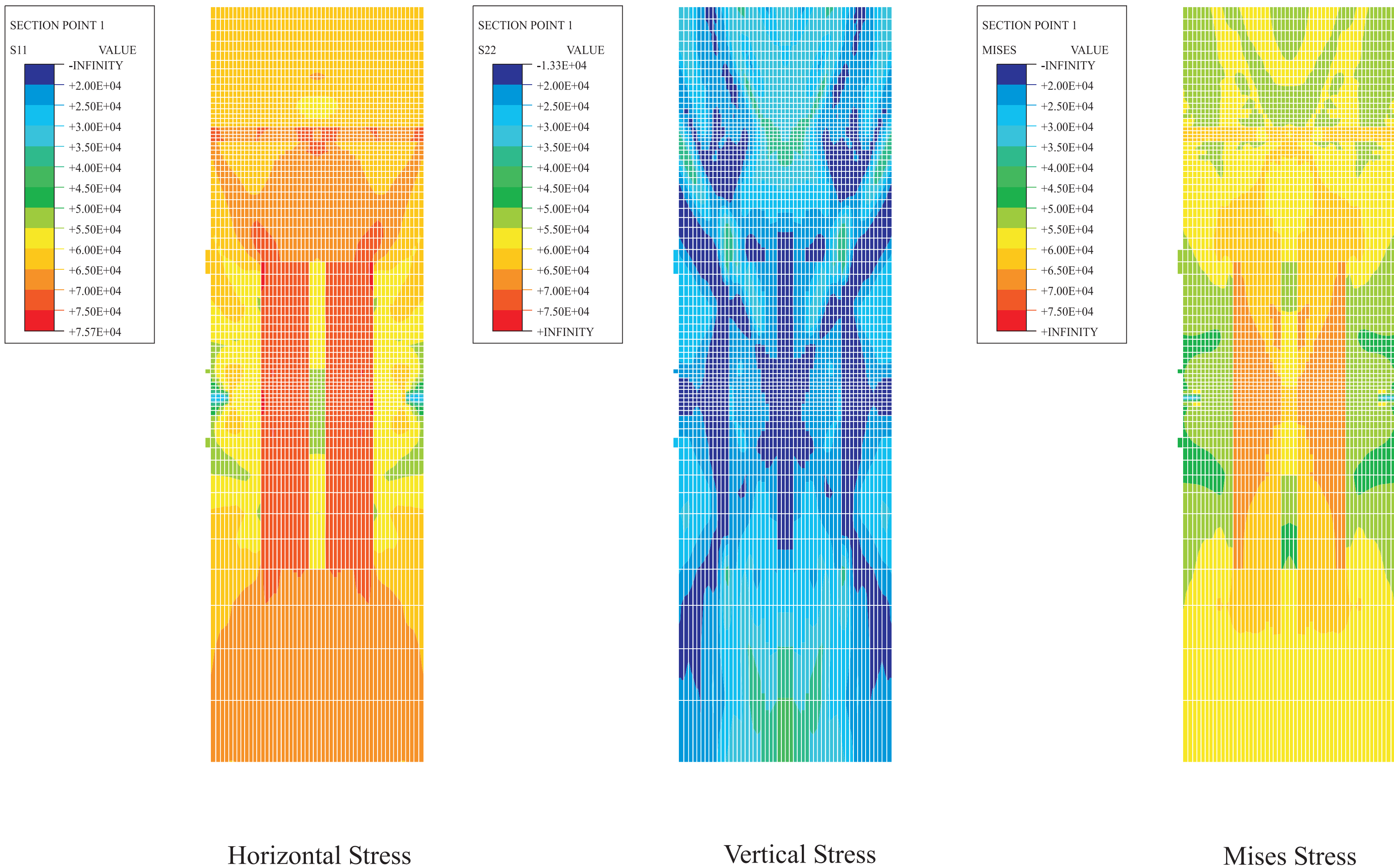

Figure 8-28. PCCV Liner Model, Posttest Analysis, Case 8, Stress Contour, at P = 3.3 Pd
(Stresses in psi; multiply by 0.00690 for MPa)

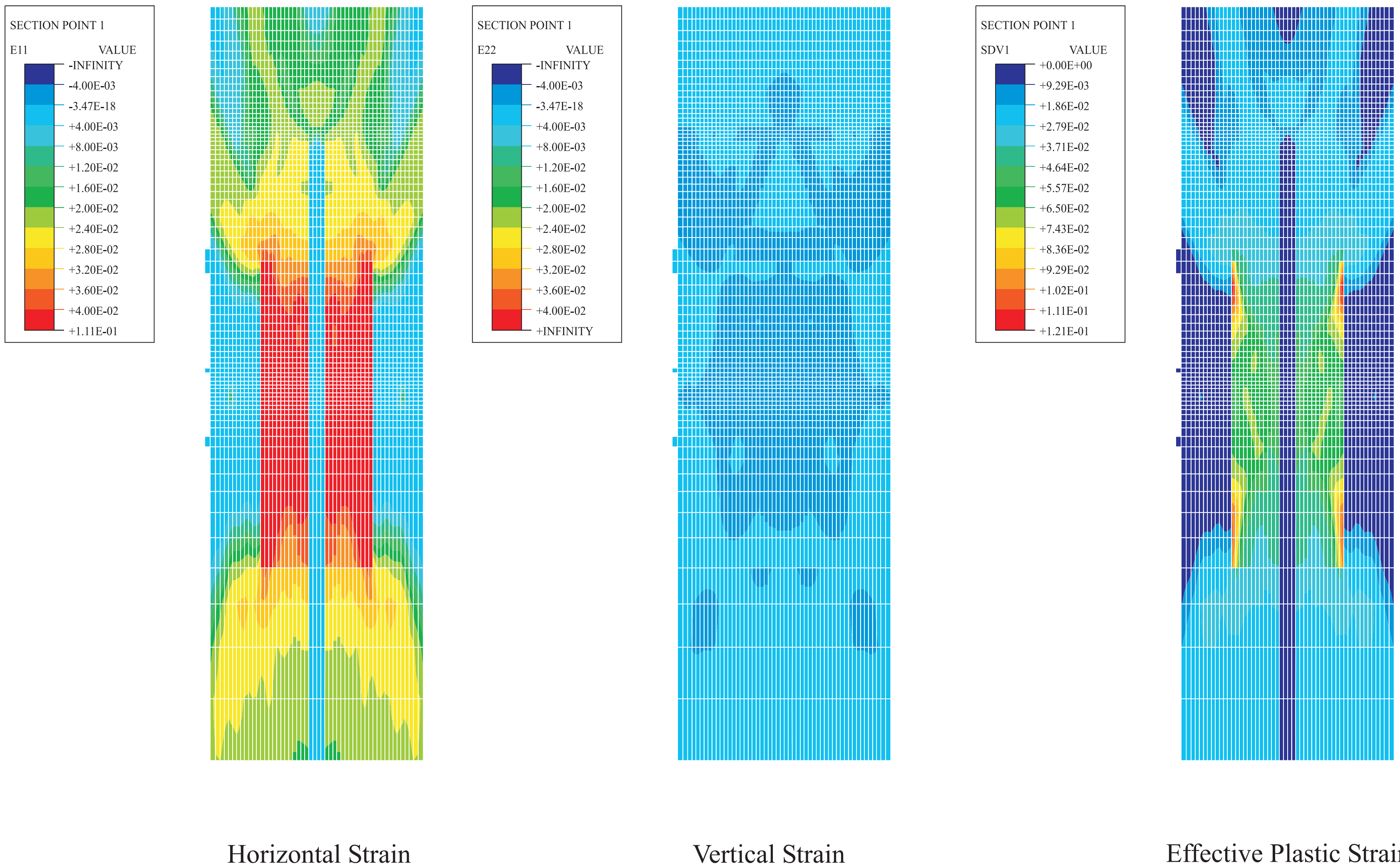

Figure 8-29. PCCV Liner Model, Posttest Analysis, Case 8, Strain Contour, at P = 3.3 Pd

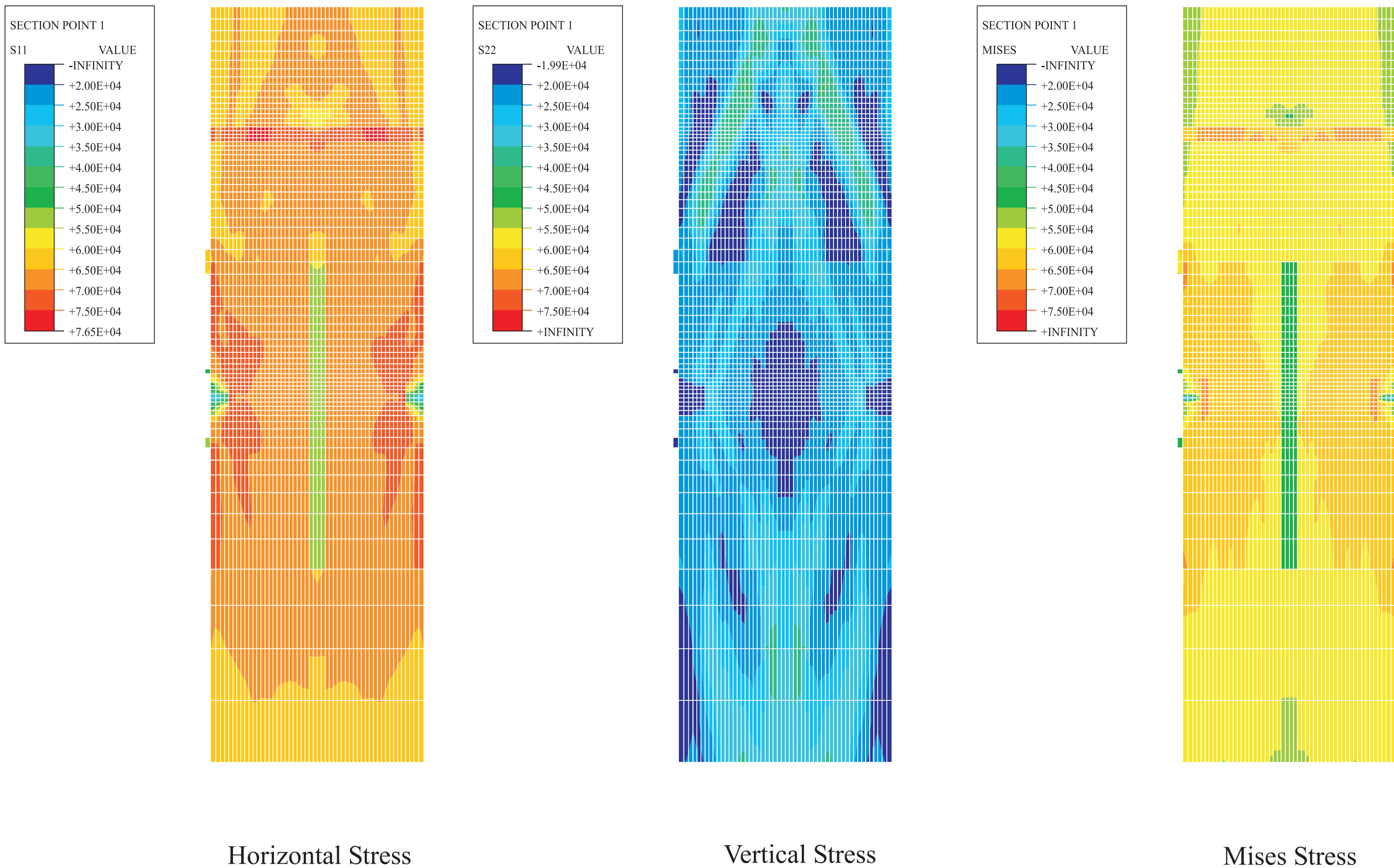

Figure 8-30. PCCV Liner Model, Posttest Analysis, Case 9, Stress Contour, at P = 3.3 Pd
(Stresses in psi; multiply by 0.00690 for MPa)

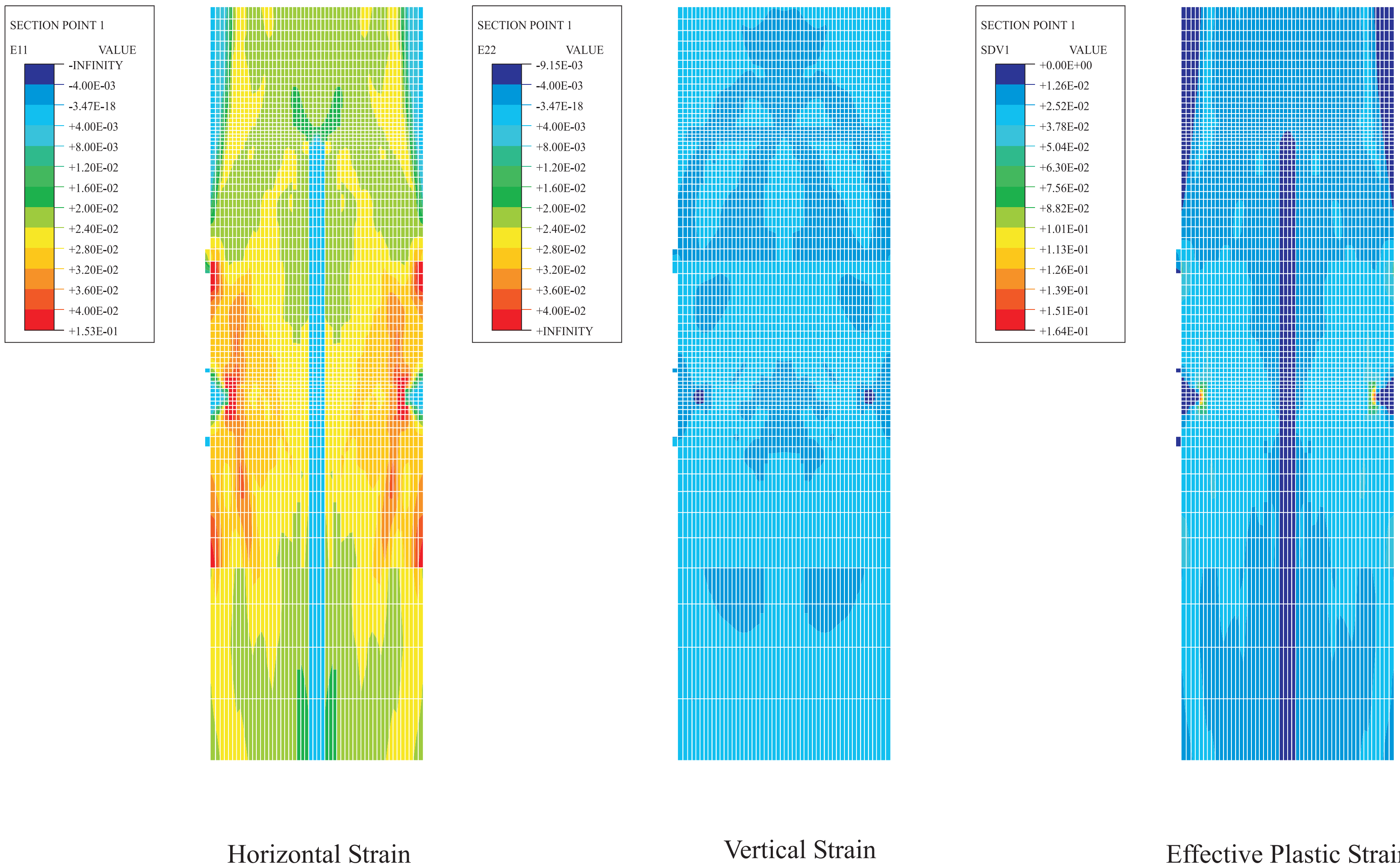

Figure 8-31. PCCV Liner Model, Posttest Analysis, Case 9, Strain Contour, at P = 3.3 Pd

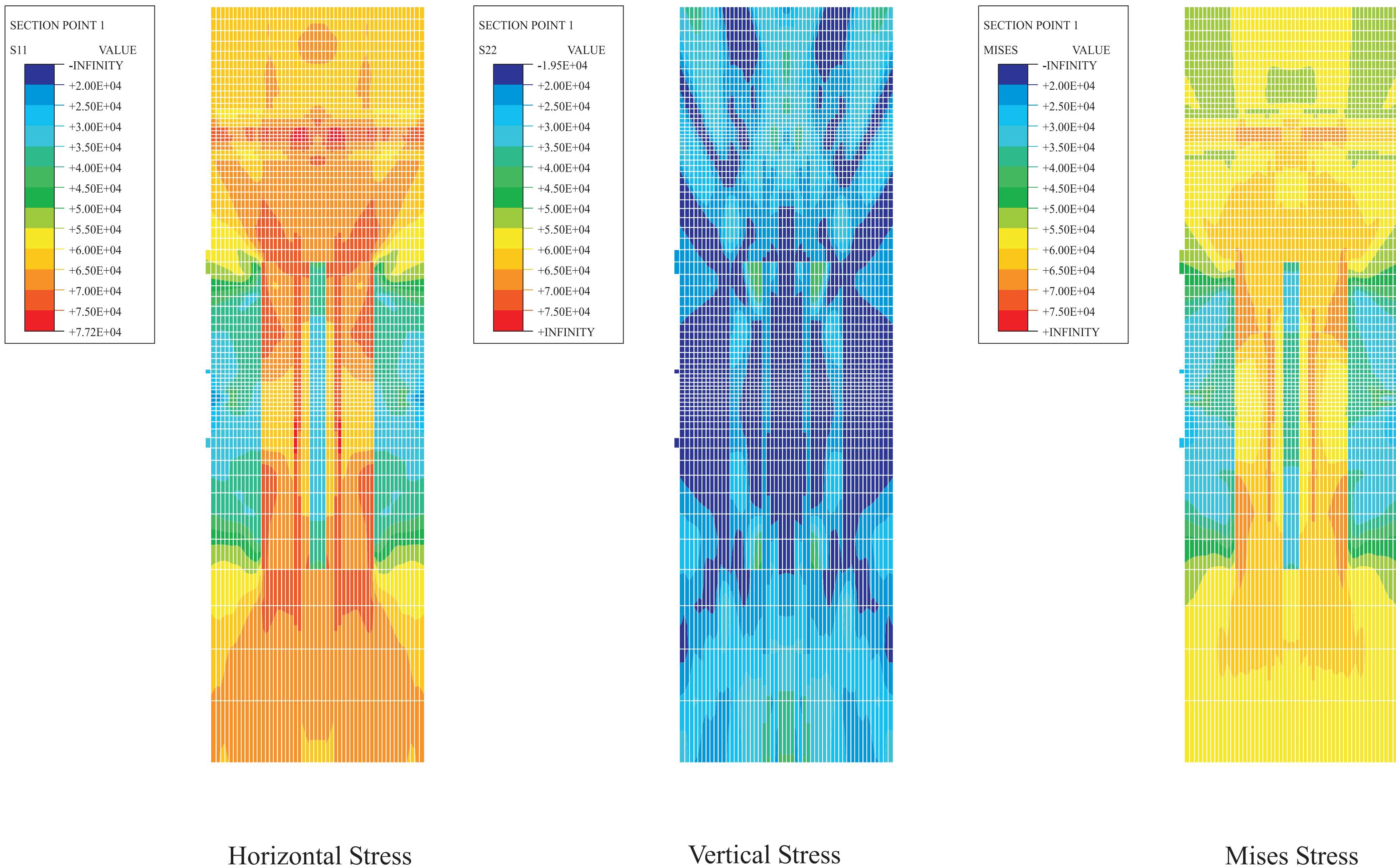

Figure 8-32. PCCV Liner Model, Posttest Analysis, Case 10, Stress Contour, at P = 3.3 Pd
(Stresses in psi; multiply by 0.00690 for MPa)

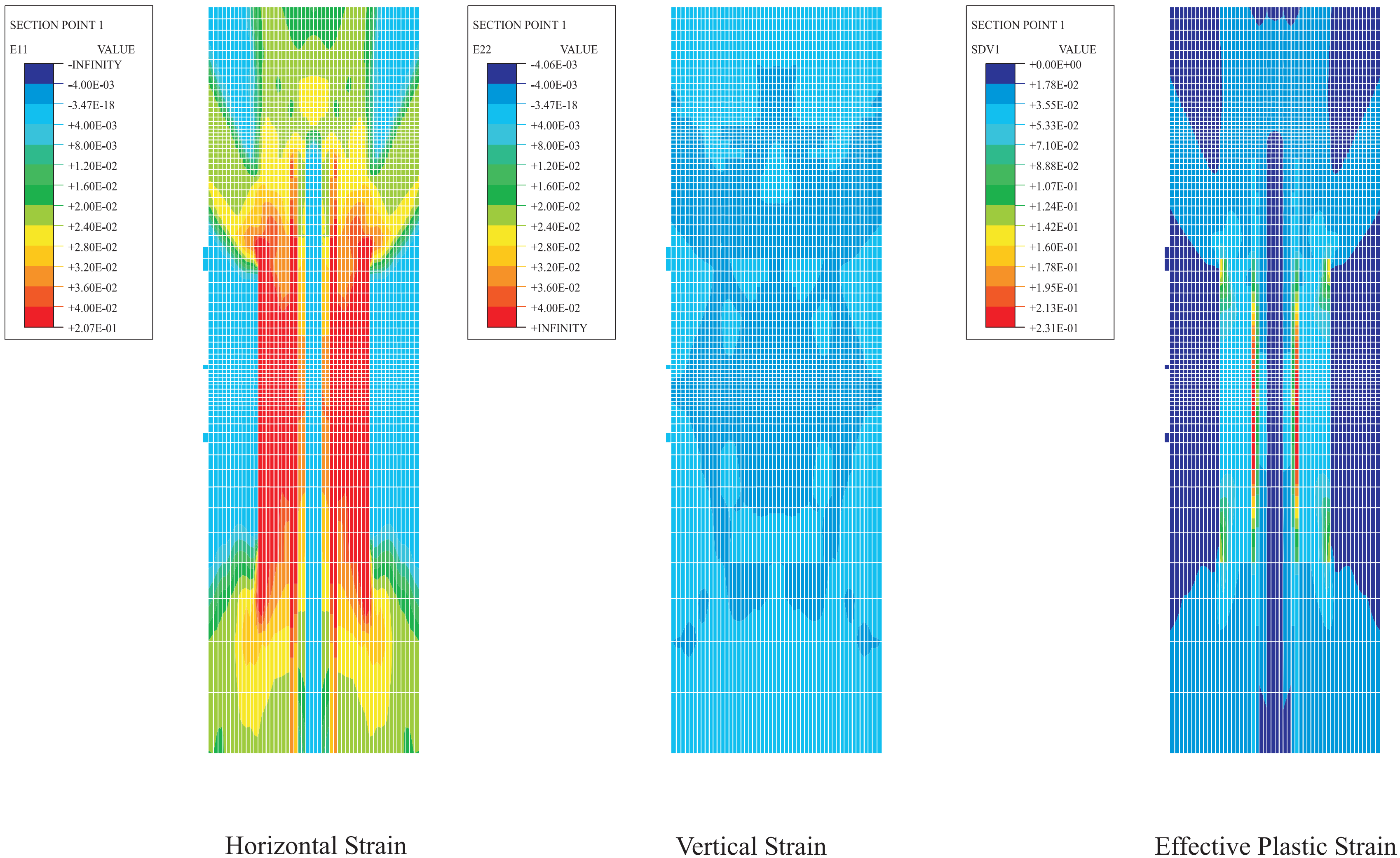

Figure 8-33. PCCV Liner Model, Posttest Analysis, Case 10, Strain Contour, at P = 3.3 Pd

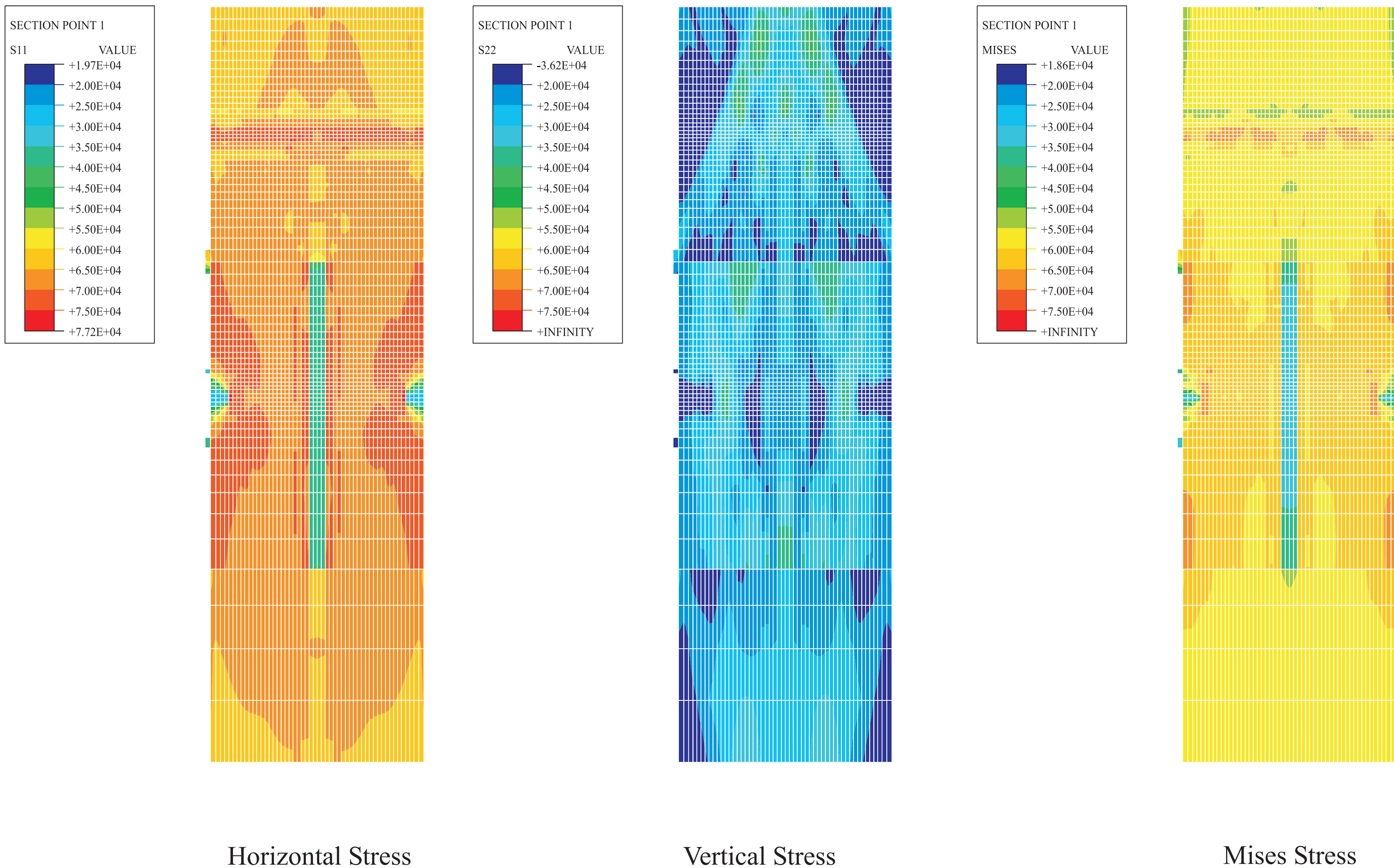

Figure 8-34. PCCV Liner Model, Posttest Analysis, Case 11, Stress Contour, at P = 3.3 Pd
(Stress in psi, multiply by 0.00690 for MPa)

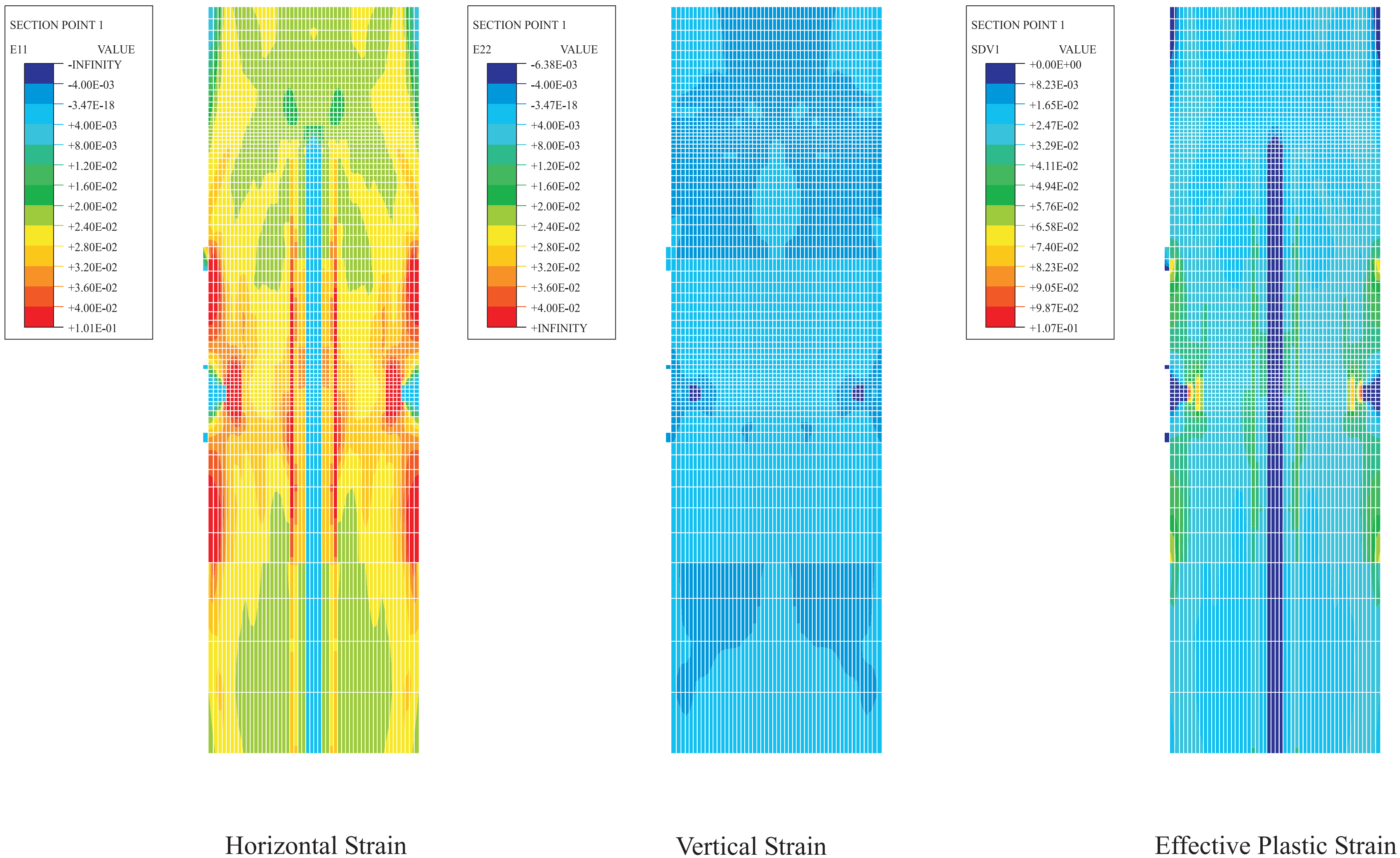

Figure 8-35. PCCV Liner Model, Posttest Analysis, Case 11, Strain Contour, at P = 3.3 Pd

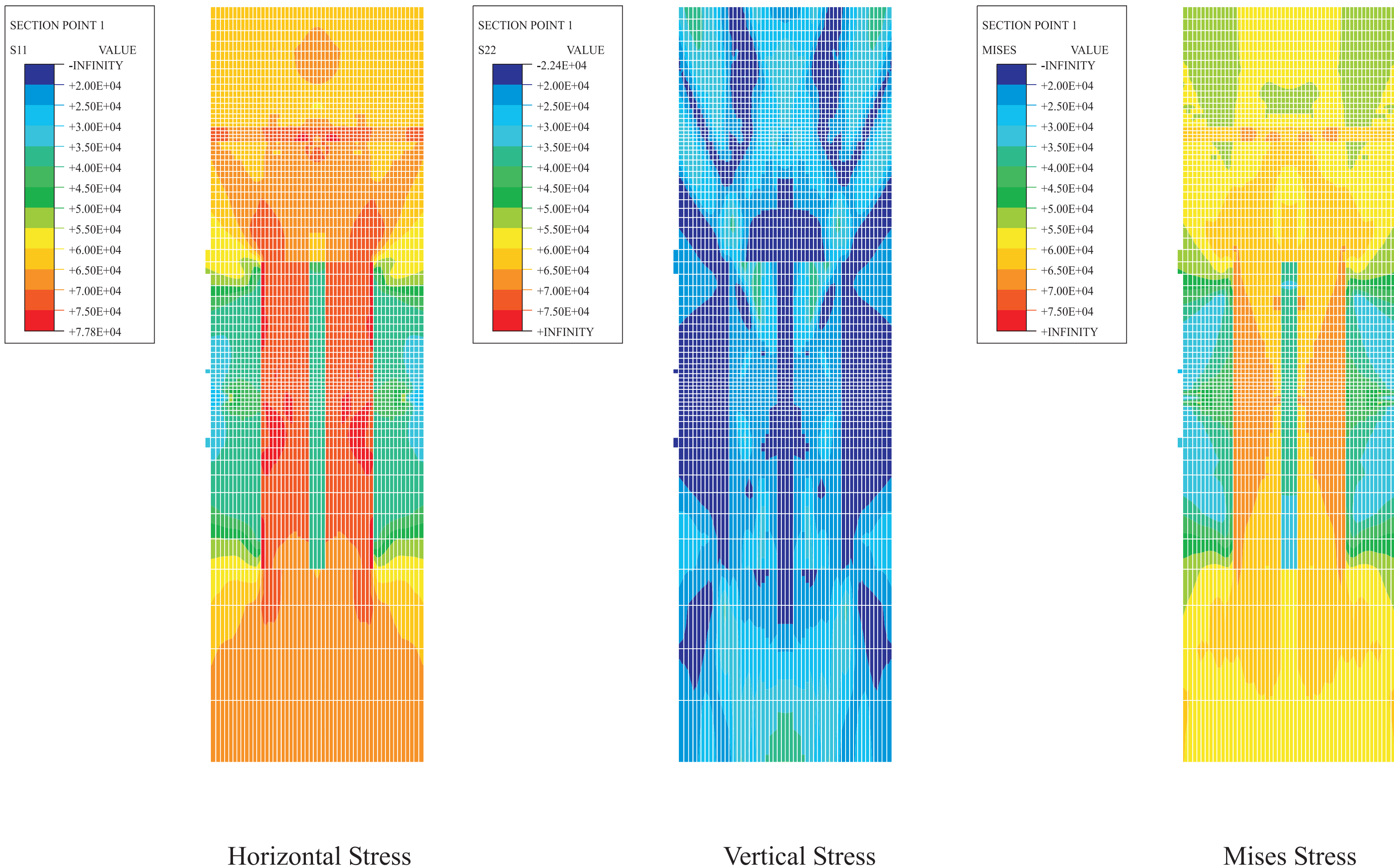

Figure 8-36. PCCV Liner Model, Posttest Analysis, Case 12, Stress Contour, at P = 3.3 Pd
(Stresses in psi; multiply by 0.00690 for MPa)

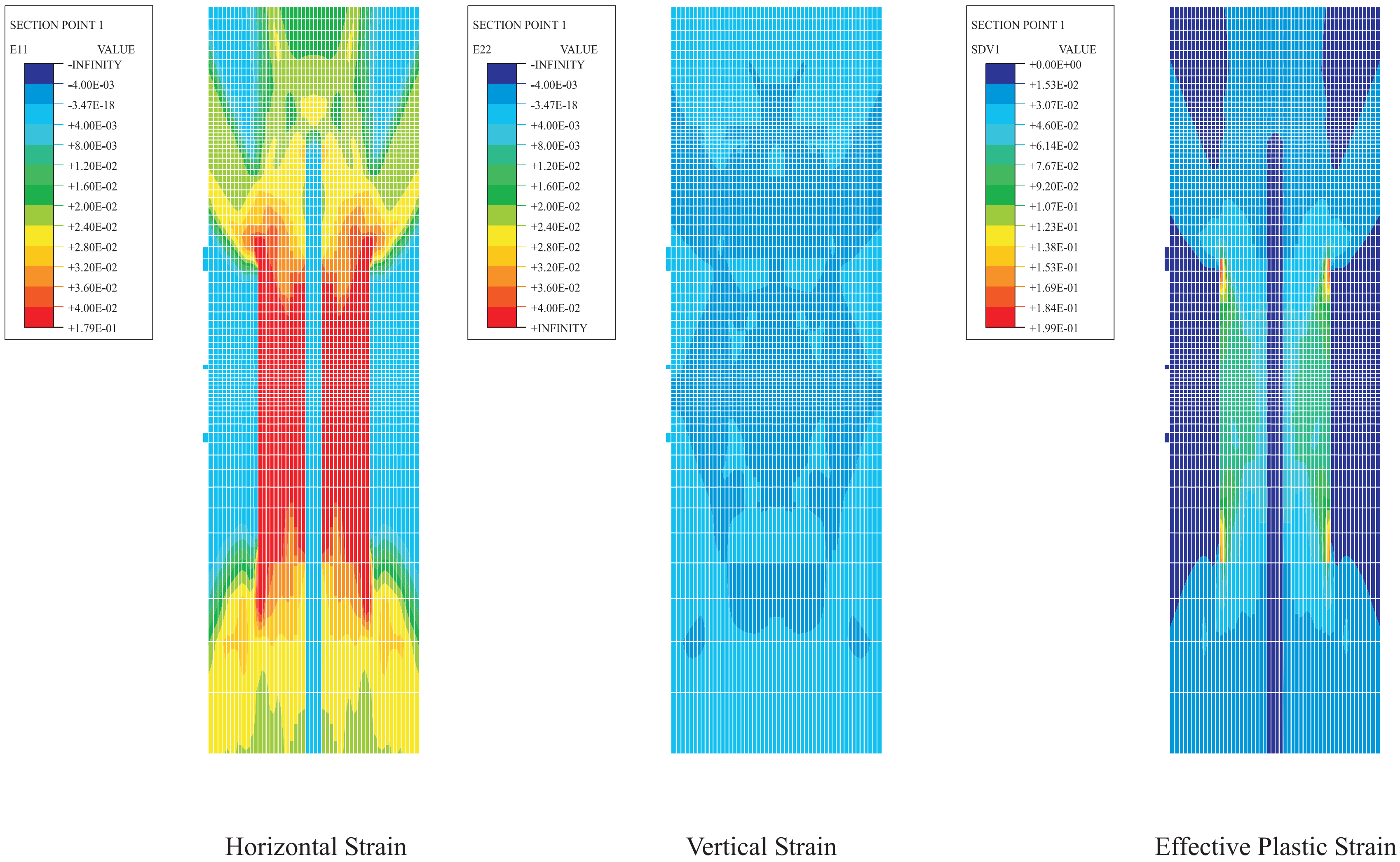

Figure 8-37. PCCV Liner Model, Posttest Analysis, Case 12, Strain Contour at P = 3.3 Pd

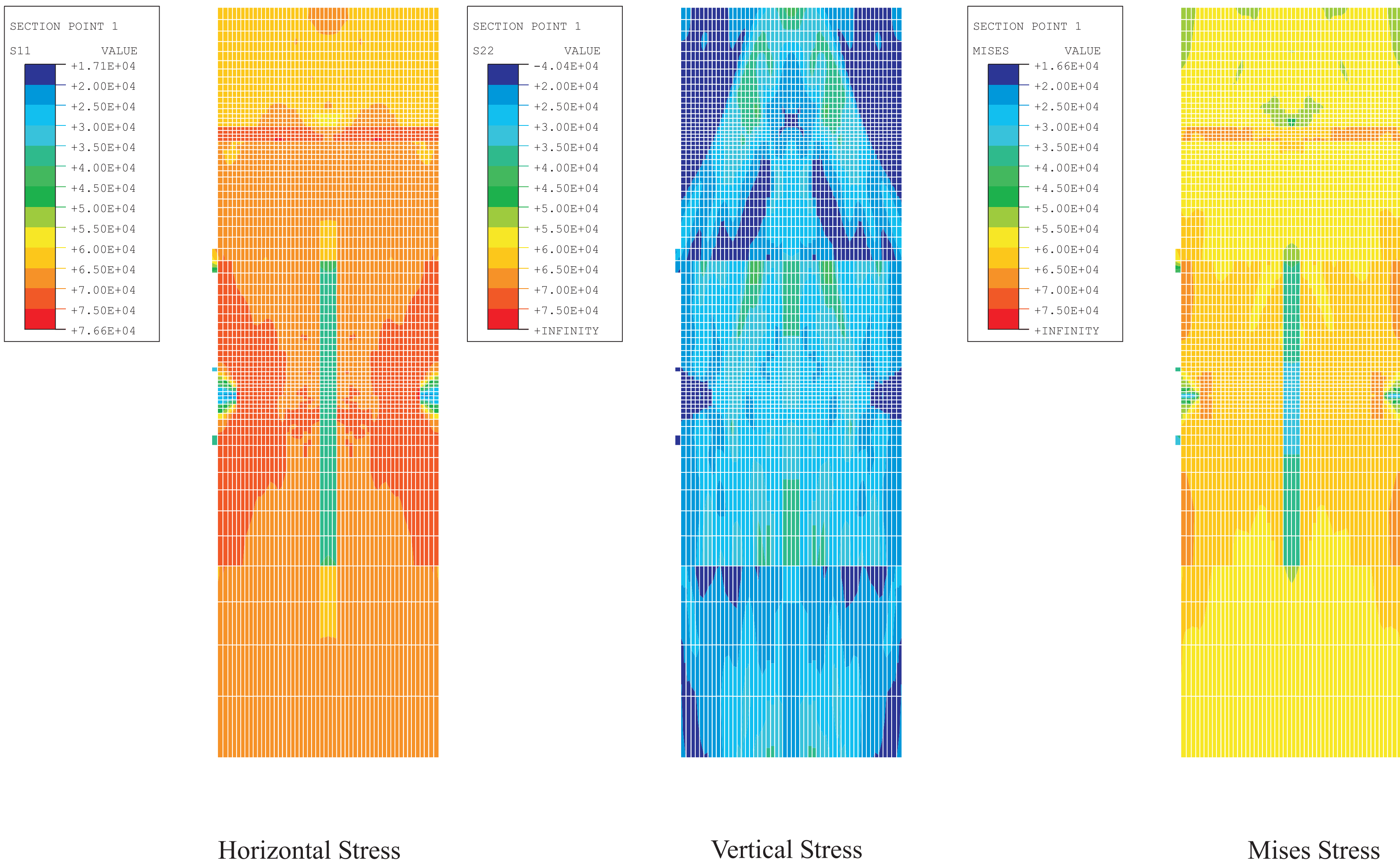

Figure 8-38. PCCV Liner Model, Posttest Analysis, Case 13, Stress Contour, at P = 3.3 Pd
(Stresses in psi; multiply by 0.00690 for MPa)

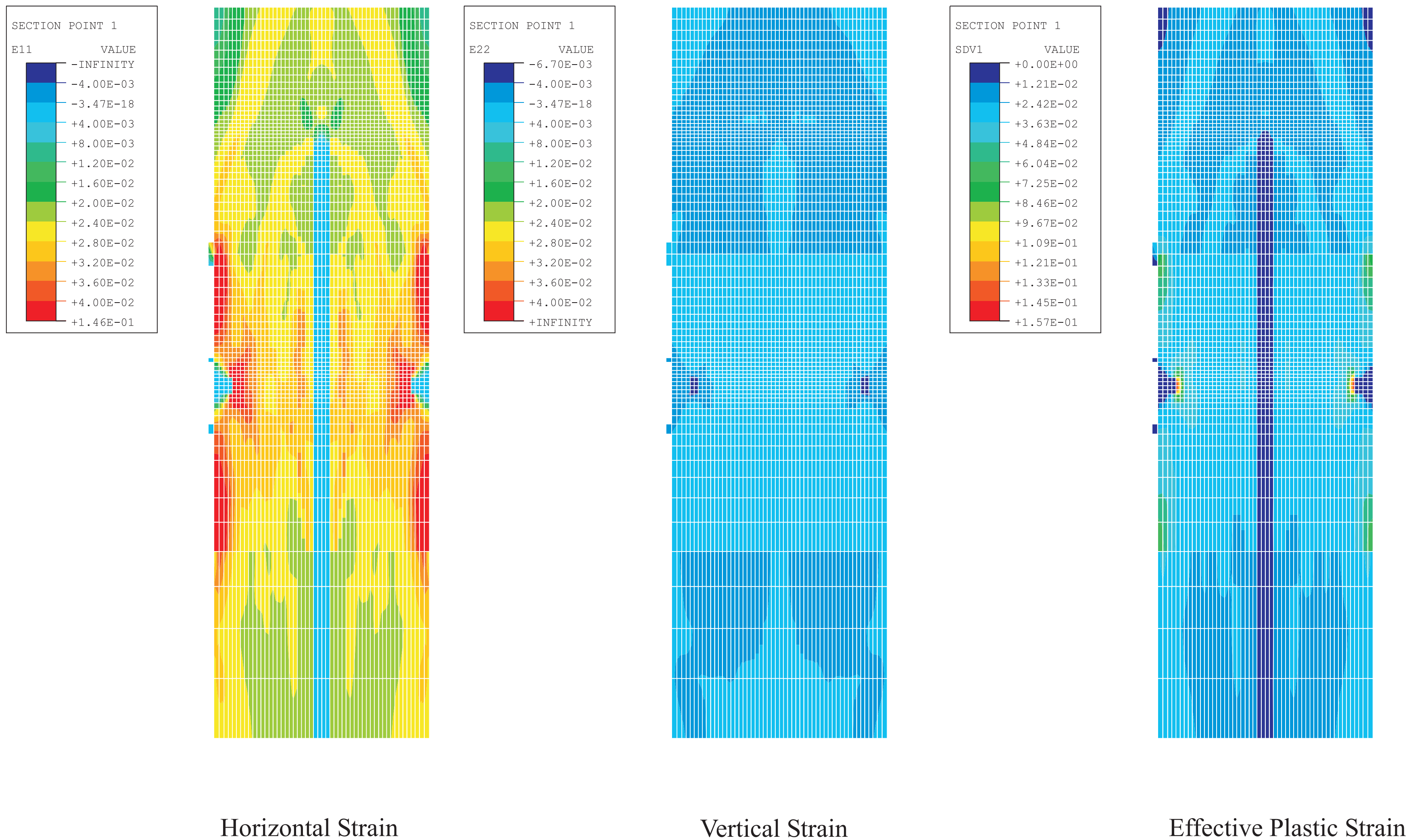

Figure 8-39. PCCV Liner Model, Posttest Analysis, Case 13, Strain Contour, at P = 3.3 Pd

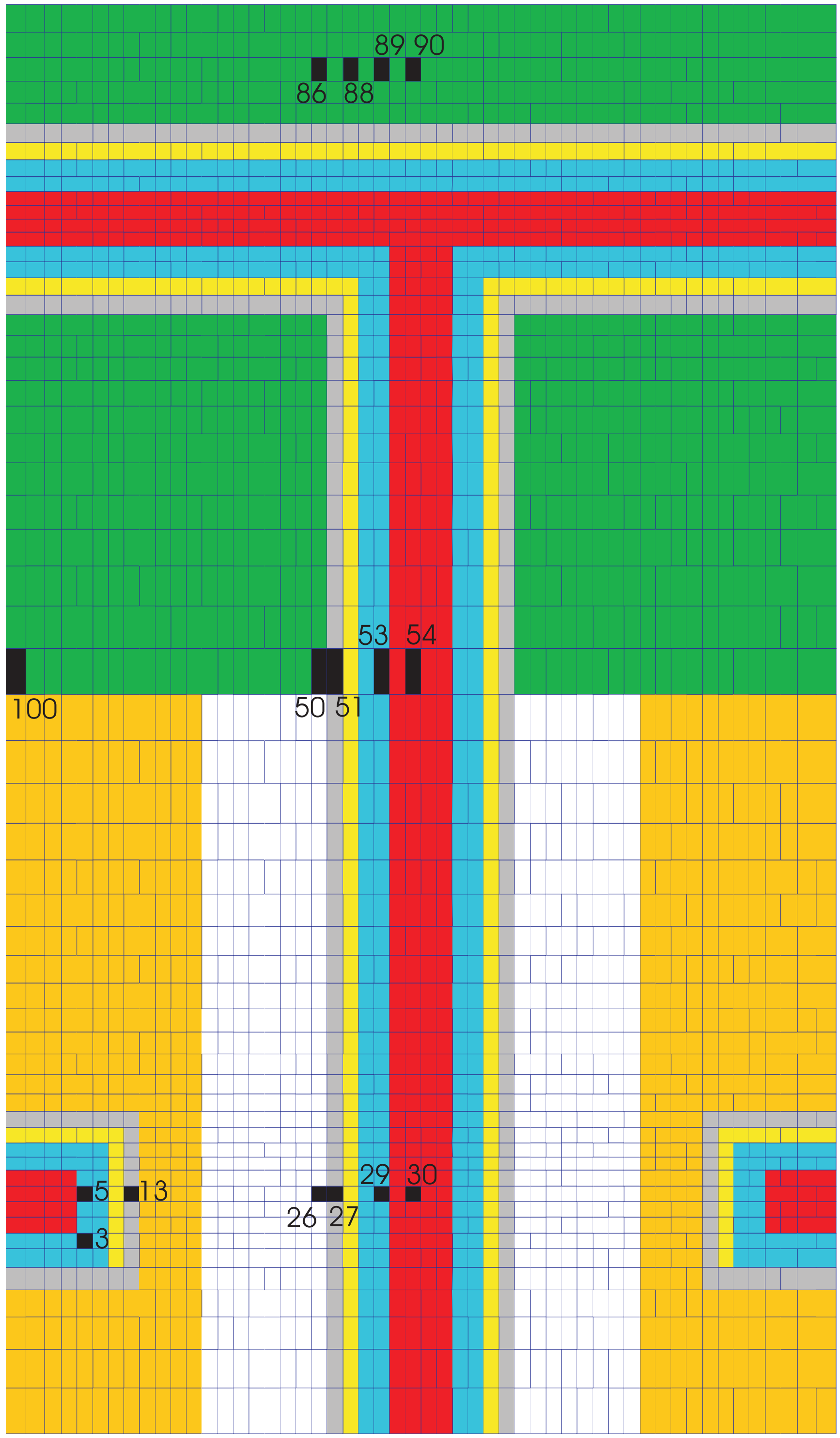

Figure 8-40. PCCV Liner Weld/Rat-Hole Study; Locations of Strain Profile Comparisons

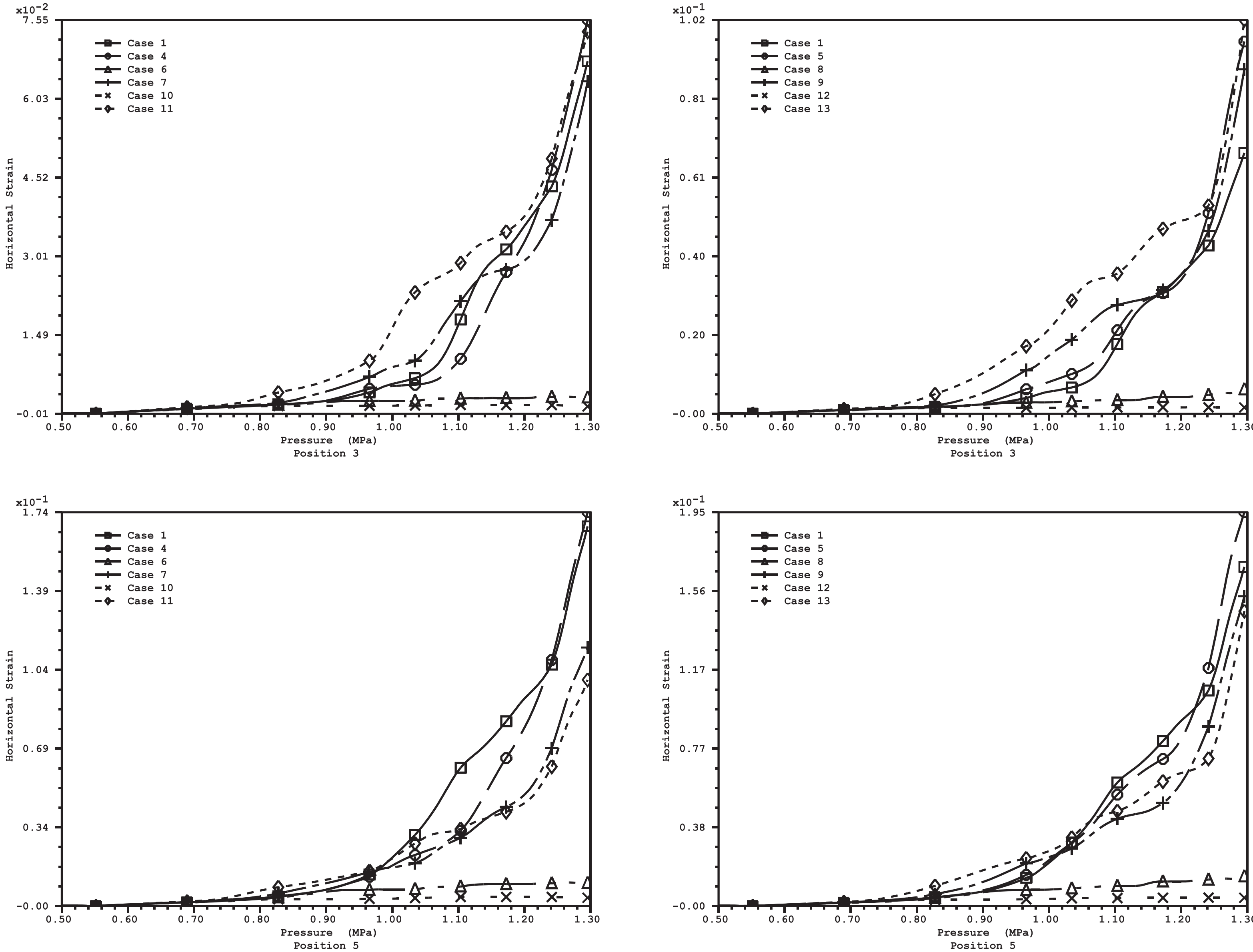

Figure 8-41. PCCV Liner Weld/Rat-Hole Study; Horizontal Strain Comparisons

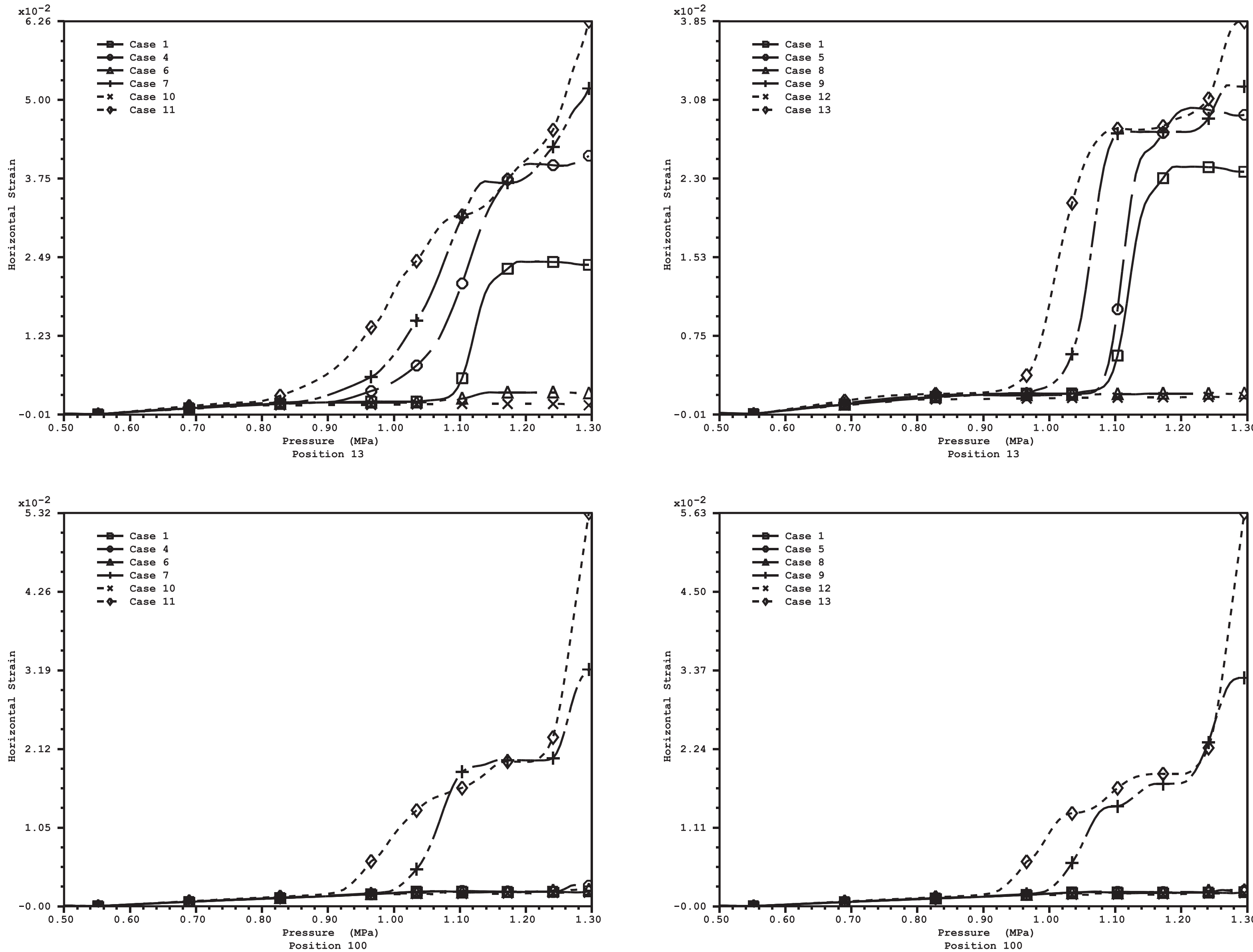

Figure 8-42. PCCV Liner Weld/Rat-Hole Study; Horizontal Strain Comparisons

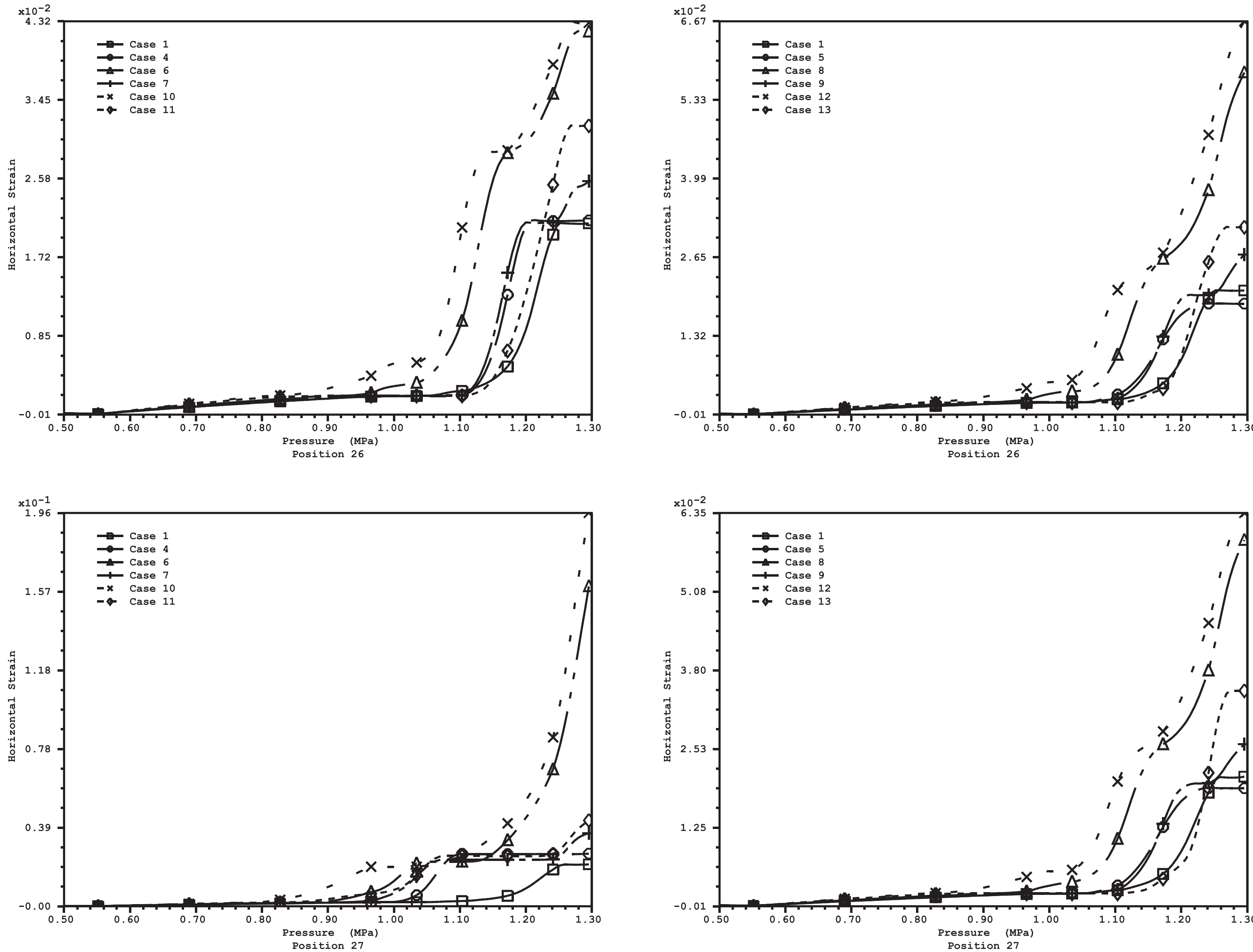

Figure 8-43. PCCV Liner Weld/Rat-Hole Study; Horizontal Strain Comparisons

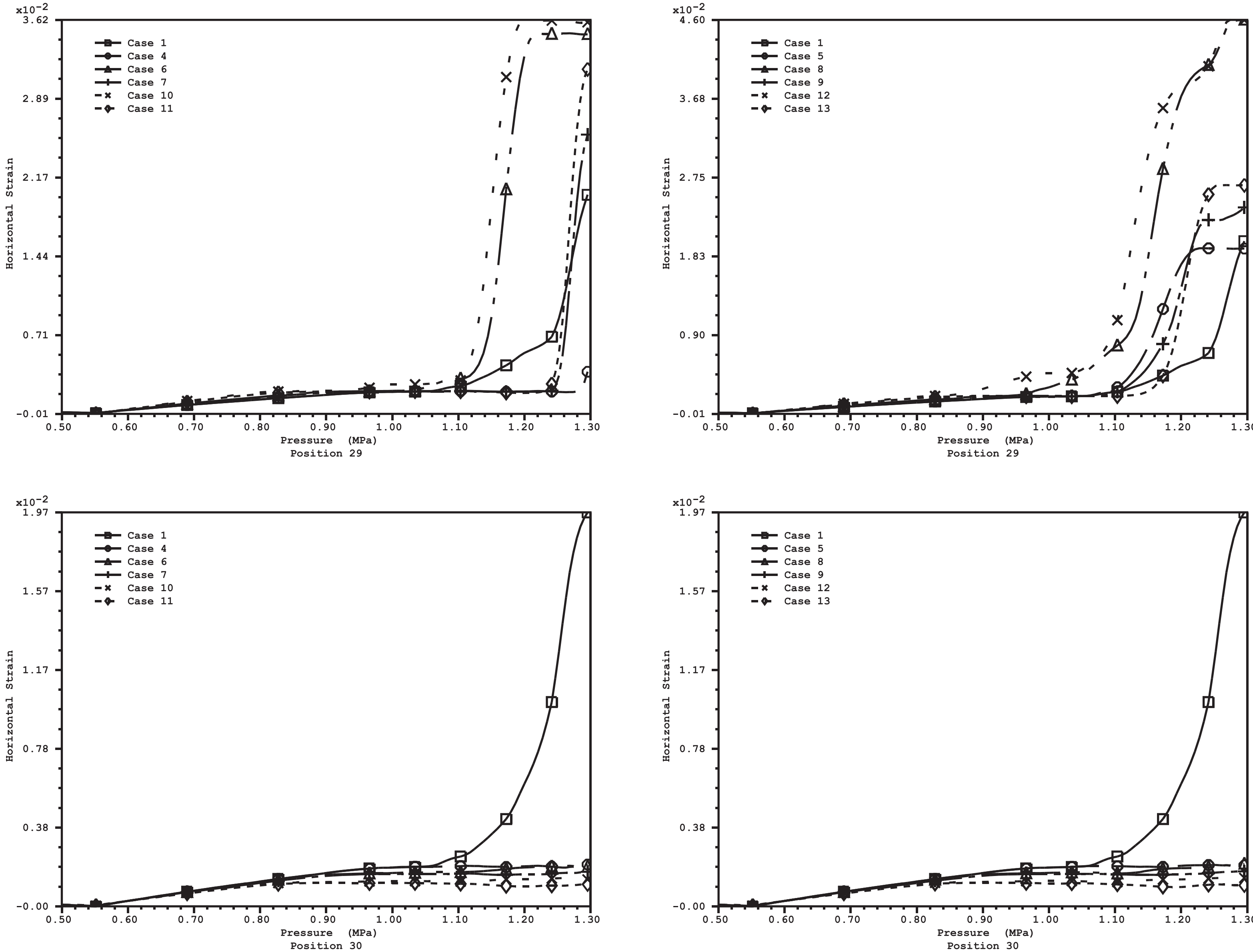

Figure 8-44. PCCV Liner Weld/Rat-Hole Study; Horizontal Strain Comparisons

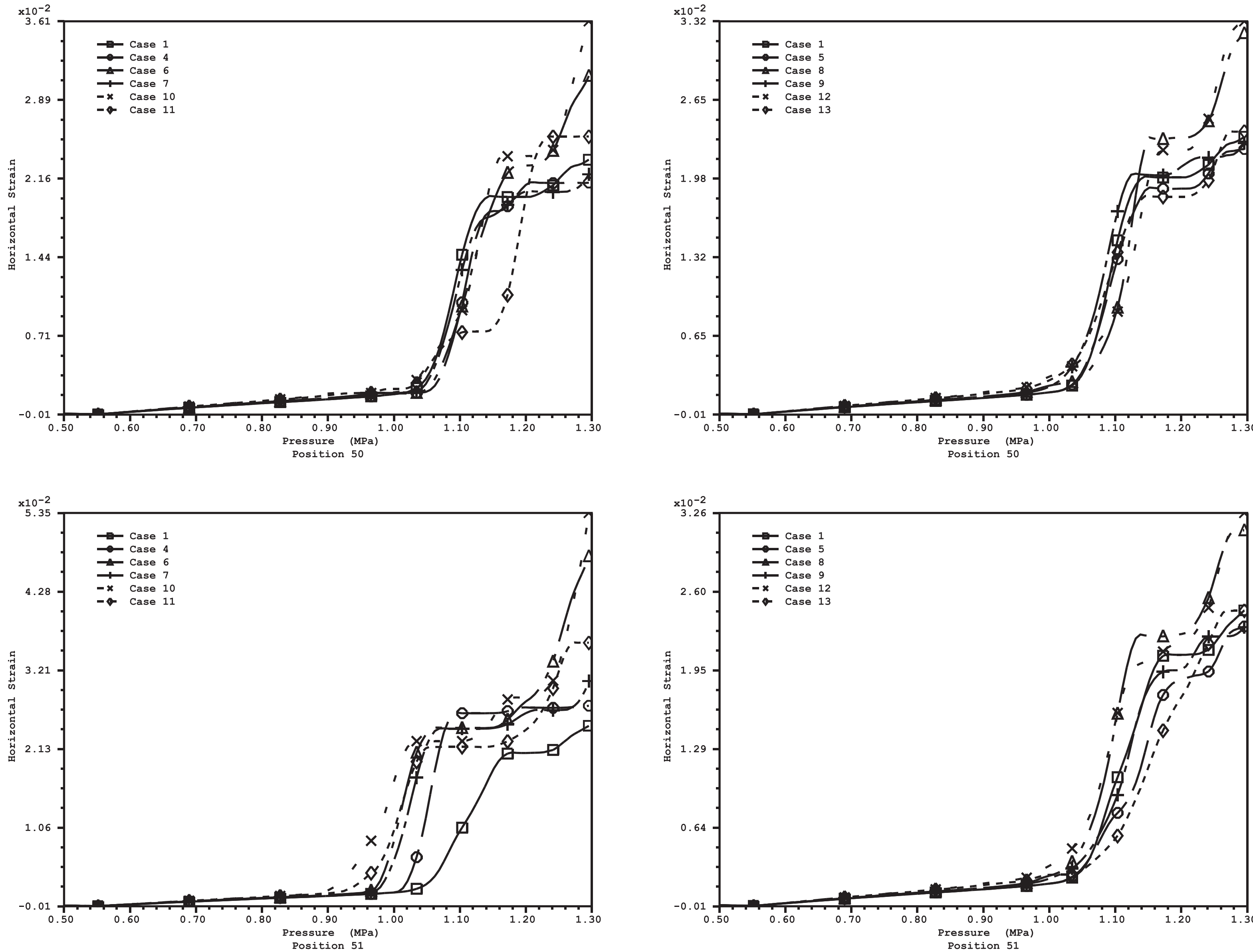

Figure 8-45. PCCV Liner Weld/Rat-Hole Study; Horizontal Strain Comparisons

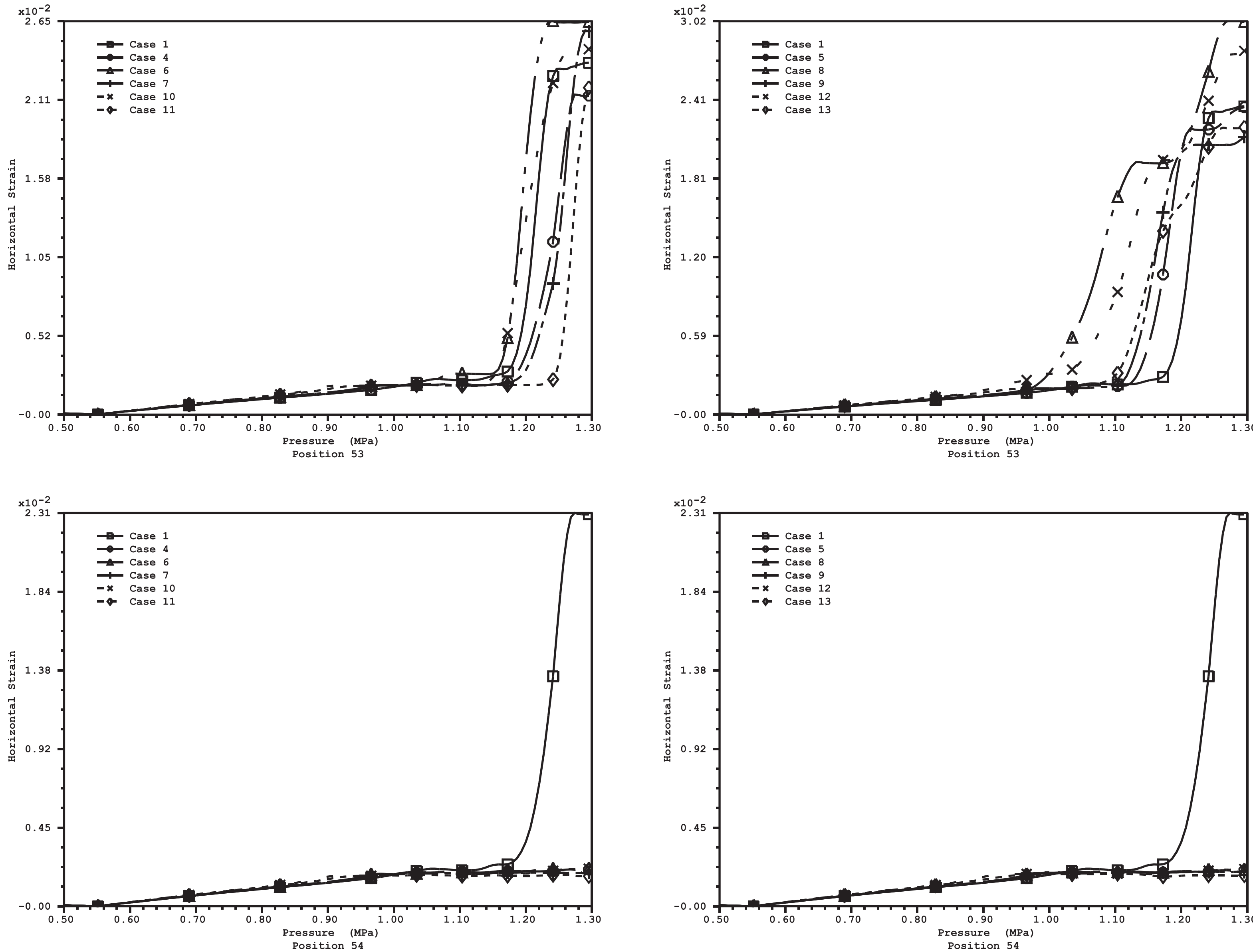

Figure 8-46. PCCV Liner Weld/Rat-Hole Study; Horizontal Strain Comparisons

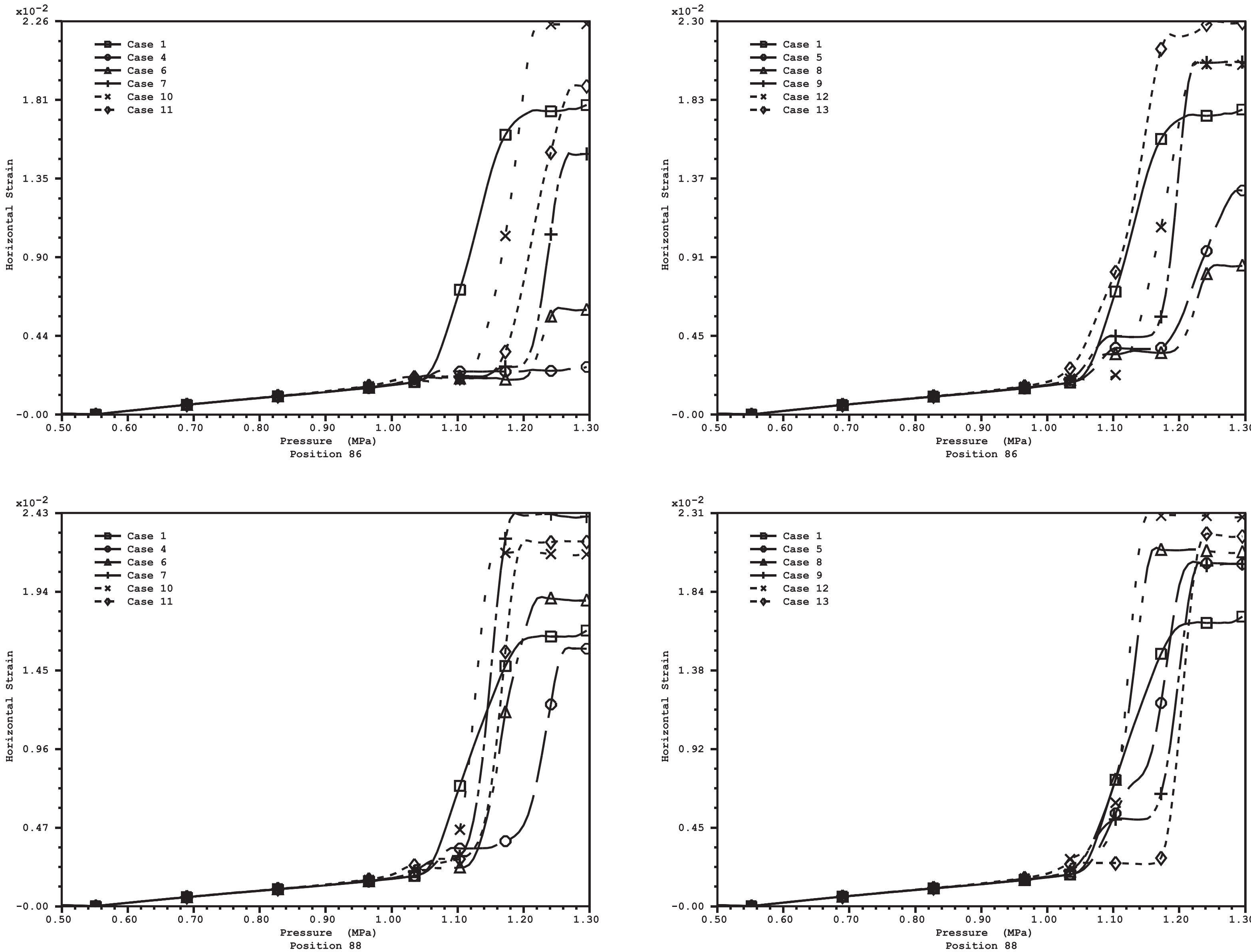

Figure 8-47. PCCV Liner Weld/Rat-Hole Study; Horizontal Strain Comparisons

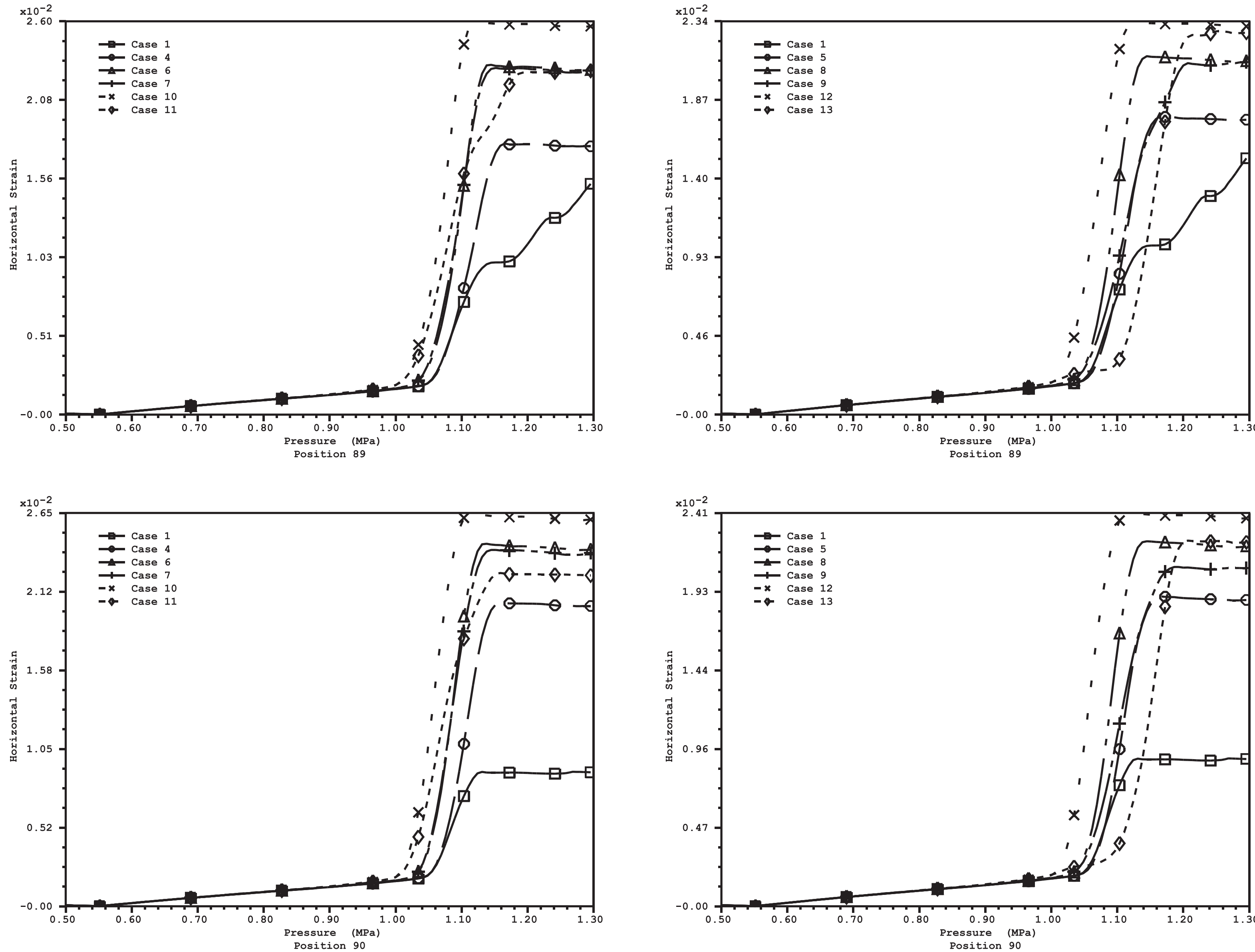

Figure 8-48. PCCV Liner Weld/Rat-Hole Study; Horizontal Strain Comparisons

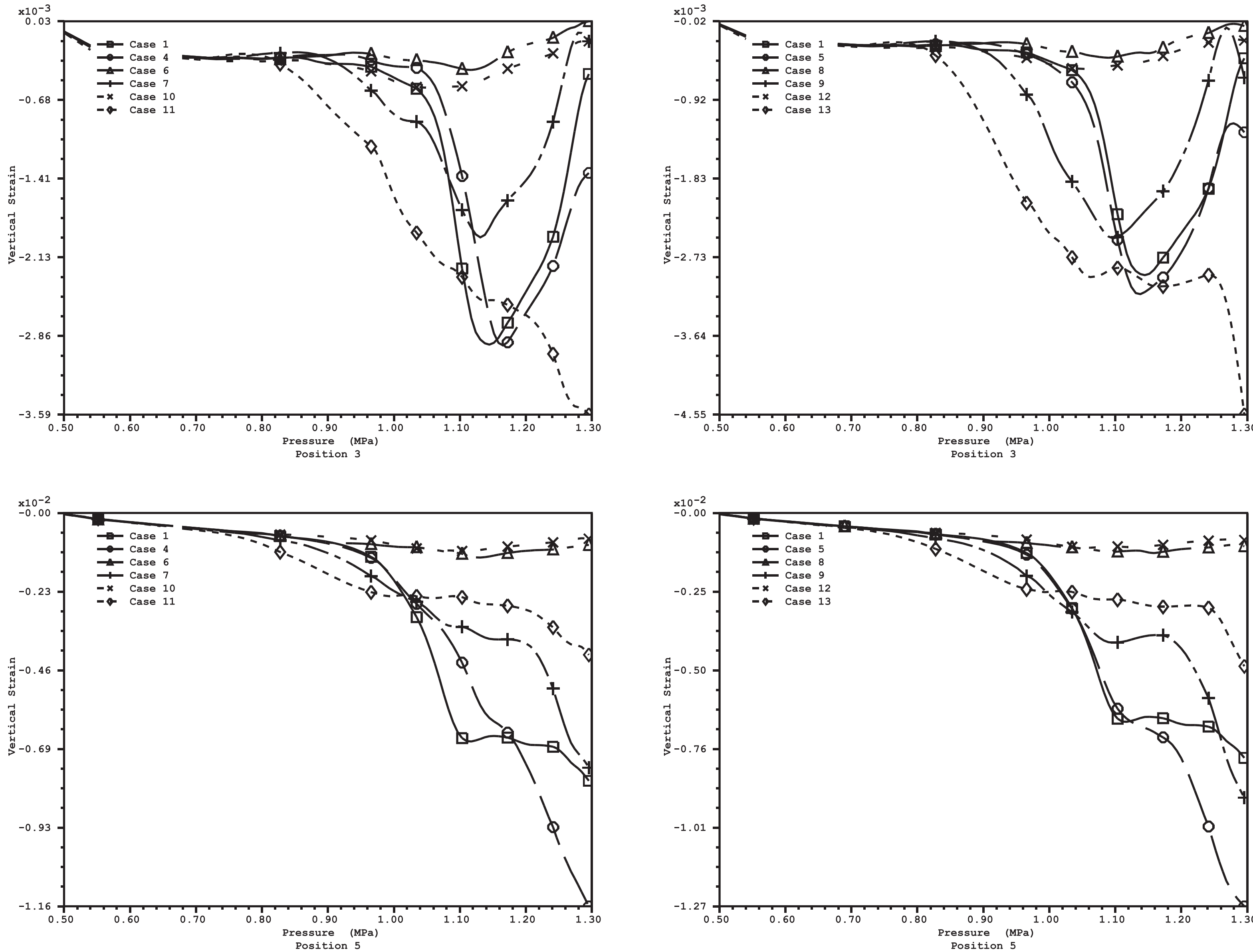

Figure 8-49. PCCV Liner Weld/Rat-Hole Study; Vertical Strain Comparisons

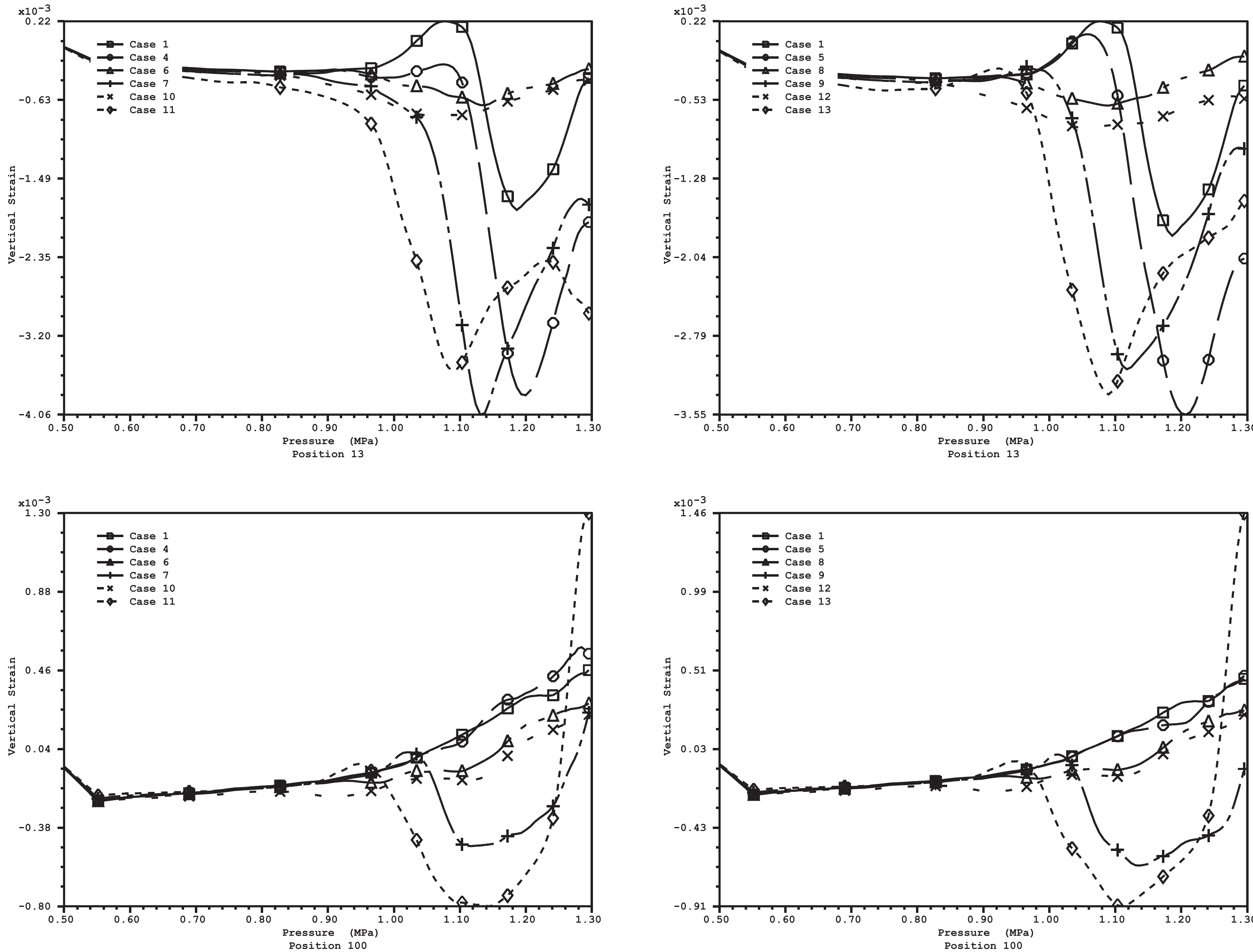

Figure 8-50. PCCV Liner Weld/Rat-Hole Study; Vertical Strain Comparisons

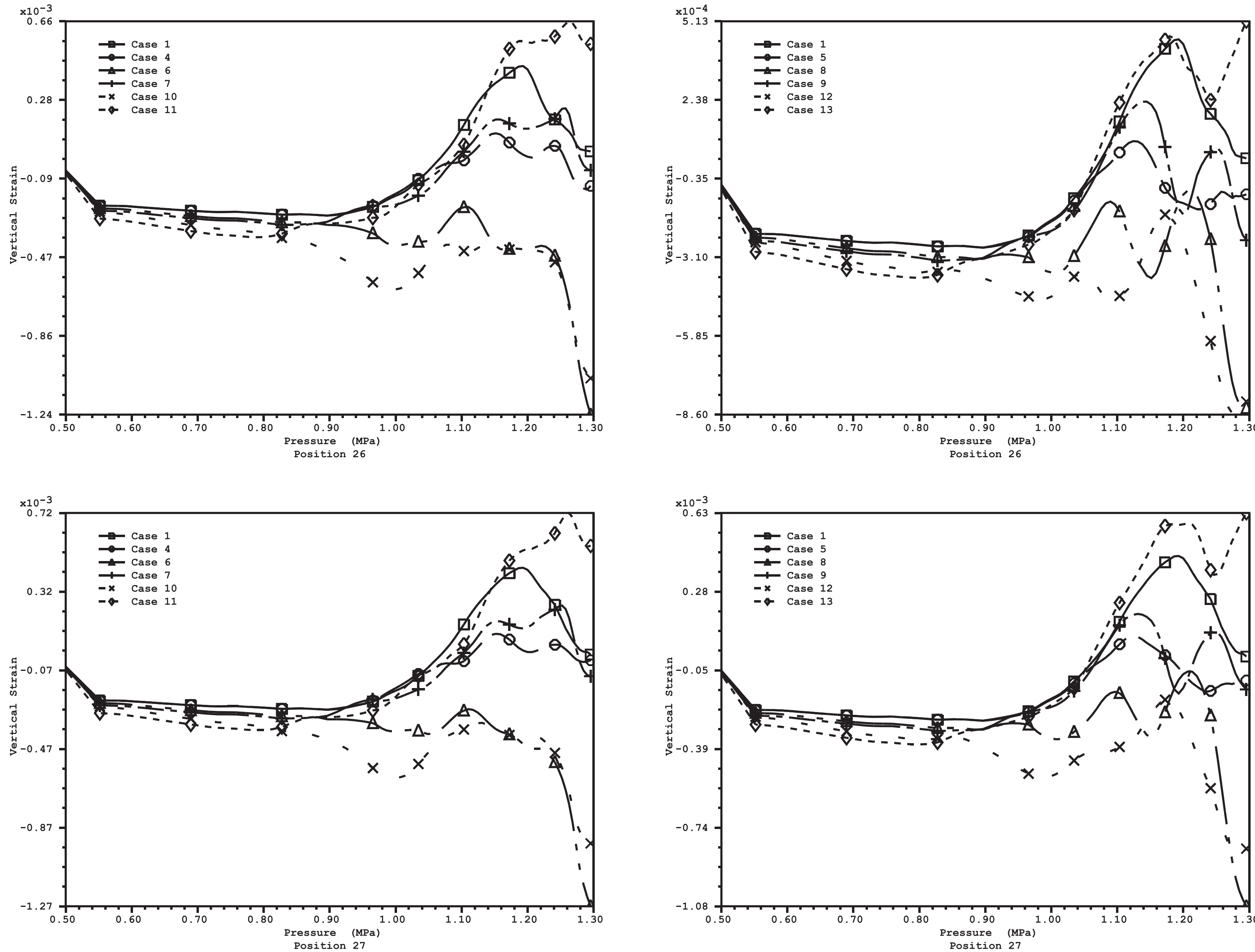

Figure 8-51. PCCV Liner Weld/Rat-Hole Study; Vertical Strain Comparisons

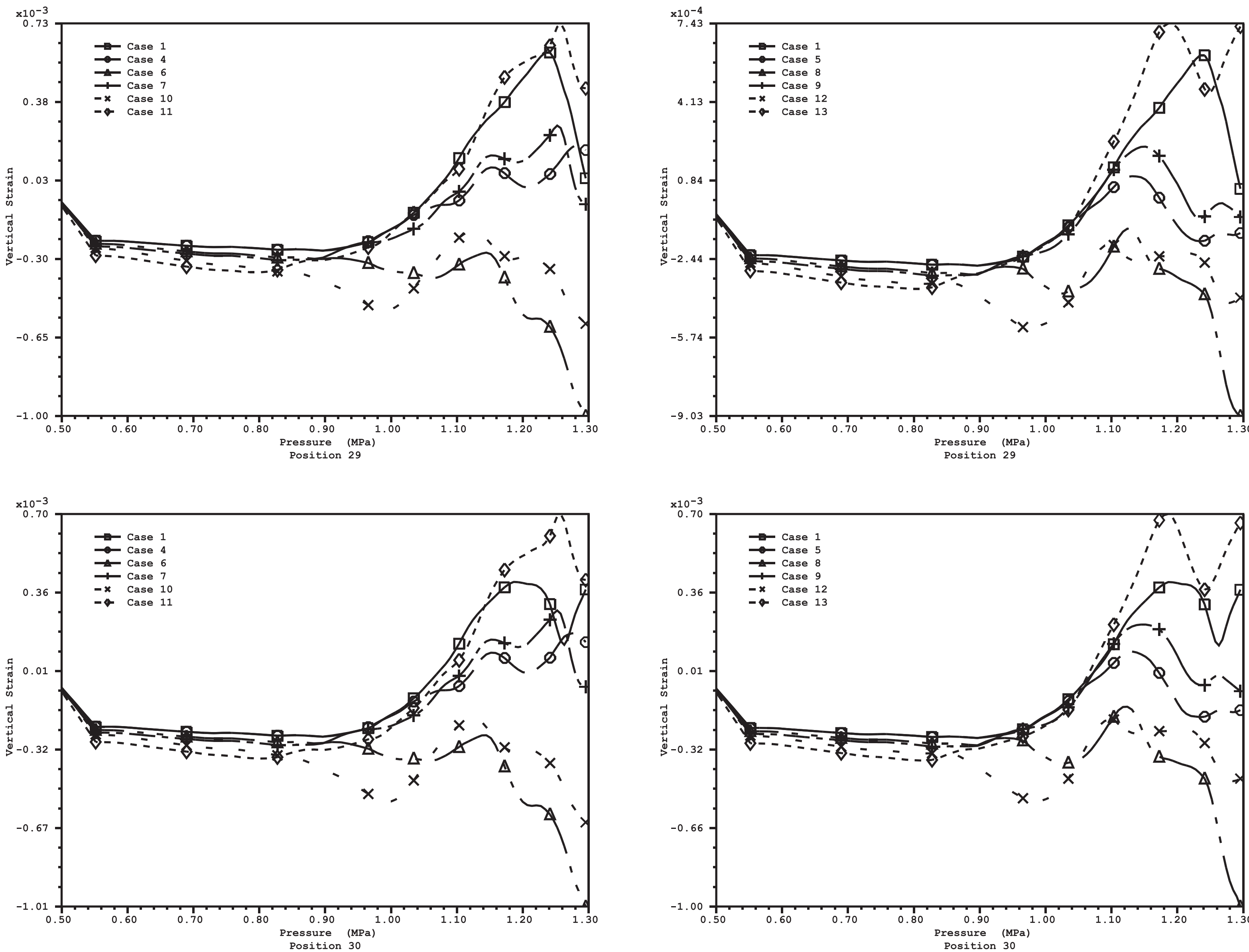

Figure 8-52. PCCV Liner Weld/Rat-Hole Study; Vertical Strain Comparisons

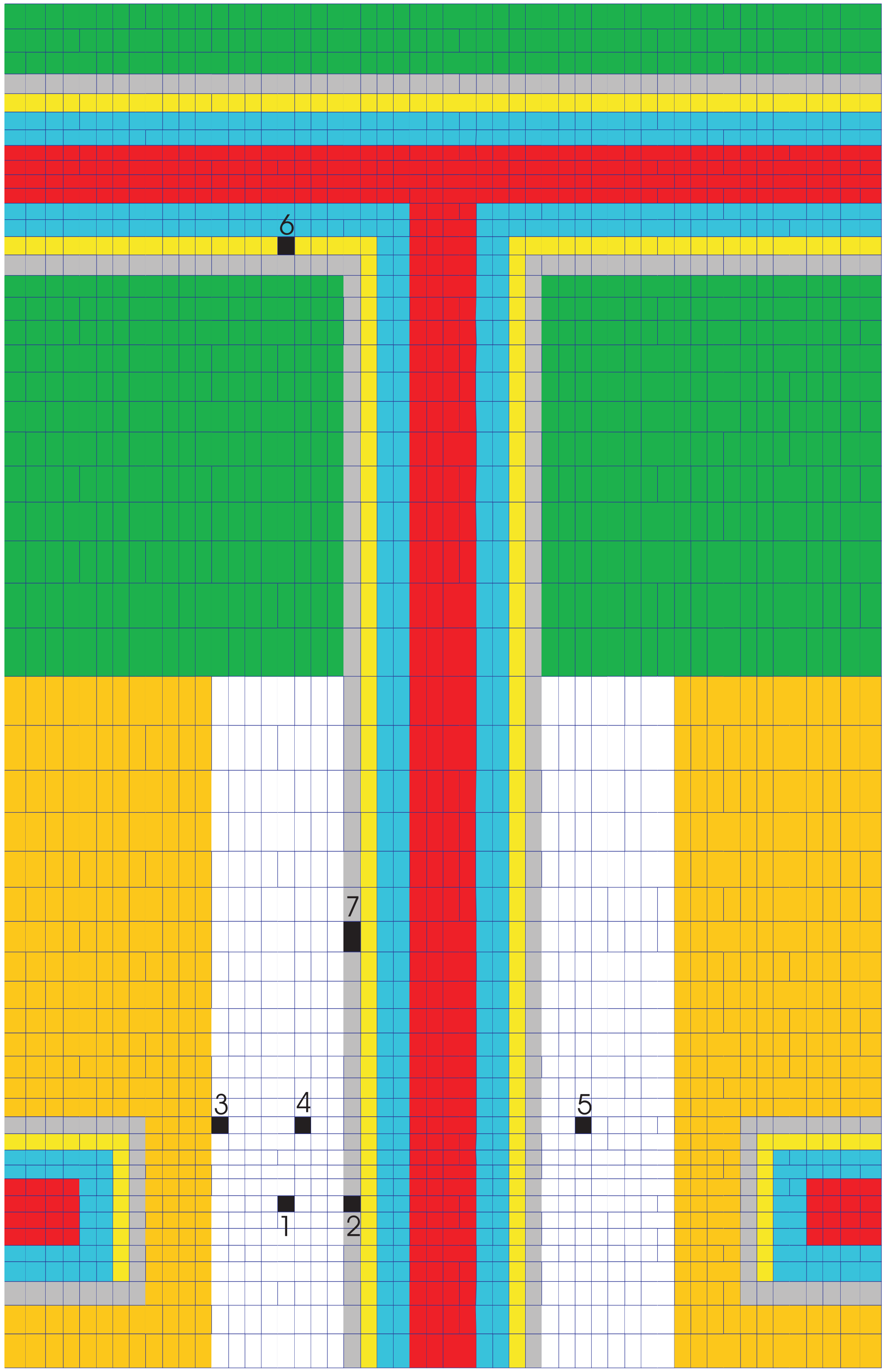

Figure 8-53. PCCV Liner Weld/Rat-Hole Study; Strain Profile Gage Locations

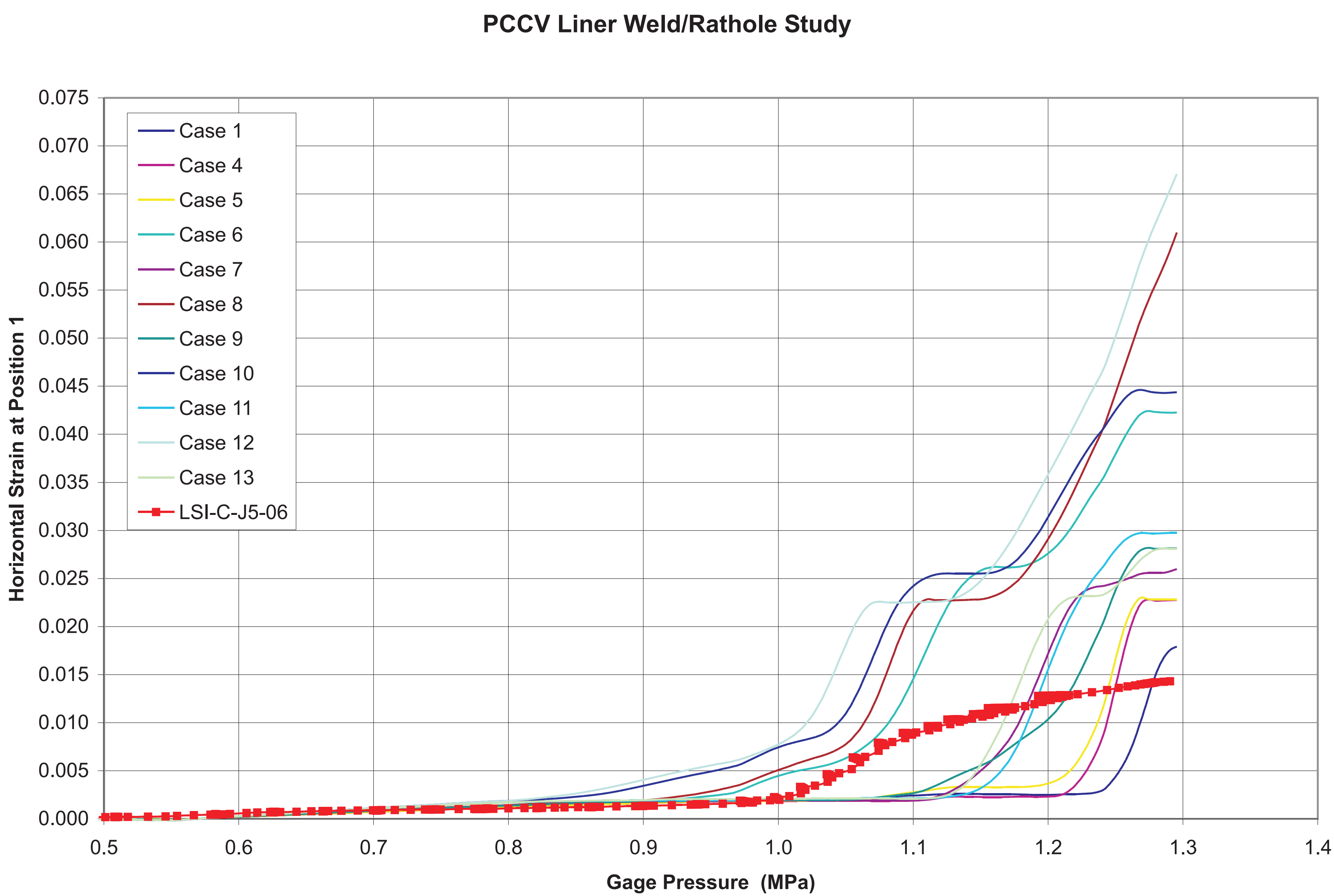

Figure 8-54. PCCV Liner Weld/Rat-Hole Study Mesh Sensitivity, Horizontal Strain Comparisons at Gage Position 1

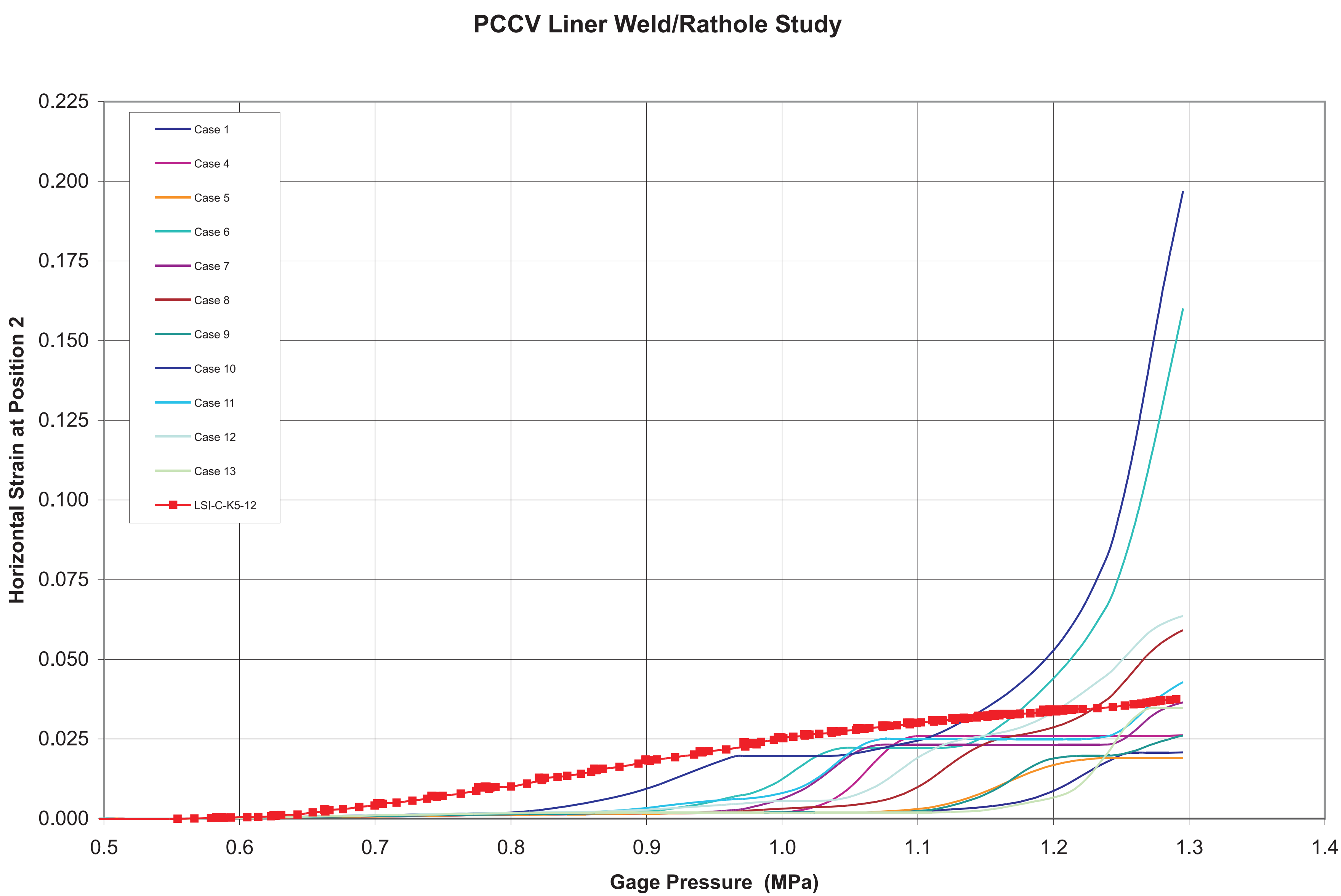

Figure 8-55. PCCV Liner Weld/Rat-Hole Study Mesh Sensitivity, Horizontal Strain Comparisons at Gage Position 2

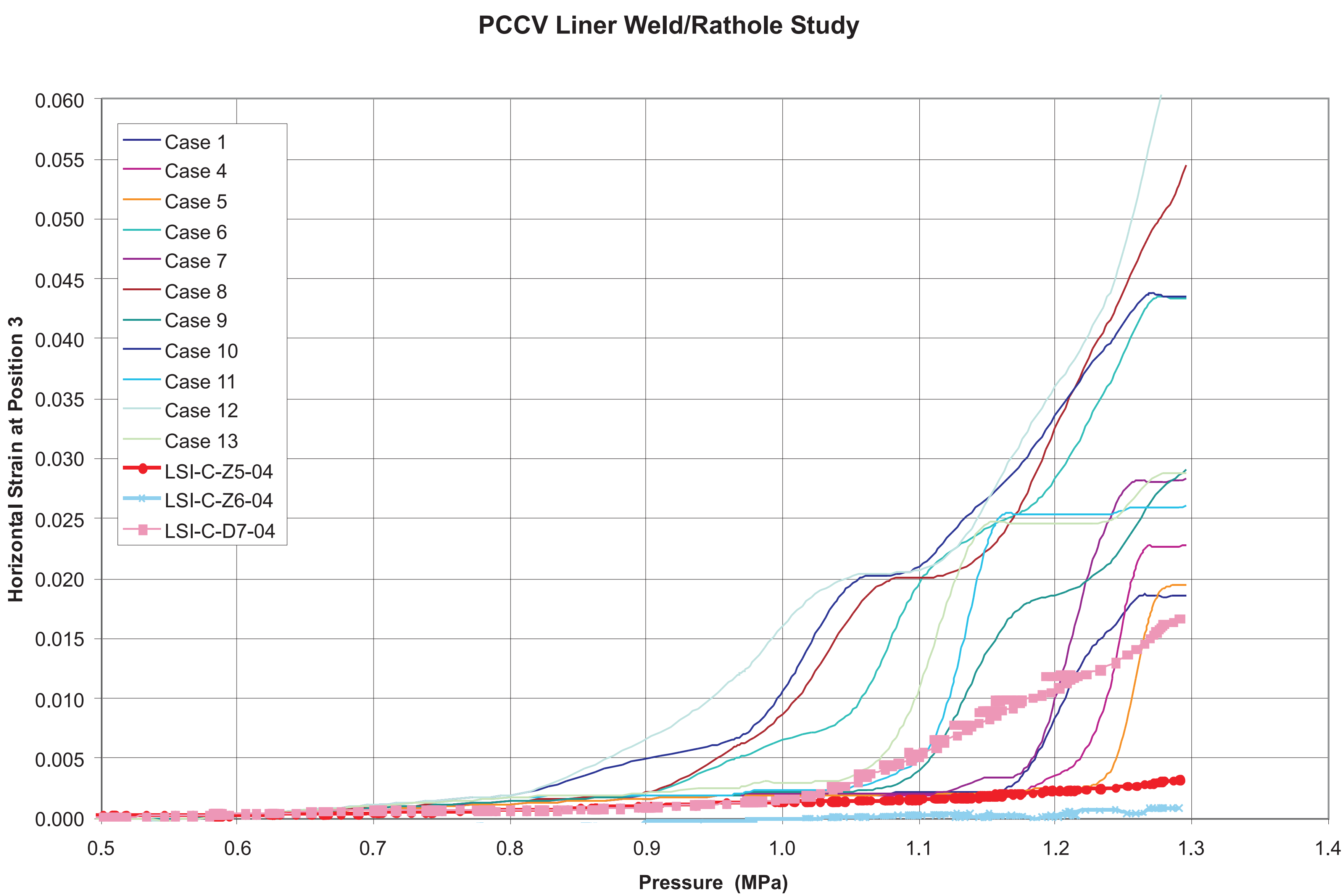

Figure 8-56. PCCV Liner Weld/Rat-Hole Study Mesh Sensitivity, Horizontal Strain Comparisons at Gage Position 3

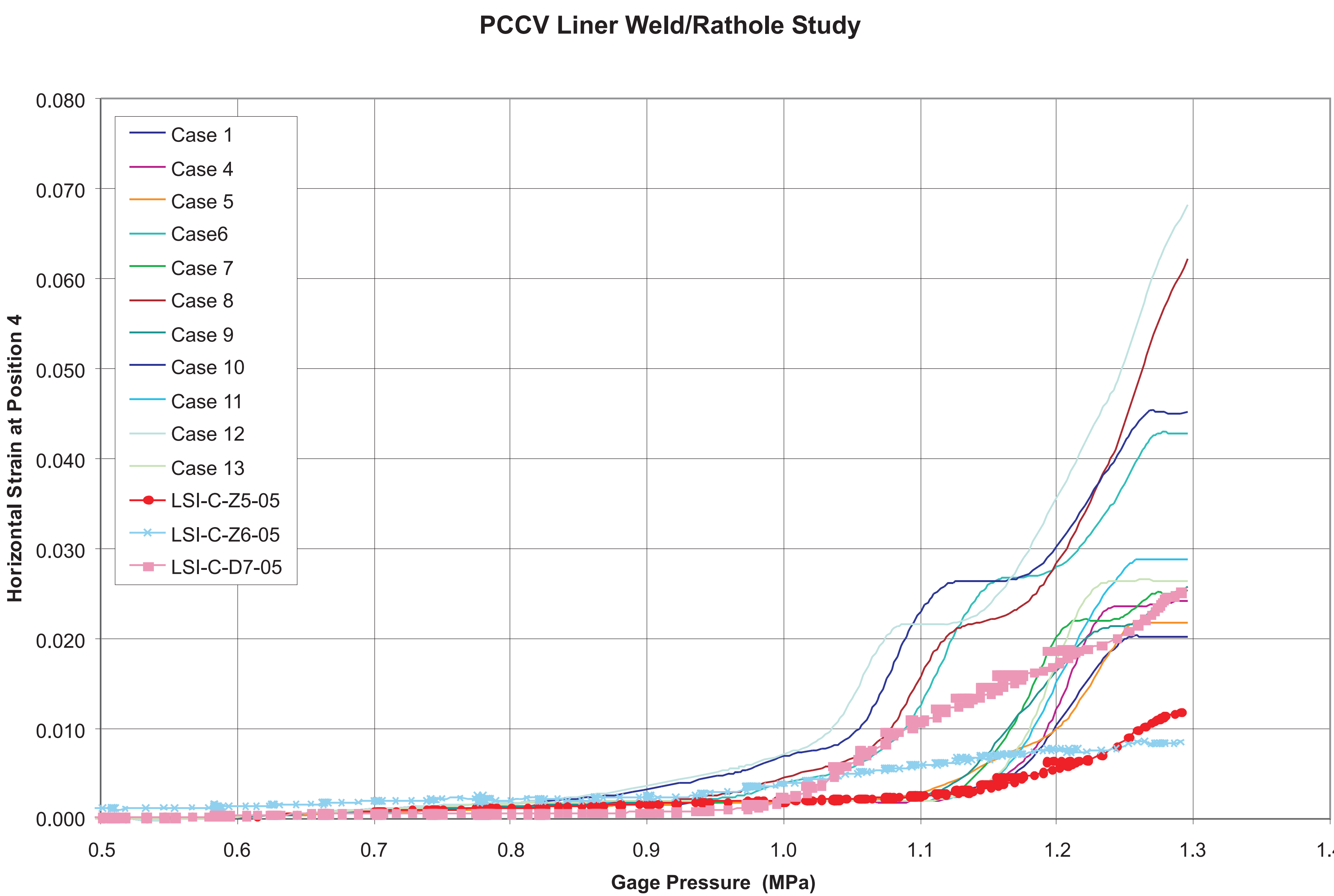

Figure 8-57. PCCV Liner Weld/Rat-Hole Study Mesh Sensitivity, Horizontal Strain Comparisons at Gage Position 4

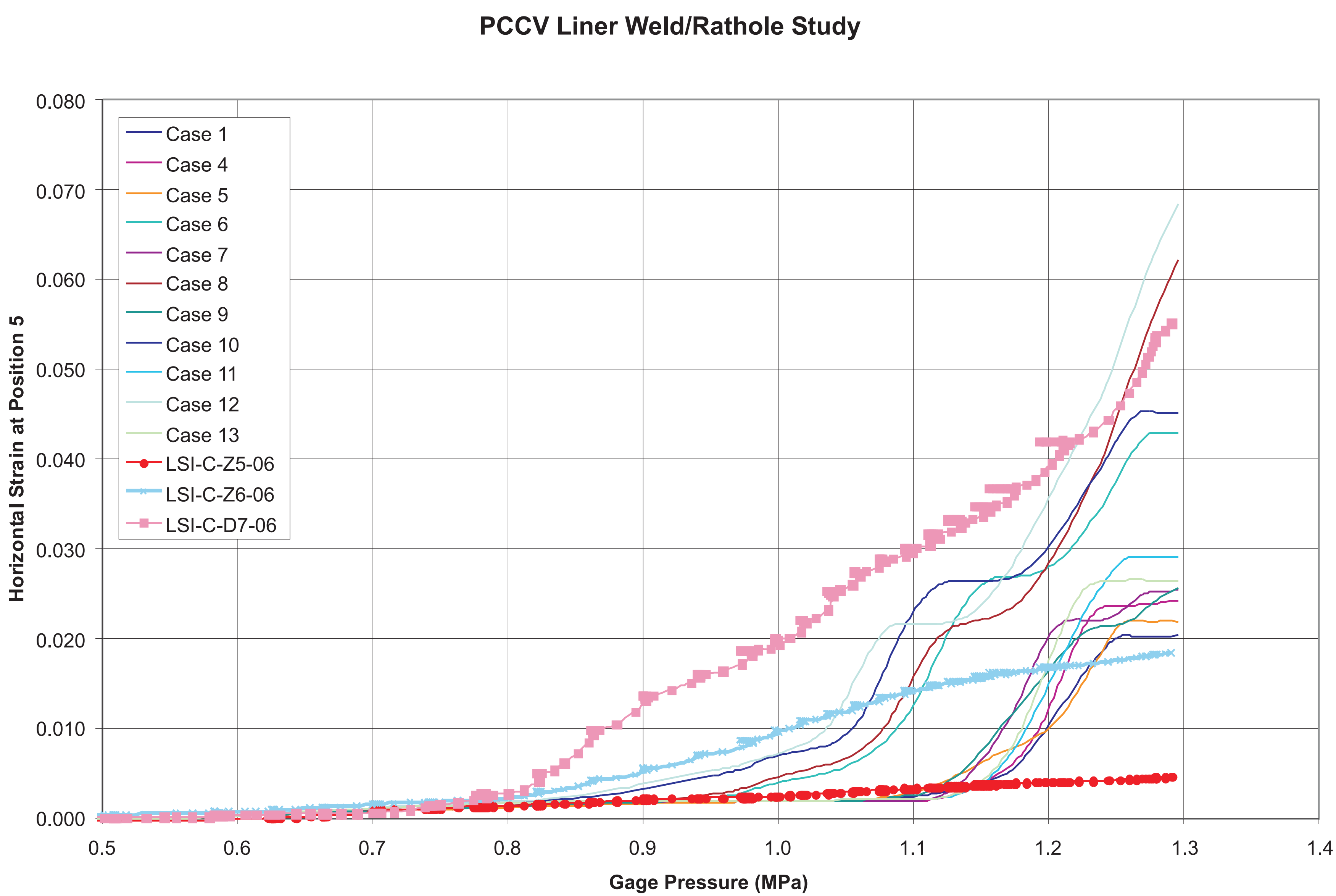

Figure 8-58. PCCV Liner Weld/Rat-Hole Study Mesh Sensitivity, Horizontal Strain Comparisons at Gage Position 5

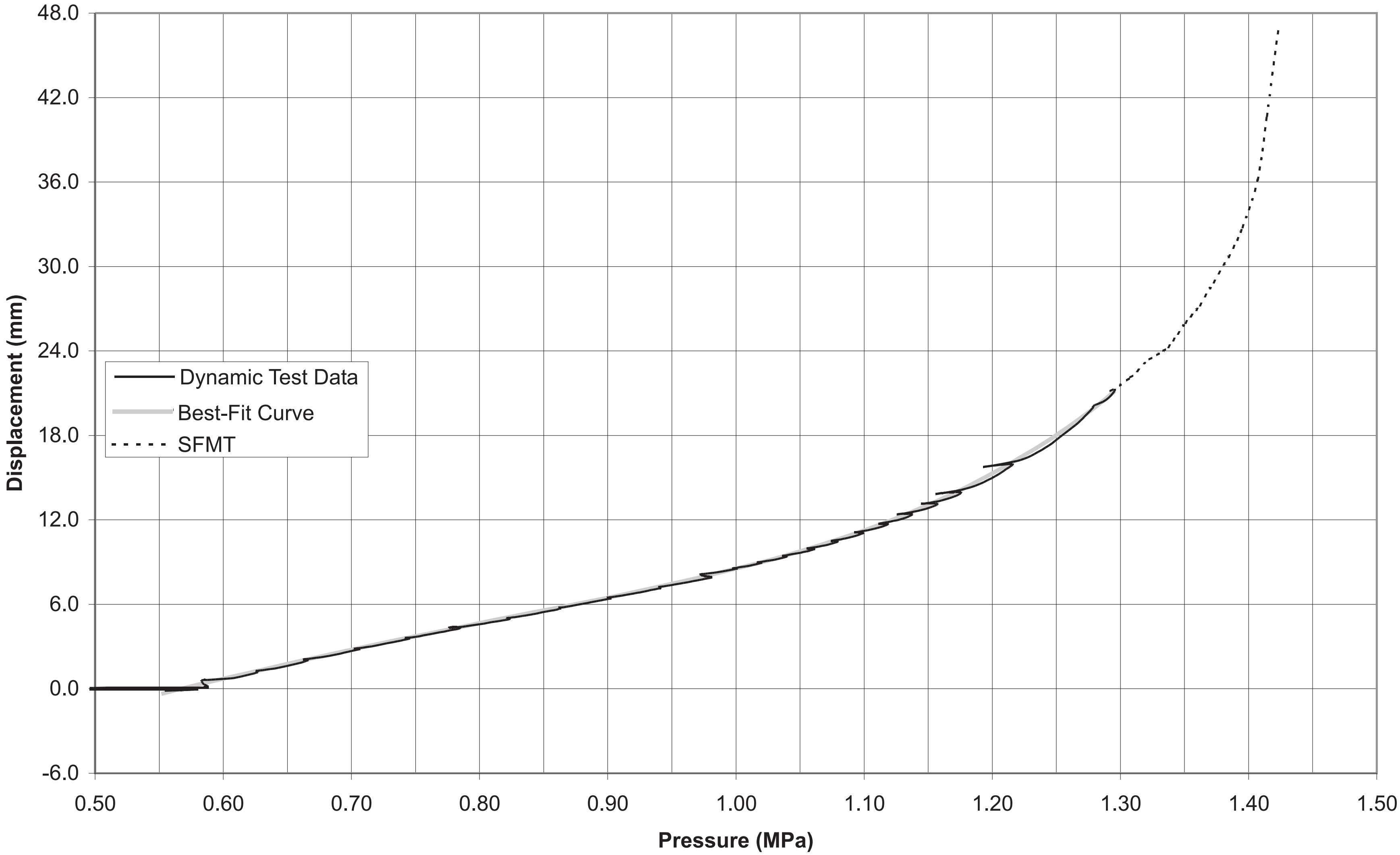

Figure 8-59. PCCV - Radial Displacement; 135, 4.68m, Gage DT-R-Z5-01

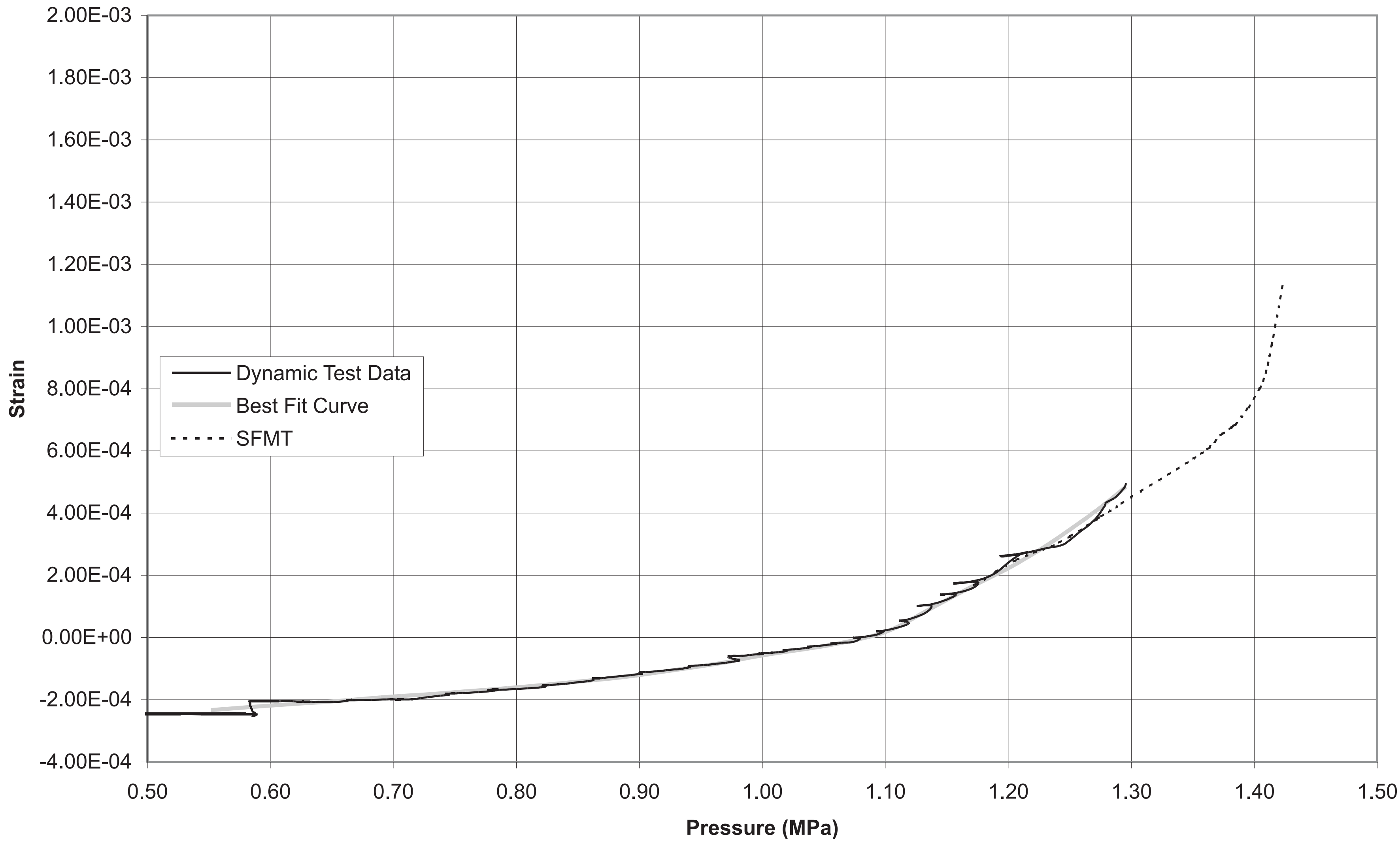

Figure 8-60. PCCV Liner Meridonal Strain; 135, 6.2 m, Gage LSI-M-Z06-01

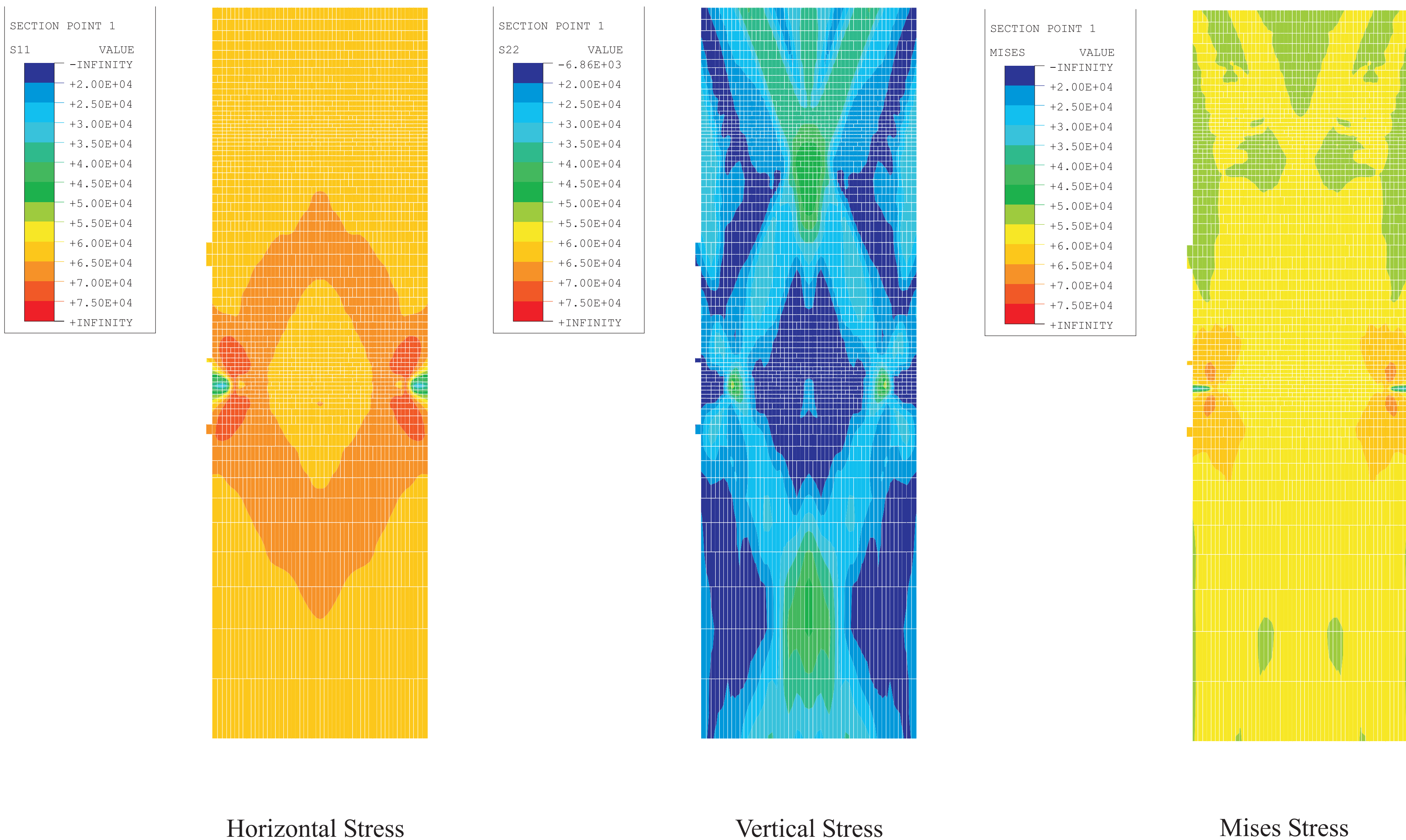

Figure 8-61. PCCV Liner Model, Liner Seam Rat-Hole Study Case 1, Stress Contour, Analysis To 3.4 Pd
(Stresses in psi; Multiply by 0.00690 for MPa)

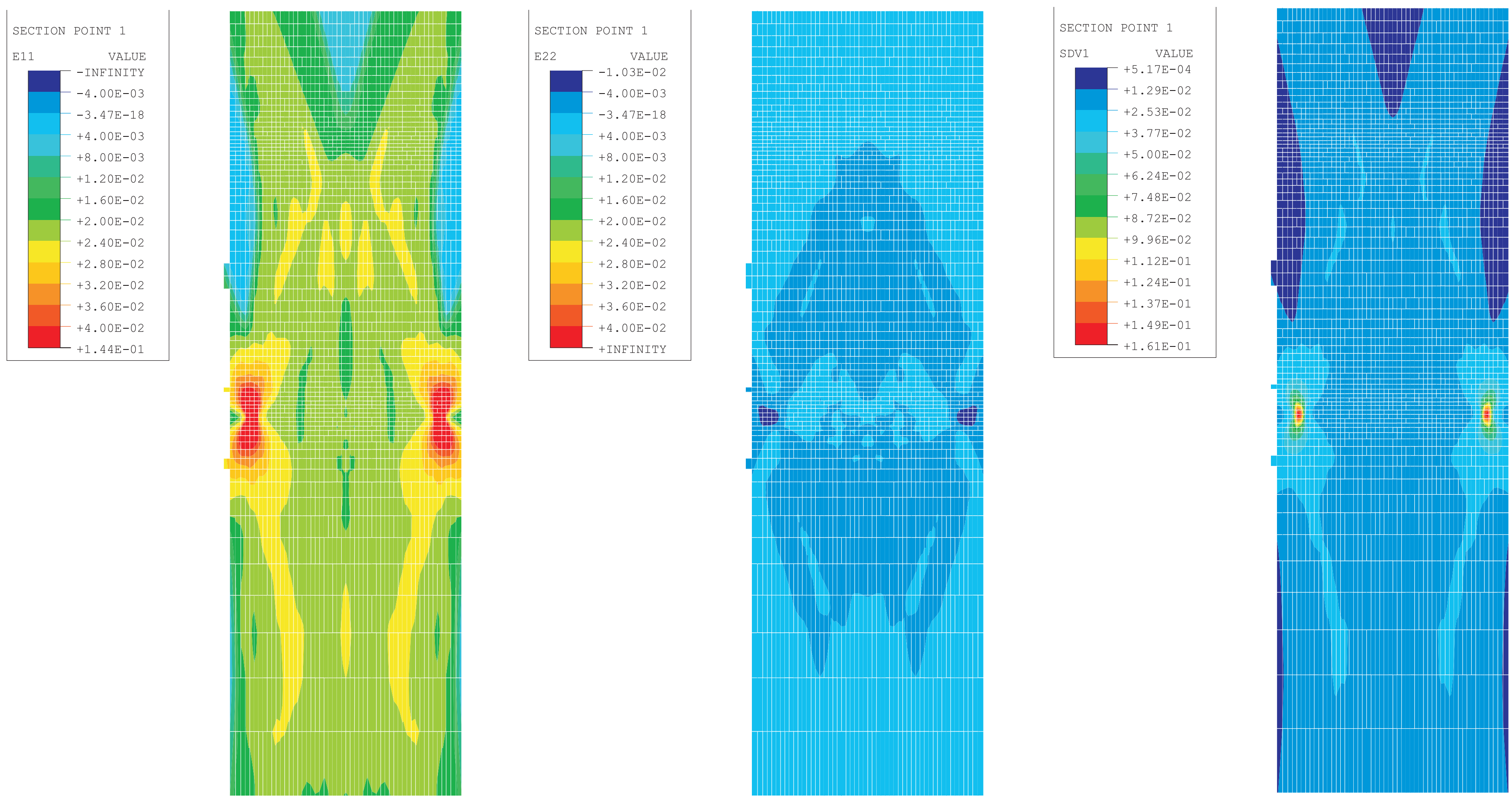

Horizontal Strain | Vertical Strain | Effective Plastic Strain

Figure 8-62. PCCV Liner Model, Liner Seam Rat-Hole Study Case 1, Strain Contour, Analysis To 3.4 Pd

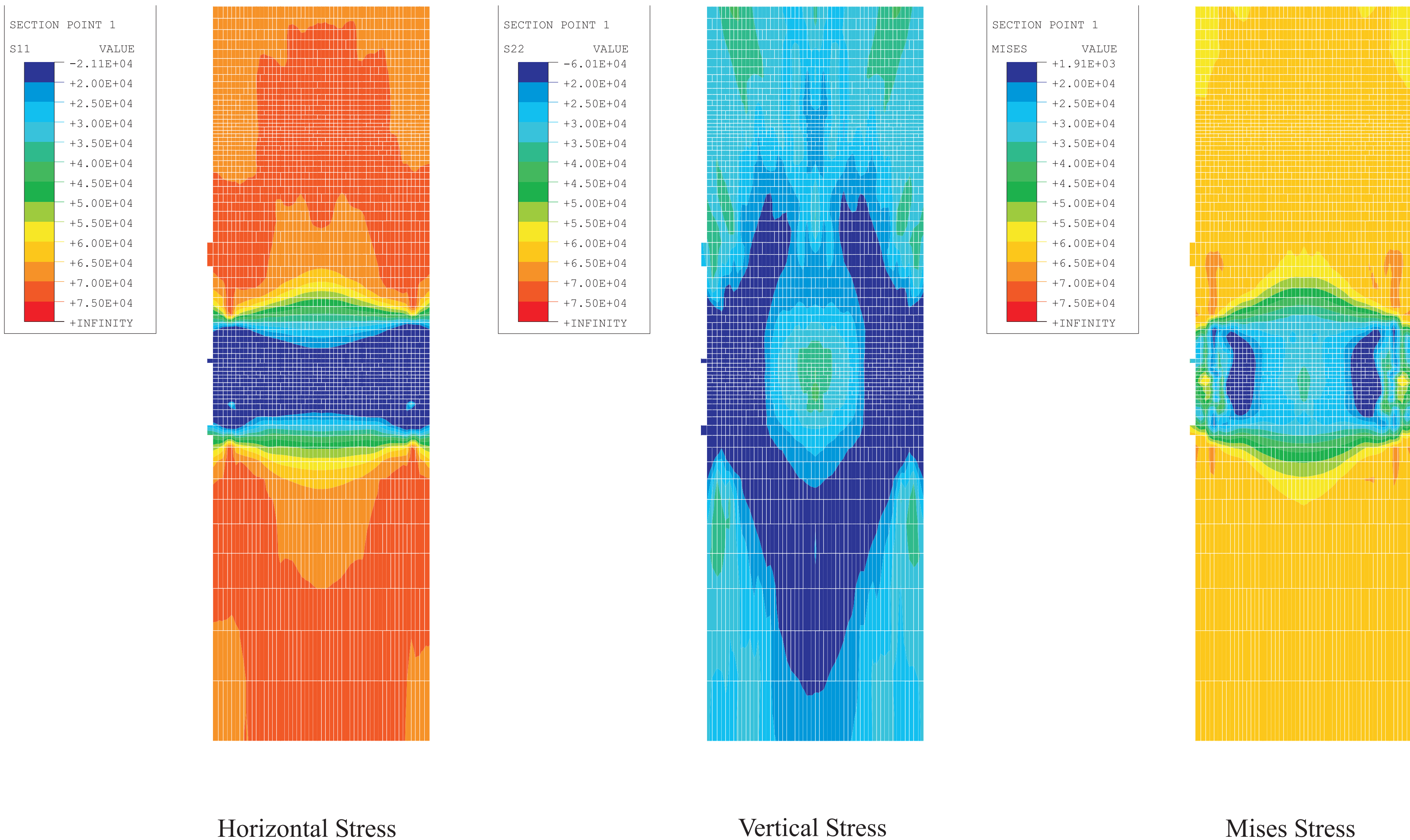

Figure 8-63. PCCV Liner Model, Liner Seam Rat-Hole Study Case 1, Stress Contour, Analysis To 3.6 Pd
(Stresses in psi; Multiply by 0.00690 for MPa)

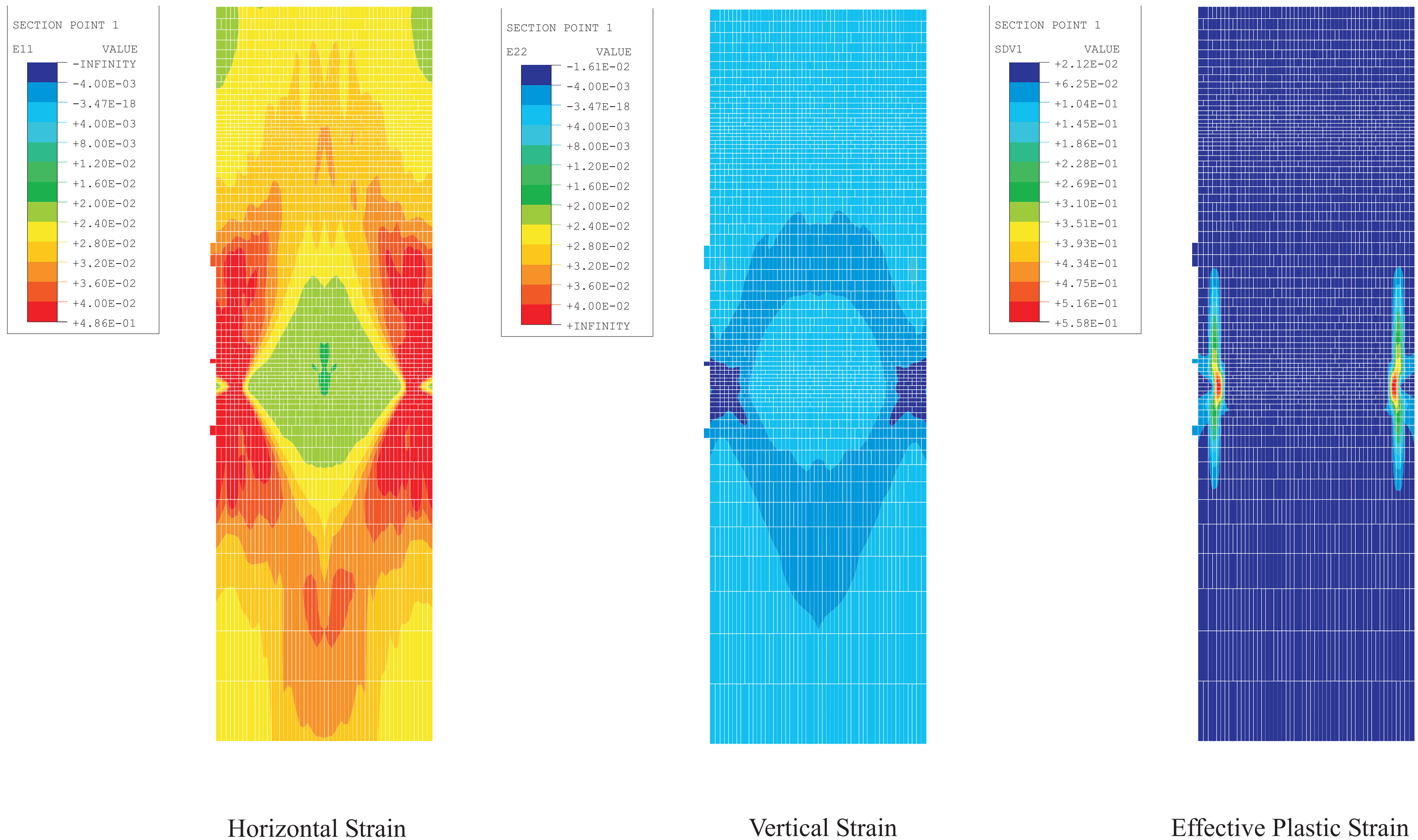

Figure 8-64. PCCV Liner Model, Liner Seam Rat-Hole Study Case 1, Strain Contour, Analysis To 3.6 Pd

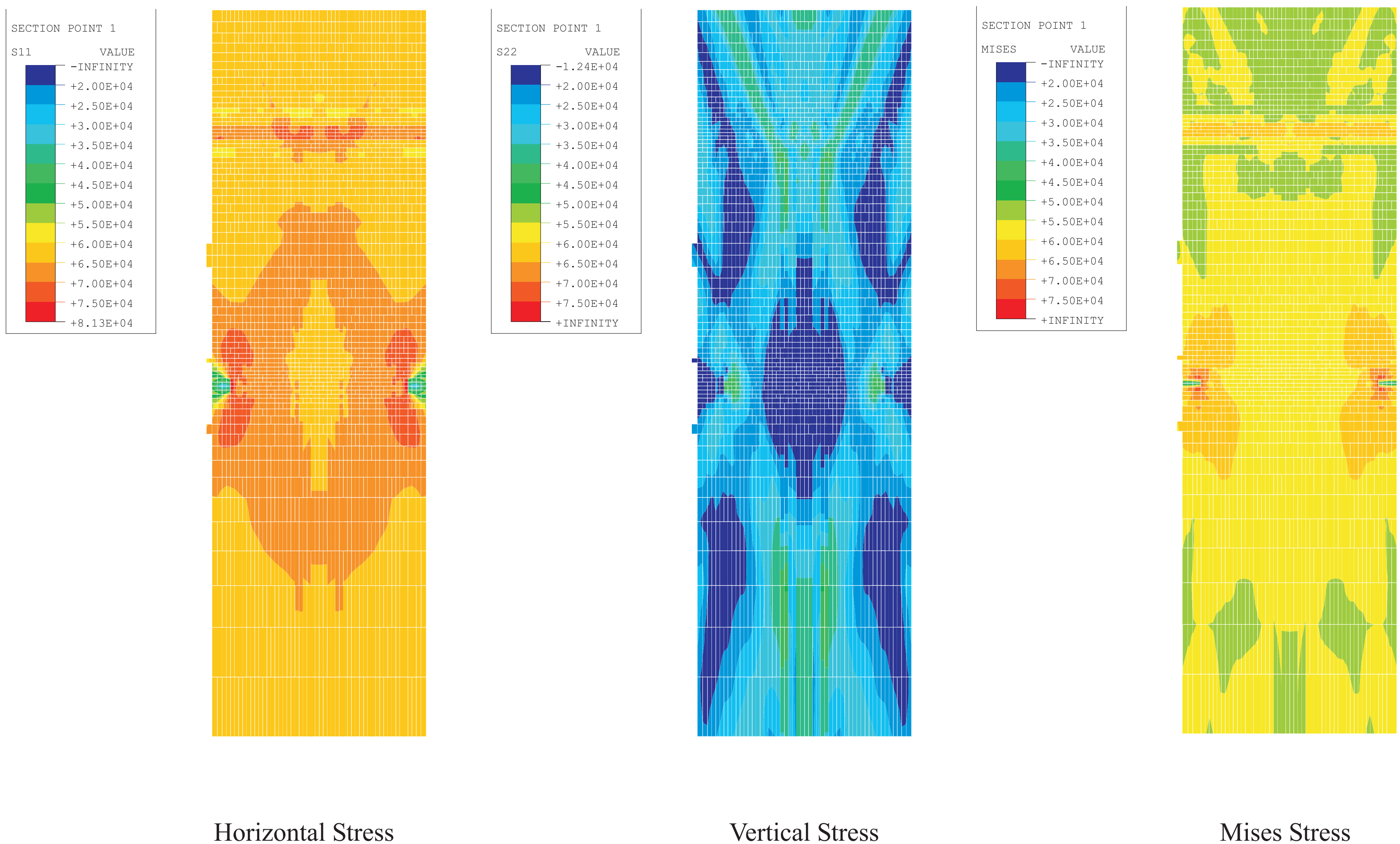

Figure 8-65. PCCV Liner Model, Liner Seam Rat-Hole Study Case 4, Stress Contour, Analysis To 3.4 Pd
(Stresses in psi; Multiply by 0.00690 for MPa)

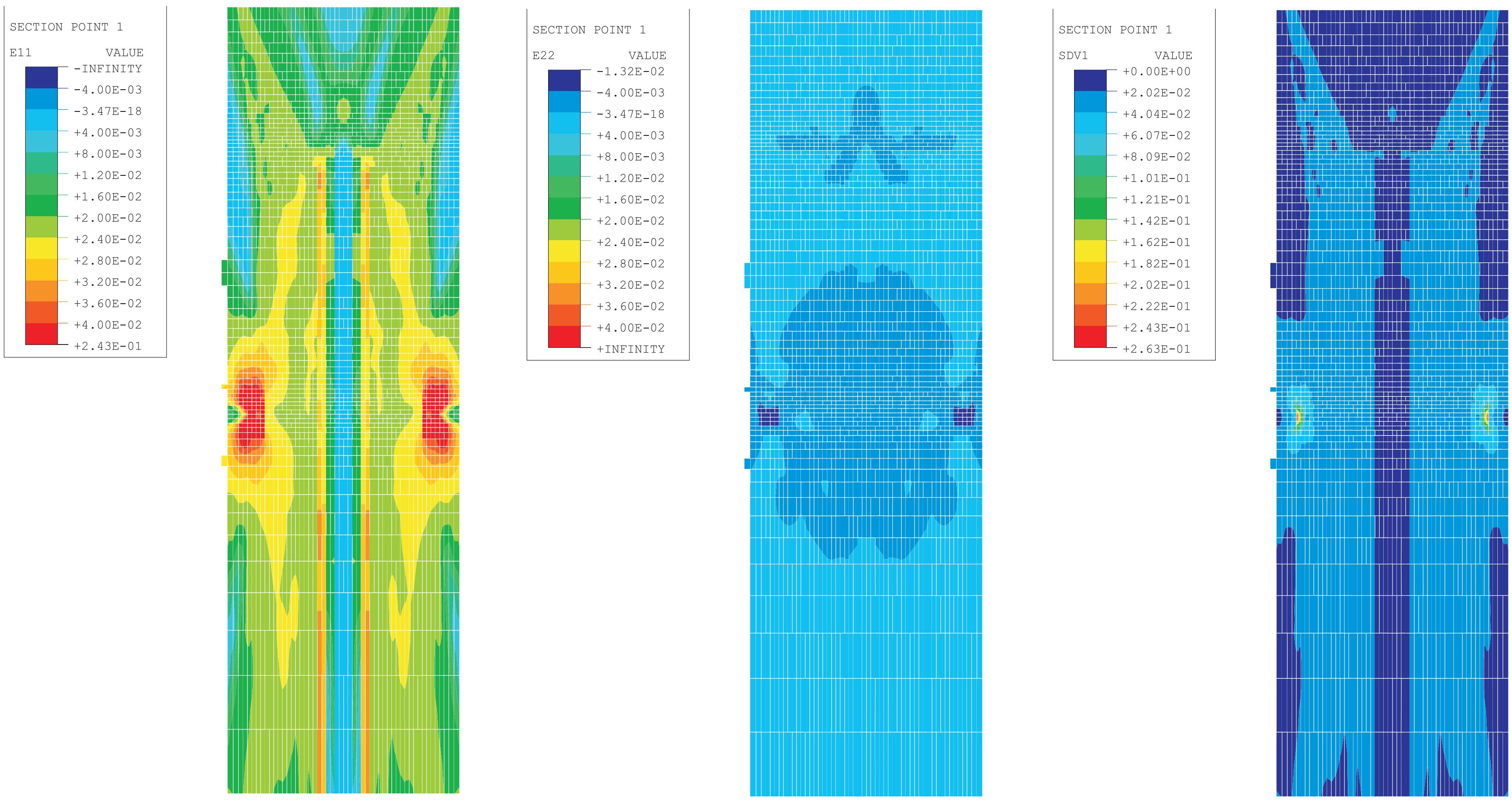

Horizontal Strain

Vertical Strain

Effective Plastic Strain

Figure 8-66. PCCV Liner Model, Liner Seam Rat-Hole Study Case 4, Strain Contour, Analysis To 3.4 Pd

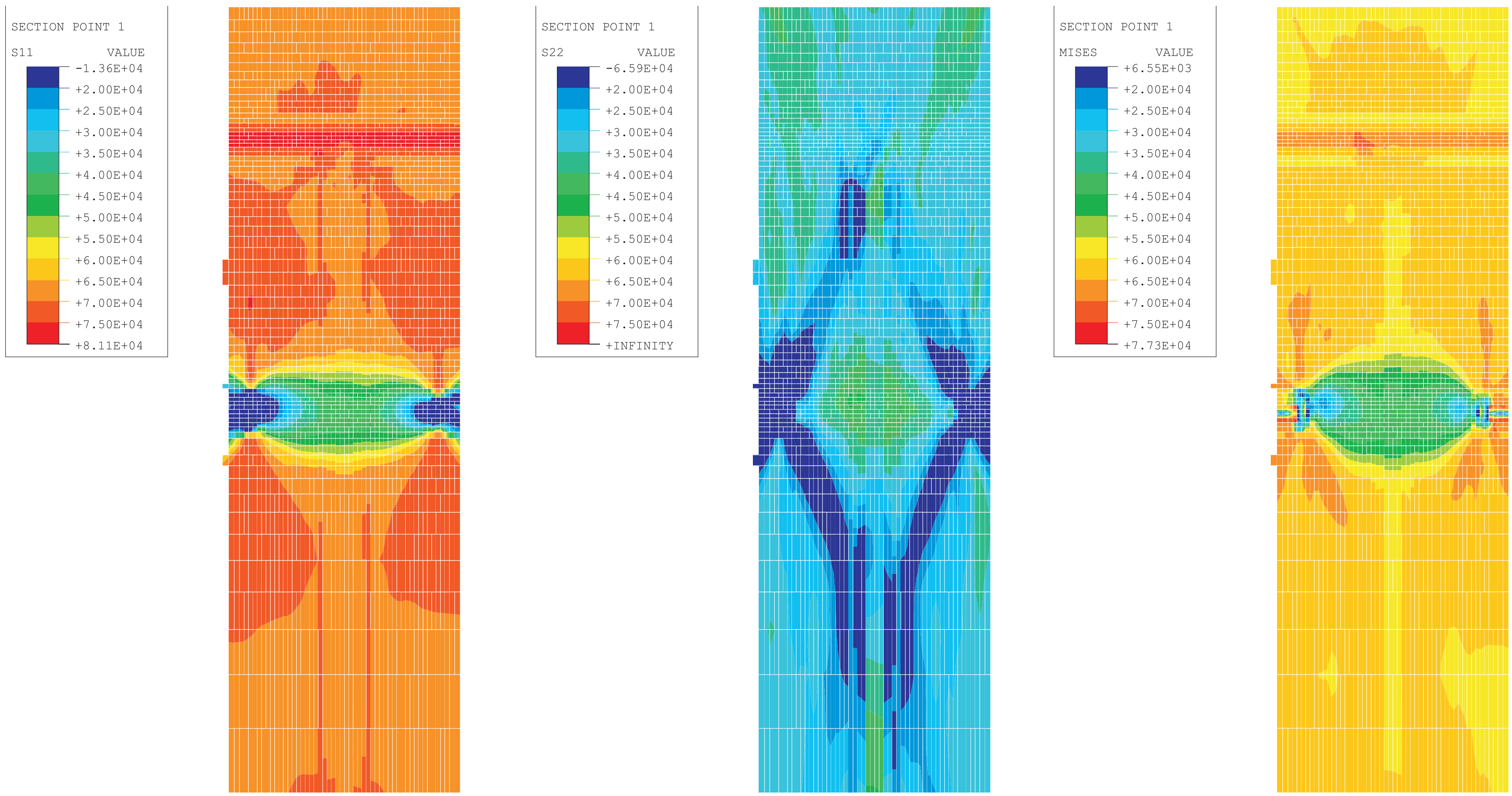

Horizontal Stress | Vertical Stress | Mises Stress

Figure 8-67. PCCV Liner Model, Liner Seam Rat-Hole Study Case 4, Stress Contour, Analysis To 3.6 Pd
(Stresses in psi; Multiply by 0.00690 for MPa)

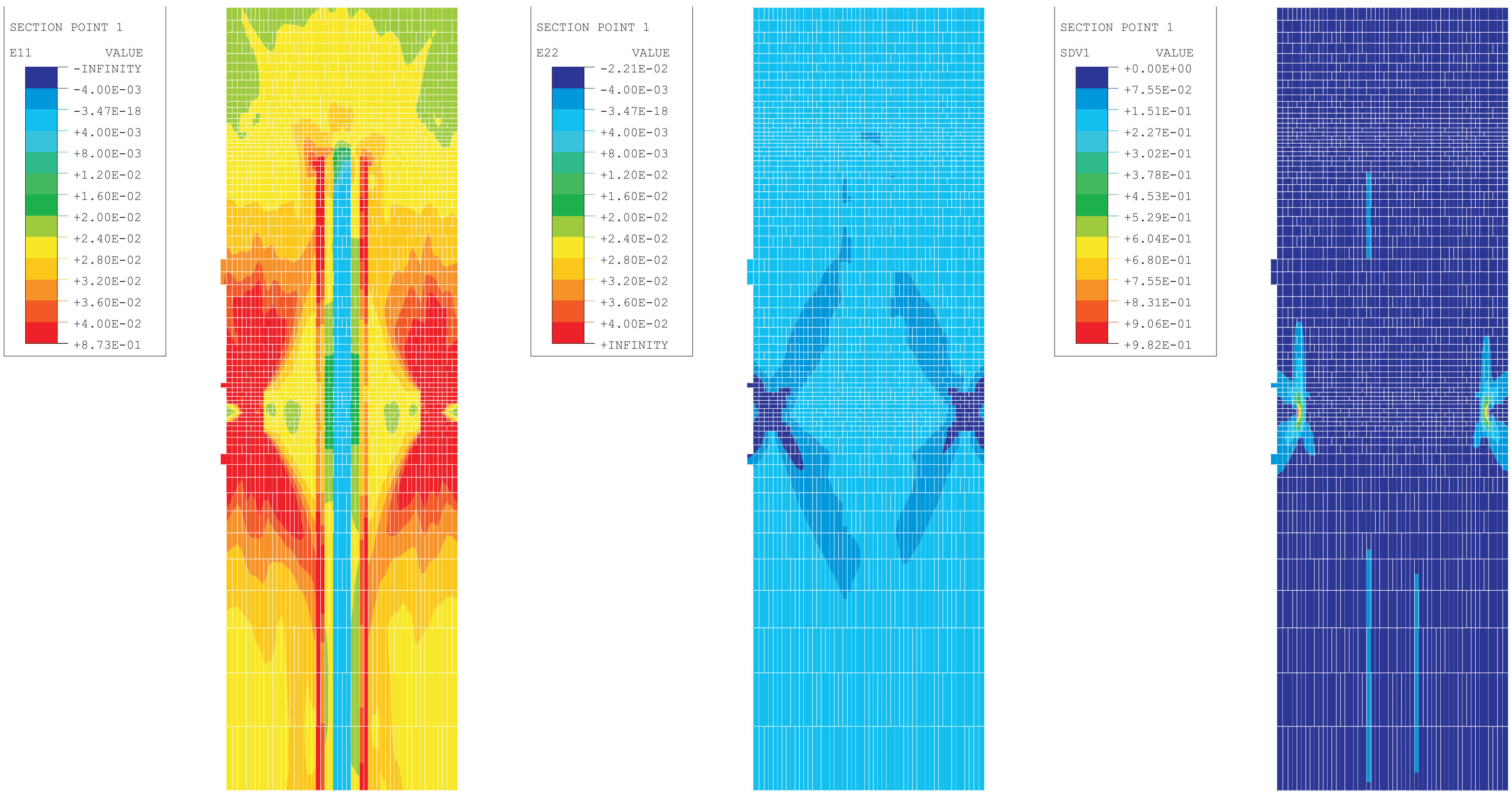

Horizontal Strain | Vertical Strain | Effective Plastic Strain

Figure 8-68. PCCV Liner Model, Liner Seam Rat-Hole Study Case 4, Strain Contour, Analysis To 3.6 Pd

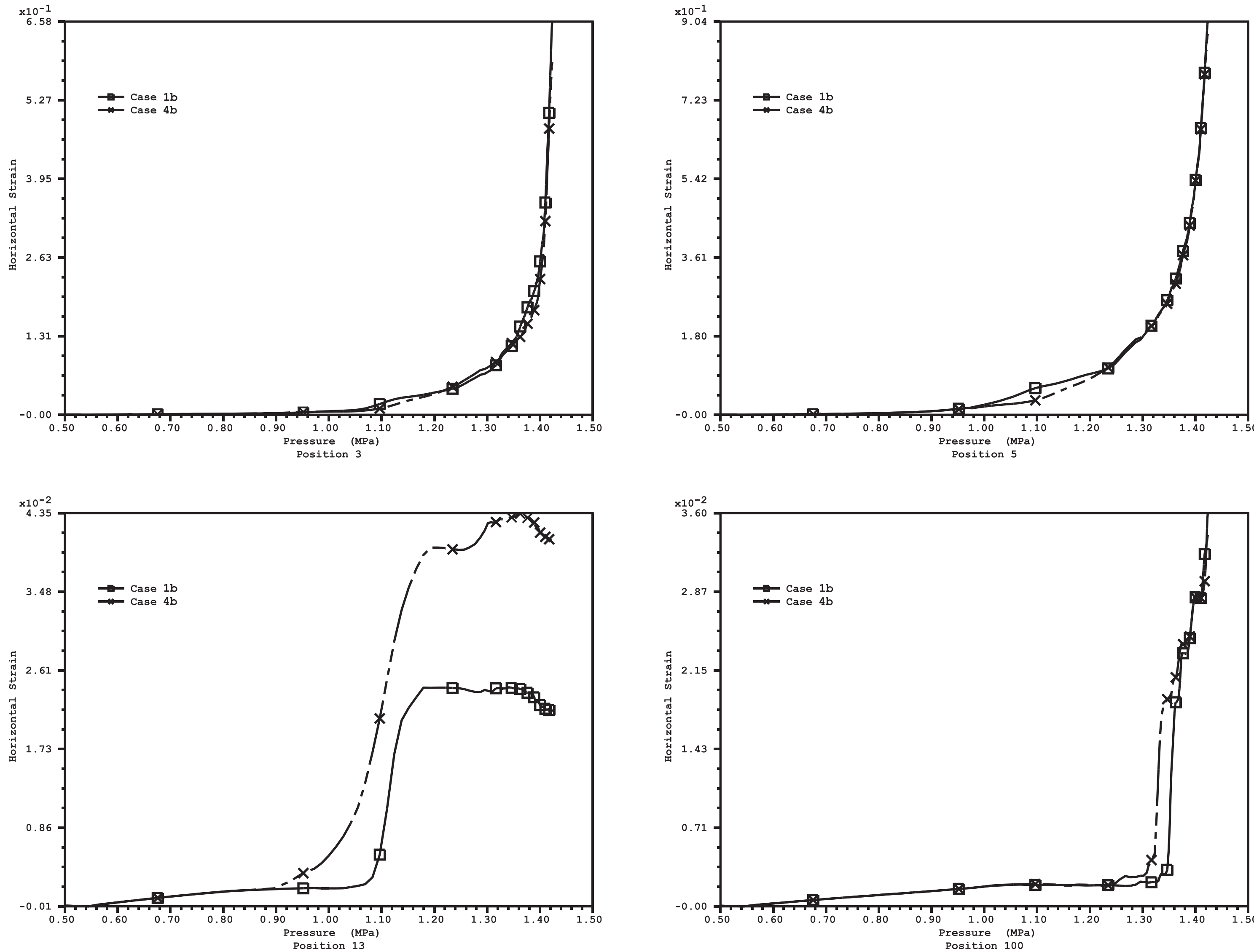

Figure 8-69. PCCV Liner Weld/Rat-Hole Study; Horizontal Strain Comparisons

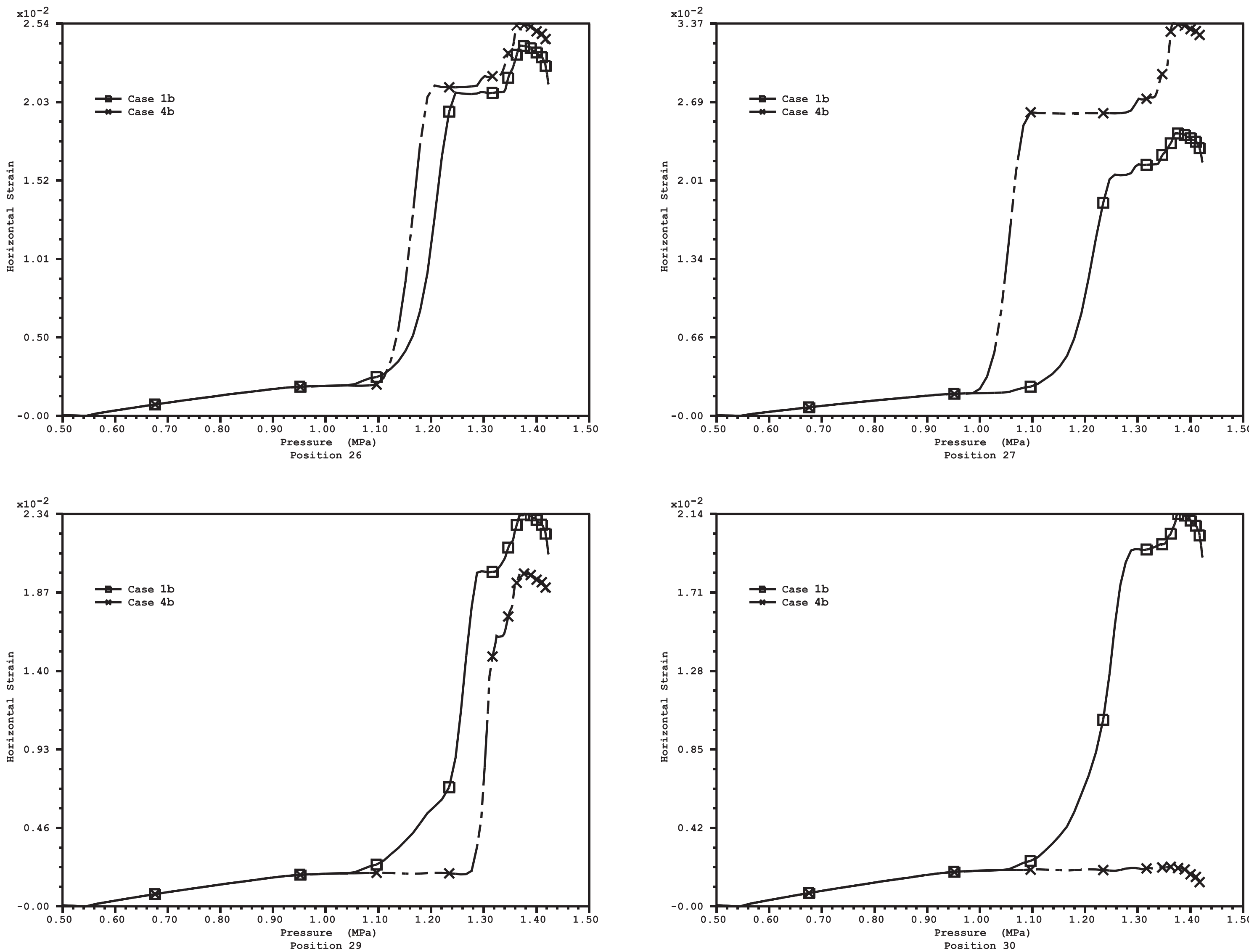

Figure 8-70. PCCV Liner Weld/Rat-Hole Study; Horizontal Strain Comparisons

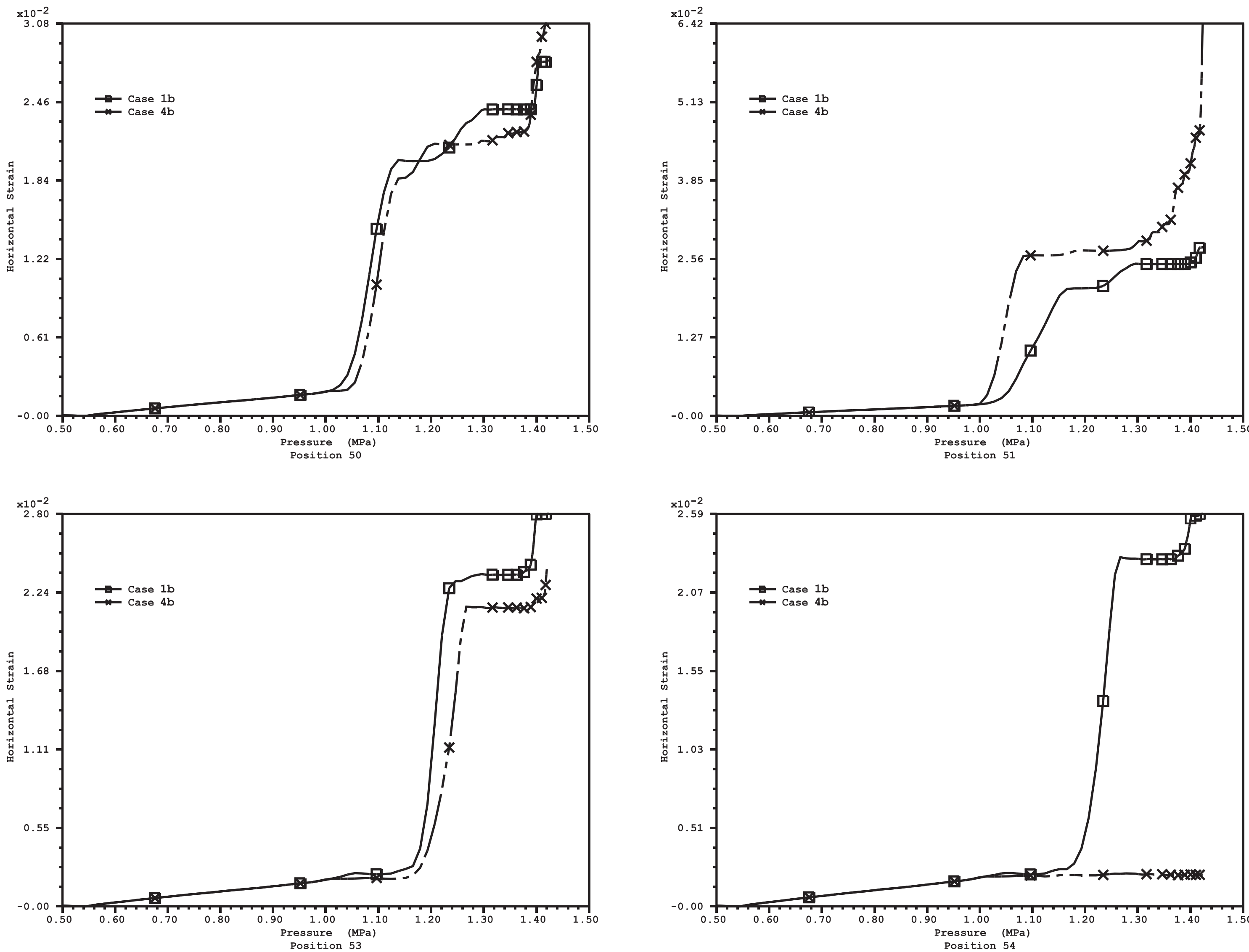

Figure 8-71. PCCV Liner Weld/Rat-Hole Study; Horizontal Strain Comparisons

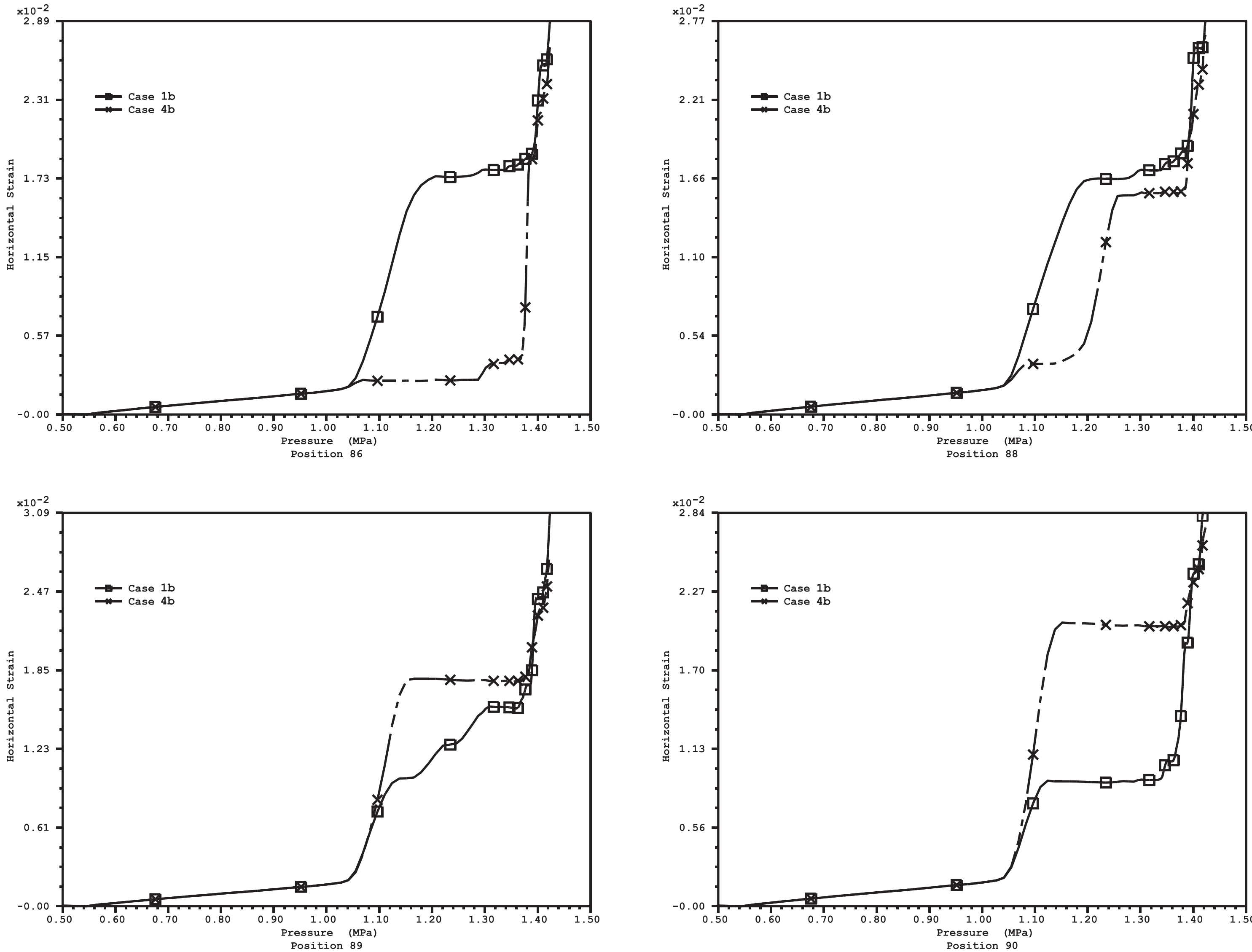

Figure 8-72. PCCV Liner Weld/Rat-Hole Study; Horizontal Strain Comparisons

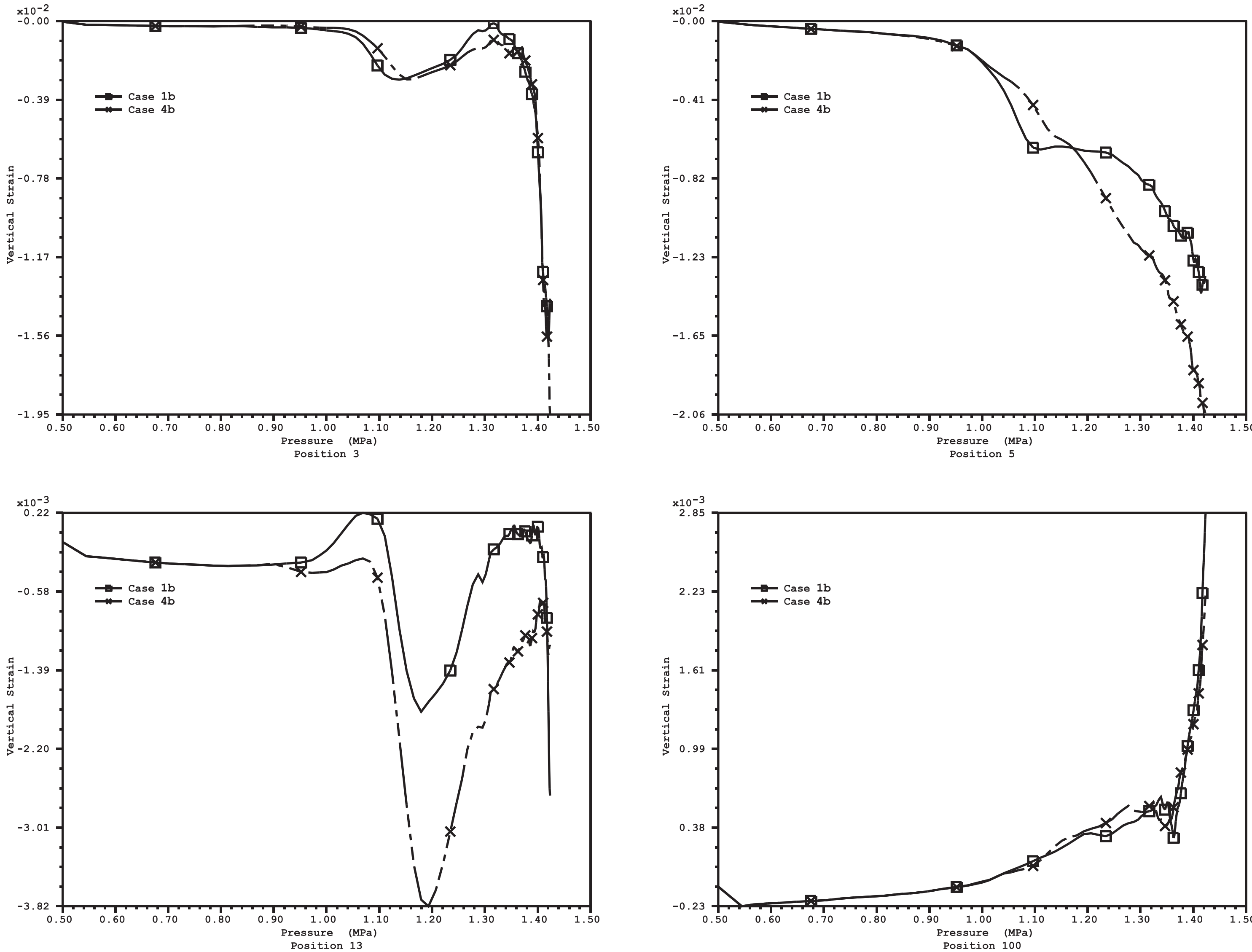

Figure 8-73. PCCV Liner Weld/Rat-Hole Study; Vertical Strain Comparisons

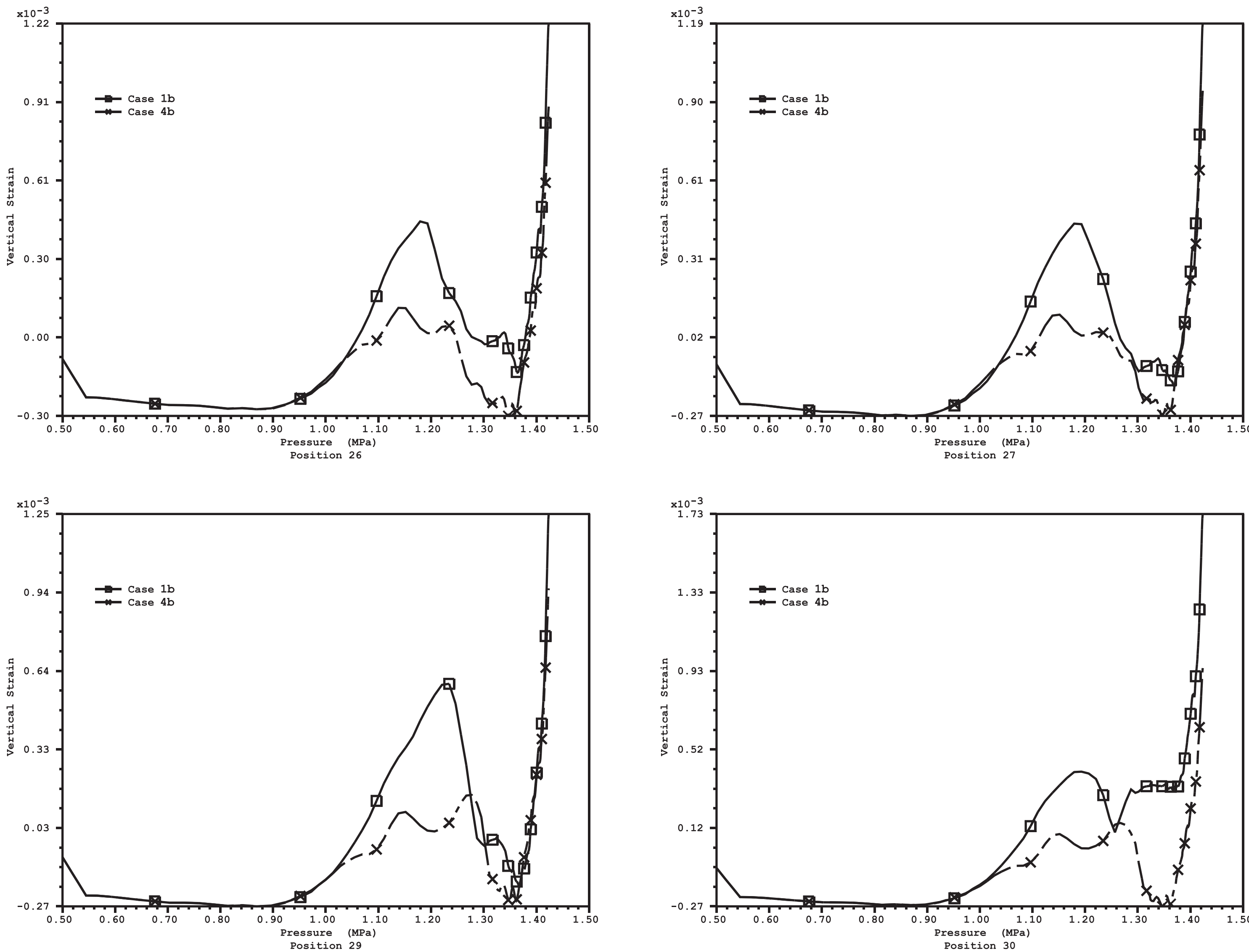

Figure 8-74. PCCV Liner Weld/Rat-Hole Study; Vertical Strain Comparisons

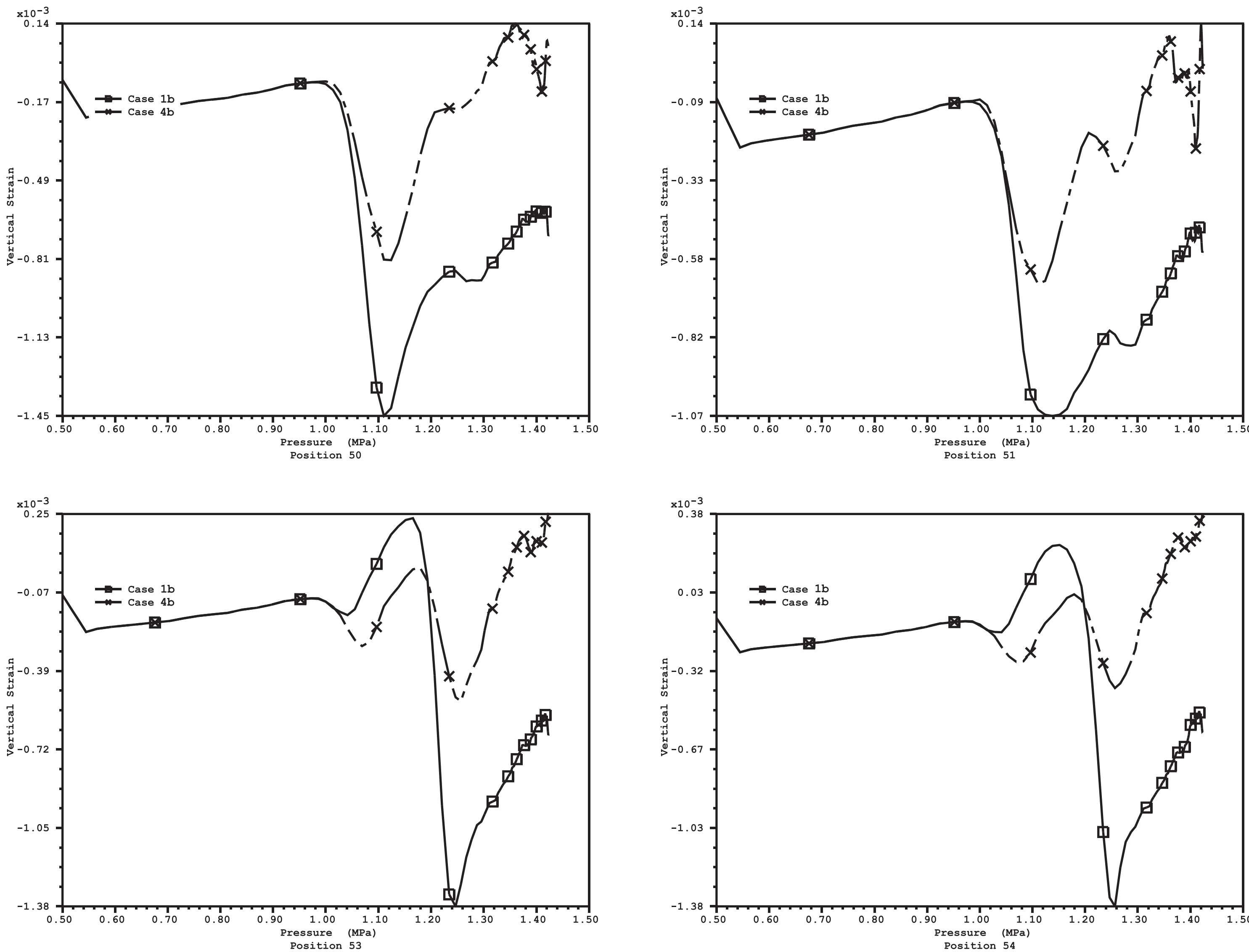

Figure 8-75. PCCV Liner Weld/Rat-Hole Study; Vertical Strain Comparisons

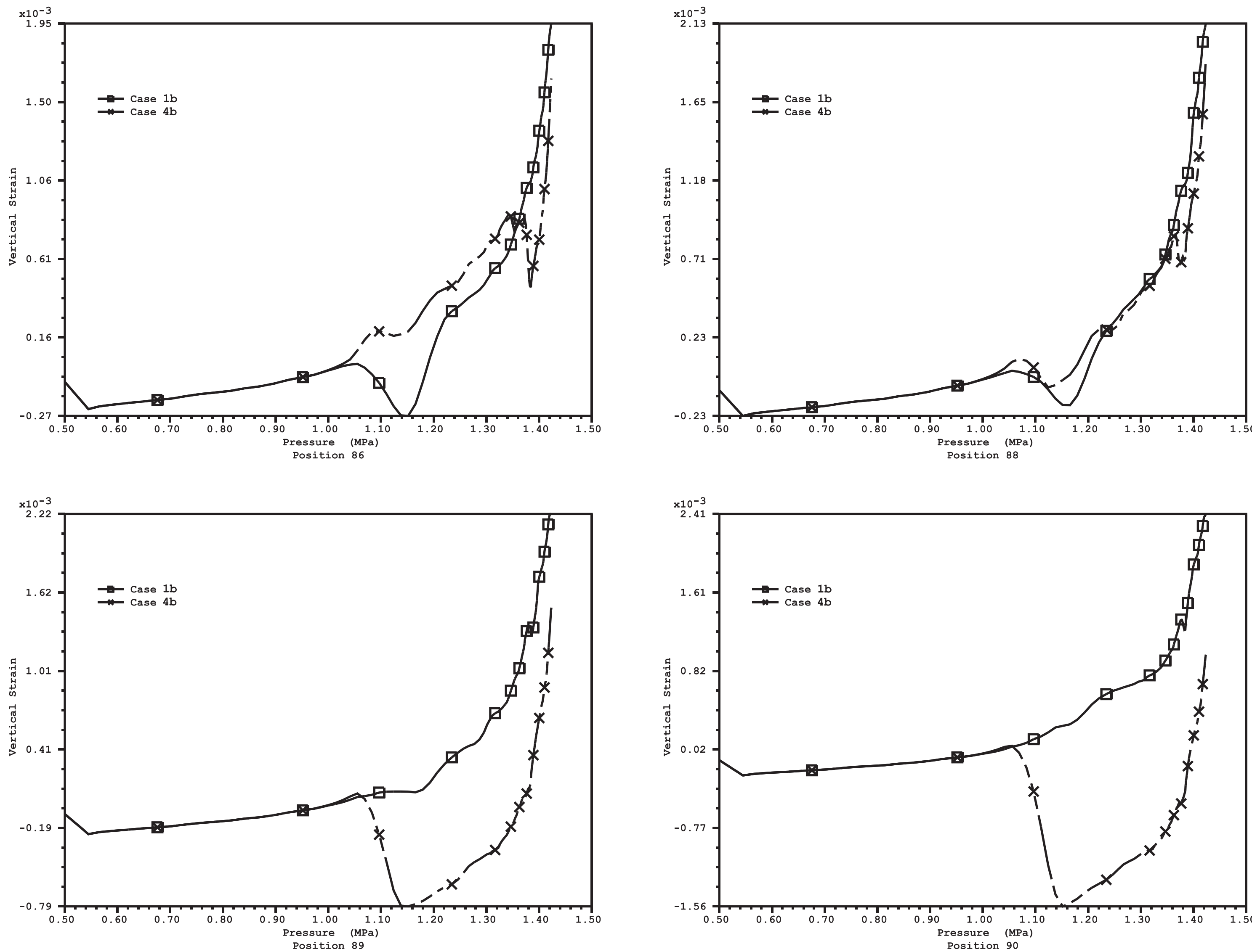

Figure 8-76. PCCV Liner Weld/Rat-Hole Study; Vertical Strain Comparisons

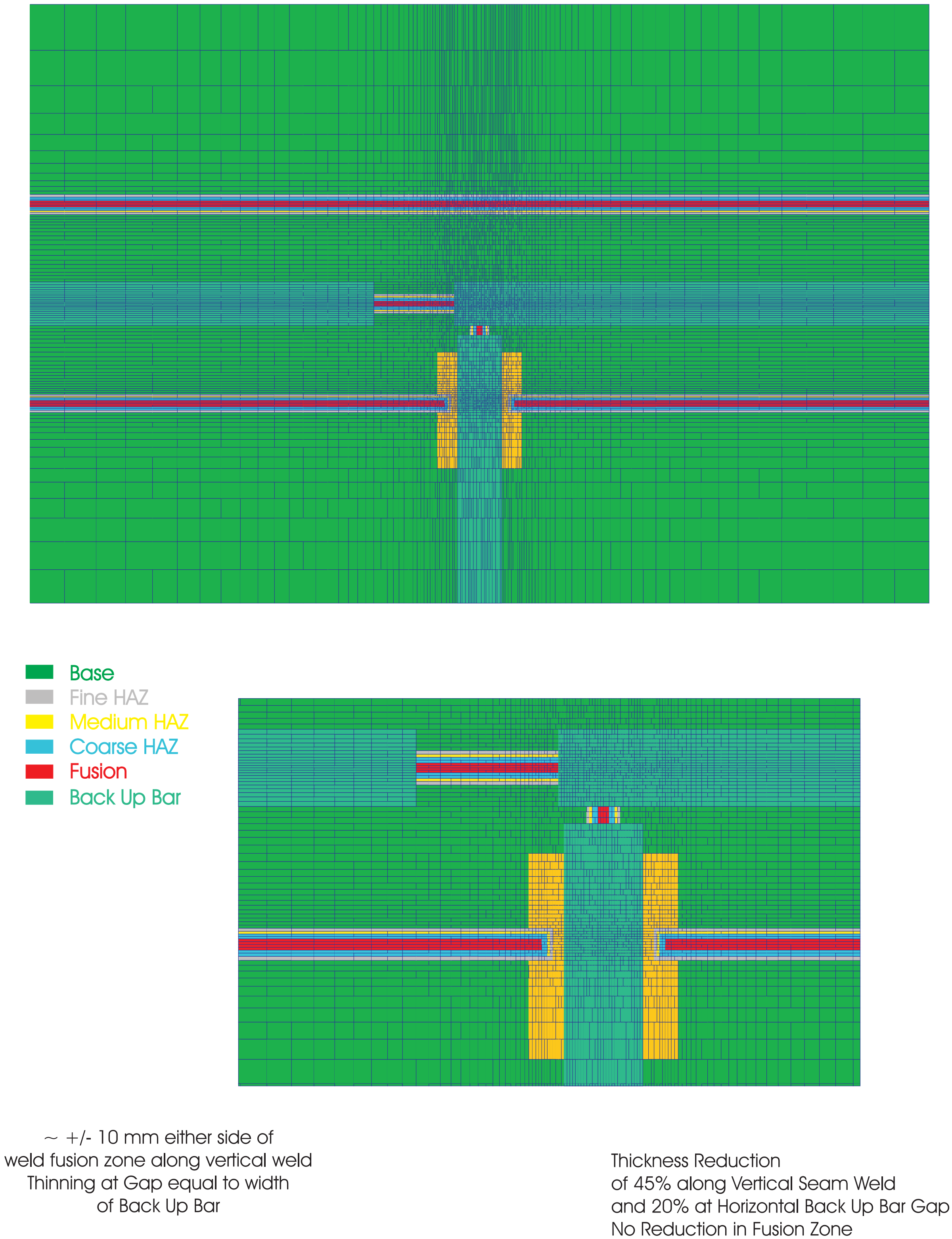

Figure 8-77. PCCV Liner Weld Seam Rat-Hole Study, Base, HAZ, and Fusion Regions, Extent of Thinning Zones, Back Up Bars and Horizontal Gap

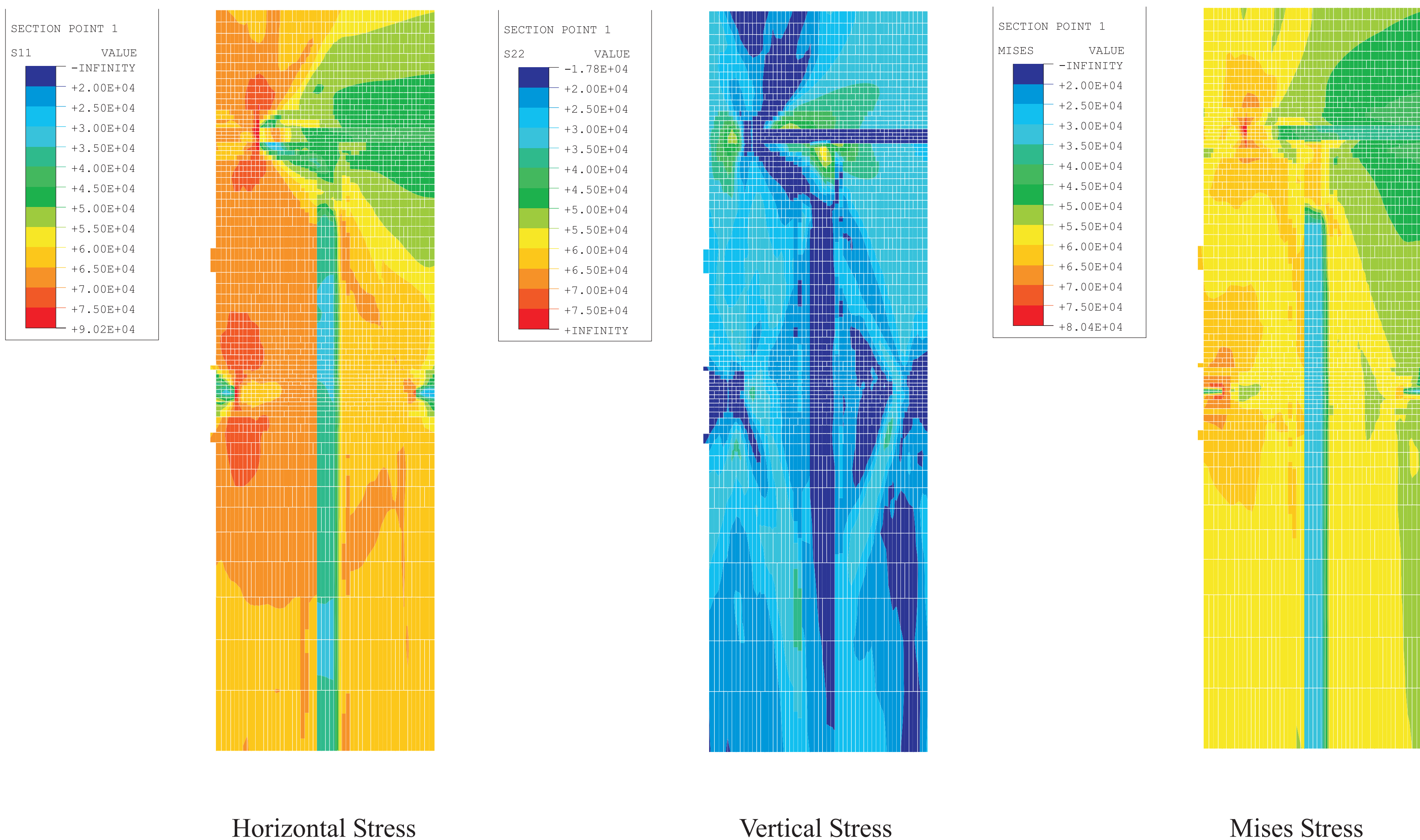

Figure 8-78. PCCV Liner Model, Liner Seam Rat-Hole Study Case 3c, Stress Contour, Vertical and Horizontal Back-Up Bars With Horizontal Gap, Similar to Case 4b, No Thinning In Gap Region (Stresses in psi; Multiply by 0.00690 for MPa)

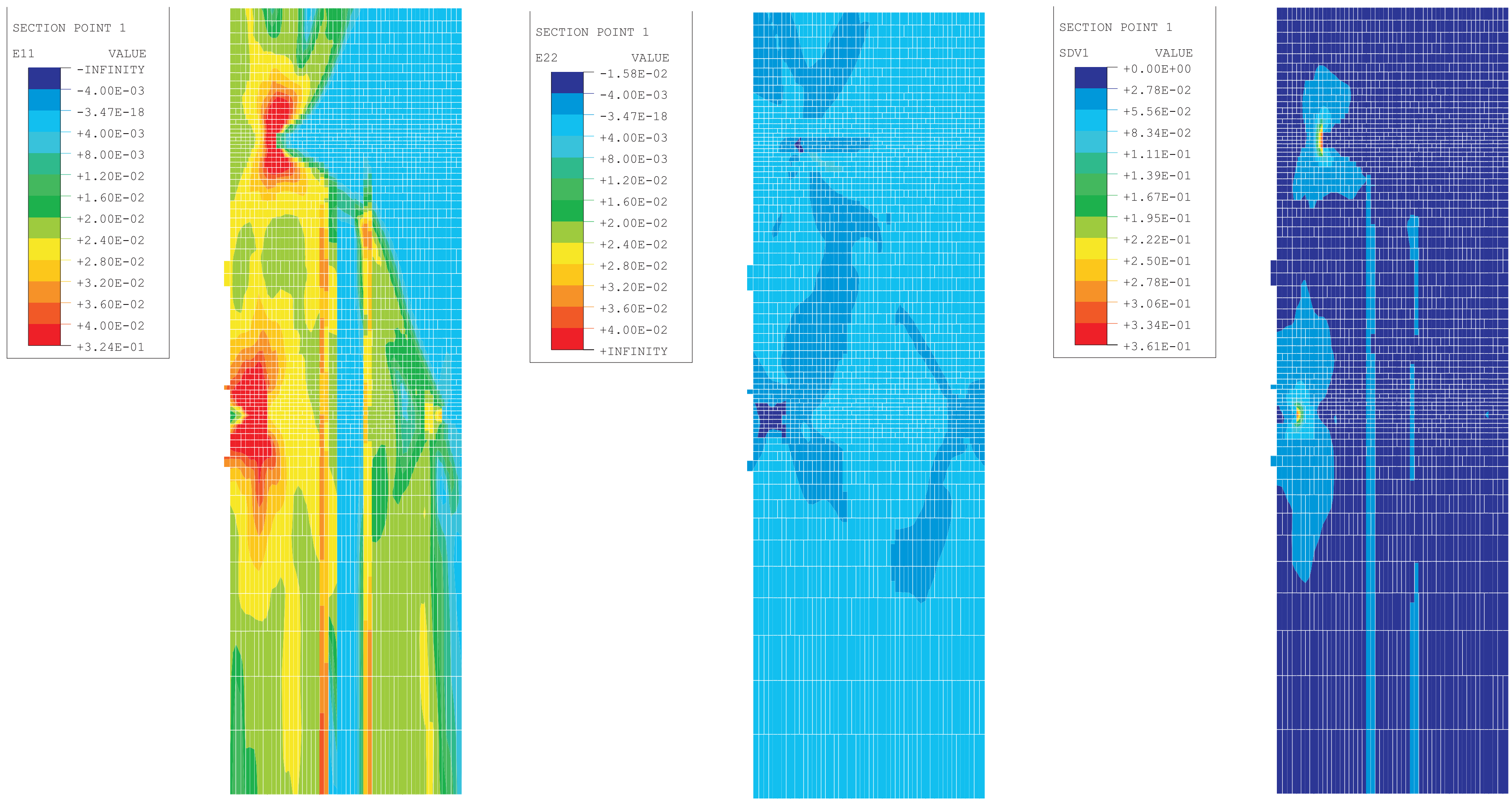

Horizontal Strain

Vertical Strain

Effective Plastic Strain

Figure 8-79. PCCV Liner Model, Liner Seam Rat-Hole Study Case 3c, Strain Contour, Vertical and Horizontal Back-Up Bars With Horizontal Gap, Similar to Case 4b, No Thinning In Gap Region

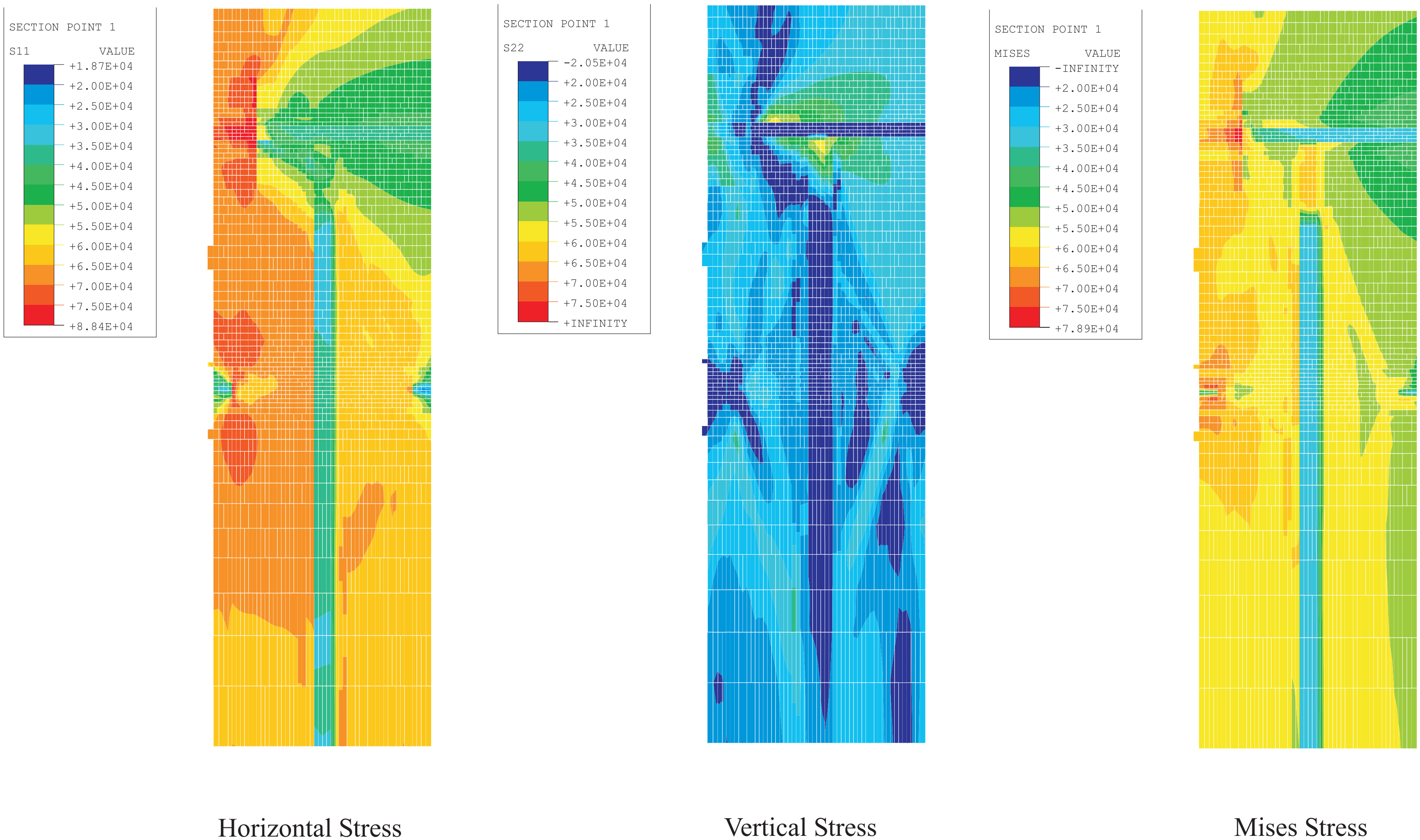

Figure 8-80. PCCV Liner Model, Liner Seam Rat-Hole Study Case 4c, Stress Contour, Vertical and Horizontal Back-Up Bars With Horizontal Gap, Similar to Case 4b, Thinning In Gap Region (Stresses in psi; Multiply by 0.00690 for MPa)

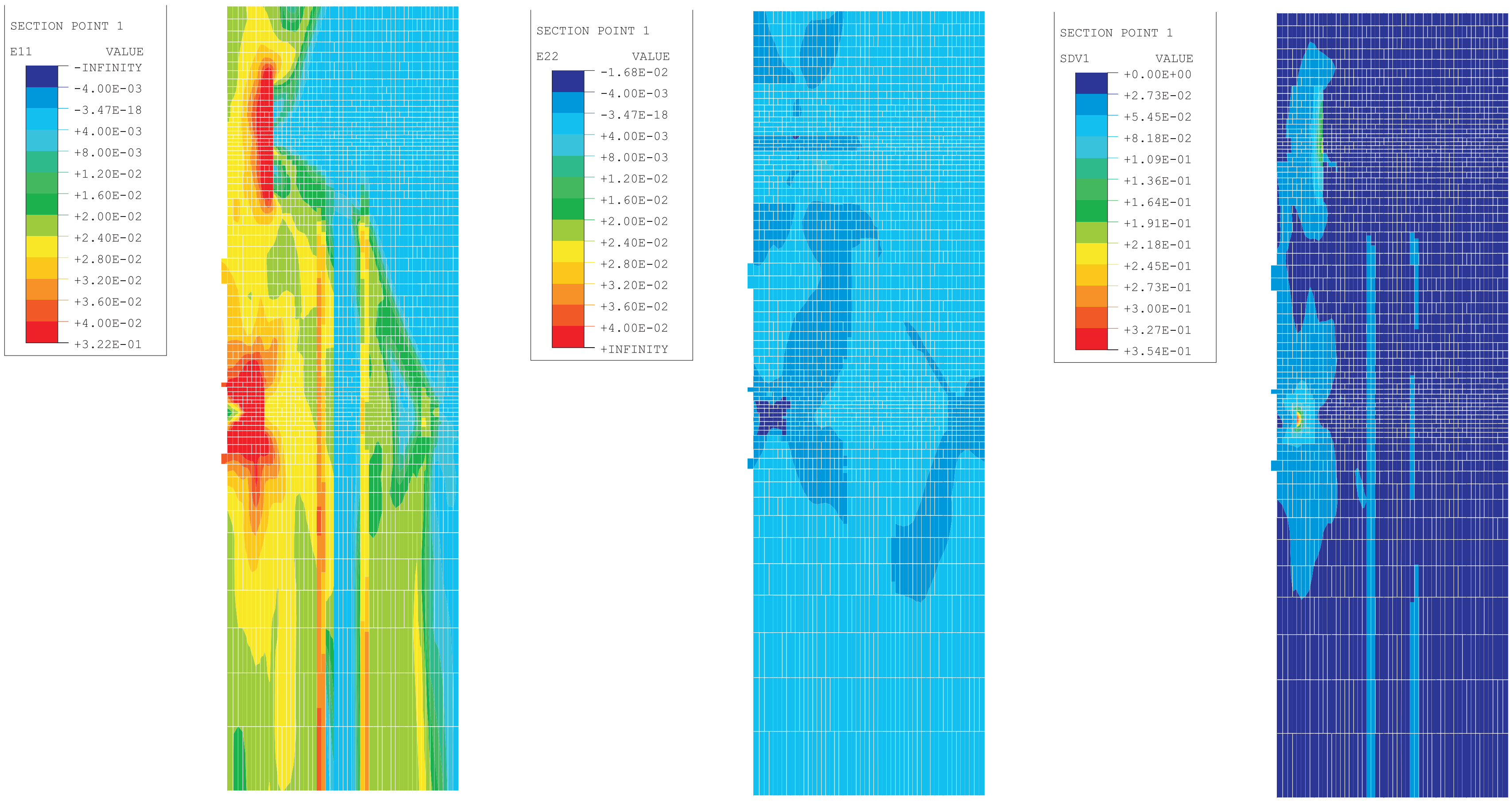

Horizontal Strain

Vertical Strain

Effective Plastic Strain

Figure 8-81. PCCV Liner Model, Liner Seam Rat-Hole Study Case 4c, Strain Contour, Vertical and Horizontal Back-Up Bars With Horizontal Gap, Similar to Case 4b, Thinning In Gap Region

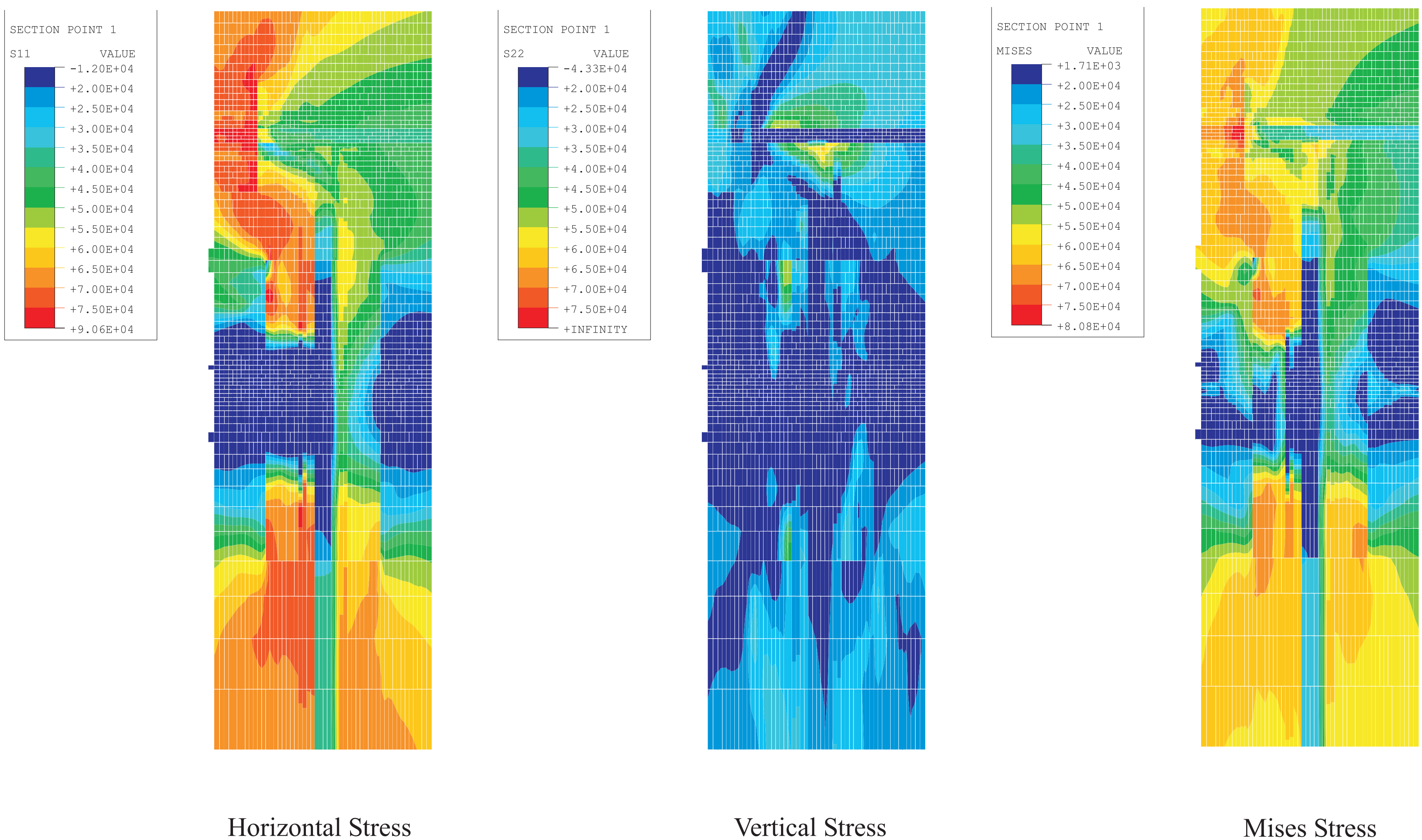

Figure 8-82. PCCV Liner Model, Liner Seam Rat-Hole Study Case 5c, Stress Contour, Vertical and Horizontal Back-Up Bars With Horizontal Gap, Similar to Case 10b, Thinning In Gap Region (Stresses in psi; Multiply by 0.00690 for MPa)

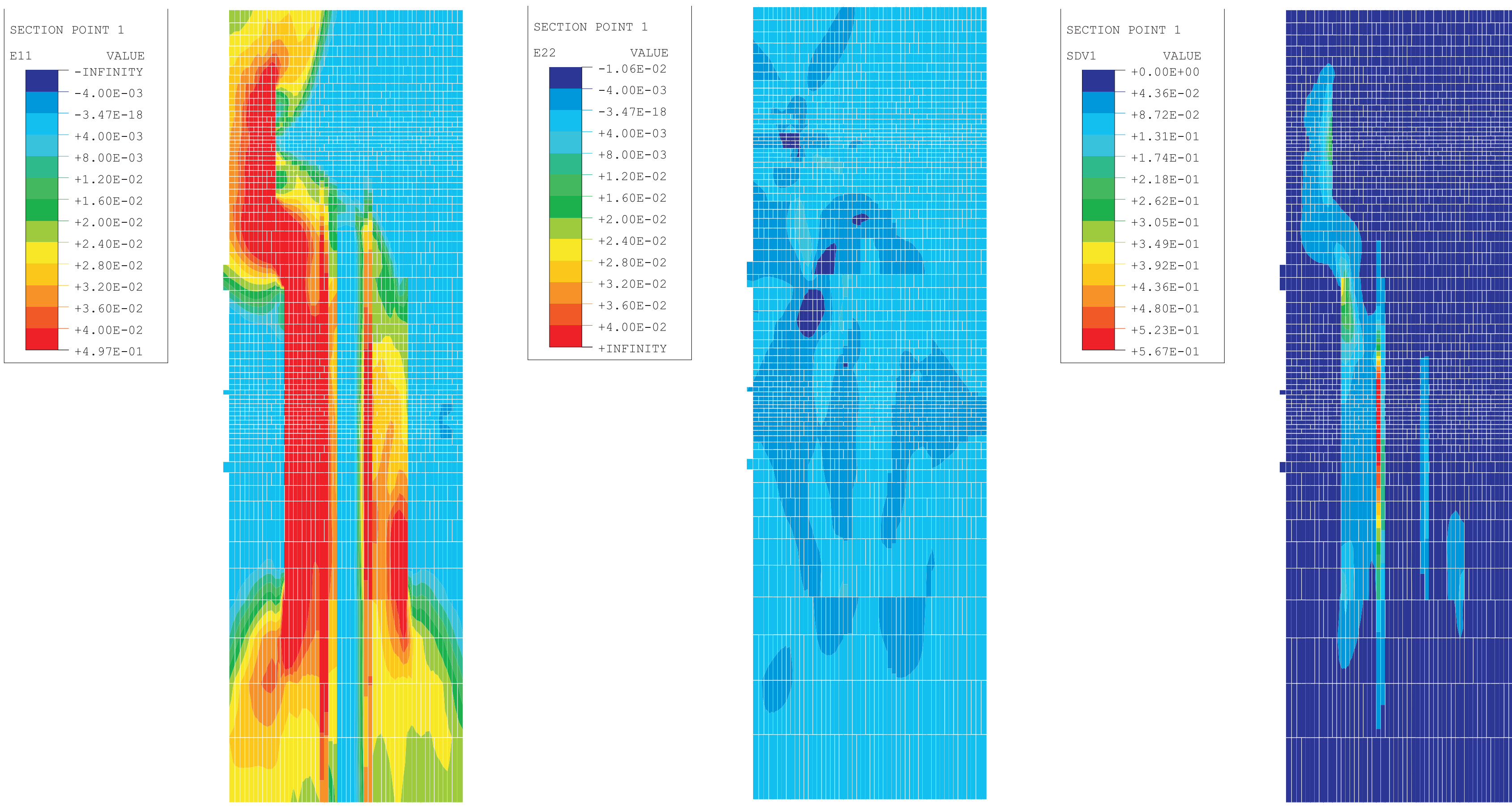

Horizontal Strain

Vertical Strain

Effective Plastic Strain

Figure 8-83. PCCV Liner Model, Liner Seam Rat-Hole Study Case 5c, Strain Contour, Vertical and Horizontal Back-Up Bars With Horizontal Gap, Similar to Case 10b, Thinning In Gap Region

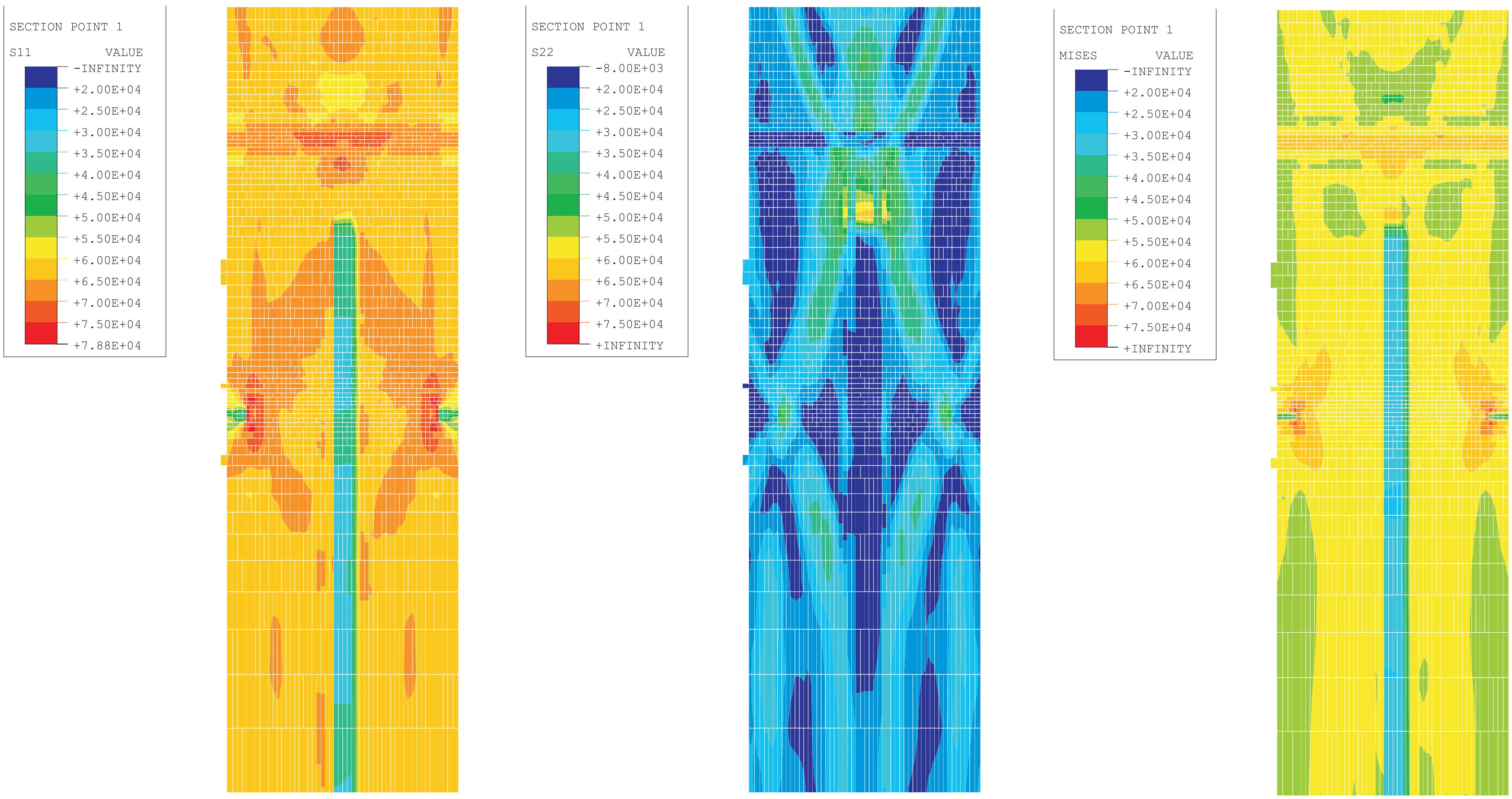

Horizontal Stress | Vertical Stress | Mises Stress

Figure 8-84. PCCV Liner Model, Liner Seam Rat-Hole Study Case 6c, Stress Contour, Vertical and Horizontal Back-Up Bars, No Horizontal Gap, Similar to Case 4b, No Thinning in Gap Region (Stresses in psi; Multiply by 0.00690 for MPa)

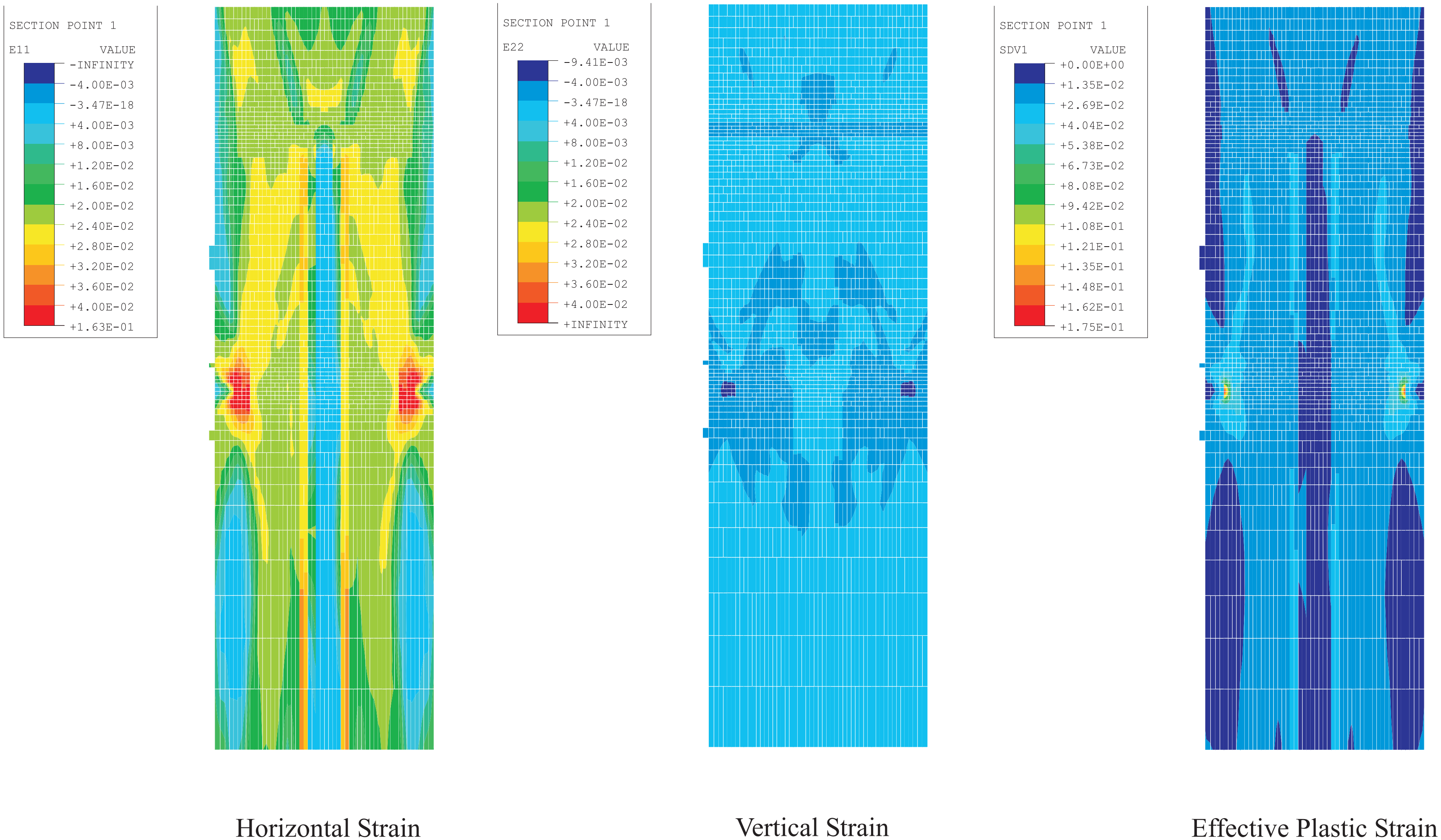

Figure 8-85. PCCV Liner Model, Liner Seam Rat-Hole Study Case 6c, Stress Contour, Vertical and Horizontal Back-Up Bars, No Horizontal Gap, Similar to Case 4b, No Thinning in Gap Region

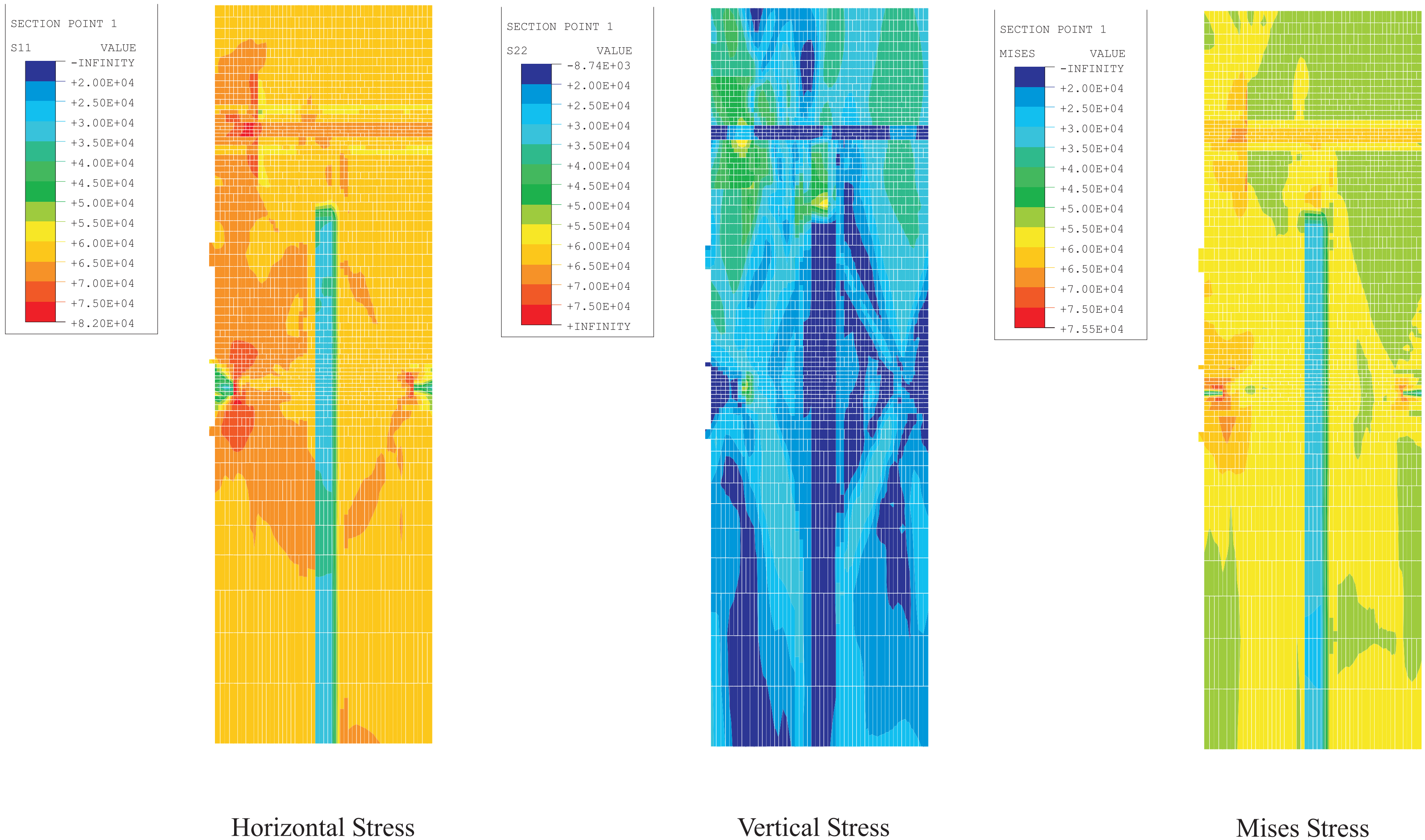

Figure 8-86. PCCV Liner Model, Liner Seam Rat-Hole Study Case 7c, Stress Contour, Vertical and Horizontal Back-Up Bars, No Horizontal Gap, Similar to Case 4b, Thinning in Gap Region (Stresses in psi; Multiply by 0.00690 for MPa)

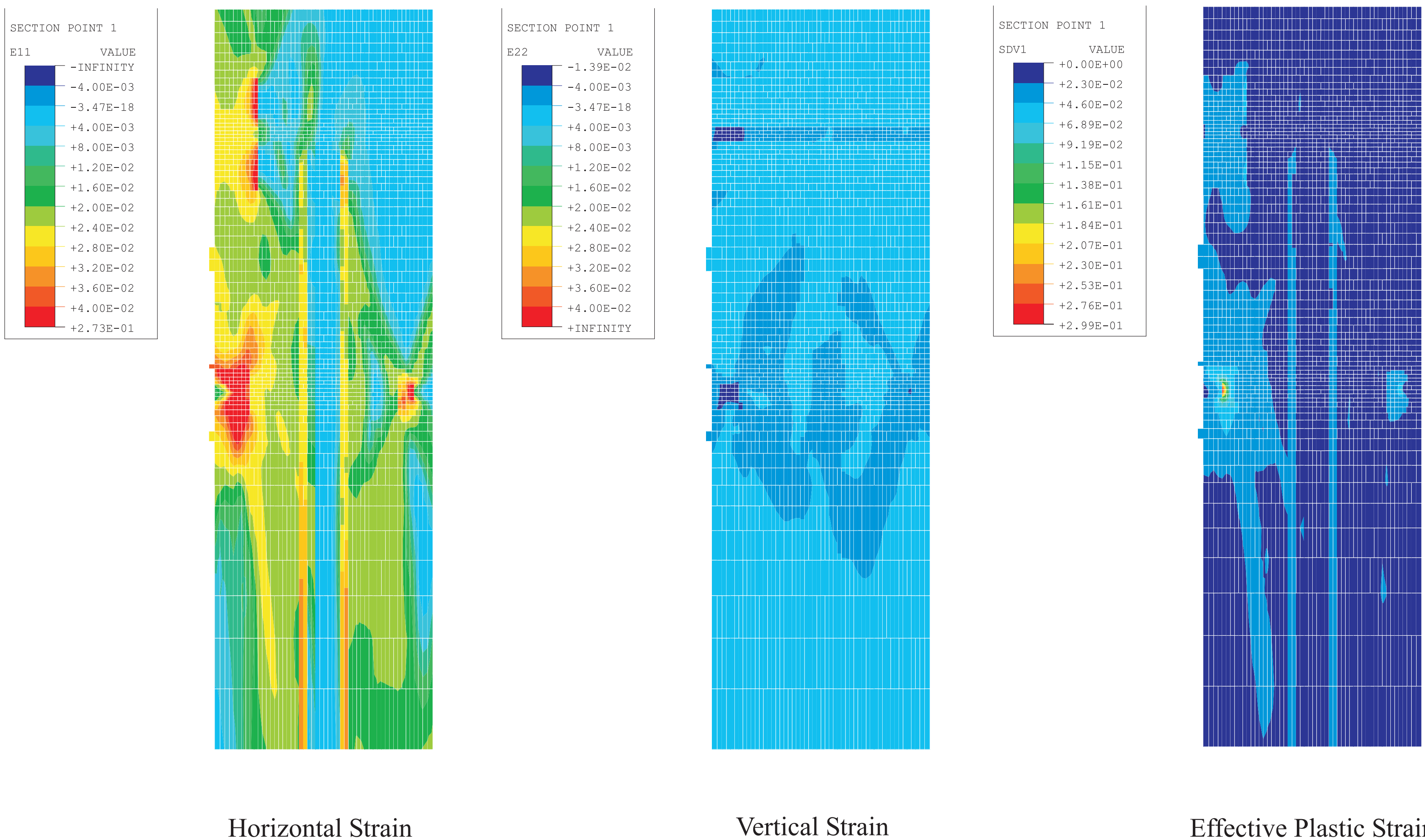

Figure 8-87. PCCV Liner Model, Liner Seam Rat-Hole Study Case 7c, Stress Contour, Vertical and Horizontal Back-Up Bars, No Horizontal Gap, Similar to Case 4b, Thinning in Gap Region

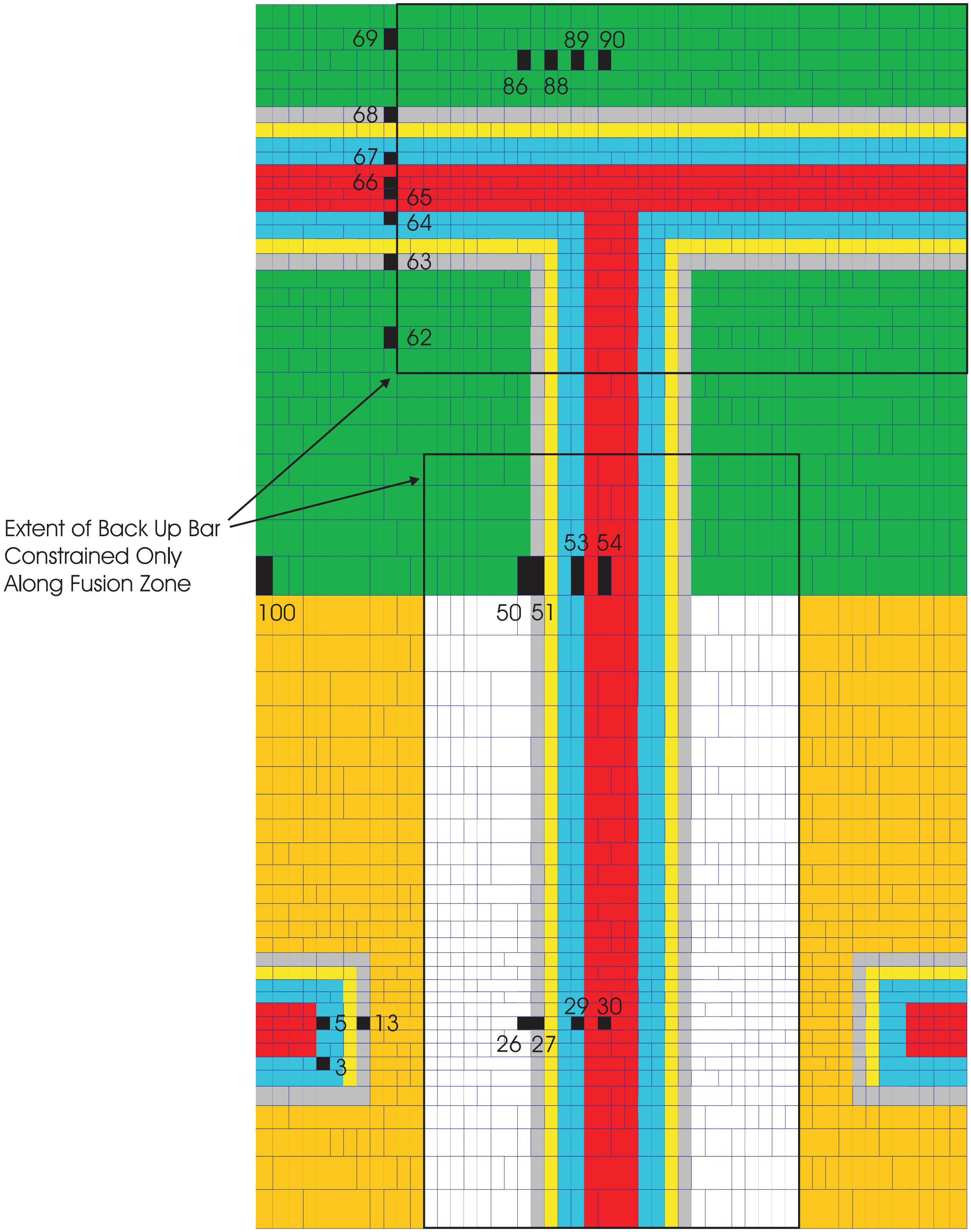

Figure 8-88. PCCV Liner Weld/Rat-Hole Study; Locations of Strain Profile Comparisons

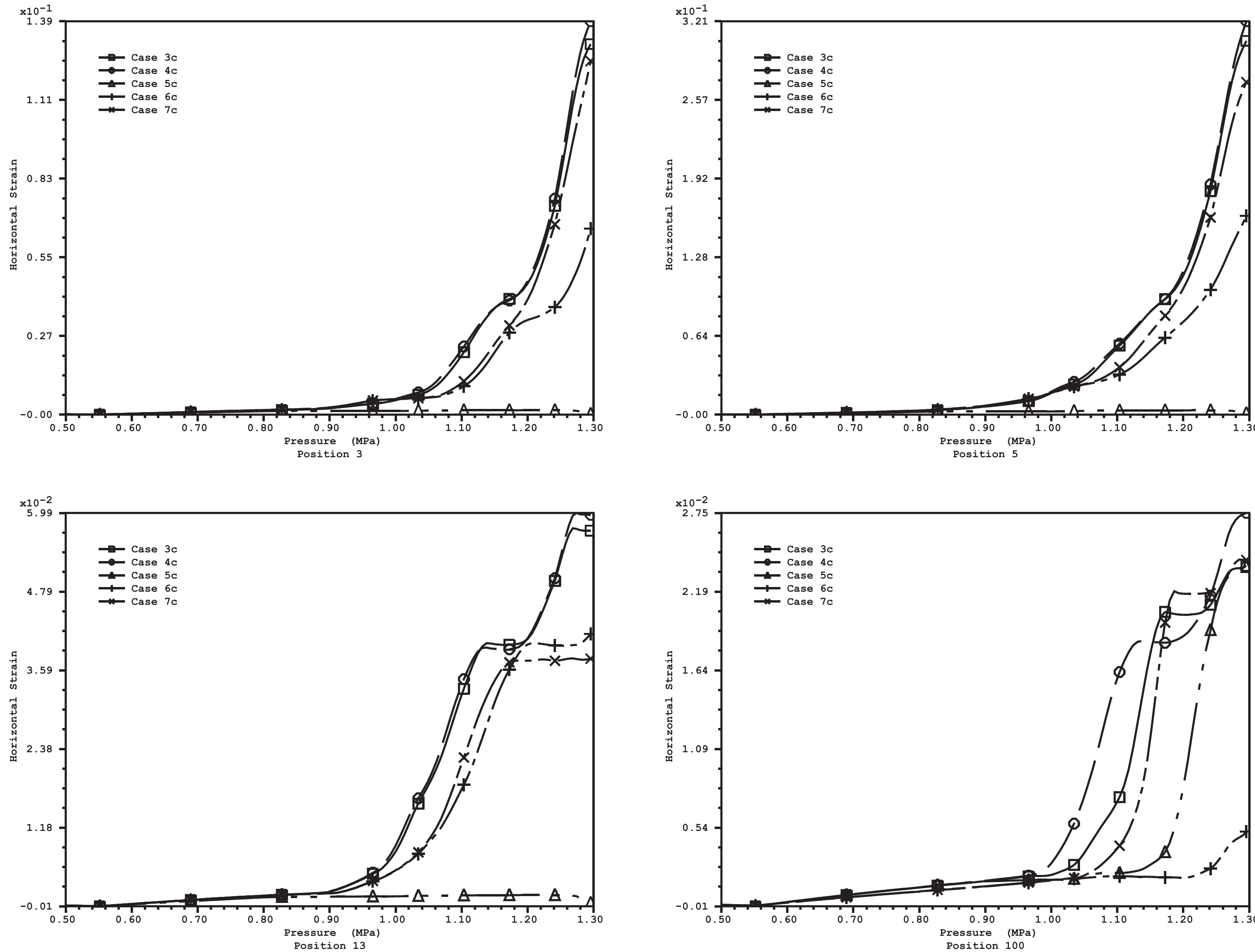

Figure 8-89. PCCV Liner Weld/Rat-Hole Study; Horizontal Strain Comparisons

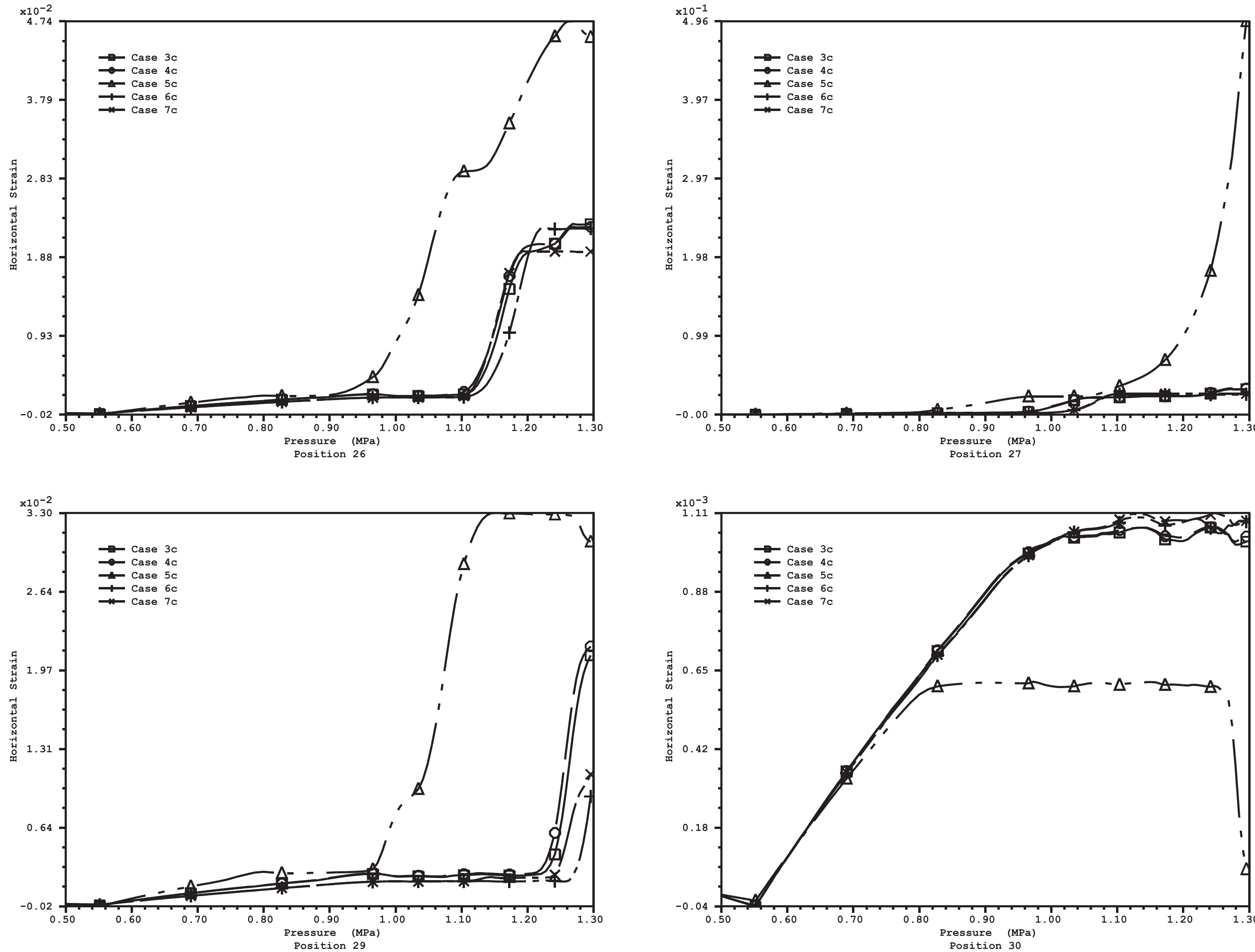

Figure 8-90. PCCV Liner Weld/Rat-Hole Study; Horizontal Strain Comparisons

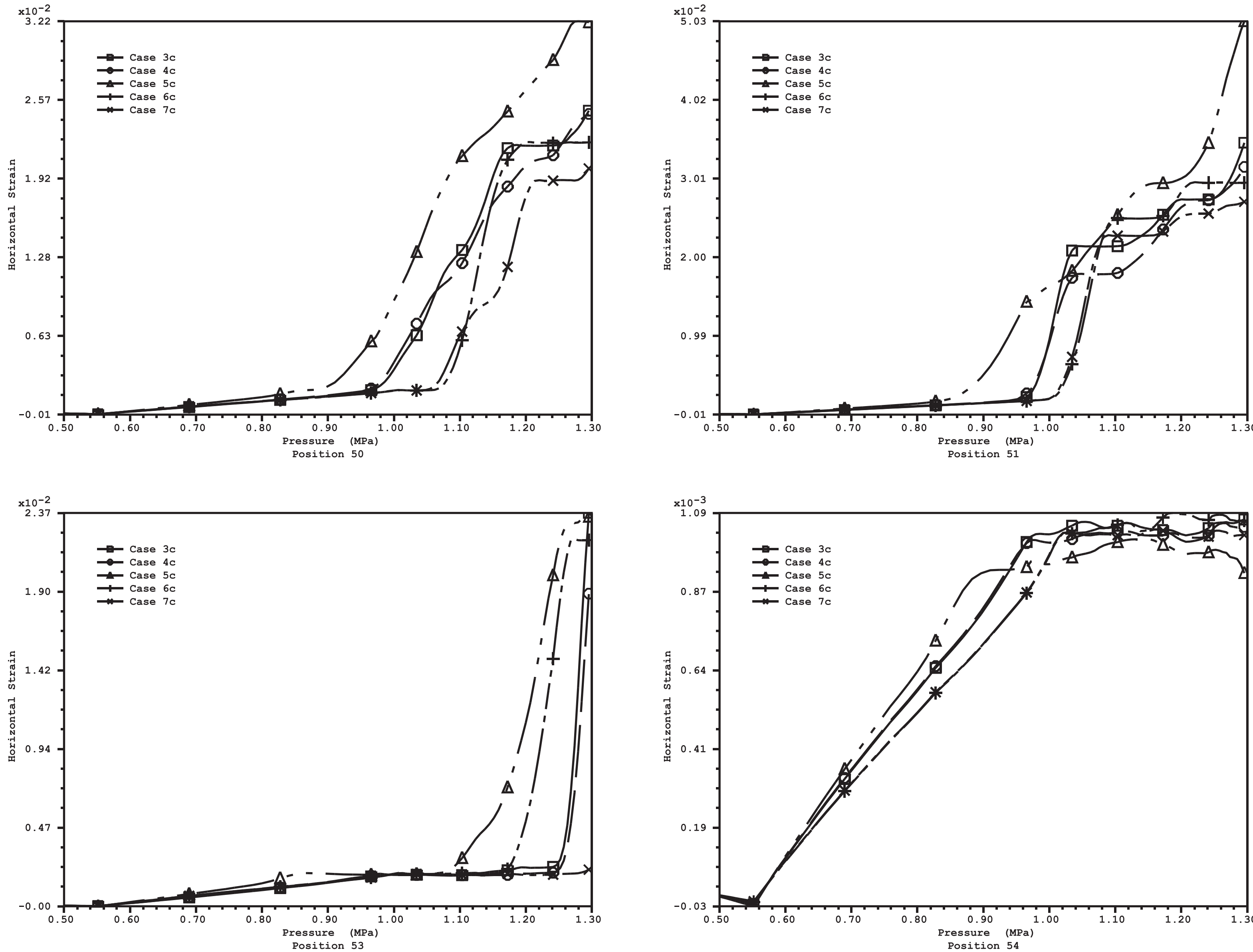

Figure 8-91. PCCV Liner Weld/Rat-Hole Study; Horizontal Strain Comparisons

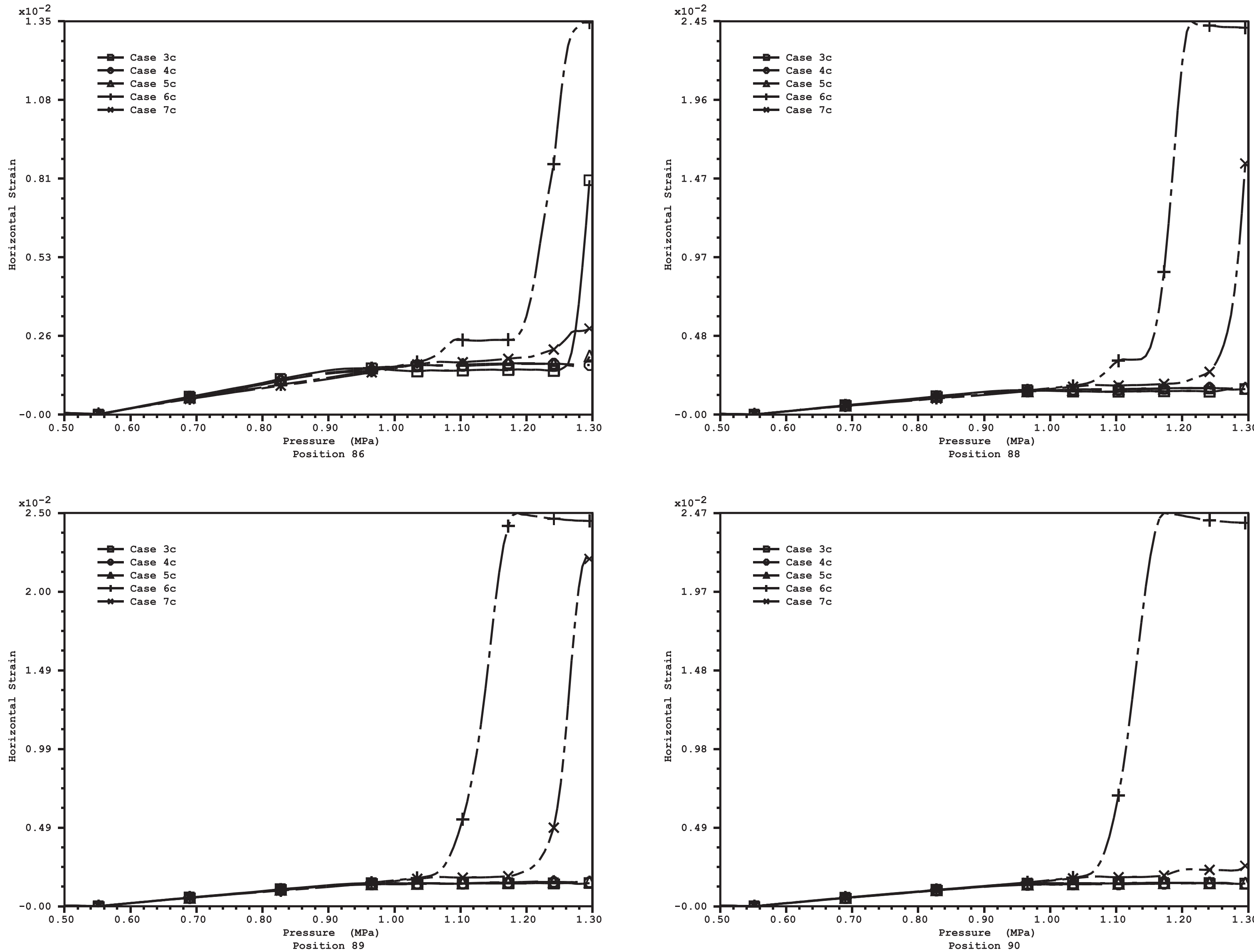

Figure 8-92. PCCV Liner Weld/Rat-Hole Study; Horizontal Strain Comparisons

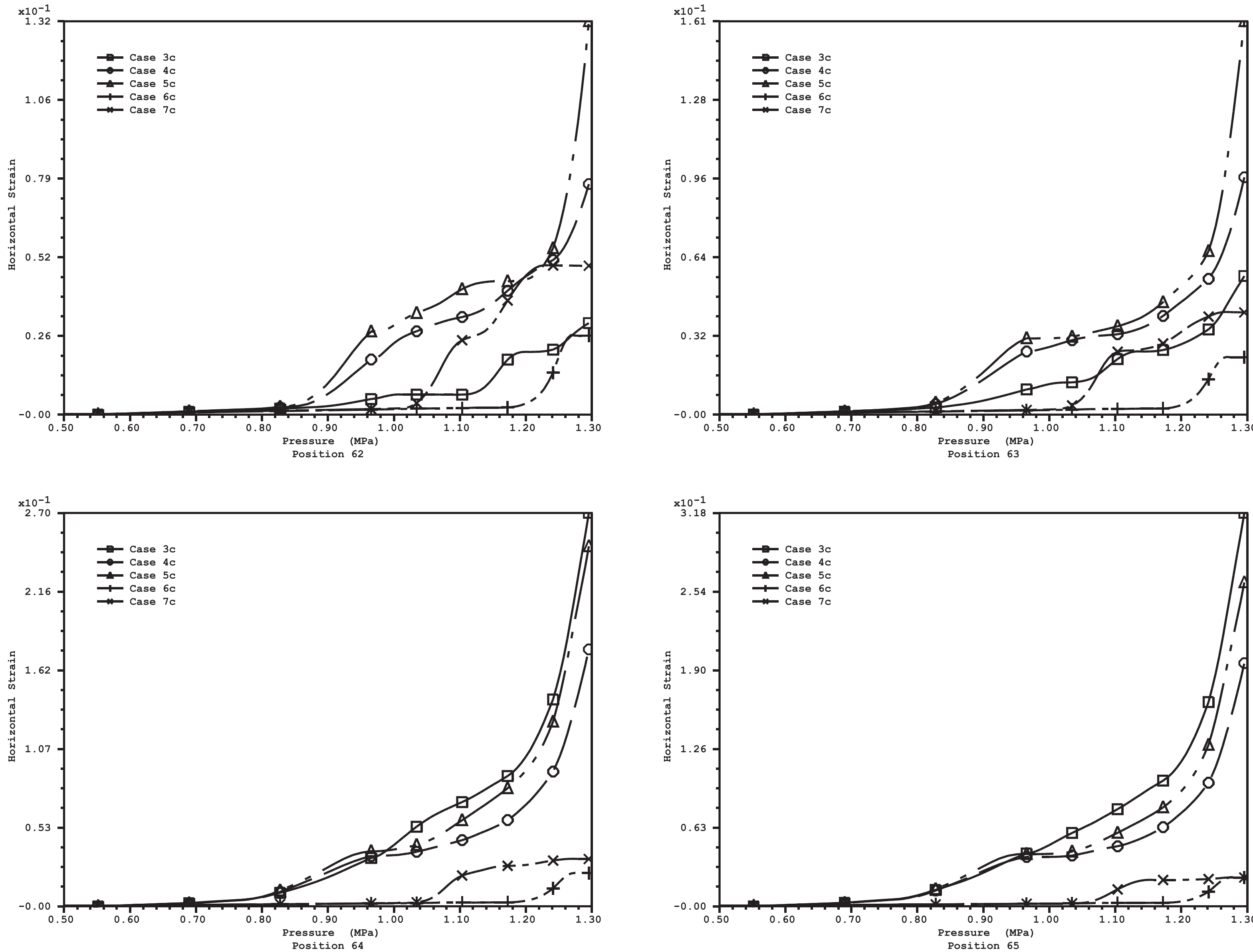

Figure 8-93. PCCV Liner Weld/Rat-Hole Study; Horizontal Strain Comparisons

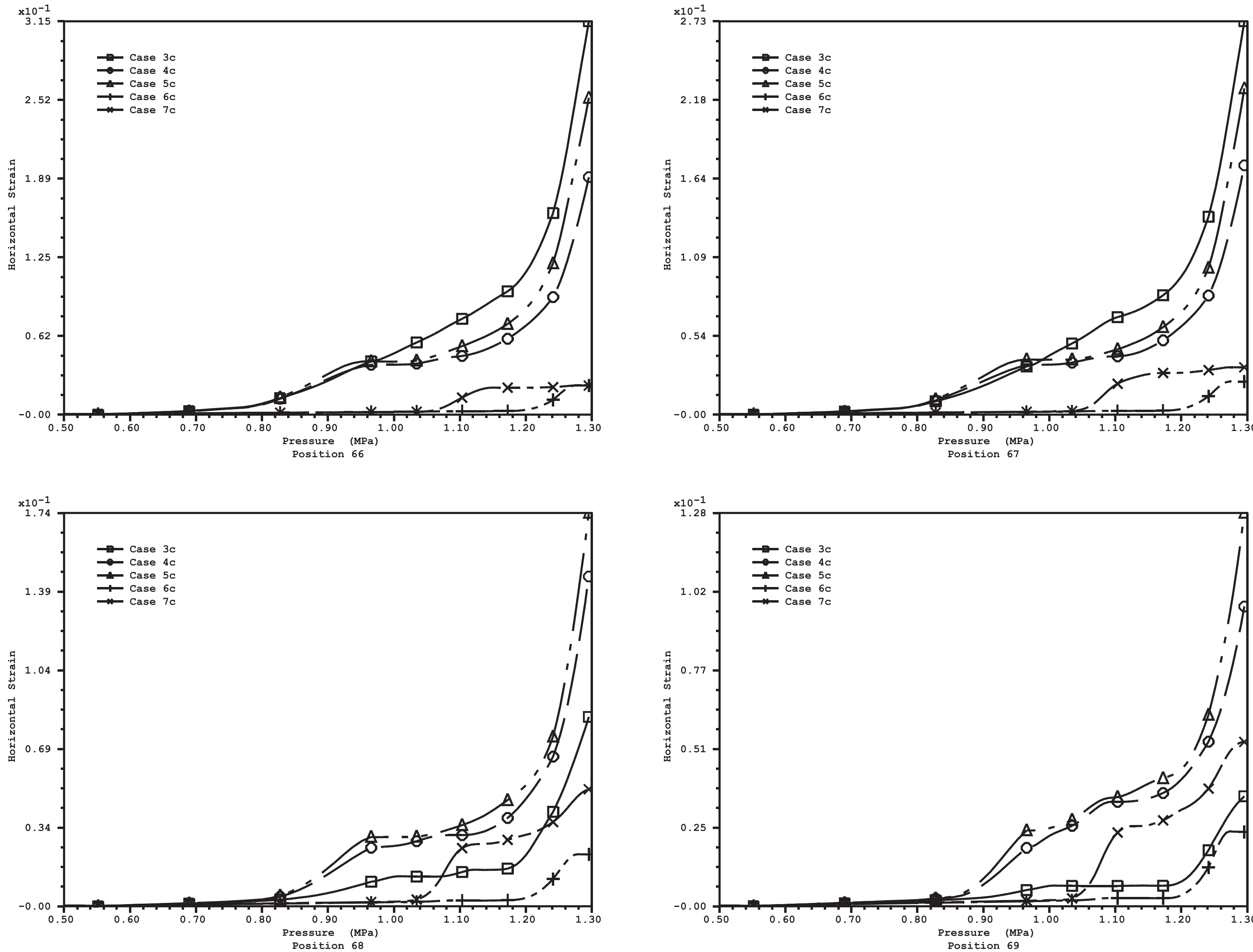

Figure 8-94. PCCV Liner Weld/Rat-Hole Study; Horizontal Strain Comparisons

Additional Strain Gages Near Buttress

	Gage ID	Azimuth (°)	Elevation (m)
1	LSI-C-J5-05	271.9	4.750
2	LSI-C-J5-06	271.9	4.700
3	LSI-C-J5-07	274	4.750
4	LSI-C-J5-08	276	4.750
5	LSI-C-J5-09	278	4.750
6	LSI-C-J5-10	280	4.750

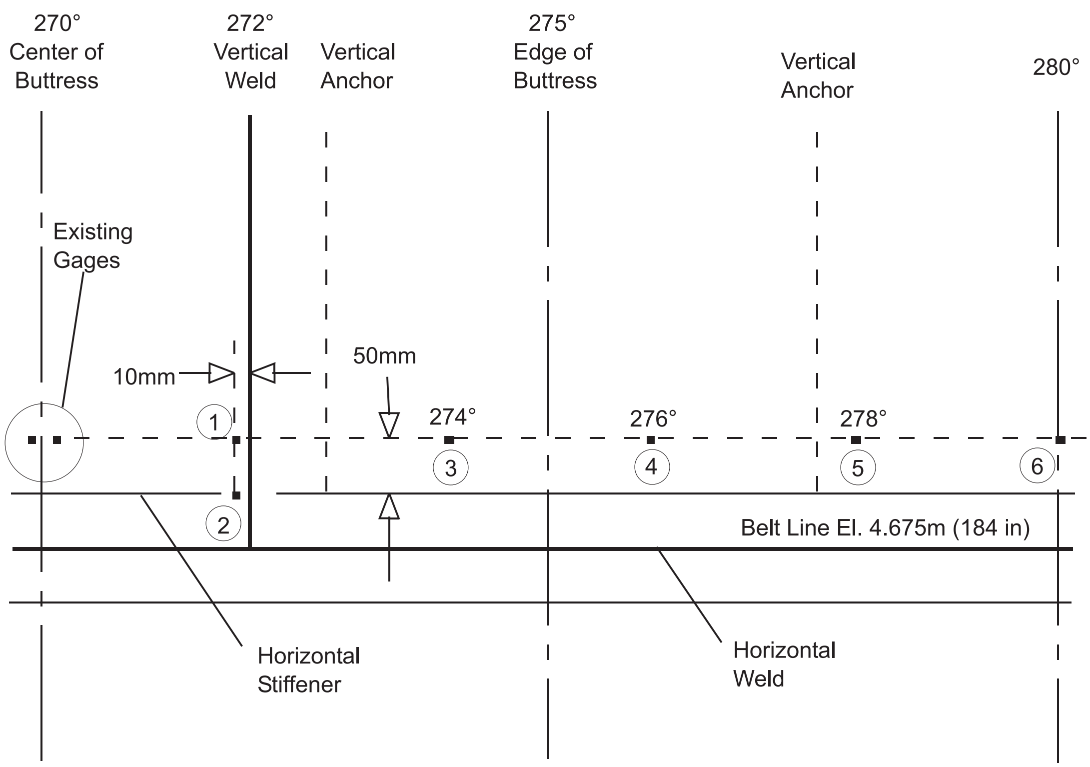

Figure 8-95. Locations of Liner Strain Gages at “J5”

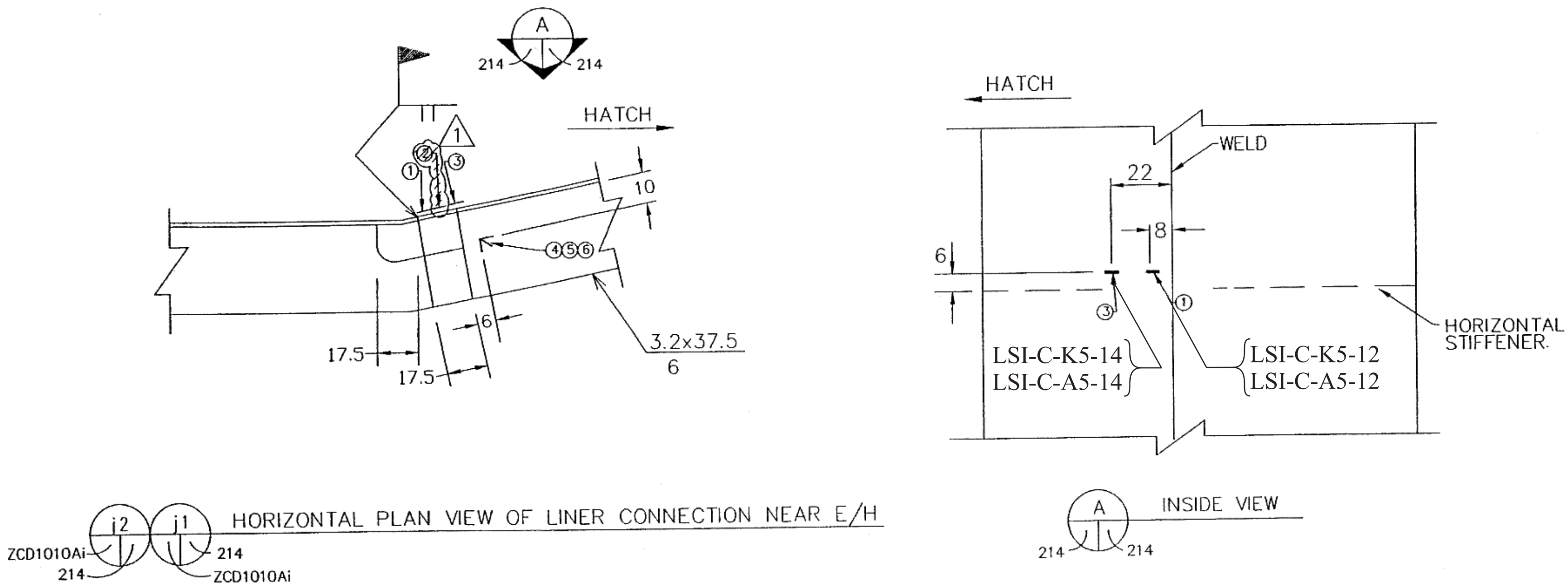

Figure 8-96. Locations of Liner Strain Gages at "KS" and "AS"
(Dimensions in mm)

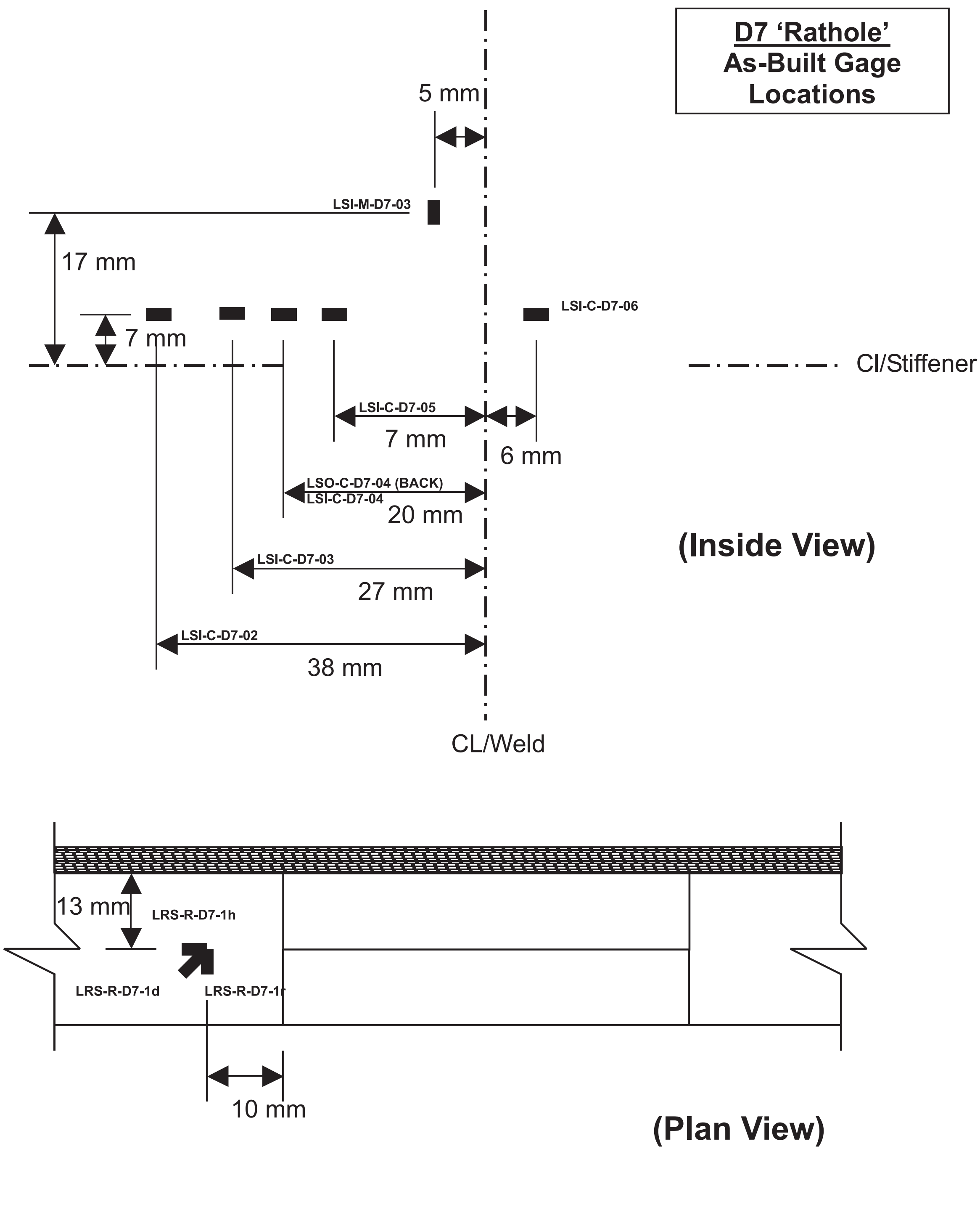

Figure 8-97. Locations of Liner Strain Gages at "D7"

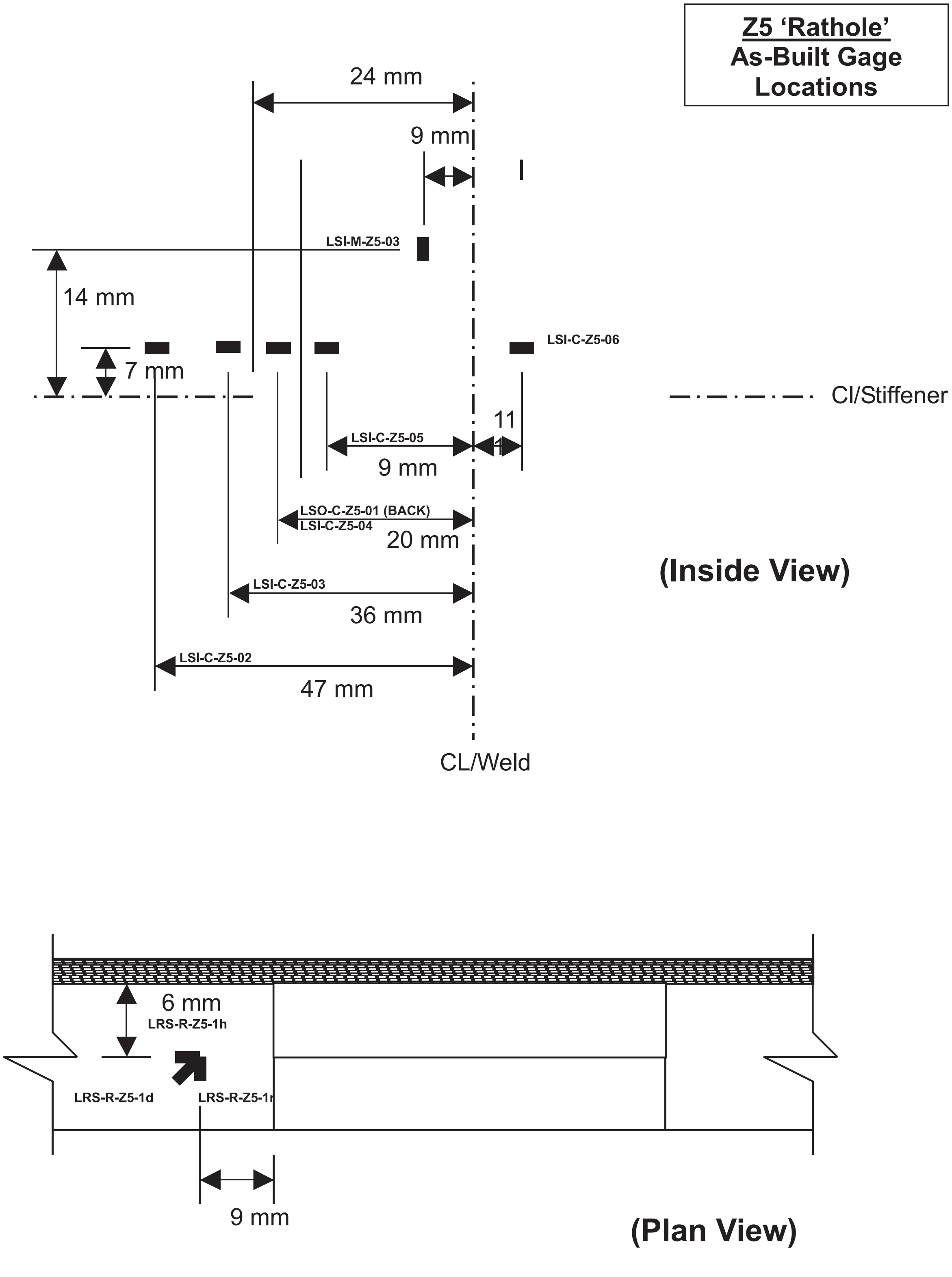

Figure 8-98. Locations of Liner Strain Gages at "Z5"

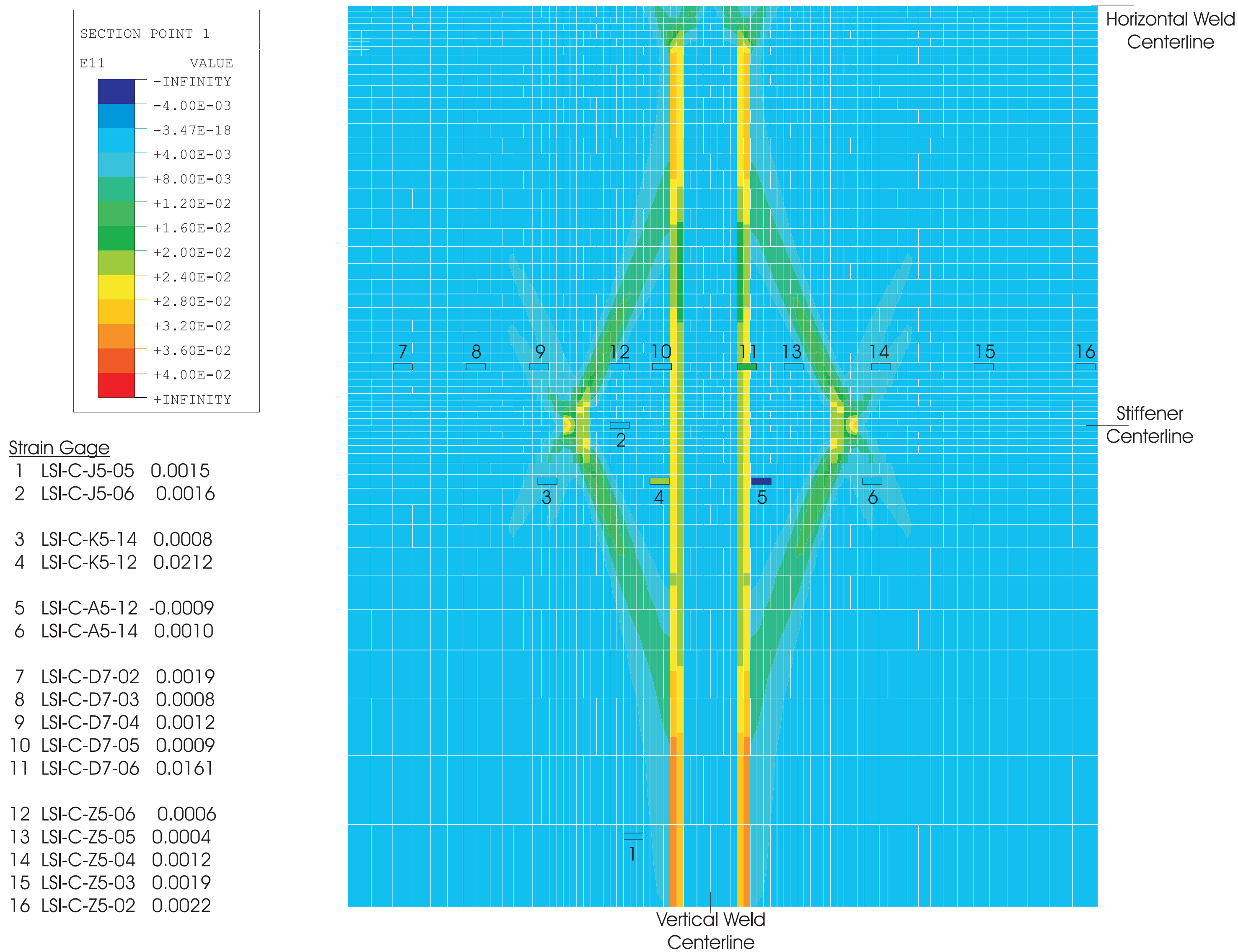

Figure 8-99. PCCV Liner Seam Rat-Hole Study, Horizontal Strain Contour, Case 4, LST Strain Gage Data Superimposed at 2.8 Pd

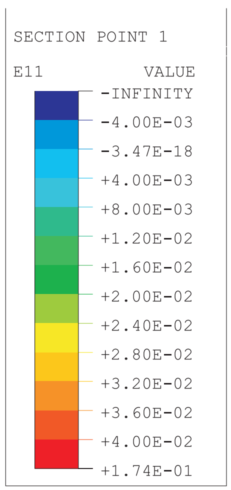

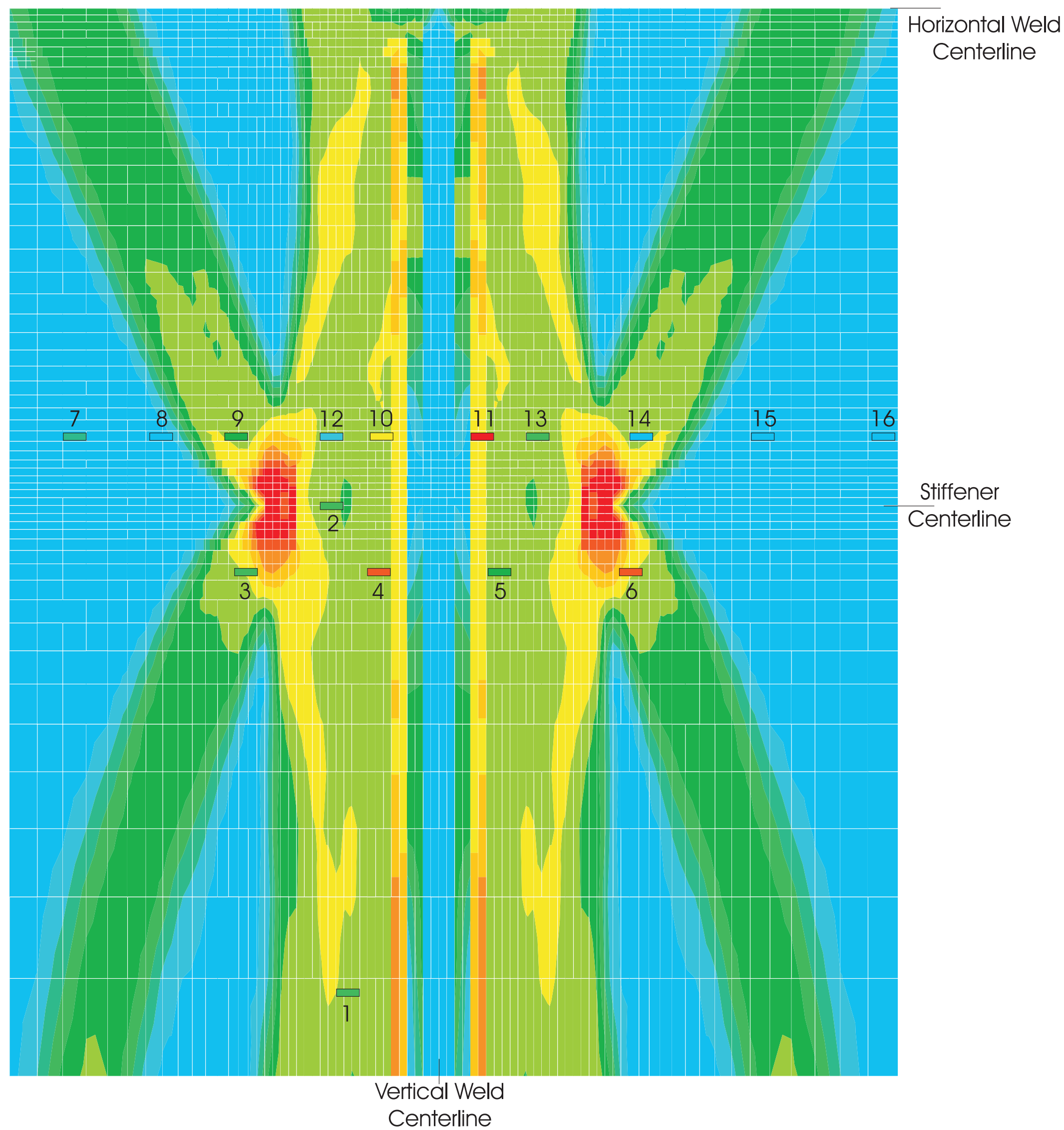

Strain Gage		
1	LSI-C-J5-05	0.0126
2	LSI-C-J5-06	0.0145
3	LSI-C-K5-14	0.0123
4	LSI-C-K5-12	0.0380
5	LSI-C-A5-12	0.0194
6	LSI-C-A5-14	0.0388
7	LSI-C-D7-02	0.0089
8	LSI-C-D7-03	0.0021
9	LSI-C-D7-04	0.0173
10	LSI-C-D7-05	0.0263
11	LSI-C-D7-06	0.0574
12	LSI-C-Z5-06	0.0046
13	LSI-C-Z5-05	0.0124
14	LSI-C-Z5-04	0.0034
15	LSI-C-Z5-03	0.0026
16	LSI-C-Z5-02	0.0023

Figure 8-100. PCCV Liner Seam Rat-Hole Study, Horizontal Strain Contour, Case 4, LST Strain Gage Data Superimposed at 3.3 Pd

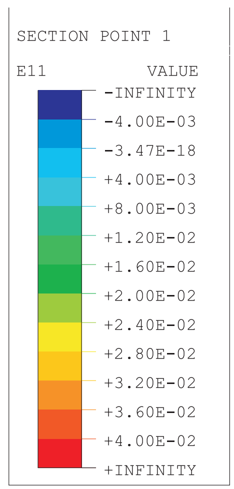

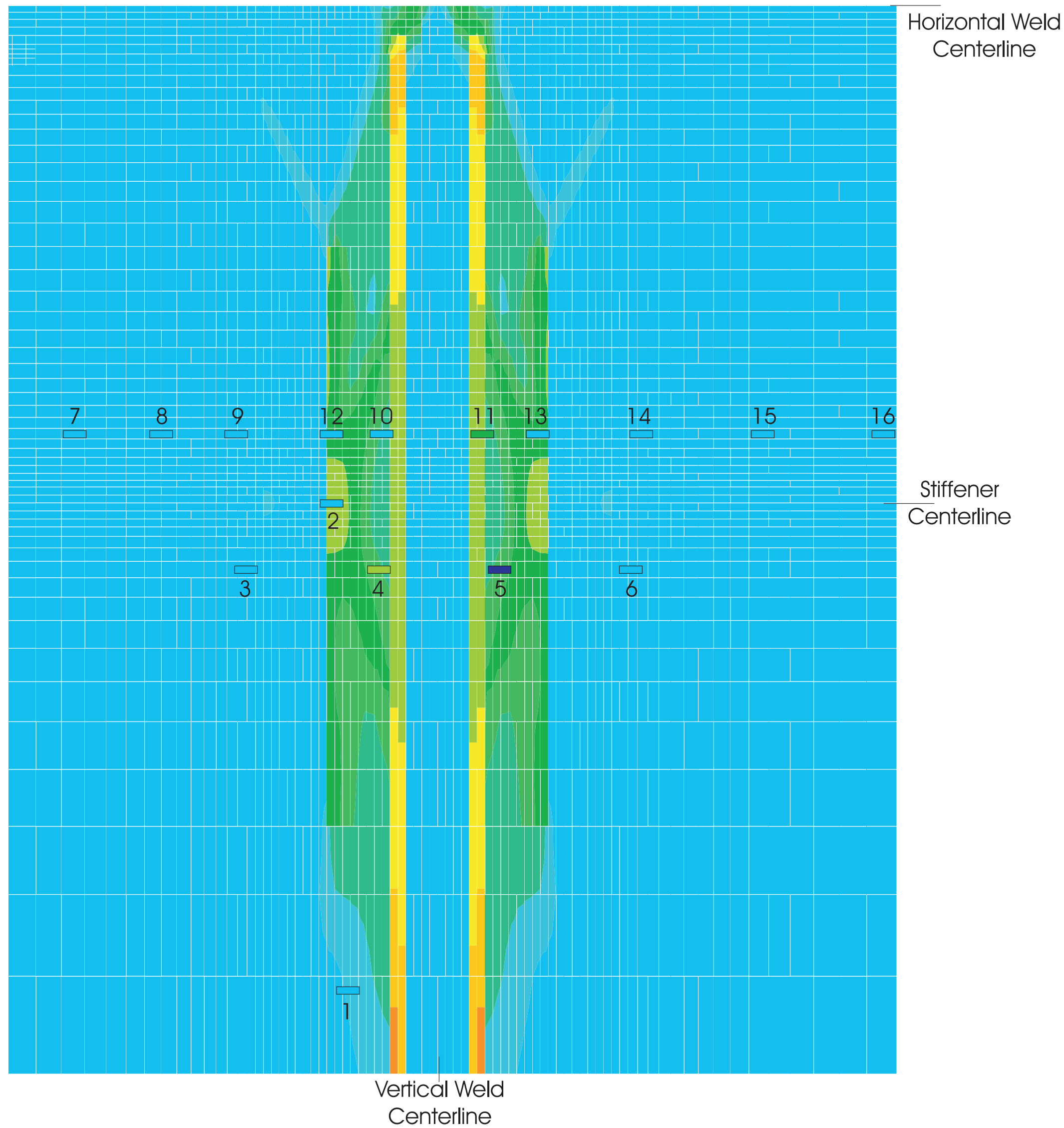

Strain Gage

1	LSI-C-J5-05	0.0015
2	LSI-C-J5-06	0.0016
3	LSI-C-K5-14	0.0008
4	LSI-C-K5-12	0.0212
5	LSI-C-A5-12	-0.0009
6	LSI-C-A5-14	0.0010
7	LSI-C-D7-02	0.0019
8	LSI-C-D7-03	0.0008
9	LSI-C-D7-04	0.0012
10	LSI-C-D7-05	0.0009
11	LSI-C-D7-06	0.0161
12	LSI-C-Z5-06	0.0006
13	LSI-C-Z5-05	0.0004
14	LSI-C-Z5-04	0.0012
15	LSI-C-Z5-03	0.0019
16	LSI-C-Z5-02	0.0022

Figure 8-101. PCCV Liner Seam Rat-Hole Study, Horizontal Strain Contour, Case 6, LST Strain Gage Data Superimposed at 2.8 Pd

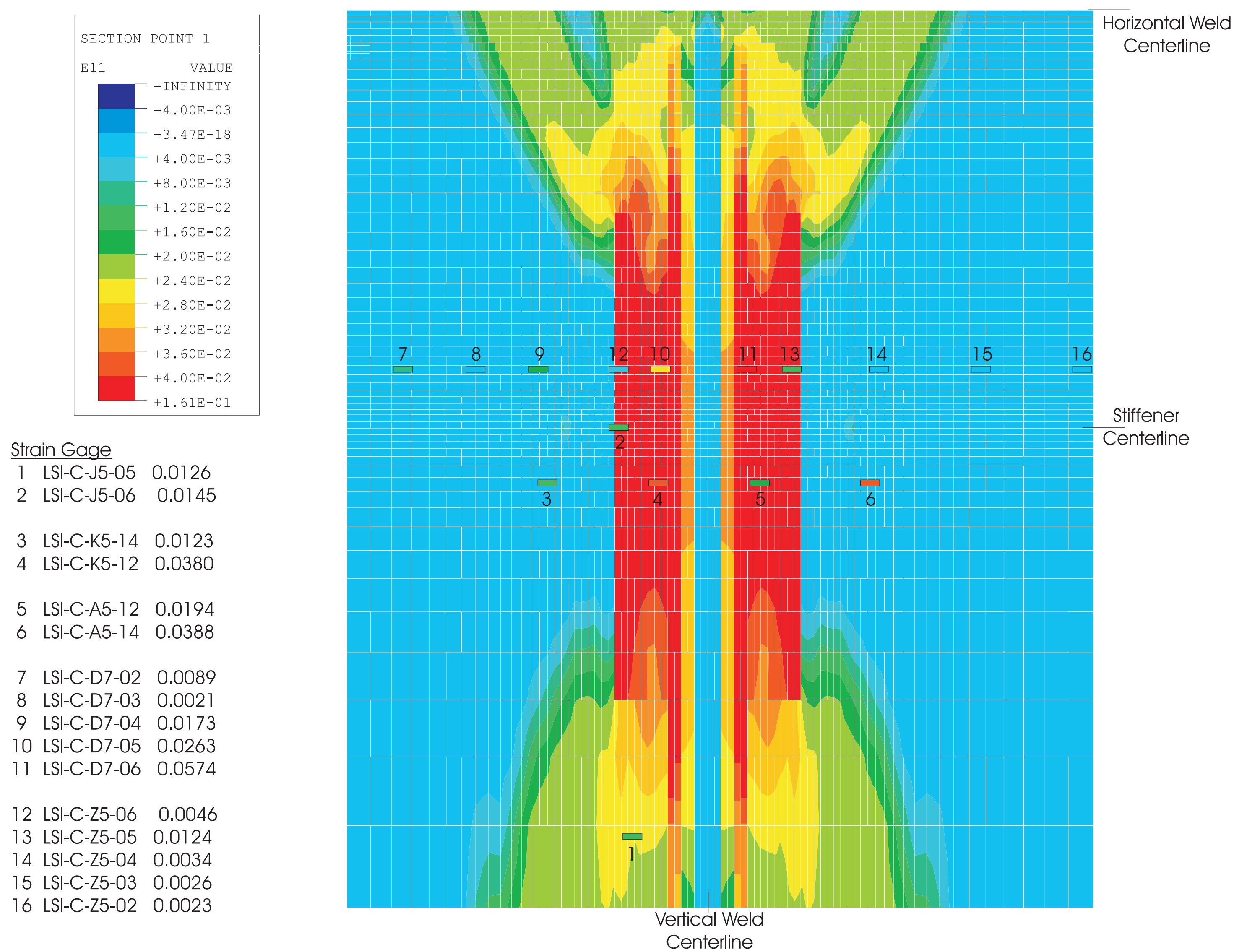

Figure 8-102. PCCV Liner Seam Rat-Hole Study, Horizontal Strain Contour, Case 6, LST Strain Gage Data Superimposed at 3.3 Pd

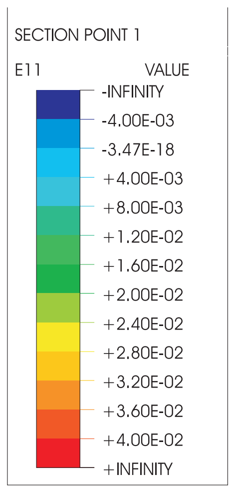

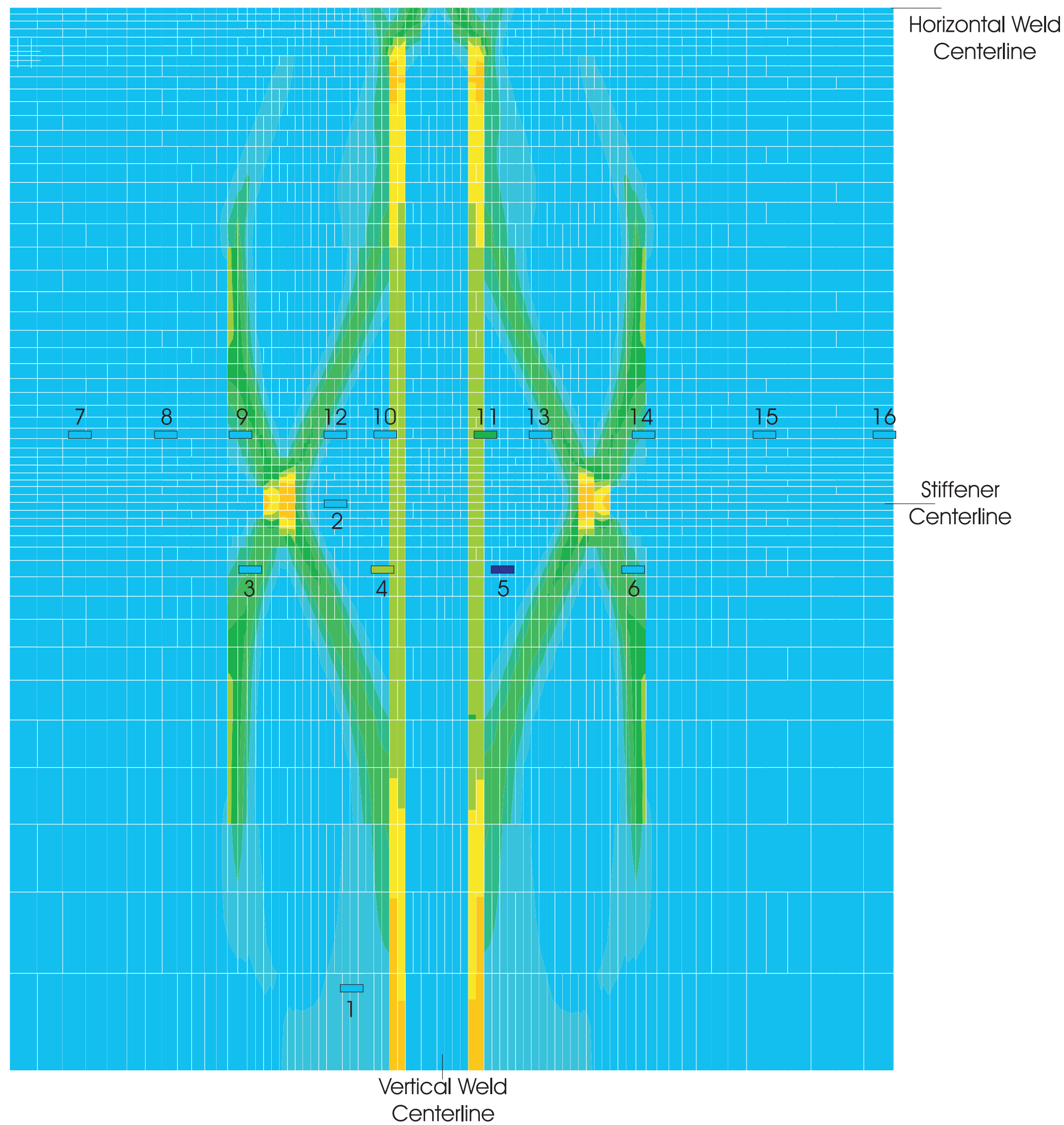

Strain Gage

1	LSI-C-J5-05	0.0015
2	LSI-C-J5-06	0.0016
3	LSI-C-K5-14	0.0008
4	LSI-C-K5-12	0.0212
5	LSI-C-A5-12	-0.0009
6	LSI-C-A5-14	0.0010
7	LSI-C-D7-02	0.0019
8	LSI-C-D7-03	0.0008
9	LSI-C-D7-04	0.0012
10	LSI-C-D7-05	0.0009
11	LSI-C-D7-06	0.0161
12	LSI-C-Z5-06	0.0006
13	LSI-C-Z5-05	0.0004
14	LSI-C-Z5-04	0.0012
15	LSI-C-Z5-03	0.0019
16	LSI-C-Z5-02	0.0022

Figure 8-103. PCCV Liner Seam Rat-Hole Study, Horizontal Strain Contour, Case 7, LST Strain Gage Data Superimposed at 2.8 Pd

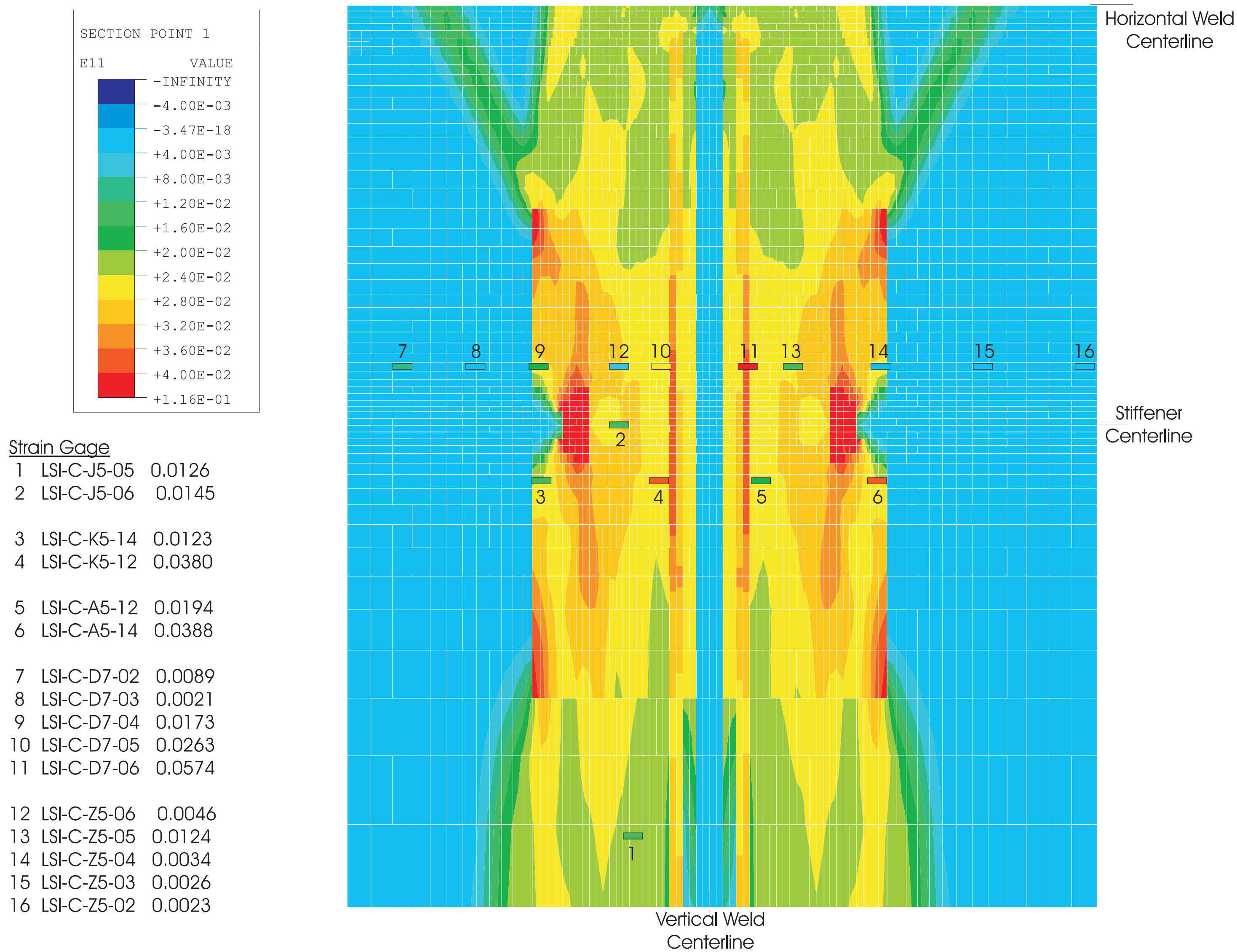

Figure 8-104. PCCV Liner Seam Rat-Hole Study, Horizontal Strain Contour, Case 7, LST Strain Gage Data Superimposed at 3.3 Pd

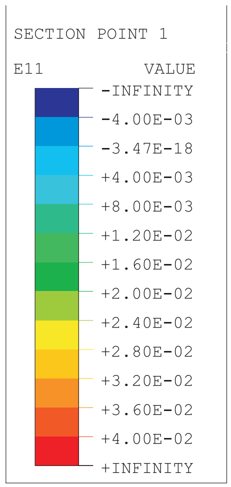

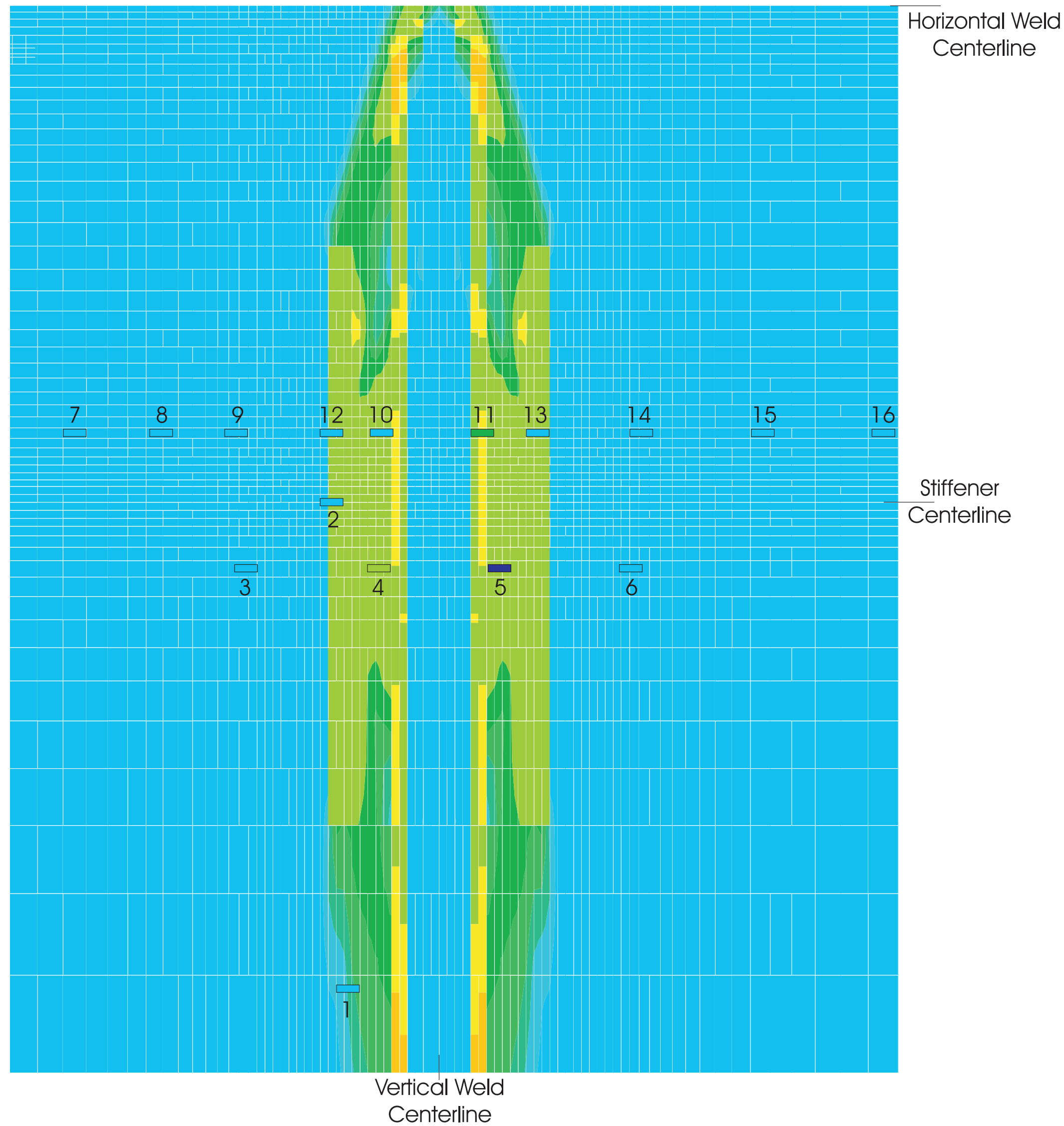

<u>Strain Gage</u>

1	LSI-C-J5-05	0.0015
2	LSI-C-J5-06	0.0016
3	LSI-C-K5-14	0.0008
4	LSI-C-K5-12	0.0212
5	LSI-C-A5-12	-0.0009
6	LSI-C-A5-14	0.0010
7	LSI-C-D7-02	0.0019
8	LSI-C-D7-03	0.0008
9	LSI-C-D7-04	0.0012
10	LSI-C-D7-05	0.0009
11	LSI-C-D7-06	0.0161
12	LSI-C-Z5-06	0.0006
13	LSI-C-Z5-05	0.0004
14	LSI-C-Z5-04	0.0012
15	LSI-C-Z5-03	0.0019
16	LSI-C-Z5-02	0.0022

Figure 8-105. PCCV Liner Seam Rat-Hole Study, Horizontal Strain Contour, Case 10, LST Strain Gage Data Superimposed at 2.8 Pd

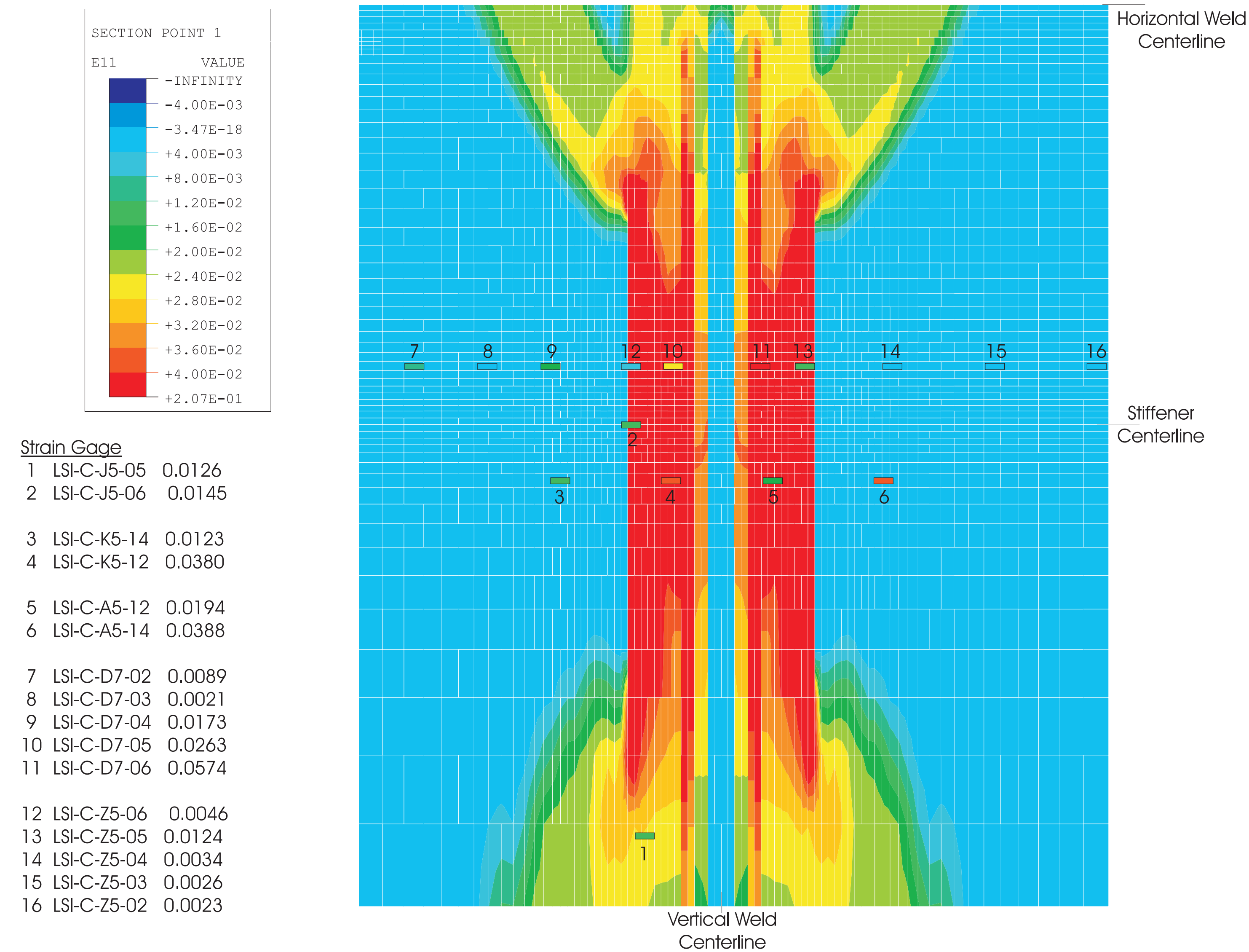

Figure 8-106. PCCV Liner Seam Rat-Hole Study, Horizontal Strain Contour, Case 10, LST Strain Gage Data Superimposed at 3.3 Pd

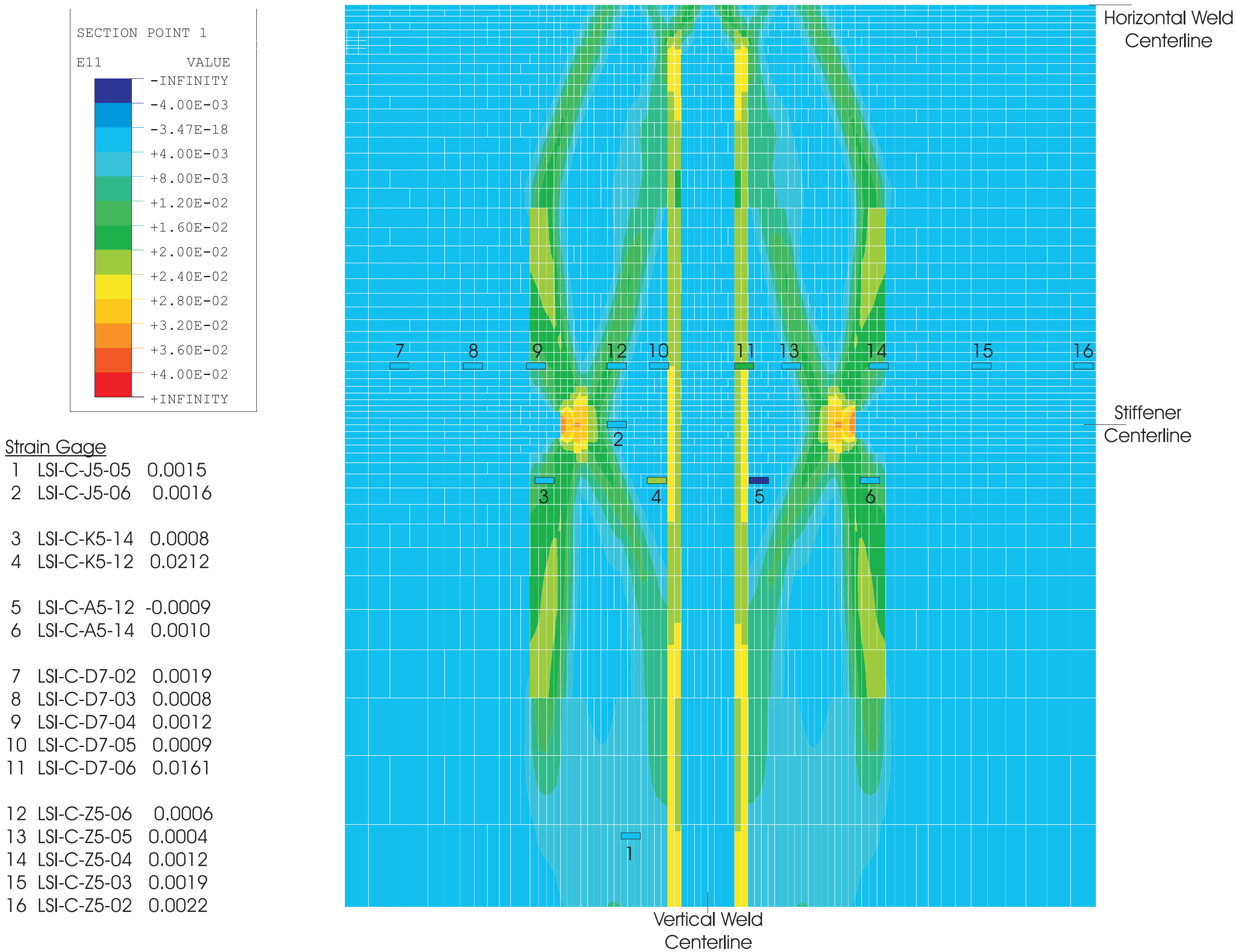

Figure 8-107. PCCV Liner Seam Rat-Hole Study, Horizontal Strain Contour, Case 11, LST Strain Gage Data Superimposed at 2.8 Pd

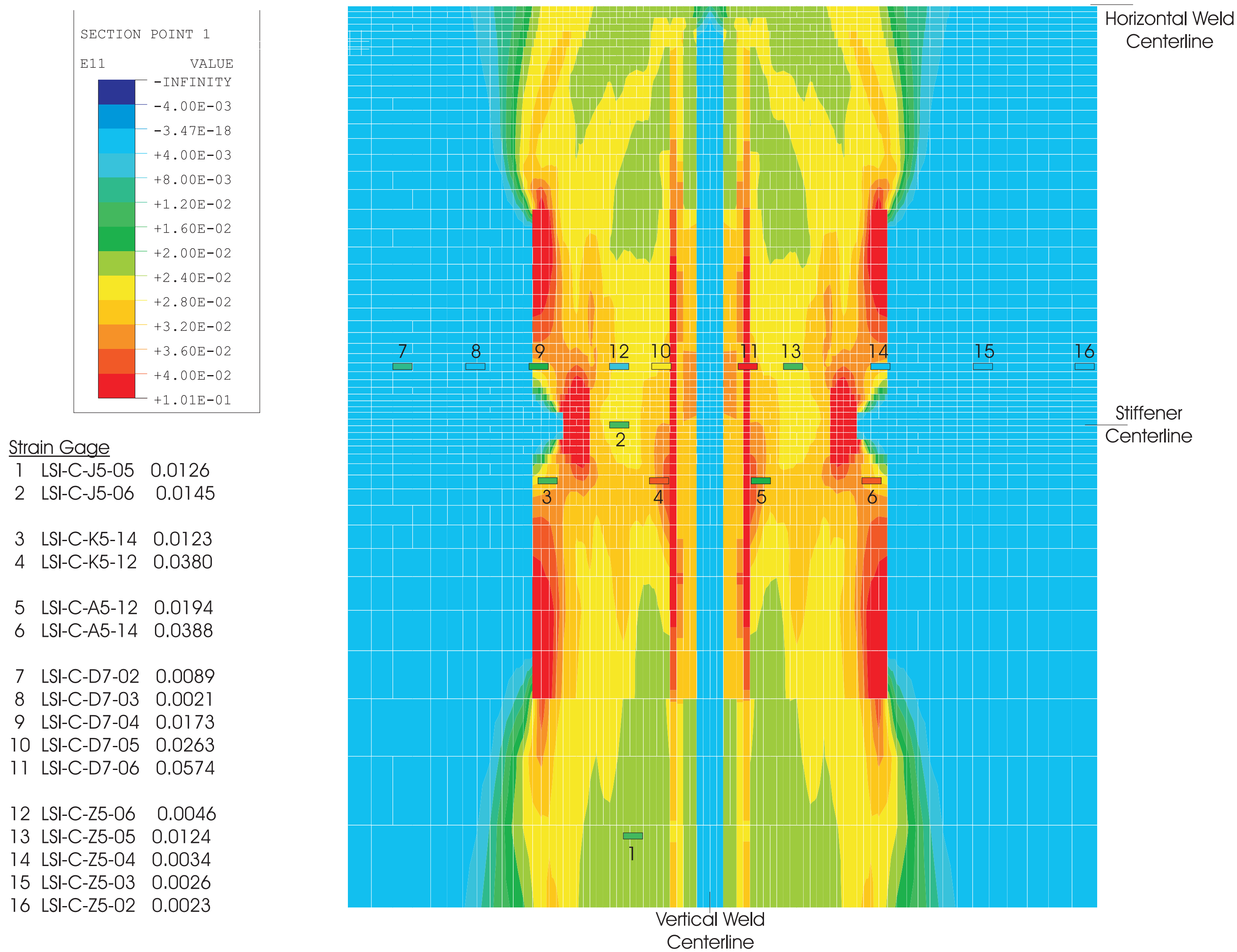

Figure 8-108. PCCV Liner Seam Rat-Hole Study, Horizontal Strain Contour, Case 11, LST Strain Gage Data Superimposed at 3.3 Pd

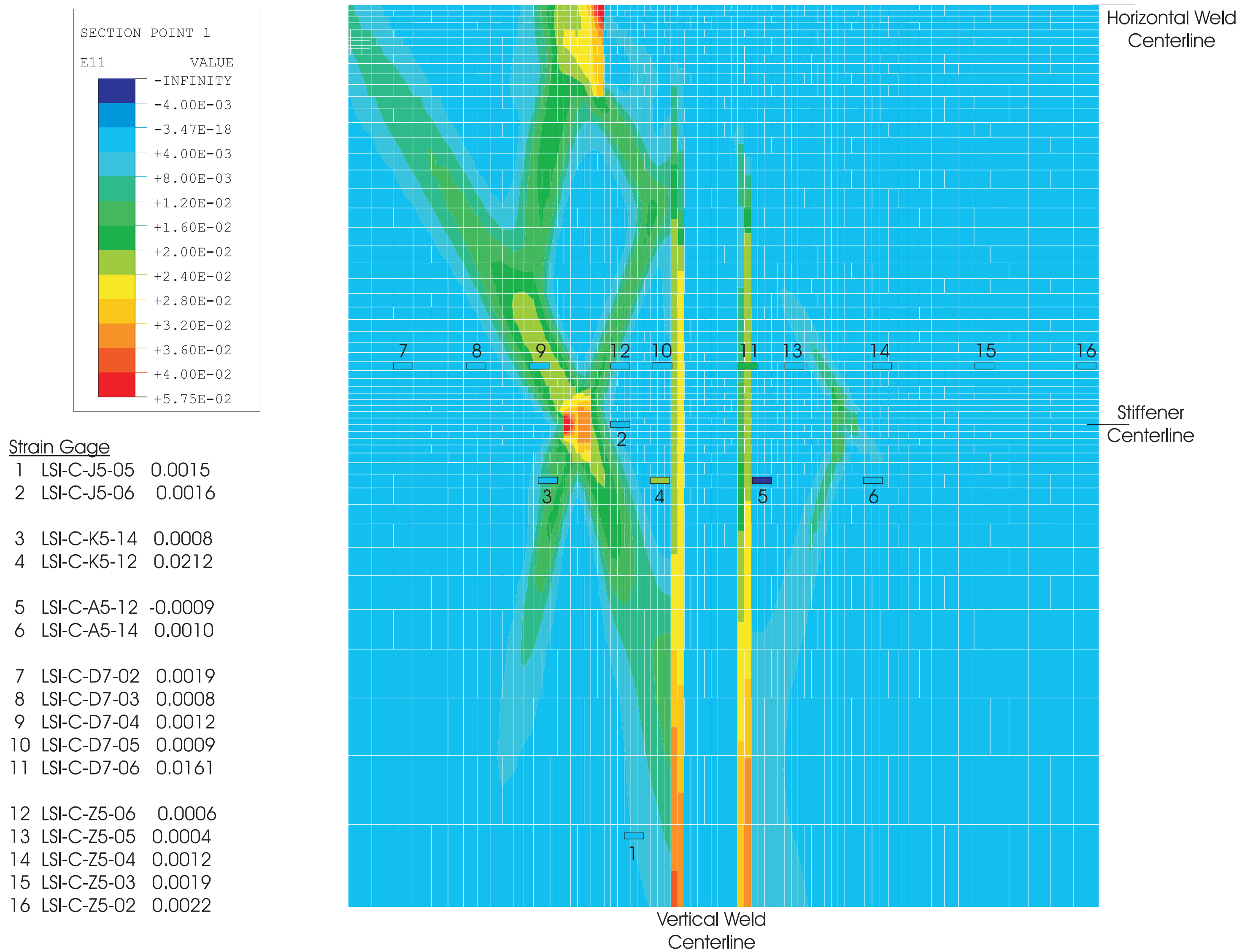

Figure 8-109. PCCV Liner Seam Rat-Hole Study, Horizontal Strain Contour, Case C4,
LST Strain Gage Data Superimposed at 2.8 Pd

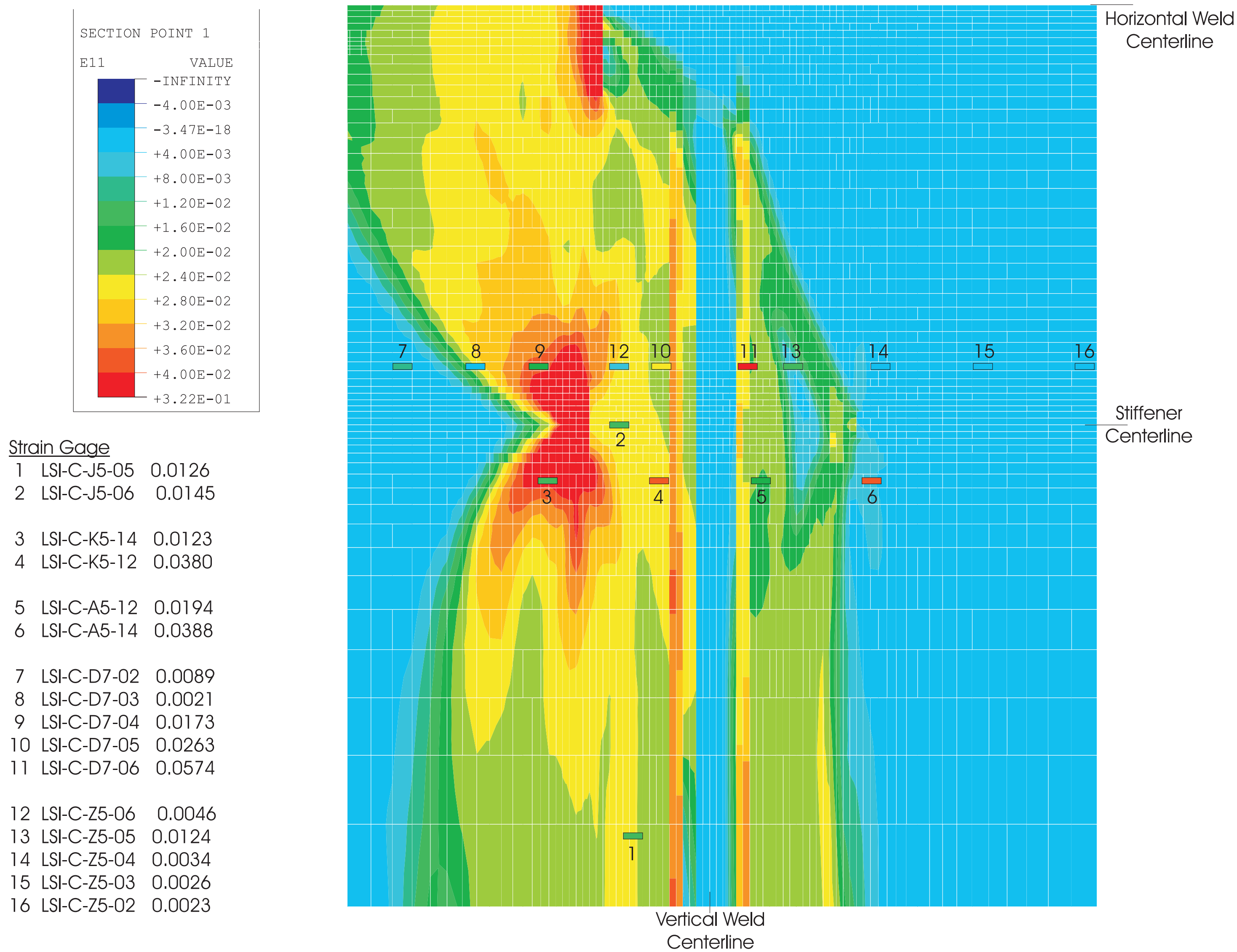

Figure 8-110. PCCV Liner Seam Rat-Hole Study, Horizontal Strain Contour, Case C4, LST Strain Gage Data Superimposed at 3.3 Pd

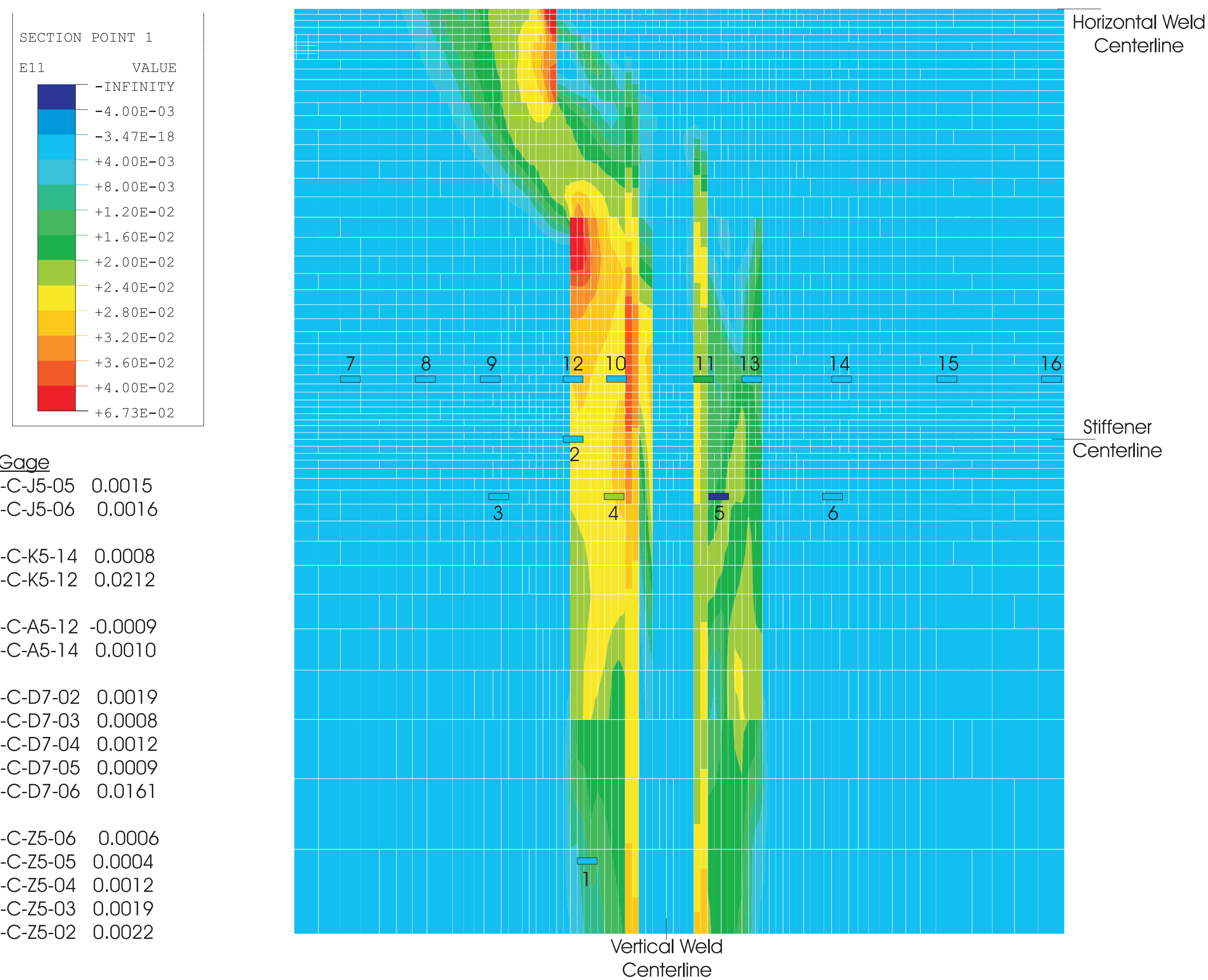

Strain Gage

1	LSI-C-J5-05	0.0015
2	LSI-C-J5-06	0.0016
3	LSI-C-K5-14	0.0008
4	LSI-C-K5-12	0.0212
5	LSI-C-A5-12	-0.0009
6	LSI-C-A5-14	0.0010
7	LSI-C-D7-02	0.0019
8	LSI-C-D7-03	0.0008
9	LSI-C-D7-04	0.0012
10	LSI-C-D7-05	0.0009
11	LSI-C-D7-06	0.0161
12	LSI-C-Z5-06	0.0006
13	LSI-C-Z5-05	0.0004
14	LSI-C-Z5-04	0.0012
15	LSI-C-Z5-03	0.0019
16	LSI-C-Z5-02	0.0022

Figure 8-111. PCCV Liner Seam Rat-Hole Study, Horizontal Strain Contour, Case C5, LST Strain Gage Data Superimposed at 2.8 Pd

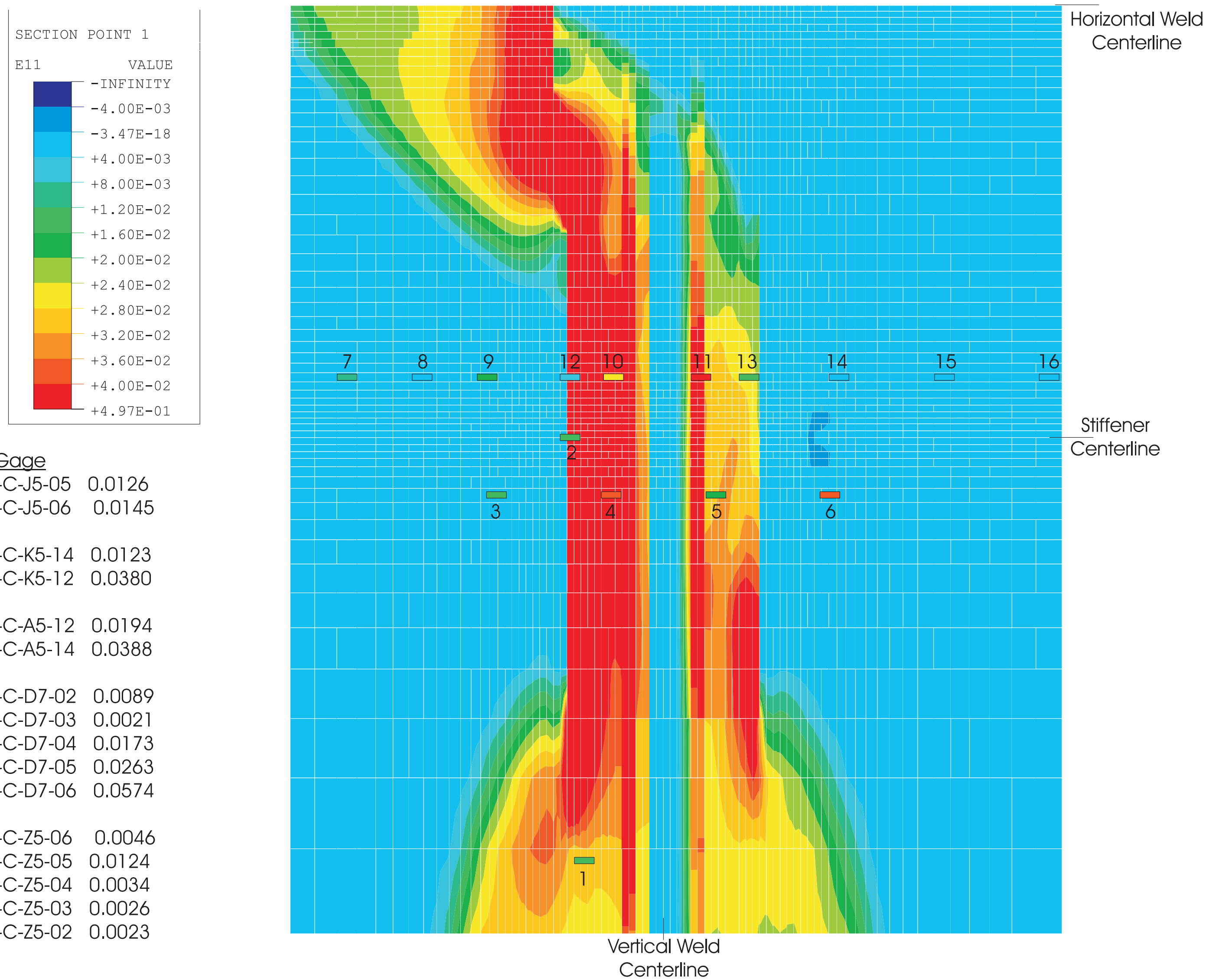

Strain Gage		
1	LSI-C-J5-05	0.0126
2	LSI-C-J5-06	0.0145
3	LSI-C-K5-14	0.0123
4	LSI-C-K5-12	0.0380
5	LSI-C-A5-12	0.0194
6	LSI-C-A5-14	0.0388
7	LSI-C-D7-02	0.0089
8	LSI-C-D7-03	0.0021
9	LSI-C-D7-04	0.0173
10	LSI-C-D7-05	0.0263
11	LSI-C-D7-06	0.0574
12	LSI-C-Z5-06	0.0046
13	LSI-C-Z5-05	0.0124
14	LSI-C-Z5-04	0.0034
15	LSI-C-Z5-03	0.0026
16	LSI-C-Z5-02	0.0023

Figure 8-112. PCCV Liner Seam Rat-Hole Study, Horizontal Strain Contour, Case C5, LST Strain Gage Data Superimposed at 3.3 Pd

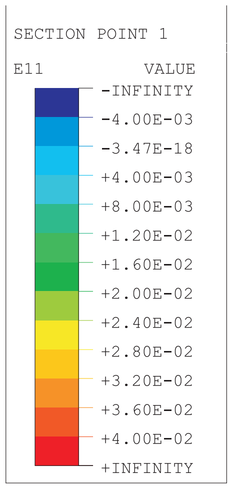

<u>Strain Gage</u>

1	LSI-C-J5-05	0.0015
2	LSI-C-J5-06	0.0016
3	LSI-C-K5-14	0.0008
4	LSI-C-K5-12	0.0212
5	LSI-C-A5-12	-0.0009
6	LSI-C-A5-14	0.0010
7	LSI-C-D7-02	0.0019
8	LSI-C-D7-03	0.0008
9	LSI-C-D7-04	0.0012
10	LSI-C-D7-05	0.0009
11	LSI-C-D7-06	0.0161
12	LSI-C-Z5-06	0.0006
13	LSI-C-Z5-05	0.0004
14	LSI-C-Z5-04	0.0012
15	LSI-C-Z5-03	0.0019
16	LSI-C-Z5-02	0.0022

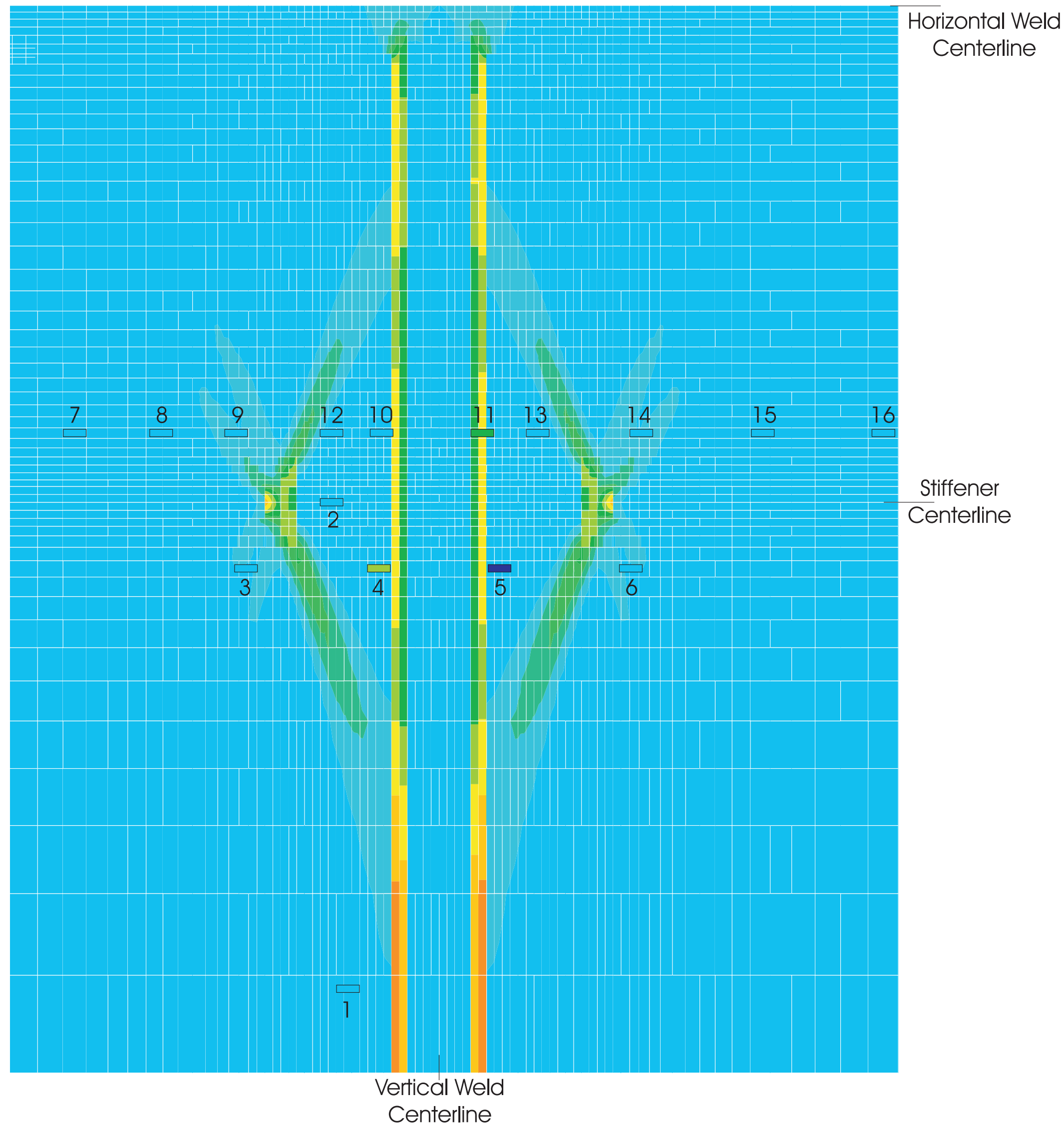

Figure 8-113. PCCV Liner Seam Rat-Hole Study, Horizontal Strain Contour, Case C6, LST Strain Gage Data Superimposed at 2.8 Pd

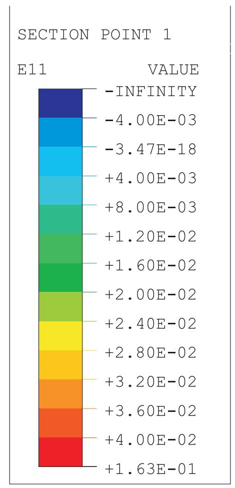

Strain Gage

1	LSI-C-J5-05	0.0126
2	LSI-C-J5-06	0.0145
3	LSI-C-K5-14	0.0123
4	LSI-C-K5-12	0.0380
5	LSI-C-A5-12	0.0194
6	LSI-C-A5-14	0.0388
7	LSI-C-D7-02	0.0089
8	LSI-C-D7-03	0.0021
9	LSI-C-D7-04	0.0173
10	LSI-C-D7-05	0.0263
11	LSI-C-D7-06	0.0574
12	LSI-C-Z5-06	0.0046
13	LSI-C-Z5-05	0.0124
14	LSI-C-Z5-04	0.0034
15	LSI-C-Z5-03	0.0026
16	LSI-C-Z5-02	0.0023

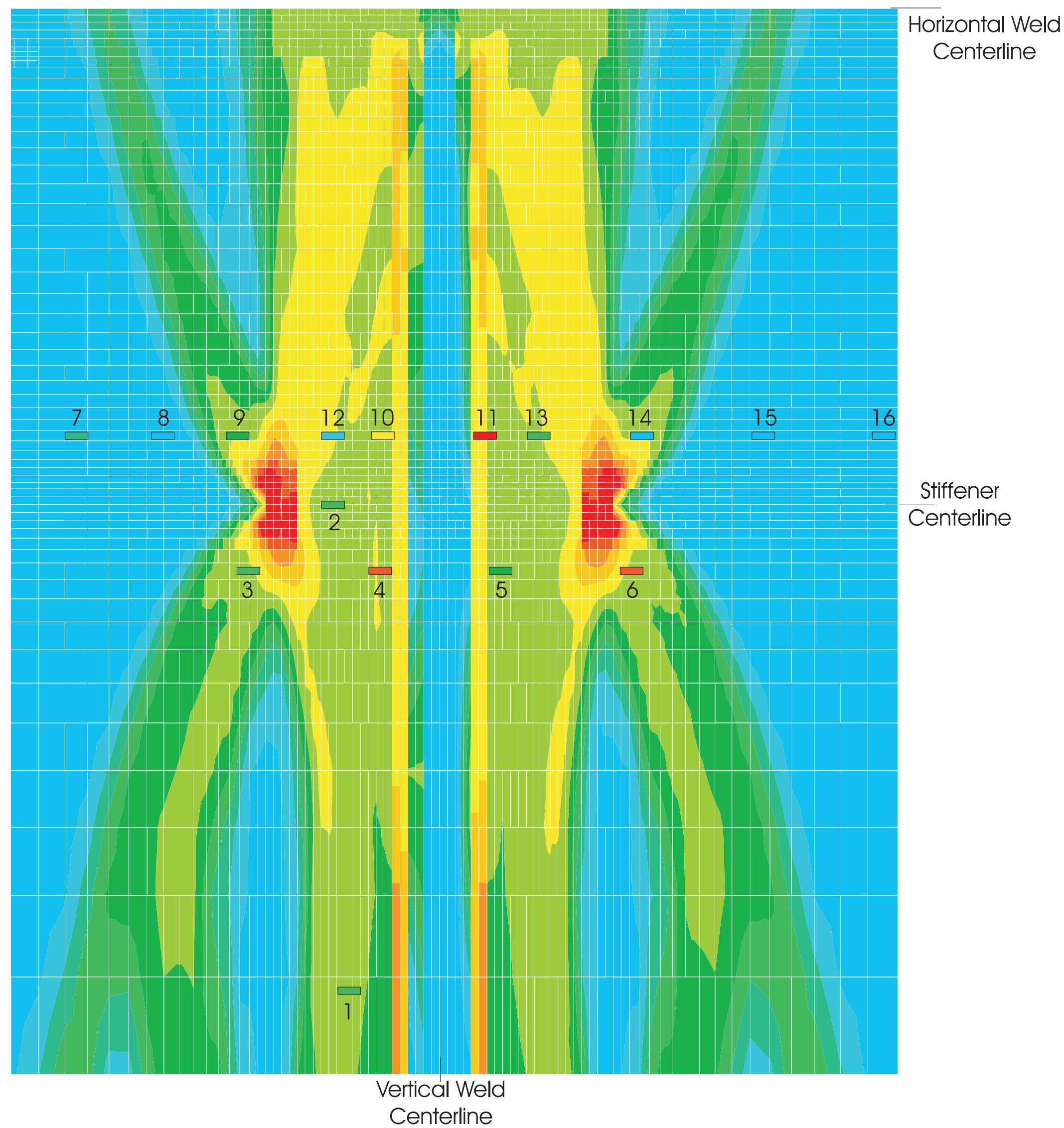

Figure 8-114. PCCV Liner Seam Rat-Hole Study, Horizontal Strain Contour, Case C6, LST Strain Gage Data Superimposed at 3.3 Pd

9.0 GLOBAL SFMT POSTTEST ANALYSIS

9.1 The Structural Failure Mode Test and SFMT Analysis Objectives

The work described in this report provided detailed documentation of comparisons of the pretest analyses to the test measurements, made adjustments to analytical models for measured material properties or material conditions, and explained and quantified behaviors and failure modes observed in the test. The overall goal of documenting analysis improvements and lessons learned, however, was limited to the context of what was learned from the LST; namely, that associated with PCCV pressure response out to global hoop strains was only about 0.5%, and liner tearing failure modes may have occurred prematurely due to welding irregularities. To obtain further information from the PCCV model, a SFMT was conducted in November 2001. In this test, the existing steel liner was relined with a heavy plastic liner and the testing medium was changed to hydrostatic, driven by nitrogen, which was pumped into a much smaller gas volume, as shown in Figure 9-1.

The SFMT resulted in a completely different failure mode: a catastrophic burst of the vessel. Additional measurement data was obtained much further into the nonlinear response range of the structure than in the LST, i.e., up to global hoop strains of nearly 2%. The rapid failure mode that followed was also captured on video. Some still photos from this video are shown in Figures 9-2 and 9-3, and the rupture pattern that occurred is shown in Figure 9-4. SNL provided some posttest observations of the SFMT.

- The maximum pressure reached (average pressure by volume) was ~1.424 MPa, or ~3.6 Pd.
- The water level inside the model visibly dropped slightly just before the rupture of the PCCV.
- Four to six tendons failed in the final minute before the vessel ruptured, and nearly all cylinder hoop tendons were ruptured by the end of the test.
- Rupture initiated at approximately midheight of the cylinder near azimuth 6 degrees, then radiated vertically in both directions; a subsequent rupture line radiated circumferentially approximately 1.5 m above the top of the basemat.
- The vessel "telescoped" over the stem of the cylinder wall and came to rest on the instrumentation frame.
- Approximately 12 tendon segments were completely ejected from the model (all remained within test site boundaries).
- Hoop tendons and rebar at the rupture line exhibited significant necking, indicating that rupture was ductile in nature.
- The model displaced 3 inches horizontally and tipped in the opposite direction from the rupture. This was likely caused by the momentum transfer that resulted from water jetting from the rupture zone.

In order to maximize the utility and lessons learned from the SFMT, analytical studies of this final test were undertaken. The additional studies consisted of two subtasks:

1. Comparing the measurements taken to existing analyses, and to new analyses which replicate the conditions of the SFMT, and
2. Conducting a new analysis using a simplified 3D model.

9.2 Posttest SFMT Global Model

The SFMT posttest analysis model is a fully 3D model of the entire containment cylinder, dome, and basemat, which focuses on capturing the global behavior versus pressure up to the tendon rupture observed in the SFMT. The containment was modeled with shell elements, which required a bonded tendon assumption for the post-tensioned tendons and was simpler to model than the pretest 3DCM model. The ABAQUS general-purpose finite element program Version 5.8-18, along with the ANACAP-U concrete and steel constitutive modeling program, was used for the SFMT analysis, just as for the other posttest work.

A layered shell model was developed that included the liner and concrete as separate layers; rebar subelements were used to model the reinforcement and tendons. The E/H and A/L penetrations of the PCCV were explicitly modeled, with emphasis on their associated perturbations in rebar and tendon patterns and increased wall thickness. The M/S and

F/W penetrations were not modeled explicitly, since these penetrations cause negligible perturbation of the tendon pattern. However, the additional reinforcement associated with these penetrations and the thickening of the liner was included. The model consisted of 4-node composite (layered) shell elements. The inner layer simulated the 1.6 mm thick steel liner and the outer layer was given properties consistent with the concrete wall, including the differing thickness of the wall at the buttress, springline, dome, and E/H and A/L penetration regions. Both the liner and concrete layers were each assigned three integration points through the thickness. The basemat was also modeled with composite shell elements and rebar subelements, but the tendon gallery was not explicitly modeled. The horizontal plane of nodes making up the basemat was located at the geometric centerline of the region, approximately 180 cm (70 inches) below the base of the containment wall. The nodes at the base of the cylinder wall were tied to corresponding nodes in the horizontal plane of the basemat with multipoint constraint equations. The bottom of the basemat was modeled with nonlinear spring elements with an average spring constant of 150.5 kips per square inch in compression; the tensile/uplift stiffness was very small. The finite element mesh is shown in Figure 9-5.

The reinforcement was modeled as subelements within the shell elements at the correct section depth. Figure 9-6 shows the inner and outer layers of vertical reinforcement in the cylinder and the dome regions. The two layers of hoop reinforcement are shown in Figure 9-7. The bonded post-tensioned tendons are also modeled as rebar subelements within the shell elements, as shown in Figure 9-8. The perturbation of the meridonal and hoop tendons around the A/L is accurately simulated. In the local region of the E/H where the hoop tendons overlap through the thickness, they were combined in groups of two with the total properties of the pair located at the geometric centroid of the two tendons. The tendons were post-tensioned by applying an initial stress to the specific tendon subelements. To address the issue of tendon friction, which was studied in detail in the 3DCM analysis, two versions of tendon initial stress were analyzed: one with variable stress around the circumference, as a function of friction and setting losses, and the other uniform tendon prestress, set to the average value of tendon stress.

Figure 9-9 shows additional local reinforcement in the buttresses at 90 and 270 degrees and the ring hoops at the E/H and A/L openings.

Pressure load was applied to all interior model surfaces. At the E/H and A/L openings, the pressure load was increased on the first row of elements around the circumference to apply the same load at these regions that would develop due to pressure applied on the covering over these penetrations. The load sequence included a preloading step that pressurized the model to 3.2 Pd (1.257 MPa), approximately the pressurization achieved in the LST test, and then unloaded it. After the preloading, a hydrostatic water pressure load was applied to the interior surfaces equivalent to a head of approximately 14.8 m to simulate the PCCV filled with water to 1.3 m from the top of the dome. Additional pressure was then ramped up on the interior surfaces in addition to the hydrostatic loading.

9.3 Results and Comparisons

Displacement versus pressure histories at various locations are compared to the SFMT in Figures 9-10 through 9-15. The displacement data from the test is plotted along with posttest analysis data from the model with uniform average tendon stress, and from the analysis with variable tendon post-tensioning stresses. The displacements are plotted versus the total internal pressure, including the hydrostatic component. The average pressure is the gas pressure plus the hydrostatic pressure that exists near the midheight of the cylinder (i.e., at an elevation of approximately 5.0 m). Table 9-1 summarizes the figure number, gage location, azimuth, elevation, and displacement component used for these comparisons.

At azimuth 135 degrees, elevations 2.63 and 6.2 m, the pretest analysis results were also added to the plots.

Maximum principal strain contour plots for the analysis with tendon friction losses are shown in Figures 9-16 through 9-23. The series shows views from azimuth locations 0 and 90 degrees, and views from 180 and 270 degrees. The inside liner strains at a total pressure load of 1.28 MPa, approximately 3.25 Pd, are shown in Figures 9-16 and 9-17. At the same pressure, the outer concrete strains are shown in Figure 9-18 and 9-19. Figures 9-20 to 9-23 show the maximum liner and concrete strains, respectively, at a pressure load of 1.44 MPa, approximately 3.65 Pd. This is approximately equal to the maximum pressure achieved during the SFMT.

Table 9-1. Gage Displacement Comparison

Figure	Gage	Azimuth	Elevation	Displacement
9-10	R-Z4-05	135 degrees	2.63 m	Radial
9-11	R-D5-05	90 degrees	4.68 m	Radial
9-12	R-I5-05	240 degrees	4.68 m	Radial
9-13	R-Z6-05	135 degrees	6.20 m	Radial
9-14	R-L9-05	324 degrees	10.75 m	Radial
9-15	M-L9-05	324 degrees	10.75 m	Vertical

The plots in this section generally show a good correlation between the analysis and the PCCV SFMT response. The displacement behavior predicts the actual displacement well (to within a few percent over most of the pressure response range), and the strain contour plots indicate that failure is predicted between 0 degrees azimuth and 6 degrees azimuth, which agrees well with observations from the SFMT. The pretest axisymmetric analysis also agrees well with the SFMT response, at least for midheight of cylinder radial displacement. It is interesting to note the effects of running LST pressurization first. The LST pressure response of the vessel shows a little larger stiffness (slope of displacement versus pressure curve) than the SFMT reload. The tendon behavior plots indicate that for the baseline analysis, the first tendons rupture at elevation 5.5 m at a pressure load of 3.51 Pd (1.381 MPa).

To address the shear failure that occurred about 1.5 m from the basemat the element section forces were saved for a circumferential band of elements that straddled the 1.5 m elevation point.

9.4 Tendon Rupture Analysis

In order to simulate and examine the sequence of events that likely occurred just before vessel failure, a "tendon rupture" analysis was run where the tendon failure criteria for rupture was adjusted to occur at 2% strain. (The non-tendon rupture analysis had tendon rupture set at 4% strain, which was the mean from tendon tests. The 2% is justified by the lower bounds of the tendon tests [8].) This was incorporated into the global shell model with the distributed friction losses. Figures 9-24 and 9-25 show outer concrete maximum principal strain contours at pressure loads of 3.47, 3.49, 3.51, and 3.53 Pd (1.365, 1.372, 1.381, and 1.388 Mpa, respectively). The first failure occurs near the 0 degrees azimuth. The adjacent elements span approximately 6 degrees at this region, so this could be considered to be a measure of the precision of the location prediction. Figures 9-26 and 9-27 show deformation plots of a circumferential band of elements at an elevation of 5.4 m and 6.5 m for each of the pressure loads shown in the previous strain contour plots. These plots also confirm the presence of a significant bulge predicted at pressures larger than 3.5 Pd.

A series of hoop tendon stress versus strain history plots are shown in Figures 9-28 through 9-34. These plots show the stress/strain status of individual tendons and demonstrate analytical prediction of tendons rupturing one at a time. Each plot shows the stress-strain response of hoop tendons at elevations 1.7, 2.6, 3.7, 4.7, 5.4, 6.5, 7.8, 8.6, 9.4, and 10.6 m above the basemat at the 0 degrees azimuth. The individual plots show a snapshot of the tendon behavior at pressure loads of 3.45 Pd (1.357 MPa) in Figure 9-28, and 3.47 Pd (1.365 MPa), 3.49 Pd (1.372 MPa), 3.51 Pd (1.381 MPa), 3.53 Pd (1.388 MPa), 3.57 Pd (1.403 MPa), and 3.65 Pd (1.435 MPa) in Figure 9-34. Hoop tendon strain profiles around the circumference at elevations of 5.8, 6.1, 6.3, 6.5, 6.8, and 7.1 m are shown in Figures 9-35 through 9-41. These plots are at the same load steps as the previous hoop tendon stress strain response plots. They show the variation of hoop strain around the circumference and show how maximum strain always occurs near 0 degrees azimuth. Note that the relatively sharp strain gradients evidenced in these figures may be artifacts of the bonded tendon assumption.

Figures 9-42 and 9-43 show the shear forces and stresses, respectively, around the circumference for design load pressure multiples of 3.05, 3.25, 3.45, and 3.65. It is clear that there are elevated shear stresses at the buttresses and between azimuths 20 to 50 degrees.

The progression of tendon stress-strain, Figures 9-28 through 9-34, is also summarized in Table 9-2.

Table 9-2. Peak Strain in Hoop Tendons from SFMT Rupture Analysis at Multiples of Design Pressure

Tendon Elev. (m)	3.45	3.47	3.49	3.51	3.53	3.57	3.65
1.7	.00771	.00775	.00780	.00784	.00789	.00812	.00977
2.6	.00886	.00898	.00914	.00930	.00951	.010343	.01547
3.7	.01121	.01176	.01238	.01313	.01411	.01807	.05976
4.7	.01346	.01420	.01506	.01621	.01836	.02451	.08797
5.4	.01702	.01807	.01928*	.02136	.03112	.06738	.12572
6.5	.01685	.01788	.01909	.02293	.03715	.06734	.12342
7.8	.01082	.01125	.01176	.01238	.01323	.01580	.04466
8.6	.01027	.01065	.01109	.01158	.01219	.01385	.02163
9.4	.00942	.00976	.01008	.01046	.01090	.01203	.01642
10.6	.00812	.00833	.00854	.00880	.00906	.00969	0.0117

* Approaching first rupture (i.e., tendon rupture redefined to be $\varepsilon = 0.02$)

The plots and table show that first rupture initiates at elev. 5.4 m, P = 3.49 Pd, but then quickly spreads up to elev. 6.5 m by 3.51 Pd. By 3.57 Pd, rupture spreads down to 4.7 m, and by 3.65 Pd, it has spread to as low as elev. 3 m and as high as 8.6 m.

9.5 Conclusions of the SFMT Analysis

The SFMT posttest analysis has shown that good simulation of the PCCV global behavior up through and including tendon rupture failures is possible with a 3D shell model. Although the model is still very complex, the shell element simplification allowed model development and analysis in just a few months and reasonable run-time, i.e., a couple of hours rather than days on a modern workstation. The main limitations of the shell model are lack of local liner strain concentration prediction and lack of accuracy in the predictions of local wall-base-juncture behavior. Significant accuracy in global behavior prediction did not seem to be lost when a bonded tendon assumption was used, but some method of accounting for initial friction losses was still desirable.

It is clear from the video coverage of the test that the rupture occurred near cylinder midheight and near 6 degrees azimuth. The SFMT analysis model provides additional insight as to how this failure likely developed. Prior to P = 3 Pd the 0 to 6 degrees azimuth location, elev. 5 m was behaving similarly to other azimuths away from penetrations. After 3.2 Pd, a few hot spots emerged around this elevation: a) edge of E/H wall embossment, b) edges of M/S penetration, and c) this ~ 0 degree location. In each case, the cause of the hot spot appears to be the location's position relative to a stiffness discontinuity. In the case of the 0 degree location, the discontinuity is a step down in inner and outer hoop rebar area totaling 38% (step-down from alternating D19, D16 bars to a pattern of 1D16/3D13 bars). Then at 3.49 Pd, while the other locations also showed elevated strain, the wall and tendon strain at the 0 to 6 degree location was the highest, and a tendon ruptures. Once this occurs, the analysis shows the neighboring tendons rupturing and the deformations spread quickly at this azimuth. It is interesting to note that the analysis predicts the secondary tendon ruptures spread upward. Shortly after the first rupture at 5.4 m, analysis predicts the tendon ruptures to spread up through 6.5 m. From review of the test video, this appears to also agree with observations. By 3.65 Pd, the analysis shows rupture to have spread over a vertical line spanning up to 6 m. This also agrees with observations.

After wall rupture, a secondary event occurred in the SFMT; the through-wall failure around the circumference of the wall at about 1.5 m elevation. While it is difficult to say at what azimuth this failure initiated, it seems clear that this was a shear or combined shear/flexural failure of the wall. The plotting of analysis shear results (force and stress) in Figures 6-42 and 6-43 show that such failure may have initiated at the buttresses (evidenced by the high shear stresses predicted there) and then "unzipped." Upon reviewing the plans again, it can be noted that at elev. 1.60 m there is a step-down in vertical rebar from D19 to D16, which may have focused this shear failure plane. Moreover, at the buttresses, the outer vertical rebar step down occurs slightly lower: at 1.22 m there is a change from a total of 19D19 bars down to a total of 10D19 bars placed within the buttress. This may explain why the circumferential failure (see Figure 9-4) ran through the buttresses at a lower elevation than the rest of the wall. As a point of comparison, the shear failure threshold calculation performed in the pretest work [1] is compared to the demand (both pretest axisymmetric and posttest SFMT) in Figure 9-44. This figure shows that without the trigger of rupture of the vessel, the capacity (a modified compression field theory calculation shown here as an average shear stress through the wall) exceeds the demand throughout the pressurization. But with the triggering event of a massive wall rupture, one of two mechanisms may have caused shear demand to exceed capacity.

1. Large deformation of the wall opening, creating large rotations near the base of the wall, would crush the outer concrete of the flexural section and thereby reduce the capacity (as would be predicted by modified compression field theory or other methods);
2. The water jet-induced momentum imbalance would cause added shear demand; using beam theory, this would create tangential shear at some azimuths that would be maximum at the buttresses; such shear acting in combination with the already high radial shear stresses could have increased shear stress demand enough to induce the shear failure.

Both of these potential mechanisms are illustrated in Figure 9-44.

The SFMT posttest analysis showed that reasonable simulation of the PCCV global behavior through and including tendon rupture was possible with a 3D shell model. The main limitations of the shell model were lack of local liner strain concentration prediction and lack of accuracy in the predictions of local wall-base-juncture behavior. However, significant accuracy in global behavior prediction was not lost when a bonded tendon assumption was used. Analysis considering initial tendon friction did provide slightly closer correlation to the test than analysis without considering initial friction losses. The SFMT model provided additional insight as to how the structural failure likely developed. Near the 0-6 degrees azimuth of the cylinder, there is a discontinuity of a step-down in inner and outer hoop rebar area of 38% (step-down from alternating D19, D16 bars to a pattern of 1D16/3D13 bars). Then at 3.49 Pd, the wall and tendon strain at the 0-6 degrees location is a little higher than all other azimuths, and a tendon rupture occurs. After this, the analysis shows neighboring tendons rupturing and the deformations spreading quickly along this azimuth. Shortly after the first rupture at 5.4 m elevation, the analysis predicted the tendon ruptures to spreading up through 6.5 m. From a review of the test video, this appears to agree with observations. By 3.65 Pd, the analysis shows rupture to have spread over a vertical line spanning about 6 m. This also agrees with observations. After wall rupture, a secondary event occurred in the SFMT: through-wall failure around the circumference of the wall at about 1.5 m elevation. While it is difficult to say at what azimuth this failure initiated, it seems clear that this was a shear or combined shear/flexural failure of the wall. The shell model provided only limited information for studying this phenomena, but it did provide the radial shear demands at all azimuths, which indicated that shear demands were highest at the buttresses. As with the vertical failure line in the cylinder, the circumferential failure line near the bottom of the cylinder appears to have occurred at or near a step-down in reinforcement.

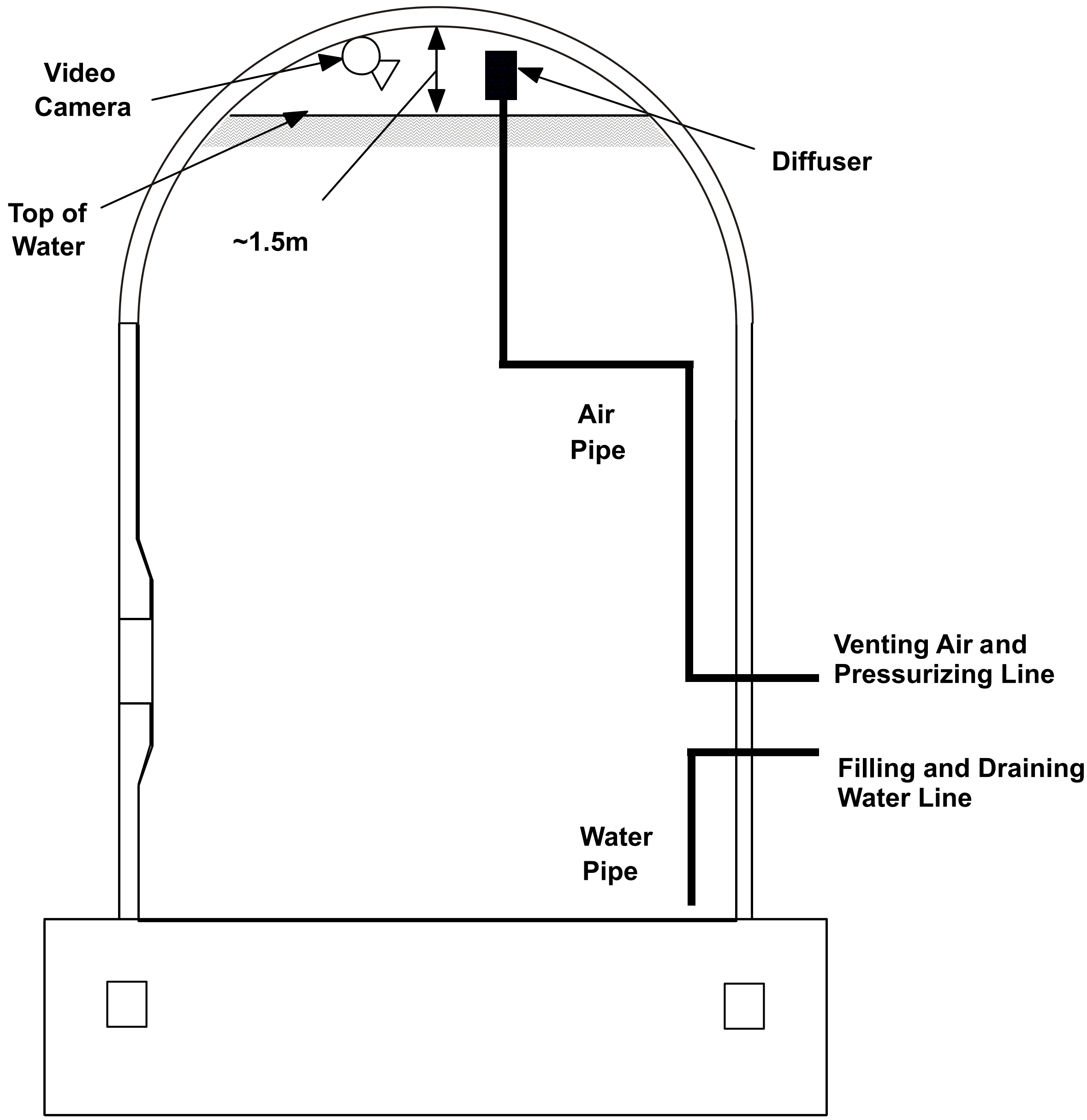

Figure 9-1. PCCV SFMT Pressurization Configuration

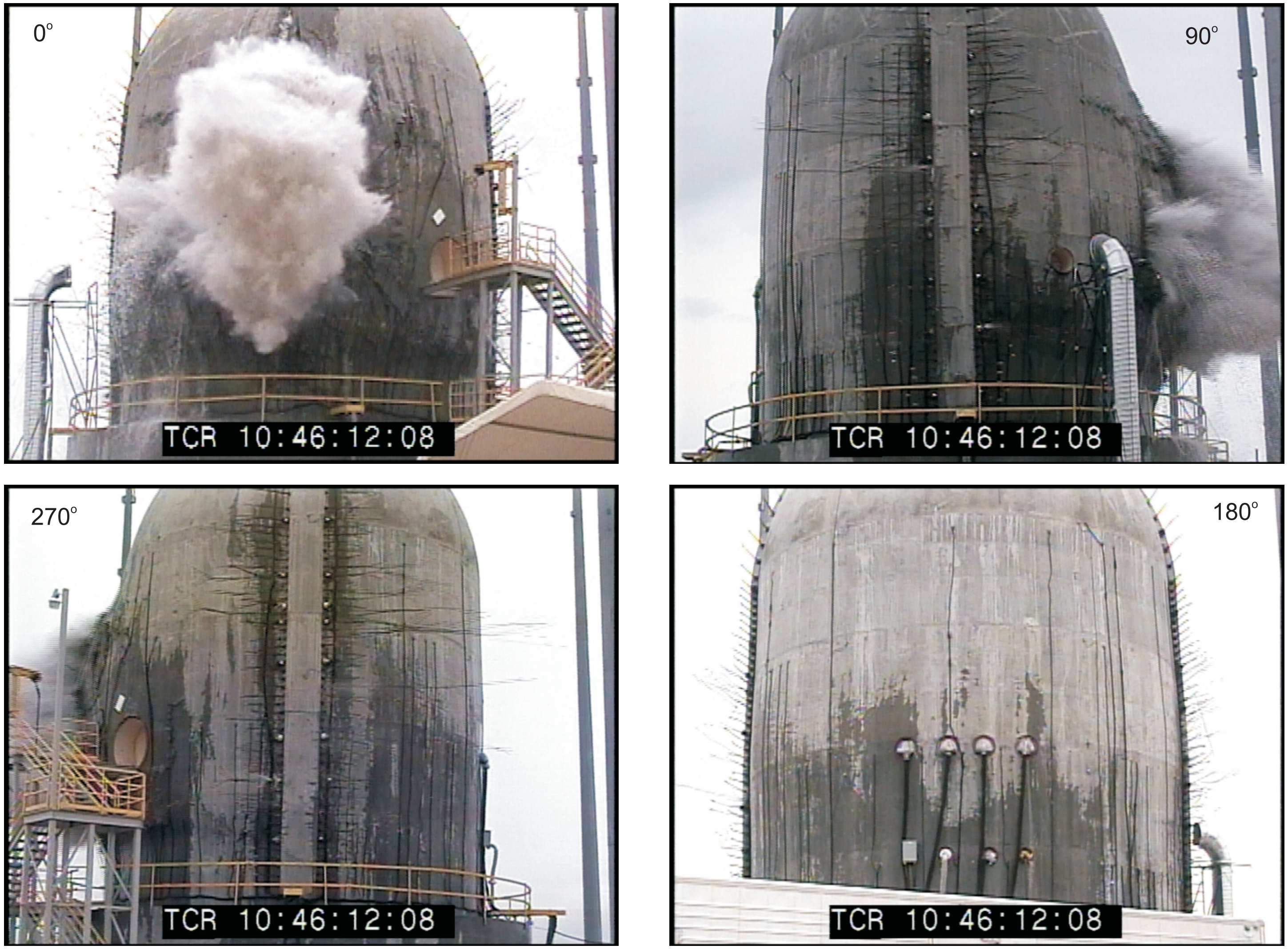

Figure 9-2. PCCV SFMT: Photograph of Exterior of PCCV at Instant of Failure

Figure 9-3. PCCV SFMT: Photograph of Exterior of PCCV After Test

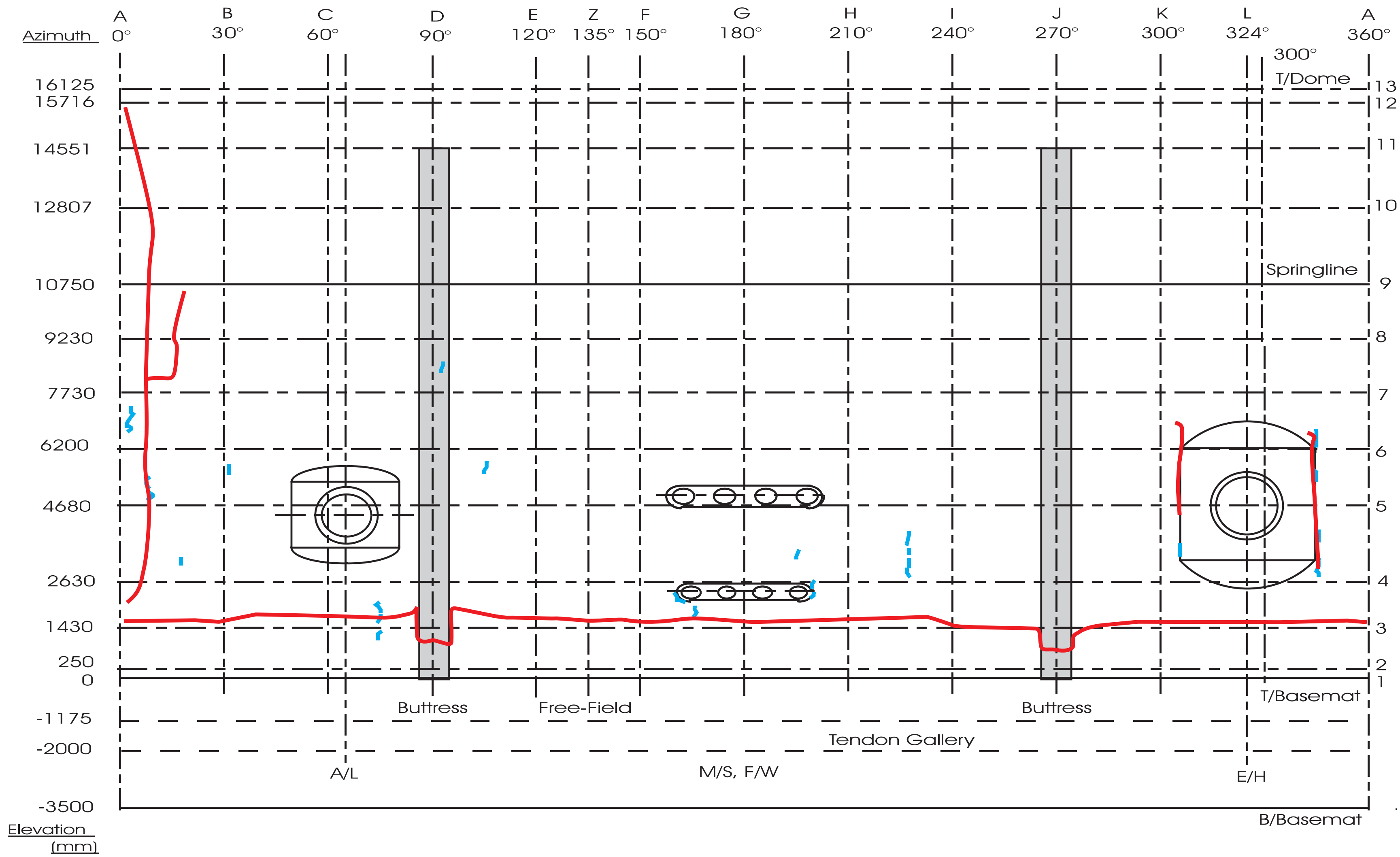

Figure 9-4. PCCV SFMT Rupture Map

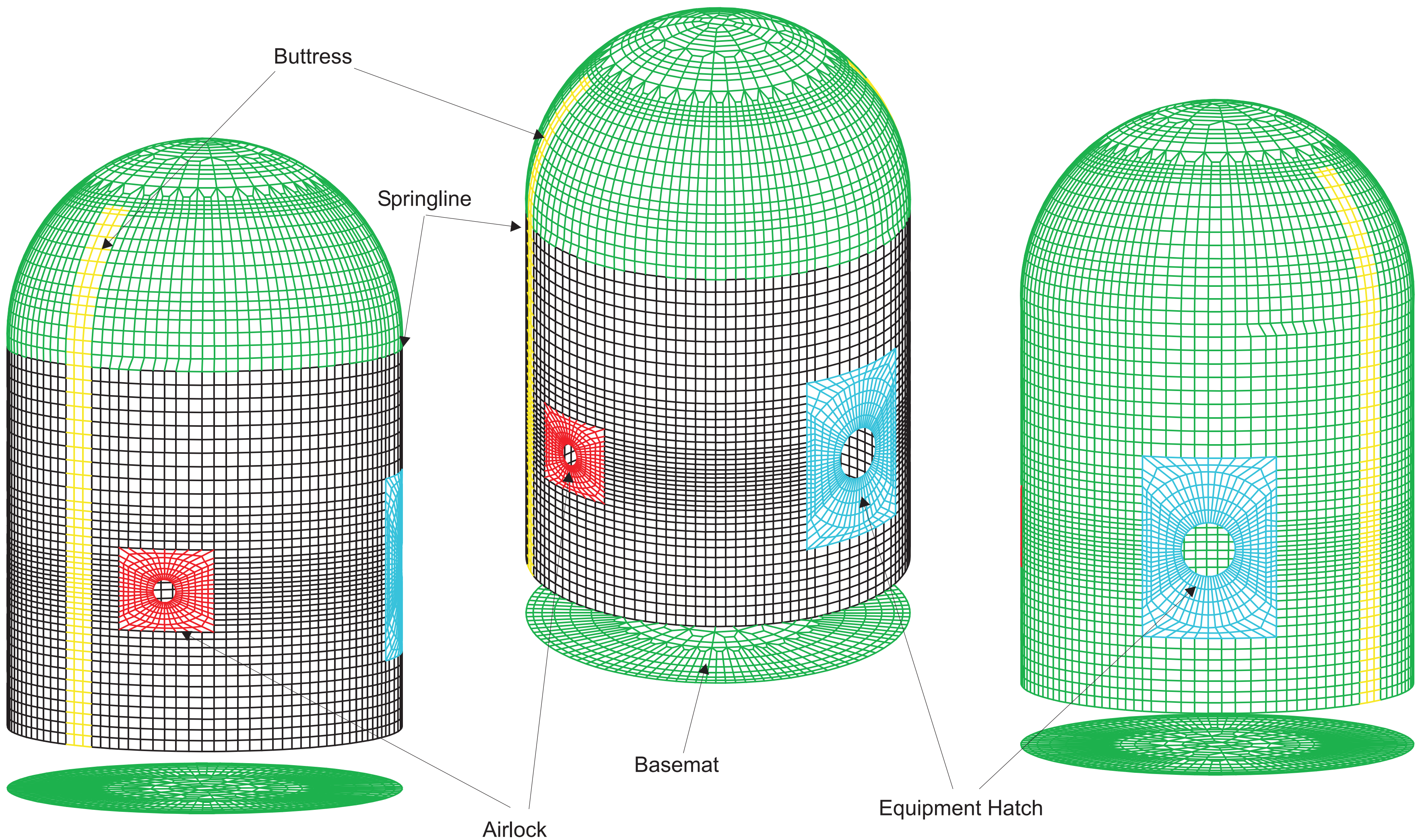

Figure 9-5. PCCV SFMT, 3D Global Shell Model

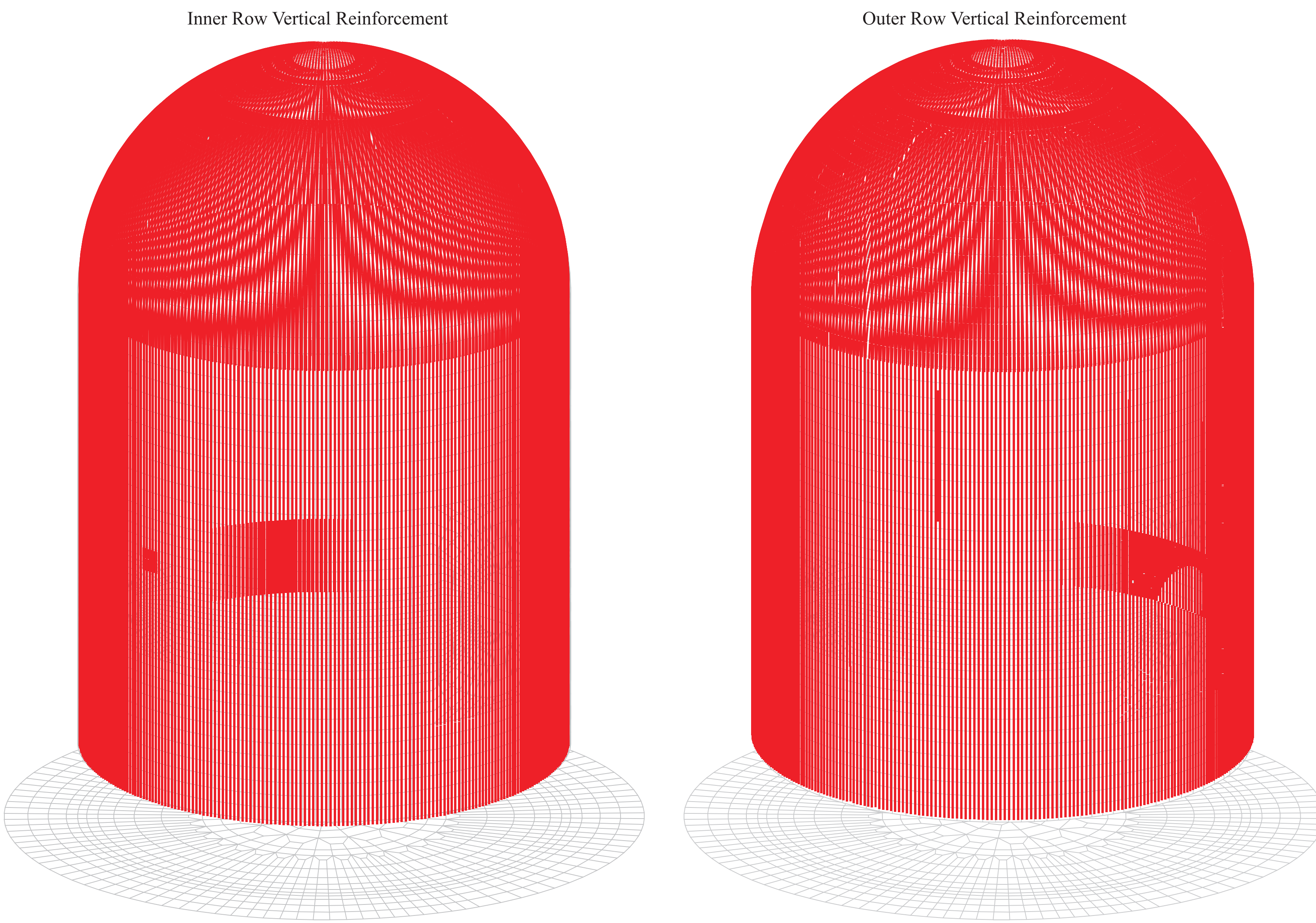

Figure 9-6. PCCV SFMT 3D Global Shell Model, Reinforcement Subelements
Vertical Reinforcement in Cylinder and Dome

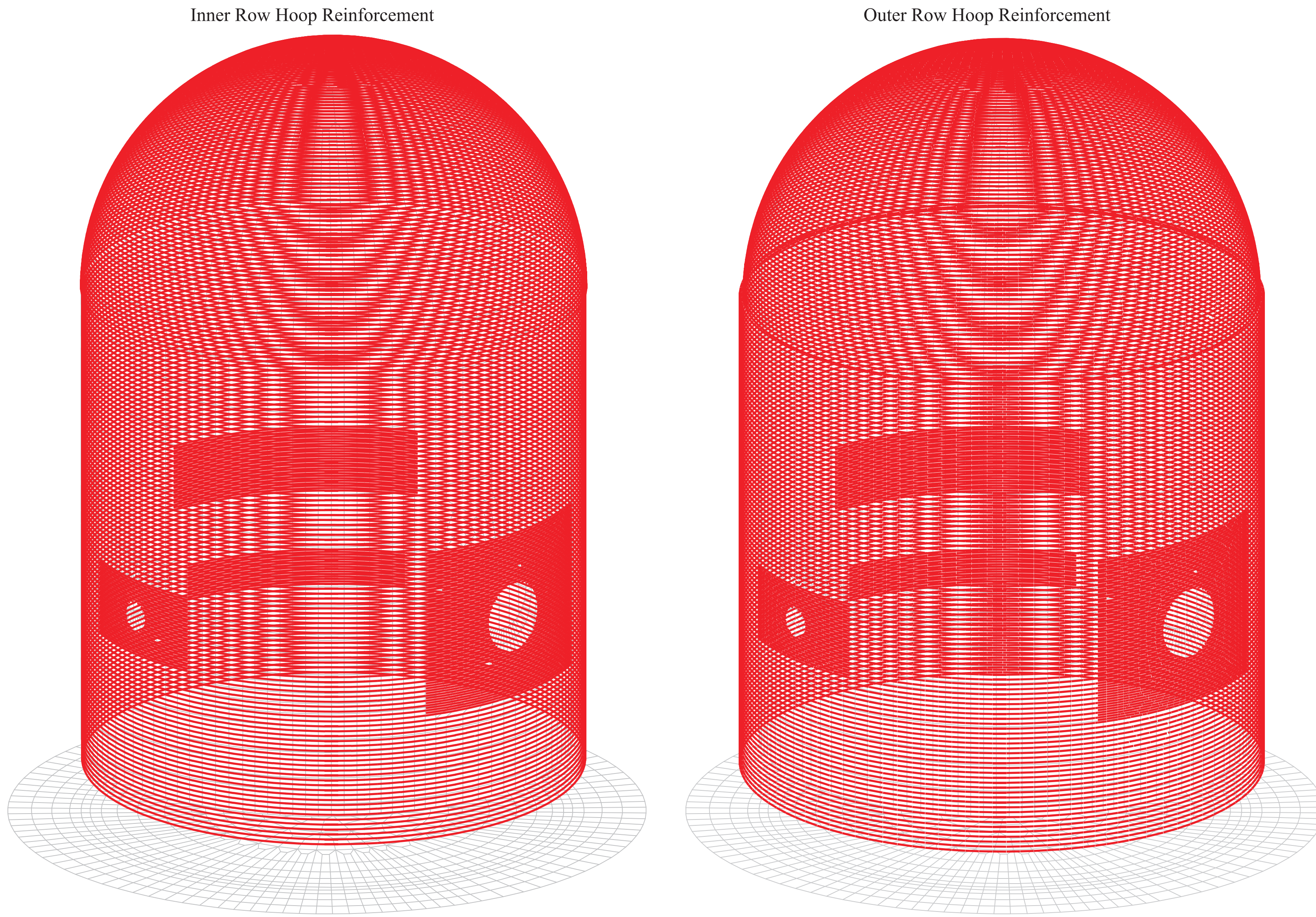

Figure 9-7. PCCV SFMT 3D Global Shell Model, Reinforcement Subelements
Hoop Reinforcement in Cylinder and Dome

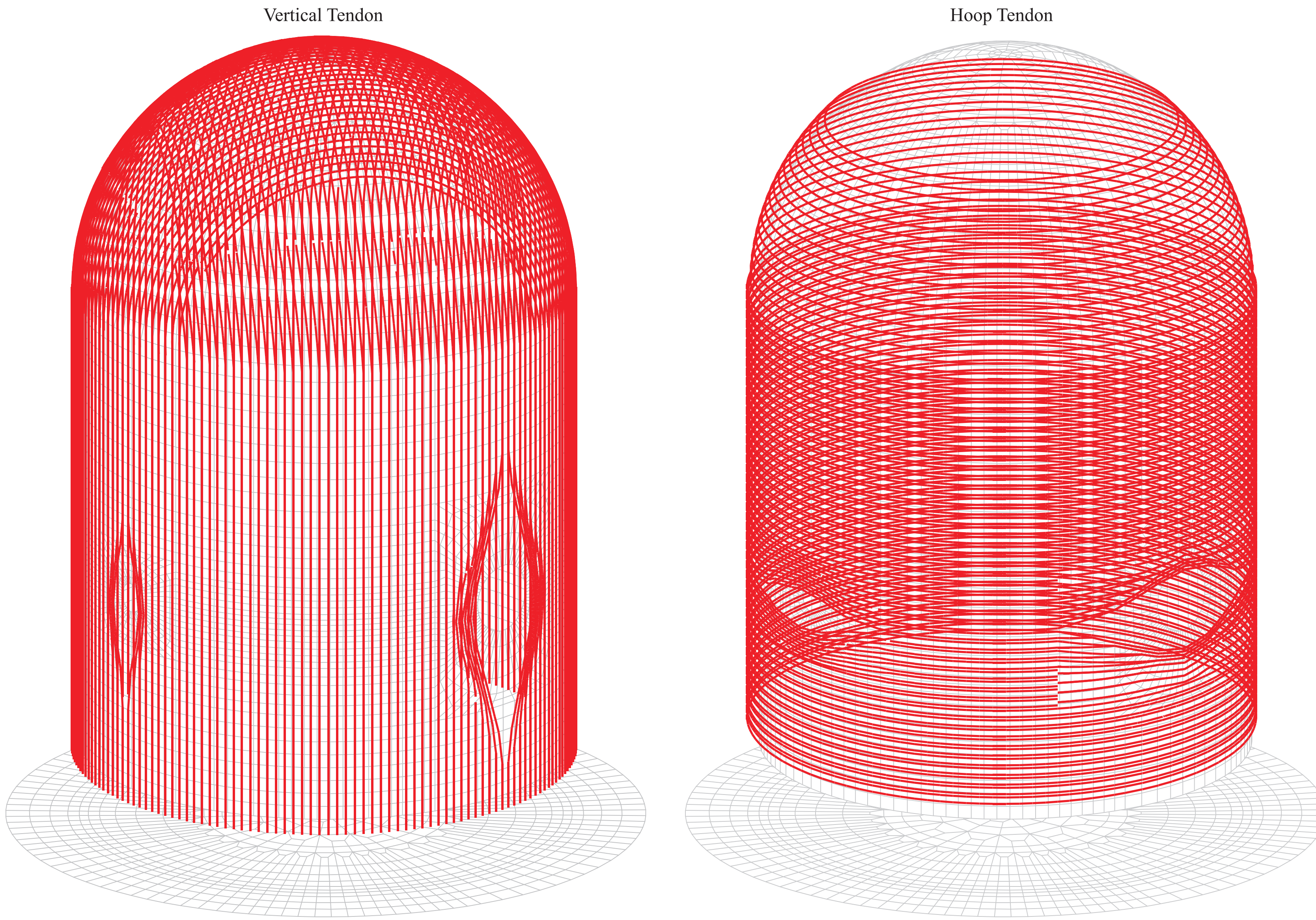

Figure 9-8. PCCV SFMT 3D Global Shell Model, Reinforcement Subelements
Prestress Tendons in Cylinder and Dome

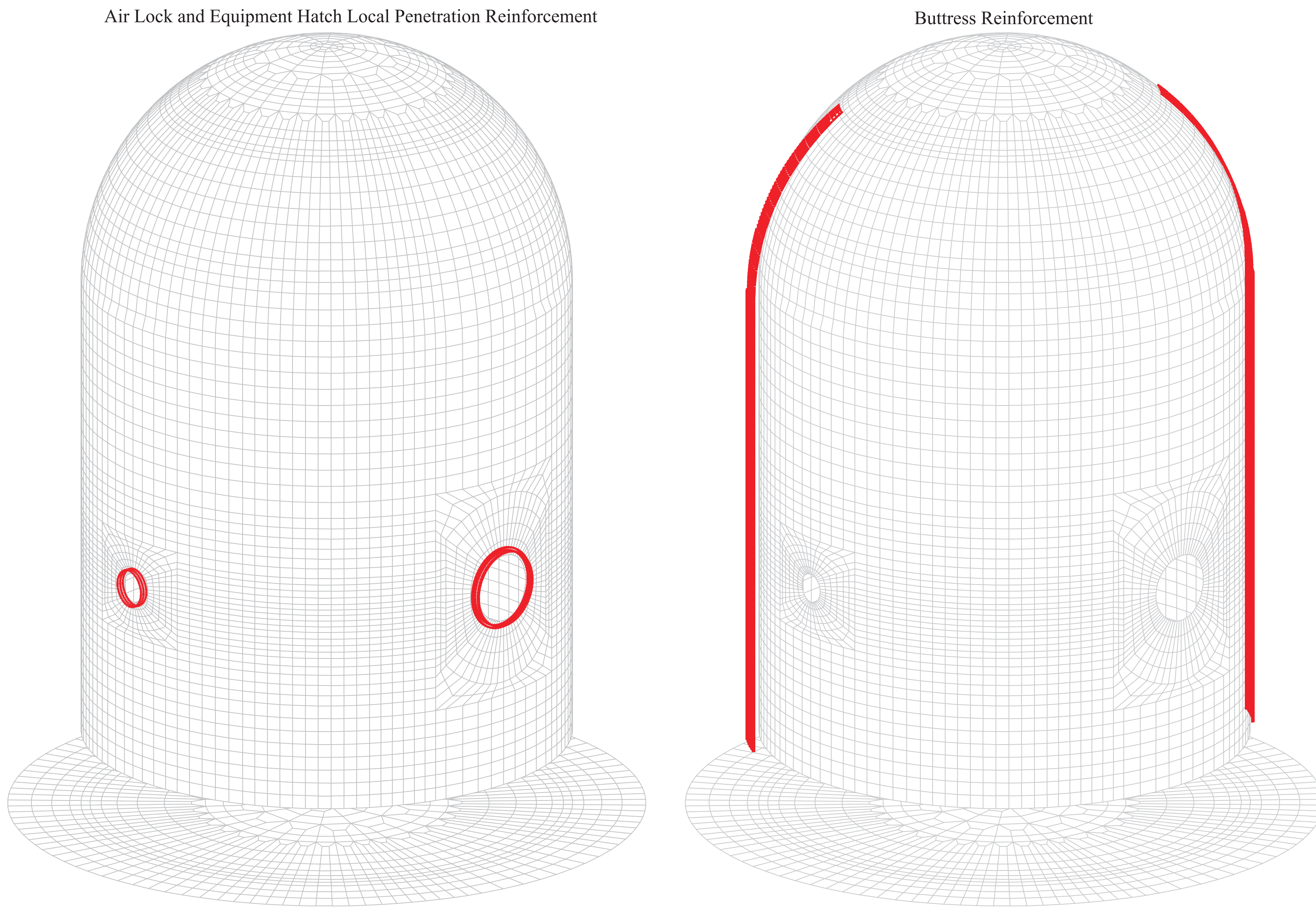

Figure 9-9. PCCV SFMT 3D Global Shell Model, Reinforcement Subelements
Buttress and Local Penetration Reinforcement

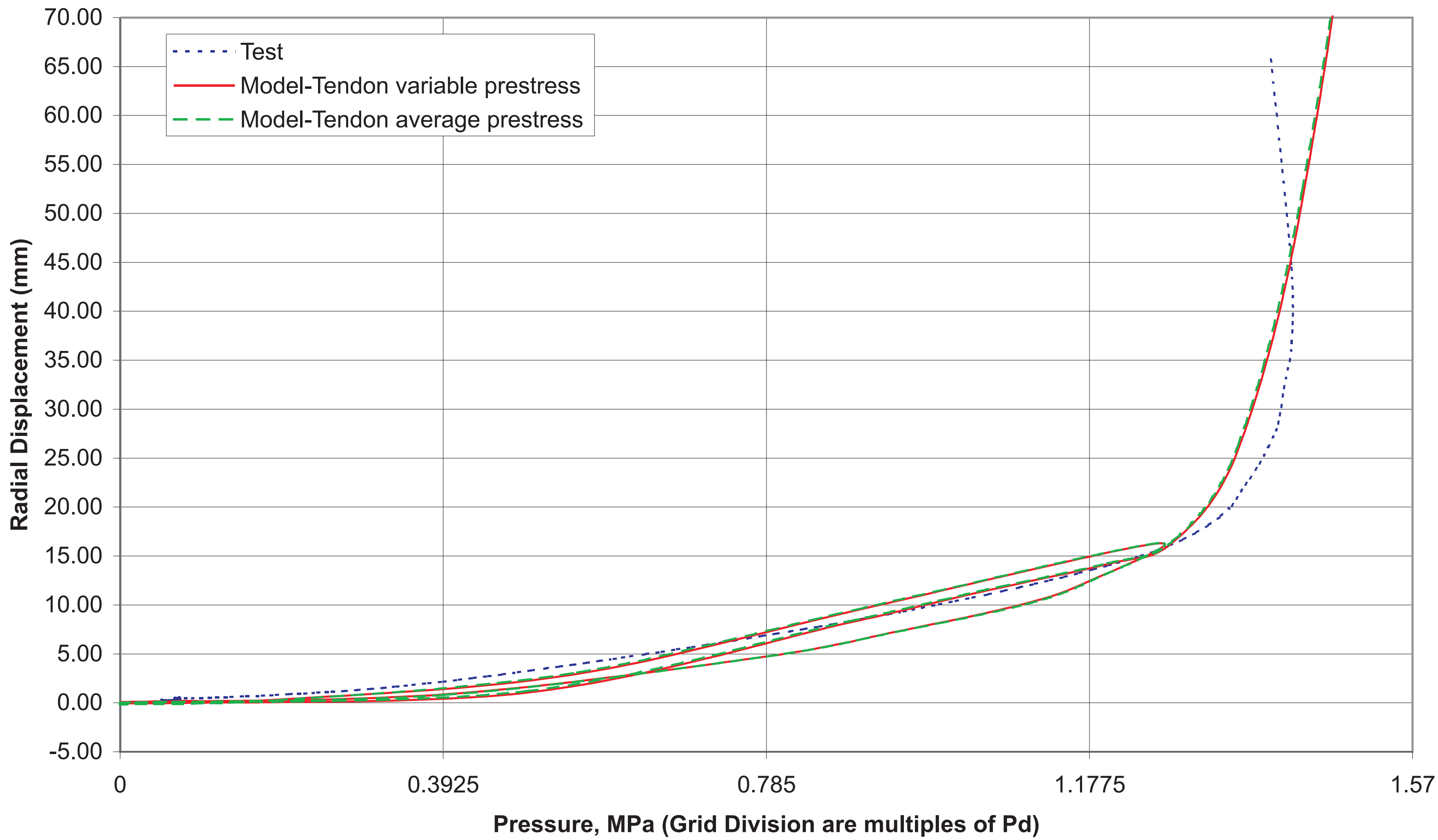

Figure 9-10. PCCV SFMT, 3D Global Shell Model - Gage R-Z4-05 Comparison
Radial Displacement, 135 Degrees, Elevation 2.63 m

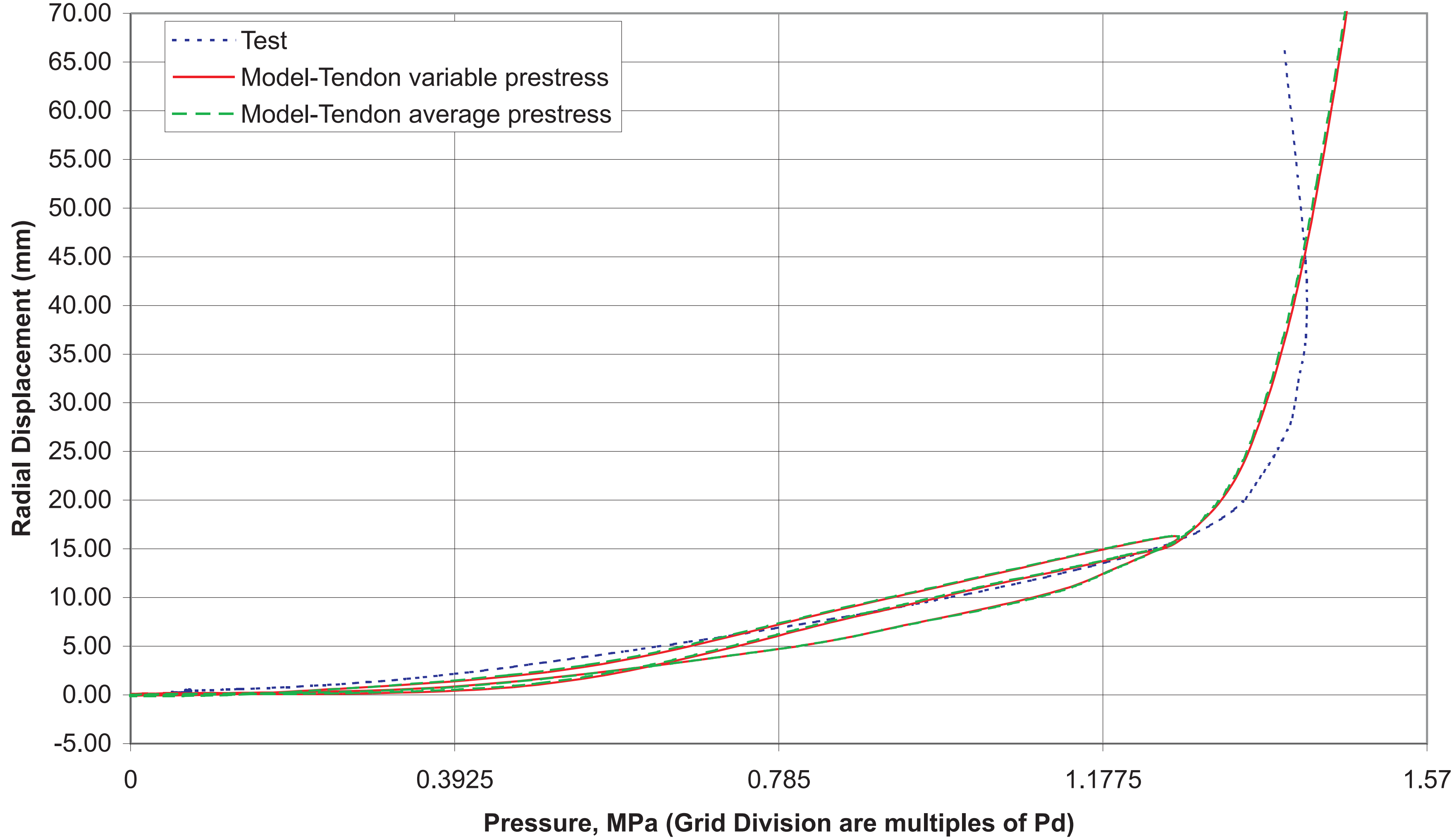

Figure 9-11. PCCV SFMT, 3D Global Shell Model - Gage R-D5-05 Comparison
Radial Displacement, 90 Degrees Buttress, Elevation 4.68 m

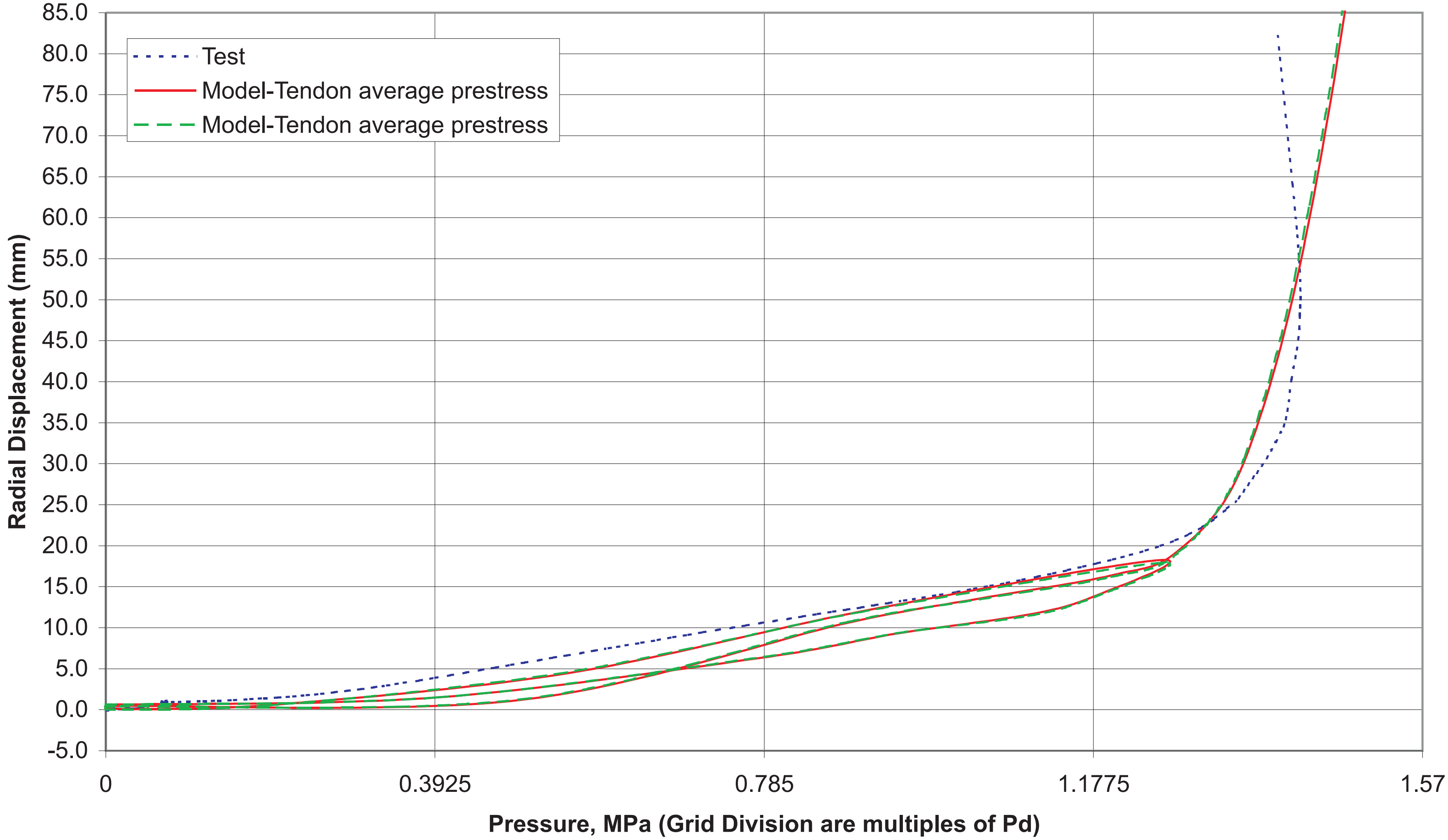

Figure 9-12. PCCV SFMT, 3D Global Shell Model - Gage R-15-05 Comparison
Radial Displacement, 240 Degrees, Elevation 4.68 m

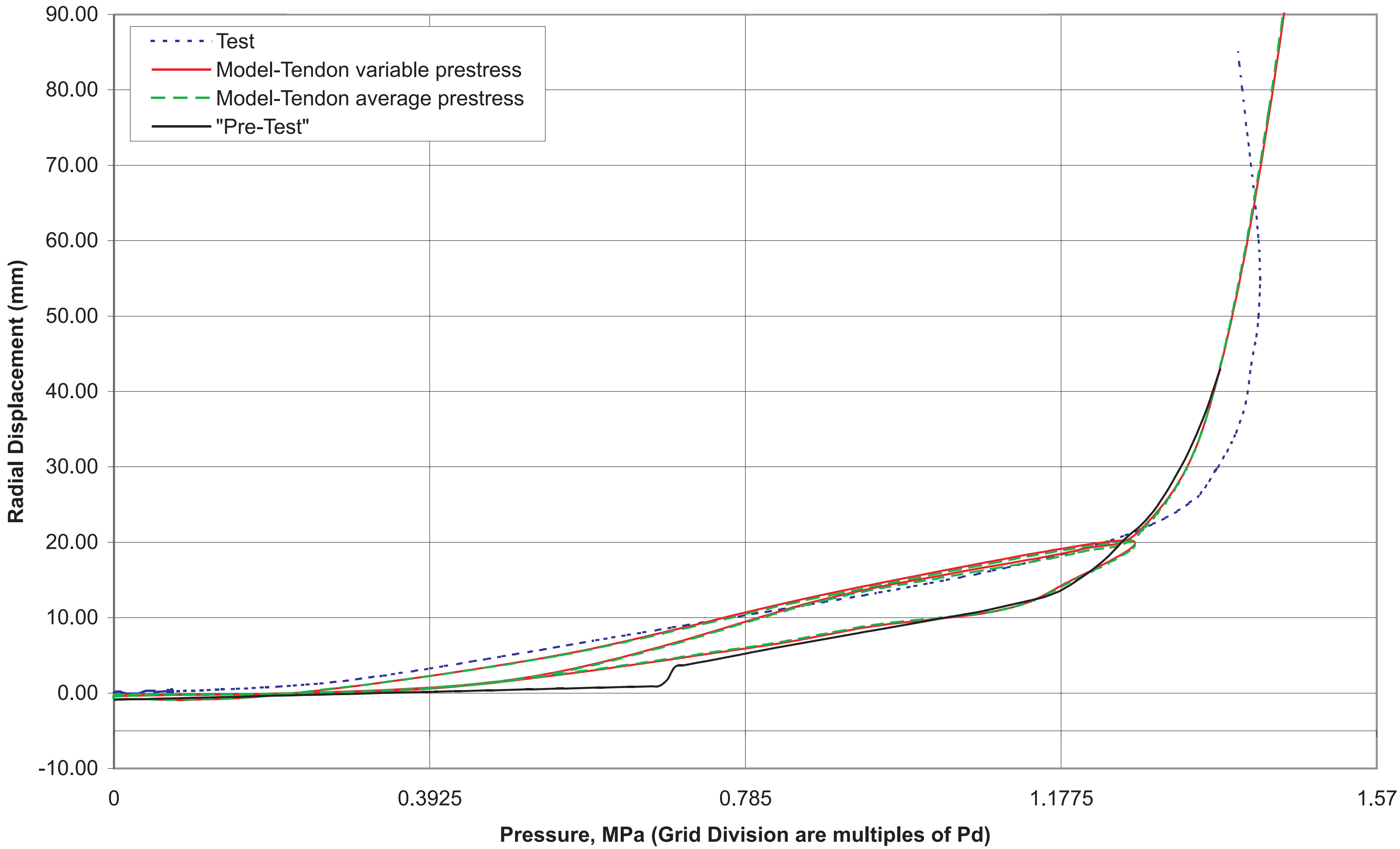

Figure 9-13. PCCV SFMT, 3D Global Shell Model - Gage R-Z6-05 Comparison
Radial Displacement, 135 Degrees, Elevation 6.20 m

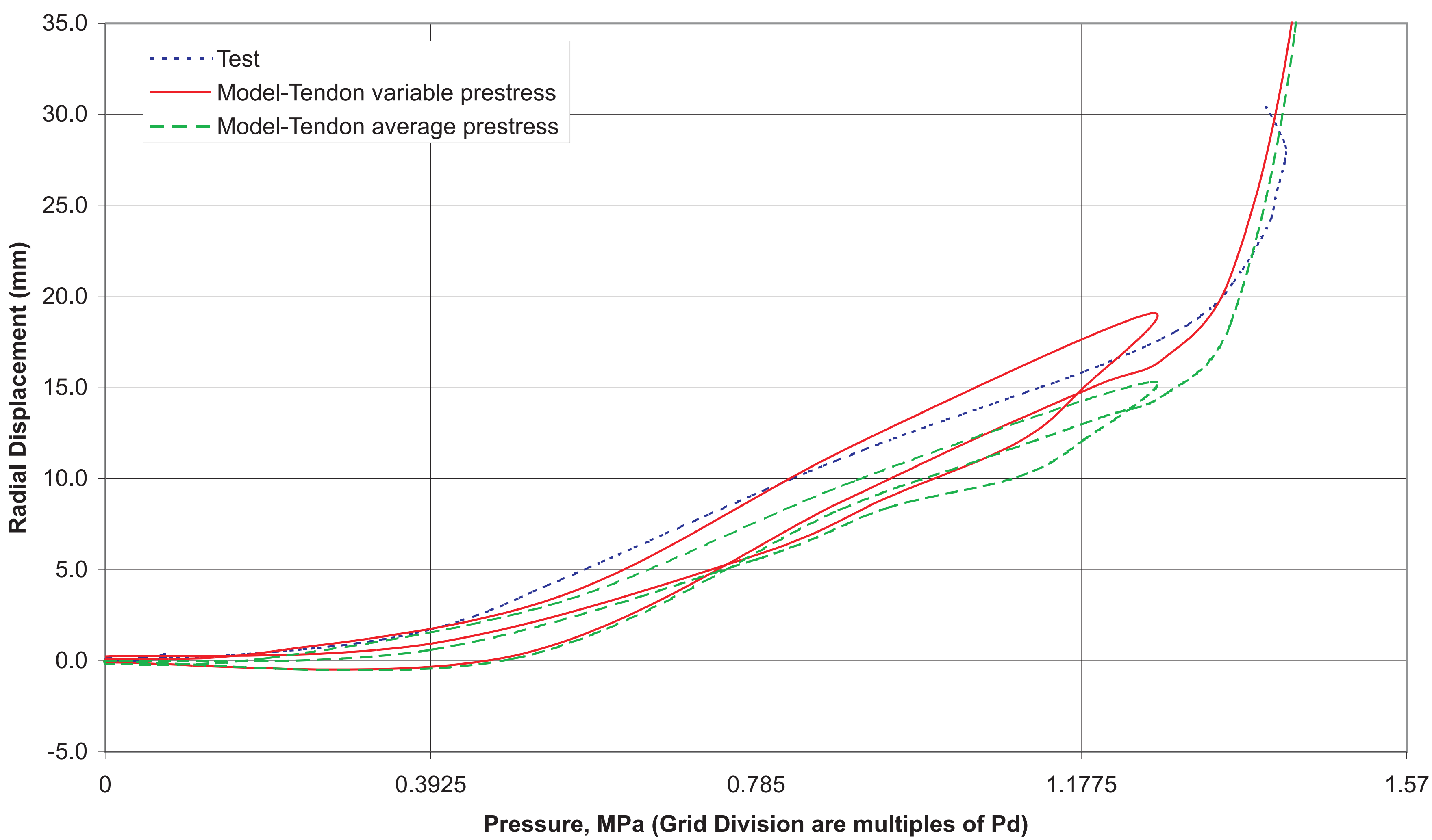

Figure 9-14. PCCV SFMT, 3D Global Shell Model - Gage R-L9-05 Comparison Radial Displacement, 324 Degrees, Elevation 10.75 m Springline

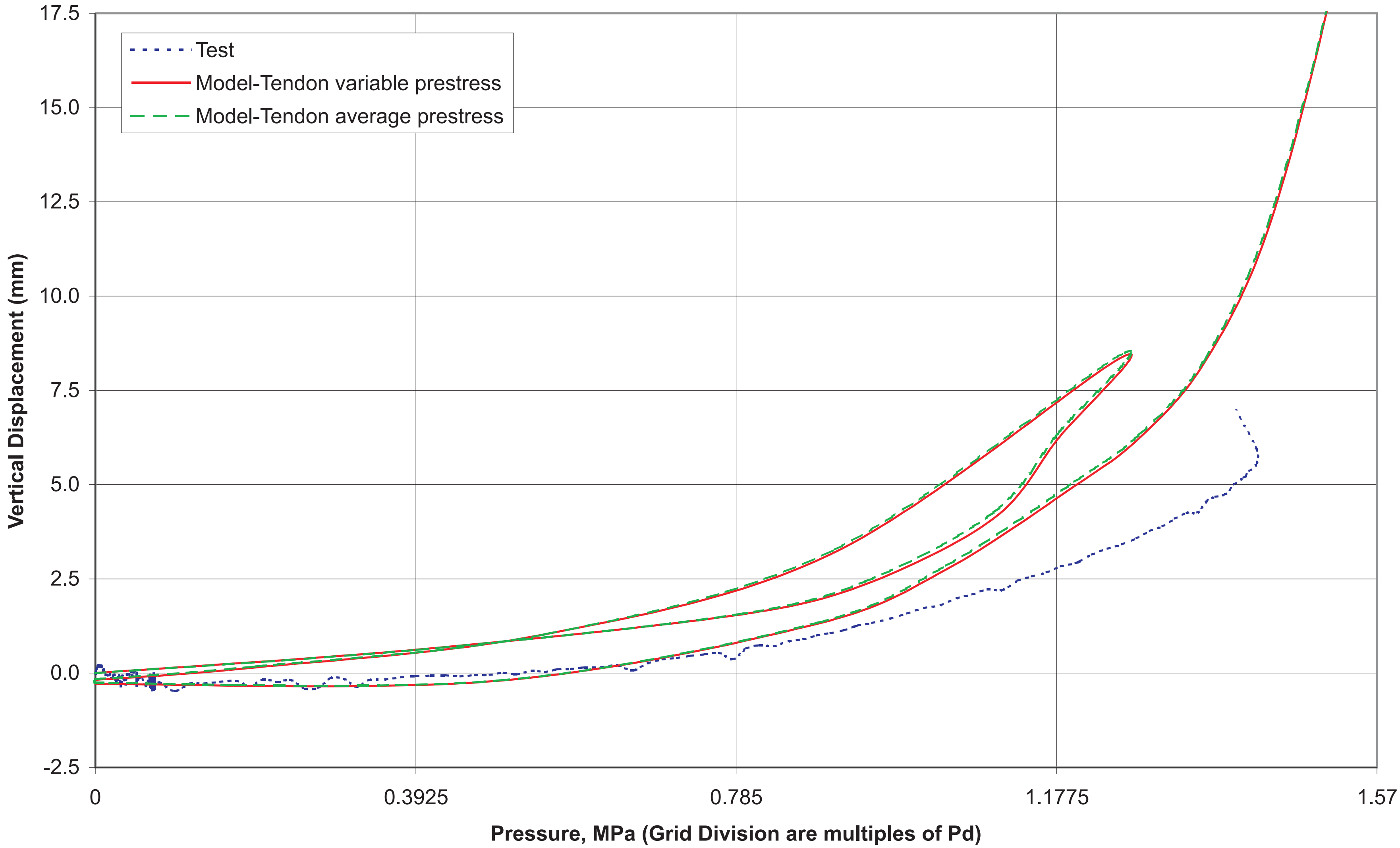

Figure 9-15. PCCV SFMT, 3D Global Shell Model - Gage M-L9-05 Comparison
Vertical Displacement, 324 Degrees, Elevation 10.75 m Springline

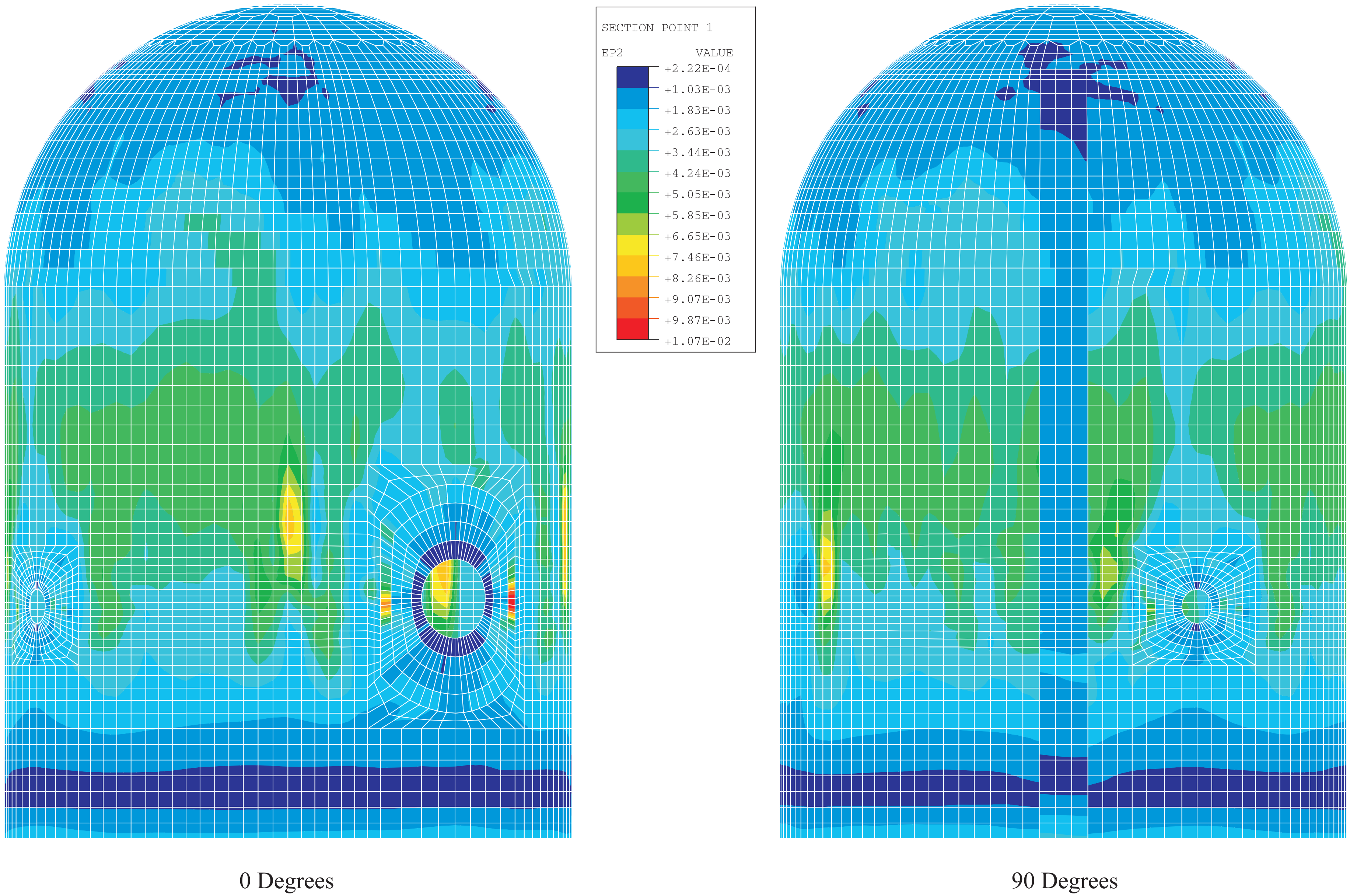

Figure 9-16. PCCV SFMT, 3D Global Shell Model. Liner Maximum Principal Strain. For Azimuth: 0 and 90 Degrees at 1.279 MPa (3.25 Pd)

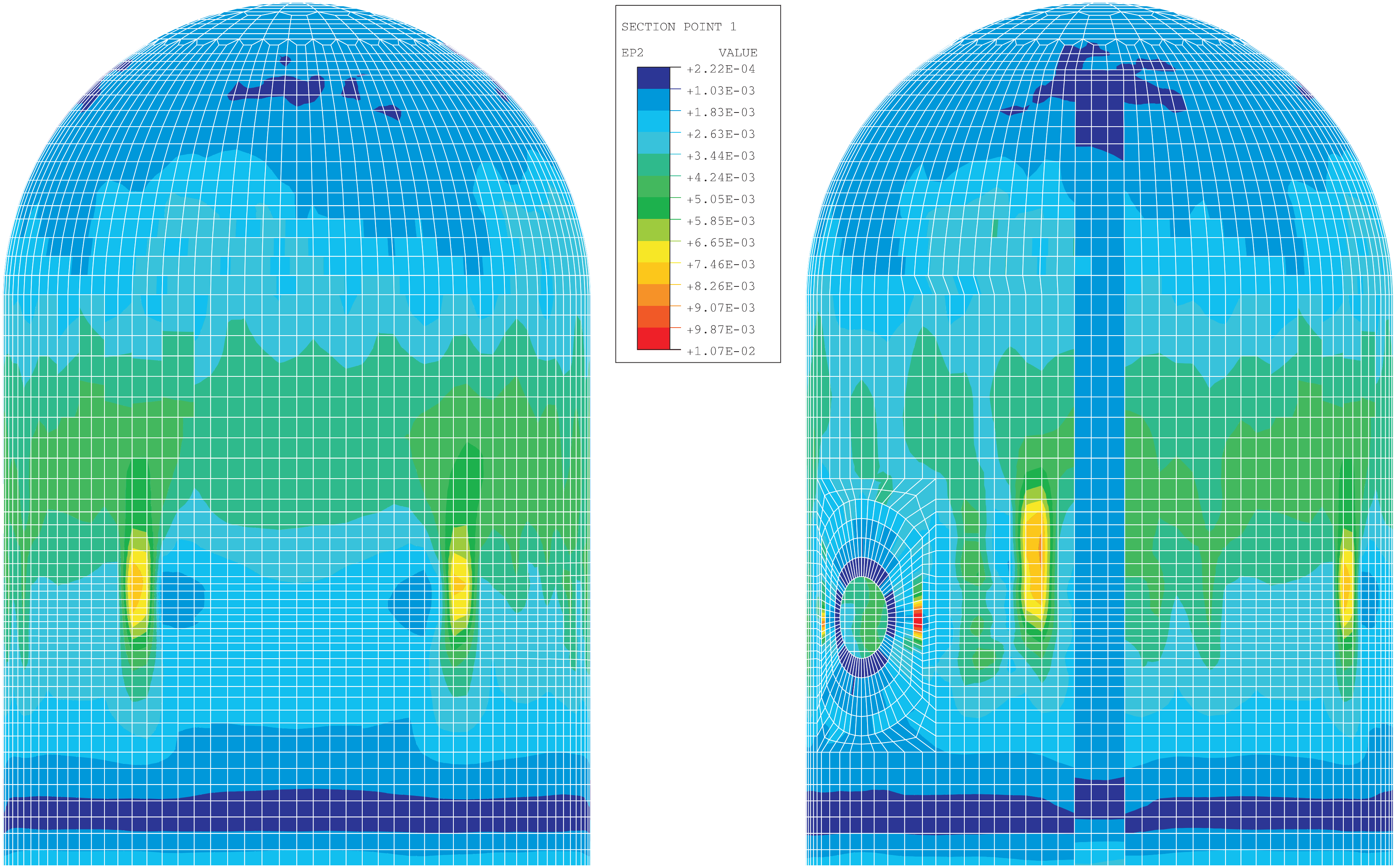

180 Degrees

270 Degrees

Figure 9-17. PCCV SFMT, 3D Global Shell Model. Liner Maximum Principal Strain.
For Azimuth: 180 and 270 Degrees at 1.279 MPa (3.25 Pd)

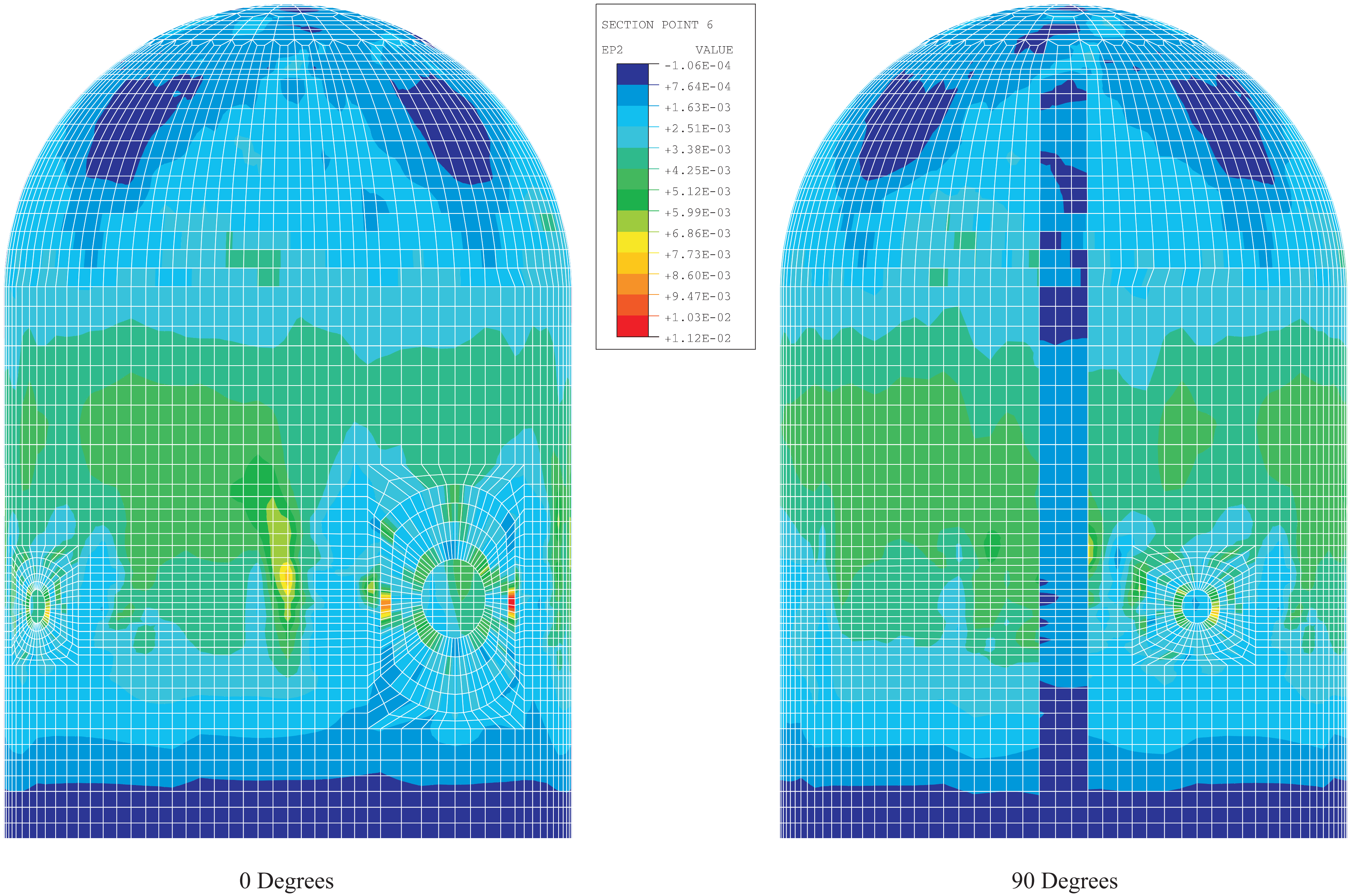

Figure 9-18. PCCV SFMT, 3D Global Shell Model. Concrete Maximum Principal Strain. For Azimuth: 0 and 90 Degrees at 1.279 MPa (3.25 Pd)

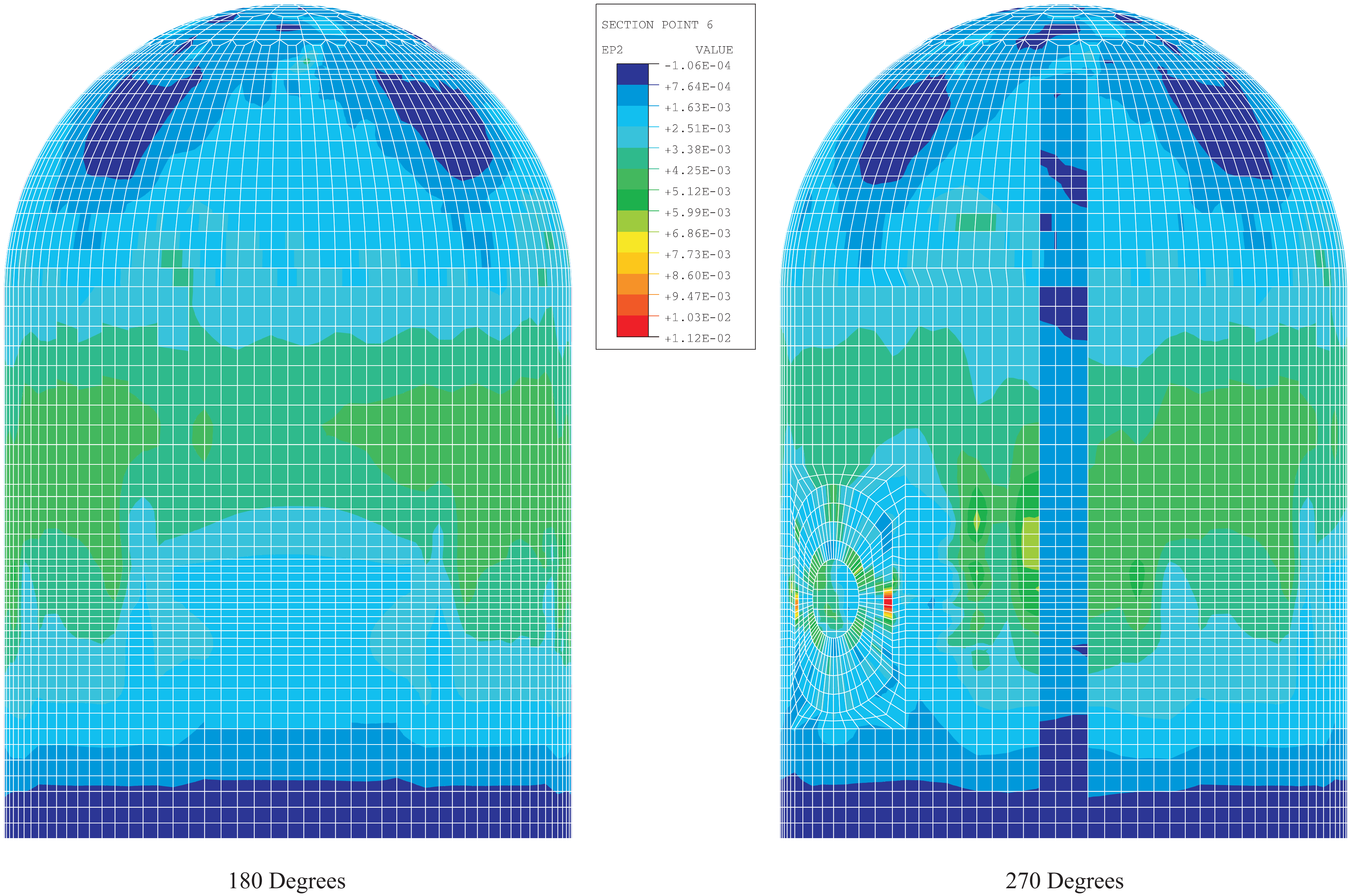

Figure 9-19. PCCV SFMT, 3D Global Shell Model. Concrete Maximum Principal Strain.
For Azimuth: 180 and 270 Degrees at 1.279 MPa (3.25 Pd)

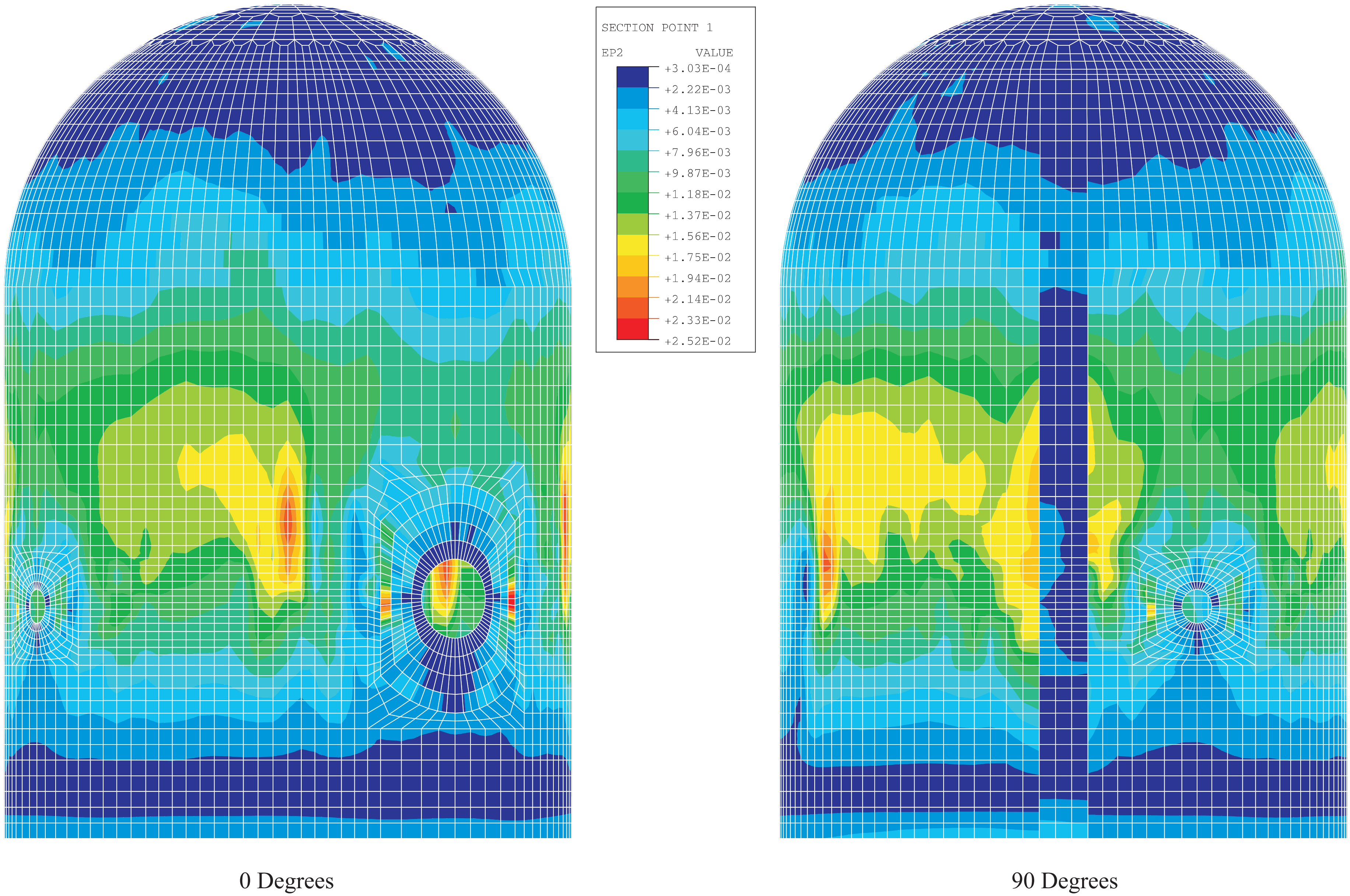

Figure 9-20. PCCV SFMT, 3D Global Shell Model. Liner Maximum Principal Strain.
For Azimuth: 0 and 90 Degrees at 1.437 MPa (3.65 Pd)

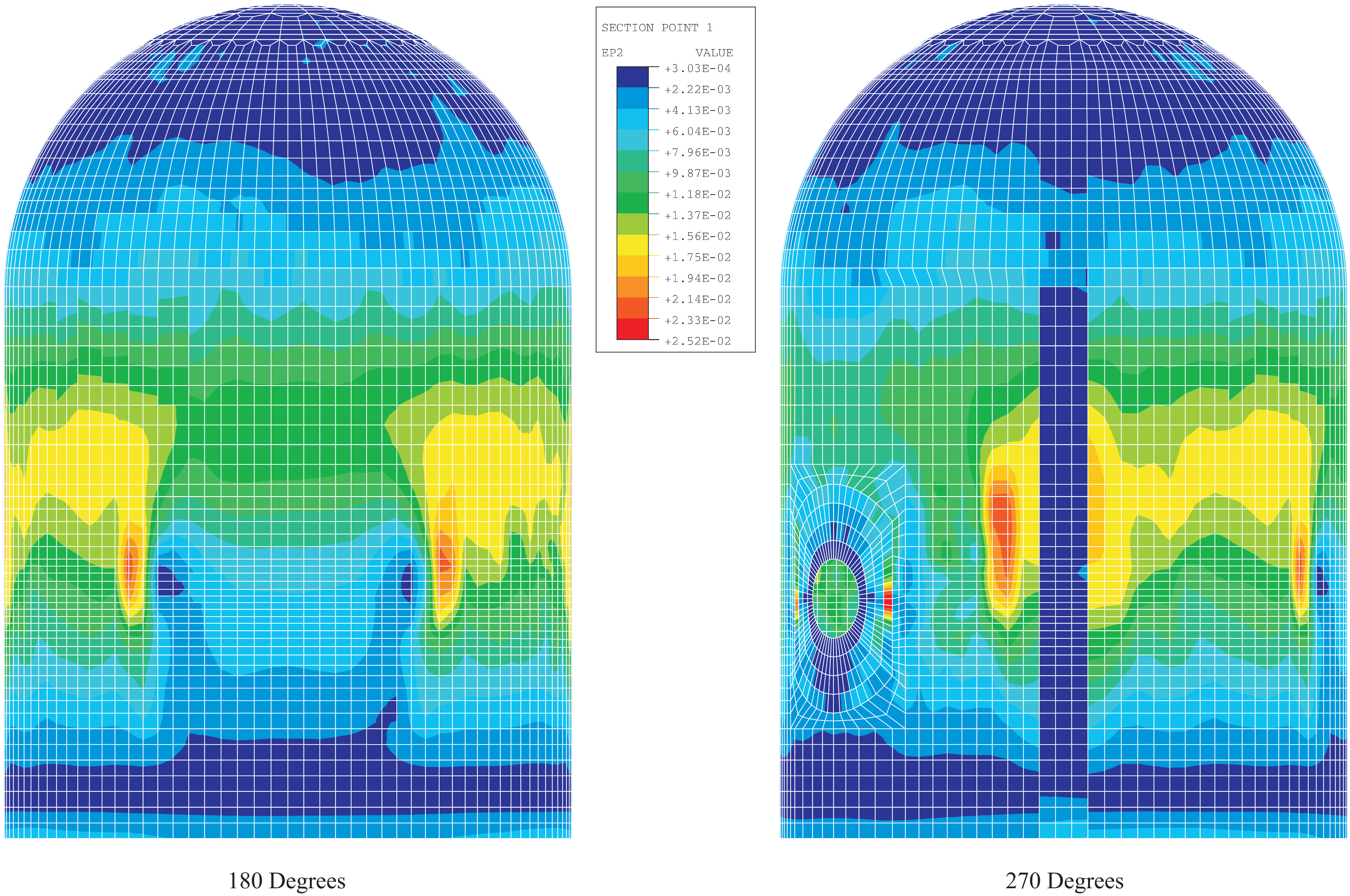

Figure 9-21. PCCV SFMT, 3D Global Shell Model. Liner Maximum Principal Strain.
For Azimuth: 180 and 270 Degrees at 1.437 MPa (3.65 Pd)

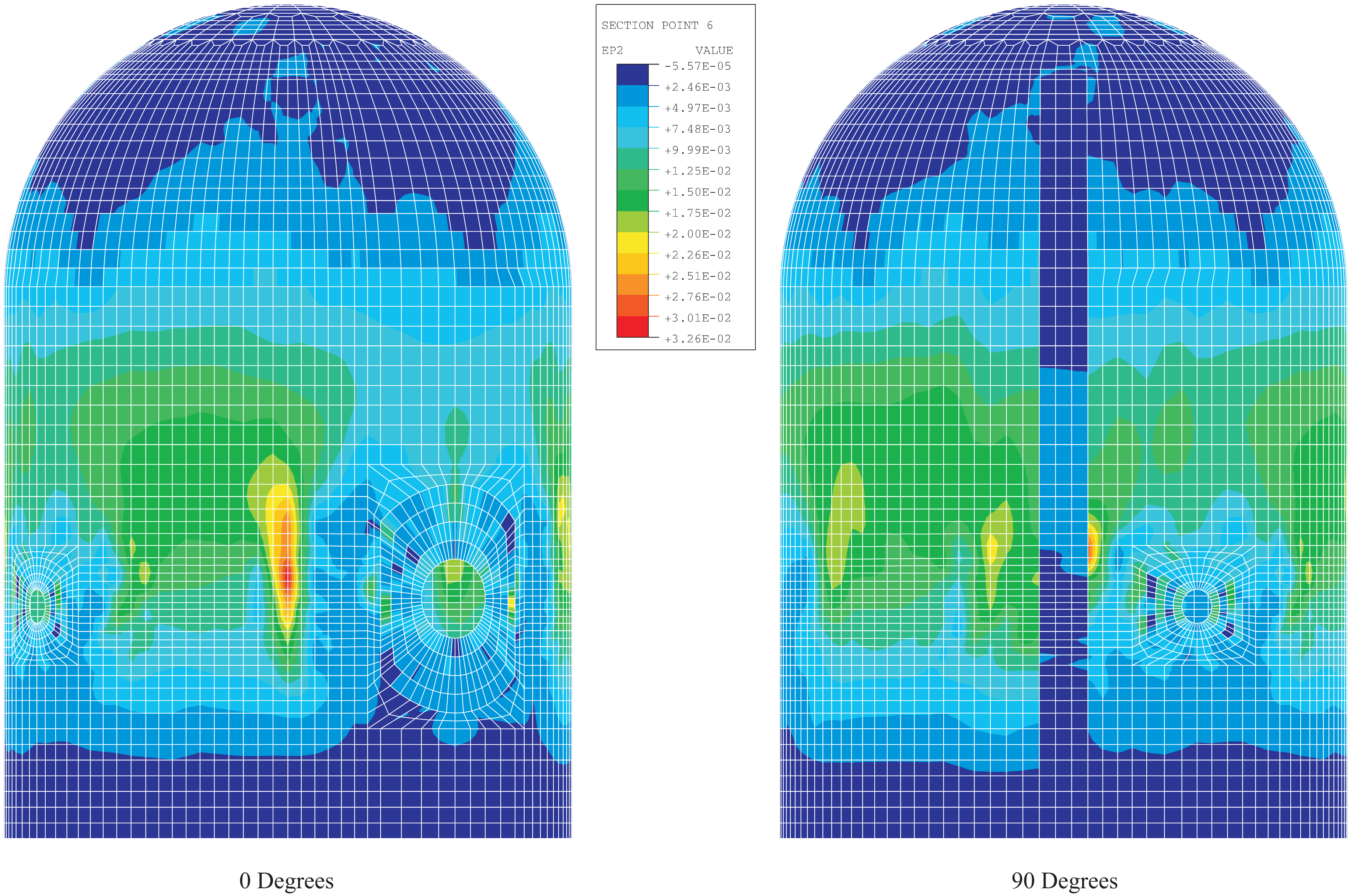

Figure 9-22. PCCV SFMT, 3D Global Shell Model. Concrete Maximum Principal Strain.
For Azimuth: 0 and 90 Degrees at 1.437 MPa (3.65 Pd)

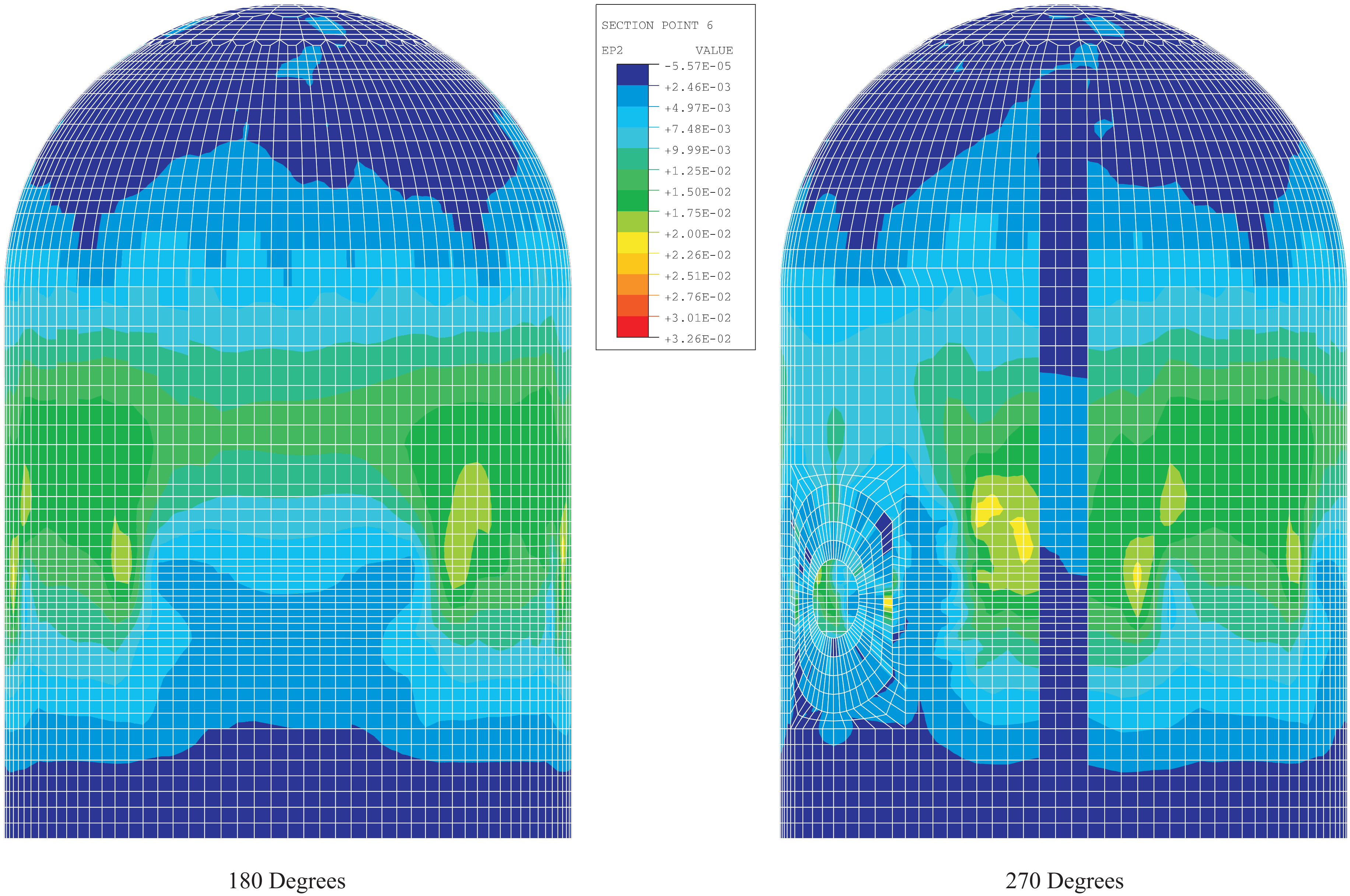

Figure 9-23. PCCV SFMT, 3D Global Shell Model. Concrete Maximum Principal Strain. For Azimuth: 180 and 270 Degrees at 1.437 MPa (3.65 Pd)

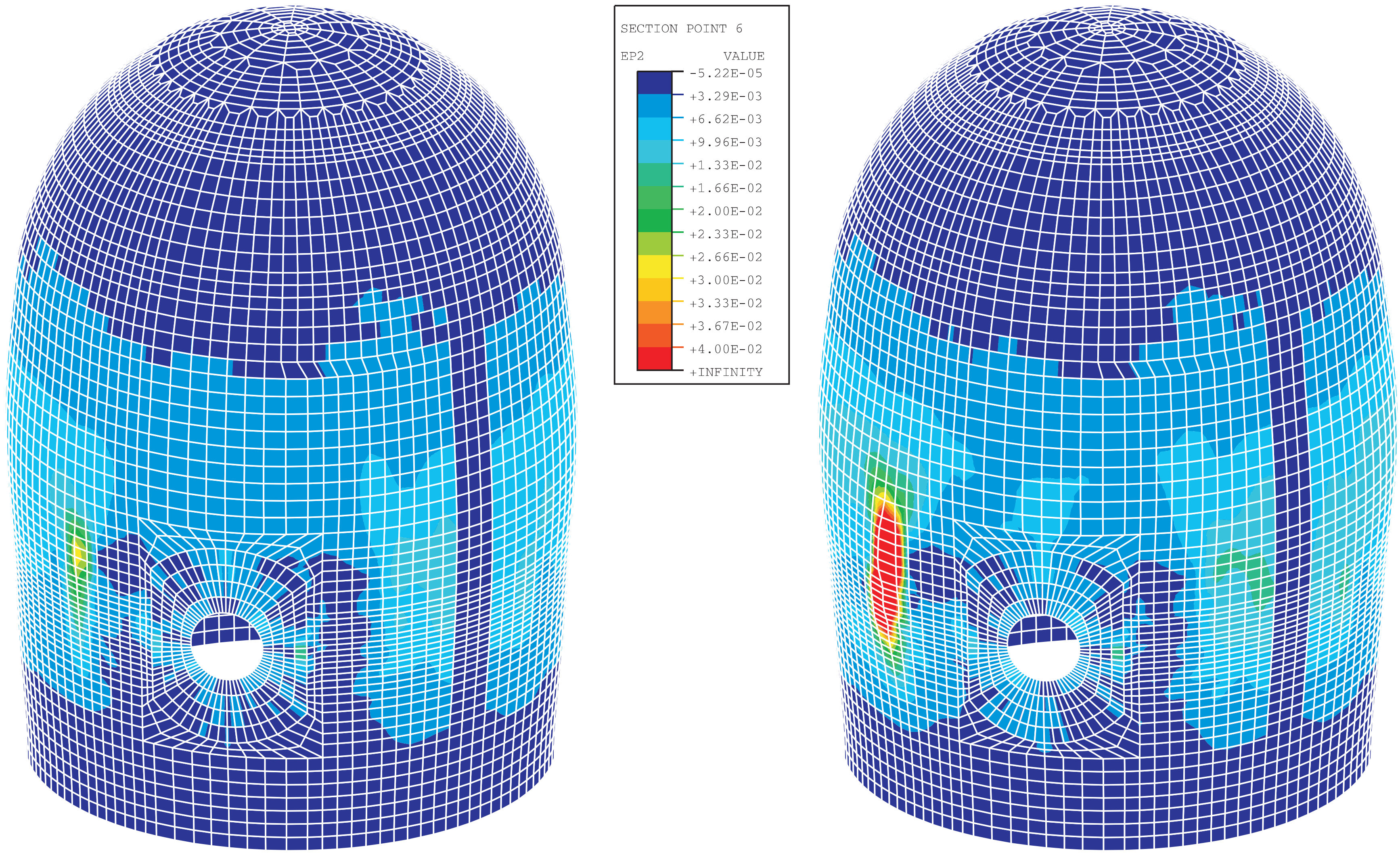

1.366 MPa

1.373 MPa

Figure 9-24. PCCV SFMT, 3D Global Shell Tendon Rupture Model. Concrete Maximum Principal Strain. For Pressure at 1.366 MPa (3.47 Pd) and 1.373 MPa (3.49 Pd), Displacement ×10.

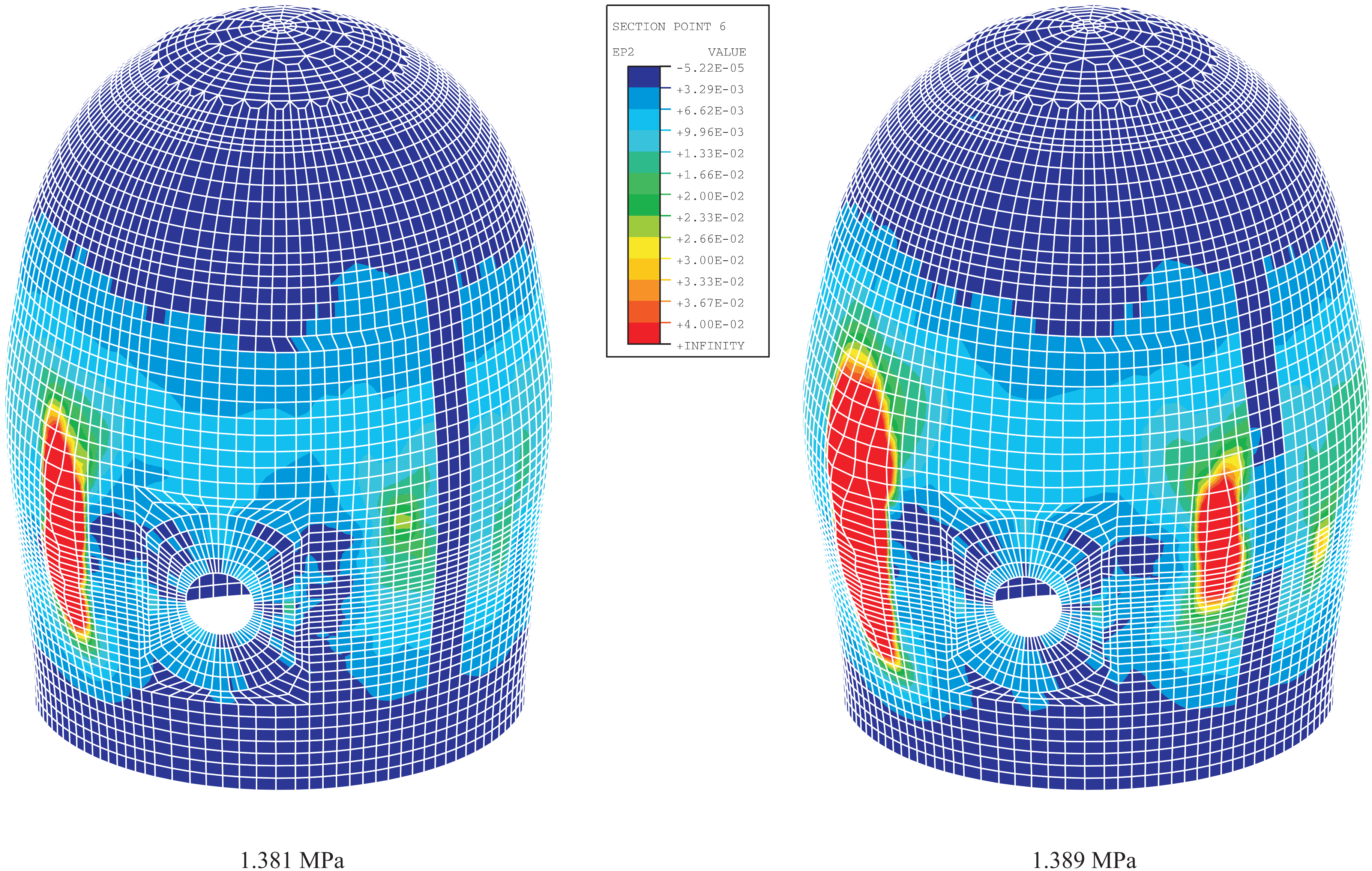

Figure 9-25. PCCV SFMT, 3D Global Shell Tendon Rupture Model. Concrete Maximum Principal Strain. For Pressure at 1.381 MPa (3.51 Pd) and 1.389 MPa (3.53 Pd), Displacement ×10.

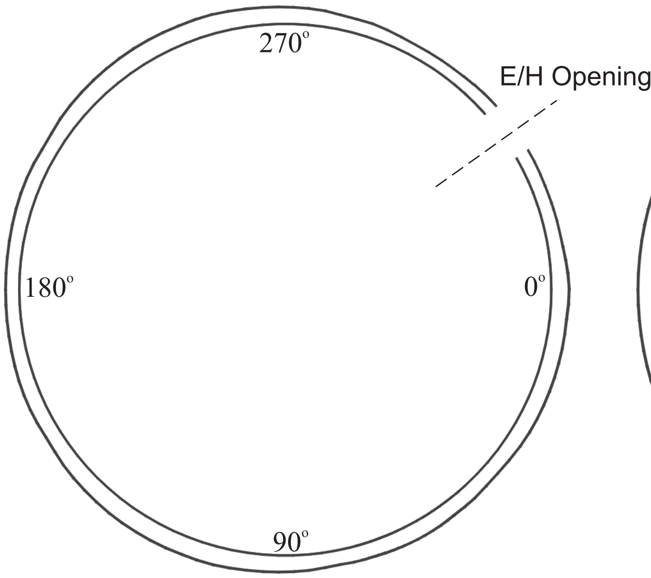

Pressure 1.366 MPa (3.47 Pd)

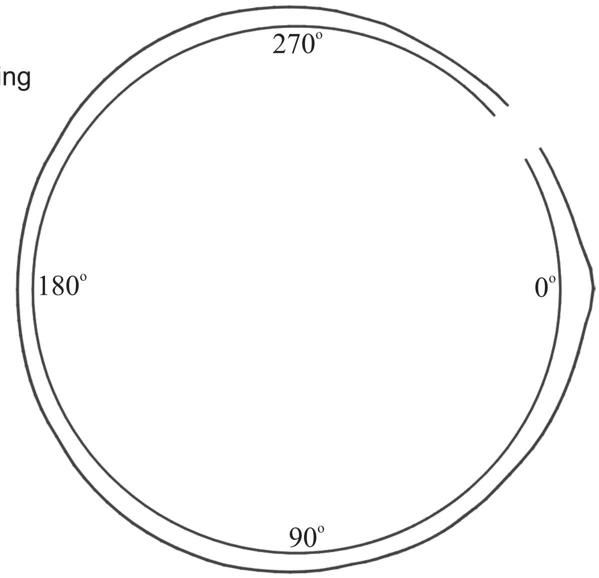

Pressure 1.373 MPa (3.49 Pd)

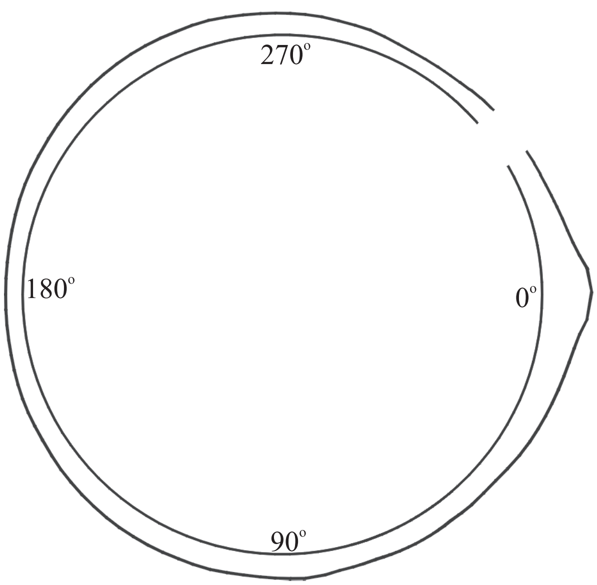

Pressure 1.381 MPa (3.51 Pd)

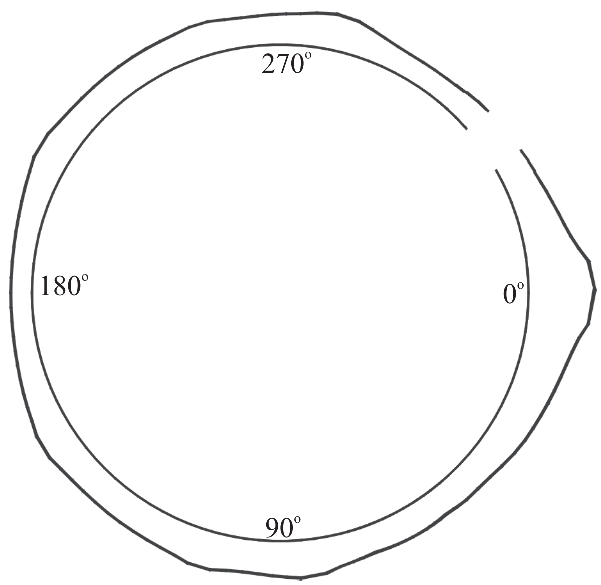

Pressure 1.389 MPa (3.53 Pd)

Figure 9-26. PCCV SFMT, 3D Global Shell Tendon Rupture Model.
Deformed Shape. For Elevation of 5.4 m. Displacements × 10.

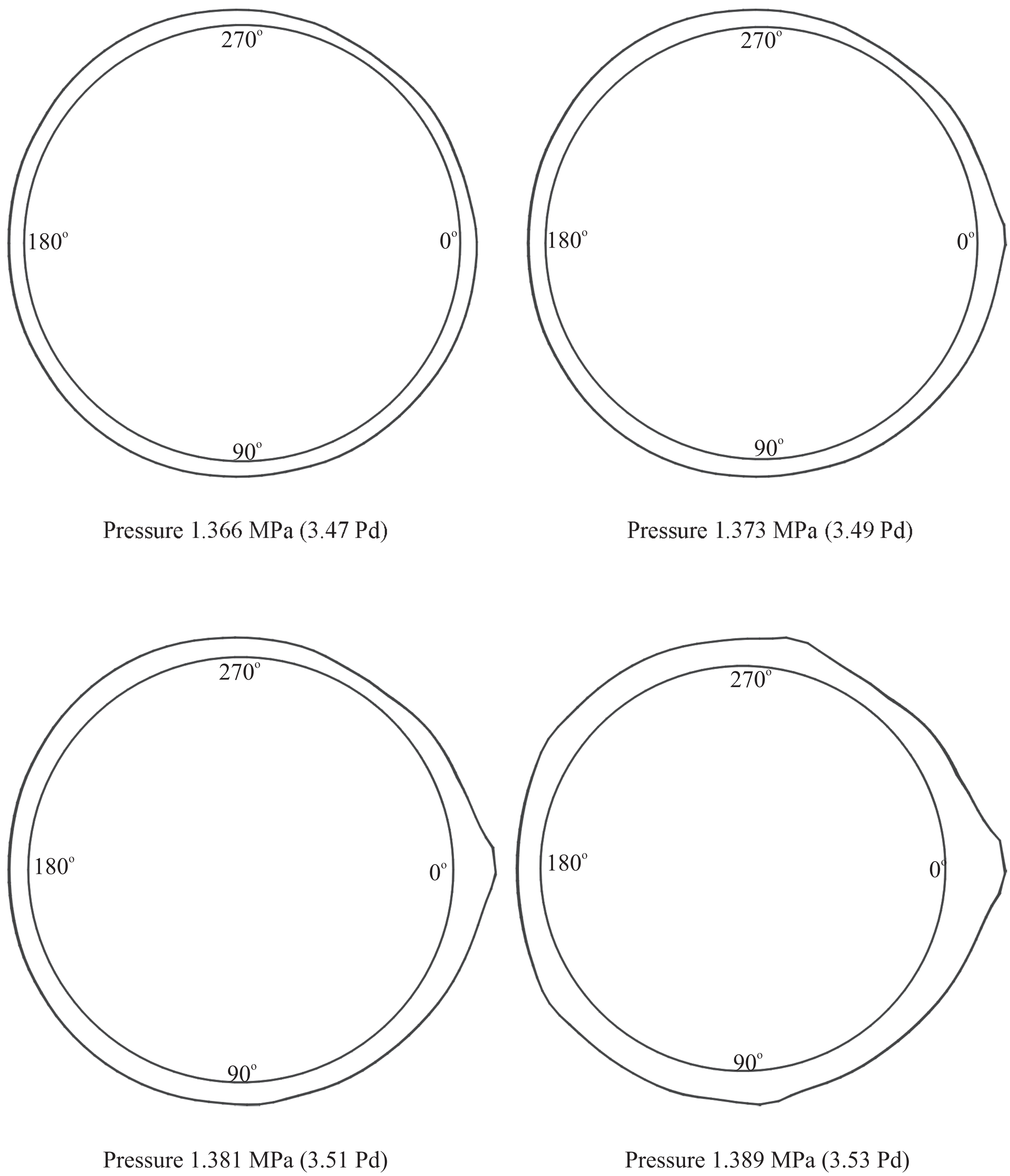

Figure 9-27. PCCV SFMT, 3D Global Shell Tendon Rupture Model.
Deformed Shape. For Elevation of 6.5 m. Displacements × 10.

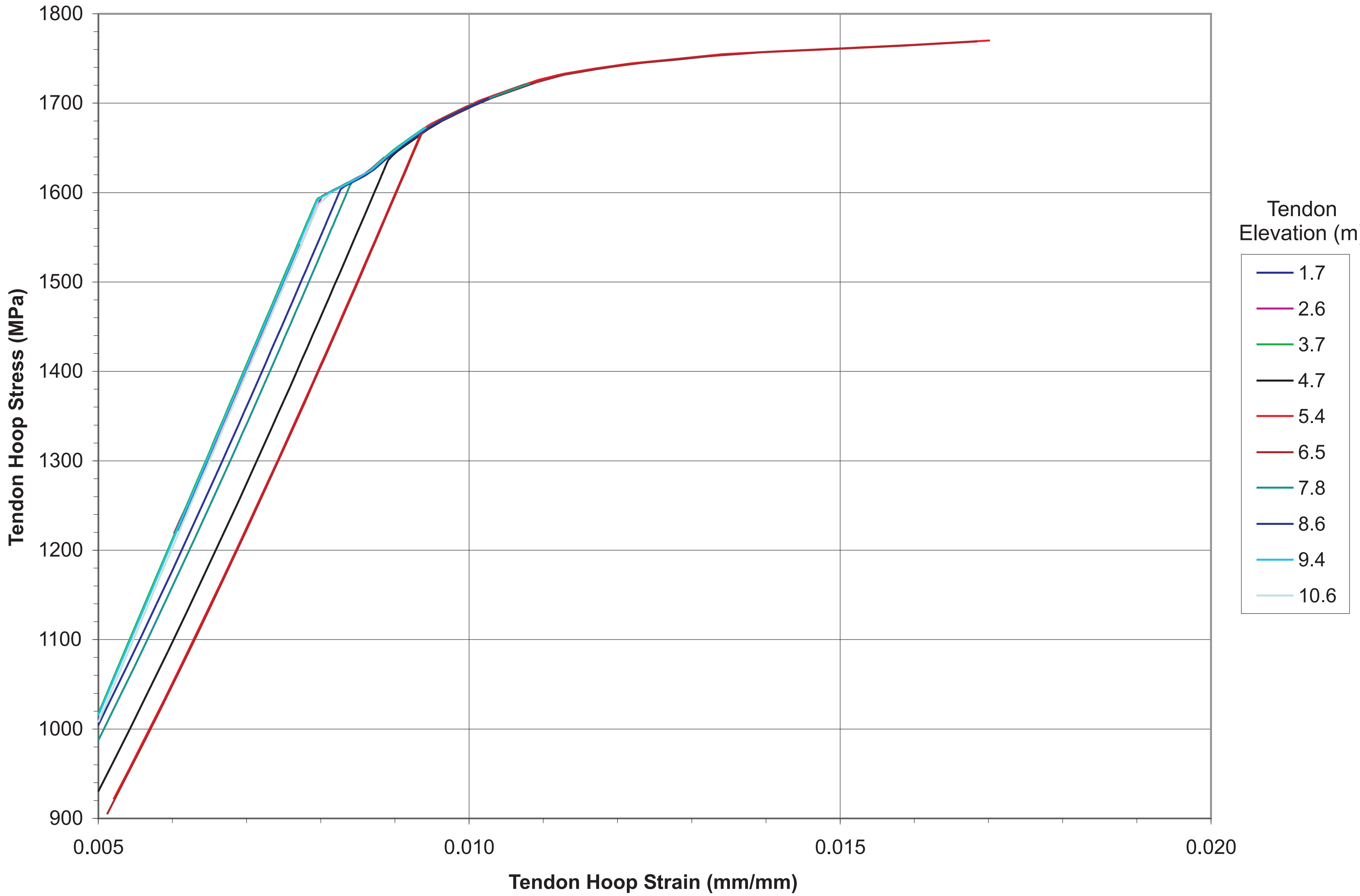

Figure 9-28. PCCV SFMT, 3D Global Shell Model-Hoop Tendon Stress Versus Strain History, Tendon History at 0 Degrees Azimuth, P = 1.357 MPa, 3.45 Pd

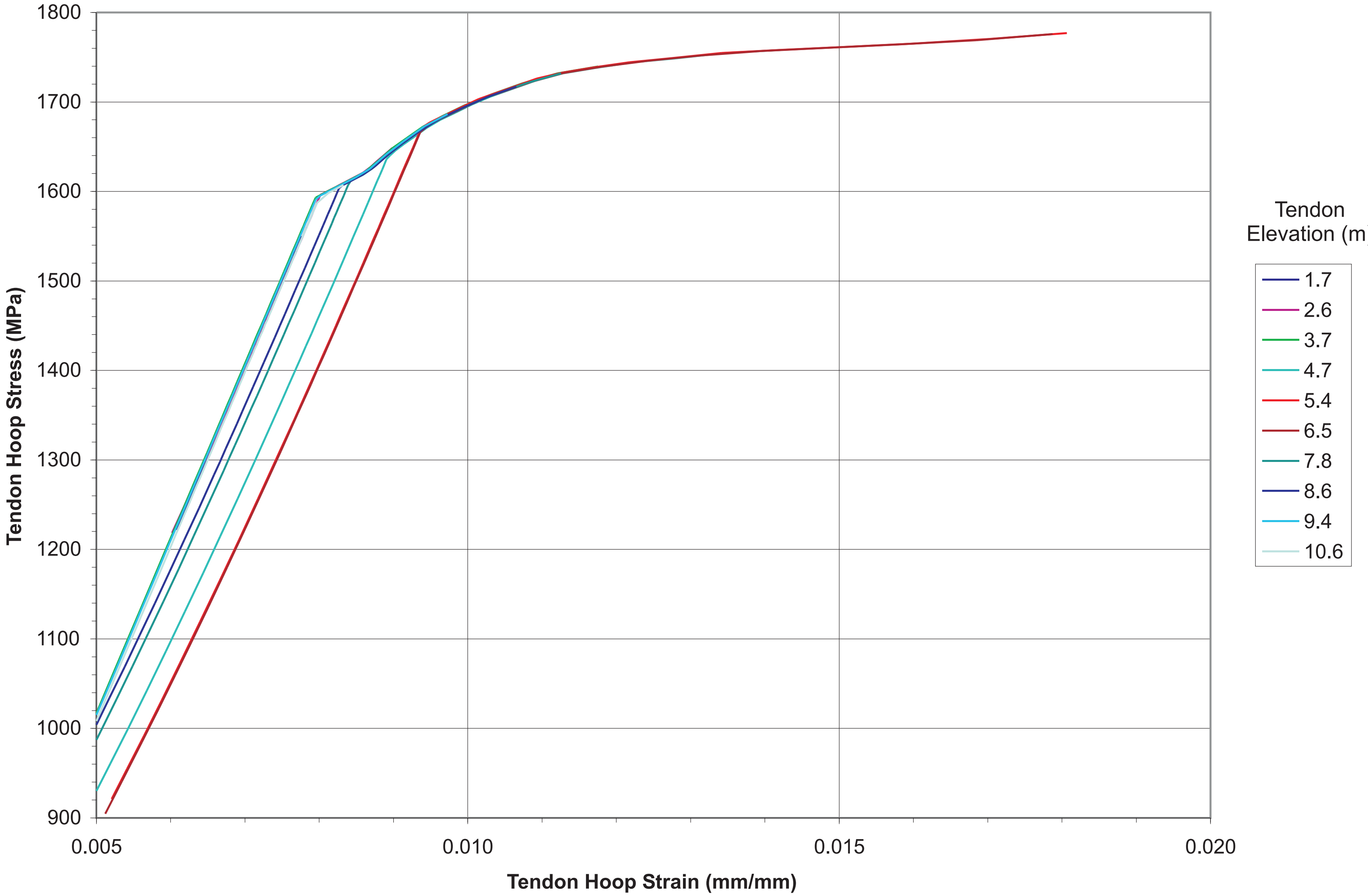

Figure 9-29. PCCV SFMT, 3D Global Shell Model-Hoop Tendon Stress Versus Strain History, Tendon History at 0 Degrees Azimuth, P = 1.366 MPa, 3.47Pd

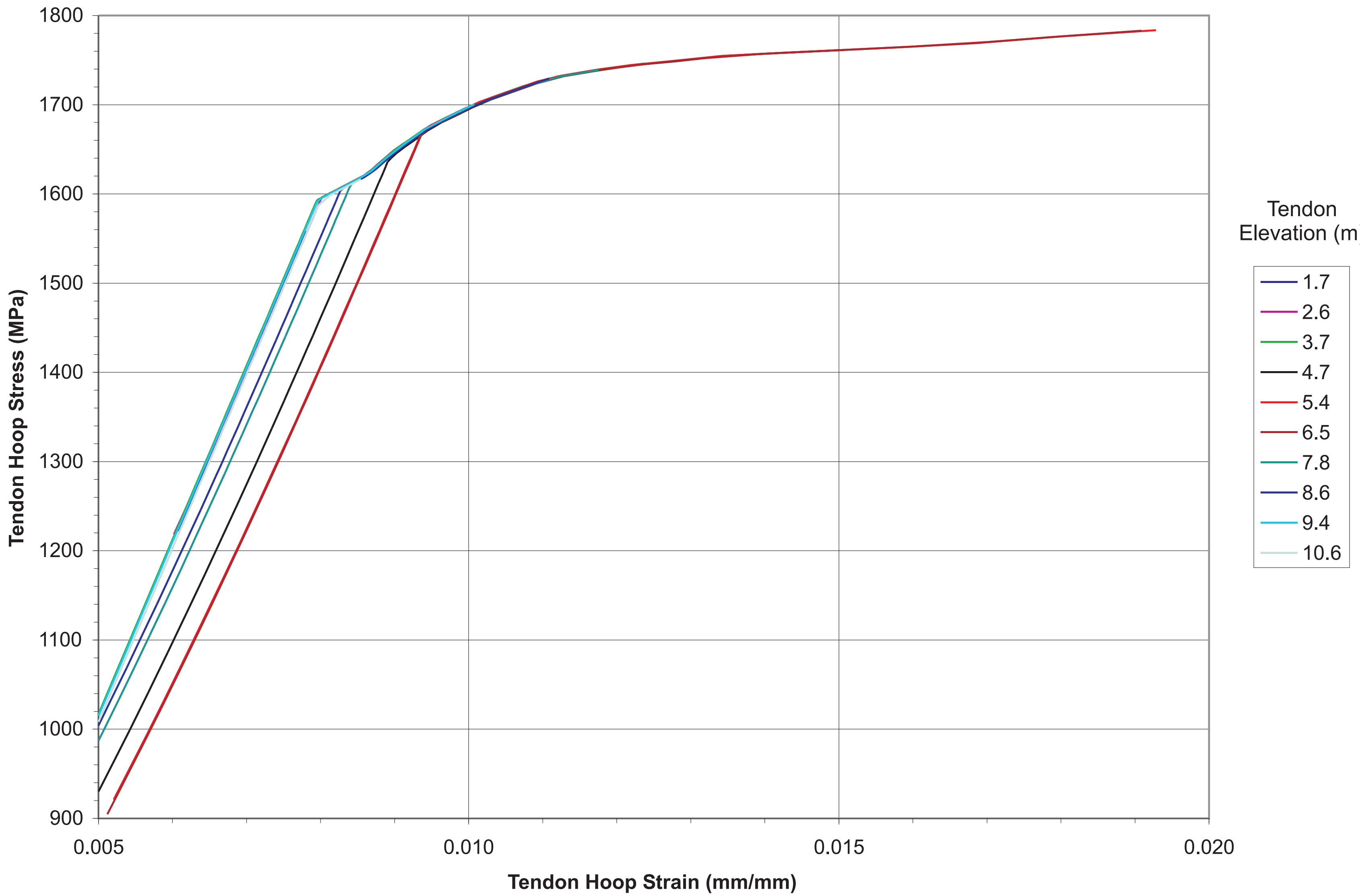

Figure 9-30. PCCV SFMT, 3D Global Shell Model-Hoop Tendon Stress Versus Strain History, Tendon History at 0 Degrees Azimuth, P = 1.373 MPa, 3.49 Pd

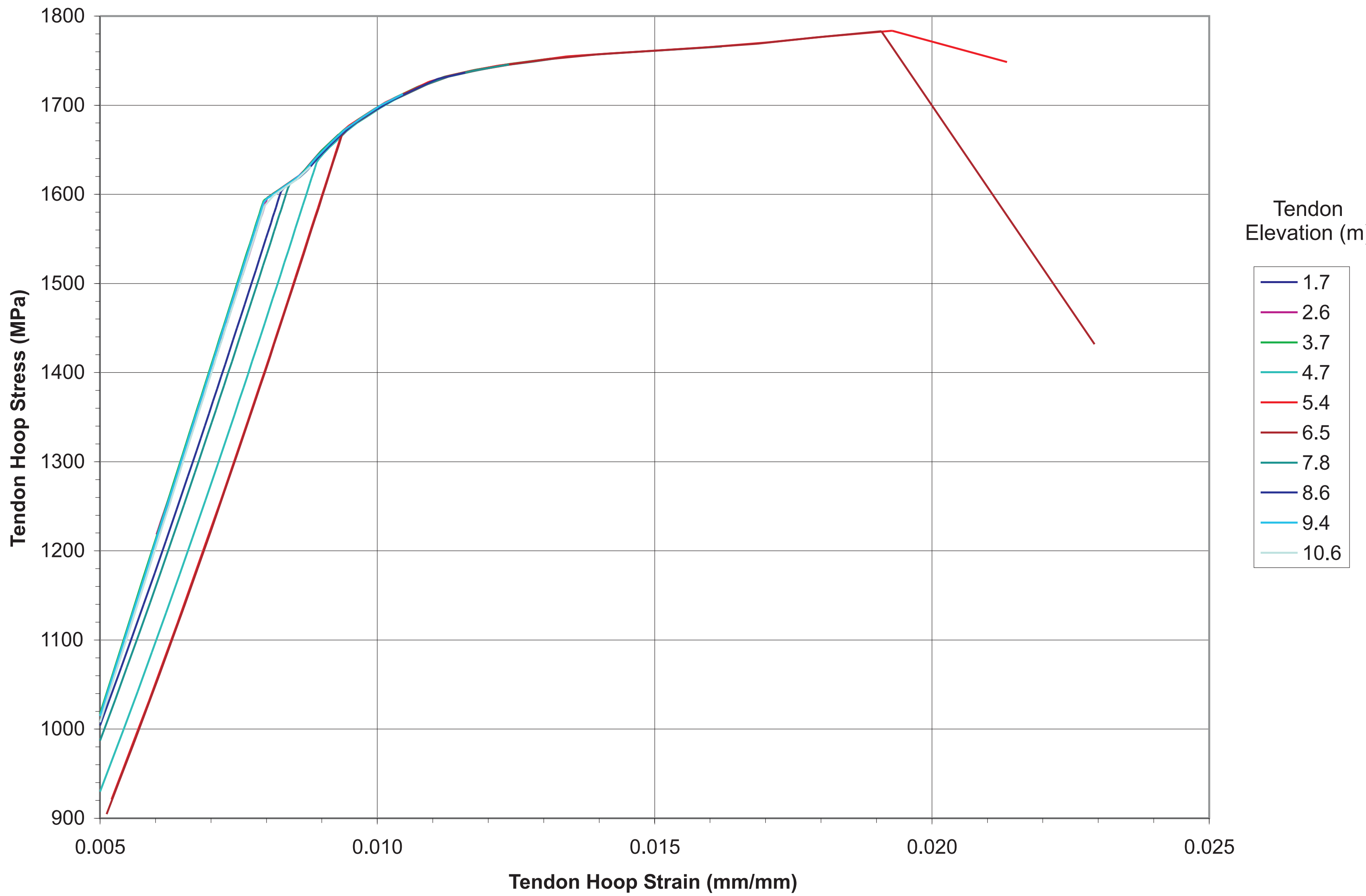

Figure 9-31. PCCV SFMT, 3D Global Shell Model-Hoop Tendon Stress Versus Strain History, Tendon History at 0 Degrees Azimuth, P = 1.381 MPa, 3.51 Pd

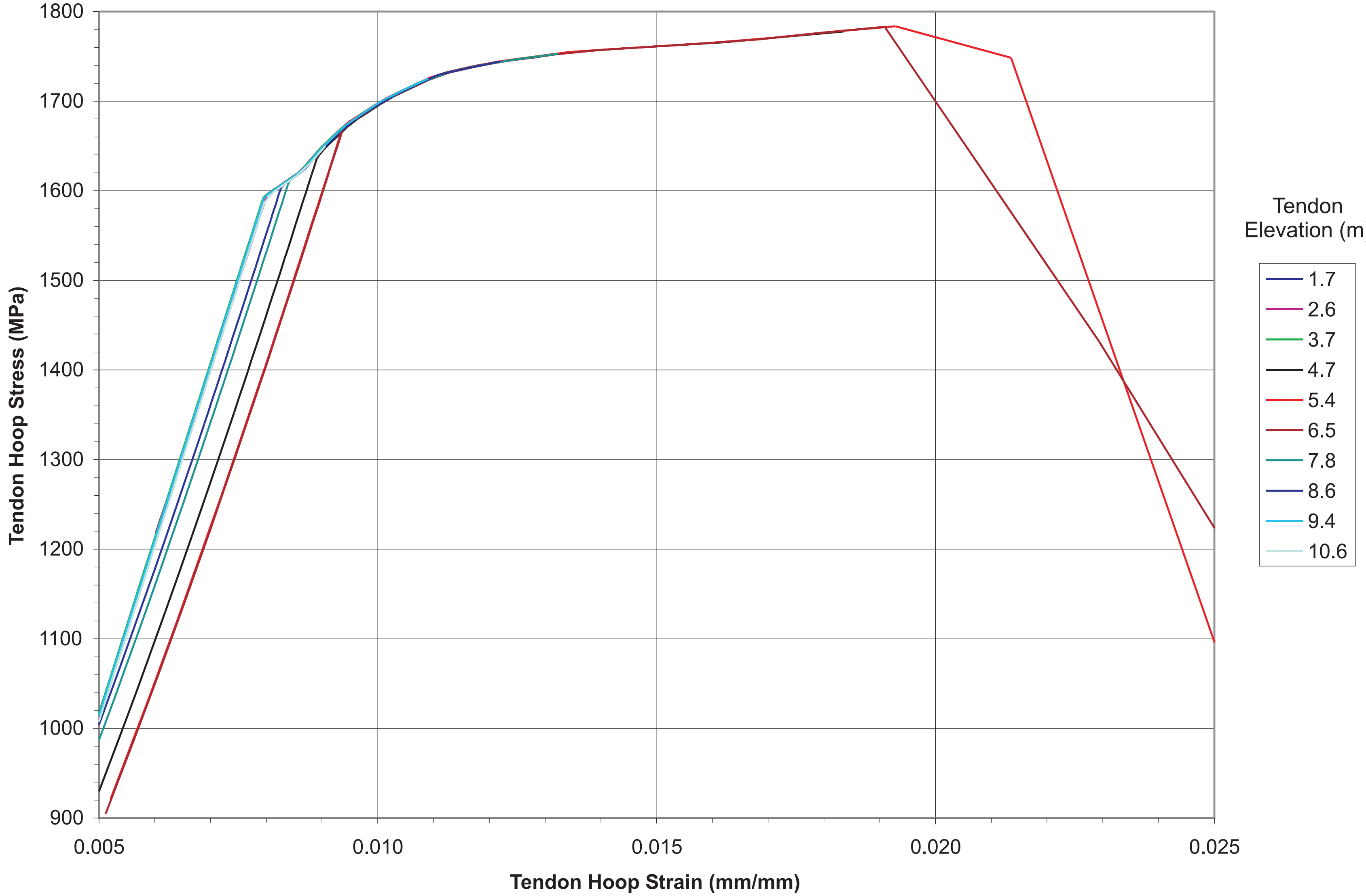

Figure 9-32. PCCV SFMT, 3D Global Shell Model-Hoop Tendon Stress Versus Strain History, Tendon History at 0 Degrees Azimuth, P = 1.389 MPa, 3.53 Pd

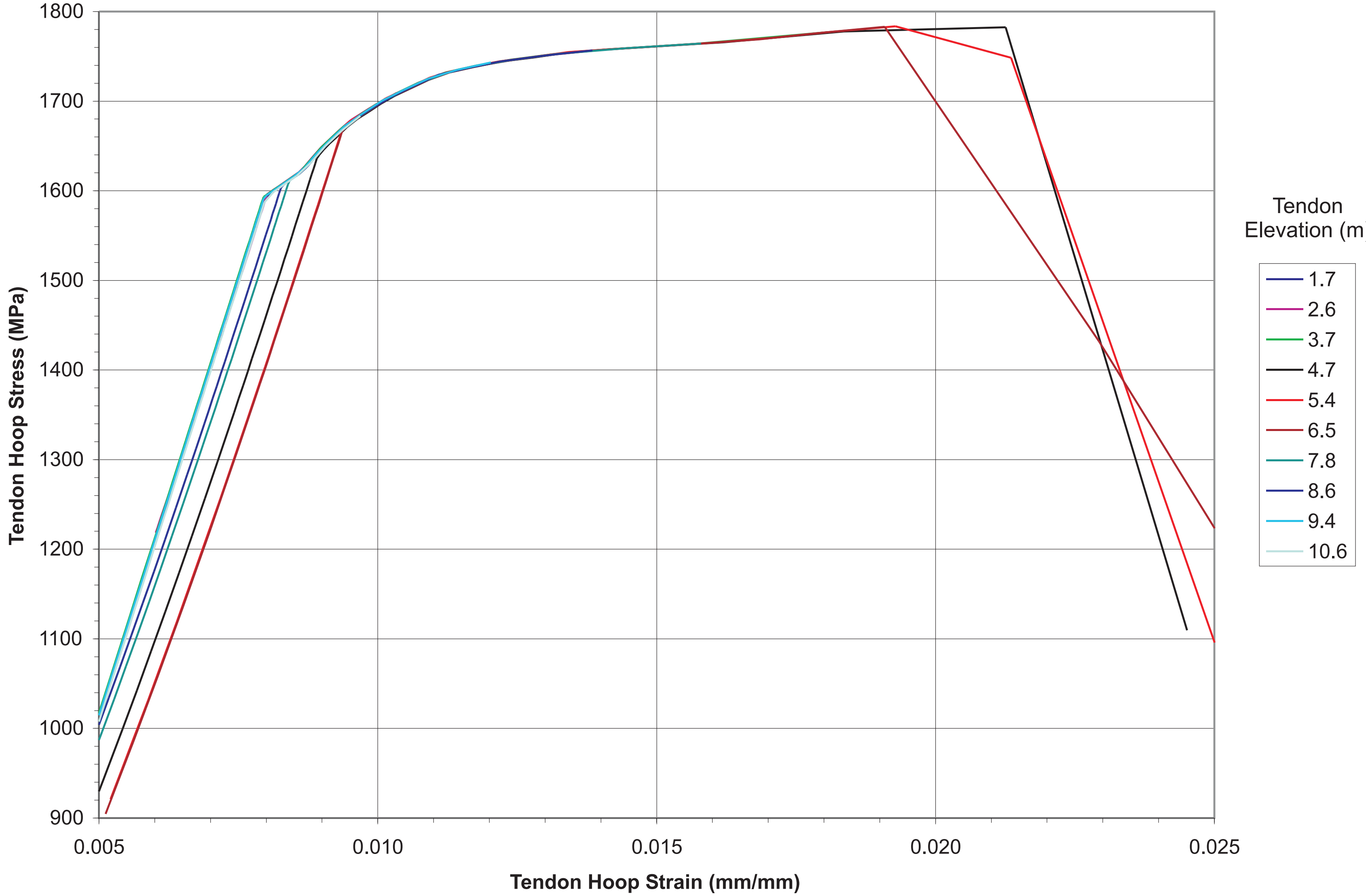

Figure 9-33. PCCV SFMT, 3D Global Shell Model-Hoop Tendon Stress Versus Strain History, Tendon History at 0 Degrees Azimuth, P = 1.404 MPa, 3.57 Pd

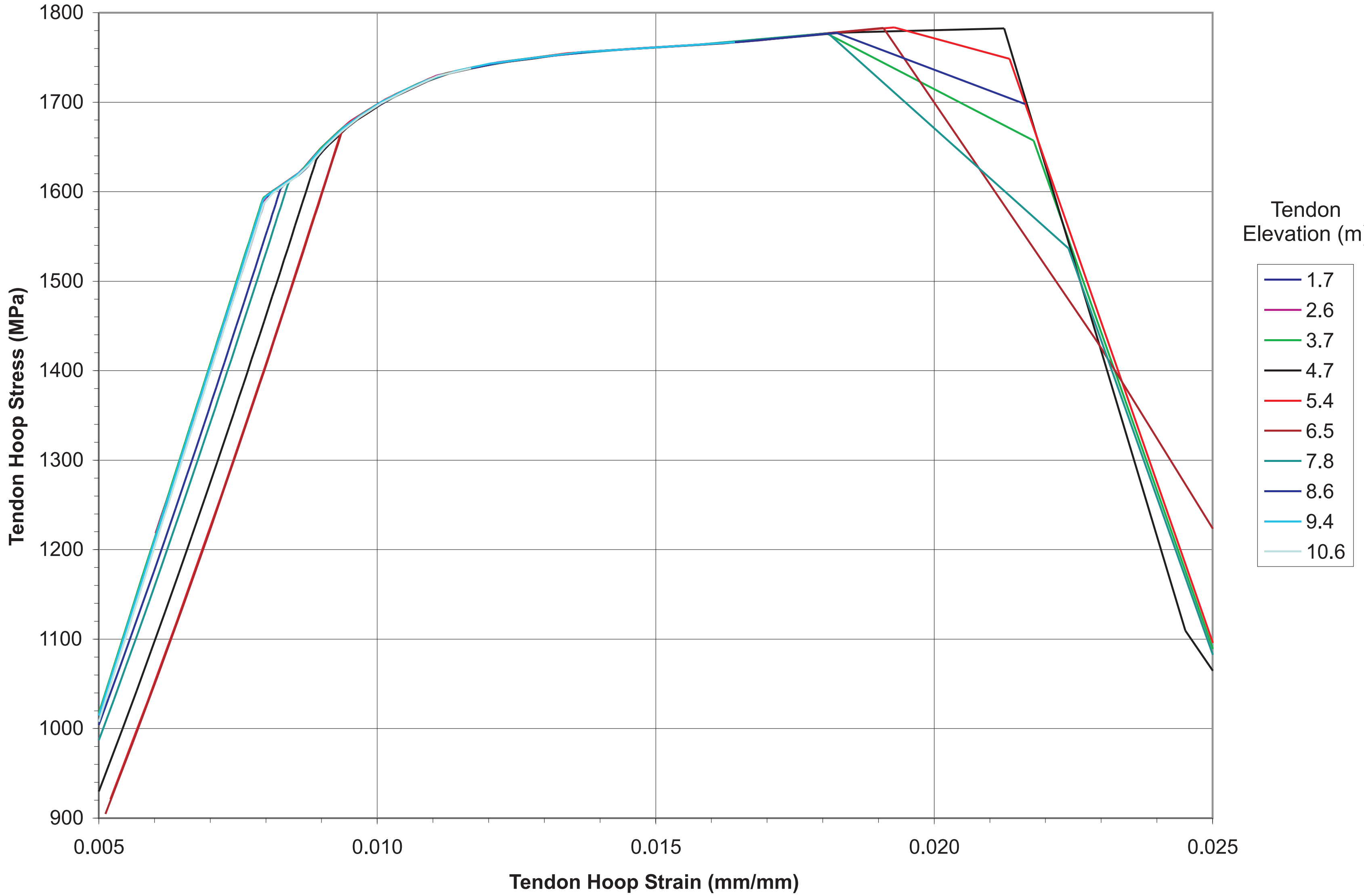

Figure 9-34. PCCV SFMT, 3D Global Shell Model-Hoop Tendon Stress Versus Strain History, Tendon History at 0 Degrees Azimuth, P = 1.436 MPa, 3.65 Pd

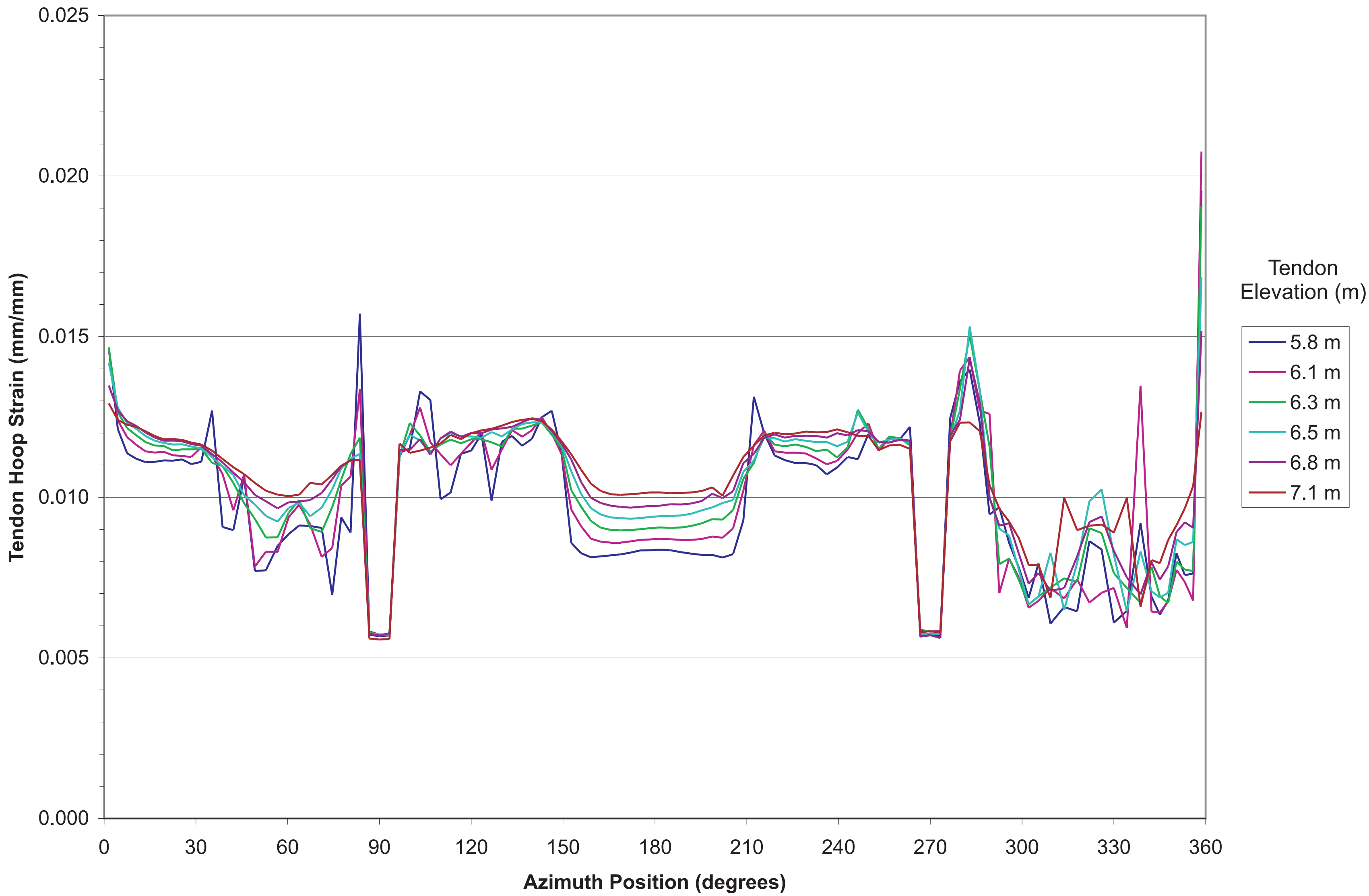

Figure 9-35. PCCV SFMT, 3D Global Shell Model-Hoop Tendon Strain Profile, Tendon History, P =1.357 MPa, 3.45 Pd

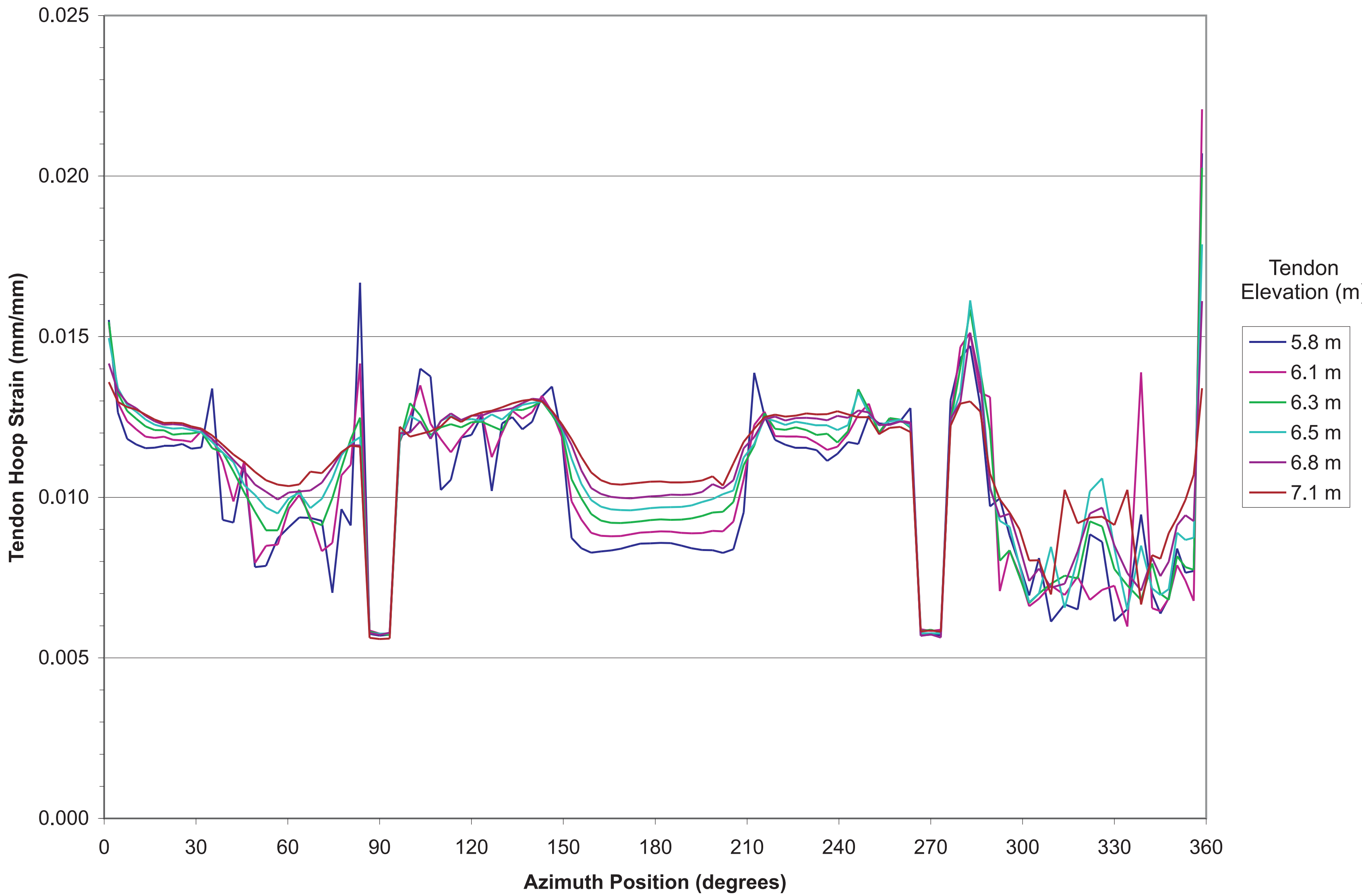

Figure 9-36. PCCV SFMT, 3D Global Shell Model-Hoop Tendon Strain Profile,
Tendon History, P =1.366 MPa, 3.47 Pd

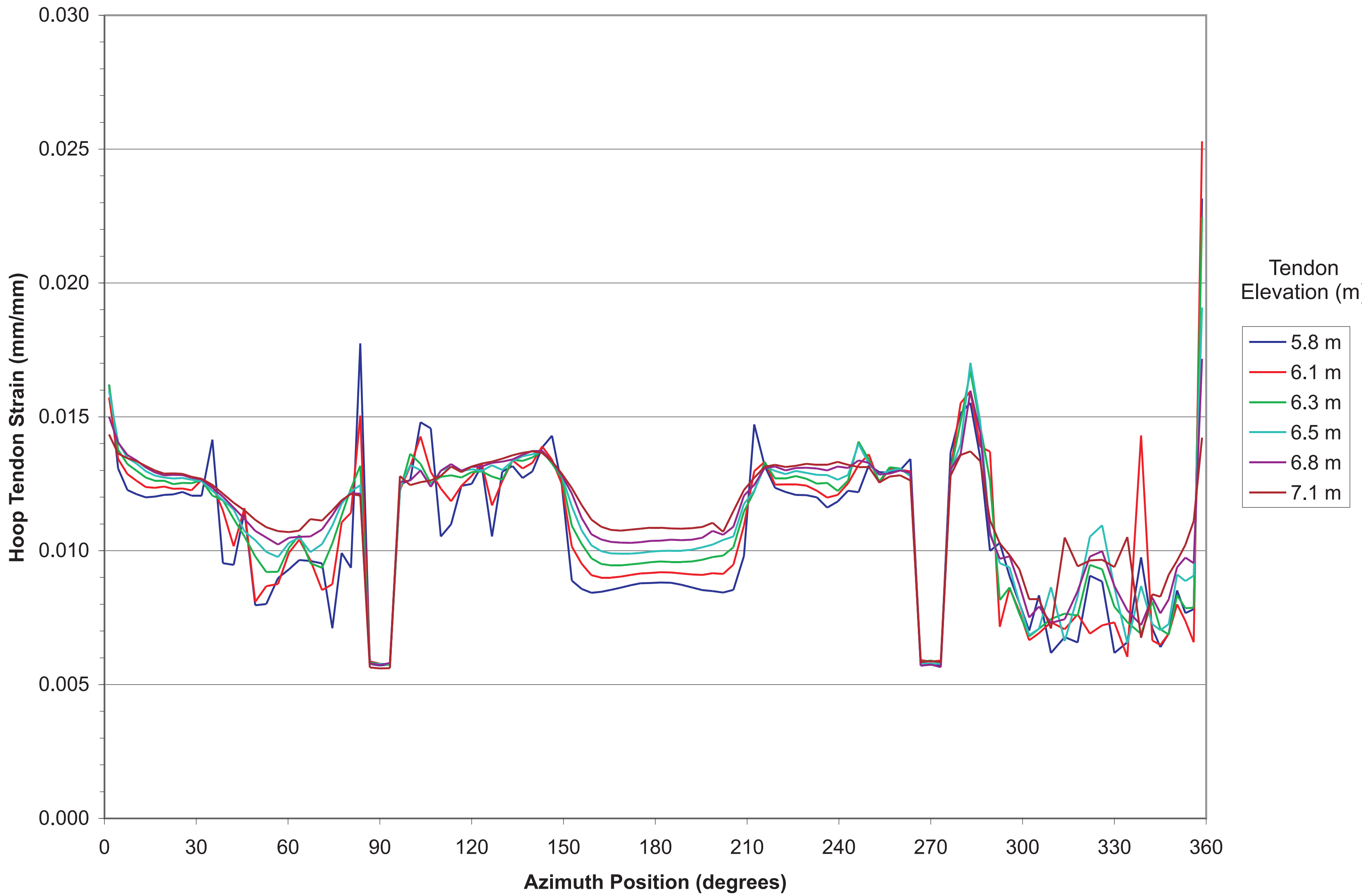

Figure 9-37. PCCV SFMT, 3D Global Shell Model-Hoop Tendon Strain Profile,
Tendon History, P = 1.373 MPa, 3.49 Pd

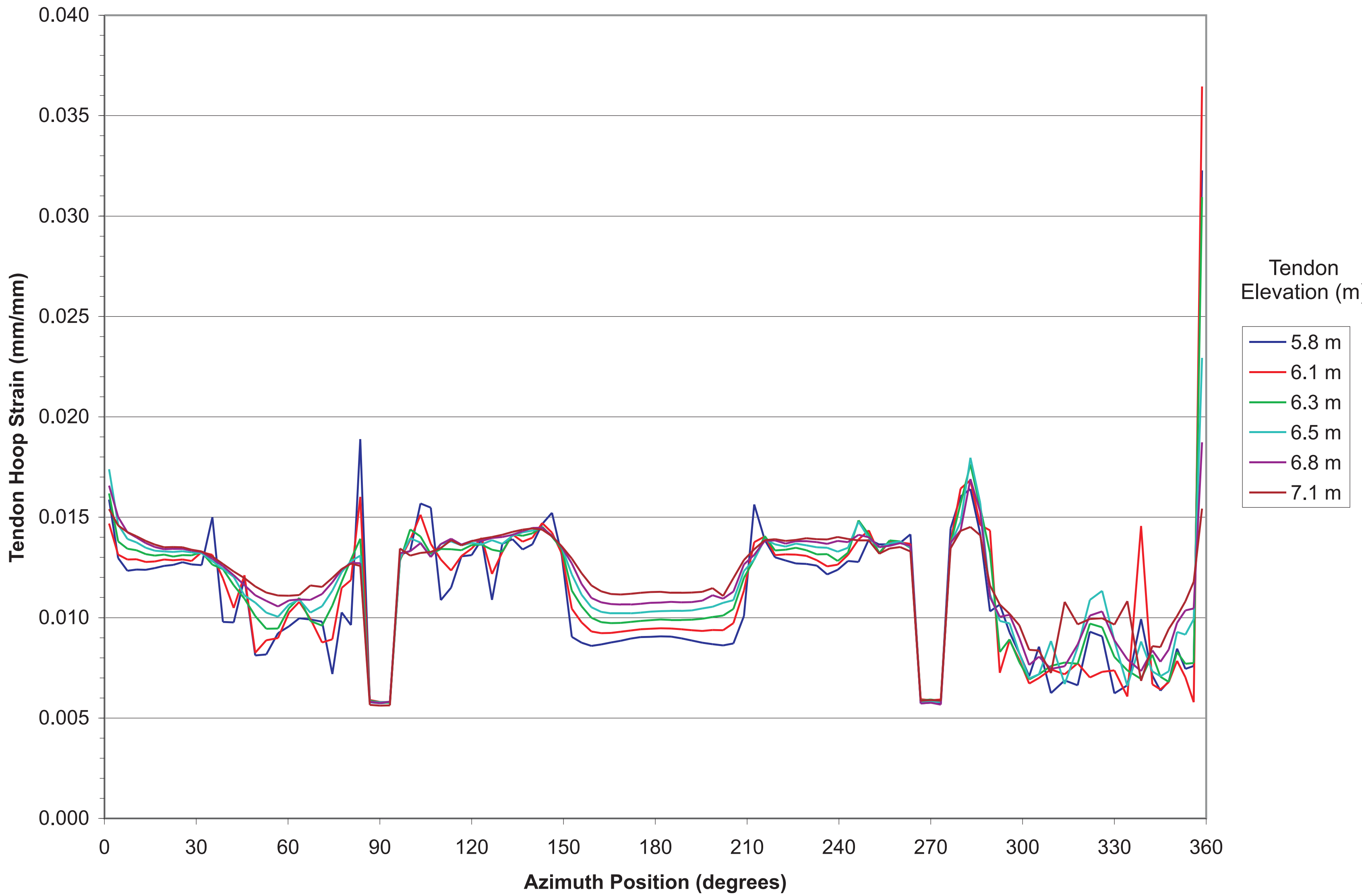

Figure 9-38. PCCV SFMT, 3D Global Shell Model-Hoop Tendon Strain Profile,
Tendon History, P = 1.381 MPa, 3.51 Pd

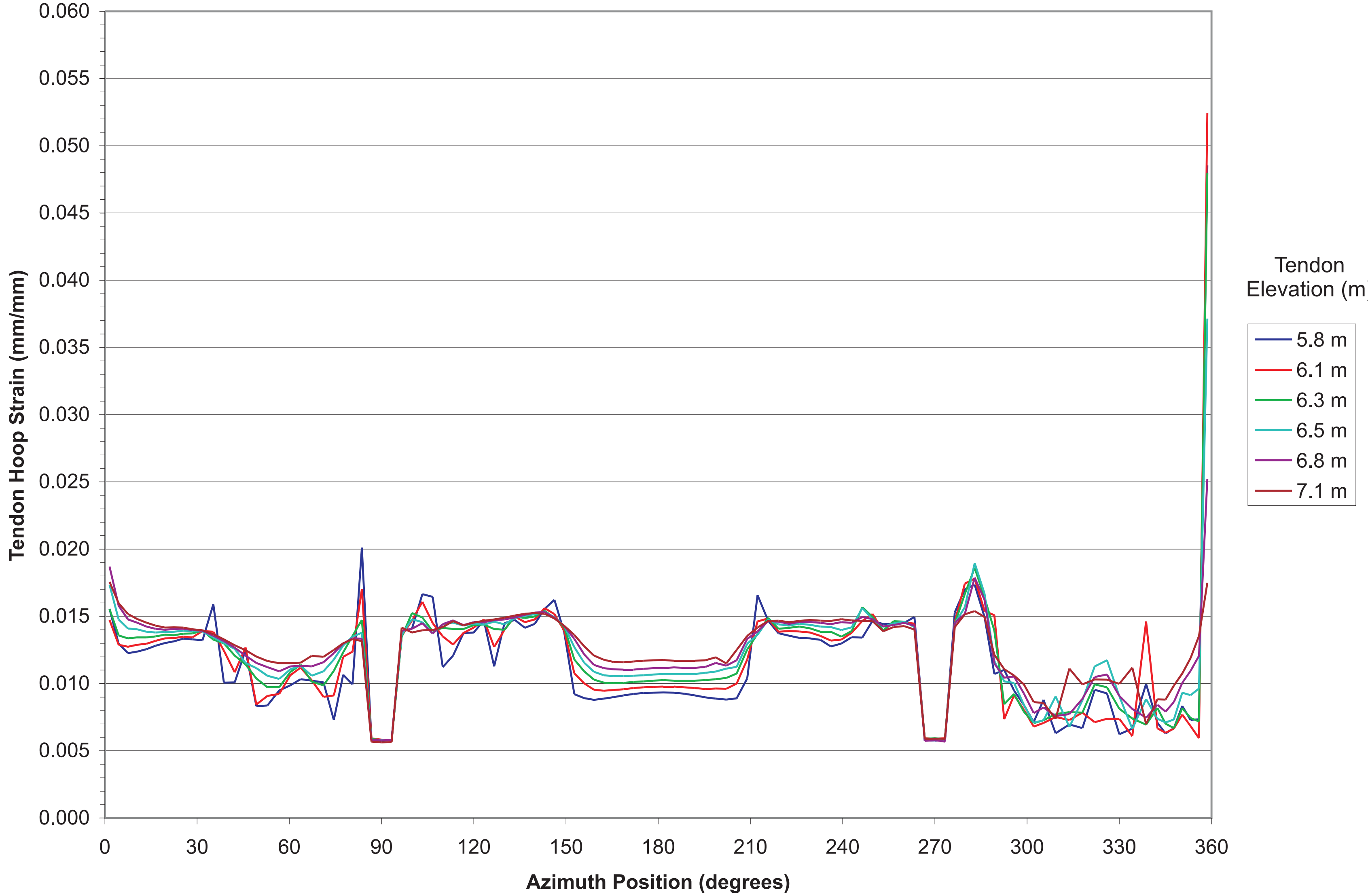

Figure 9-39. PCCV SFMT, 3D Global Shell Model-Hoop Tendon Strain Profile,
Tendon History, P = 1.389 MPa, 3.53 Pd

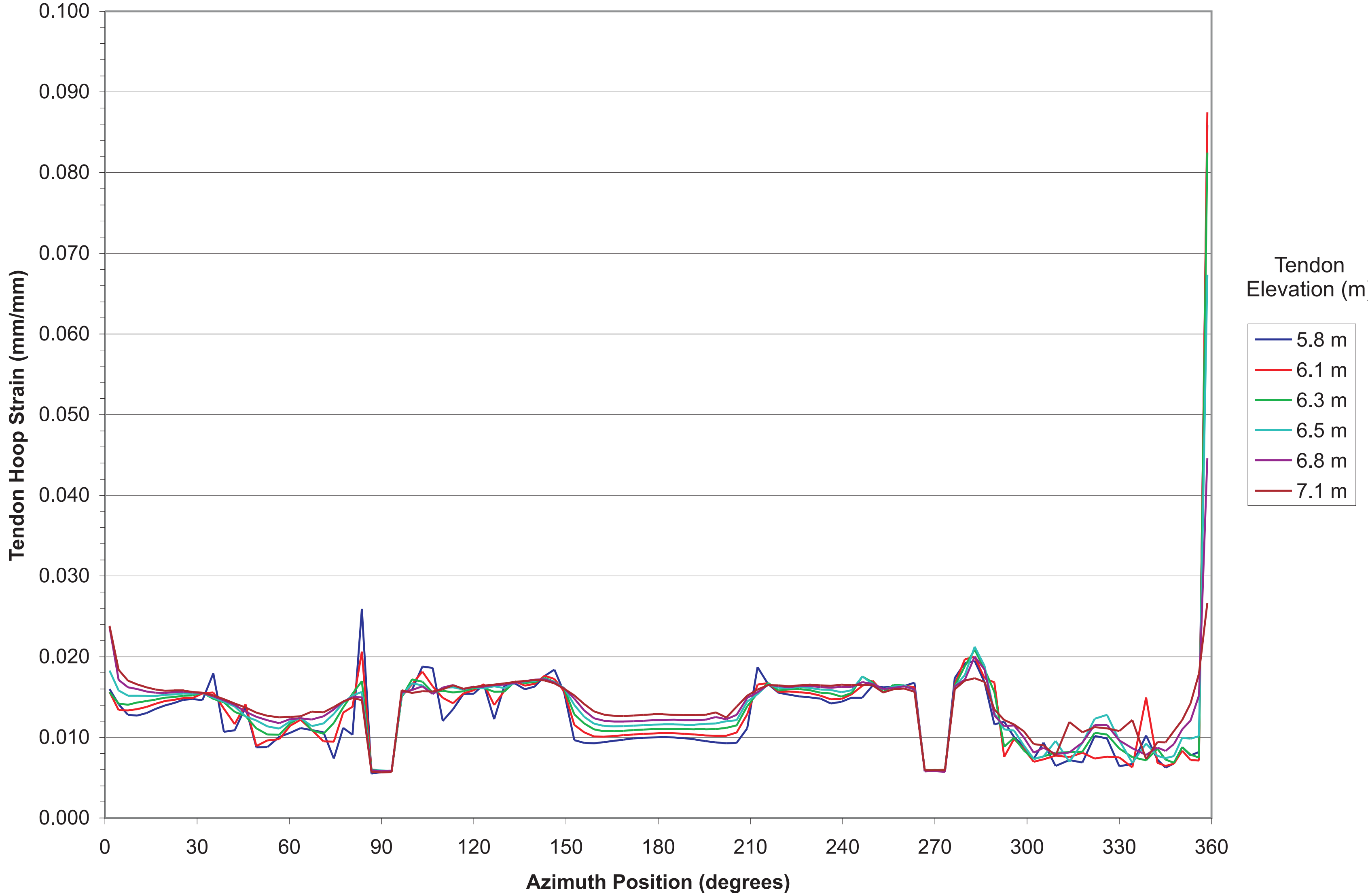

Figure 9-40. PCCV SFMT, 3D Global Shell Model-Hoop Tendon Strain Profile, Tendon History, P = 1.404 MPa, 3.57 Pd

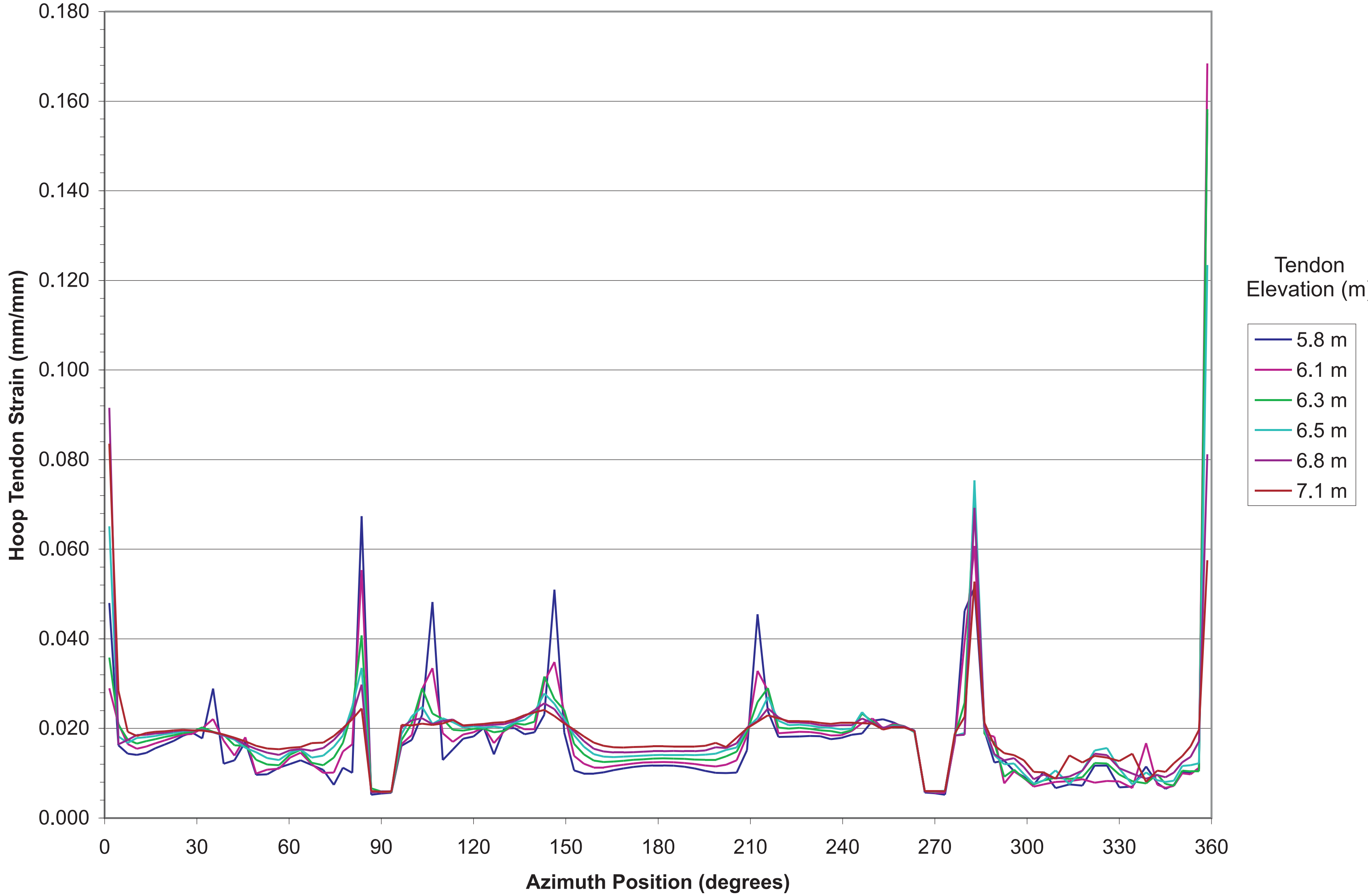

Figure 9-41. PCCV SFMT, 3D Global Shell Model-Hoop Tendon Strain Profile, Tendon History, P = 1.436 MPa, 3.65 Pd

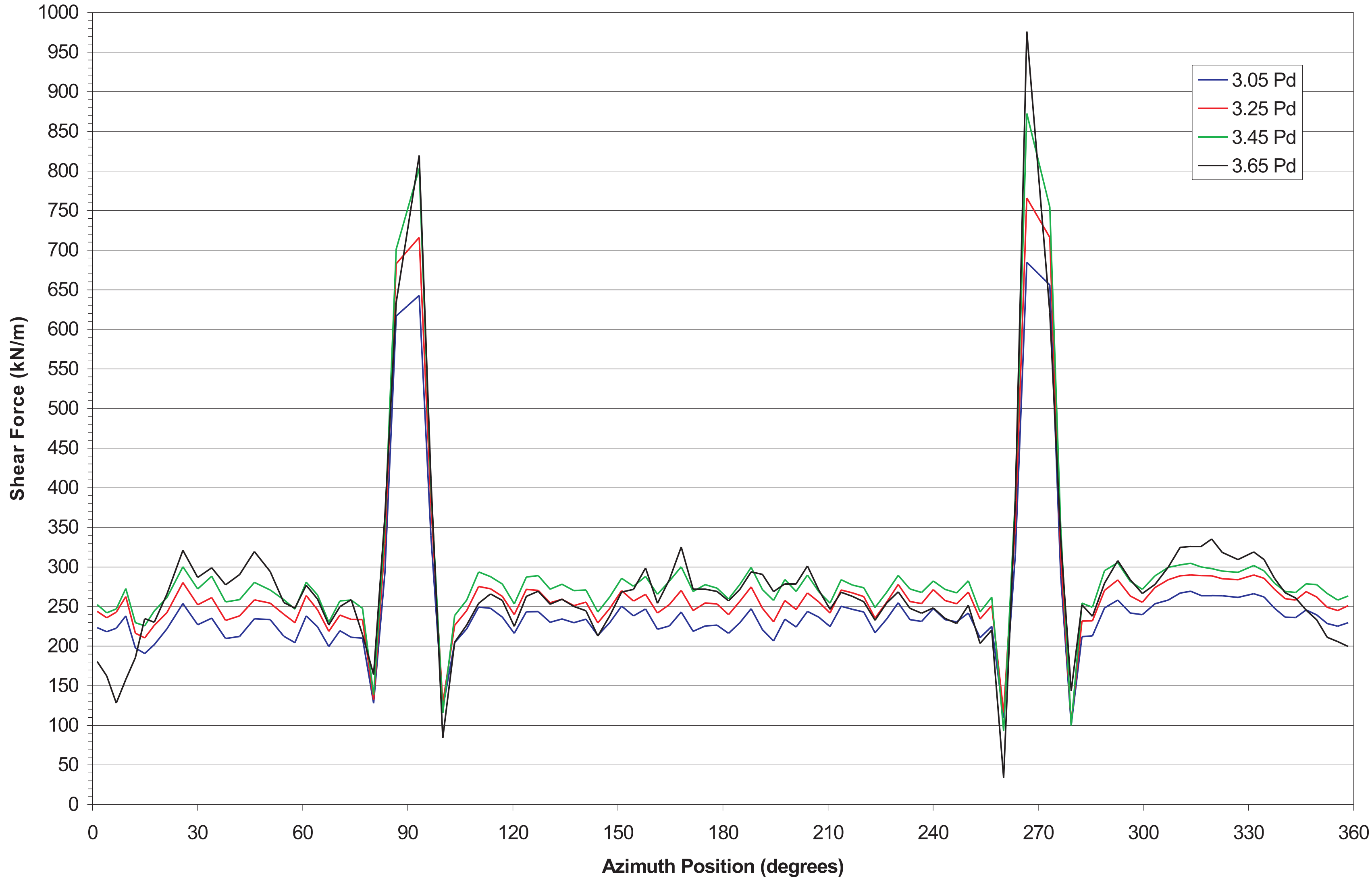

Figure 9-42. PCCV SFMT, 3D Global Shell Model - Cylinder Shear Profile 1 m Above Basemat

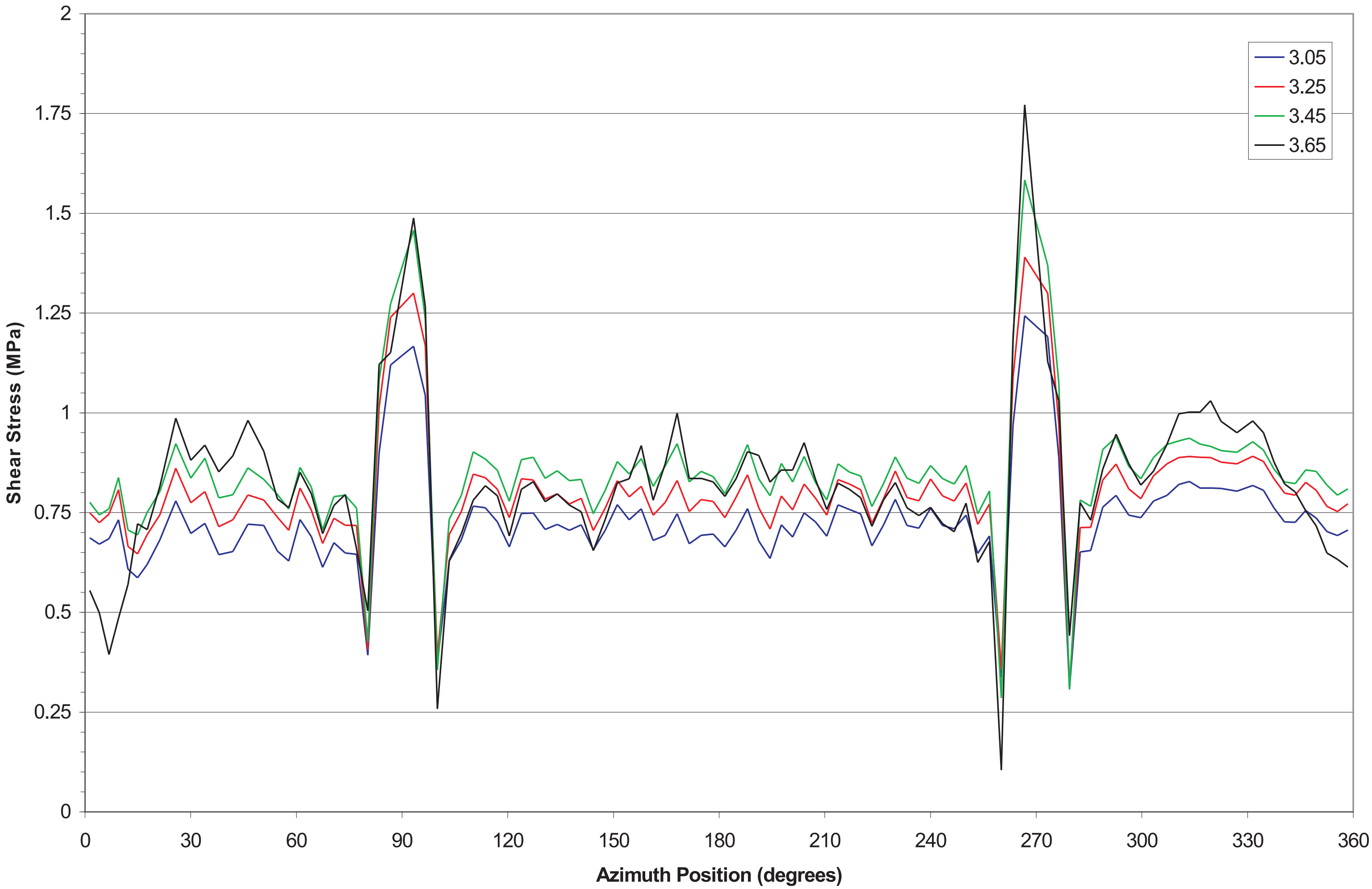

Figure 9-43. PCCV SFMT, 3D Global Shell Model - Cylinder Shear Profile 1 m Above Basemat

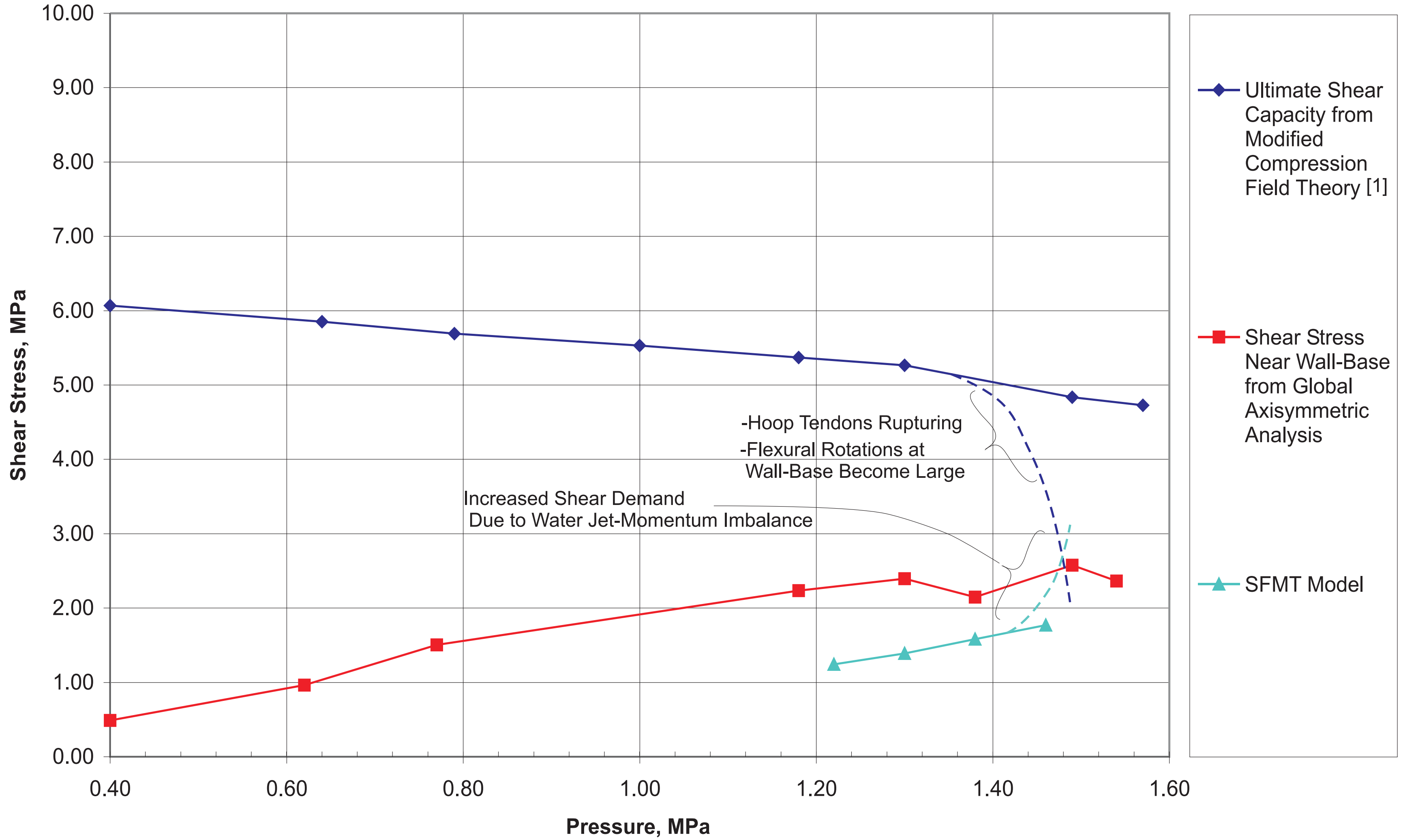

Figure 9-44. PCCV Wall-Base Shear Strength from Modified Compression Field Theory Compared to Shear Demand from the Global Analysis Model [1] and the SFMT Model

10.0 CONCLUSIONS AND LESSONS LEARNED

10.1 Conclusions of Post-Test Analytical Studies of the PCCV LST

As part of the NUPEC and NRC-sponsored Containment Research Program conducted at Sandia National Laboratories, a 1:4 scale model of a prestressed concrete containment vessel (PCCV) has been constructed, pressure tested to failure, and studied with preliminary, pretest, and post-test analytical evaluations. All analyses were performed using the nonlinear concrete constitutive model, ANACAP-U, in conjunction with the ABAQUS general purpose finite element code. The documentation of post-test analysis work herein has included: a final series of pretest analyses (performed to support test operations and account for information, such as tendon prestress levels, learned in the final months prior to the test); a comprehensive set of comparisons of test measurements to pretest analyses; review, model modification, and re-analysis of pretest analytical models to incorporate as-built conditions or improve levels of correlation with the test; and development and study of liner seam/rat-hole detailed models to gain insight on the behavior mechanisms surrounding the liner tears that occurred in the test. Review and standardization of measurements taken during the LST have also been conducted.

The effects and phenomena studied in the "data correction" effort were temperature, rigid body motion of the model, and strain localization. Temperature, as a direct influence on structure strains and displacements and as a secondary influence on voltage readouts of strain gages, was corrected for, the former being calibrated by direct observation of model response during the spring and summer of 2000, and the latter being calibrated by formulae provided by the gage manufacturer. To correct for either phenomena, a temperature mapping algorithm based on interpolation between the matrix of temperature gages, was developed. Additional correction was considered for rebar gages, but was ultimately left up to end users to apply as deemed appropriate. Without such correction, however, users should note that the rebar gage measurements tend to overpredict the apparent engineering strain, especially in the strain range just past initial yield, i.e. between $\varepsilon = 0.002$ and $\varepsilon = 0.015$. The cause for this is area reduction associated with grinding for gage-preparation.

The overall conclusions from the comparisons of the pretest analyses with the test data are as follows:

- Radial displacements were well predicted by global axisymmetric analysis, but dome and overall vertical displacements were significantly overpredicted.
- Measured basemat uplift was much smaller than predicted, but this is judged to be an artifact of how this quantity was measured.
- Wall-base juncture behavior, including many rebar and liner strain measurements, was well predicted by the detailed wall-base juncture (axisymmetric) modeling.
- The maximum pressure, 1.30 MPa (187.9 psig) or $3.30P_d$, which was primarily a function of the onset of global yielding, was very close to the prediction of liner tearing at the equipment hatch at a pressure of 1.28 MPa (185 psi), although the predicted tears did not occur. The strains occurring in the test model at the primary tear prediction location were very small.
- An initial small leak occurred at $2.5P_d$ that was not predicted by analysis, but this may be due to defects associated with weld seam repair.
- The average radial displacement of 23mm, equivalent to an average hoop strain of 0.0040, was well predicted by global analysis.
- The maximum radial displacement at the E/H of 29mm, equivalent to a hoop strain of 0.0054, was well predicted by 3DCM model, but prediction of some displacements at other azimuths, like the buttresses, was poorly predicted by 3DCM model.
- Tendon stress distribution simulated by analysis at start of LST shows fair agreement with measurements, implying that the angular friction and anchor set modeling assumptions at start of test were reasonable.
- Hoop tendon stress distributions during pressurization showed poor agreement with the pretest analysis. In particular, the gages interior from the ends were underpredicted and the anchor forces were overpredicted.
- Cylinder hoop tendon data shows evidence that angular friction forces were overcome by differential tendon forces resulting in the tendons sliding, relative to the ducts, during pressurization. The measurements indicate that the shape of the tendon stress profile completely changes during pressurization. The increase in tendon

strain, which is greater than the corresponding cylinder wall hoop strain, implies that portions of the tendons are slipping in order for higher deformation at other azimuths to be accommodated.

- As with the hoop tendons, there was about 8% to 10% loss in vertical tendon force between the initial prestressing and the start of the LST caused by long term effects and by the SFT and SIT. Only one tendon, V85 showed significant friction losses below the springline, and the other two gaged vertical tendons showed only about half of the friction loss in the dome than what was assumed by designers and incorporated in analysis.

Initial post-test analyses were run with ABAQUS Version 5.8-15. When ABAQUS Version 5.8-18 was used in post-test analysis, a significant program bug was found in 5.8-18 (and 5.8-21) related to the use of "Prestress Hold" and small deflection theory. (Small deflection theory was used in conjunction with the tendon friction modeling strategy adopted for the curved portions of tendons.) The bug was finally resolved by ceasing to use the "Prestress Hold" option. Now Version 5.8-18 was used for all post-test analyses, but without "prestress hold" - by increasing the prestress to account for elastic shortening. The conclusions reached about post-test global axisymmetric analyses are summarized below.

- Uplift and dome displacement simulations were significantly improved by redistributing soil basemat springs according to tributary area, and by thickening the dome meridional tendon representation due to the rectilinear "hairpin" layout.
- Predictions were also improved by using no vertical tendon friction in the cylinder.
- Analysis using ABAQUS should not use the Prestress Hold option.

The important conclusions from comparing the 3DCM model pretest analysis to the LST follow:

a. The 3DCM model predicted significantly larger radial deformations than the test measurements and more than the axisymmetric analysis.
b. At pressures lower than $3.0P_d$, the buttresses (90/ and 270/) bulge out radially more than most other azimuths. This trend reverses itself beyond $3.0P_d$, but at $P < 3.0P_d$ the trend is at odds with test observation.
c. While the 3DCM model did provide a good simulation of the distribution of tendon stress at the test's initial conditions, as pressure increased it is clear that very different stress redistribution occurred in the tendons than was simulated by the analysis.

The first change introduced for post-test 3DCM modeling was that the buttresses above and below the 3DCM model boundaries were given vertical beam stiffnesses that was not accounted for in the pretest analysis. The next and only other modeling assumption found to be at significant variance with observed test behavior was the tendon friction modeling. Two important observations were made about the hoop tendon measurements as pressure increases:

1. When pressure reaches the "Pressure to overcome prestress," P = 0.59 MPa, tendon stress distributions change from the classical angular friction design assumption to approximately uniform distribution; toward the end of the test, some tendon interior forces slightly exceed the force at the anchor.
2. The "apparent strain" increases in the tendons corresponding to the force/strain gage readings are significantly larger than the strain that corresponds purely to radial expansion. This can only be explained by force redistribution associated with sliding.

These observations led to changes and studies of the tendon friction modeling. The final analyses performed were:

Run 6. Apply Prestress. Then by using the ABAQUS *MODEL CHANGE capability, fix the tendon nodes at their initially deformed position relative to the concrete. In other words, start from classical design prestress with friction and then grout (bond) the tendons.

Run 7. Perform Run #5 (the Run with only the buttress springs added) up to $P = 1.5P_d$ (0.59 MPa), then "Model Change" all friction elements to non-friction elements (truss ties aligned perpendicular to the tendons. In other words, at $P = 1.5P_d$, perfectly "grease" (unbond) the tendons.

Run 9. After prestress, keep the initial friction elements, but add a new set of friction elements in the reverse orientation so that if points on the tendon move relative to concrete in the reverse direction from that of initial prestress, they will experience reverse direction friction.

The tendon friction simulation runs 6, 7, 9 showed progressively better agreement with test measurements, with Run 9 showing quite good agreement at the anchors and at most points interior to the tendon ends. The results of Run 9 were used for driving the M/S (and estimated F/W) penetrations post-test analysis. On tendon friction behavior, the test measurements and analytical evidence support the conclusion that tendon friction is important to the tendon behavior, but traditional friction design formulas that predict tendon stress distribution begin to break down once pressurization exceeds the pressure that "overcomes" prestress (in this case, roughly 1.5Pd). The coefficient of angular friction appears to lessen to allow sliding and force redistribution as the vessel expands, but more importantly, some parts of the tendon are forced to reverse direction of travel relative to the duct, reverse it from the direction of travel experienced during prestressing. Under this action, angular friction properties probably still hold, but perhaps with a reduced coefficient, and the direction of friction changes sign from that assumed in a design calculation.

Liner strains measured in the vicinity of the E/H penetration collar were much lower than predicted by pretest analysis. Two hypotheses were developed and subsequently proven by the post-test analyses. Post-test analysis showed that by preventing relative slip between liner and concrete, the overall behavior of the system (concrete strains, tendon strains, liner strains away from the hatch) remained the same, but the elevated strains close to the collar were eliminated. This supports a conclusion that the liner in the E/H area had a high degree of bond-friction with concrete, preventing slippage of the liner relative to the concrete; relative slippage is required for elevated strains to develop near local discontinuities like T-anchors and stiffeners. In a final case, directed cracks were introduced to one row of elements, and a discrete crack was formed by adding double rows of nodes along an assumed crack line. This was found to create a liner elevated strain phenomenon. This supports a conclusion that formation of a major crack near the edge of the E/H embossment further concentrated the liner strains at the edge of the embossment. The mild strain concentration coincides, in location, with rat-hole weld seam details, and in the LST, numerous tears occurred at these details. Based on results of detailed liner rat-hole (weld-seam) analysis, the additional strain concentration associated with these details was found to be enough to make a tear prediction at the edge of the embossment. This shows that with discrete crack modeling and local rat-hole modeling, a liner tear could have been predicted to occur as early as $2.8P_d$. Based on the evidence provided by liner strain gages and by acoustic monitoring, one of the tears along this embossment edge may have even occurred as early as $2.5P_d$. A higher strain prediction might be possible if a discrete crack (separate rows of nodes) were propagated all the way through the concrete wall, but this would require a change in rebar modeling strategy - one that is probably not practical even for very detailed analytical evaluations of containments.

The Mainsteam (M/S) and Feedwater (F/W) Penetration "hot spots" (both analysis and LST observations) occurred near the vertical T-anchor terminations and near the thickened insert plate surrounding the penetration group, e.g. at the 3 o'clock and 9 o'clock positions. For the post-test analysis effort no changes to the M/S model were found to be necessary, other than updating the applied displacement versus pressure histories, which were obtained from 3DCM post-test model 9. The M/S and F/W locations were well instrumented with liner strain gages. These provided the following observations and conclusions relevant to response prediction for containment penetrations.

- Many of the highest strains recorded during the LST were near the M/S and the F/W.
- There was a wide variation in peak strain data, even at locations which were theoretically identical in geometry; factors contributing to these differences: slight variations in liner thickness (due to manufacturing and weld repair grinding), gage position relative to the collar/weld, material properties (including welding heat effects), etc.
- The highest strain measurements can, but do not always, correspond to tear locations. Examples supporting this are: 1) a gage near the F/W tear shows evidence of rising strain prior to tear occurrence, then starting at $2.9P_d$, declining strain due to the stress relief caused by the tear; a gage located near the crack tip, on the other hand, showed quite low strain up to $3.1P_d$ and then a sudden jump. This supports a hypothesis that this tear initiated at a pressure of $2.9P_d$ at about the 7:30 o'clock position (mid-point of the tear) and then between $2.9P_d$ and $3.1P_d$, the tear ran around the perimeter of the thickened collar and up to the 9 o'clock position.

Comparisons of analysis to the M/S and F/W liner strain gages show that the post-test analysis of the M/S penetrations captured the strains measured in the LST quite well for both the M/S and F/W penetrations.

Post-test liner seam studies led to the following conclusions and insights on liner seam/rat-hole modeling and behavior:

- By comparison with strain gage measurements and post-test liner tear observations, some of the finite element weld seam meshes capture the strain concentrations in and around the rat-holes and liner welds very well.
- Because of competing mechanisms (between the weld zone and the ends of stiffeners) making yield and ultimate strength adjustments to the HAZ material properties appears to be justified and necessary to correctly predict strain concentration location and intensity.
- Including back-up bars, nominal geometric properties and best estimate material properties, is the best way to predict behavior of defect-free rat-hole/weld-seam details, as probably occurred in the PCCV model at locations such as D7 and J5; however, even without back-up bars, also provided reasonable correlation with gages at these locations.
- A case with severe (~40%) amounts of thinning provided best simulation of behavior of tears with severe liner thinning (due to weld repair grinding as reported in [7]) and back-up bars absent; these conditions existed at Tears 7, 8, 10, 12, 13, 14, 15, and 16.
- A case specifically representing the Tear 16 detail provided reasonable simulation of the tears that occurred <u>with</u> back-up bars present, namely, Tears 1, 2, 6, 9, 11, and 16. The severity of the strain at this case also shows that a tear ($\varepsilon_{eff} > 20\%$) at the geometry simulated would have been predicted to occur as early as $3.0P_d$.
- If a section of liner with a rat-hole/liner-seam such as at Tears 7, 12, 13, 15 is subjected to elevated strain (i.e. strain across the liner model that is larger than free-field strain) a tear even earlier than $3.0P_d$ can be justified. In practice, such a prediction could be approximated using a strain concentration factor approach. The strain concentration factors (K = peak ε_{eff} divided by global ε_{hoop}) implied by this liner seam study are as follows: K = 48 (tear at Stiffener End, no back-up bar); K = 45 (tear at Stiffener End, with back-up bar); K = 59 (tear at HAZ, no back-up bar, and 40% thickness reduction due to grinding); K = 91 (tear at Tear 16, if a short segment of horiz. weld seam back-up bar is missing)
- Using a model of the rat-hole/seam locations without defects, such as location D-7, showed that liner tears still would have developed by pressure of $3.4P_d$, so liner tearing and leakage would still have been the failure mode (for quasi-static pressurization) even in the absence of liner welding irregularities.

10.2 Summary of Lessons Learned and Guidelines for Prestressed Concrete Containment Analysis

The 1:4 Scale PCCV test has, as with other containment pressurization tests, shown that the driving response quantity which leads to limit state of the vessel is the radial expansion of the cylinder. This aspect of response must be predicted correctly in order to reasonably predict vessel capacity and predict, at least approximately, the many other local aspects of response (local liner strains, etc.) that are driven by the cylinder expansion. With this test, as with the 1:6 Scale RCCV model [9], many competing strain concentrations occur around the midheight of the cylinder. Although it is difficult to predict which local liner detail will tear first, and although some particular response quantities, like basemat uplift, were not predicted exactly by the ANATECH/SNL pretest analysis of the PCCV model, the radial expansion of the cylinder was predicted very accurately.

A response mechanism which also appears to have been well predicted was cylinder wall-base flexure and shear and this is another mechanism that, if predicted grossly incorrectly, could lead to very erroneous pressure capacity/failure mode conclusions.

The local analyses and 3DCM analyses provided additional insights into local behaviors, albeit with some inaccuracies that have been identified herein – in particular, tendon friction and liner friction modeling considerations. Thus, in the author's opinion, the combination of the pretest analysis [1] and post-test analysis conducted for the PCCV provides a good road map and example for conducting a detailed analytical evaluation of a containment vessel. As followed in this road map, therefore, a detailed containment evaluation should consist of the following steps. The steps are listed in order of descending priority and in order of increasing complexity and accuracy. The minimum requirement for a containment overpressure evaluation should certainly be a robust axisymmetric analysis, Step 4 shown below:

1. Review drawings, geometry, and material property information
2. Based on what is known about containment behaviors from the last two decades of research (SNL/USNRC, EPRI, and international containment research), list the potential failure modes and failure mechanisms that are possible for the structure. (This was done in [1].)
3. Idealize material property information. This should include digitization of concrete, liner, rebar, and tendon stress-strain curves. For tendons, stress-strain input should be the net axial stress and strain, adjusting for the wrap angle of the strands, if applicable.
4. Develop and analyze axisymmetric analysis model. This model can be relatively coarse in the cylinder wall and dome, but should be fine and detailed at the wall-basemat juncture. The methods and assumptions described in the post-test analyses of this report can be used for guidance.
5. Develop and analyze a 3D model that captures the 3D aspects of the cylinder deformed shape. This could be either a 3D model of the entire structure, or a ring model of a portion of the cylinder. The ring idea was used here, because of the difficulty to model individual tendons with friction simulation for a full global 3D model. Various lessons learned on tendon modeling have been identified in this report and are highlighted again here. (It should be noted that a 3D "slice" model is not adequate for capturing the non-asixymmetric aspects of the structure which affect the response, i.e., the positions of the penetrations, etc.)
6. Develop and analyze local models as needed to predict liner tearing.

Below are some other "lessons learned" about axisymmetric analysis:

- Comparisons between the test and the axisymmetric analysis show that assuming no friction along the straight portion of tendon and smaller friction in the dome than designers calculate will provide improved simulation of the vertical tendon behavior.
- Uplift and dome displacement predictions were significantly improved by redistributing soil basemat springs according to tributary area, by allowing up to 10 psi tensile "stick" under the basemat, and by thickening the dome meridional tendon representation due to the rectilinear "hairpin" layout.
- Analysis using ABAQUS should not use the "Prestress Hold" option.
- The best calculation methods that can now be recommended for tendon friction modeling are, in descending order of preference,
  1) an advanced contact friction surface between the tendons and the concrete (not manageable for the current problem size and complexity),
  2) Pre-set friction ties applied in one direction during prestressing and then added in the other direction during pressurization (3DCM Run #9), and
  3) if neither of these methods are practical within the scope of the calculation, it is best to start with an "average" stress level (using a friction loss design formula), but assume uniform stress distribution in the tendons throughout pressurization, i.e., an unbonded tendon assumption, and finally
  4) same as 3, but using a bonded tendon assumption. (It should be recognized for method 4, however, that this can lead to a premature prediction of tendon rupture, because the tendon strain increments during pressurization will match the hoop strain increments of the vessel wall one-to-one, and this is not what was observed to occur during the PCCV LST.)

11.0 REFERENCES

1. Dameron, R. A., et al. 2000. *Pretest Analysis of a 1:4-Scale Prestressed Concrete Containment Vessel Model*, NUREG/CR-6685, SAND2000-2093. Albuquerque, NM: Sandia National Laboratories.

2. Dameron, R. A., Rashid, Y. R., Luk, V. K. and Hessheimer, M. F. 1997. "Preliminary Analysis of a 1:4 Scale Prestressed Concrete Containment Vessel Model," in *Proceedings of the 14th International Conference on Structural Mechanics in Reactor Technology,* Vol. 5, pp 89-96, Lyon France.

3. Luk, V. K. 2000. *Pretest Round Robin Analyses of a Prestressed Concrete Containment Vessel Model.* NUREG/CR-6678, SAND00-1535. Albuquerque, NM: Sandia National Laboratories.

4. *ANACAP-U User's Manual*, Version 2.5, 1997. San Diego, CA: ANATECH Corp.

5. *ABAQUS Users Manual*, Version 5.8, 1998. Providence, RI: Hibbitt, Karlsson & Sorensen, Inc.

6. Klamerus, E. L., et al. 2001. "NUPEC/NRC PCCV Structural Behavior Test Model-Instrumentation Plan," Plan, Gage Locations, and Final As-Built Drawings, issued 1/31/01. Albuquerque, New Mexico: Sandia National Laboratories.

7. Eckelmeyer, K. H., Van Den Aryle, J. A., Kilgo, A. C. and Lambert, L. D. 2001. "Metallurgical Analysis of PCCV Liner Tears," Sandia Internal Report - Draft, October 26, 2001, Albuquerque, New Mexico: Sandia National Laboratories.

8. Hessheimer, M. F., Klamerus, E. W., Rightley, G. S., Lambert, L. D. and Dameron, R. A. 2003. *Overpressurization Test of a 1:4-Scale Prestressed Concrete Containment Vessel Model*, NUREG/CR-6810, SAND2003-0840P, Sandia National Laboratories, Albuquerque, NM.

9. Clauss, D. B., et al. 1987. *Round-Robin Pretest Analyses of 1:6 Scale Reinforced Concrete Containment Model Subject to Static Interval Pressurization*, SAND87-0891, NUREG/CR-4913, Albuquerque, NM: Sandia National Laboratories.